Heat Transfer and Pressure Drops in Micro-Tubes for ground and Space applications

Facoltà di Ingegneria

Corso di Dottorato in Energia & Ambiente

A cura di:

Luca Gugliermetti

Matricola n. *1249893*

Relatore: Correlatore:

Prof. Fabrizio Cumo   *Prof. Gianfranco Caruso*

*"I really don't trust **s**tatistics much. A man with his head in a hot oven*
and his feet in a freezer has statistically an average body temperature"

- Charles Bukowski

Sommario

<u>Figure Index</u>

Table Index

Nomenclature

Symbol	Description	SI unit
Roman		
a_α	Pressure drop contribution by inertia	$-$
A	Cross-sectional area	m^2
c_p	Specific heat at constant pressure	$J/kg \cdot K$
C	Constant into a specific equation	$-$
D, d	Diameter	m
e	Thickness	m
E	Electrical tension	V
f	Friction factor	$-$
g	Acceleration due to gravity	m/s^2
G	Mass flux	$kg/m^2 \cdot s$
h	Convective heat transfer coefficient	$W/m^2 \cdot K$
i	Enthalpy	J/kg
I	Electrical current	A
k	Thermal conductivity	$W/m \cdot K$
l	Axial length	m
L	Heated length	m
$\dot{m}$	Mass flow rate	kg/s
M	Molecular weight	g/mol
P	Pressure	Pa

$\dot{q}$	Effective heat flux	W
q	Heat flux	W/m^2
r	Radial distance from the center	m
R	General variable dependent of y	*
T	Temperature	$°C$
u	Velocity	m/s
w	Radial length (width)	m
v	Specific volume	m^3/kg
$\dot{V}$	Volume flow rate	m^3/s
x	Thermodynamic quality	$-$
z	Axial distance from the inlet	m

Greek

α	Void fraction	$-$
β	Coefficient of thermal expansion	K^{-1}
ΔP	Pressure drop	Pa
ΔT	Temperature difference	K
μ	Dynamic viscosity	$kg/m \cdot s$
ν	Kinematic viscosity (diffusivity of momentum)	m^2/s
ρ	Density	kg/m^3
Ω	Inclination angle of the channel	$°$

act	Actual
amb	Ambient
b	Bubble
$cond$	Conduction
$conv$	Convection
df	Down flow
$elec$	Electrical
fr	Frictional
F	Pure forced convection
Fa	Fanning
hom	Homogeneous model
in	Inlet of the heated length
l	Liquid
le	Liquid equivalent
ll	Liquid and vapor in laminar regime
$loss$	Loss
$l0$	Liquid only
lt	Liquid in laminar and vapor in turbulent regime
lv	Vaporization
max	Maximum
n	Nose of the bubble
o	External

out	Outlet of the heated length
pres	Present condition
prev	Previous condition
sat	Saturation
sp	Single phase
tl	Liquid in turbulent and vapor in laminar regime
tp	Two-phase
tt	Liquid and vapor in turbulent regime
v	Vapor
v_0	Vapor only
w	Wall. When alone, it refers to internal wall.
z	Axial position from the inlet
0	Axial local position where $x = 0$

Dimensionless numbers and parameters

Bo	Boiling number, $\dfrac{\dot{q}''}{G i_{lv}}$
Fr	Froude number, $\dfrac{G^2}{g D_i \rho^2}$
Gr	Grashof number, $\dfrac{g \beta (T_w - T_f) D_i^3}{v^2}$
Ja	Jakob number, $\dfrac{\bar{c}_p (T_{in} - T_{sat,0})}{i_{lv}}$
Nu	Nusselt number, $\dfrac{h D_i}{k}$
Re	Reynolds number, $\dfrac{G D_i}{\mu}$

We	Weber number, $\dfrac{G^2 d_i}{\rho \sigma}$
X	Martinelli parameter, $\left[\dfrac{(dP/dz)_l}{(dP/dz)_v}\right]^{1/2}$

Introduction

During the curse of physics, we learn that "heat" is a form of energy associated with the motion of atoms or molecules and capable of being transmitted through solid and fluid by conduction, convection and radiation. Instead, "temperature" is a measure of the average kinetic energy of the particles in a portion of matter, expressed in terms of degrees. It is common knowledge that "temperature" and "heat" are related. In fact, "heat" is the flux of energy associated with "temperature". In addition, Energy and related quantities are connected to the capacity of a system to perform work. Energy moves from one place to another and cannot be destroyed, at least it can be converted in matter $(E= MC^2)$. Two bodies with different temperatures exchange heat. It moves from the warmer body to the colder, naturally. Only using more energy is possible to invert this process by some specific processes.

Now, an important question is: "why we study these phenomena?". The answer is because we can use it for our purposes, harnessing the forces of nature to optimize process and reducing human's labor. However, everything has a price. Every form of energy transmission is associated with a degradation of a part of that energy. "Entropy" is the name of that process and it is related with an increment of the chaos in the system, which usually mean an increment of the temperature. This process is irreversible and slowly degrade energy distributing it across the universe. Moreover, the use of "Heat Energy" can be dangerous rising the temperatures and bringing to an uncontrolled and destructive states. We can remember the explosion of chemical industries at Seveso[1] in Italy caused by a temperature increment of a process tank.

Thermodynamics studies the laws of heat, how heat moves through space and materials and how transform Heat into useful Energy. A correct understanding of thermodynamics can bring to an increment of machine efficiency, a reduced cost, and to a better energy production.

In this work, flow boiling in micro-tubes is studied in deep. Micro-exchangers are the next generation of cooling systems useful for both terrestrial and space applications where weight and dimensions are important.

Flow boiling is the best way to reach high heat flux, heat transfer improves with fluid velocity and, within certain limits, with the temperature difference between the liquid and the tube.

---

[1] *1* The Seveso disaster was an industrial accident that occurred around 12:37 pm July 10, 1976, in a small chemical manufacturing plant approximately 15 kilometres (9 mi) north of Milad in Italy. It resulted in the highest known exposure to 2,3,7,8-tetrachlorodibenzo-p-dioxin (TCDD) in residential populations. A total of 3,300 animals were found dead, mostly poultry and rabbits. Emergency slaughtering commenced to prevent TCDD from entering the food chain, and by 1978 over 80,000 animals had been slaughtered. 15 children were quickly hospitalised with skin inflammation. By the end 1,600 people of all ages had been examined and 447 were found to suffer from skin lesions or chloracne.

Micro-tubes, thanks to their dimension, might be employed in a wide range of microgravity systems such as satellites for communications, thermal management of the International Space Station, cooling of electronic devices subjected to high thermal load (i.e. high heat flux), thermal transport, cooling of nuclear space reactors, etc. In order to develop and design thermal systems for small applications, it is necessary to achieve a detailed understanding of all flow boiling aspects, also under low gravity conditions.

1. State of the Art Review

1.1. From Macro to Micro Scale

First, must be defined when a channel is micro or in macro scale. There is no proven criterion in literature that define this difference. Scientific community has not reach a universal agreement or definition for the transition. This chapter describes the most used criterion to define the transition from micro to macro-scale for flow boiling heat transfer. Two-phases flow pattern maps are reported to make a visual comparison.

Several researches proposed transition criteria for macro to micro scale transition ranging from physical channel size classifications to approaches based on bubble confinement and bubble departure diameter.

1.1.1. Channel Size Classifications for Single Phase

For single-phase the transition can be defined basing on rarefaction effects related on the Knudsen number:

$$K_n = \frac{k_B T}{\sqrt{2}\pi\sigma^2 pL}$$

Where k_B is the Boltzmann constant (1.380×10^{-23} J/K), σ is the particle hard shell diameter, p is the total pressure. Following are reported three examples:

Mehendale et al. (2000) proposed a fixed classification based on the physical size of the channels:

- *Micro-channels* for a size range *1 μm - 100 μm,*

- *Meso-channels* for channel sizes from *100 μm to 1.0 mm,*

- *Compact channels* from *1.0 mm to 6.0 mm*,

- *Macro-channels* for all channel sizes exceeding *6.0 mm.*

Kandlikar et al. (2001, 2002, 2003) instead proposed a classification based on flow considerations:

- *Conventional channels* for hydraulic diameters of *3.0 mm or larger*

- *Mini-channels* for hydraulic diameters of *200 μm to 3.0 mm,*

- *Micro-channels* for hydraulic diameters smaller than *200 μm*.

Kandlikar recommend the above criteria for both liquid and two-phases flow applications to provide uniformity in channel classification.

Furthermore Shah (1986) define compact heat exchangers as exchangers with surface-to-volume ratio *> 700 m²/m³*, which translates to a threshold diameter for the macro-micro transition of *< 6.0 mm* irrespective of the fluid properties.

1.1.2. Bubble Confinement

To define the transition between singe phase and two-phases, it is necessary to analyze the bubble confinement. This method studies the confined growth of a bubble in small channels. When hydraulic diameter decreases the role of surface tension forces becomes more important and the gradual imminent suppression of the gravity forces increases. Kew et al. (1997) proposed the Confinement number for the distinction between macro and micro scale channels:

$$Co = \frac{1}{D_h} \sqrt{\frac{4\sigma}{g(\rho_L - \rho_G)}}$$

Where D_h is the hydraulic diameter. For the criterion $Co = 0.5$ is the threshold:

- $Co > 0.5$ is for micro-scale,
- $Co < 0.5$ for macro-scale.

Kew et al. (1997) investigated diameters of *1.10, 1.80, 2.80* and *3.60 mm* and for a square channel of *2.0 x 2.0 mm.*

Triplett et al. (1999) proposed two-phase flows smaller than the order of the capillary length as the threshold of micro-channel flows in *1.10* and 1.*49 mm* circular micro-channels.

Brauner et al. (2006) studied the effect of channel diameter on the mechanisms leading to adiabatic flow pattern transitions in single channels. The Eötvos number evidences the macro to micro threshold, it is like the Bond number *Bo* and represents the ratio of buoyancy force to surface tension forces. The number can be expressed as:

$$Eo = \frac{\Delta\rho_{lg} g D_h^2}{\sigma}$$

Where D_h is the hydraulic diameter.

Eötvos number plays a key role dictating the relevant characteristics of dispersed flows and wall-wetting in separated flows. *Eo = 0.2* is considered as the threshold value for micro-scale flows. Triplett et al. (1999) for air-water in a *1.1 mm* channel (*Eo = 0.021*) inspect that *Eo = Bo/8.*

Ullmann and Brauner (2006) concluded that the Eötvos number play a significant role in flow pattern transitions and in determining the characteristic length of dispersed two-phases flows and in wall-wetting effects in separated flows. Moreover, it is an important parameter in the disappearance of stratified flows.

Bretherton et al. (2004) suggested a transition at *Eo < 0.84* as the threshold at which a Taylor bubble would no longer rise only under the influence of gravity in a vertical, water filled capillary tube.

Cheng et al. (2006) classified the work of *Li* et al. (2003) on phase changing heat transfer into micro, meso and macro channels in terms of the Bond number:

$$Bn = \frac{\rho g L^2}{\sigma}$$

L is the diameter of a capillary tube and σ is the surface tension of the interface.

The proposed classifications:

1. **$Bn < 0.05$** Micro scale flow. Gravity effects can be neglected.

2. **$0.05 < Bn < 3.0$** Meso scale flow. Surface tension is dominant.

3. **$Bn > 3.0$** Macro scale flow. Gravity forces are dominant.

Bond number and dimensionless numbers are related in this equivalence:

$$Bn = Eo = 2Go^2 = 2De^2$$

Where *Eo, Go*, and *De* are respectively the Eötvös, Goucher, and Deryagin numbers. The "difference" between the Goucher and Deryagin numbers is expressed in the work of Pierre-Gilles et al. (2004). The Goucher number (used for coating problems) uses the letter *R* to represent length scales while the Deryagin number (used for plate film thickness problems) uses L.

Kew et al. (2001) based the division on confinement of a bubble within a channel. According to them, for hydraulic diameters lower than D_{th}, the macroscopic laws are not suitable to predict either flow boiling heat transfer coefficients or flow pattern transitions. D_{th} is given by:

$$D_{th} = \sqrt{\frac{4\sigma}{g(\rho_L - \rho_G)}}$$

Figure (1) shows the comparison recommended by Kandlikar et al. (2002) for the transition diameters between conventional and mini channels and between mini channels and micro channels compared with the variation of D_{th} with the reduced pressure of *CO2* and *water*:
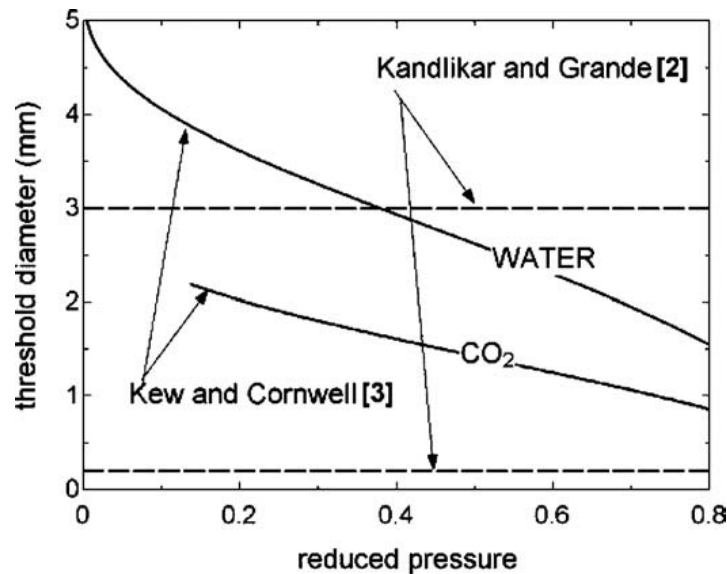
Figure 1: Threshold diameters recommended by Kandlikar and Grande (2002), compared to the macro to micro scale threshold of Kew and Cornwell (2001) for CO2 and water.

Serizawa et al. (2000) provided another interpretation for the micro channel transition. Figure (2) shows a flow pattern in a *0.05 mm* glass channel with steam and water. A new flow pattern was observed and named *liquid ring flow*. Moreover, for air-water in a *0.020 mm* channel, was identified another flow pattern named *liquid lump flow,* following the liquid ring flow.
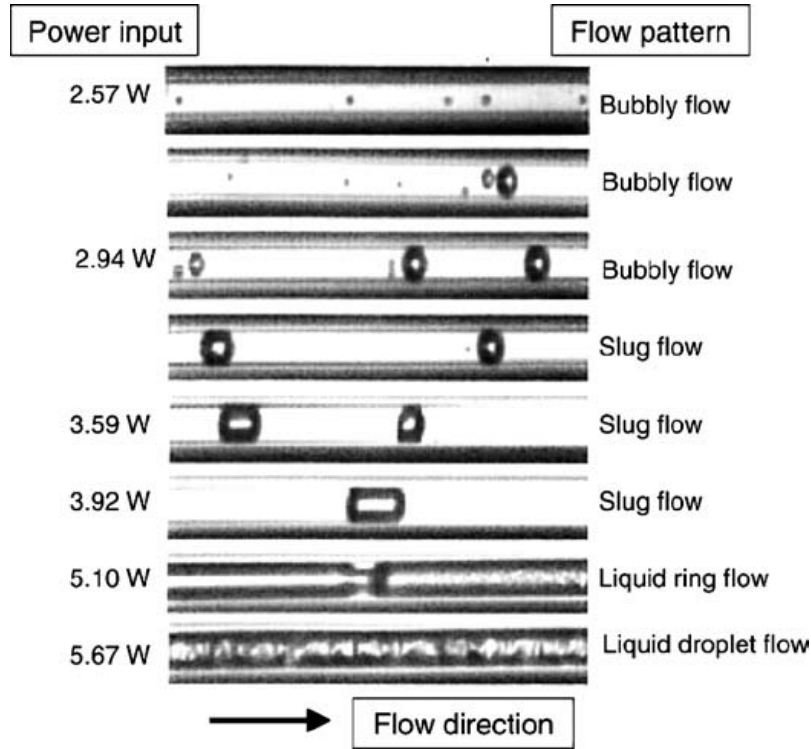
Figure 2: Flow regimes observed by Serizawa and Feng (2000) in a 0.050 mm channel for steam-water flows.

Probably there are some transition between Kandlikar et al. (2003) definitions. Some examples could be:

- macro channel,
- macro to mini transition,
- mini channel,
- mini to micro transition.

Kawaji et al. (2004) reviewed the characteristics of two-phase flow and proposed the following recommendation as a threshold criterion for defining micro channel for two-phase flows. This criterion analyzes a set of six dimensionless numbers and two velocities for threshold:

- Bond number:

$$Bn = \frac{g(\rho_L - \rho_L)D^2}{\sigma} \ll 4$$

- Superficial liquid and vapor Weber numbers:

$$We_L = \frac{\rho_L U_L^2 D}{\sigma} \ll 1 \; ; \; We_G = \frac{\rho_G U_G^2 D}{\sigma} \ll 1$$

- Superficial liquid and vapor Reynolds numbers:

$$Re_L = \frac{\rho_L U_L D}{\mu_L} \ll 2000 \; ; \; Re_G = \frac{\rho_G U_G D}{\mu_G} \ll 2000$$

- Capillary number:

$$Ca_L = \frac{\mu_L U_L}{\sigma} \ll 1$$

- Superficial vapor and liquid velocities:

$$U_g = \frac{\dot{Q}_G}{A}; \; U_L = \frac{\dot{Q}_L}{A}$$

Further researches determinate more accurately the actual thresholds. It is now unclear how to define or predict any of these transitions.

1.1.3. Bubble Departure

The heat transfer model proposed by Jacobi et al. (2000) base their assumption on elongated bubble flow in micro scale channels. An important assumption for micro scale flow is that the bubble diameter fills the tube internal diameter before detaching from the wall surface. In their heat transfer model, the effective nucleation wall superheat considers the critical bubble radius. The idea is that no stratification exists at micro scale.

Thome et al. (2002) proposed the use of nucleate pool boiling bubble detachment to predict bubble departure diameters for confined bubble flow. They noted that bubbles grow in length as they flow downstream. No results or prediction methods are available when the bubble nearly blocks the channel during its growth while is still attached to the wall. Using bubble departure diameter methods for nucleate pool boiling can give an approximate idea of bubble departure diameters expected under, neglecting imposed cross flow or confinement of the bubble.

Jensen et al. (1986) reviewed the most popular methods available to predict bubble departure diameters in nucleate pool boiling and compared them. The Fritz (1935) correlation gives the detachment bubble diameter "d_{bub}" as:

$$d_{bub} = 0.0208\beta \sqrt{\frac{\sigma}{g(\rho_l - \rho_v)}}$$

Where β is the contact angle expressed in degrees.

Nishikawa (1985) gave the following expression:

$$d_{bub} = \left[0.12 + 0.08 \left(\frac{C_{pl} T_{sat}}{h_{lg}} \right)^{\frac{2}{3}} \right] \sqrt{\frac{\sigma}{g(\rho_l - \rho_v)}}$$

Kutateladze et al. (1979) proposed the equation:

$$d_{bub} = \left[0.25(1 + 10^5 K_l)^{\frac{1}{2}} \right] \sqrt{\frac{\sigma}{g(\rho_l - \rho_v)}}$$

Where K_l is a parameter expressed as:

$$K_l = \left(\frac{\rho_l C_{pl}(T_w - T_{sat})}{\rho_l h_{lv} Pr_l} \right)^2 \left[\frac{\mu_l^2 C_{pl} \sqrt{g(\rho_l - \rho_v)}}{\rho_l \sigma^{\frac{3}{2}}} \right]$$

This expression adds the influences of the wall superheat, liquid Prandtl number and liquid dynamic viscosity to the bubble departure criterion but, again, not the contact angle.

Jensen et al. (1986) proposed a more accurate definition of d_{bub} based on their database:

$$d_{bub} = \left[0.19(1.8 + 10^5 K_l)^{\frac{1}{2}} \right] \sqrt{\frac{\sigma}{g(\rho_l - \rho_v)}}$$

The Bond number ($\frac{g(\rho_L - \rho_L)D^2}{\sigma}$) have a key role in all these relations, which are theoretically valid only for pool boiling, while the flow in a micro channel will tend to promote the detachment of the bubble before it completely spans the channel.

Bubble Departure criterion probably overestimate the value of the channel diameter of the threshold. These methods are "preliminary" because they are still not validated.

1.1.4. Young-Laplace Approach

Li et al. (2003) studied the gravitational effect on the transition from symmetric flow, where gravity can be neglect, to asymmetric flow, where gravity cannot be neglect, during condensation in micro horizontal tubes. Based on the Young-Laplace equation, they proposed the following critical and threshold values. The capillary length, L_{cap}, is the division criteria for micro to macro scale transition. The threshold diameter is:

$$d_{th} = 1.75 L_{cap}$$

L_{cap}, the capillary length is defined as:

$$L_{cap} = \sqrt{\frac{\sigma}{g(\rho_l - \rho_v)}}$$

Their critical diameter (capillary length) is similar to the bubble departure diameter in the Fritz (1935) equation above if the contact angle is set to *10°*. Furthermore, their threshold diameter differs from that of Kew et al. (1997) only by the value of the multiplier of *1.75* rather than *2.0*. Based on these definitions, Li et al. (2003) proposed to subdivide condensation flow regimes, relative to the channel diameter d_{in}, as follows:

1. $d_{in} < d_{crit}$ Surface tension forces are dominant. The flow regimes are symmetrical.

2. $d_{crit} < d_{in} < d_{th}$ Gravity and surface tension forces have the same importance. A thin stratification on the flow distribution is observed.

3. $d_{th} < d_{in}$ Gravity forces are dominant and the flow regimes are similar to macro scale flows.

Figure (3) shows a comparison of selected macro to micro scale threshold criteria for *R-134a* as a function of reduced pressure.

Only two of the three Mehendale et al. (2000) divisions are shown in the diagram. The diagram is subdivided in four class: micro-scale, meso-scale, compact and macro scale.

Two of the three Kandlikar et al. (2003) divisions are shown that separate the channel diameters: nano-scale, micro-scale, mini-scale and macro-sizes.

The Kew et al. (1997) Confinement number, the Ullmann et al. (2006) Eötvos number and the Li et al. (2003) threshold diameter give approximately similar values and trends.

The critical diameter of Li et al. (2003) is similar to the bubble departure diameter prediction of Jensen et al. (1986) assuming a contact angle of *35°*. The effect of fluid properties is important. The fixed diameter threshold is not very realistic but only act as rough guidelines.
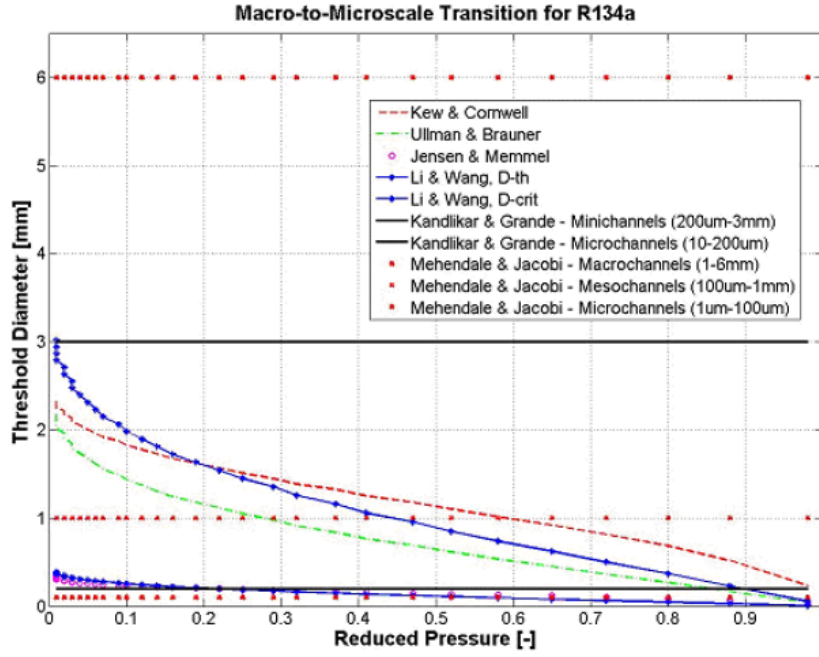
Figure 3: Comparison of selected macro-to-micro scale transition criteria for *R-134a* as a function of reduced pressure (the points come from a simulation, there are not data points).

1.1.5. Numerical Approaches

Onbasioglu (2004) applied the Volume of Fluid (VOF) and Eularian methods in a commercial numerical fluid dynamics software to simulate two-phase flows inside small channels. He validated the computation procedures with macro-scale flow pattern experiments changing the channel size to discern the transition point where the conventional governing equations fails. Based on his simulations, he proposed a qualitative two-phase macro to micro-scale transition for *air* and *water*.

Zun (2007) also presented a detailed numerical simulation of elongated bubble flows in horizontal channels comparing the liquid film thickness at the top of the bubble to that at the bottom of the bubble. He used *R-134a* at a saturation pressure of *7.74 bar*. Channel diameters were compared in terms of:

- Reynolds number: $Re = \dfrac{\rho_l u_g d_{bub}}{\mu_l}$

- Eötvos number: $Eo = \dfrac{g(\rho_l - \rho_v) d_{bub}^2}{\sigma}$

- Archimedes number: $Ar = \dfrac{g \rho_l (\rho_l - \rho_v) d_{bub}^3}{\mu_l^2}$

- Weber number: $We = \dfrac{\rho_l u_g^2 d_{bub}}{\sigma}$

- Froude number: $Fr = \dfrac{u_g^2}{g d_{bub}}$

- Capillary number: $Ca = \dfrac{\mu_l u_g}{\sigma}$

The dimensionless numbers refer to the bubble "nose diameter" denoted by d_{bub} while u_g is for the bubble velocity. The top to bottom liquid film thickness ratio was to account for the different forces acting on the shape of the moving bubble and the resulting relative thickness of the liquid films. The values from this method is comparable with Li et al (2003) above.

1.2. Flow Boiling Heat Transfer

This section describes the flow boiling heat transfer mechanisms and the heat transfer trends during flow boiling in small channels. Experimental results from different studies are difficult to compare since there is not any officially accepted benchmark. It is possible to divide heat transfer mechanisms into three different categories:

1. nucleate boiling dominant, dependent from heat flux,

2. convective boiling dominant, with the heat transfer coefficient dependent on mass flux and vapor quality but not from heat flux,

3. heat flux dominant, dependent from liquid film evaporation around elongated bubbles.

1.2.1. Macro-scale Flow Boiling

During 1950 and 1960, scientists have recognized that the heat transfer coefficient, in macro scale flow boiling, is an interaction of nucleate and convective boiling. In macro scale flow boiling channels, the heat transfer can be classified according to nucleate boiling, dependent from the formation of vapor bubbles at the tube wall surface, and to convective boiling, where the heat is transferred through conduction and convection through a thin liquid film at the evaporative liquid-vapor interface.

For simplicity, only one type of flow boiling at time is analysed at time, and the heat transfer mechanism can switch from one type to other at same point. More than one flow boiling mechanism can coexist and the changing is associated with vapor quality increase. The convective boiling gradually substitutes the nucleate boiling. Boiling is a complicated phenomenon where drag force of convection mechanism gradually superimposes buoyancy force of nucleation mechanism. Steiner et al. (1922), studying the characteristic of flow boiling in vertical tube, discovered that convective boiling is the only mechanism for heat fluxes below the onset of boiling where the heat transfer coefficient is independent of heat flux over a wide range of vapour quality. Moreover, heat transfer coefficient is also independent from mass flux and vapour quality for high heat flux in a fully developed nucleate boiling. Next Figures (4, 5) illustrate a classical flow boiling process:
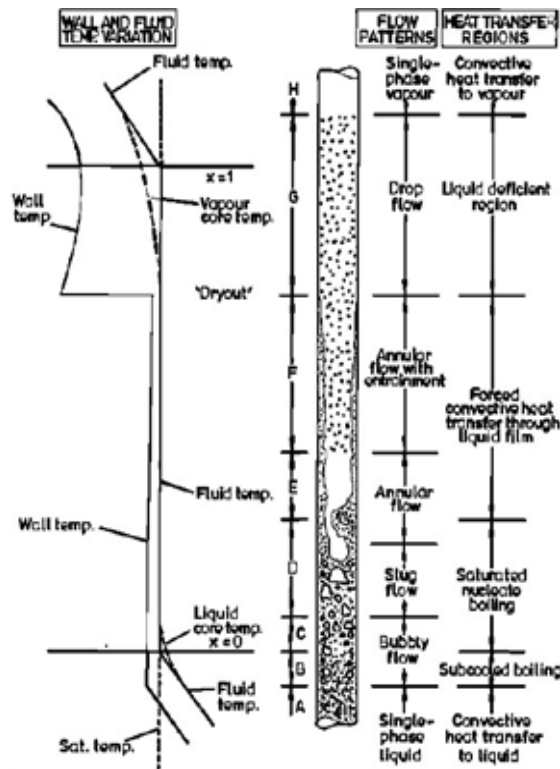
Figure 4: Heat transfer regions in convective boiling in a vertical tube from Collier and Thome (1994)
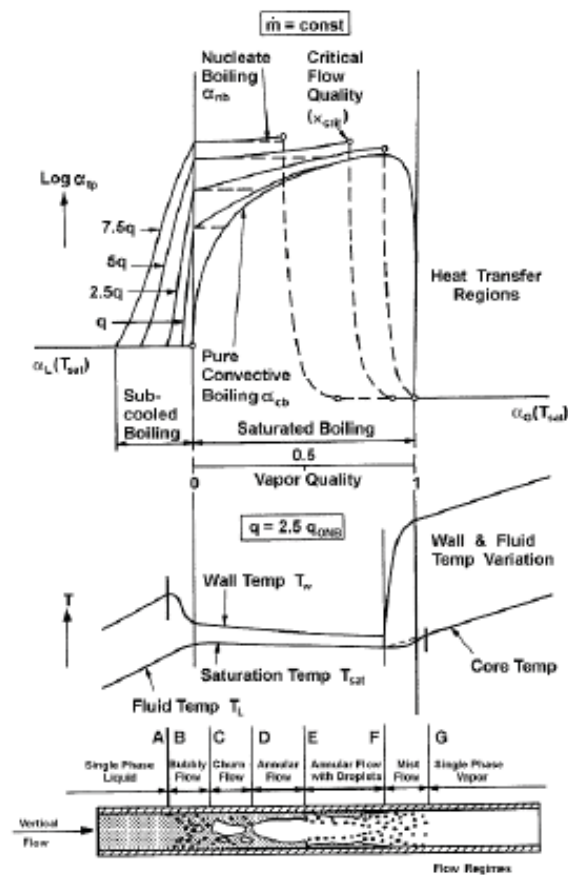
Figure 5: Heat transfer regions in a vertical tube from Steiner (1992)

A careful analysis of the images brings to the following conclusions:

1. Nucleate boiling onset is reached near initial quality X = 0 (subcooled boiling is possible) and the heat transfer coefficient increases.

2. For low heat fluxes, convective boiling is significant and becomes the dominant mechanism when the vapour quality increases.

3. For intermediate heat fluxes, the heat transfer coefficient is largely independent of vapour quality before reaching a constant value at higher vapour qualities where convective boiling becomes dominant.

4. For high heat flux nucleate boiling is dominant before critical heat flux.

5. The nucleate boiling coefficient values increase with the increasing of saturation pressure.

Kattan et al. (1998) performed in-tube flow boiling experiments for five refrigerants, (*R134a, R-123, R-402A, R-404A* and *R-502*) in a *11.9 mm* copper tube for a wide range of parameters to study the effects of local flow patterns on flow boiling heat transfer.The authors proposed a flow boiling model that uses a more fundamental approach in predicting the local heat transfer coefficients by incorporating a simplified flow structure into the heat transfer prediction as a function of the local flow pattern, i.e. Stratified-wavy, fully Stratified, Intermittent and Annular flows.

Next figure (6) illustrates the simplified two-phase flow structure used in their heat transfer prediction:
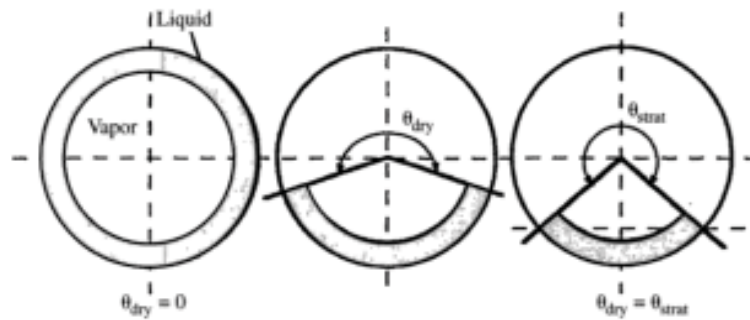
Figure 6: Liquid-vapor regions, stratified and dry angles from Kattan et al. (1998)

Wojtan et al. (2005) performed some flow boiling tests for *R22* and *R410A* in horizontal tubes with 8.0 and 13.84 *mm* internal diameters. Their work implements several important modifications to the flow pattern map of Kattan et al. (1998) by subdividing the stratified wavy region into three sub-zones: slug, slug/stratified wavy and stratified wavy. The extension of heat transfer prediction model includes dry-out and mist flow by the addition of an annular to dry-out and a dry-out to mist flow transition. Figure (7) show the comparison of their new prediction method and a macro scale flow pattern map with the flow boiling experimental data of Lallemand et al. (2001) for refrigerant *R22* in a *10.7 mm* diameter tube.
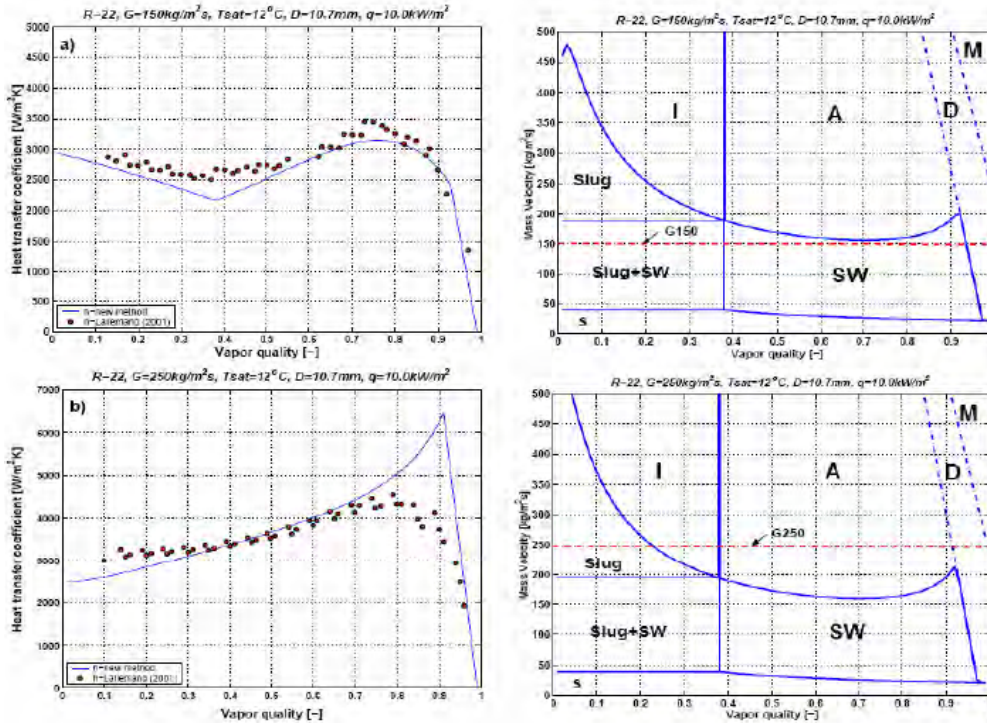
Figure 7: Wojtan et al. (2005) and Lallemand et al. (2001) flow boiling comparison charts

Jabardo et al. (2000) investigated on convective boiling for *R22*, *R134a* and *R404a* refrigerants in a copper channel with an internal diameter of *12.70 mm*. They studied the influence of physical parameters of mass flux and heat flux on flow boiling heat transfer. Figure (8) shows the obtained flow boiling heat transfer.
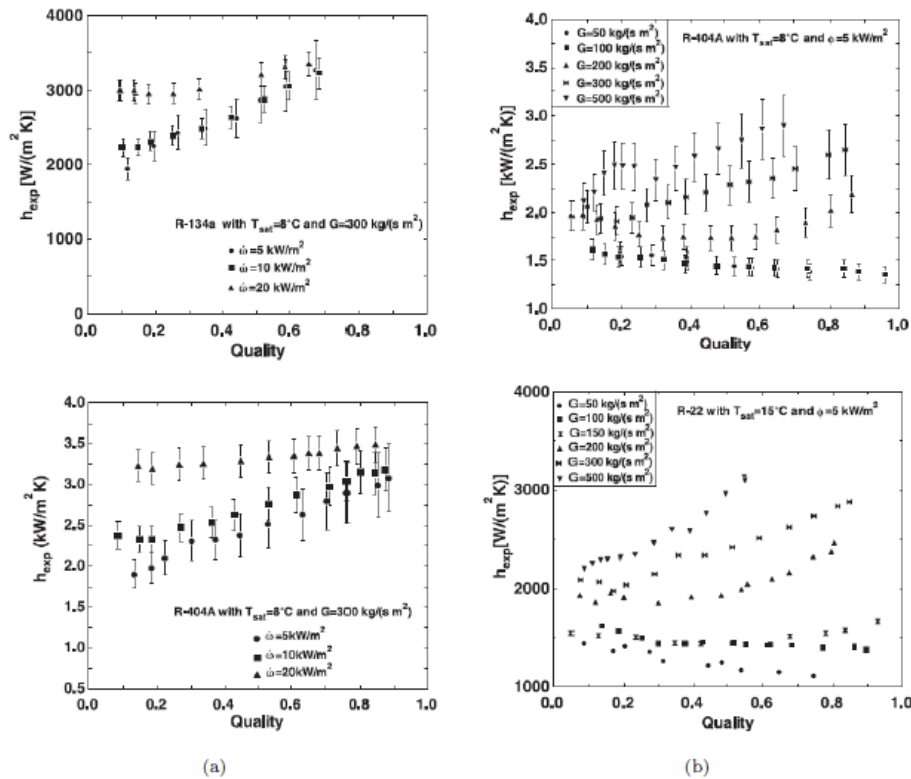
Figure 8: Heat transfer results for *R141b* in the *1.10 mm* channel, *Co=1.1*: (a) *G=365kg/m²s* and (b) *G=505 kg/m²s*.

1.2.2. Flow Boiling in Micro-channels

Over the past several years, single micro channel tubes have been investigated. Today, multi micro channels have gained attention for microelectronics and power electronics applications due to the challenge of removing high heat fluxes produced by transistors. Thome et al. (2005), Cheng et al. (2004), and Consolini et al. (2008) have made the most important studies about flow boiling in micro channels. Agostini et al. (2012) presented a comprehensive state of the art of high heat flux cooling technology. Furthermore Hetsroni et al. (2005), Xu et al. (2006), and Harirchian et al. (2009) have contributed broadly to the field of multi micro channel two phase flow boiling. Below the most important works are described.

Jiang et al. (2002) tested a transparent micro channel heat sink fabricated by bonding a Pyrex glass cover plate onto a silicon wafer. The chip is about *10 x 20mm²* in size, comprising either *34* or *35* micro channels with triangular cross-sectional areas. The authors distinguished three stable boiling modes during the experiments. Moreover, they investigate the dependence of the flow regime on the input power level:

- At low input power local nucleate boiling is prevalent.

- At high input power a stable annular flow is prevalent.

No bubbly flow regime appears in the test section (in contrast to macro channels).

Zhang et al. (2002) made another experiment with channel diameters from *25* to *60 μm*, without any bubbly or slug flow.

Wu et al. (2003) investigated on convective heat transfer and pressure drop for silicon parallel micro channels of trapezoidal cross-sectional areas with water as refrigerant. The number of parallel channels varied from *8* to *15*. They observed an alternative two-phase and single-phase flow. Temperature and pressure oscillations were present in the fluid. The authors associated these instabilities with contradictory results found in the literature by Wang et al. (2003).

Chen et al. (2004) studied boiling heat transfer of FC-77 in 24 silicon micro channels of *389 x 389 μm* of cross-sectional area. The experiment showed that:

- For low heat flux bubbly flow is dominant.

- For higher heat flux wispy-annular and churn flows appears

A partial wall dry-out can cause a drop of heat transfer coefficient and instabilities in wall temperature that increase with heat fluxes. The experiment showed how heat transfer coefficient and pressure drop in a fully developed flow boiling are independent of flow rate.

Zhang et al. (2005) extend the Chen et al. (2002) correlation for heat transfer analyzing and confronting *13* separate databases with some of the most widely quoted correlations for two-phase heat transfer in conventional systems. Chen's superposition model gave the best outcome. The authors observed that for liquid Reynolds numbers less than $Re_l < 2000$ the calculated heat transfer coefficient was inconsistent. Chen's superposition model for convective boiling states that heat is transferred by two competing mechanisms: the nucleate boiling and the convective vaporization. The Zhang model instead proposed an overall heat transfer coefficient that is given by an additive law that combines the different contributions:

$$\alpha = \alpha_{nb} + \alpha_{cv}$$

The nucleate boiling term is expressed as the product of the nucleate pool boiling value (α_{npb}) with an enhancing factor computed at the corresponding wall superheat. Forster et al. (1995) correlation was used with a boiling suppression factor, S, that accounts the suppression of bubble nucleation due to the convective nature of the two-phase system. Besides, the convective contribution depends on the flow properties and is given as an all liquid heat transfer coefficient multiplied by a two-phase correction factor, F. It can be expressed as follows:

$$\alpha_{nb} = S \, \alpha_{npb}$$

$$\alpha_{cv} = F \, \alpha_l$$

Zhang et al. (2005) suggested to use a laminar or turbulent expression for the all liquid heat transfer coefficients according to the value of the liquid Reynolds number. Moreover, for the two-phase factor, F, they used the larger value of 1 and an expression, F' based on the Martinelli parameter, X:

$$F' = 0.64 \sqrt{\left(1 + \frac{C}{X} + \frac{1}{X^2}\right)}$$

where C is the Chisholm's constant. For the suppression factor S, they propose to use the following expression:

$$S = \frac{1}{1 + 2.53 \times 10^{-6} Re_l^{1.17}}$$

This expression is like the one proposed by Chen et al. (2002) but it has the liquid Reynolds number in the place of the two-phase Reynolds number. This is due to their choice to assume the nucleate boiling suppression mechanism to remain the same as in the macro-scale.

Lee et al. (2008) used deionized water to study saturated flow boiling heat transfer and pressure drop in a *400 µm* deep silicon micro-channels. The channel width varied from *102 µm* to *997 µm*. They developed a new heat transfer coefficient and pressure drop models and compared it with existing prediction methods obtaining a good agreement.

Lazarek et al. (1982) investigated the evaporation of *R-113* in a *3.1 mm* stainless steel tube in a vertical test section divided in two parts. They performed their experiments starting with sub-cooled liquid at the inlet. Figure (10) show their data for sub-cooled and saturated flow boiling. The tests result indicates a strong dependence on heat flux but a negligible influence of vapor quality. This is quite different than the usual trend in macro-scale flow boiling where the heat transfer coefficient rises with increasing vapor quality and be less sensitive to heat flux. This suggested that nucleate boiling was controlled by heat transfer process in their *3.1 mm* test section.
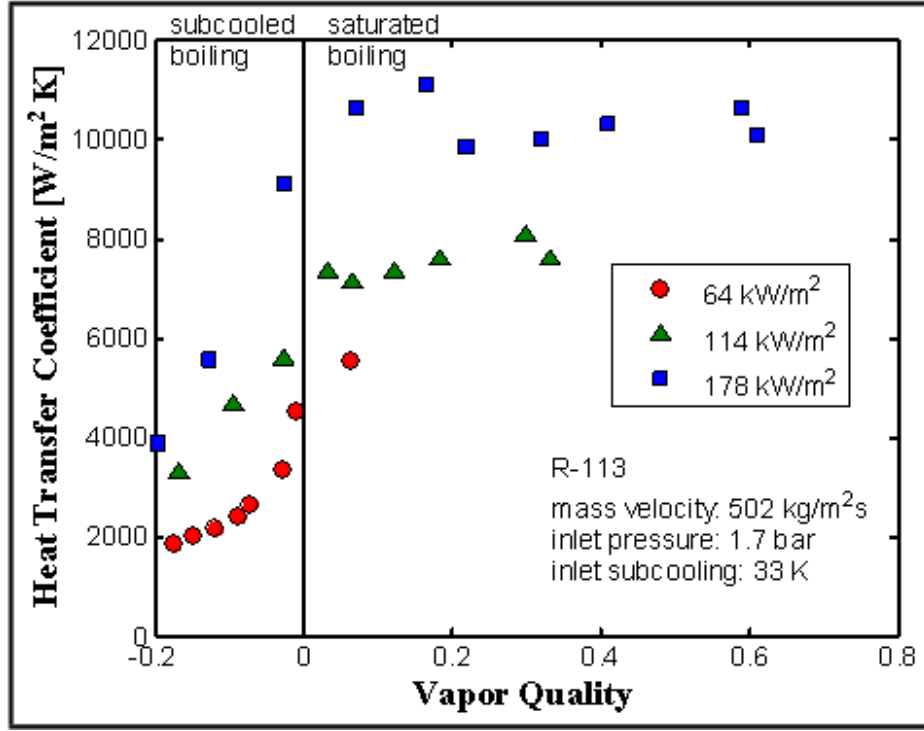
Figure 9: Flow boiling data of Lazarek et al. (1982) for R-113 in a *3.1 mm* channel.

The equation is:

$$Nu_l = 30Re_{lo}^{0.857}Bo^{0.714}$$

With:

- $Re_{lo} = GD/\mu_l$, the all-liquid Reynolds number,
- $Bo = q/(G * h_{lv})$ the Boiling number,
- *G* the mass velocity of the total flow of liquid and vapor.

The equation expresses no dependence of the heat transfer process on the local vapor quality.

Schneider et al. (2007) studied convective heat transfer for a cavitation and non-cavitation flow of *R-123* in *silicon* multi micro-channels having a hydraulic diameter of *227 μm*. In order to initiate cavitation and enhance heat transfer a *20 μm x 200 μm* rectangular micro orifices were installed at the entrance of each channel. The experiment returned a heat transfer coefficient for flashing flow *84%* higher in comparison to non-flashing flow. Thus, the two-phase flashing flow dominates the convective boiling, while for the non-flashing flow, it was hypothesized to be either the nucleate boiling or convective boiling depending on vapor quality.

Kandlikar et al. (2004) made a correlation for conventional tubes. Traditionally the local two-phase heat transfer coefficient was determined according to the value of the dominant mechanism between nucleate boiling (*nb*) and convective evaporation (*cv*):

$$\alpha = \max(\alpha_{nb}; \alpha_{cv})$$

The equation for the two coefficients were developed for all-liquid Reynolds numbers, $Re_{l0} > 3000$. Coefficients was expressed in function of:

$$\frac{\alpha_{nb}}{\alpha_l} = f_{nb}\left[\left(\frac{\rho_v}{\rho_l}\right)^{0.5}\left(\frac{1-x}{x}\right)^{0.8}, \frac{q}{Gh_{lv}}, \frac{G^2}{\rho_l^2 gD}, x\right]$$

$$\frac{\alpha_{cv}}{\alpha_l} = f_{cv}\left[\left(\frac{\rho_v}{\rho_l}\right)^{0.5}\left(\frac{1-x}{x}\right)^{0.8}, \frac{q}{Gh_{lv}}, \frac{G^2}{\rho_l^2 gD}, x\right]$$

The characteristic sets are: the Convection number Cv, the Boiling number Bo, the all-liquid Froude number Fr_{lo}, and the vapor quality. For developed flux, the author recommended to use the Gnielinski transition correlation and, Petukhov and Popov correlation for full-turbulent low. Moreover, for smaller channels where $Re < 3000$, the authors said that the preceding single-phase correlations are inconsistent. Furthermore, due to the reduced effect of gravity in micro-channels, the Froude number can be removed from relations. Therefore, the following modified correlations for α_{nb} and α_{cv} are:

$$\frac{\alpha_{nb}}{\alpha_l} = 0.6683Cv^{-0.2}(1-x)^{0.8} + 1058Bo^{0.7}(1-x)^{0.8}F_{sf}$$

$$\frac{\alpha_{cv}}{\alpha_l} = 1.136Cv^{-0.9}(1-x)^{0.8} + 667.2Bo^{0.7}(1-x)^{0.8}F_{sf}$$

F_{sf} is a constant that was used to fit the expressions to each particular tube material-fluid combination. The authors also suggest some variation in the model for different Reynolds number range:

- For $3000 \leq Re_{lo}$ use the standard model relations.
- For $1600 \leq Re_{lo} < 3000$ interpolate between laminar and transition correlations for $\alpha_{l.}$
- For $100 \leq Re_{lo} < 1600$ the flow is laminar; a laminar correlation like $Nu = \alpha_l * \frac{D}{k} * l$ is applicable.
- For $Re_{lo} \leq 100$ the heat transfer equation is $\alpha = \alpha_{nb}$.

Note that the nucleate boiling and convective boiling heat transfer correlations are both identical, except for values of the two constants and one of the exponents. Thus, it is not clear how one represents nucleate boiling and the other convective boiling.

Bogojevic et al. (2009, 2011) studied the flow boiling instabilities in a *silicon* heat sink with uniform and non-uniform heating. The test section was composed of *40* parallel channels having a hydraulic diameter of *194 μm* and a length of *15 mm*. They demonstrated the existence of different flow regimes in channels along the transverse direction. From the experiment resulted that inlet liquid sub-cooling have an influence on the stability and uniformity of wall temperature. It rises with the increase of liquid inlet temperatures. They confirmed the observation of Hetsroni et al. (2003) that non-uniform heating enhances the micro-channel flow boiling instabilities.

Bertsch et al. (2008, 2009) proposed a heat transfer correlation for saturated flow boiling considering the effect of channel size and applying a superposition of nucleate boiling and convective contributions. They developed a model based on a database from *14* studies, which included *12* different fluids, vertical and horizontal channels (both single and multiple) with diameters ranging from *0.16* to *2.92mm* and confinement numbers from *0.3* to *4.0*. The correlation is in a good agreement with the experimental results.

Harirchian et al. (2012) presented a flow regime map for *FC-77* in parallel *silicon* micro-channels. Only one fluid at one saturation temperature were tested. This work developed a predicting heat transfer method for: slug, confined annular, bubbly, and alternating churn/annular/wispy-annular flows. To predict the liquid film thickness in the elongated bubble they used a modified three-zone model of Thome et al. (2004). The channel locations where the flow transforms from bubbly to slug, and consequently to annular, flow were determined, and then the pressure drop for each regime occurring along the channel was separately calculated.

Tran et al. (2008) in their experiments on *R-12* and *R-113* observed that for wall superheats above *2.75 K* the heat transfer data express a strong dependence from the heat flux. They explained this with the macro-scale mechanism of nucleate boiling. The authors therefore modified the correlation of Lazarek and Black (1982), by replacing the Reynolds number with the Weber number:

$$We_{lo} = \frac{2GD}{\rho_l \sigma}$$

They removed viscous effects in favor of surface tension. The liquid to vapor density ratio was added to further account for variations in fluid properties. They proposed the following expression:

$$\alpha = (8.4 * 10^5)Bo^{0.6}We_{lo}^{0.3}\left(\frac{\rho_l}{\rho_v}\right)^{-0.4}$$

The first coefficient is dimensional and has the units of *W/(m²K)*. The equation removes any dependence on bulk velocity of the heat transfer coefficient. Moreover, it yields the following proportionality between the heat transfer coefficient and the channel diameter: $\alpha(D^{0.3})$, which seems to be the opposite of experimental trends found in later studies. Figure (10) shows their results. Their data shows a little influence of vapor quality on the heat transfer coefficient but a large effect on the heat flux. They attributed this heat flux effect to the dominance of nucleate boiling in their small channel.
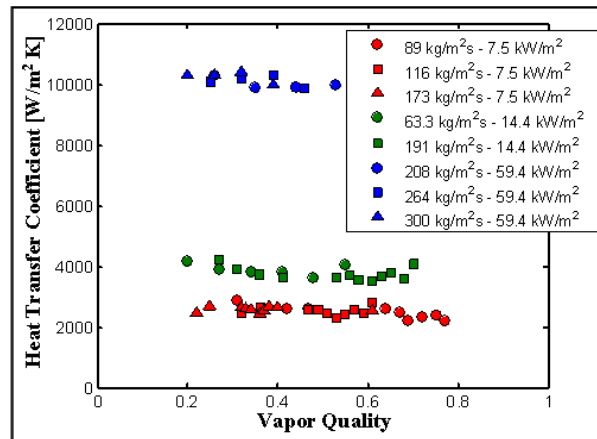
Figure 10: Flow boiling data of Tranet et al. (2008) for R- 12 evaporating in a *2.46 mm* circular channel.

Jacobi et al. (2002) proposed a simple analytical two-zone model of thin film evaporation for elongated bubbles. They demonstrated that film evaporation is the dominant heat transfer mechanism in micro-channels in comparison to macro-channel nucleate pool boiling mechanism.

Thome et al. (2004) modified the previous two-zone model to take in account the time averaged local heat transfer. He made a new three-zone model that treats evaporation of elongated bubbles as a cyclic passage of a liquid slug, an evaporating elongated bubble, and a vapor slug. They compared their local heat transfer coefficients with an experimental database including more than *1500* data points from seven independent studies.

Lin et al. (2012) studied evaporation of *R-141b* in a vertical *1.1 mm* tube. Their test section has an atmospheric outlet pressure and the inlet pressure ranged between *1.34* and *2.19 bar*. Due to the relatively low pressure compared to environment temperature, their data includes a small saturation pressure effect. They found a significant influence of vapor quality on the heat transfer coefficient that is in opposition from different studies. At high heat fluxes, their data exhibit a sharp peak at low vapor qualities followed by a monotonic decrease. At low heat fluxes, they had a significant monotonic rise in value of vapor qualities up to a peak of *x = 0.60*. At intermediate heat fluxes, from *42* to *48 kW/m²*, the heat transfer coefficients were nearly independent of vapor. Their results show a complex dependency of the heat transfer coefficient on heat flux and vapor quality than those in previous studies. Lin et al. (2012) hypothesized that nucleate boiling dominate at low vapor qualities and that convective boiling dominate at high vapor quality. Next Figure shows some of their results.
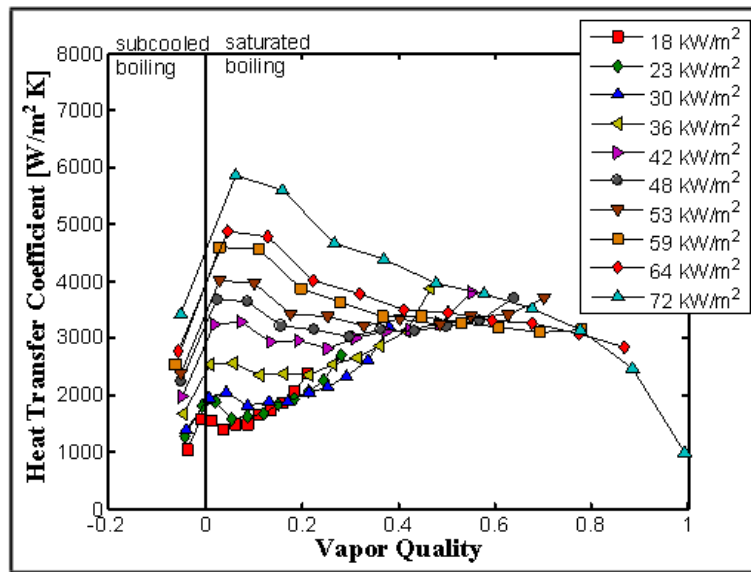
Figure 11: Flow boiling data of Lin et al. (2012) for R-141b inside a vertical tube of *1.1 mm* at *510 kg/m²s*.

Agostini et al. (2008) investigated on a two-phase flow cooling a silicon chip at high heat fluxes. They used *R236fa* and *R245fa* as working fluids. The experimental section had *67* channels and was *223 μm* wide, *680 μm* high and *20 mm* long. The base temperature of the multi micro-channel heat sink was *52 C°* while the maximum heat flux was *255 W/cm²*. The inlet sub-cooling was *10K* and the pressure drop across the channel *90 Kpa*. The cooling performance provided by two-phase flow for such chip is better than the single-phase liquid cooling at the same pumping power. The top of the channels was closed with a transparent plate for flow visualization while small rectangular orifices were made at the entrance to each individual channel by the connection of the inlet distributor to the channels. These orifices uniformed flow and prevented back flow into the inlet distributor. In

addition, they flashed the sub-cooled inlet liquid to "jump start" of the boiling process with a stream of bubbles. Bubbles grew along the channels avoiding any temperature overshoot to initiate the boiling process. This phenomenon resolved several annoying problems with multi micro-channel evaporator elements in one stroke. Fig. (12) shows some of their results.
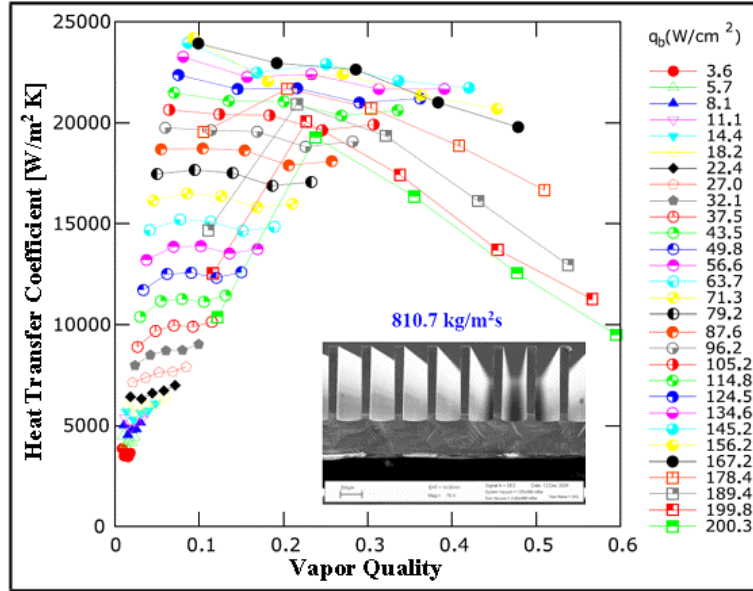
Figure 12: Flow boiling data of Agostini et al. (2008) for *R-236fa* for mass velocity of *810.7 kg/m²s*, and pressure of *2.73 bar*. The photograph shows the silicon test section without its cover plate.

In figure 12, heat transfer coefficients at low heat fluxes increase with vapor quality until intermediate heat fluxes, where they first increase with vapor quality and then show nearly no influence of vapor quality. At higher heat fluxes the heat transfer coefficients start to decline with increasing vapor quality. The local heat transfer coefficients have a base heat fluxes over *200 W/cm²*, which are in the range of those required for the design of computer microprocessor cooling elements.

Agostini et al. (2008) have also measured local flow boiling heat transfer coefficients in the same experimental section. They used one central inlet at the center of the channel length and two outlets, one at each end, to reduce the two-phase pressure drop. They could uniform base temperatures at base heat fluxes up to *210 W/cm²*. The highest base heat flux they reached was *255 W/cm²*. It is not the critical heat flux. This was a limitation of the pump. The pressure drop at this condition was about *0.9 bar*, but about one-third of this was due to the orifices not necessary in actual cooling application. In their tests, they reached flow boiling heat transfer coefficients, up to *180 kW/m²K*.

Borhani et al. (2010) developed a new time strip technique to analyze the image sequences taken by a high-speed camera during the flow boiling of R245fa in the test section Agostini et al.(2008). The results were in conflict each other and with heat transfer coefficients. The authors explained that by an intermittent dry-out and rewetting mechanism of the liquid film trapped between the channel wall and the elongated bubble.

Saitoh et al. (2005, 2007) investigated flow boiling of *R-134a* in *0.51*, *1.12* and *3.1 mm* horizontal tubes over a significant range of conditions. They found that mass velocity decrease with decreasing tube diameter even though an increase of heat transfer. The fluid entered their experimental section

as a two-phase flow. They only observed annular flows and intermittent (plug and slug) flows. Their section had a vapor qualities limit to *x > 0.2*, which precluded from obtaining any data in the bubbly flow regime. The heat transfer was highest in *0.51 mm* tube for vapor qualities less than *0.05*.

Owhaib et al. (2010) studied the tube diameter effects with *R-134a*. They found that the heat transfer coefficient becomes higher as tube diameter decreases. Their experimental section had vertical glass tubes of *0.83, 1.22* and *1.70 mm* diameters.

Martin-Callizo et al. (2007, 2010) presented results for a vertical *0.64 mm* stainless steel micro-channel. They found that the dominant effect in flow boiling for micro-channels is the heat flux while mass velocity is less important. In addition, they observed that heat transfer coefficient is barely influenced by vapor quality until high heat fluxes are reached.

Park et al. (2009) and Thome et al. (2010) presented a new saturated critical heat flux (CHF) database for multi micro-channel copper elements with low-pressure refrigerants (R134a, R236fa, and R245fa). They tested two different heat sinks with a different aspect ratio on a wide range of mass and heat fluxes. The channels were *467 x 4052 μm^2* and *199 x 756 μm^2*, respectively. The comparison of the data with the available CHF methods showed good agreement with predictions of Katto et al. (2002), Revellin et al. (2005, 2006) and Wojtan et al. (2005). A flow visual inspection assessed the effect of inlet orifices used for each channel. The authors reported a substantial improvement of flow stability with the micro-orifices in place. Furthermore, no back flow appeared and they observed a better flow uniformity. The orifices produced an additional pressure drop, with the consequent reduction of sub-cooling and in some cases vapor flashing. Moreover, if a lower heat flux was imposed at the start of experimental section, the wall-temperature distribution becomes uniform and the overshoot for the onset of boiling is significantly reduced.

Mauro et al. (2010) makes new tests with the split flow configuration (one inlet and two outlets) in *199 x 756 μm^2* channels with same refrigerants used by Park et al. (2009). They found a lower pressure drops accompanied by higher CHFs if compared with the single inlet-outlet system. The correlations of Wojtan et al. (2005), and Katto et al. (2002), agreed with the obtained CHF database for R134a, R236fa, and R245fa. The mean absolute error was 8.92% considering an error range of 30%. The numerical model of Revellin et al. (2008) provided a Mean Average Error of 14.2%.

Bao et al. (2000) studied local flow boiling for *R-11* and *R-123* inside a copper channel of *1.95 mm*. They used a single piece of tubing, *870 mm* long where first *400 mm* was unheated followed by *270 mm* of hated test zone and ended with another a *200 mm* of unheated zone. They tested the section for mass velocities from *50* to *1800 kg/m^{2}s*, enthalpies from sub-cooled to saturated and, heat fluxes from *5* to *200 kW/m^2*. Everything in a wide range of saturation pressures. Figure (14) shows some of their results.
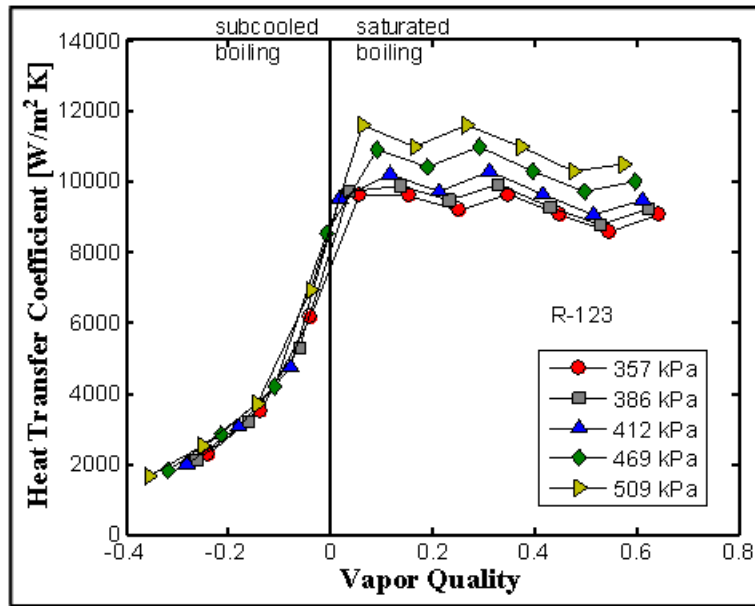
Figure 13: Flow boiling data of Bao et al. (2000) for *R-123* inside a copper tube with a diameter of *1.95 mm*.

The heat transfer coefficient is in a straight relationship with heat flux, it increases with saturation pressure, while the effects of vapor quality and mass flux is small, although there was a slight decreasing trend in the heat transfer with increasing vapor quality. Thus, they concluded that nucleate boiling dominates the heat transfer process. Baird et al. (2006), using the same quantities of heat fluxes, saturated pressures and mass velocities, reported local heat transfer data for *R-123* in a *0.92* mm diameter tube and for CO_2 in the *1.95* mm tube of Bao et al. (2000). They observed the same trends.

Ong et al. (2009) investigated flow boiling heat transfer phenomenon for R134a, R236fa, and R245fa in a horizontal heated tube. Experimental section used tubes of *1.03 mm*. They classified the slug flow in micro-channel systems into isolated and coalescing bubble flow, which converts into annular flow for higher vapor qualities. A dependence of heat flux on heat transfer coefficients at low vapor qualities was observed. Moreover, in the annular flow regime for low-pressure fluids, the convective boiling mechanism becomes dominant with the vapor quality increase. The method proposed by Ong et al. (2010) was in a good agreement with the database of Arcanjo et al. (2010). The model of Saitoh et al. (2007) described the heat transfer data bank of Tibirica et al. (2012). The new criterion was developed for the threshold from micro to macro scale; the confinement number, *Co*.

Consolini et al. (2010) studied the coalescing bubble flow during convective boiling heat transfer in micro tubes. They present a new one-dimensional model for evaporation of confined bubbles. The model, like the model of Thome et al. (2004), is based on the hypothesis that the thin film evaporates into elongated bubbles. The comparison of the model to the experimental database revealed the conclusion that the film evaporation mechanism governs the heat transfer, as widely confirmed in literature.

Costa et al. (2011) examined two-phase flow of R245fa and R236fa in *135* silicon multi micro-channels heated by *35* local heaters. The channels were *85 μm* wide, *560 μm* high and, *127 mm* long. Channels are separated by a *46 μm* wide fins. They developed a new experimental technique to determine the outlet restriction pressure drop which represent up to *30%* of the total pressure loss

through the micro-channels. The experimental results were in a good agreement with the annular flow model of Cioncolini et al. (2011) that used the Lockhart and Martinelli criterion for the isolated bubble regime.

Madhour et al. (2007) tested flow boiling of R134a at a saturation temperature of *63 °C*. The experimental section was developed with a copper heat sink with *100* parallel channels and *35* local heaters and temperature sensors. They made many tests; 3D-IC chips with interlayer cooling were the main subject of their work.

1.2.3. Conclusions

All the experimental work here reviewed showed a dominant effect of heat flux on the heat transfer coefficient. Besides the influence of forced convective boiling on heat transfer is insignificant (an exception is i.e. works of Lin et al. (2012)). The increasing of heat transfer in the annular flow regime suggests that forced convection are dominant in confined channels. The experimental data under stable two-phase micro-channel flows indicated the importance of the fluid properties on the flow boiling heat transfer process in confined micro-scale channels. Most studies have not measured sub-cooled liquid laminar and turbulent flow heat transfer coefficients. In addition, many studies do not report the internal surface roughness of the test section, which may influence the heat transfer process. Achieving steady-state conditions seems to be the most important thing and hence it is important to label data as being obtained at stable or unstable conditions. Finally, for non-circular channels the channel perimeters are often not reported.

1.3. Flow Pattern and Maps for Micro-channels

This paragraph disserts on the two-phases flow pattern studies for micro channels and their difference from macro channels due to differences in the phase change phenomena. Appling an extrapolation method to use heat transfer and flow pattern studies for the macro scale on micro scales is unrealistic for heat transfer. Usually the flow patterns are recognized by visual inspection, though other means such as analysis of the spectral content of the unsteady pressures or the fluctuations in the volume fraction have been devised for those circumstances in which visual information is difficult to obtain. In transiting from macro scale to micro scale flows, gravity dominance is successively surmounted by surface tension forces. It results in a gradual suppression of some macro scale flow regime that came gradually with the diminishing of channel size to a condition where gravity force is negligible. The suppressed flow regime is the stratified flow because stratification is a consequence of buoyancy forces. In addition, slug, plug and stratified wavy flows converge into elongated bubble regime in reason of the predominance of surface force due to the reduced channel size. Following in this paragraph a review of two-phase flow patterns for macro and micro scale channels is reported. In summary, there are many challenges associated with a better understanding of flow patterns and considerable work is necessary before a reliable design tools become available.

1.3.1. Flow Pattern in Macro-scale

For the simpler macro scale flows, such as those in vertical or horizontal pipes, many investigations were made to determine the dependence of the flow pattern on volume fluxes, volume fraction and on the fluid properties such as density, viscosity, and surface tension. Flow regime maps display the results that identify the flow patterns occurring in various parts of a parameter space defined by the component flow rates. The used flow rates may be the volume fluxes, mass fluxes, momentum fluxes, or other similar quantities depending on the author. The boundaries between the various flow patterns in a flow map occur because a regime becomes unstable at transition to another flow pattern. Like the laminar to turbulent transition in single-phase flow, these multiphase transitions can be rather unpredictable since they may depend on otherwise minor features of the flow, such as the roughness of the walls or the entrance conditions. There are many problems in the using of flow maps. One of the basic fluid mechanical problems is that these maps are often dimensional and therefore apply only to the specific pipe, sizes and fluid, but sometimes is possible to generalize. However, generalizations can only have limited value because several transitions are represented in most flow pattern maps and the corresponding instabilities are governed by different sets of fluid properties. Neither for the simplest duct geometries exist a universal and dimensionless flow pattern maps that incorporate dependence of the boundaries on the fluid characteristics. In general, the type of two-phase flow pattern observed in a channel depends on the respective distribution of the different phases taking a particular configuration. There are some possible distinguishing criteria, such as the relative importance of various forces, i.e. inertia, viscosity, buoyancy and surface tension. Some schematic of evaporative flow patterns occurring in both horizontal and vertical tubes are illustrated in Figure (15).
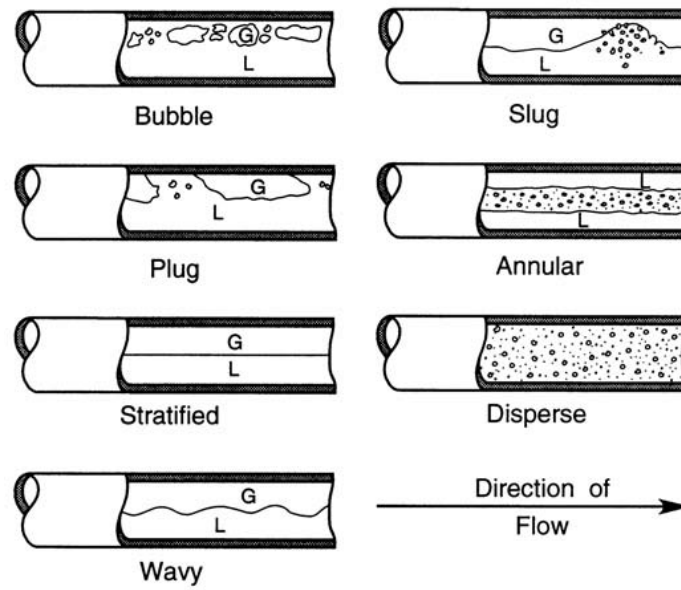
Figure 14: Sketches of flow regimes for flow of air/water mixtures in a horizontal, *5.1cm* diameter pipe from Weisman et al. [1995]
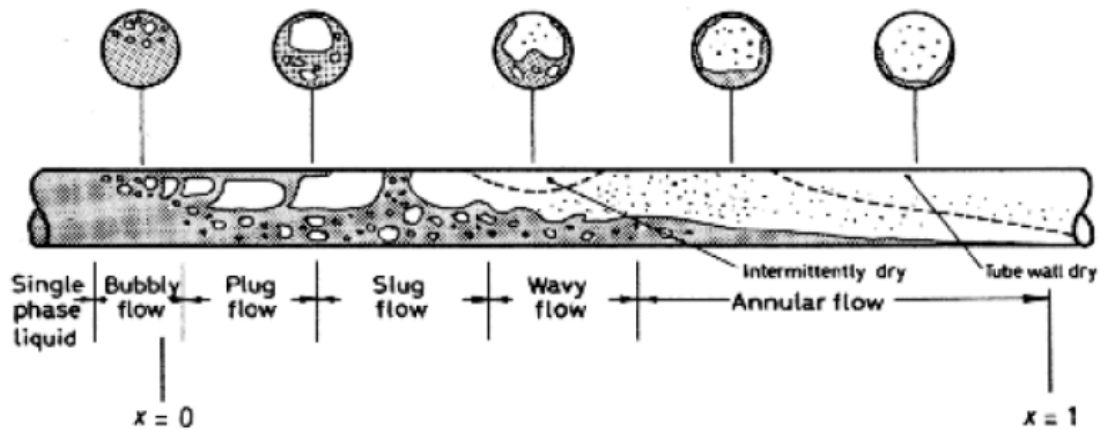
Figure 15: Illustration of the sequence of two-phase flow patterns during evaporation from Colier et al. (1994)

Figure 16: Sketches of flow regimes for two-phase flow in a vertical pipe from Weisman et al (1995).
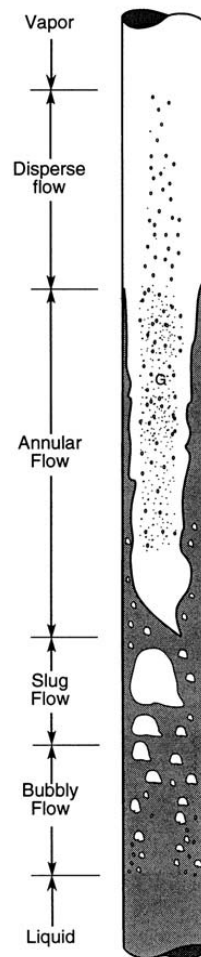
Figure 17: Illustration of the sequence of two-phase flow patterns during evaporation from Collier et al. (1994).

Numerous two-phase flow pattern observations are available in the literature. Apparently Suo et al. (1963), who observed three different flow patterns in channels of *1.03* and *1.60 mm* diameter, made the first study on flow patterns in micro-channels. Their study covered heptane and water as the liquid phase, and helium and nitrogen as the gas phase.

Another study came from Cornwell et al (2001) who noted three different flow patterns in rectangular channels of *1.2 × 0.9 mm* and *3.5 × 1.1 mm*. They used *R-113* and *R-141b* for tests: isolated bubbles, confined bubbles, and slug/annular flow.

Hewitt et al. (1969), Baker (1954), Taitel et al. (1976) studied adiabatic flow maps. Sato et al. (1971), Kattan et al. (1998) and Wojtan et al. (2005) studied instead adiabatic flow maps.

Sato et al. (1971) studied saturated flow boiling of water in a vertical rectangular cross section of internal diameter *15×10 mm* and with a heated length of *1 m*. The author classified the flow patterns into bubbly, slug, slug/annular, annular and annular/bubbly flow. Figure (19) shows the flow pattern data for water with transitions lines included.
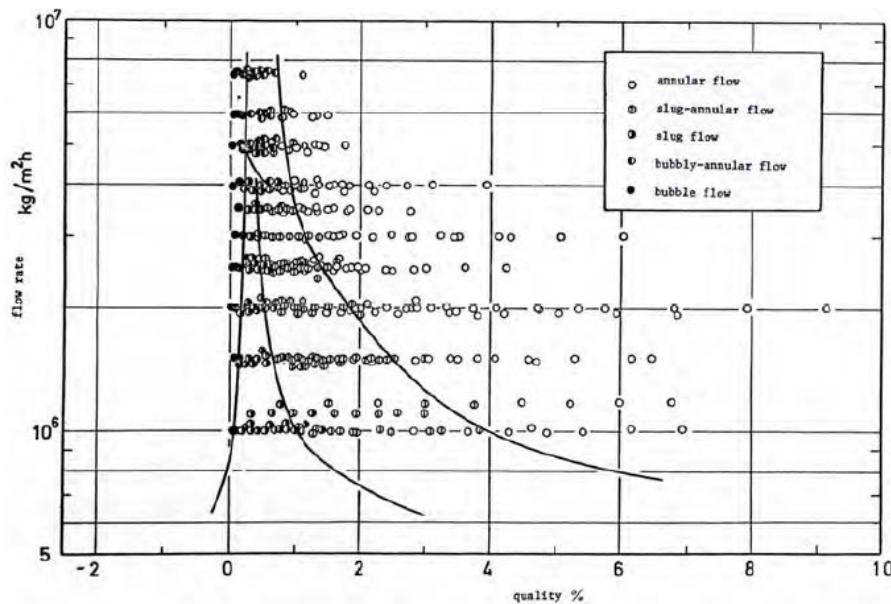
Figure 18: Flow pattern map for flow boiling of water in a *15×10 mm* channel from Sato et al. (1971).

Many others have observed these three basic flow patterns: Damianides et al. (1988), Wien et al. (1995)], Kasza, Didascalou et al. (1997), Lin, Kew et al. (1998) Sheng et al. (2001) and more over.

Instead, Coleman et al. (2002) divided, their observations of 16 different regimes, into four traditional sets: dispersed, intermittent, wavy and annular.

These sets were then subdivided as follows:

- dispersed flow into 3 types of bubbly flow,
- intermittent flow into 4 types of slug and plug flow,
- wavy flow into 4 types of waves,
- annular into 5 categories of annular films.

Following are reported two different flow maps for both vertical and horizontal tubes. Figure (20, 21)
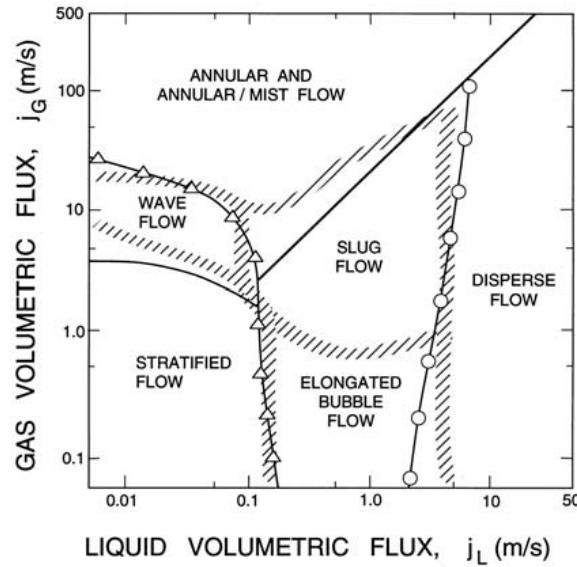
Figure 19: A flow regime map for the flow of an air/water mixture in a horizontal, *2.5 cm* diameter pipe at 25°C and 1bar. Solid lines and points are experimental observations of the transition conditions while the hatched zones represent theoretical predictions. From Mandhane et al. (2002)
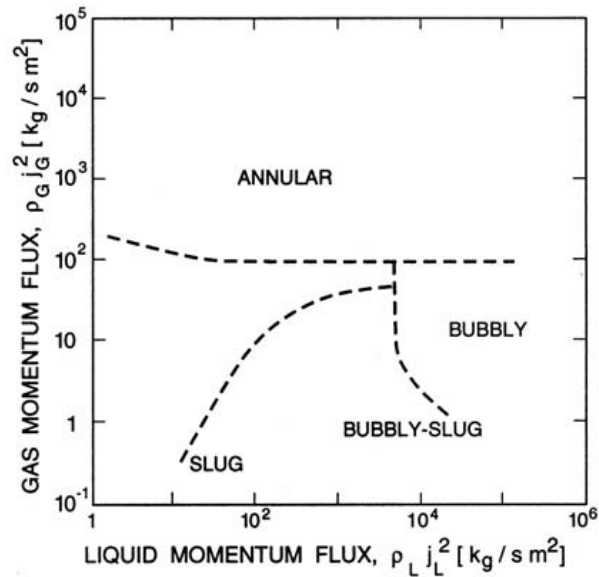
Figure 20: The vertical flow regime map of Hewitt et al. (1969) for flow in a *3.2 cm* diameter tube, validated for both air/water flow at atmospheric pressure and steam/water flow at high pressure.

Hetsroni et al. (2003) realized some high-speed videos that documents the intermittent dry-out phenomenon in single and multi-micro channels due to the very rapid vaporization at high heat fluxes with water in a *0.150 mm* channel. In his videos, the channel dries out and remains locally dry until flow is reestablished and a liquid meniscus can be seen that arrives and rewets the surface. They observed the Liedenfrost effect on a rewetting or not rewetting surface at high thermal flux, the latter of which would result in CHF if the substrate is not able to conduct the heat away from the local hot spot to wetted zones.

Xu et al. (2005) performed a visualization study that included an explosive evaporation in microchannels. Next figure (22) shows the cyclical process at very high heat fluxes.
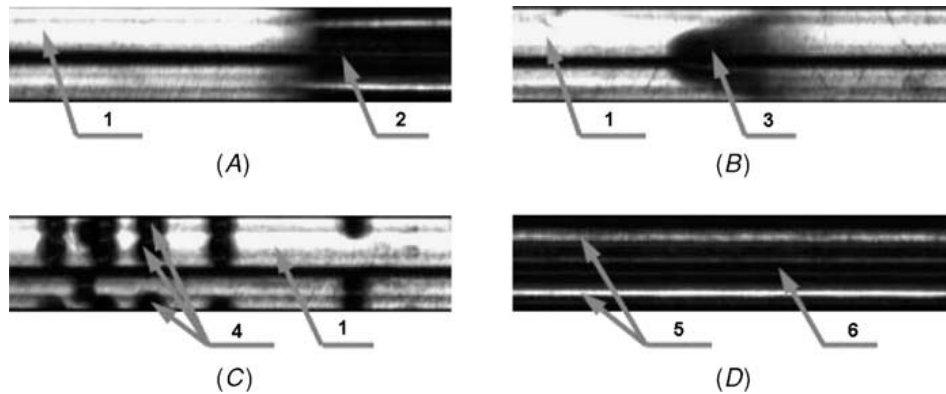
Figure 21: Sequence of flow patterns observed by Xu et al. (2005) in a rectangular microchannel during high heat flux operating conditions

Figure A shows the elongated bubble flow with a liquid slug and vapor bubble:

1. liquid slug,
2. vapor bubble.

Figure B shows a bubble apparition inside the liquid slug:

3. bubble in liquid slug,
4. multiple bubbles in liquid slug.

Figure C shows numerous bubbles evident within the liquid slug:

Figure D shows annular flow after the liquid expunge:

5. liquid film in corner of channel,
6. vapor core.

The flow expands away very rapidly in both directions from the point of occurrence. This sequence of events documents the activation of nucleate boiling sites within the liquid slug that occurs because of the high heat flux.

Nino et al. (2000) and Jassim et al. (2001) have approached two-phase flow mapping in horizontal micro-channels in a new manner. Instead of categorizing a specific flow regime they determined the time fraction that each type of flow regime. Analyzing the flow by image processing they observed evaporators at a given mass velocity and quality in a singular channel or in multi micro channels. This probabilistic flow mapping technique captures simultaneously different flow regimes in different channels. Figure (23) exemplify the result, some of the channels are in annular flow and others are in intermittent flow.
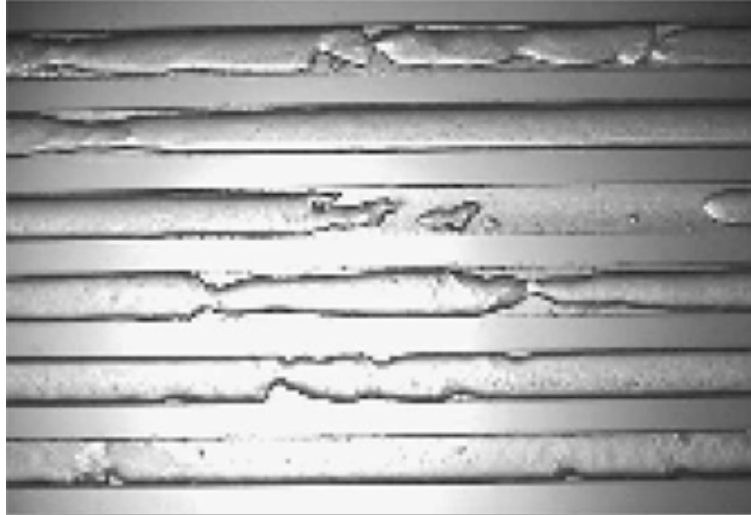
Figure 22: *R410A* at *10°C* in a multi micro channel from Nino (2000) for flow in flat channels of *1.54 mm* hydraulic diameter at ×= *0.17* at *100 kg/m²s*

In the proximity of a transition boundary, this yields a statistical approach act to characterize the beginning and the ending of the transition band. Their probabilistic map was used to model pressure drops and void fractions for each type of regime and for every probability of occurrence.

1.3.2. Micro-scale Two-Phase Flow and Flow Maps

This paragraph presents a short of numerous mini and micro scale, adiabatic and not, two-phase flow pattern studies. Literature is full of works on micro scale two-phase flow maps, hence, in this thesis there are described only the most important.

Kawaji et al. (2004) presented a comparative review of adiabatic two-phase flow patterns. They recognized that two-phase flows in macro channels and mini channels exhibit morphological similarity. They based the analysis on the study of Triplett et al. (1999), Damianides et al. (1988) and Fukano et al. (1995). They also reviewed the work done by Serizawa et al. (2000), Kawahara et al. (2005) and Chung et al. (2004) pointing out the significant difference in the observed two-phase flow patterns unique to micro channels.

Figure (24) presents schematics of mini channel and micro channel flow. Here the use of the term "mini channels" is given to flows thought to be in the transitions state between macro scale and micro scale.
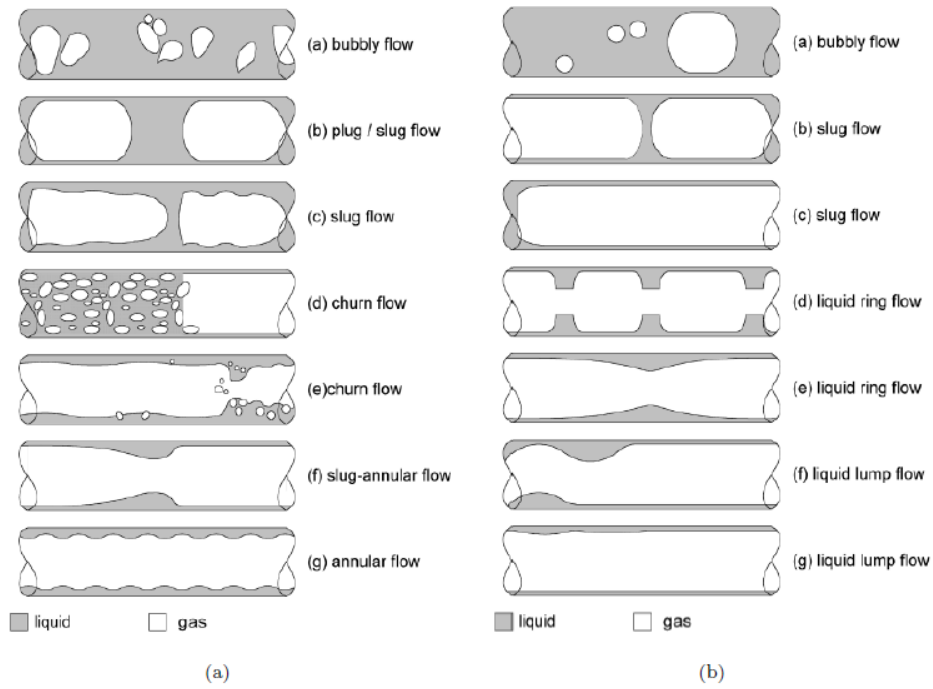
Figure 23: Two-phase flow regimes from Kawaji et al. (2004): (a) Mini channel flow patterns and (b) micro channel flow patterns.

Suo et al. (1963) involved gas to liquid two-phase flow pattern observations in capillary tubes providing the first insight of the two-phase distribution in micro scale channels. They used as working fluid a mix of *air−water*, *water−nitrogen* and *N2−heptane* with *nitrogen*. The experimental section have channels of *1.03* and *1.60 mm* diameter. They identified, by the experiments, only three distinct flow patterns: bubbly-slug, slug and annular flow. The flow pattern map proposed by Suo et al. (1963) as a function of capillary number, *Ca* and volumetric quality is shown in Figure (25).
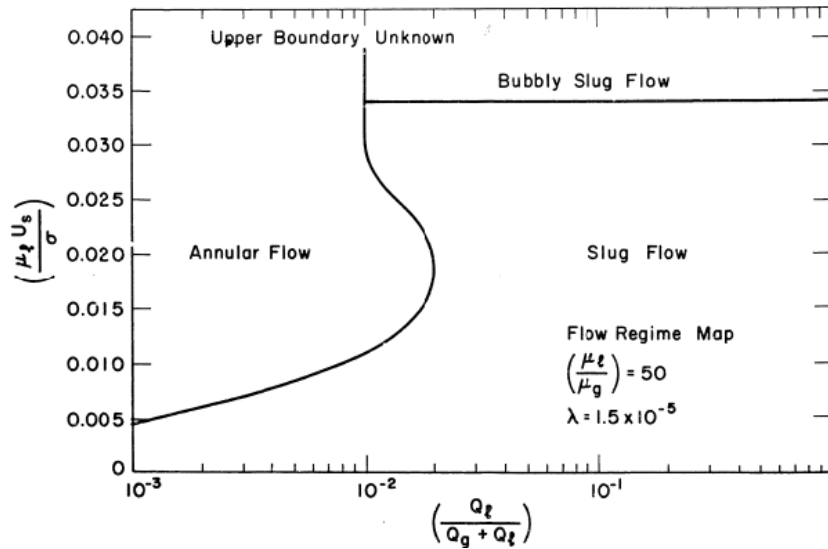
Figure 24: Flow pattern map of Suo et al. (1963).

Serizawa et al (2002) provided an interesting overview of the two-phase flow patterns for micro-channels. Figure (26) shows their flow pattern observations made for a *0.100 mm* glass channel with steam-water. Here, a new flow pattern type was identified, namely *liquid ring flow*. They also ob-

served, for air-water in a *0.020 mm* channel, a liquid ring flow that they named *liquid lump flow*. Hence, this is apparently the first experimental evidence to support the case that there should be another sub scale after micro-channel.
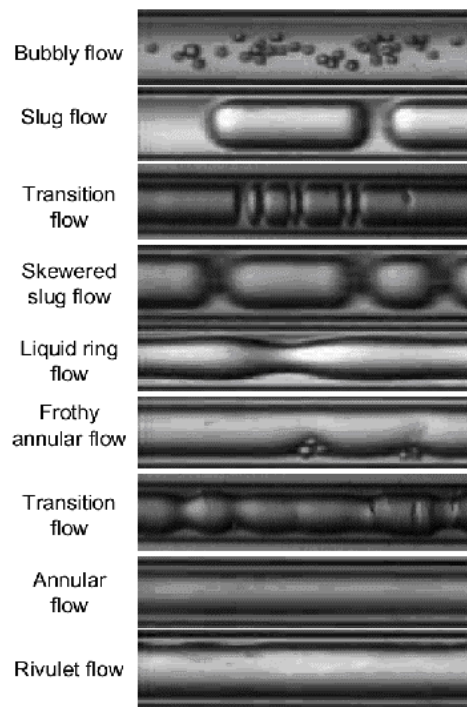
Figure 25: Flow regimes observed by Serizawa et al (2002) in a *0.100 mm* channel for steam-water flows

Cubaud et al. (2004) studied *air-water* flows in small square channels. They observed that the liquid film was continuous around the channel near the nose end of elongated bubbles and that near the rear there were dry patches at the middle of each face. They called these *wedge flows*. This regime is due to the large surface tension and contact angle of water and does not occur for other liquids.

A critical issue of two-phase flow patterns in micro-channels is how to identify them. High-speed camera is not always able to distinguish flow regimes due to the difficulty to identifying and interpreting images, as it depends mainly from the reseracher. A better approach is to use optical techniques as described below.
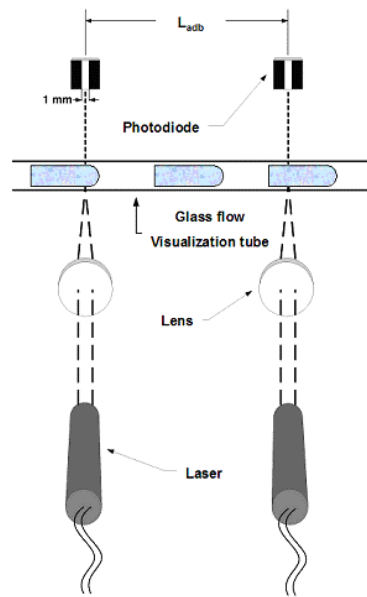
Figure 26: Optical flow pattern identification technique by Revellin et al. (2008) for a micro-channel.

Figure (27) depicts the two-laser and two-diode optical technique developed by Revellin et al. (2008) for micro-channels. As the name can suggest the technique uses two low power lasers, of a power less *1 mW*, and two diodes. These are mounted together with a lens to focus the laser light through the glass tube, the fluid, and then onto the diode. Using two lasers instead of one gives two high frequency, light intensity signals, which can then be cross-correlated using signal processing to determine the velocity of bubbles, for instance.

Figures (28, 29) of Revellin et al. (2008) show the obtained laser signals for the respective flow patterns observed. First figure expresses the intensity of light in function of time for the light incident on the diode. Even without any signal processing, it is possible to identify some flow patterns only by comparing the signals to the corresponding images.

By the signal processing procedure described in Revellin et al. (2008), it is possible to distinguish:

- the flow pattern,
- the bubble frequency,
- the bubble velocity (by the delay time between two signals),
- the bubble length,
- the void fraction (from the elongated bubble velocity).
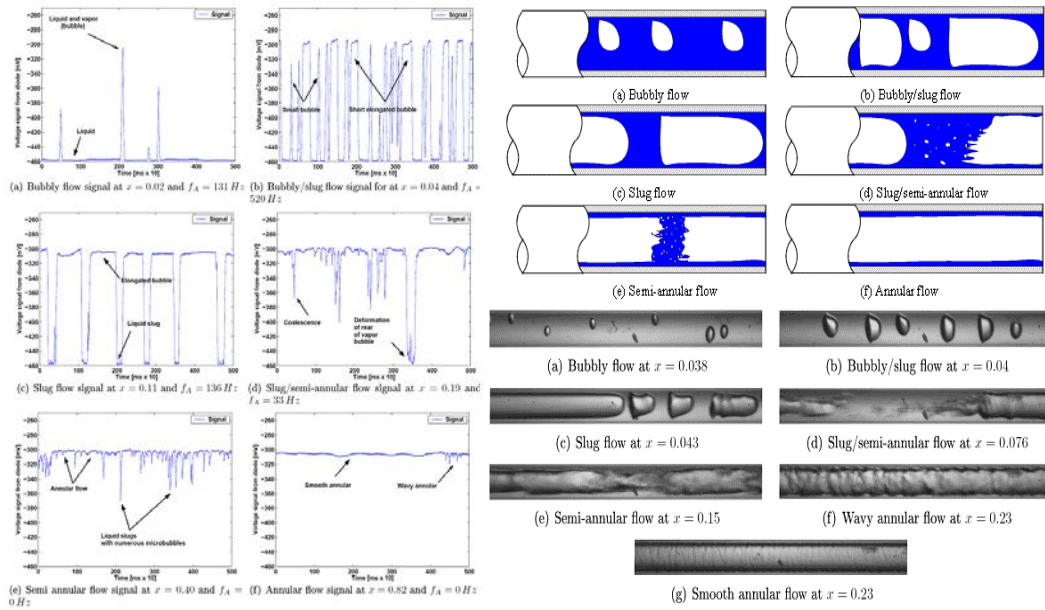
Figure 27, 28: Temporal laser light intensity signals of and Revellin et al. (2008) for R-134a in a 0.509 mm glass channel at with mass velocity of 500 kg/m2s and temperature of 30°C and flow patterns and transitions observed.

Figure (30) show the flow map proposed by Triplett et al. (1999), it is in function of the superficial liquid velocity versus the superficial vapor velocity. They based their flow pattern on observations of *air-water* in a *1.1 mm* horizontal glass channel; a mixer was used to create the air and water flow. They also made observations in a *1.45 mm* channel and in several small semi-triangular tubes. The created map shows some significant differences in the transition locations, probably caused by the large difference in physical properties of *air-water* compared to *R-134a*. Hence, a flow pattern transition prediction method that incorporate the properties of the gas and liquid phases to generalize the map for more fluids, is necessary.
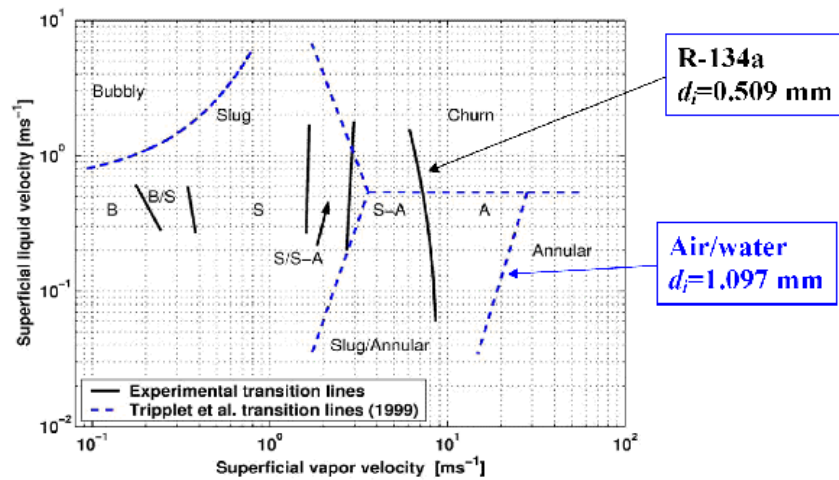
Figure 29: Flow pattern map of Triplett et al. (1999) for air-water in a 1.1 mm horizontal channel.

Coleman et al. (2003) and Killion et al (2002) proposed a graphical flow pattern maps based on their extensive observations of *air-water* flows and *R-134a* in circular and non-circular channels. They have also proposed an empirical expression for some of the transitions.

Yang et al. (2001) proposed a flow pattern map of superficial liquid velocity in function of the superficial vapor velocity. They based on their observations made in a *2.0 mm* channel. The transition lines were quite different for *air-water* flows compared to *R-134a* flows.

Akbar et al. (2012) proposed a flow pattern map based on all available *air-water* observations with hydraulic diameters less or equal than *1.0 mm* following the methodology adopted by Lowe and Rezkallah (1999). For their surface tension dominated zone (comprised of bubbly, plug and slug flows), its upper threshold boundary is determined in terms of the liquid (SL) and vapor (SG) superficial *Weber* numbers.

- $We_{SG} \leq 1.0$ for $We_{SL} > 3.0$

- $We_{SG} \leq 0.11*We_{SL}^{0.315}$ for $We_{SL} \leq 3.0$

Where We_{SG} is below this boundary, the flow is in the surface tension dominated zone. Moreover, the transition threshold bound the annular flow zone:

- $We_{SG} \geq 11*We_{SL}^{0.14}$ and $We_{SL} \leq 3.0$

For all conditions above and to the left of this boundary, the flow is in the annular flow zone. In addition, the transition threshold bound the dispersed flow zone:

- $We_{SL} > 3.0$ and $We_{SG} > 3.0$

Therefore, at all conditions above and to the right of this boundary, the flow is in the dispersed flow zone. The transition zone falls below the annular zone and above the surface tension dominated zone as follows

- $0.11*We_{SL}^{0.315} < We_{SG} < 11*We_{SL}^{0.14}$ and $We_{SL} \leq 3.0$

Next figure (30) shows these boundary conditions within different studies and the one proposed by the author.
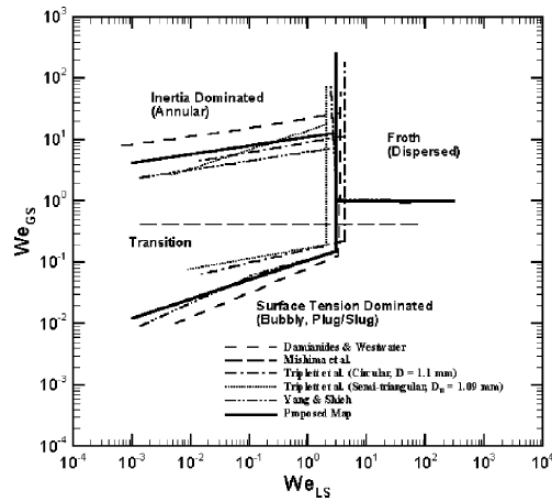
Figure 30: Flow pattern map comparison for circular and near-circular channels with diameter of *1mm* from Akbar et al. (2012).

This map agrees very well with *air-water* data in channels of *1 mm* diameter. Furthermore, they observed that the superficial vapor and liquid Weber numbers work better for distinguishing flow pattern transitions than the tradition superficial vapor and liquid velocities in micro-channels. However, the map did not predict their flow pattern observations for R-134a in vertical small tubes of *1.10,*

2.01, 2.88 and *4.26 mm*. The main suggested reason is that the map is in a good agreement with the results when the Bond number is less than *0.3*, which corresponds to a channel diameter of about *0.25 mm* at *6 bar* for *R-134a*. Moreover, they concluded that non-circular channels with sharp corners might support different flow regimes and transition boundaries as compared to near circular channels.

Chen et al. (2008) studies are in full contradiction with the results obtained by Coleman et al. (2003) and the flow evaporation study of Revellin et al. (2008) for *R134a* and *R245fa* in a *0.5* and *0.8 mm* channel.

Ong et al. (2005) showed an expansion of the annular flow regime when channel confinement number increases. From all their experiments in small channels, they noticed an increased dominance of the annular flow regime.

Starting from the flow pattern observation of Triplett et al. (1999), Ullmann et al. (2006) proposed a micro-scale flow pattern map that considers controlling mechanisms for each flow pattern transition. To make work macro scale flow pattern to micro-scale many significant modifications were made by the authors to predict the transitions by their method for each transition. Farther, they noted that the stratified flow region shrinks to a very small zone on their map at relatively very low liquid flow rates and at very high gas flow rates. Therefore, their analysis showed that the difference between a stratified flow, whose interface, is curved up to the top of the channel by capillary forces and that the definition of annular flow becomes ambiguous in small channels since both regimes look essentially equal, and can be classified only as annular flow.

Revellin et al. (2008) utilized flow pattern data, bubble frequency data and the CHF correlation of Wojtan et al. (2006) work to create a new type of flow pattern map. This map classifies evaporating flow regimes as described:

- *Isolated bubble regime*:
  - ➢ *Bubbly flow*: bubbles shorter in length than the channel diameter;
  - ➢ *Slug flow:* bubbles longer than the channel diameter;
  - ➢ *Mixed bubble flows:* where the frequency of bubbles increases with increasing heat flux and vapor quality at a fixed mass velocity;
- *Coalescing bubble regime*:
  - ➢ *Slug flows*: long bubbles followed by aerated liquid slugs. Some short bubbles may still exist, where the frequency of the bubbles decreases with increasing heat flux and thus vapor quality at a fixed mass velocity;
  - ➢ *Churn flows*: equal to *coalescing slug flows;*
- *Annular flow regime*:
  - • *Smooth annular flows*: nearly no interfacial waves;
  - • *Wavy annular flow*: interfacial waves are very evident;
- *Dryout regime*
  - • *Post dry-out region*: after CHF at the critical vapor quality.

Figure (31) shows an example of some bubble frequency data obtained in a *0.5 mm* channel of glass detected using the laser/diode measurement technique earlier described.
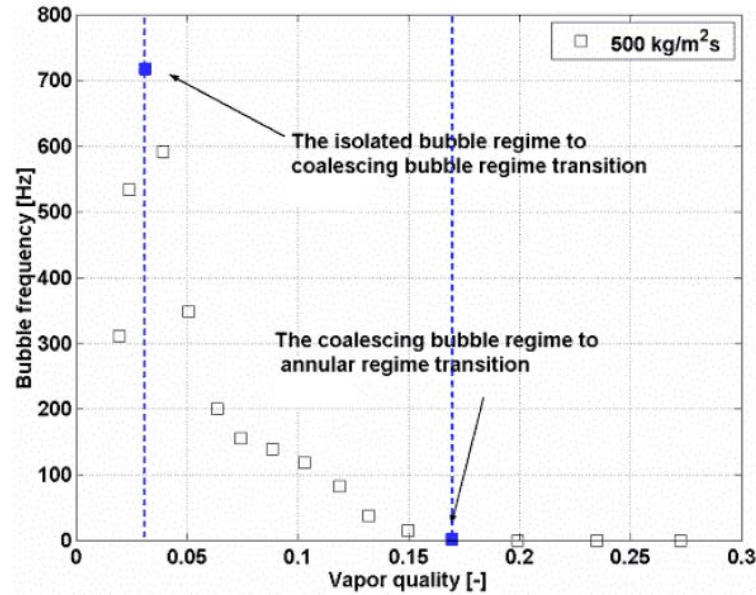
Figure 31: Bubble frequency data measured by Revellin et al. (2008) for *R-134a* for a *0.509 mm* micro-channel using their laser technique.

At a fixed mass velocity, the bubble frequency increase rapidly up to a peak. After the peak, the frequency decreases first very sharply and then faster up to zero. The first slow decreasing tract involves the coalescence of the smaller bubbles into long bubbles, and the slower fall off then is due to the coalescence of the long bubbles into even longer. At the end annular flow is reached.

Figure (32) shows this new type of flow pattern map with the transition equations evaluated for *R134a* at *30°C*.

The local length along the uniformly heated channel can be obtained from an energy balance between the latent heat absorbed by the fluid and from the perimeter of the tube subjected to a heat flux. The heat flux is also used to establish the location of the transition between the isolated bubble regime and coalescing bubble regime. The lower end of the transition lines represents an extrapolation below the lowest mass velocity, where notable flow instabilities begin.
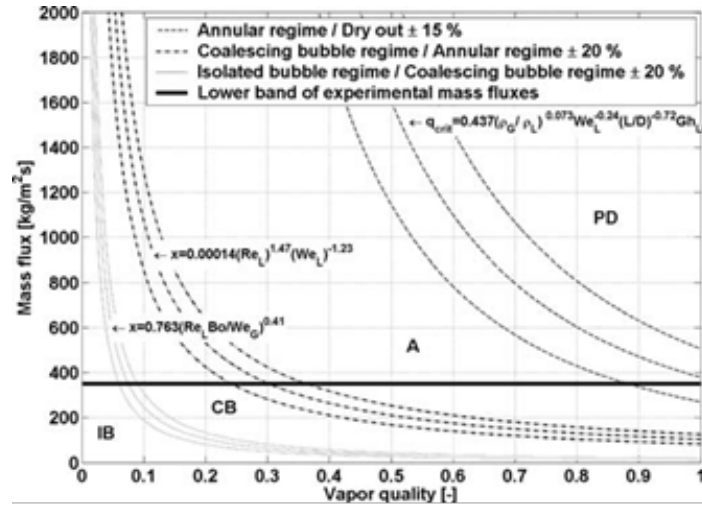
Figure 32: Flow pattern map from Revellin et al (2008) for evaporating flow in uniformly heated micro-channel. Presently evaluated for *R134a* for diameter of *0.5 mm*, length of *70 mm*, saturation temperature of *30°C*, heat flux of *50 kW/m2* with no sub-cooling at inlet. Transition boundaries (center curve of each set) are shown with their error bandwidth.

In the figure:

- *Bo* is the boiling number,
- Re_l is the liquid Reynolds number,
- We_L is the liquid Weber number,
- We_G is the and vapor Weber number,
- IB is the isolated bubble regime,
- CB is the coalescing bubble regime,
- A is the annular regime,
- PD is the post dry-out regime.

1.3.2.1. Conclusions

Many two-phase flow pattern and maps studies have been analyzed. The analysis evidences the dominance of surface tension forces on micro-scale channels. When the channel size increases, the buoyancy force suppress the surface tension forces. The fluid properties also play a key role in the flow pattern transitions from one regime to another. The suppression of the stratified flow regime and the convergence of the macro-scale intermittent flow regime into the elongated bubble flow regime in micro-scale supports the idea of a macro-scale to micro-scale transition in between. In micro-channel flow, the isolated and coalescing bubble regime is suppressed, such as the annular flow region that spans over an ever-wider range of vapor quality before reaching the onset of dryout. The developing of mechanistic models able to predict local flow boiling heat transfer coefficients requires significant information about the flow regime and its structure. For example, modeling flow boiling in the slug flow regime in a micro-channel requires knowledge of the bubble frequency, bubble length, liquid slug length and thickness of the liquid film trapped between the bubble and the wall, etc.

1.3.3. Trends in Micro-channel Flow Boiling Data

Fig. (33) summarizes the trends in local flow boiling heat transfer coefficient α versus vapor quality x as categorized by Agostini et al. (2008) reviewing 13 different studies.
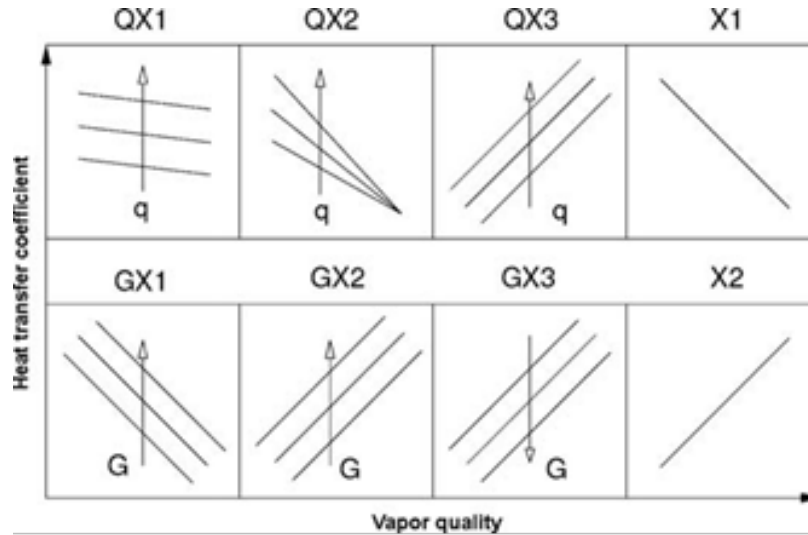
Figure 33: Heat transfer trends versus vapor quality by Agostini et al (2008)

The array of lines shows the trends found for local boiling heat transfer coefficient in function of the vapor quality. The map denotes how the heat transfer coefficient vary with the parameter in the frame. An arrow with the symbol shows the nature of the variation. A short description of the array is reported as follow:

- QX1 showed that the heat transfer coefficient has a decreasing trend regard the vapor quality and that heat transfer increased with increasing heat flux q.
- QX2 showed a similar trend except that the data all come together at higher vapor quality.
- QX3 showed the data in which α increased versus x and with q.
- X1 data decreased sharply with vapor quality but did not depend on mass velocity or heat flux.
- X2 data increased only with vapor quality and independent from mass velocity or heat flux.
- The GX1, GX2, and GX3 showed three types of trends with respect to mass velocity and vapor quality.

Most of the studies analyzed follow the boiling heat transfer trends represented by QX1 and X1 (11 out of 13). It can be concluded that:

- at low to medium vapor qualities ($x < 0.5$), the heat transfer coefficient increases with heat flux and decreases or is relatively constant with respect to vapor quality;
- at higher vapor qualities ($x > 0.5$), the heat transfer coefficient decreases sharply with vapor quality and does not depend on heat flux or mass velocity;
- the effect of heat flux is always to increase the heat transfer coefficient except at high x, whereas mass velocity varies from no effect, an increasing effect, or a decreasing effect.

1.4. Near Zero Gravity Conditions

While gravity plays an important role in the macro-scale, it has less effect in the micro-scale due to the contrasting effects of surface tension. Hence, operating in micro-gravity conditions the behavior of a micro-channel should not change. Micro-gravity studies are not common due to the difficulty to make the experiments without the gravity force. The state-of-the-art review of two-phase flow and heat transfer in zero gravity conditions is presented in the following sections, but because it is a recent topic, the literature is not very wide and often contradictory.

1.4.1. Flow Boiling in Micro-gravity

Cooper et al. (1989) and Van Helden et al. (1995) during their studies obtained bubble growth and displacement in terrestrial gravity and for short duration microgravity flow. They observed the vapor bubbles departing from their nucleation cavity by sliding away from the site along the heated surface. Moreover, they also observed the bubble dynamics and how detachment phenomenon is influenced by bulk flow velocity and sub-cooling, flow regime, heat flux, flow direction, heater surface orientation relative to gravity, and the strength of the gravitational field.

Zeng et al. (1997) studied the vapor bubbles on an upward heated surface exposed to low velocity flow. Their work showed the vapour bubbles rising directly off the boiling surface and then are carried away by liquid. However, if the velocity of liquid increases to a critical value, the hydrodynamic forces compels bubbles to depart from the nucleation site sliding them along the heated surface. Heat is absorbed during sliding and bubble growth continues until the bubble lifts off the surface due to the influence of buoyancy and shear forces.

Thorncroft et al. (1997) observed the mean departure point and the lift off diameters in a vertical upward and downward flow boiling for *FC-87*. During the vertical upward flow, bubbles departed the heating surface by sliding upward and tended to remain attached to the heating surface. In contrast, bubbles in downward flow departed by sliding either upward or downward along the heating surface. This behavior is probably dictated by the interaction of hydrodynamic forces and buoyancy forces on the bubble. The bubbles that departed from nucleation sites for low fluid velocity tended to slide upward against the flow due to the buoyancy forces that are larger compared to drag force. The buoyancy force was overcome at higher flow velocities and the bubble slides downward. The dependence of bubble dynamics upon the buoyancy force indicated a corresponding dependence upon the gravitational field.

Mikic et al. (1970) developed an early model for bubble growth in a uniformly superheated liquid under inertia and diffusion controlled growth conditions. After they extended their work to bubble growth in non-uniform temperature fields.

Van Stralen et al. (1975) and Mei et al. (1995) identified clear discrepancies between many such early modeling efforts and extensive data available at the time. Mei et al. (1995) submitted a numerical analysis detailing bubble growth in saturated heterogeneous boiling that considered:

- energy balance on the vapor bubble,
- liquid microlayer under the bubble,
- the heater.

They used a vapor bubble shape parameter and micro-layer wedge parameter to provide an agreement with experimental data. Whereupon, in the second part of the study they presented an assay on the dependence of bubble growth rate and the thermal field within the heater on four governing dimensionless parameters:

- Jacob number,
- Fourier number,
- solid-liquid thermal conductivity ratio,
- solid-liquid thermal diffusivity ratio.

Klausner et al. (1993) created a prediction model for vapor bubble departure. The model is based on the onset instability between a quasi-steady drag force, the unsteady component of the drag force due to asymmetrical bubble growth, and the surface tension force in the flow direction. They noted a significant dependence on wall superheat and liquid velocity. The departure diameters that was increased and decreased basing on, respectively, an increase and decrease in vapour quantities.

Zeng et al. (1997) updated this model including determination of the bubble inclination angle as part of the solution rather than as a required input to the model. They supposed that surface tension force at departure and lift-off can be neglected, and the bubble contact area and contact angles are not necessary to solve the model. Obtained data is in a good agreement with available experimental data.

Thorncroft et al. (1999, 2001) proposed another model constructed from first principles and related the forces affecting a vapor bubble during its life through Newton's Law. Bower et al. (2002) discussed the model. The force balance can be expressed as:

$$\vec{F} = \vec{F}_{Body} + \vec{F}_S + \vec{F}_B + \vec{F}_{CP} + \vec{F}_{FS} + \vec{F}_{AM} + \vec{F}_{QS} + \vec{F}_{SL} + \vec{R} = m_b \frac{dV}{dt}$$

Where the described forces are:

- Fr_{Body} is the body force acting on the bubble.
- Fr_S is the surface tension force integrated around the base of the bubble.
- Fr_B is the buoyancy force due to the liquid-vapor density difference.
- Fr_{CP} is the contact pressure force due to the pressure difference inside and outside the top of the liquid-vapor interface.
- Fr_{SL} is the shear lift force due to pressure gradients around a growing bubble.
- Fr_{QS} is a quasi-steady drag force of the bulk fluid.
- Fr_{AM} is the mass force from unsteady Bernoulli equation
- Fr_{FS} is the free-stream acceleration force
- R is the reaction force at the heated surface

The detailed forces are applicated to the bubble growth in a bulk liquid flow parallel to a heater surface oriented at some angle relative to the direction of gravity, as shown in Figure (34).
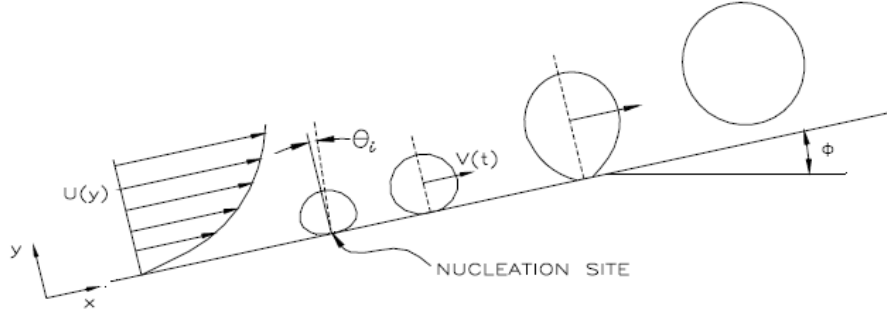
Figure 34: detailed forces are applicate to the bubble grow for Thorncroft et al. (2001)

The velocity field at the center of the bubble, the inclination angle, and the growth rate are inputs of Thorncroft et al. (2001) model. The Reichardt's expression is used to estimate the velocity of the bulk liquid at the bubble center of mass. Growth rates are approximated by the diffusion-controlled bubble growth solution as described by Zuber et al. (1997). The inclination angle is difficult to determinate due to the deformable nature of the bubble interface. However, the inclination angle is approximated to 45° in horizontal upper flow. The comparison of the departure diameters generated from computational solutions of this model at various conditions are in a good agreement with experimental results.

The model works well with a good range of fluids and Jacob numbers. For high mass velocity, the model is gravity independent. The correlating parameter ψ is plotted versus Jacob number, in figure (35), to give an indication of this phenomena.
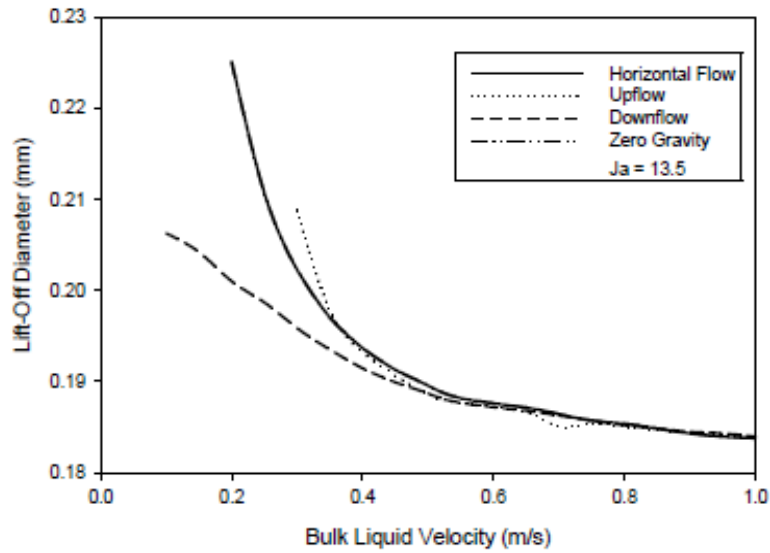
Figure 35: Lift-off diameters for different flows with different liquid velocity for Thorncroft et al. (2001)

These correlating parameters are defined as:

$$Ja = \frac{\rho_l c_{p,l} \Delta T_{sat}}{\rho_v h_{fg}} \quad \psi = \frac{U_l \mu}{\sigma} \frac{\rho_l}{\rho_l - \rho_v} = \frac{We}{Re} \frac{\rho_l}{\rho_l - \rho_v}$$

Due to its governing influence on heat transfer, the vapor bubble growth rate and the related departure phenomena have been the subject of considerable investigation. However, the study of Thorncroft et al. (2001) does not report growth rate. Instead the critical bubble dynamics to assessing the nature of a varying gravitational field on boiling heat transfer was investigated. Figure (36) gives an indication to the gravity dependent range.

$$\psi = \frac{U_l \mu}{\sigma} \frac{\rho_l}{\rho_l - \rho_v}$$
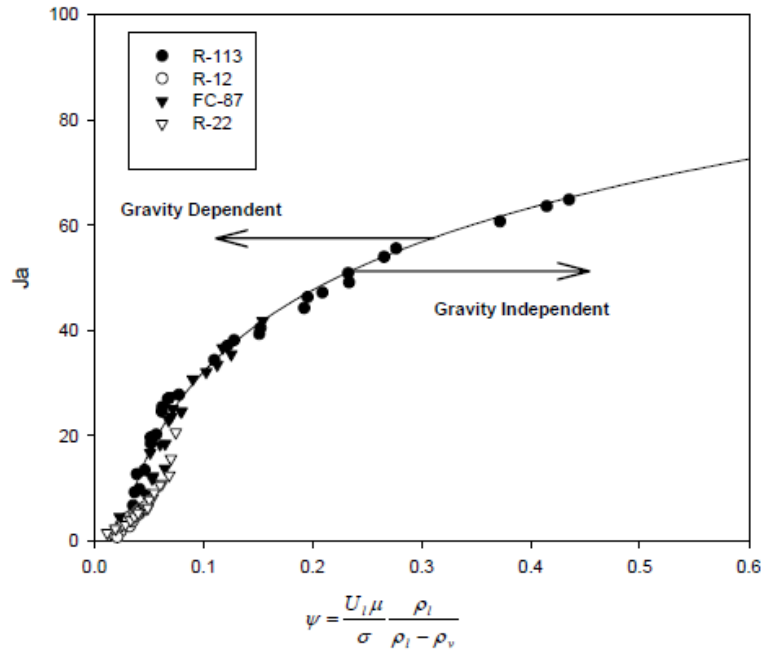
Figure 36: Gravity dependent range in function of Ja and ψ for Thorncroft et al. (2001)

Zhao et al. (2007), Rezkallah et al. (1999) and Lowe et al. (1999) made a two-phase flow pattern study under microgravity conditions in a *9.5 mm* diameter channel. The authors proposed a two-phase flow transition model for channels under microgravity conditions based on various Weber numbers. They observed that inertia and surface tension forces were dominant as opposed to buoyancy for microgravity flows and thus used a new Weber number in a new correlation to determinate flow regime transitions. The proposed flow pattern map can be divided into three distinct zones:

- the surface tension dominated zones where the bubbly and slug regimes coexist;
- the inertia dominated zone corresponding to the annular flow regime;
- a transition zone where both surface tension and inertia forces exhibit coexist.

Van Helden et al. (1995), Nydahl et al. (1989) and Zeng et al. (1999) studies indicate how buoyancy forces play a significant role in bubble growth dynamics. The buoyancy forces influence the heat transfer from the boiling surface by either assisting or impeding the bubble departure and liftoff from the heater surface.

Kirk et al. (1995) identified for low velocity a flow regime dependent on the buoyancy force. They demonstrated that vertical up-flow produced significant heat transfer enhancement when compared with horizontal flow. The study also showed how the buoyancy effect is neglected at sufficiently high velocities, where hydrodynamic forces dominate over the buoyancy forces. Bulk fluid velocity remove vapor from the heating surface, postponing an eventually onset burnout due to the higher heat fluxes. The effect of zero gravity accelerates dry-out, buoyancy forces normally aid in sweeping large vapor volumes from the surface and allow liquid replenishment, in no-gravity environment

this phenomenon is absent. This reduced critical heat flux at micro-g conditions is a severe barrier to the implementation of two-phase flow systems.

Gersey et al. (1995) developed a model for critical heat flux based on a wavy vapor layer that can breaks down on the surface due to hydrodynamic instability. When fluid velocity increases buoyancy forces, and thus critical heat flux, became independent from the orientation of gravity.

Zhang et al. (2002) made a visual study and CHF measurements describing the effects of the direction of buoyancy force. They noted how orientation is an important factor only for lower velocities.

1.4.1.1. Conclusions

The practical difficulties of obtaining experimental data at microgravity conditions combined with the excessive cost of a spatial pumping system have hindered the utilization of two-phase flow boiling systems in space applications. However, insight into behavior of flow boiling systems at various levels of gravitational influence can be gained in some experiments on earth by varying the gravitational influence; the effect of gravity on flow boiling may be discerned. Parabolic flights are another possibility to obtain experimental results useful to create and validate models. The main effects of gravity reflect on the bubble dynamics, the buoyancy forces and the detachment point.

1.4.2. Heat Transfer in Micro-gravity

Next frontier of space heat transfer is the phase change due to the very large heat fluxes available. High thermal fluxes impact on the reduction of the size, weight, and cost of thermal management power systems. It is an central problem in space applications. As such, numerous research studies have attempted to gain a fundamental understanding and predictive capability of the phase change in reduced gravity conditions.

Roshenow et al. (1952) introduced an important concept for flow boiling heat transfer correlations. They suggested that two-phase heat transfer rate is due to two independent and additive mechanisms: bulk turbulence and ebullition.

Chen et al. (1966) proposed an extension of this concept, asserting that the application of empirical factors to these two mechanisms could allow the researcher to obtain agreement with experimental observations. Many correlations reported in the literature, used the flow boiling data obtained with Chen's technique. The Chen approach recently met some critics due to new discovered physical phenomena, which was not considered.

Gungor et al. (1986) introduced a dependence factor on heat flux due to the convective portion of boiling heat transfer. This determined that the generation of vapor could result a significant disturbance of flow at the wall and a changing in the convective heat transfer.

Kenning et al. (1989, 1991), studying the effect described by Gungor et al. (1986), hypnotizing that the micro-convection and macro-convection components of two-phase heat transfer were not independent and additive. They correlated the convective heat transfer data based on a small dependence heat flux to demonstrate their hypothesis.

Shah et al. (1982) studied the proper heat transfer coefficient. They supposed that the coefficient is larger than the convective or nucleate terms and not the simply sum of the two. However, the ther-

mal transport data for two-phase flow related with micro-gravity conditions are scarce and inconclusive.

Standley et al. (1991) conducted micro-gravity experiments using *R-11* as the working fluid in parabolic flights. The large systematic variations on the temperature and pressure measured result in a difficult interpretation of data.

Saito et al. (2005, 2007) studied heat transfer and report their data of flow boiling of water in a horizontal annulus equipped with a central heater rod during parabolic flight, which had about *22 s* of microgravity conditions. They observed that under microgravity condition, contrarily to terrestrial conditions, bubbles are hardly detached from the heater rod due to the reduction of the buoyancy. They flowed along the heater rod, and grew due to the heating by the heater rod. The coalescence become much larger, surrounding the heater in the downstream. This microgravity behavior was more noticeable in the cases of lower inlet fluid velocity, higher heat flux and lower inlet fluid subcooling. The differences between earth gravity and microgravity in the local heat transfer coefficients were very small despite the large differences of the flow regimes.

Lui et al. (1998) studied heat transfer in sub cooled flow boiling with *R113* in a tubular tests section of *12 mm* diameter and *914.4 mm* length. They observed that sub-cooled boiling heat transfer increment in microgravity conditions. Heat transfer coefficients were approximately *5* to *20%* higher in microgravity and increase with qualities. Therefore, they suggested how the greater movement of vapor bubbles on the heater surface caused a localized turbulence, which is the responsible for the increased heat transfer coefficients.

Ohta et al. (1982) studied flow boiling with *R113* in a vertical transparent tube of *8 mm* diameter and *100 mm* length. Their experimental section was internally coated with a *gold* film. The flow rate ranged from *150* to *600 kg/m²s*, and the heat flux from *2.5* to *80 W/m²*. They examined bubbly, slug and annular flow regimes observing a big variation in bubble and slug sizes due to the gravity. Moreover, they observed that the heat transfer coefficient was barely affected by the various gravity levels. Hence, they supposed that heat transfer was controlled by nucleate boiling. Figure (37) shows their results:
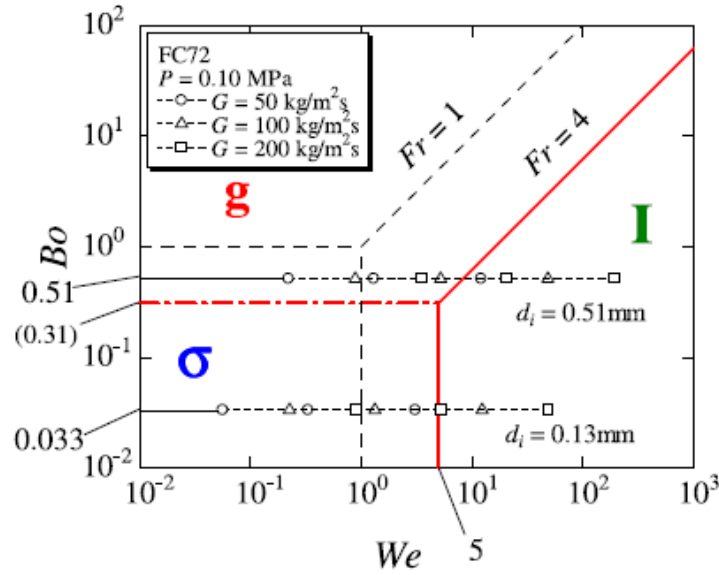
Figure 37: Boundaries for dominated regimes of buoyancy(g), surface tension(σ), and inertia(I) represented by a-dimensional sets

Ma et al. (2001) studied force convection boiling in normal and micro gravity conditions. They used *FC-72*, in a drop tower that reach *1 s* of micro-gravity conditions. The test section was uniformly heated by a flat square plate. They obtained boiling curves and flow maps for different flow rates in microgravity. From the observations resulted how the forced flow decreased the average bubble size and sustain boiling in the nucleate boiling regime in microgravity. Moreover, when flow rate increases, the heat transfer coefficient increases as well, while the average superheat of the heater surface decreases. An important result of the studies was that forced convection increases the departure of bubbles from their nucleation sites. Finally, they noted how, for high heat flux the curves, both in normal or micro gravity, bubbles tend to be close together as Reynolds numbers increase. For *Re > 10.000*, no influence of gravity has been found.

Westheimer et al. (2001), conducted a visualization experiment on flow boiling in a glass annular heat exchanger, using *R-113* as fluid, in parabolic flight. They obtained the following trends:

- flow regime transitions in micro gravity can be caused with less heat addition;
- normal gravity flow regime maps and visual data did not correspond with visual data and flow regime maps in micro gravity;
- all micro-gravity flow regime maps give a similar result for calculations of: quality, heat-transfer coefficient, and heat-exchanger temperature.
- the maximum heat transfer occurred somewhere in the heat exchanger near the transition from bubble to slug flow.

Ohta et al. (1982) studied the critical heat flux. They made few experiments, finding that *CHF* is independent from the gravity level as the fluid flow rate is increasing above a critical value.

Ma et al (2001) performed a *CHF* experiment using the same test section described previously. They observe how *CHF* in microgravity is lower than that in terrestrial gravity, but, when the flow rate increases, the two lines tend to approach each other. The authors underlined how the *CHF* values in normal and micro gravity tend to be similar in magnitude above a certain value of the flow rate.

Zhang et al. (2002) performed a *CHF* experiment in a rectangular channel on a parabolic flight using *FC-72* as process fluid. They founded how *CHF* in microgravity at low velocities is significantly smaller than in horizontal flow at terrestrial gravity. The difference in *CHF* magnitude between the two environments decreases with the increase of fluid velocity. It converges at *1.5 m/s* for *FC-72*. This result proves that is possible to design an inertia-dominated space system by maintaining flow velocities above the convergence limit.

Crowley et al. (1991) used parabolic flights to measure the liquid temperature and wall temperature in a condensing section at micro-gravity. They observed an increase in the heat transfer coefficient in micro-gravity conditions. However, no steady-state conditions were reached during the entire *20 s* micro-gravity window. The large systematic variations in time were large enough to made impossible ad interpretation of the results.

Hill et al. (1994) studied the condensation heat transfer using the data obtained by Baranek et al. (1991) to construct a micro-gravity condensation heat transfer model.

Rite et al. (1993) measured with a parabolic flight the two-phase heat transfer coefficient for various air-fluid combinations with no phase change. They founded that the differences between normal and micro-gravity heat transfer data were less than *10%* and within the uncertainty of the available heat transfer correlations.

Kirk et al. (1995) observed an increment of the heat transfer when the heating surface is rotated from horizontal towards vertical. They also found an increment for very low heat flux if the heater was downward facing and if velocity is sufficient to sweep away vapor bubbles. The slide of vapor bubbles along the heated surface was reputed the bolstering element of the heat transfer. A reduced effect manifest for test section orientation at the highest tested mass flow velocity of *0.32 m/s*.

Rite et al. (1997) performed both normal and micro-gravity experiments aboard a parabolic flight and observed low heat transfer coefficients in micro-gravity. The heat transfer coefficient drops along the length of the heating surface in micro-gravity while it increases in normal gravity. The authors supposed how the liquid-vapor slip reduces the thermal flow entry lengths in normal gravity flow. While it was not present in micro-gravity flow due to the absence of buoyancy forces. It is the most probable cause of the reduction of the heat transfer. This influence is weaker for higher velocities.

Miller et al. (1993) and Rite et al. (1997) studied a flow boiling regimes in which the pressure drops and heat transfer coefficient seemed to not be related with gravity. The purpose of this investigation is to investigate the bounds of gravity independent heat transfer and assess the predictive capabilities of the detailed bubble dynamics model that analytically exhibits the diminishing effects of gravity.

1.4.2.1. Conclusions

Considering the totality of the prior gravity experiments appears to be a significant confusion in flow boiling. It was due to the insufficient data. Therefore, is difficult to design heat exchangers for microgravity applications that cover all boiling and two-phase flow regimes.

The convection phenomena guide the heat transfer in a two-phase flow at low gravity. Can be distinguished two types of convection, the micro and macro-convection:

- Micro-convection refers to the heat transfer due to the liquid vaporization during the bubble nucleation and the subsequent growth, it continues up to the detachment from the heating surface.
- Macro-convection refers to the heat transfer that is facilitated by the bulk two-phase turbulent flow.

Both processes, as well as the overall heat transfer rate, depend on the dynamics and detachment of vapor bubbles. As suggested in the last paragraph, bubble dynamics govern the boiling process in the sub-cooled region and is independent from the gravitational field. The heat transfer coefficient should also remain constant as orientation of the gravitational force is changed. However, due to the limited availability of flight opportunities, the experimental activity in this area is still quite fragmentary and phenomenon involved in flow boiling in microgravity is far to be comprehended. The main conclusions that can be taken are:

- results on heat transfer are contradictory, spanning form increase to decrease with respect to terrestrial gravity;
- the effect of gravity level on heat transfer strongly depends on the flow pattern;
- inertial effects play a fundamental role in microgravity flow boiling heat transfer as, added up to the buoyancy force, it may overcome it; the thresholds beyond which inertial effects are dominant over buoyancy effects must be carefully determined;
- a systematic study of flow boiling heat transfer is necessary to create a consistent data set for design purposes and to better establish the flow boiling heat transfer knowledge in microgravity.

1.5. Flow Instabilities

During the experiments researchers found problems with attaining stable flows. Some report large flow oscillations that result in a vapor back flow into the inlet header, while others report smaller, periodic fluctuations. A discussion on these instabilities on two-phase flows in micro-channels is presented below.

Wen et al. (2010) made a particularly well documented study on periodic pressure and saturation temperature. They made simultaneous measurements of local pressures and their difference and filmed with high-speed camera the process determining the velocity of the bubbles, and located local nucleation sites. Figure (38) shows the results of their work. Nucleation sites are visible in the image.
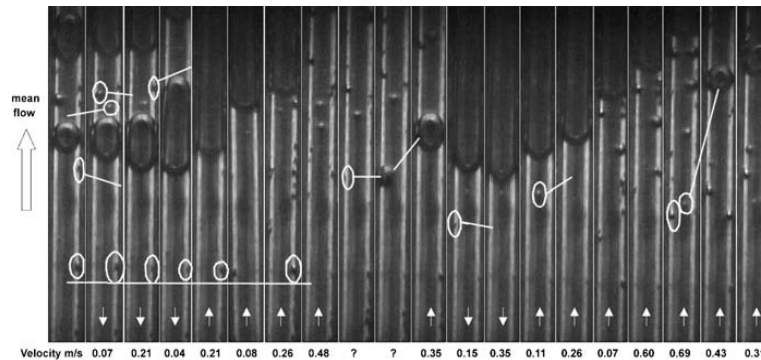
Figure 38: Images of Wen et al. (2010) with velocities during boiling of water in a *2 mm* channel

They observed that the nucleation and growth of bubbles were influenced by the compressibility of the vapor at the inlet and by other less meaningful events happening along channel, including at the exit. These events could be the cause variability in the frequency of formation of elongated bubbles and the length of the bubbles. They also observed the bubbles coalescence that combines small bubbles in an elongated bubble. This phenomenon causes a significant and cyclical fluctuation in the saturation and wall temperatures. A preliminary model was also proposed to explain the pressure waves they measured.

Some researcher studied the dynamic flow instability in a macro or micro channel. They combined set of parameters that seemed to be reflected on the flow instability process. For macro-channels that there are three types of origin of oscillation: pressure drop, density wave, and thermal. With respect to microchannel, there have been only a handful of studies.

Peles et al. (2010, 2011) observed the flow boiling in microchannels and developed a non-dimensional model. Their model work for outlet vapor quality less than unity. The unsteady flow was divided in two parts that used different models, one for the vapor and one for the liquid.

Hetsroni et al. (2003) studied the high heat fluxes created in a semi-periodic rewetting and refilling multi-microchannel. They observed a cyclic period on the order of *1 Hz* that was attributed to the cyclic bubble growth and collapse.

Brutin et al. (2009, 2011) performed a two-phase instability experiment on a single rectangular microchannel of *0.9 mm* diameter, observing two types of behavior:

- a steady state: low amplitude pressure oscillations without a characteristic frequency
- a highly unsteady flow: fluctuations frequencies of about *3.6-6.6 Hz*.

Wu and Cheng (2006) studied boiling in silicon micro-channels with hydraulic diameters of *0.083* and *0.158 mm*. Their study established that once boiling has started, there is a cyclic variation between single phase liquid flow and two-phase flow in their channels, producing oscillations in the measured pressure drops, wall temperatures, inlet and outlet temperatures, and mass flow rate. They concluded that the unsteady flow was sustainable if the pressure drop and mass flow were out of phase.

Xu et al. (2006) investigated on static and dynamic flow instabilities in a multi-micro channel heat sink. They explained the instability exploiting the curve shown in the next Figure (39).
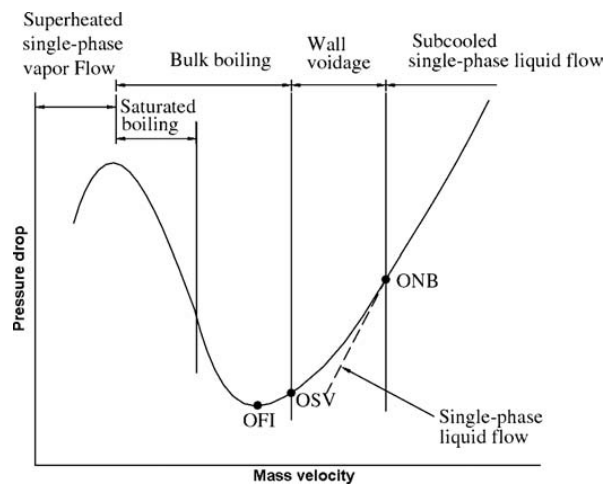
Figure 39: Demand curve of Xu et al. (2006) showing the pressure drop plotted versus the mass velocity at a given inlet temperature and heat flux.

Where:

- OFI is Onset of Flow Instability,
- OSV is Onset of Significant Void,
- ONB is Onset of Nucleate Boiling

In this diagram sub-cooled liquid flow occurs in the channel. When the mass velocity decrease to the value at which the actual curve deviates from the calculated one the fluid reaches the onset of nucleate boiling (ONB). Decreasing mostly the mass velocity leads to the Onset of Significant Void (OSV), which occur at a slightly higher mass velocity than the Onset of Flow Instability (OFI). When the pressure drop is higher than Onset of Flow Instability the two different mass velocities yield the same pressure drop and hence the fluid oscillates between these two conditions. Later they proposed an expression to predict the OFI mass velocity.

Piasecka et al. (2004) extensively studied the instabilities due to the boiling incipience in narrow channels. In their studies, only one side of the channel is heated. They found the location of incipience at the minimum local heat transfer coefficient and maximum local wall temperature. System pressure, inlet sub-cooling, and flow rate influenced the heat transfer coefficient at the location of boiling incipience.

1.6. Pressure drops

Pressure drops in saturated flow boiling were largely analyzed at macro scale, Ould Didi et al. (2002) compared seven of the most quoted macro-scale methods in the literature to determinate frictional pressure drop on a 788 points database in two horizontal macro-scale test sections of 10.92 and 12.00 mm diameter for five fluorocarbon refrigerants. They found that the methods of Muller-Steinhagen and Heck (1986) and Gronnerud (1972)] gave the best predictions. Ribatski el al. (2006) compared twelve prediction methods and found as the most effective the macro-scale method proposed by Muller-Steinhagen and Heck (1986). However, they showed how none of the analyzed methods can be classified as a design tool for microscale tubes. As described in Lee and Mudawar (2008), the inlet subcooling enhances the heat fluxes transferred in the exchanger by using both the sensible and latent heat of the fluid compared to the mostly latent heat in saturated flow boiling.

Most common micro-heat exchangers have two shapes: small straight circular tubes and rectangular channels. Due to the nature of the geometries involved, the pressure drop vary widely from large to small tubes and channels. The implementation of this kind of heat exchanger is hampered by the limited understanding of the momentum and thermal transport characteristics in micro-scale. Due to the small hydraulic diameter used in micro- and mini-exchangers, excessive pressure drop is always a concern, since these devices are typically used in combination with pumps with limited pumping power capability. A few published studies discuss pressure drop and hydrodynamic instability of flow boiling in mini/micro-tubes. These concerns are compounded when the fluid flow is in transition between laminar and turbulent flows, where there is no valid and established model. In microscale Zhang and Webb (2001), Kuwahara et al. (2004) obtained good predictions of their data for R134a by using the Friedel (2004) correlation. Also, Lazarek and Black (1982) studied the problem obtaining good forecasts by using a value of C = 30 in the generalized Chisholm (1967) and Lockhart–Martinelli (1949) correlations. Along this direction, Qu and Mudawar (2003), Lee and Mudawar (2005) and Lee and Garimella (2008) developed their individual flow boiling pressure drop models based on their experimental data developed in microchannel heat sinks. Mishima and Hibiki (1996) obtained reasonably good predictions for their frictional pressure drop data by correlating the Chrisholm (1967) parameter in the Lockhart–Martinelli (2005) correlation as a function of the tube diameter. Bowers and Mudawar (1994) analyzed flow boiling pressure drop of refrigerant R-113, using a homogenous equilibrium model, in both mini and micro-channel obtaining a good agreement. Two-phase hydrodynamic instabilities in parallel mini/micro-channels were addressed by Kandlikar et al. (2001) and Hetsroni et al. (2001). Tran et al. (2000) studied flow boiling pressure drop of three different refrigerants in single tubes and for a single rectangular channel. Kim and Mudawar (2013) developed a model, using a database of 2378 experimental points, that considers six dimensionless parameters to calculate the Lockhart–Martinelli C parameter.

2. Python Programming

2.1. What Is Python?

Python is a modern, general-purpose, object-oriented, high-level programming language. The main Python characteristics are the clean and simple language that is easy to red and intuitive. The best technical features are:

- *The dynamical type*: The code does not need to define the type of variables, function arguments or return types.
- *The automatic memory management*: No need to explicitly allocate and reallocate memory for variables and data arrays. No memory leak bugs.
- *The interpreter*: No need to compile the code. The Python interpreter reads and executes the python code directly.

The main advantages are easiness of programming, minimization of the time required in development and debugging.

Moreover, a well-designed language may encourage many good programming practices:

- Modular and object-oriented programming, good system for packaging and re-use of code.
- Documentation tightly integrated within the code.

Python have a large standard library, and an ample collection of add-on packages.

Obviously, the code has some disadvantages. Since Python is an interpreted and dynamically typed programming language, the execution of python code can be slow compared to compiled programming languages, such as C++ and Matlab. Python is also decentralized, with different environment, packages and documentation spread out at separate places. It is harder to get started.

2.2. What Makes Python Suitable for Scientific Computing?

Python has a strong position in scientific computing due to the large community of users. It makes easy to find help and documentation. Moreover, many scientific libraries and environments are available:

- numpy: Numerical Python
- scipy: Scientific Python
- matplotlib: Graphics library

A reliable performance is granted due to close integration with time-tested and highly optimized codes written in C and Fortran:

- blas, altas blas, lapack, arpack, Intel MKL, ...

Python can support:

- Parallel processing with processes and threads
- Inter-process communication (MPI)
- GPU computing (OpenCL and CUDA)

In addition, the code is readily available and suitable for use on high-performance computing clusters. At the end it has no license costs that can be traduced in no unnecessary use of research budget.

Figure (40) shows an example of scientific python software stack
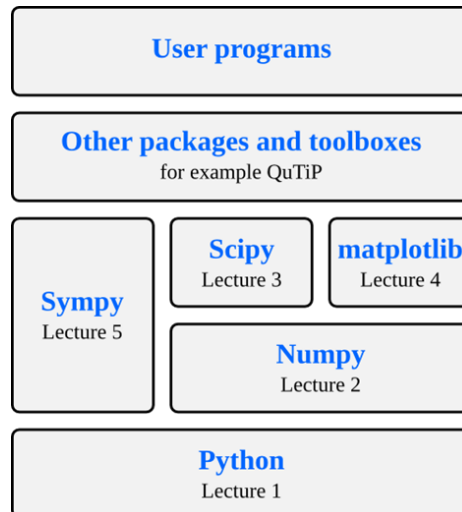
Figure 40: scientific python software stack

2.3. Python Environments

Often referred to Python not only for a programming language, but also the interpreter, *CPython*, that runs the python code on a windows computer.

There are also many different environments through which the python interpreter can be used. Each environment has different advantages and is suitable for different workflows. One strength of python is its versatility and that it can be used in complementary ways.

2.3.1. Python Interpreter

Python programming language use the Python interpreter to run python code. The interpreter is a program that read and execute the python code in files passed to it as arguments. At the command prompt, the command `python` is used to invoke the Python interpreter. Next figure (41) shows the interpreter.

Figure 41: Python interpreter

The standard python interpreter is not very convenient for work, due to many evident limitations.

2.3.2. Spyder

Spyder is a MATLAB like IDE for scientific computing with python. It has the advantages of a traditional IDE environment. Everything from code editing, execution and debugging is supported in a single environment and work on different calculations can be organized as projects in the IDE environment.

Some advantages of Spyder:

- Powerful code editor, with syntax highlighting, dynamic code introspection and integration with the python debugger.
- Variable explorer, IPython command prompt.
- Integrated documentation and help.

Next figure (42) shows Spider.
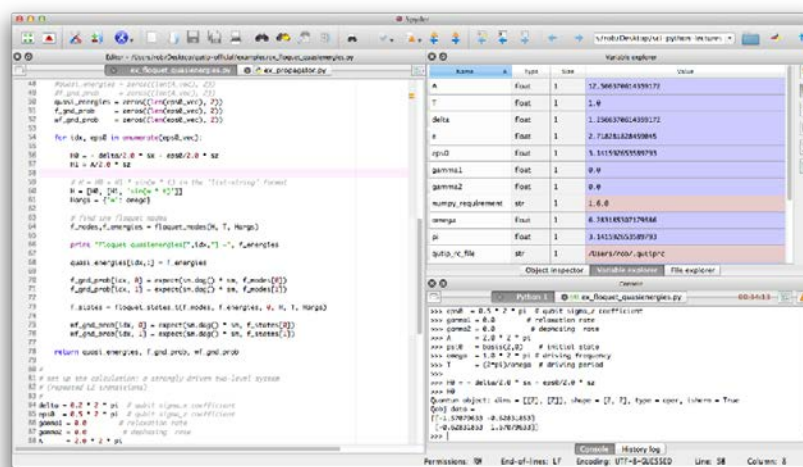
Figure 42: Spyder

2.3.3. Versions of Python

There are currently two versions of python: Python 2 and Python 3. Python 3 will eventually update Python 2, but the backward compatibility it is not granted. A lot of existing python code and packages has been written for Python 2, and it is still the most common version. It is probably easier to work with Python 2 for now, because it is more widespread and readily available via prebuilt packages or binary installers. Several versions of Python can be installed in parallel. The programs in annex is programmed with Python 2.7.

2.4. Why Python Is Better Than Matlab

It is not easy to choose a programming language for scientific applications. The most spread languages for science is probably Matlab. This paragraph discuss why was chosen python and not Matlab for this research. The main arguments on behalf of python are:

- Python is free and open source, whereas Matlab is a closed-source commercial product.
- The Python language is easies that Matlab's one.
- Python integrates better with other languages
- Python includes natively a large number of general-purpose or more specialized libraries, and Python users continuously develop external libraries.

3. Heat transfer models

This chapter is an analysis in full detail of the correlation used to calculate the heat transfer coefficient. The programs that use correlations are in annex. Following analysis starts from the models' assumptions to arrive to the used formula. These descriptions are important to understand models' behavior and the range of usability. No modification to suite the model to the experiment are made.

3.1. The Three-Zone Model

The three-zone model describes the evaporation of an elongated bubble in a micro-channel as a sequential and cyclical passage of a liquid slug, an evaporating elongated bubble, and a vapor slug if the liquid film dries out.

3.1.1. Introduction to model

The first draft of flow boiling model for micro-channels was made by Jacobi (2002) and Thome. They modelled the thin film evaporation of the liquid film trapped between these bubbles and the channel wall, accounting for the liquid-phase convection in the liquid slugs between the bubbles. They want to demonstrate that the thin film evaporation mechanism was the principal heat transfer mechanism in micro channels for slug flows. Specifically, they showed that the thin film heat transfer mechanism along the length of the bubbles is dominant if compared to the liquid convection occurring in the liquid slugs. Thin film evaporation heat transfer mechanism, without any local nucleation sites in slug flows, yields the same type of functional dependency as the nucleate boiling curve. Therefore, being nucleate boiling in micro channels the only heat transfer mechanism upstream at or near the onset of boiling for very low vapor qualities, they concluded that for a downstream flux the main mechanism is the thin film evaporation. It dominates boiling in micro channels in the slug flow regime, up until the flow regime changes to annular. Thus, for this reason the macro scale flow boiling correlations cannot fit for micro channel flow boiling data unless such models include a nucleate boiling heat transfer dependency. However, macro scale flow boiling correlations and nucleate pool boiling correlations do not actually model nucleate boiling. The heat flux dependency of process is considered empirically. The Jacobi and Thome slug flow model shows a strong, direct dependency of heat transfer by the bubble frequency in the thin film evaporation process of elongated bubbles. Therefore, this probably explains why this pseudo-nucleate boiling dependency is incorrectly identified earlier papers.

Thome, Dupont and Jacobi (2004) proposed a three-zone flow boiling model for slug flow in micro channels. This model is an updated version of the prior two-zone model. Only the three-zone model will be described here in this chapter in detail.

3.1.2. Model description

Figure (43) shows a representation of the three-zone model with the evolution of successive bubbles.
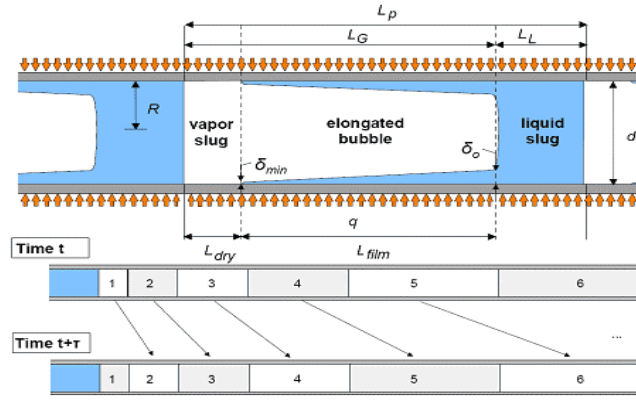
Figure 43: Three-zone heat transfer model of Thome, Dupont and Jacobi (2004) for the elongated bubble flow regime in micro channels.

Where:

- L_p is the total length of the pair or triplet,
- L_L is the length of the liquid slug,
- L_{dry} is the length of dry wall in the vapor slug,
- L_G is the length of the bubble including the length of the dry wall,
- L_{film} is the length of the liquid film trapped by the bubble,
- R is the internal radius of the tube,
- δ_0 is the thicknesses of the liquid film trapped between the elongated bubble,
- δ_{min} is the channel wall at its formation and at dry out of the film.

The local vapor quality, heat flux, micro channel internal diameter, mass flow rate and fluid physical properties at the local saturation pressure are input parameters to the model.

The three-zone model predicts the heat transfer coefficient of each zone and the cyclic local time-averaged heat transfer coefficient at a fixed location. The model works for a micro channel during the evaporation of an elongated bubble and with a constant, uniform heat flux. The elongated bubbles grow in axial length, trapping a thin film of liquid between the bubble and the inner tube wall as they flow along the channel. The thickness of this film plays a key role in heat transfer. At a fixed location, the process is assumed to proceed as follows:

1. a pure liquid slug passes; which not have any entrained vapor bubbles,
2. an elongated bubble passes; the liquid film is formed from liquid removed from the liquid slug,
3. a vapor slug passes; if the thin evaporating film of the bubble dries out before the arrival of the next liquid slug.

The cycle repeats itself for every arrival of the next liquid slug. The repetition frequency is:

$$f_p = \left(\frac{1}{\tau}\right)$$

Hence, a liquid slug and an elongated bubble pair, or a triplet of liquid slug, an elongated bubble and a vapor slug pass this fixed point at a certain frequency that is a function of the formation rate of the bubbles upstream, and that is assumed to be constant downstream.

In brief, the heat transfer model was reassumed by the authors as follows.

"The homogeneous model of two-phase flow is utilized to obtain the void fraction and two-phase velocity along the channel at the desired vapor quality. From the pair or triplet frequency, the local length of the pair or triplet in the channel passing by this point is calculated as a function of the vapor quality. It is obtained from an energy balance of the mass flow rate and the uniform heat flux applied to the inner channel wall. The respective lengths of the liquid slug L_L and vapor L_G in the pair or triplet are obtained directly from the void fraction at this location, ignoring the small fraction of liquid in the film. Then, from the local mean velocity of the liquid slug, the initial liquid film thickness δ_0 is calculated and dry out of the wall occurs if the film thickness reaches a predetermined value of δ_{min} before the arrival of the next liquid slug. Mean heat transfer coefficients are determined from the liquid and vapor slugs while the average value of the heat transfer coefficient of the evaporating film is determined from conduction across its varying thickness. The time-averaged heat transfer coefficient is then determined at the local vapor quality for one pair or triplet passing by this location of the channel with respect to the residence time of each process during one time cycle τ."

The model makes the following assumptions:

1. The flow is assumed to be an elongated bubble slug flow.
2. The flow is homogeneous: vapor and liquid travel at the same velocity.
3. The heat flux is uniform and constant with time along the inner wall.
4. The fluid is saturated liquid at the entrance of the channel with elongated bubbles generated at an unknown frequency f_p.
5. The temperatures of the liquid and vapor remain constant, which means that all the energy delivered to the fluid is used for vaporization. Neither the liquid nor the vapor is superheated or sub-cooled.
6. The local saturation pressure is used to determine the local saturation temperature. Pressure drop is ignored.
7. The liquid film remains attached to the wall whilst the influence of vapor shear stress on the liquid film is negligible. Therefore, the film remains smooth without ripples.
8. The film thickness δ_0 is much smaller than the tube radius of R.
9. The thermal inertia of the channel wall can be neglected during this cyclical heat transfer process.

To develop the model, an experimental database of local heat transfer coefficients was taken from six different laboratories, it covers seven different fluids: *R-11*, *R-12, R-113, R-123, R-134a, R-141b* and *CO2*. Dupont, Thome and Jacobi (2004) took *1591* test from the literature. The database comprehended channel diameters from *0.77* to *3.1 mm*, mass velocities from *50* to *564 kg/m²s*, pressures from *1.24* to *57.66 Bar*, heat fluxes from *5* to *178 kW/m²*, and vapor qualities from *0.01* to about *0.99* with a setup of five single channel and two multi-micro channels.

3.1.2.1. Bubble Frequency

One of the model hypothesis is that bubble nucleation occurs at the location where the fluid reaches saturation. This place is at *x = 0*. The earlier model of Thome et al. (2002) assumed that these small bubbles grew in a uniformly superheated liquid to a diameter equal to the internal diameter of the channel before departing. Instead, Plesset et al. (1994) proposed a heat diffusion limited model to obtain the rate of bubble growth:

$$r(t) = \frac{\rho_L c_{pL} \Delta T_{sat}}{\rho_G h_{LG}} \left[12 a_L t / \pi \right]^{1/2}$$

Where:

- a_L is the liquid thermal diffusivity,
- t is the bubble growth time,
- ΔT_{sat} is the wall superheat.

Each bubble divides the liquid flow into successive pairs or triplets. If there is no waiting time between successive bubbles, the frequency of bubble departure f_p and period of pair or triplet generation τ was obtained from the bubble growth rate and the internal radius of the tube R is:

$$f_p = \frac{1}{\tau} = \left[\frac{\rho_L c_{pL} \Delta T_{sat}}{\rho_G h_{LG} R} \right]^2 \left[12 a_L / \pi \right]$$

The predicted pair frequency f_p for *R-134a* using the above equation for two different superheats of *ΔT_{sat} 1 °C* and *20 °C*, in a channel of *0.5 to 2 mm* diameter, cause a bubble frequency variation from *20 Hz* to *0.05 Hz*. The frequency depends on the diameter of the micro channel. The shear stress exerted by the liquid flow in the channel force the departure of the bubble before it reached the channel diameter. Therefore, a hydrodynamic model is required to predict bubble departure and hence also bubble frequency. The bubbles tend to depart with diameters much smaller than the channel diameter before rapidly grow and coalesce downstream to form elongated bubbles. The values of f_p will be discussed later in the chapter about adjustable parameters.

3.1.2.2.   Basic Equations

By the homogeneous model hypothesis, the liquid and the vapor travel at the same mean velocity:

$$u_L = u_G$$

Where:

$$u_G = \frac{\dot{Q}_G}{A \varepsilon} = \frac{\dot{m}}{\rho_G} \left(\frac{x}{\varepsilon} \right)$$

$$u_L = \frac{\dot{Q}_L}{A(1 - \varepsilon)} = \frac{\dot{m}}{\rho_L} \left(\frac{1 - x}{1 - \varepsilon} \right)$$

The cross-sectional void fraction can be obtained matching velocity as a function of vapor quality:

$$\varepsilon = \frac{1}{1 + \left(\frac{1 - x}{x} \right) \frac{\rho_G}{\rho_L}}$$

The assumptions are:

- it is a homogeneous void fraction model,

- the volumetric void fraction is equal to the cross-sectional void fraction in a homogeneous flow.

Form the equality, the pair or triplet velocity is:

$$u_p = \dot{m}\left(\frac{x}{\rho_G} + \frac{1-x}{\rho_L}\right)$$

For a normal fluid:

$$\rho_L >> \rho_G$$

Therefore, the pair or triplet velocity can be assumed to vary almost linearly along the tube:

$$u_p \approx \dot{m}\left(\frac{x}{\rho_G}\right)$$

A pair or triplet passes during each time τ. It is thus possible to deduce the mean equivalent length of this pair or triplet using the following expression:

$$L_p = u_p\tau = \tau\dot{m}\left(\frac{x}{\rho_G} + \frac{1-x}{\rho_L}\right)$$

L_p is the apparent length of the pair or triplet that can be seen by an observer at any location on z. To evaluate the residence time t_G of an elongated bubble at location z ($z = 0$ is assumed to be at the saturation point $x = 0$). The equivalent length of the vapor L_G is calculated using the local void fraction:

$$L_G = \varepsilon L_p = \frac{\tau\dot{m}}{\rho_G}x$$

Instead, the vapor residence time t_G is:

$$t_G = \frac{L_G}{u_p} = \frac{\tau}{1 + \dfrac{\rho_G}{\rho_L}\dfrac{1-x}{x}}$$

The time t_G corresponds to the period employed by vapor to pass through the cross section in a point on z.

The equivalent length of the liquid slug L_L and the liquid residence time t_L is:

$$L_L = (1-\varepsilon)L_p = \frac{\tau\dot{m}}{\rho_L}(1-x)$$

$$t_L = \frac{L_L}{u_p} = \frac{\tau}{1 + \dfrac{\rho_L}{\rho_G}\dfrac{x}{1-x}}$$

The time t_L corresponds to the period employed by a liquid slug to pass through the cross section at location z. Finally, the following relations are valid:

$$t_G + t_L = \tau$$

$$L_G + L_L = L_p$$

3.1.2.3. Liquid Film Thickness

The initial liquid film thickness δ_0 at the front of the bubble is an important parameter for the model. The thickness influences the evaporation process and thus a relation for predicting the initial thickness of the film δ_0 is required. Thome, Dupont and Jacobi (2004), elaborate two film thickness correlations proposed by Moriyama and Inoue (1996), changing the Bond number into Weber number and expressing δ_0 as a function of the pair velocity u_p.

Moriyama and Inoue (1996) in their model experimentally measured the radial liquid film thickness of bubbles growing between two parallel, heated transparent plates. To obtain data set they used an experimental technique comprehensive of video vapor front tracking and a wall transient temperature analysis. The experimental section has a gap between the two plates of about *0.100* to *0.400 mm* and the tests were conducted with *R-113*. From their experiments resulted a large superheat or high bubble velocity at the viscous boundary layer controlled the liquid film formation thickness δ_0. Instead of a low bubble speed or for a small gap between the plates, the surface tension force is dominant. Moriyama and Inoue (1996) proposed two empirical correlation to take in account both regimes.

In the three-zone model by Thome, Dupont and Jacobi (2004), these two expressions were combined with an asymptotic *8th* power expression. To combine the expression some assumptions from parallel plate geometry to the present circular channel geometry were necessary. However, the two expressions for δ_0 of Moriyama and Inoue (1996) are valid only for *R-113* and for the analyzed range of gaps. Therefore, an empirical correction factor $C_{\delta o}$ was added. Its value was statistically taken out by the heat transfer database. The default given value is $C_{\delta o} = 0.29$. This parameter is included in the asymptotic initial liquid film thickness model:

$$\frac{\delta_o}{d_i} = C_{\delta_o} \left[3 \left(\frac{\mu_L}{\rho_L u_p d_i} \right)^{1/2} \right]^{0.84} \left[\left(0.07 \, We_p^{0.41} \right)^{-8} + 0.1^{-8} \right]^{-1/8}$$

The Weber number We_p was incorrectly labeled as a Bond number in the first paper of Thome, Dupont and Jacobi (2002). It ca be expressed using the pair velocity u_p and channel diameter d_i:

$$We_p = \frac{\rho_L d_i u_p^2}{\sigma}$$

Figure (46) shows the predicted variation of the initial thickness for a liquid *R-113* film at a saturation temperature of *47.2°C* in function of the pair velocity u_p for two micro channel diameters.
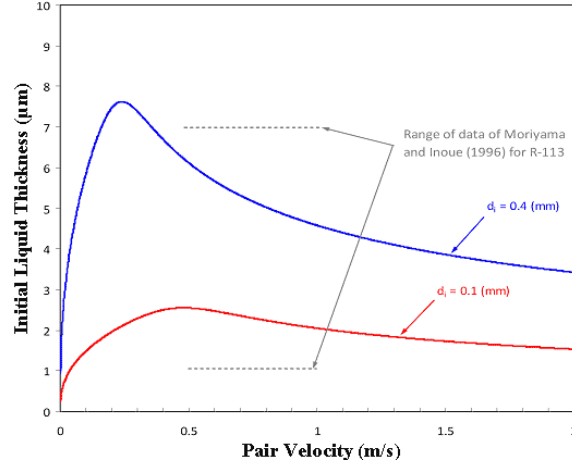
Figure 44: Predicted thickness measured by Moriyama and Inoue (1996) between two parallel plates.

The values of δ_0 change in a range from *2.1* to *6.1 μm* for pair velocities from *0.5* to *1.0 m/s*. The obtained value has the same order of magnitude as those measured by Moriyama and Inoue (1996) for *R-113* for small gaps of *0.1* to *0.4 mm* for the corresponding range of velocity.

The liquid film thickness varies from its initial value of δ_0 due to vaporization by the uniform heat flux q at the inner wall of the tube. Its actual value can be obtained by an energy balance over the differential length of the film d_z. For hypothesis it is assumed that all the energy transferred by conduction from the wall is used to vaporize the liquid. The rate of latent heat transfer depends on the rate of evaporation of the liquid phase, $\frac{dM_L}{dt}$, and hence from the assumption that $\delta \ll R$ for an annular film, this is:

$$Q = -\frac{dM_L}{dt}h_{LG} = -\rho_L 2\pi(R-\delta)\frac{d\delta}{dt}dz\,h_{LG}$$

The heat dissipated from the wall is:

$$d\delta = -\frac{q}{\rho_L h_{LG}}\frac{R}{R-\delta}dt$$

Being from assumption $\delta \ll R$, then $R - \delta \approx R$.

At $t = 0$ the film is created at position z. Integrate the above expression with the initial condition:

$$\delta(z,0) = \delta_0(z)$$

Results in:

$$\delta(z,t) = \delta_o(z) - \frac{q}{\rho_L h_{LG}}t$$

The value of $\delta_0(z)$ is obtained with the above expression. Moreover, the maximum duration of the film $t_{dry\text{-}film}$ at position z is obtained in function of the minimum thickness at dry-out δ_{min} :

$$t_{dry\,film}(z) = \frac{\rho_L h_{LG}}{q}\left[\delta_o(z) - \delta_{min}\right]$$

The actual final film thickness δ_{end} and residence time of the film t_{film} depend on if the film dries out. If the maximum duration of the film arrives is more than time employed by vapor to pass through the cross section hence the next liquid slug arrives before dry-out occurs. It can be summarized by the following equations:

$$t_{dry,film} > t_G$$

$$\delta_{end}(z) = \delta(z, t_G)$$

$$t_{film} = t_G$$

Instead if the maximum duration of the film arrives is lesser than time employed by vapor to pass through the cross section hence local dry-out occurs when the liquid film thickness reaches the minimum feasible film thickness δ_{min}. It can be summarized by the following equations:

$$t_{dry,film} < t_G$$

$$\delta_{end}(z) = \delta_{min}$$

$$t_{film} = t_{dryfilm}$$

Thus, the time duration of the liquid film on the local wall is t_{dry}:

$$t_{dry} = t_G - t_{film}$$

The equivalent length of the dry zone at the location z is obtained by the time duration of the liquid film and the velocity of the pair:

$$L_{dry} = u_p t_{dry}$$

The minimum film thickness at dry-out δ_{min} is related to the roughness of the surface, the thermophysical properties of the fluid, the contact angle between the vapor, liquid and wall, and the local hydrodynamics of the flow. Figure (45) shows the film layout.
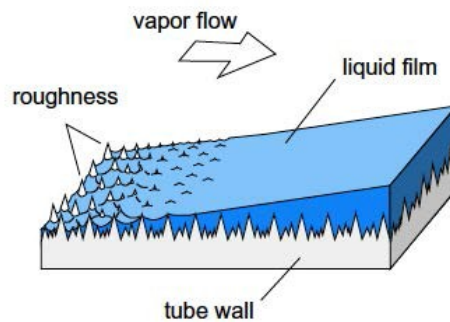
Figure 45: Transition from film evaporation to vapor convection in the dry zone from Thome et al. (2004)

Obtain δ_{min} value is beyond current modeling capabilities and thus a fixed empirical value was statistically taken out from the heat transfer database. It means value is $\delta min = 0.0000003\ m = 0.3\ \mu m$.

3.1.2.4. Heat Transfer Model

The time-averaged local heat transfer coefficient α_{film} is expressed by the following integral:

$$\alpha_{film}(z) = \frac{1}{t_{film}} \int_0^{t_{film}} \frac{k_L}{\delta(z,t)} dt$$

The hypotheses are:

- The liquid film evaporates only between the bubble and the wall,
- The thin liquid film is stagnant
- The heat transfer is only one-dimensional conduction across the film.

Integrate over the bubble passage period gives:

$$\alpha_{film}(z) = \frac{k_L}{\delta_o - \delta_{end}} \ln\left(\frac{\delta_o}{\delta_{end}}\right)$$

The value of δ_{min} is assumed to be different from zero and of the same order of magnitude as the surface roughness.

The minimum film thickness δ_{min} was taken as one of the three adjustable parameters in the three-zone model along with f_p and $C_{\delta 0}$. It was determined statistically comparing the model results to an experimental heat transfer database of seven fluids from six different laboratories.

The heat transfer coefficients for the liquid and vapor slugs are calculated from their respective local Nusselt numbers. These values are then applied to the respective equivalent lengths of the liquid slug L_L and dry wall zone L_{dry} passing by a given location z. The Nusselt number is assumed to be hydro-dynamically and thermally developing.

For laminar developing flow, for which *Re* <=2300, the London and Shah (1978) correlation is used to obtain the local tubular flow Nusselt number:

$$Nu_{lam \text{ or } turb}(z) = \frac{h * d_i}{k}$$

$$Nu_{lam}(z) = 0.455 \sqrt[3]{Pr}\left(\frac{d_i Re}{L(z)}\right)^{1/2}$$

To obtain the averaged value over the length z was used the liquid slug length L_L or vapor slug length L_{dry} as $L(z)$:

$$Nu_{lam,z} = 2 Nu_{lam}(z)$$

For transition and turbulent developing flows, the Gnielinski (1976) correlation is used for *Re* >= *2300* so that the local Nusselt number is:

$$Nu_{turb}(z) = \frac{(f/2)(Re-1000)Pr}{1+12.7\sqrt{f/2}(Pr^{2/3}-1)}\left[1+\frac{1}{3}\left(\frac{d_i}{L(z)}\right)^{2/3}\right]$$

The friction coefficient f is:

$$f = (1.58 \ln Re - 3.28)^{-2}$$

To obtain the averaged value over the length z was used again the liquid slug of length L_L or vapor slug of L_{dry} for $L(z)$. This value on z is obtained from:

$$\text{Nu}_{turb,z} = \frac{(f/2)(\text{Re}-1000)\,\text{Pr}}{1+12.7\sqrt{f/2}\left(\text{Pr}^{2/3}-1\right)}\left[1+\left(\frac{d_i}{L(z)}\right)^{2/3}\right]$$

Reynolds number Re for the phase is obtained using the channel diameter d_i, the local pair velocity u_p, and the dynamic viscosity of that phase:

$$\text{Re} = \frac{\rho u_p d_i}{\mu}$$

To avoid a discontinuity in the value of the Nusselt number at $Re = 2300$, it is used a continuous expression of the mean convective heat transfer coefficient. It is a function of Reynolds number and apply a 4th power asymptotic expression. It can be expressed as follows:

$$\alpha_{slug} = \left[\alpha_{lam}^4 + \alpha_{turb}^4\right]^{1/4} = \frac{k}{d_i}\left[\text{Nu}_{lam}^4 + \text{Nu}_{turb}^4\right]^{1/4}$$

The expression is valid for the liquid in the slug and for the vapor in the dry zone in their respective equivalent lengths, L_L and L_{dry}.

At the end, from these three heat transfer coefficients, one for every zone, the time-averaged local heat transfer coefficient α_{tp} is calculated. It is mean over the period τ. Hence the local, time-averaged heat transfer coefficient of a pair or triplet passing by location z is:

$$\alpha_{tp} = \frac{t_L}{\tau}\alpha_{slug,L}(z) + \frac{t_{film}}{\tau}\alpha_{film}(z) + \frac{t_{dry}}{\tau}\alpha_{slug,G}(z)$$

3.1.2.5. Modified Relations

To simplify the model is possible to change some equations. One of the simplification that are made is on the minimum film thickness. It is changed to the measured wall roughness because the roughness breaks the liquid film. It is important to mention that this has been already proposed in the previous studies of Agostini et al. (2008) in *silicon* test section, Ong and Thome (2011) in *stainless steel* micro tubes, Vakili-Farahani et al. (2012) in *aluminium* tubes, while the study of Costa-Patry et al. (2011, 2012) included *silicon* and *copper* test sections.

Moreover, the developing flow Nusselt number correlations were replaced by fully-developed ones for laminar and turbulent flow, respectively:

$$Nu_{lam} = 4.36$$

$$Nu_{turb} = \frac{\text{Pr}\frac{\xi}{8}(\text{Re}-1000)}{1+12.7\left(\frac{\xi}{8}\right)^{0.5}\left(\text{Pr}^{\frac{2}{3}}-1\right)}$$

Where ξ is the frictional pressure drop coefficient.

Finally, the liquid film heat transfer from is modified in:

$$\alpha_{film} = \frac{k_l}{\delta_0 - \delta_{end} + 1 \times 10^{-9}} \ln\left(\frac{\delta_0}{\delta_{end}}\right)$$

3.1.2.6. Adjustable Parameters

The three-zone model has three adjustable parameters, all of which are difficult to predict theoretically. They are:

- δ_{min} is the minimum film thickness reached at dryout. It is related to roughness of the surface, the thermo-physical properties of the fluid and the hydrodynamics of the flow. It can be approximated with the value to the surface roughness as a first estimation when available;
- $C_{\delta 0}$ is the correction factor used on the prediction of δ_0. It considers the difference between the fluids and the geometries. In the standard database used for examples it came from to the original *R-113* test;
- f_p is the pair or triplet frequency. It is a complex function of the bubble formation and coalescence process. Moreover, it is influenced by the diameter of the channel, its surface roughness, the nucleation process, the bubble departure dynamics, the coalescence phenomena, etc.

Dupont, Thome and Jacobi (2004) made a first analysis for the optimum values of the parameters f_p, $C_{\delta 0}$ and δ_{min} in the second part of their study. This was done by applying the three-zone model to each individual series of local boiling data points of their entire database to find the optimum values of the parameters for each individual set of data. Once the set of optimum values for all the series were determined, they were then used to develop the general methods.

The optimum values for f_p were found to be strongly dependent only on the heat flux. Moreover, it has no clear dependency on any other parameter. Therefore, plotting the identified pair frequencies in function of the heat fluxes for each series in the database, shows nearly parallel lines for each fluid in each study. Hence, the following power law expression give the best fit to these semi-empirical values:

$$f_p = \frac{1}{\tau} = \left(\frac{q}{q_o}\right)^{1.74}$$

The expression has the units of *Hz* while the units of q and q_0 are *W/m²*. The pair frequency is supposed to be a function of the fluid physical properties. A reduced pressure relation gives the effect of the fluid physical properties on the expression via the reference heat flux q_0:

$$q_o = 3328 \left(\frac{p_{sat}}{p_{crit}}\right)^{-0.5} = 3328\, p_r^{-0.5}$$

However, these equation permits to calculate the pair or triplet from the local heat flux and from the local saturation conditions in first approximation. It is important that the model is based on a local energy balances, which makes the model impossible to be implemented for a non-uniform heat flux q along the channel and around its circumference.

The correction parameter $C_{\delta 0}$ results from all experimental tests in the database to be ranged from *0.34* to *1.23* with the mean value of *0.84* and a standard deviation of *0.28*. This mean value near unity gave means a good approximation capacity for the expression used to calculate δ_0. However, the best value for $C_{\delta 0}$ is *0.29* and this is the value that must be used with the three-zone model.

If the minimum film thickness δ_{min} coming from the database is used to obtain the standard logarithmic expression for $\alpha_{film}(z)$ it is possible to takes some errors due to the sensibility of the relation to δ_{min}. In fact, when the value of δ_{min} tends to zero the value of $\alpha_{film}(z)$ tends to infinity. In order to reduce the sensitivity of the model to this parameter, a new expression based on the average value of the film thickness is used to calculate the mean heat transfer coefficient in the film:

$$\alpha_{film}(z) = \frac{2k_L}{\delta_o(z) - \delta_{min}(z)}$$

This expression is the substitute of the logarithmic expression presented in the standard three-zone model. From the database of studies, the specific values of δ_{min} is ranged from *0.01* to *3.0 μm*. However, the statically best value was equal to *0.0000003 m = 0.3 μm* and this is the value to use in the model. Finally, it is possible to use the surface roughness of the channel in place of this value.

The three-zone model, using these empirical values, predicted about *67%* of total database to within a *±30%* error. Moreover, it capture the *83%* of the single-channel database within the same range. Next two figures (46, 47) show the comparisons.
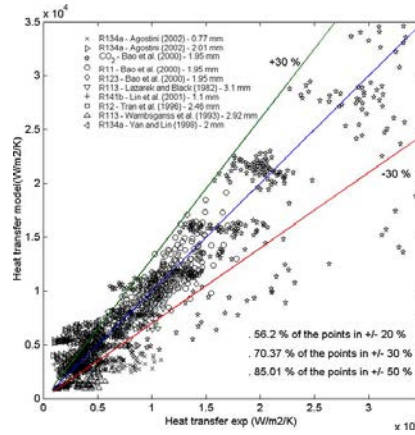
Figure 46: Comparison between experimental heat transfer and the corresponding values given by the model using the general model**.**
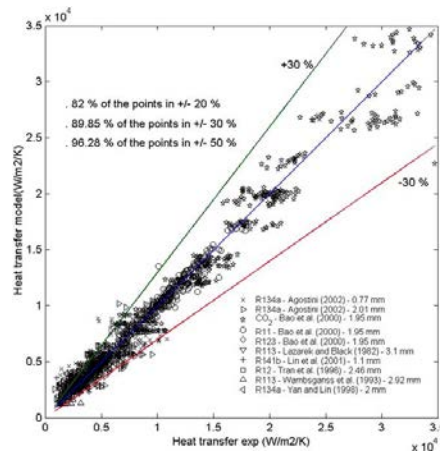
Figure 47: Comparison between experimental heat transfer and the corresponding values given by the model with different constant values for parameters resulting from an optimization on each database**.**

The elongated bubble model for slug flow was developed using the entire heat transfer database, thus including bubbly flow and annular flow heat transfer data. Does not exist any proven method at that time to distingue only slug flow heat transfer data points.

The three-zone model shows the importance of the cyclic variation in the heat transfer coefficient in the elongated bubble flow regime and the strong influence of heat transfer on:

- the bubble frequency,
- the minimum liquid film thickness at dry-out,
- the initial liquid film thickness.

It provides a physically based guideline for what parameters should be measured in future flow boiling experiments, in addition to the time-averaged local heat transfer coefficients, to better understand the fundamentals of the elongated bubble heat transfer process.

3.1.2.7. Comparisons

To validate the three-zone model comparison are made in some publications with new experimental data sets.

Shiferaw et al. (2007, 2009) measured local flow boiling data in a *2.01 mm* diameter *stainless steel* tube at *8 bar* with *R-134a* as fluid. The three-zone model predicted most of their data within a *±20%* error. The prediction seems to be irrespective of flow regime. However, their data at *12.0 bar* were bad predicted, yielding a spread of *±30%*. It shows a under prediction tendency with increasing pressure.

Agostini et al. (2008) compared their multi micro-channel database with the three-zone methods. The test section was made by a silicon heat sink constitute of 67 parallel rectangular channels with a high aspect ratio. The channels were *0.223 mm* wide, *0.680 mm* high and *20.0 mm* long with *0.080 mm* fins between one to other. They used vapor qualities above *5%* and orifices at the entrance of the channels to eliminate the inlet effects of the *90°* turn in the flow. The database used for the comparison consisted of *1438* data points for *R-245fa* and *R-236f* that considers the fin efficiency effects. They used for the three-zone model the measured surface roughness of *0.17 μm* due to silicon channels instead of the original value of *0.3 μm*. The model predicts *90%* of these data within *±30%*. The Kandlikar et al. (2004) correlation captured *58%* and Zhang et al (2004) correlation captured only the *19%* of the data within *±30%*.

Agostini et al. (2010) measured local flow boiling heat transfer coefficients for *R- 236fa* in a silicon test section equipped with *134* parallel rectangular channels. The channel dimensions is *0.067 mm* in wide and *0.680 mm* in high with fins of *0.092 mm* thick. The experimental section has one central inlet and two outlets to each side. The three-zone model badly predicts the heat transfer, even using the measured surface roughness of *0.160 μm* in place of the original value of *0.3 μm*. The most probably reason is the significant influences of the jet created by the inlet orifice at the center of each channel united with the recirculation created on these short channels of *10 mm* to each side from the inlet and with the *90°* bends in the flow at the inlet and outlet. These effects are not accounted from the three-zone model.

Consolini et al. (2008) compared their extensive database for *R-134a, R-236fa* and *R-245fa* obtained in stable flow conditions and near ambient saturation temperature in *stainless steel* channels of *0.510* and *0.790 mm* with five different methods. They used the Revellin et al. (2008) diabatic

flow pattern map described earlier in the second chapter to eliminate the annular flow data from the comparison. Therefore, they keep only the data identified to be in the Isolated Bubble and Coalescing Bubbles regimes. The results are that *77%* of the data are predicted within *±30%* by the three-zone. However, excluding the bubble flow data or low vapor qualities, the accuracy prediction improved. In comparison, the Lazarek et al (1982) correlation captures *88%* of the entire database within *±30%* while the Tran et al (2000) correlation captures only *4%* within this range, Kandlikar et al (2004) correlation captures *21%* and the Zhang et al (2004) correlation captured *58%.*

3.1.2.8.   Conclusions

The three-zone model was compared to many fluids data taken by many independent laboratories. From the comparison results that the three-zone model sometimes gives reasonably accurate predictions of the data while sometimes it does not. Not surprisingly, it seems to significantly under predict data at very low vapor qualities where the flow regime is bubbly flow and apparently nucleate boiling is the controlling heat transfer mechanism. Moreover, it does not apparently capture the effect of micro channel tube diameter correctly. However, this is a first-generation model for boiling in micro channels and it must be improved. Using the annexed programs, it is possible to simulate predictions of the three-zone model for specific applications or compare the model to new experimental test data. To improve its prediction for a specific fluid for a specific application when such data is available, it is suggested to play with one or all the three empirical factors or, for instance, to set the minimum film thickness as the surface roughness if known.

3.2. Bubble Coalescence Model

The bubble coalescence model is one-dimensional and predicts a confined coalescing bubble flow in a micro-channel where a convective boiling heat transfer exists. Coalescing bubble flow was identified in chapter 1 as one of the characteristic flow patterns for micro channels. This regime occurs at intermediate vapor qualities between the isolated bubble and the fully annular regimes.

3.2.1. Introduction to the Model

The Bubble coalescence model extended the work of Thome et al. (2004) expressed in the previous chapter by "the three-zone model". Their old model (Jacobi and Thome) for micro-channel slug flow was for purely convective boiling and for confined slug flow. In the model the local flow was modeled as a cyclical passage of three different phase, with constant bubble frequency:

- a saturated liquid slug without entrapped bubbles,
- an elongated bubble with an evaporating thin film at the heated wall,
- a dry vapor zone if the dry-out is reached.

The local heat transfer coefficient was time-averaged over the total passage period ϑ and specific phase passage time ϑ_{film}, $\vartheta_{,liquid}$, ϑ_{dry} . The heat transfer mechanisms can be expressed, as expressed in the previous chapter:

$$\bar{\alpha} = \frac{1}{\vartheta}(\vartheta_{liquid}\bar{\alpha}_{liquid} + \vartheta_{film}\bar{\alpha}_{film} + \vartheta_{dry}\bar{\alpha}_{dry})$$

The first and third terms represent single-phase contributions of liquid and dry zone. Instead, the second heat transfer coefficient, for the film evaporation zone, was postulated as pure conduction through the film's thickness without the presence of bubble nucleation. In the model is supposed that film evaporation governs the slug flow heat transfer, which may have the same features as in nucleate. The passage of bubble trains is generally classified as a slug flow and normally is found at low and intermediate vapor qualities in micro-channel systems.

Revellin and Thome (2008) with more recently Ong and Thome (2010) divided flow into two parts:

- *Isolated bubble*: where the formation rate of bubbles by the nucleation process is much higher than their rate of coalescence,
- *Coalescing bubble*: where the characteristic bubble passage frequency reduces from a peak value to zero that represent the transition to annular flow.

Figure (48) shows the micro-channel flow pattern map proposed.
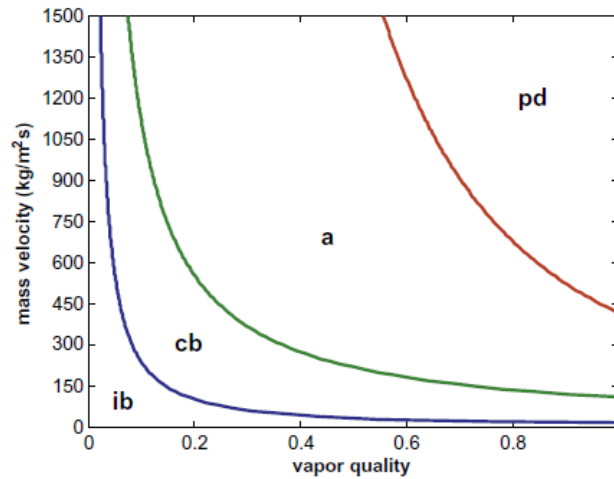
Figure 48: The flow pattern map of Revellin and Thome (2008) updated by Ong and Thome (2010). The map was simulated for *R-134a* at *7 bar* with a mass velocity of *500 kg/m²* s and a heat flux of *50 kW/m²* in a *500 µm* diameter channel.

Where, in the figure:

- *ib* – isolate bubble flow,
- *cb* – coalescing bubble flow,
- *a* – annular flow,
- *pd* – post dry-out flow.

3.2.2. Model Description

This model considers the coalescence of two or more bubbles by the action of inertia and surface tension. Due to the coalescence, the frequency passage of slug's decreases and the liquid redistribute among the remaining flow structures. In the model is assumed that heat transfer occurs only by conduction through the thin evaporating liquid film trapped between the bubbles and the channel wall. This model includes a simplified description of the formation and flow dynamics of the liquid film and the thin film evaporation process. Moreover, the model considers the mass transfer caused by breakup of the bridging liquid slugs.

This model includes the coalescence in the description of the thin evaporating film and its impact on the calculation of heat transfer coefficients. As a further development to the previous model, this investigation therefore presents a simplified analysis of one-dimensional slug flow with bubble coalescence.

The main assumption made for this model are listed following:

1. Two-phases are in thermodynamic equilibrium without liquid superheat.
2. Bubbles are nucleated periodically only at the origin of the heated length, where $x = 0$.
3. Bubble departure from the wall occurs axially, with no radial detachment.
4. Liquid film surrounding the confined bubble is laminar. No inertial effects are present, and is driven only by interfacial shear.
5. Flow presents axial symmetry.
6. Interface of the liquid film varies linearly only in the axial direction,
7. Pressure drop is negligible the fluid properties are constant.
8. Liquid film thickness is small compared to the channel size.
9. Heat flux is constant and uniform.

10. Heat is used only to evaporate the liquid.
11. No heat transfer to the liquid slug and any dry patch may occur.

Some of the above assumptions have strong impacts on the effectiveness of the model. The assumption (2) of bubbles to nucleation at x = 0 may be acceptable at higher mass velocities, where the extent of the bubbly flow regime collapses towards the saturated liquid curve, for lower flow rates in fact nucleation may take place over a substantial length of the heated section. Moreover, the assumption of axial symmetry and no radial departure of the bubble (3) simplifies the treatment of the problem, neglecting circumferential flows induced by gravity or surface tension, but it applies well only for high confinement number where this type of flow geometry is common. Also, the assumption of neglecting pressure drop (7) is arguable, particularly when bubbles reach high acceleration. However, many recent studies have suggested that the pressure drop develops mainly within the liquid slugs rather than in the bubbles. Finally, taking the liquid–vapor interface as linear (6) gives a good representation of the bubble far from the high-curvature extremities, and in the absence of interfacial waves.

3.2.2.1. Bubble Dynamics

The analysis starts from a mass balance over the finite control volume, *CV*. It presents a stationary boundary, an all liquid flow enters the heated sector and a move to boundary, with velocity equal to the bubble nose velocity, *WN*. Expressing the balance at the nose of the unspecified bubble, yields:

$$\frac{dm_{CV}}{dt} = \frac{1}{4} G \pi D^2$$

m_{CV} is the mass inventory of the control volume. Expressing the balance with V_{CV} and V_v that are, respectively, the total volume of *CV*, and *v* the vapor within it:

$$\frac{dV_{CV}}{dt} = \frac{1}{4} W_N \pi D^2$$

Then:

$$\frac{dm_{CV}}{dt} = \rho_l \frac{dV_{CV}}{dt} - (\rho_l - \rho_v)\frac{dV_v}{dt} = \frac{1}{4}\rho_l W_N \pi D^2 - (\rho_l - \rho_v)\frac{dV_v}{dt}$$

Combining previous equations brings to the expression of velocity at the bubble nose:

$$W_N = \frac{G}{\rho_l} + \left(1 - \frac{\rho_v}{\rho_l}\right)\frac{4}{\pi D^2}\frac{dV_v}{dt}$$

Next figure (49) shows the control volume.
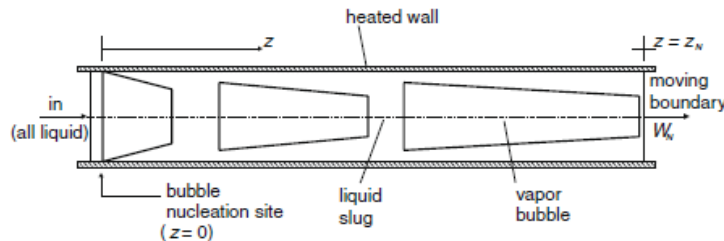
Figure 49: The control volume for the determination of the velocity and position of the bubble nose.

The last expression gives the slug velocity as the sum of the speed of the liquid entering the channel plus a contribution of the phase-change that occur within the control volume. Assuming the phases to be saturated. The energy balance can be expressed as:

$$\frac{dE_{CV}}{dt} = \frac{1}{4}G\pi D^2 h_l + \pi D q z_N - p\frac{dV_{CV}}{dt}$$

Where z_N is the axial position of the moving boundary. Once the kinetic energy contribution is neglected, the time derivative of the total energy in the control volume became:

$$\frac{dE_{CV}}{dt} = \rho_l\left[\frac{d(V_{CV}u_l)}{dt} - \frac{d(V_v u_l)}{dt}\right] + \rho_v\frac{d(V_v u_v)}{dt}$$

Where u_l and u_v are respectively the specific internal energies of the two-phases. Applying the definition of enthalpy:

$$h = u + \frac{p}{q}$$

Previous expression became:

$$\frac{dE_{CV}}{dt} = \rho_l h_l\frac{dV_{CV}}{dt} - (\rho_l h_l - \rho_v h_v)\frac{dV_v}{dt} - p\frac{dV_{CV}}{dt}$$

Combining the volume, mass and energy expression in the *CV*:

$$\frac{dz_N}{dt} = \frac{G}{\rho_l} + \frac{4q}{\rho_v h_{lv}}\frac{z_N}{D}$$

Setting:

$$W_N = \frac{dz_N}{dt},$$

Merge last expression with the *CV* balance and velocity bubble nose, and remove the term:

$$\frac{dV_v}{dt} = 0$$

Can be obtained:

$$W_N = \frac{G}{\rho_l} + \left(1 - \frac{\rho_v h_v}{\rho_l h_l}\right)\frac{4}{\pi D^2}\frac{dV_v}{dt} + \frac{4q}{\rho_l h_l}\frac{z_N}{D}$$

Where it was assumed that:

$$q_v \ll q_l$$

For a time varying heat flux, the equation of z_N has to be integrated to obtain the general solution:

$$z_N(t) = \exp\left(\frac{4}{\rho_v h_{lv}D}\int q\,dt\right)\left[\frac{G}{\rho_l}\int \exp\left(-\frac{4}{\rho_v h_{lv}D}\int q\,dt\right)dt + C\right]$$

C is the integration constant.

For hypothesis thermal flux q is constant and the initial bubble generation condition $z_N(0) = 0$ must be imposed. Taking the assumption gives the following time law for governing the motion of the bubble nose:

$$z_N(t) = \frac{G}{\rho_l} \frac{\rho_v h_{lv} D}{4q} \left[\exp\left(\frac{4q}{\rho_v h_{lv} D} t \right) - 1 \right]$$

3.2.2.2.   Thin Film Evaporation Process

Figure (50) illustrates an elongated bubble during its flow through a heated circular channel.
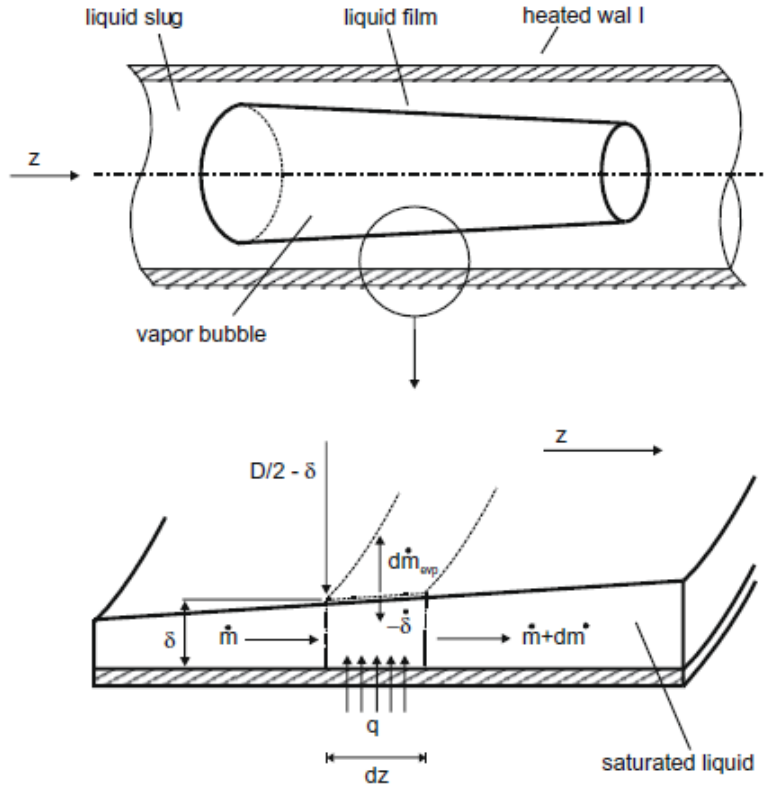
Figure 50: Schematic representation of an elongated bubble, and the control volume for the analysis of the liquid film.

From an analysis of the thin evaporating film surrounding the bubble it is possible to express the conservation of mass:

$$\frac{\partial}{\partial t}\left[\frac{\delta}{D}\left(1 - \frac{\delta}{D}\right) \right] + \frac{\partial}{\partial z}\left[W\frac{\delta}{D}\left(1 - \frac{\delta}{D}\right) \right] = -\frac{1}{\rho_l D}\left(1 - 2\frac{\delta}{D}\right)\dot{m}''_{evp}$$

Where $\dot{m}_{evp}{}''$ is the evaporating mass flux and W the average liquid film velocity in the axial direction. Expressing in the same way the conservation of energy:

$$\frac{\partial}{\partial t}\left[\frac{\delta}{D}\left(1 - \frac{\delta}{D}\right) \right] + \frac{\partial}{\partial z}\left[W\frac{\delta}{D}\left(1 - \frac{\delta}{D}\right) \right] = -\frac{1}{\rho_l D}\frac{h_v}{h_l}\left(1 - 2\frac{\delta}{D}\right)\dot{m}''_{evp} + \frac{q}{\rho_l h_l D}$$

The film thickness governing equation is obtained combining both conservation equations:

$$\frac{\partial}{\partial t}\left[\frac{\delta}{D}\left(1 - \frac{\delta}{D}\right) \right] + \frac{\partial}{\partial z}\left[W\frac{\delta}{D}\left(1 - \frac{\delta}{D}\right) \right] = -\frac{q}{\rho_l h_{lv} D}$$

From the assumption the film is driven only by interfacial shear, s_i. Thus, is possible to neglect the pressure drop and inertial terms. The mean cross-sectional velocity of the film in the axial direction is given from an axial momentum balance:

$$W = \frac{\tau_i D}{2\mu_l}\left[\frac{(1-2\frac{\delta}{D})^3}{4\frac{\delta}{D}(1-2\frac{\delta}{D})}\ln\left(1-2\frac{\delta}{D}\right)+\frac{1}{2}\left(1-2\frac{\delta}{D}\right)\right]$$

From hypothesis the thin film approximation is:

$$d/D << 1$$

Moreover, simplifies the expression to the following asymptotic expansion:

$$W \sim \frac{\tau_i D}{2\mu_l}\frac{\delta}{D}+O\left[\left(\frac{\delta}{D}\right)^2\right]$$

Using last two equations before the terms expansion and dropping the higher order terms yields to the quasi-linear expression:

$$\frac{\partial \delta}{\partial t}+\frac{\tau_i}{\mu_l}\delta\frac{\partial \delta}{\partial z}=-\frac{q}{\rho_l h_{lv}}$$

In virtue of the hypothesis of the axial film thickness linear variation (which is deemed acceptable far from the bubble nose and its tail) the solution of last equation may be rearranged in a more convenient form:

$$\delta(t,z) = \delta_0(t) + z\delta_1(t)$$

Where δ_0 and δ_1 are two unknown functions of time. Using the previous equation:

$$\left(\frac{d\delta_0}{dt}+\frac{\tau_i}{\mu_l}\delta_1\delta_0\right)+z\left(\frac{d\delta_1}{dt}+\frac{\tau_i}{\mu_l}\delta_1^2\right)=-\frac{q}{\rho_l h_{lv}}$$

Confronting the two parts gives the following system of ordinary differential equations:

$$\frac{d\delta_0}{dt}+\frac{\tau_i}{\mu_l}\delta_1\delta_0=-\frac{q}{\rho_l h_{lv}} \qquad \frac{d\delta_1}{dt}+\frac{\tau_i}{\mu_l}\delta_1^2=0$$

That solute for δ_0 gives:

$$\delta_0(t)=\frac{1}{t+C_1}\left[C_0-\frac{1}{\rho_l h_{lv}}\int(t+C_1)qdt\right]$$

And for δ_1:

$$\delta_1(t)=\frac{\mu_l}{\tau_i(t+C_1)}$$

Where C_0 and C_1 are the two integration constants. Therefore, the sum of the last two equation give the expression that govern the local film thickness:

$$\delta(t,z)=\frac{\frac{\mu_l}{\tau_i}z+C_0}{t+C_1}-\frac{1}{\rho_l h_{lv}}\frac{\int(t+C_1)qdt}{t+C_1}$$

The equation can be simplified by the constant heat flux hypothesis:

$$\delta(t,z)=\frac{\frac{\mu_l}{\tau_i}z+C_0}{t+C_1}-\frac{q}{2\rho_l h_{lv}}(t+C_1)$$

3.2.2.3.   Initial and Boundary Conditions

The last two equations for film thickness obtained in the previous section represent the behavior of the liquid film deposited by a liquid slug during its passage. Initial and Boundary conditions must be found to determine the values of C_0 and C_1. The last equation considering the constant heat flux and assuming bubble nucleation at $t = 0$ and $z = 0$, yields that no liquid-vapor interface should exist for $t \to 0$ over $z > 0$. This can be expressed with a limit:

$$\lim_{t \to 0} \delta(t, z) = +\infty$$

Thus, the bubble does not exist near the nucleation site at the beginning time. This is satisfied when:

$$C_1 = 0 ; \; C_0 \geq 0$$

As for the boundary condition at $z = 0$, $\delta^{(0)}(t)$, for hypothesis the bubble detachment process occurs only axially, that comport $\delta^{(0)}(t) \leq 0$. In fact, $z = 0$ represents either a contact location of the bubble with the channel wall, or a dry perimeter, a negative value for $\delta^{(0)}(t)$ implies a local condition of film dry-out. $\delta^{(0)}(t)$ for $C_1 = 0$ can be expressed from $\delta(t,z)$ equation:

$$\delta^{(0)}(t) = \frac{C_0}{t} - \frac{q}{2\rho_l h_{lv}} t \leq 0$$

The above inequality can be satisfied only if $C_0 = 0$:

$$\delta(t, z) = \frac{\mu_l}{\tau_i} \frac{z}{t} - \frac{q}{2\rho_l h_{lv}} t$$

Figure (51) shows the temporal evolution of the film thickness and the bubble nose near $t = 0$.
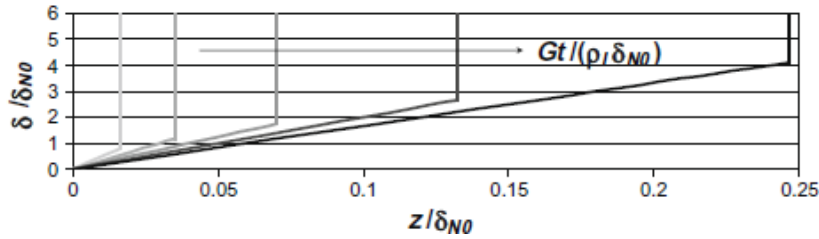
Figure 51: Temporal evolution of the liquid film and the bubble nose at the initial stages of the bubble development.

It can be observed that, the film shrinks in time due to the combined effect of the vaporization process and the drag exerted by the vapor phase.

Merging the last equation of two previous paragraphs gives the time law of the nose film thickness:

$$\delta_N(t) = \frac{G\mu_l}{\rho_l \tau_i} \frac{\rho_v h_{lv} D}{4q} \left[\frac{\exp\left(\frac{4q}{\rho_v h_{lv} D} t\right) - 1}{t} \right] - \frac{q}{2\rho_l h_{lv}} t$$

In order to obtain the initial film thickness the limit for $t \to 0$ has to be make for last expression:

$$\delta_{N0} \equiv \lim_{t \to 0} \delta_N(t) = \frac{G\mu_l}{\rho_l \tau_i}$$

The obtained value represents the nose film thickness when the bubble forms. Moreover for the adiabatic case for $q \to 0$ $\delta_{N,adiabatic} = \delta_{N,0}$, assuming that the interfacial adiabatic shear is approximately

equal to that for a diabatic flow. Therefore, the bubble's nose film thickness remains unchanged in adiabatic flows.

Rearranging last equation, and utilizing the inverse of $z_n(t)$, gives:

$$\frac{\delta_N}{D} = \frac{\left(\frac{\rho_l W_N}{G} - 1\right)\frac{\delta_{N0}}{D}}{\ln\left(\frac{\rho_l W_N}{G}\right)} - \frac{1}{8}\frac{\rho_v}{\rho_l}\ln\left(\frac{\rho_l W_N}{G}\right)$$

The obtained value, δ_{N0}/D, represent the non-dimensional nose film thickness for an adiabatic flow.

Figure (52) shows the predicted nose film thicknesses in function of the Capillarity number for adiabatic conditions and for highly viscous fluids, the relation follows the Taylor's law.
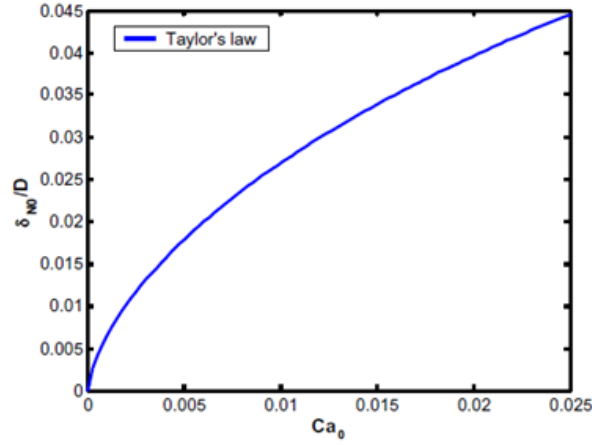
Figure 52: Taylor's law versus the adiabatic capillary number

The non-dimensional nose film thickness is only a function of the bubble's capillary number:

$$Ca_0 = \frac{\mu_l W_{N0}}{\sigma}$$

Therefore, the new expression is:

$$\frac{\delta_{N0}}{D} = \frac{0.67 Ca_0^{2/3}}{1 + 2.5 \times 1.34 Ca_0^{2/3}}$$

When Ca_0 increases, for higher mass velocity, the initial film thickness increases together and causes an increment of the diabatic nose film thickness δ_{N0}/D. Moreover, the vaporization accelerates bubble, incrementing its nose film thickness. This trend is in agree with previous relation for slow bubbles that have values of the Bond number:

$$Bn = \rho_l W_N^2 D/\sigma \le 2$$

In this case, the liquid film is thinner than the boundary layer in the liquid slug, and δ_N increases with bubble nose speed. Instead for:

$$Bn > 2$$

The film scales with the thickness of the boundary layer, and an acceleration of the fluid brings to a thinner liquid films.

3.2.2.4. Bubble Frequency and Coalescence

The transition between different phases in the model has a cyclical nature. However, when a certain vapor quality is exceeded the passage frequency falls due to the rapid increase of bubble coalescence. Thus, the frequency presents a maximum value, f_{max}, at the transition quality between the isolate bubble and coalescing bubble flow. Furthermore, the value tends to zero at the transition to annular flow. Next figure (53) shows this trend in an experimental test.
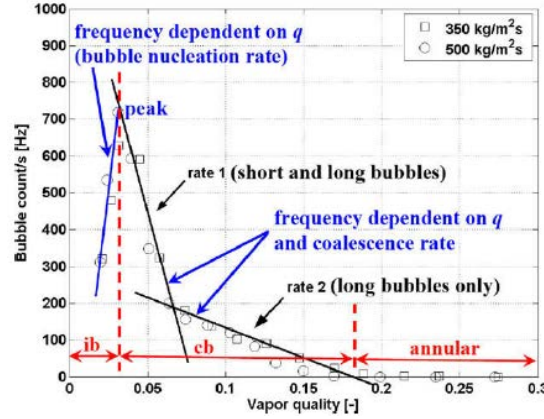
Figure 53: Experimental bubble passage frequency versus exit vapor quality for a two-phase flow of R-134a at 30 °C in a uniformly heated 510 μm circular micro-channel.

Form the figure the transition quality described x_c is evident. It is the transition between the isolate bubble and coalescing bubble flow and $x_{a,}$ for the transition to annular flow. The bubble frequency function may be expressed as:

$$\frac{f}{f_{max}} = \left(\frac{x_a - x}{x_a - x_c}\right)^\beta$$

Where β is a shape factor normally equal to 1. Any change in the liquid for a pair bubble-slug during its travel is due to:

- Variation of the vapor quality from the heating process
- Change in frequency associated to coalescence.

The liquid mass crossing a given location over one passage period is:

$$m_L = \frac{G\pi D^2(1-x)}{4f}$$

From that can be obtained the mass variation due to a unitary change in frequency:

$$\frac{\partial m_L}{\partial f} = -\frac{G\pi D^2(1-x)}{4f^2}$$

Multiplying the equation by the elementary change in frequency gives an estimation of the mass of liquid redistributed to the bubble–slug pair during coalescence. Figure (54) shows this redistribution.
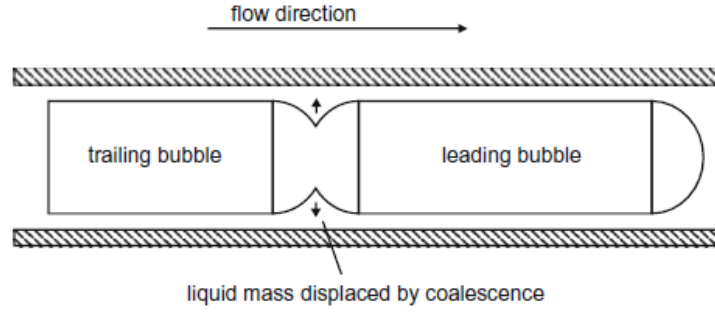
Figure 54: Schematic diagram of coalescence of two bubbles

For assumption a constant fraction of the film mass will be distributed to the liquid slug, while the remaining fraction, $\xi \leq 1$ participates in the film evaporation process. The liquid intake by the film is an incoming flux, m''_c. It is assumed that the residence time of the liquid slug is negligible with respect to that of the bubble, the incremental mass added to the liquid film cause to a change in frequency. It can be expressed as:

$$dm_c = \frac{\dot{m}''_c \pi D dz}{f} = \xi \frac{\partial m_L}{\partial f} df$$

From the expression for the vapor quality gradient:

$$\frac{dx}{dz} = \frac{4q}{G h_{lv} D}$$

The mass flux may be expressed as:

$$\dot{m}''_c(x) = \frac{q}{h_{lv}} \psi(x)$$

Where $\psi(x)$ is:

$$\psi(x) \equiv \xi \beta \left(\frac{1-x}{x_a - x} \right)$$

Inserting the incoming mass of liquid given by last equation is the differential expression of the film thickness gives:

$$\frac{\partial \delta}{\partial t} + \frac{\tau_i}{\mu_l} \delta \frac{\partial \delta}{\partial z} = -\frac{q}{\rho_l h_{lv}} [1 - \psi(x(z))]$$

To obtain a simple closed solution for the film thickness the equation is simplified by the following expansion:

$$\psi(x) \sim \psi(x_c) + O(x - x_c)$$

The term $\psi(x)$ is calculated near x_c. The expression became:

$$\frac{\partial \delta}{\partial t} + \frac{\tau_i}{\mu_l} \delta \frac{\partial \delta}{\partial z} = -\frac{q}{\rho_l h_{lv}} (1 - \psi_c)$$

Therefore $\psi(x)$ have to be calculated in x_c:

$$\psi_c \equiv \psi(x_c) = \xi \beta \left(\frac{1-x_c}{x_a - x_c} \right)$$

In the hypothesis of constant heat flux the film thickness equation is:

$$\delta(t,z) = \frac{\frac{\mu_l}{\tau_i}z + C_0}{t + C_1} - \frac{q}{2\rho_l h_{lv}}(1 - \psi_c)(t + C_1)$$

To assure continuity between last equation and the film thickness expression at initial condition in which coalescence starts, the values of the constants must satisfy the following conditions:

$$C_0 = -\frac{q\psi_c}{2\rho_l h_{lv}}t_c^2$$

$$C_1 = 0$$

Inserting the constants in previous equation gives:

$$\delta(t,z) = \frac{\mu_l}{\tau_i}\frac{z}{t} - \frac{q}{2\rho_l h_{lv}}t\left[1 - \psi_c\left(\frac{t^2 - t_c^2}{t^2}\right)\right]$$

This expression is valid for:

$$t \geq t_c$$

t_c is the transition time at which coalescing ebullition is reached, where the vapor quality is $x = x_c$. Using the expression for vapor quality:

$$x = \frac{4qz}{G h_{lv} D}$$

Inserting it in the equation for $z_n(t)$, gives:

$$t_c = \frac{\rho_v h_{lv} D}{4q} \ln\left(1 + \frac{\rho_l}{\rho_v}x_c\right)$$

To express the value of the film thickness in function of the local vapor quality the following expression must be used in combination with the previously:

$$z = \frac{G h_{lv} D x}{4q}$$

It gives:

$$\hat{\delta}(t,x) = \frac{\mu_l}{\tau_i}\frac{G h_{lv} D}{4q}\frac{x}{t} - \frac{q}{2\rho_l h_{lv}}t\left[1 - \psi_c\left(\frac{t^2 - t_c^2}{t^2}\right)\right]$$

Matching all the equation obtained for the film thickness with the last one it is possible to express the liquid film thickness at the bubble nose as:

$$\frac{\delta_N}{D} = \frac{\delta_{N0}}{D}\frac{\rho_l}{\rho_v}\frac{x}{\ln\left(1 + \frac{\rho_l}{\rho_v}x\right)} - \frac{1}{8}\frac{\rho_v}{\rho_l}\ln\left(1 + \frac{\rho_l}{\rho_v}x\right)\left[1 - \psi_c + \psi_c\frac{\ln^2\left(1 + \frac{\rho_l}{\rho_v}x_c\right)}{\ln^2\left(1 + \frac{\rho_l}{\rho_v}x\right)}\right]$$

Moreover, the expression calculated for tail of the bubble gives:

$$\frac{\delta_T}{D} = \frac{\delta_{N0}}{D}\frac{\rho_l}{\rho_v}\frac{x}{\ln\left(1 + \frac{\rho_l}{\rho_v}x\right) + 4Bo\left(\frac{x_a - x_c}{x_a - x}\right)^\beta} - \frac{1}{8}\frac{\rho_v}{\rho_l}\left[\ln\left(1 + \frac{\rho_l}{\rho_v}x\right) + 4Bo\left(\frac{x_a - x_c}{x_a - x}\right)^\beta\right] \times \left\{1 - \psi_c + \psi_c\frac{\ln^2\left(1 + \frac{\rho_l}{\rho_v}x_c\right)}{\left[\ln\left(1 + \frac{\rho_l}{\rho_v}x\right) + 4Bo\left(\frac{x_a - x_c}{x_a - x}\right)^\beta\right]^2}\right\}$$

Where *Bo* is the modified Boiling number:

$$Bo = \frac{q}{\rho_v h_{lv} D f_{max}}$$

Due to the approximation adopted for the liquid film thickness the limit for $x \to x_a$ yields:

$$\lim_{x \to x_a} \frac{\delta_T}{D}(x; \psi_c) = \begin{cases} +\infty & \psi_c > 1 \\ 0 & \psi_c = 1 \\ -\infty & \psi_c < 1 \end{cases}$$

This limit provides three different scenarios depending the non-dimensional mass flux, ψ_c:

1. $\psi_c > 1$; liquid mass accumulates in the film, destabilizing it;
2. $\psi_c = 1$; film is stable in the range of vapor qualities, $x_c < x \le x_a$, and the flow is at a threshold;
3. $\psi_c < 1$; liquid film remains stable and dry-out occurs at the tail of the bubble.

The last two cases yield stable bubbles, with the boundary film that reach the dry-out approaching $x = x_a$. Its residence time tends to infinity. In the last case the liquid film is unbounded, and the liquid film equation do not give the liquid depletion as the flow approaches the annular flow transition. Reassuming:

- If $\psi_c \le 1$, a coalescing bubble flow persists up to the dry-out where $x_a = 1$,
- If $\psi_c > 1$, the film is unstable and $x_a < 1$

The relation can be expressed in term of ξ as following and for quality in range:

$$\xi > \xi_a$$

$$x_c < x_a < 1$$

ξ_a can be expressed as:

$$\xi_a \equiv \frac{1}{\beta}\left(\frac{x_a - x_c}{1 - x_c}\right)$$

Next figures (55, 56) show the trends:
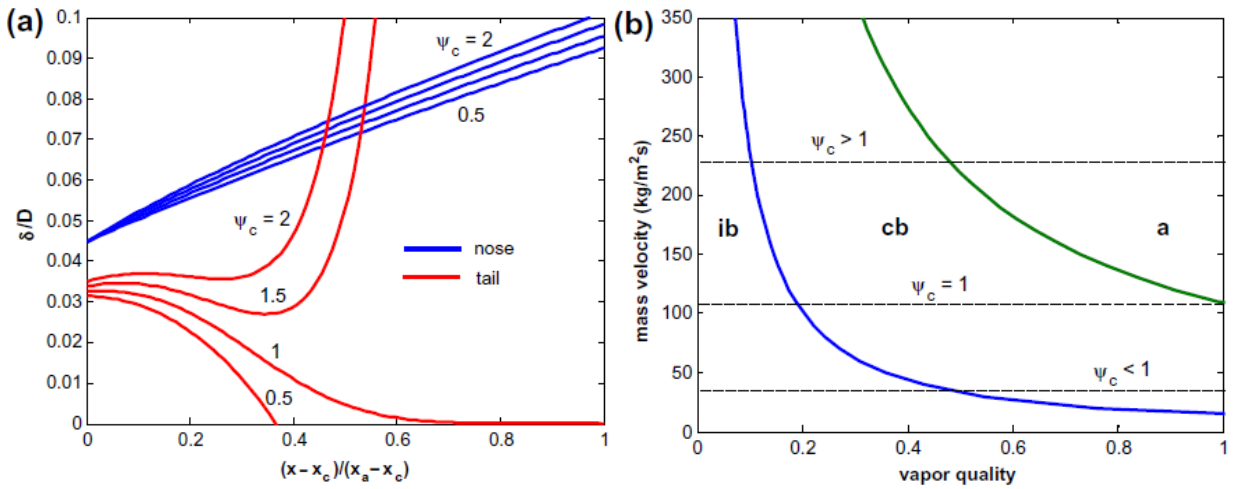
Figure 55, 56: (a) Non-dimensional bubble nose and tail film thicknesses versus reduced vapor quality for $\delta_{N0}/D = 0.02$, $GD/\mu_l = 1310$, $G^2 D/(\rho_l \sigma) = 13.0$, $q/(Gh_{lv}) = 6.0 * 10^4$, $\beta = 6$, and $0.5 < \psi_c < 2$, (b) three paths on a micro-channel flow pattern map for different values of ψ_c: *ib* is isolate bubble flow, *cb* is coalescing bubble flow and *a* is annular flow.

3.2.2.5.   Local Heat Transfer Coefficients

For hypothesis the heat is transmitted only by conduction through the laminar film of liquid surrounding the elongated bubbles. The residence time of the liquid slug is neglected. Considering that, the expression of the local time-averaged heat transfer coefficient is:

$$\bar{\alpha}(x) = f \int_{1/f} \frac{k_l}{\hat{\delta}(t,x)} dt$$

Integrating the equation and utilizing the expression for $z_n(t)$ for bubble dynamics, the expression f_{max} for bubble frequency, the expression for t_c and the expression for $\delta(x,t)$ gives the following expression for the local time-averaged heat transfer coefficient for $\psi_c \neq 1$:

$$\bar{\alpha}(x) = \frac{k_l}{D} \frac{\left(\frac{\rho_l}{\rho_v}\right)\left(\frac{x_a-x}{x_a-x_c}\right)^\beta \ln\left(\frac{1-\Theta_1(x)}{1-\Theta_2(x)}\right)}{Bo(1-\psi_c)}$$

Where the functions Θ_1 and Θ_2 are defined as:

$$\Theta_1(x) \equiv \frac{(1-\psi_c)\ln^2\left(1+\frac{\rho_l}{\rho_v}x\right)}{\Theta_3(x)}$$

$$\Theta_2(x) \equiv \frac{(1-\psi_c)\left[\ln\left(1+\frac{\rho_l}{\rho_v}x\right) + 4Bo\left(\frac{x_a-x}{x_a-x_c}\right)^{-\beta}\right]^2}{\Theta_3(x)}$$

In addition, the function Θ_3 is:

$$\Theta_3(x) \equiv 8\frac{\mu_l}{\tau_i}\frac{G}{\rho_v D}\frac{\rho_l}{\rho_v}x - \psi_c\ln^2\left(1+\frac{\rho_l}{\rho_v}x_c\right)$$

The heat coefficient equation is applied to the range of vapor quality close to x_c. Therefore, the replacement of $\psi(x)$ with ψ_c is acceptable, but, from an operative point of view, is necessary to have an equation for all vapor qualities, from x_c to x_a. The expression of the heat transfer coefficient must be corrected to represent where the coalescing bubble flow regime approaches annular flow. It is possible to represents in a more general form of the equation for the two-phase heat transfer coefficient in the range $x_c \leq x < x_a$, expressing the dependencies in function of the Nusselt number, Nu:

$$Nu(x) = \frac{\left(\frac{\rho_l}{\rho_v}\right)\left[\left(\frac{x_a-x}{x_a-x_c}\right)^\beta\right]^{\gamma(x;x_c,x_a)} \ln\left(\frac{1-\Theta_{1c}}{1-\Theta_{2c}}\right)}{Bo(1-\psi_c)}$$

Where Θ are all calculated in $x = x_c$. Extrapolating from the Nusselt number the simplified heat transfer coefficient:

$$\bar{\alpha}(x) = \frac{k_l}{D} \frac{\left(\frac{\rho_l}{\rho_v}\right)\left[\left(\frac{x_a-x}{x_a-x_c}\right)^\beta\right]^{\gamma(x;x_c,x_a)} \ln\left(\frac{1-\Theta_{1c}}{1-\Theta_{2c}}\right)}{Bo(1-\psi_c)}$$

Where γ is a function of the vapor quality expressed as:

$$\gamma(x;x_c,x_a) = \left(\frac{x_a-x}{x_a-x_c}\right)^\chi$$

Where χ is an empirical constant.

3.2.2.6.   Empirical Paramters

The model is based on five parameters that remain unknown and that must be defined. The parameters are: τ_i, ξ, β, χ and f_{max}. Many of them can be evaluated by physical quantity by either direct or indirect measurements. The following list reassume the parameters assumption:

- τ_i is the interfacial shear stress and is directly related to the initial film thickness, δ_{N0}. The expression result from the confrontation of the model prediction with a database of two-phase heat transfer coefficients, ranged within the coalescing bubble flow mode. The empirical correlation obtained is:

$$\tau_i = (fr_q + fr_v)\frac{G^2 x_c^2}{2\rho_v}$$

Where fr_v is the Blasius single-phase vapor friction factor:

$$fr_v = 0.079\, Re^{0.25}$$

While fr_q is an added term that accounts the flow evaporation and it is expressed as:

$$fr_q = 304\left(\frac{GD}{\mu_l}\right)^{-1.16}\left(\frac{\rho_l}{\rho_v}\right)^{1.74}\left(\frac{\mu_l}{\mu_v}\right)^{1.43} x_c^{-2}\left[1 - \exp\left(-\frac{qD}{h_{lv}\mu_l}\right)\right]$$

If $fr_q = 0$ when $q = 0$ the approximation that $\tau_{i,adiabatic} = \tau_{i,diabatic}$ has a limited applicability. (ρ_l e ρ_v are inverted in the relation)

- f_{max} is the maximum bubble frequency. It depends on the heat flux, on the fluid physical properties and on the channel size, which influences the bubble confinement. The frequency can be extrapolated by a non-dimensional analysis:

$$f_{max} = 0.004\left(\frac{q}{\sigma}\right)\left(\frac{\sigma^3}{q^2 D^3 \rho_v}\right)^{0.25}$$

- β describes the decline in bubble frequency at the transition to annular flow. From the data sets result that the best fitting value of β is $\beta = 1$. This conclusion accuracy should be further verified on more data sets.
- χ is an entirely empirical parameter, and its best approximation is:
$$\chi = 3$$
- ξ is a physical quantity that indicates the liquid fraction to film and that must be deduced indirectly. Their proposed value is:

$$\xi = 0.02$$

- x_c and x_a are the flow pattern boundaries and are expressed by the following correlations:

$$x_c = 0.763\left(\frac{q\rho_v\sigma}{\mu_l h_{lv} G^2}\right)^{0.39}$$

$$x_a = 4.1 \times 10^{-4}\left(\frac{p}{p_{134a}}\right)^{0.45}\left(\frac{GD}{\mu_l}\right)^{1.47}\left(\frac{G^2 D}{\rho_l \sigma}\right)^{-1.23}$$

Figure (57) shows the calculated trends for the heat transfer coefficients simplified and not within the range $x_c \leq x < x_a$.
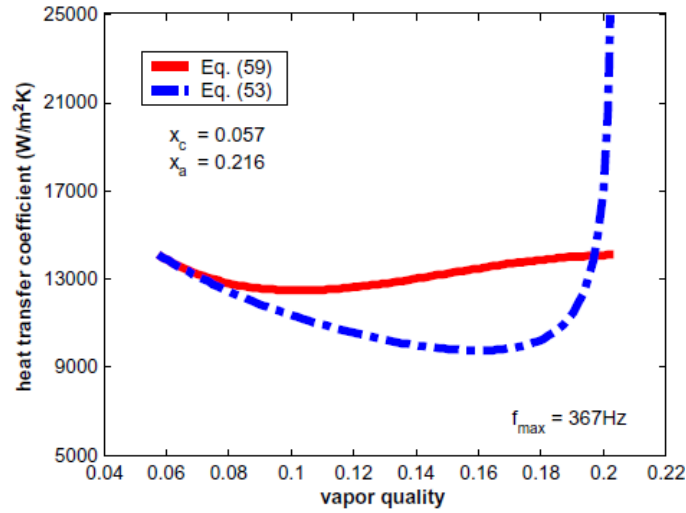
Figure 57: Predictions from heat transfer simplified equation (59) and standard equation (53) for the flow boiling heat transfer coefficients of *R-134a* at *31 °C* in a *500 μm* micro-channel at a heat flux of *50 kW/m²* and mass velocity of *500 kg/m²s*.

The two curves start at the same point and both decline near x_c due to an average thickening of the liquid film. The standard relation has a gross reduction of the heat transfer coefficient at the intermediate vapor qualities, while increase asymptotically approaching to the annular flow due to the acute reduction in the film thickness by evaporation up to the film dry-out. This behavior is not verified experimentally and thus suggests the better solution is given by simplified relation. Both equations have two minimum values. One at the limit between of the coalescence region, where the film dynamics give thicker films and lower heat transfer coefficient and the other where film depletion by evaporation and shear either dominates or balances the coalescing mass flow that comport a thinner film and higher heat transfer coefficient.

3.2.3. Model Summary and Modified Relations

The coalescence model can be reassumed with the following relations:

- For the heat transfer the simplified relation gives the best results with the empirical data

$$\bar{\alpha}(x) = \frac{k_l}{D} \frac{\left(\frac{\rho_l}{\rho_v}\right)\left[\left(\frac{x_a-x}{x_a-x_c}\right)^\beta\right]^{\gamma(x,x_c,x_a)} \ln\left(\frac{1-\theta_{1c}}{1-\theta_{2c}}\right)}{Bo(1-\psi_c)}$$

- Appling the best fit prediction based on the database the coefficients are:

$$\gamma = \left(\frac{x_a-x}{x_a-x_c}\right)^3,$$

$$\beta = 1$$

$$\psi_C = 0.002\beta\left(\frac{1-x_C}{x_a-x_C}\right)$$

- The modified Boiling number is:

$$Bo = \frac{q}{\rho_g h_{fg} Df_{max}},$$

- The three function that appear in the heat transfer for $x = x_c$ are:

$$\theta_{1C} = \frac{(1-\psi_C)\ln^2\left(1+\frac{\rho_L}{\rho_g}x_C\right)}{\theta_{3C}}$$

$$\theta_{2C} = \frac{(1 - \psi_C)\left[\ln\left(1 + \frac{\rho_L}{\rho_g}x_C\right) + 4Bo\right]^2}{\theta_{3C}}$$

$$\theta_{3C} = 8\frac{\mu_L}{\tau_i}\frac{G}{\rho_g D}\frac{\rho_L}{\rho_g}x_C - \psi_C\ln^2\left(1 + \frac{\rho_L}{\rho_g}x_C\right)$$

- The shear stress is obtained empirically as:

$$\tau_i = (f_q + f_{v,Blasius})\frac{G^2 x_C^2}{2\rho_v}$$

- The empiric friction factor is:

$$f_q = 304\left(\frac{GD}{\mu_L}\right)^{-1.16}\left(\frac{\rho_L}{\rho_g}\right)^{-1.74}\left(\frac{\mu_L}{\mu_g}\right)^{1.43}x_C^{-2}\left[1 - \exp\left(-\frac{qD}{h_{fg}\mu_L}\right)\right]$$

- The Blasius friction factor is:

$$fr_{v,Blasius} = 0.079\,Re^{0.25}$$

- The maximum bubble frequency is expressed as:

$$f_{max} = 0.004\left(\frac{q}{\sigma}\right)\left(\frac{\sigma^3}{q^2 D^3 \rho_g}\right)$$

- The transition quality from bubble to coalescence is:

$$x_c = 0.763\left(\frac{q\rho_g\sigma}{\mu_L h_{fg}G^2}\right)^{0.39}$$

- The simplified (of the relationship between saturated and critical pressure) transition quality from coalescence to annular is:

$$x_a = 1.4 \times 10^{-4}\left(\frac{GD}{\mu_L}\right)^{1.47}\left(\frac{G^2 D}{\rho_L\sigma}\right)^{-1.23}$$

3.2.4. Comparison

The model was compared with a database of *980* experimental data points in the coalescing bubble flow mode. The refrigerants in the database are *R-134a, R-236fa* and *R-245fa*. The section has a singular circular channel with diameters of *510* and *790 μm*. Temperatures varies in range between *30* and *32* °C. The mass velocities ranges from *300* to *2000 kg/m²s*, and heat fluxes up to 200 kW/m².

Next figures (58, 59) show the overall success ratio of *83%* for the data predicted within the *±30%* error band.
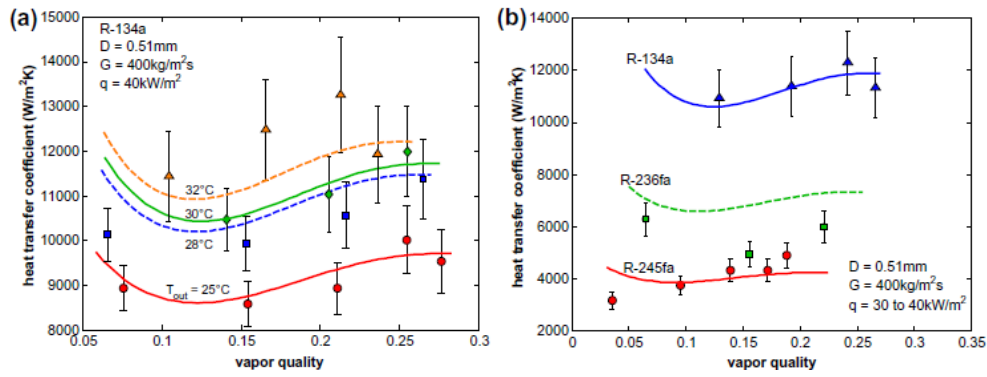
Figure 58, 59: (a) Experimental heat transfer coefficients versus the computed for a flow of *R-134a*. (b) Experimental versus predicted data for *R- 134a*, *R-236fa* and *R-245fa*.
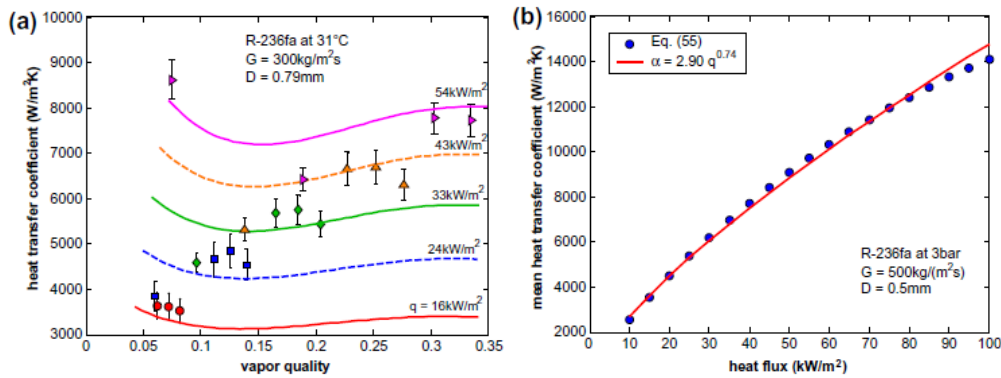
Figure 60, 61: (a) Experimental heat transfer coefficients versus the predictions for a flow of *R-236fa* at different heat fluxes. (b) Computed flow boiling curve for *R-236fa*.

The best performance is for *R-134a*, which is the highest-pressure refrigerant, with *93%* of the data inside the same error band. The other two refrigerants have ad error of *79%* for *R-236fa* and *75%* for *R-245fa* on the predicted data. The three-zone model predicted *75%* of the data within the *±30%* error band; respectively, *83%* for *R-134a*, *56%* for *R-236fa* and *87%* for *R-245fa*. The largest errors are near the transition boundary between bubble and coalescence flow.

Bertsh et al. (2008) with a new flow boiling method for micro-channels captures only *39%* of this database within *±30%*. Next figure (62, 63) compares the predictions to flow boiling data of *CO2, R-22* and *R-141b*, taken respectively from Choi et al. (2006), Bang and Choo (2007) and Lin et al. (2012).
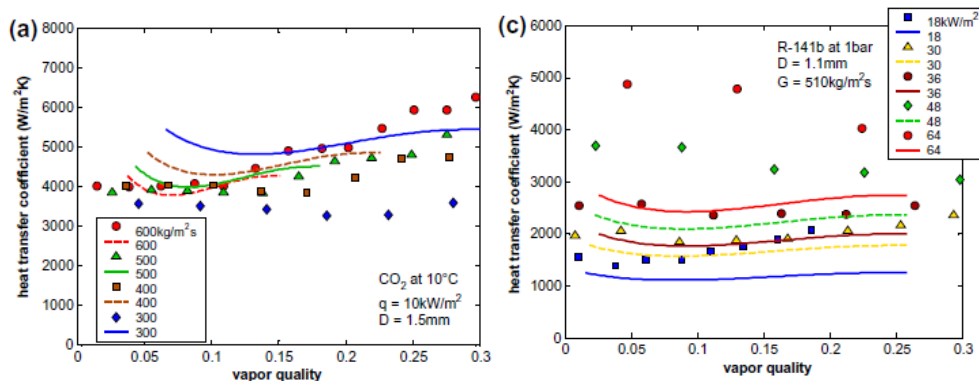
Figure 62, 63: (a) Experimental heat transfer coefficients versus the prediction for *CO2* at *10 °C* at different mass velocities. (c) *R-141b* at *1 bar* and at different heat fluxes from Lin et al. (2012).

The obtained values for the CO_2 and *R-22* show good agreement with the experimental results. However, the model does not capture the increase in the heat transfer coefficient with mass velocity for CO_2. This is probably due to the difference in the experimental and predicted film thickness. For *R-141b* data, the model reproduces the increase in heat transfer with heat flux but shows a general under-prediction of the experimental results that increase at the highest heat fluxes.

3.2.5. Conclusions

The coalescence model and its extension to the entire coalescing bubble vapor quality range, given by the heat transfer equation based on the Nusselt number, represent a micro-channel two-phase heat transfer model comprehensive of the bubble coalescence and the thin film dynamics. Model is entirely based on the prediction of the thin evaporating film. The simplified relations are in well agreement with the trends reported in the experimental literature. The accuracy of the model depends on the simplifying assumptions adopted from hypothesis. The model also depends on the empirical equations developed for closure. The heat transfer equations are flow pattern based expressions. This entails that they are rely on the precision of the adopted flow pattern map to identify the coalescing bubble flow regime boundaries. The flow pattern transition is not an exact value but range in a band of transition vapor qualities. For this reason, the predictions about the transition boundaries is subjected to the higher errors founded. Finally, this approach, which has been presently developed for a constant heat flux, may potentially be extended to the time-varying heat flux case.

3.3. Correlations

This paragraph is not intended to be a simple description of a single heat transfer model. Indeed, the paragraph presents 17th different correlation models from many authors. Models will be presented shortly with a brief description of the model, the applicability range and fluids analyzed. For a complete description is suggested to check the original papers reported in bibliography.

3.3.1. Introduction

One of purpose of this list of models is to match the transition diameter between macro and micro scale. Therefore, the correlation are divided in two main sets:

- Macro-Scale correlations:
  - Chen (1966)
  - Shah (1982)
  - Gungor and Winterton (1986)
  - Kandlikar (1989)
  - Liu and Winterton (1991)

- Micro-Scale correlations
  - Lazarek and Black (1982)
  - Tran et al. (1996)
  - Kew and Cornwell (1997)
  - Warrier et al. (2002)
  - Kandlikar and Balasubramanian (2004)
  - Zhang et al. (2004)
  - Lee and Mudawar (2005)
  - Saitoh et al. (2007)
  - Bertsch et al. (2009)
  - Mikielewicz (2010)
  - Li and Wu (2010)
  - Mohamed and Karayiannis (2012)

Models are order from the oldest to the newest. All the described models are empirical or semi-empirical.

3.3.2. Macro Scale Models

Following are presented the macro-scale models.

3.3.2.1. Chen

Chen proposed an additive mechanism to represent boiling and convective heat transfer in micro and macro tube. The model takes into account the interaction between the two mechanisms by two dimensionless functions:

- effective two-phase Reynolds number function, F,
- bubble growth suppression function, S.

Where F is a function of the Martinelli's parameter that consider both empirical correlation of heat transfer data and a momentum analysis, and S is an empirical function of the two-phase Reynolds number.

The relation was tested for: *water, methanol, cyclohexane, pentane, heptane* and *benzene* with 594 data points for both vertical upper and downward flow in tubes and annuli. The pressure range was from *1* to *34.8 bar,* for the fluid inlet velocity the range was *0.06-4.5 m/s* with a quality range of *0.01-0.71.*

Following relations express the model:

- Martinelli's parameter:

$$X_{tt} = \left(\tfrac{1-x}{x}\right)^{0.9} \left(\tfrac{\rho_v}{\rho_L}\right)^{0.5} \left(\tfrac{\mu_L}{\mu_v}\right)^{0.1}$$

- Convective boiling enhancement factor:

$$F = \begin{cases} 1 & 1/X_{tt} \leqslant 0.1 \\ 2.35\left(0.213 + \tfrac{1}{X_{tt}}\right)^{0.736} & 1/X_{tt} > 0.1 \end{cases}$$

- Reynold's Two-Phase:

$$Re_{tp} = Re_L . F^{1.25}$$

- Liquid fraction Reynold's number:

$$Re_L = \tfrac{(1-x)GD}{\mu_L}$$

- Bubble growth suppression factor:

$$S = \tfrac{1}{1 + 0.00000253 Re_{tp}^{1.17}}$$

- Forced convection heat transfer coefficient (Dittus-Boelter):

$$h_L = 0.023 Re_L^{0.8} Pr_L^{0.4} \tfrac{k_L}{D},$$

- Nucleate boiling heat transfer coefficient:

$$h_{F-Z} = 0.00122 \tfrac{k_L^{0.79} c_{pL}^{0.45} \rho_L^{0.49}}{\sigma^{0.5} \mu_L^{0.29} h_{fg}^{0.24} \rho_v^{0.24}} (\Delta T)^{0.24} (\Delta P)^{0.75}$$

- Mean heat transfer coefficient:

$$h_{tp} = S h_{F-Z} + F h_L$$

3.3.2.2. Shah

The author presented a general correlation named *CHAPT* for the estimation of heat transfer coefficients during saturated boiling at subcritical heat flux in tubes and annuli. The relation compares the convective and nucleate boiling heat transfer coefficient obtained by an analysis of prevalent phenomena in the channel. The original idea behind the Boiling number correction is to allow for the enhancement of the forced convective heat transfer mechanisms arising from the generation of vapor in the boundary layer next to the wall. However, the presence of the boiling number term appears to prevent application to sub-cooled boiling.

The correlation is applicable to both horizontal and vertical tubes with a wide range of fluids and conditions. It was compared to 780 data points from 19 independent experimental studies. The pressure range is about *0.004* to *0.8 bar.*

Following relations express the model:

- Boiling number:

$$Bo = \frac{q}{G\Delta H_{lv}}$$

- Liquid fraction Reynold's number:

$$Re_L = \frac{(1-x)GD}{\mu_L}$$

- Prandtl's number:

$$Pr_L = \frac{\mu_L C_p}{K_L}$$

- Liquid heat transfer coefficient (Dittus-Boelter):

$$h_L = 0.023 Re_L^{0.8} Pr_L^{0.4} \frac{k_L}{D}$$

- Convection number:

$$N_{Co} = \left(\frac{1-x}{x}\right)^{0.8} \left(\frac{\rho_g}{\rho_L}\right)^{0.5}$$

- Convective boiling enhancement factor:

$$F = \begin{cases} 14.7 & Bo > 0.0011 \\ 15.43 & Bo < 0.0011 \end{cases}$$

- Nucleate boiling liquid coefficients:
  - If $N_{Co} > 1$:

$$\frac{h_{nb}}{h_L} = \begin{cases} 230Bo^{0.5} & Bo > 0.0003 \\ 1 + 46Bo^{0.5} & Bo < 0.0003 \end{cases}$$

  - If $0.1 < N_{Co} < 1$:

$$\frac{h_{nb}}{h_L} = FBo^{0.5} \exp(2.74N_{Co} - 0.1)$$

  - If $0.1 > N_{Co}$:

$$\frac{h_{nb}}{h_L} = FBo^{0.5} \exp(2.74N_{Co} - 0.15)$$

- Convective boiling on liquid heat transfer coefficients:

$$\frac{h_{cb}}{h_L} = \frac{1.8}{N_{Co}^{0.8}}$$

- Mean heat transfer coefficient:

$$h_{tp} = MAX(h_{cb}, h_{nb})$$

3.3.2.3. Gungor and Winterton

The correlation is projected for forced convection boiling with the aid of a databank that consists of over 4300 data points *for water, common refrigerants (CF)* and *ethylene glycol*. Gungor and Winterton used the same layout of Chen's relation to describe an additive heat transfer constituted from two different part:

- liquid heat transfer by Dittus-Boelter relation,
- pool boiling heat transfer by Cooper relation.

The correlation is valid both for saturated boiling in vertical and horizontal tubes with diameter from *2.95* to *32 mm* and a pressure range of *0.08-202.6 bar.*

Following relations express the model:

- Liquid fraction Reynold's number:

$$Re_L = \frac{(1-x)GD}{\mu_L}$$

- Prandtl's number:

$$Pr_L = \frac{\mu_L C_p}{K_L}$$

- Boiling number:

$$Bo = \frac{q}{G\Delta H_{lv}}$$

- Reduced pressure:

$$P_r = \frac{P}{P_{crit}}$$

- Liquid heat transfer coefficient (Dittus-Boelter):

$$h_L = 0.023 Re_L^{0.8} Pr_L^{0.4} \frac{k_L}{D}$$

- Convective boiling enhancement factor:

$$E = 1 + 24000 Bo^{1.16} + 1.37(1/X_{tt})^{0.86}$$

- Bubble growth suppression factor:

$$S = \frac{1}{1 + 1.15 \times 10^{-6} F^2 Re_L^{1.17}}$$

- Nucleate boiling heat transfer coefficients (Cooper):

$$h_{nb} = 55 P_r^{0.12} (-\log P_r)^{-0.55} M^{-0.5} q^{0.67}$$

- Mean heat transfer coefficient:

$$h_{tp} = F h_L + S h_{nb}$$

3.3.2.4.   Kandlikar

This correlation is an evolution of the oldest correlation for predicting saturated flow boiling heat transfer coefficients inside horizontal and vertical tubes proposed by the same author. The model is based on the contributions of nucleate boiling and convective mechanisms and incorporated a fluid-dependent parameter F_{fl} in the nucleate boiling term. The correlation can be extended to other fluids by evaluating the fluid-dependent parameter F_{fl} for that fluid from its flow boiling or pool boiling data.

The fluid database utilized cover over 5246 data points from 24 experimental investigations with *water, R11, R12, R22, R113, R114, R152a, nitrogen* and *neon*. The diameter range is *4.6-32 mm,* the mass flux range is *13-8179 kg/m²s*, the quality range is *0.001-0.987*, the pressure range is *0.4-64.2 bar* and the Confinement number range is *0.004-52.1.*

Following relations express the model:

- All liquid Reynold's number:

$$Re_{L0} = \frac{GD}{\mu_L}$$

- Prandtl's number:

$$Pr_L = \frac{\mu_L C_p}{K_L}$$

- All liquid heat transfer coefficient (Dittus-Boelter):

$$h_{Lo} = 0.023 Re_{Lo}^{0.8} Pr_L^{0.4} \frac{k_L}{D}$$

- Convection number:

$$N_{Co} = \left(\frac{1-x}{x}\right)^{0.8} \left(\frac{\rho_g}{\rho_L}\right)^{0.5}$$

- Froude's number:

$$Fr^2 = \frac{v^2}{gD}$$

- Orientation flux exponential constant:
  - $C = 0$ for horizontal flux
  - $C = 0.3$ for vertical flux
- Nucleate boiling heat transfer coefficients

$$h_{nb} = [0.6683N_{Co}^{-0.2}(25Fr_{Lo})^c + 1058Bo^{0.7}F_{fl}]h_{Lo}$$

- Convection heat transfer coefficients

$$h_{conv} = [1.136N_{Co}^{-0.9}(25Fr_{Lo})^c + 667.2Bo^{0.7}F_{fl}]h_{Lo}$$

- Mean heat transfer coefficients

$$h_{tp} = MAX(h_{conv}, h_{nb})$$

3.3.2.5. Liu and Winterton

This model substitutes the Boiling number instead of the Prandtl number for nucleate boiling dependence. In this way an accurate predictive method covering a very wide range of parameters is constructed with an explicit nucleate boiling term and without boiling number dependence.

The correlation work for all common fluids and refrigerants with a mass flux range of *12.4-8179.3 kg/m²s*, a heat flux range of *348.9-2.62 * 10⁶ W/m²*, a quality range of *0-0.948*, a diameter of *2.95-32 mm*, reduced pressure range of *0.0023-0.895*. Raynold's number range is *568.9–8.75 * 10⁵* and Prandtl's number from *0.83* to *9.1*.

Following relations express the model:

- All liquid Reynold's number:

$$Re_{L0} = \frac{GD}{\mu_L}$$

- Prandtl's number:

$$Pr_L = \frac{\mu_L C_p}{K_L}$$

- Reduced pressure:

$$Pr = \frac{P}{P_{crit}}$$

- Convective boiling enhancement factor:

$$F = \left[1 + xPr_L\left(\frac{\rho_L}{\rho_g} - 1\right)\right]^{0.35}$$

- Bubble growth suppression factor:

$$S = \frac{1}{1 + 0.055F^{0.1}Re_{Lo}^{0.16}}$$

- All liquid heat transfer coefficient (Dittus-Boelter):

$$h_{Lo} = 0.023Re_{Lo}^{0.8}Pr_L^{0.4}\frac{k_L}{D}$$

- Nucleate boiling heat transfer coefficient (Cooper):

$$h_{nb} = 55P_r^{0.12-0.434\ln R_p}(-\log P_r)^{-0.55}M^{-0.5}q^{0.67}$$

- Two-phase heat transfer coefficient:

$$h_{tp} = \sqrt{(Fh_{Lo})^2 + (Sh_{nb})^2}$$

3.3.3. Micro Scale Models

Following micro scale models are presented.

3.3.3.1.   Lazarek and Black

Lazarek and Black measured the local heat transfer coefficient and the critical heat flux in saturated boiling of *R-113* in a round tube with an internal diameter of *0.31 cm*, and heated lengths of *12.3* and *24.6 cm*. They used both vertical upper flow and down flow configurations, the mass flux range is from *125* to *750 kg/m²s*, the heat flux range is between *14* and *380 kW/m²* and pressure range is *1.3-4.1 bar*. The obtained correlation for the local heat transfer coefficient is expressed in term of the Nusselt's number as a function of the liquid Reynolds number and Boiling number.

The resulting relations are quite simple:

- All liquid Reynold's number:

$$\mathrm{Re}_{L0} = \frac{GD}{\mu_L}$$

- Boiling number:

$$Bo = \frac{q}{G\Delta H_{lv}}$$

- Two-phase heat transfer coefficient:

$$h_{tp} = 30\mathrm{Re}_{Lo}^{0.857} Bo^{0.714}(k_L/D)$$

3.3.3.2.   Tran et al.

The correlation of Tran et al. for heat transfer has been developed for small circular channel of *2.46 mm* diameter and a small rectangular channel of hydraulic diameter of *2.40 mm* with *R-12* and *R-113*. The obtained data range over of qualities up to *0.94*, a mass flux range of *44-832 kg/m²s*, and a heat flux range of *7.5-129kW/m²*. Reduced pressure range is *0.045-0.2*. Local heat transfer coefficients were determined experimentally as a function of quality along the length of the test section. The correlation is valid for both nucleation and convection-dominant boiling heat transfer regimes.

The resulting relations are:

- Weber's number:

$$We_L = \frac{G^2 D}{\rho_L \sigma}$$

- Boiling number:

$$Bo = \frac{q}{G\Delta H_{lv}}$$

- Two-phase heat transfer coefficient:

$$h_{tp} = 840000(Bo^2 We_L)^{0.3} \left(\frac{\rho_L}{\rho_g}\right)^{-0.4}$$

3.3.3.3.   Kew and Cornwell

The correlation is for boiling in single, small-diameter tubes in a compact two-phase heat exchanger. It calculates the heat transfer coefficients for *R141b* that flow in *500 mm* long tubes with diameters of *1.39-3.69 mm*. The established correlation predicts the heat transfer coefficients reasonably well for the largest tube, but the accuracy slightly falls with the decrease of tube diameter. From the

correlation results that simple nucleate pool boiling correlations, such as that of Cooper, predicts with a well agreement the data.

The resulting relations are:

- All liquid Reynold's number:

$$\text{Re}_{L0} = \frac{GD}{\mu_L}$$

- Boiling number:

$$Bo = \frac{q}{G\Delta H_{lv}}$$

- Two-phase heat transfer coefficient:

$$h_{tp} = 30\text{Re}_{Lo}^{0.857} Bo^{0.714} \frac{k_L}{D} (1 - x)^{-0.143}$$

3.3.3.4. Warrier et al.

Warrier et al. correlation is for FC-84 in small rectangular channel. It is developed for both single-phase forced convection and for subcooled and saturated nucleate boiling. The hydraulic diameter is *0.75 mm* the Boiling number range is $0.00027 < Bo < 0.00089$ and quality range is $0.03 < x < 0.55$. The channels are oriented horizontally and uniform heat fluxes is applied at the top and bottom surfaces.

The resulting relations are:

- Boiling number:

$$Bo = \frac{q}{G\Delta H_{lv}}$$

- Two-phase heat transfer coefficient:

$$h_{tp} = [1 + 6Bo^{1/16} - 5.3x^{0.65}(1 - 855Bo)] \frac{4.36k_L}{D}$$

3.3.3.5. Kandlikar and Balasubramanian

The correlation is modified from the Kandlikar correlation for macro scale flow boiling. It was modified by using the laminar single-phase heat transfer coefficient for all liquid flow. The correlation is also extended for flow boiling in micro channels using the nucleate boiling as the dominant part of the original correlation. The trends in heat transfer coefficient versus quality are compared in the laminar and deep laminar regions in mini channels and micro channels. F_{Fl} is the same parameter of the old correlation.

The applicability range is for *water, R11, R12, R22, R113, R114, R152a, nitrogen* and *neon*, with a diameter range of *0.19-32.0 mm,* a mass flux range of *13-8179kg/m²s*, a heat flux range of *0.3-2280kW/m²*, a pressure range of *0.4-64.2 bar*.

The resulting relations are:

- All liquid Raynold's number:

$$\text{Re}_{L0} = \frac{GD}{\mu_L}$$

- Boiling number:

$$Bo = \frac{q}{G\Delta H_{lv}}$$

- Convection number:

$$N_{Co} = \left(\frac{1-x}{x}\right)^{0.8} \left(\frac{\rho_g}{\rho_L}\right)^{0.5}$$

- The liquid laminar heat transfer correlation changes in function of Reynolds liquid number:
  - $Re_{L0} < 100$ (directly two phase coefficient)

$$h_{tp} = h_{NBD}(1-x)^{0.8} h_{Lo}$$

  - $100 < Re_{L0} < 1600$:

$$h_{Lo} = 0.023 Re_{Lo}^{0.8} Pr_L^{0.4} \frac{k_L}{D}$$

  - $1600 < Re_{L0} < 3*10^3$:
    Linear interpolation between upper and lower coefficient
  - $3*10^3 < Re_{L0} < 10^4$:

$$h_{Lo} = \frac{(Re_{Lo}-1000)Pr_L(f/2)(k_L/D)}{1+12.7(Pr_i^{2/3}-1)(f/2)^{0.5}}$$

  - $10^4 < Re_{L0} < 5*10^6$:

$$h_{Lo} = \frac{Re_{Lo}Pr_L(f/2)(k_L/D)}{1+12.7(Pr_L^{2/3}-1)(f/2)^{0.5}}$$

- Convective boiling heat transfer coefficient:

$$h_{CBD} = 1.136 N_{Co}^{-0.9} + 667.2 Bo^{0.7} F_{Fl}$$

- Nucleate boiling heat transfer coefficient:

$$h_{NBD} = (0.6683 N_{Co}^{-0.2} + 1058 Bo^{0.7} F_{Fl})$$

- Two-phase heat transfer coefficient:

$$h_{tp} = \max(h_{CBD}, h_{NBD}) (1-x)^{0.8} h_{Lo}$$

3.3.3.6. Zhang et al.

The correlation is based on the existing experimental investigations of flow boiling. The correlation is for saturated flow boiling, developed for liquid-turbulent and gas-turbulent flow conditions. Therefore, the correlation may not be suitable to predict heat transfer coefficients in micro tubes when flow conditions are liquid-laminar and gas-turbulent. This regime consideration influences the Reynolds number factor F and the single-phase heat transfer coefficient h_{sp}. The model is based on the Chen correlation for four flow conditions such as liquid-laminar and gas-turbulent one often occurring in mini-channels.

The correlation applicability range is: from *0.78* to *6.0 mm* for hydraulic diameter, from *23.4* to *2939 kg/m²s* for mass flux, from *2.95* to *2511 kW/m²* for heat flux and from *1.01* to *8.66 bar* for pressure. The correlation works for *water* and *most common refrigerants (FC and R series)*.

The resulting relations are:

- Liquid fraction Reynold's number:

$$Re_L = \frac{(1-x)GD}{\mu_L}$$

- Vapor fraction Reynold's number:

$$Re_g = \frac{xGD}{\mu_g}$$

- Prandtl's liquid number:

$$Pr_L = \frac{\mu_L C_{pL}}{K_L}$$

- Prandtl's vapor number:

$$Pr_g = \frac{\mu_g C_{pg}}{K_g}$$

- Martinelli's parameter:

$$X = \left(\frac{f_L}{f_g}\right)^{0.5} \left(\frac{1-x}{x}\right) \left(\frac{\rho_g}{\rho_L}\right)^{0.5}$$

- Nusselt reation for or Re_L:
  - *If $Re_L < 2000$ (laminar flow):*

$$\max(4.36, Nu_{Collier})$$

$$Nu_{Collier} = 0.17Re_L^{0.33}Pr_L^{0.43} \left(\frac{Pr_L}{Pr_w}\right)^{0.25} \times \left[\frac{g\beta\rho_L^2 D_h^3(T_w - T_L)}{\mu_L^2}\right]^{0.1}$$

  - If $Re_L > 2300$ (Dittus-Boelter):

$$0.023Re_L^{0.8}Pr_L^{0.4}$$

  - If $2000 < Re_L < 2300$:
                Interpolate between two previous relations.
- Liquid heat transfer coefficient:

$$h_L = (k_L/D)Nu$$

- Friction factor in function of $Re_{g\ or\ L}$:
  - If $Re_{g\ or\ L} < 1000$:

$$16/Re_{L\ or\ g}$$

  - If $Re_{g\ or\ L} > 2000$:

$$0.046\ Re_{L\ or\ g}^{-0.2}$$

  - If $2000 < Re_{L\ or\ g} < 2300$:
                Interpolate between two previous relations.
- Chilsom's constant:
  - for $Re_L < 1000$ and $Re_g < 1000$, $X = X_{vv}$ and $C = 5$
  - for $Re_L > 2000$ and $Re_g < 1000$, $X = X_{tv}$ and $C = 10$
  - for $Re_L < 1000$ and $Re_g > 2000$, $X = X_{vt}$ and $C = 12$
  - for $Re_L > 2000$ and $Re_g > 2000$, $X = X_{tt}$ and $C = 20$
  - Obtained by interpolation between previous coefficients.
- Two-phase frictional multiplier:

$$\phi_L^2 = 1 + \frac{C}{X} + \frac{1}{X^2}$$

- Convective boiling enhancement factor:

$$F' = 0.64\phi_L$$
$$F = MAX(F', 1)$$

- Nucleate boiling suppression factor:

$$S = (1 + 2.53 \times 10^{-6} Re_L^{1.17})^{-1}$$

- Nucleate boiling heat transfer coefficient (Foster-Zuber):

$$h_{nb} = 0.00122 \left(\frac{k_L^{0.79} C_{pL}^{0.45} \rho_L^{0.49}}{\sigma^{0.5} \mu_L^{0.29} h_{fg}^{0.24} \rho_g^{0.24}}\right) \Delta T_{sat}^{0.24} \Delta P_{sat}^{0.75}$$

- Nucleate boiling heat transfer coefficient (Cooper):

$$h_{nb} = 55 P_r^{0.12-0.434\ln R_p} (-\log P_r)^{-0.55} M^{-0.5} q^{0.67}$$

- Two-phase heat transfer coefficient:

$$h_{tp} = S h_{nb} + F h_L$$

3.3.3.7. Lee and Mudawar

The correlation of Lee and Mudawar is for R134a in micro-channel. It is associated with different mechanisms and relation for low, medium and high qualities. The correlation is divided in function of quality in three different zones:

- low qualities: corresponding to very low heat fluxes and a nucleate boiling,
- medium quality: high thermal fluxes,
- high quality: dominated by annular film evaporation.

Because of the large differences in heat transfer mechanism between the three quality regions, better predictions are possible by dividing the quality range into smaller ranges corresponding to these flow transitions. The heat transfer coefficient correlation work for both R134a and water for a hydraulic diameter of *0.35mm.*

The resulting relations are:

- Weber's number:

$$We_L = \frac{G^2 D}{\rho_L \sigma}$$

- Reynold's numbers:

$$Re_g = \frac{xGD}{\mu_g} \quad Re_L = \frac{xGD}{\mu_L}$$

- Prandtl's numbers:

$$Pr_L = \frac{\mu_L C_{pL}}{K_L} \quad Pr_g = \frac{\mu_g C_{pg}}{K_g}$$

- Liquid heat transfer coefficient (Dittus-Boelter):

$$h_g = 0.023 Re_L^{0.8} Pr_L^{0.4} \frac{k_L}{D}$$

- Vapor heat transfer coefficient (Dittus-Boelter):

$$h_g = 0.023 Re_g^{0.8} Pr_g^{0.4} \frac{k_g}{D}$$

- Two-phase heat transfer coefficient:
  - for *x < 0.05*:

$$h_{tp} = 3.856 X^{0.267} h_L$$

  - for *0.05 < x < 0.55*:

$$h_{tp} = 436.48 Bo^{0.522} We_L^{0.351} X^{0.665} h_L$$

  - for *x > 0.55*:

$$h_{tp} = MAX(108.6 X^{1.665} h_g, h_g)$$

3.3.3.8. Saitoh et al.

The proposed correlation is Chen-type for flow boiling heat transfer of R-134a in horizontal tubes and it was modified to consider the effect of tube diameter. This effect on flow boiling heat transfer coefficient was characterized by the Weber number for the gas phase. This correlation could be applied to a wide range of tube diameters from *0.5* to *11 mm* and in a mass flux range of *150-450 kg/m²s*. The thermal flux can vary from *5* to *39 kW/m²* in a pressure range of *3.5-5 bar*. The refrigerant is *R-134a.*

The correlation is expressed by the following relations:

- Reynold's numbers:

$$\text{Re}_g = \frac{xGD}{\mu_g} \quad \text{Re}_L = \frac{(1-x)GD}{\mu_L}$$

- Weber's number:

$$We_L = \frac{G^2 D}{\rho_L \sigma}$$

- Martinelli's parameter:
    o for $\text{Re}_L > 1000$ and $\text{Re}_g > 1000$

$$X = \left(\frac{1-x}{x}\right)^{0.9} \left(\frac{\rho_g}{\rho_L}\right)^{0.5} \left(\frac{\mu_L}{\mu_g}\right)^{0.1}$$

    o for $\text{Re}_L < 1000$ and $\text{Re}_g > 1000$

$$X = \left(\frac{f_L}{f_g}\right)^{0.5} (\text{Re}_g^{-0.4}) \left(\frac{G_L}{G_g}\right)^{0.5} \left(\frac{\rho_g}{\rho_L}\right)^{0.5} \left(\frac{\mu_L}{\mu_g}\right)^{0.5}$$

- Liquid heat transfer coefficient h_L:
    o For $\text{Re}_L < 1000$ (Dittus-Boelter):

$$0.023 \frac{k_L}{D} \text{Re}_L^{0.8} \text{Pr}_L^{1/3}$$

    o For $\text{Re}_L > 1000$ (Developed flow):

$$\frac{4.36 k_L}{D}$$

- Convective boiling enhancement factor:

$$F = 1 + \left(\frac{1}{X}\right)^{1.05} / (1 + We_g^{-0.4})$$

- Bubble growth suppression factor:

$$S = 1/(1 + 0.4(F^{1.25} \times \text{Re}_L \times 10^{-4})^{1.4})$$

- Bubble diameter:

$$D_b = 0.512[\sigma/g(\rho_L - \rho_g)]^{0.5}$$

- Nucleate boiling heat transfer coefficient:

$$h_{nb} = 207 \frac{k_L}{D_b} \left(\frac{qD_b}{k_L T_L}\right)^{0.745} \left(\frac{\rho_g}{\rho_L}\right)^{0.581} \text{Pr}_L^{0.533}$$

- Two-phase heat transfer coefficient:

$$h_{tp} = S h_{nb} + F h_L$$

3.3.3.9.   Bertsch et al.

Bertsch et al. correlation is applicable over a wide range of parameters. It is developed including nucleate boiling and convective heat transfer terms while accounting for the effect of bubble confinement in small channels. The correlation is developed from a database of *3899* data points from *14* studies covering *12* different fluids. The hydraulic diameters range is from *0.16* to *2.92 mm*, and confinement numbers is from *0.3* to *4.0*. The mass fluxes included in the database range from *20* to *3000 kg/m²s*, the heat fluxes from *0.4* to *115 W/cm²*, the vapor qualities from *0* to *1*, and the saturation temperatures from -194 to *97 °C*.

The resulting relations are:

- Reynold's numbers:

$$\text{Re}_{g0} = \frac{GD}{\mu_g} \; ; \text{Re}_{L0} = \frac{GD}{\mu_L}$$

- Prandtl's numbers:

$$\text{Pr}_L = \frac{\mu_L C_{pL}}{K_L}; \text{Pr}_g = \frac{\mu_g C_{pg}}{K_g}$$

- Reduced pressure:

$$\text{P}_r = \frac{P}{P_{crit}}$$

- Confinement number:

$$Co = \frac{\sqrt{\sigma/g\Delta\rho}}{D}$$

- Liquid turbulent heat transfer coefficient (Dittus-Boelter):

$$h_{L0} = 0.023 Re_{L0}^{0.8} Pr_L^{0.4} \frac{k_L}{D}$$

- Vapor heat turbulent heat transfer coefficient (Dittus-Boelter):

$$h_{g0} = 0.023 Re_{g0}^{0.8} Pr_g^{0.4} \frac{k_g}{D}$$

- Vapor and liquid laminar heat transfer coefficient:

$$h_{Lo/go} = \frac{k_{L/g}}{D}\left[3.66 + \frac{0.0668 \frac{D}{L} Re_{Lo/go} Pr_{L/g}}{1 + 0.04\left(DRe_{Lo/go} \frac{Pr_{L/g}}{L}\right)^{2/3}}\right]$$

- Convective boiling enhancement heat transfer coefficient:

$$h_{conv} = (1 - x)h_{Lo} + xh_{go}$$

- Convective boiling enhancement factor:

$$F = 1 + 80(x^2 - x^6)\exp(-0.6Co)$$

- Nucleate boiling heat transfer coefficient (Cooper):

$$h_{nb} = 55 P_r^{0.12 - 0.434 \ln R_p}(-\log P_r)^{-0.55} M^{-0.5} q^{0.67}$$

- Bubble growth suppression factor:

$$S = (1 - x)$$

- Mean heat transfer coefficient:

$$h_{tp} = Sh_{nb} + Fh_{conv}$$

3.3.3.10. Mikielewicz

A prediction method for small-diameter channels and mini channels was presented by Mikielewicz. The correlation for heat transfer in saturated boiling regime is presented, contrary to other approaches, in the cases of both conventional and small-diameter channels. The author compared the results of calculations with some experimental data available from literature on conventional size tubes and mini channels. The model is based on the analogy between momentum transfer and energy transfer. It started with the premise that the total energy dissipation in the flow is the sum of the energy dissipation due to shearing flow without nucleation and the energy dissipation due to nucleation. Under steady state conditions in two phase flow, the energy dissipation was approximated by the viscous energy dissipation per unit volume in the boundary layer. Using the analogy between momentum and energy transfer, the two phase heat transfer coefficient was written in a form similar to the asymptotic model. The two phase heat transfer coefficient was expressed in terms of the frictional two phase multiplier of Muller-Steinhagen and Heck, the boiling number and the all-liquid Reynolds number. The Cooper pool boiling correlation was recommended for the nucleate boiling term corrected by a factor that depends on the all liquid Reynolds number, boiling number and the frictional two phase multiplier.

The correlation is expressed with the following relations:

- Reduced pressure:

$$P_r = \frac{P}{P_{crit}}$$

- Nucleate boiling enhancement heat transfer coefficient (Cooper):

$$h_{nb} = 55 P_r^{0.12-0.434 \ln R_p} (- \log P_r)^{-0.55} M^{-0.5} q^{0.67}$$

- Friction factor:
  - Tubolent flow:

$$f_1 = \frac{\rho_g}{\rho_L} \left(\frac{\mu_L}{\mu_g}\right)^{0.25} \quad f_2 = \left(\frac{k_g}{k_L}\right)$$

  - Laminar flow:

$$f_1 = \frac{\rho_g}{\rho_L} \frac{\mu_L}{\mu_g} \quad f_2 = \frac{\mu_g}{\mu_L} \frac{c_{pL}}{c_{pg}} \left(\frac{k_L}{k_g}\right)^{1.5}$$

- Convective number of Muller-Steinhagen:

$$\phi_{MS} = \left[1 + 2\left(\frac{1}{f_1} - 1\right) x Co^{-1}\right](1-x)^{1/3} + \frac{x^3}{f_2}$$

- Convective additive factor:

$$P = 0.00253 Re_{Lo}^{1.17} Bo^{0.6} (\phi_{MS} - 1)^{-0.65}$$

- Two-phase on liquid only heat transfer coefficients:

$$\frac{h_{tp}}{h_{Lo}} = \sqrt{\phi_{MS}^n + \frac{1}{1+P}\left(\frac{h_{nb}}{h_{Lo}}\right)^2}$$

3.3.3.11. Li and Wu

The correlation is based on experimental results of the saturated flow boiling heat transfer in micro and mini channels for both single and multi-band channel. The database contains about *3700* data points and cover *12* types of working fluids, in a wide range of operational conditions, and, from *0.148* to *3.25 mm* tubes diameters. The correlation uses the boiling number, Bond's number and Reynold's number in a general form to calculate the evaporative heat transfer for micro and mini channels. In addition, the authors proposed the Bond's number like a criterion to classify a flow path as a micro channel or as a conventional macro channel.

- Liquid phase Raynold's number:

$$Re_L = (1-x)\frac{GD}{\mu_L}$$

- Boiling number:

$$Bo = \frac{q}{G \Delta H_{lv}}$$

- Bond's number:

$$Bn = \frac{\rho_L g D^2}{\sigma_L}$$

- Two-phase heat transfer coefficients:

$$h_{tp} = 334 Bo^{0.3} (Bd Re_L^{0.36})^{0.4} \frac{k_L}{D}$$

3.3.3.12. Mohamed and Karayiannis

The correlation proposed is a statistical correlation for flow boiling heat transfer for *R134a* in micro tubes with diameter ranging from *4.26* to *0.52 mm*. The heat transfer coefficient was fitted as a

function of boiling number, Weber's number, liquid Reynold's number, confinement number and convection number using the multi-parameter nonlinear least square fitting. The correlation was based on *5152* data points excluding dry-out data and is valid for mass flux of *100-500 kg/m²s*, a pressure between *6-14 bar* and heat flux in between of *2.4-175.4 kW/m²*.

The expression of the correlation is reported as follow:

- Reynold's numbers:

$$Re_L = \frac{(1-x)GD}{\mu_L}$$

- Weber's number:

$$We_L = \frac{G^2 D}{\rho_L \sigma}$$

- Boiling number:

$$Bo = \frac{q}{G\Delta H_{lv}}$$

- Confinement number:

$$Co = \frac{\sqrt{\sigma/g\Delta\rho}}{D}$$

- Heat transfer coefficient in function of hydraulic diameter:
  - For $= 4.26 > D > 1.1\ mm$:

  $$h_{tp} = 3320 \frac{Bo^{0.63} We_L^{0.2} Re_L^{0.11}}{Co^{0.6}} \frac{k_L}{D}$$

  - For $D = 0.52\ mm$ and $x < 0.3$:

  $$h_{tp} = 3320 \frac{Bo^{0.63} We_L^{0.2} Re_L^{0.11}}{Co^{0.6}} \frac{k_L}{D}$$

  - For $D = 0.52\ mm$ and $x > 0.3$:

  $$h_{tp} = 5324 \left[\frac{Bo^{0.3} We_L^{0.25}}{N_{Co}^{0.25}}\right]^{1.79} \frac{k_L}{D}$$

3.3.4. Comparisons

The following comparisons came from the work of Mahmoud and Karayiannis [2012], they analyzed the heat transfer coefficients in small to micro diameter tubes. The test section has four stainless steel tubes; one tube with *D = 0.52 mm* and *L = 100 mm* and three tubes with *D = 1.1 mm* and *L = 150, 300, 450 mm*. All tubes were seamless cold drawn tubes made of stainless steel *AISI316*. Each test section consisted in an adiabatic calming section of length *150 mm*, a heated section and a borosilicate visualization section with total length of *100 mm*. The comparison was chosen for analogy with the actual experimental section that use a refrigerant with similar proprieties and tube diameters. Therefore, similar trends are expected.

3.3.4.1. Macro scale assessment

Following are presented the macro-scale comparisons:
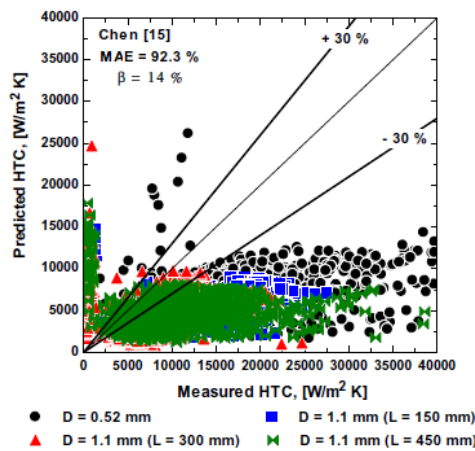
Figure 64: Global comparison of Chen correlation

The correlation predicted only *14%* of all data within the error band at a MAE value of *92.3%*. From the figure (64) is evident that the Chen correlation gives a heat transfer coefficient that increases with increasing vapor quality in the very low quality region and then shows up to a plateau as the quality increases. The behavior of the correlation at very low vapor quality values is opposite to the experimental. The maximum deviation between the predicted and measured values is expected to occur at very low vapor quality values and at high vapor quality values when the experimental heat transfer coefficient exhibits an increasing trend with vapor quality.
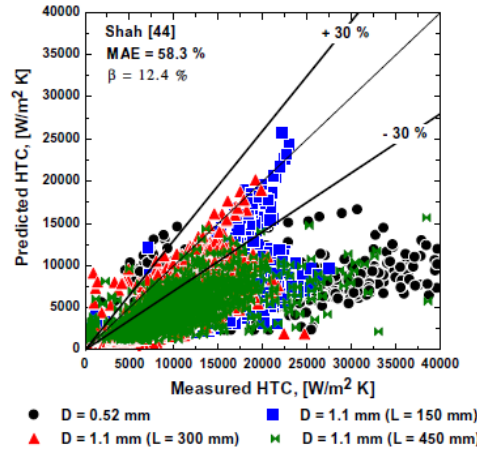
Figure 65: Global comparison of Shah correlation.

The correlation predicted *12.7%* of data within the error bands of 30% and the MAE value is *58.3%*. Figure (65) shows the heat transfer coefficient predicted by the Shah correlation. The value drops from a high value at very low vapor quality and then increases constantly with increasing vapor quality. This trend is like the current experimental trend. The correlation tends to work better in the very low quality region, at high system pressure, and at very high vapor quality.
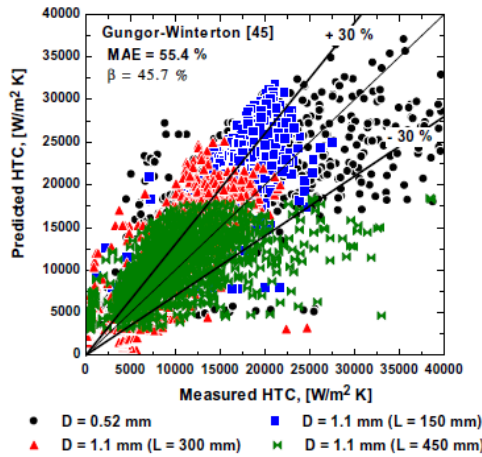
Figure 66: Global comparison of Gungor and Winterton correlation

The correlation predicted *45.7%* of all data within the *±30%* error band at a MAE value of *55.4%*. The figure (66) shows the performance of the correlation in all tubes. The correlation gives a heat transfer coefficient that is independent of vapor quality in the low quality region and it decreases slightly with quality in the high quality region. However, the correlation over-predicts the experimental values at high heat flux values. Therefore, the correlation works reasonably at low to intermediate heat flux values.
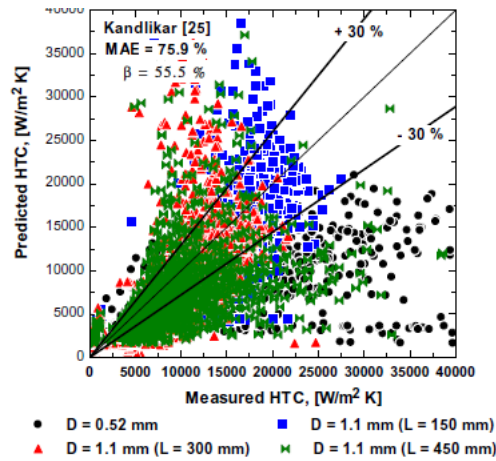
Figure 67: Global comparison of Kandlikar correlation

Kandlikar's correlation predicted *55.5%* of all data within the *±30%* error band with MAE of *75.9%*. The figures (67) shows, that for the *0.52 mm* diameter tube, there is some agreement between the predicted and experimental values over a narrow range of vapor quality. The correlation seems to underestimate most of the data in the tube. On the contrary, the correlation captured the correct experimental trend and magnitudes in the shortest *1.1 mm* diameter tube up to high vapor quality. The over-prediction depicted for the tube diameter of *1.1 mm* tube occur at high vapor qualities. Therefore, Kandlikar's correlation underestimates the trend up to intermediate vapor quality and overestimates the values for high vapor qualities.
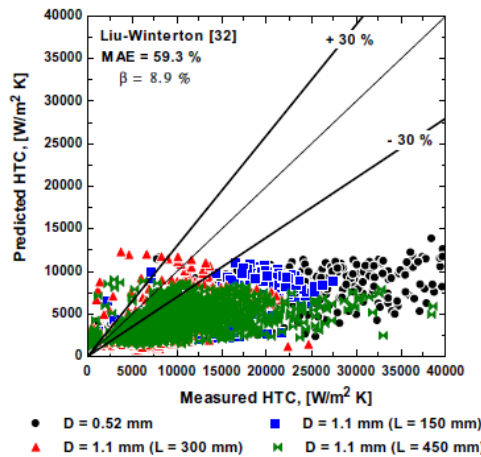
Figure 68: Global comparison of Liu and Winterton correlation

The Liu and Winterton correlation predicted *8.9%* of all data within the error band at a MAE value of *59.3%*. This correlation looks similar in performance to Chen correlation. Figure (68) shows the comparison.

3.3.4.2. Micro scale assessment

Following are presented the micro-scale comparisons:
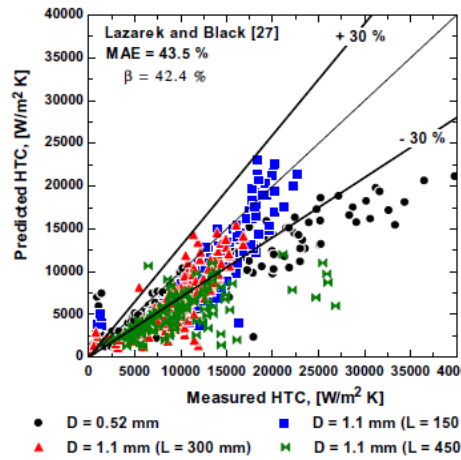
Figure 69: Global comparison of Lazarek and Black correlation

Lazarek and Black correlation predicted *42.4%* of the data within the error band and the MAE is *43.5%*. Its performance is consistent with the behavior of the measured heat transfer coefficient in the bigger tube. The measured coefficient drops from maximum value at starting ebullition, then it remains approximately constant over a low quality range. The correlation prediction remains constant with quality, so the correlation highly underestimates the experimental values at high quality. However, the correlation success in predicting most of the data in the shortest tube. The correlation was developed considering nucleate boiling as the only dominant mechanism of flow boiling and thus the predictions deteriorate as the heated length increases due to contribution of nucleate and convective boiling. Figure (69) shows the comparison.
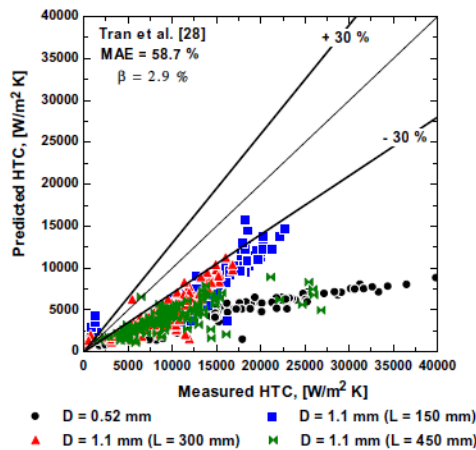
Figure 70: Global comparison of Tran et al. correlation

Tran et al. correlation predicted only *2.9%* of the data within the *±30%* error band. The model considers a dominance of nucleate boiling mechanism. However, there is a big difference in the performance of this correlations compared to the actual experimental data.Tran et al. correlation highly underestimates the experimental data and a decrease in the tube diameter results in a decrease in the heat transfer coefficient, which is contrary to the trend in Lazarek and Black. Figure (70) shows the comparison.
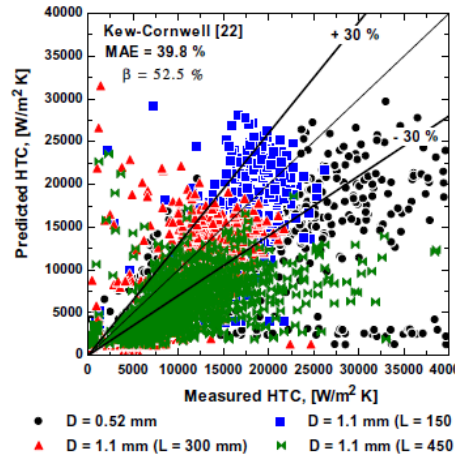
Figure 71: Global comparison of Kew and Cornwell correlation

Kew and Cornwell correlation predicted only *52.5%* of the data within the error bands with a MAE of *39.8%* as can be seen in figure (71). It is a modified version of Lazarek and Black correlation, in fact the difference in performance is not large. The correlation predicts the heat transfer coefficient increase at a slow rate with quality at the very low quality region and at a relatively faster rate in the high quality region.
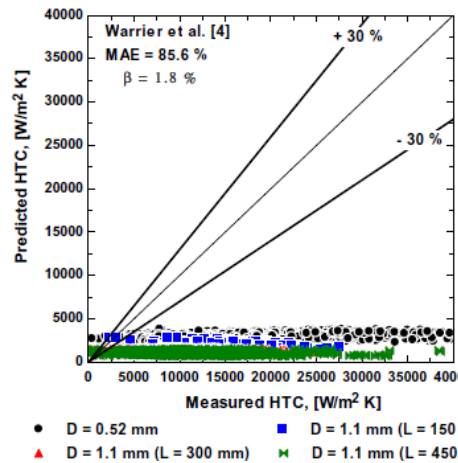
Figure 72: Global comparison of Warrier et al. correlation

Warrier et al. correlation predicted *1.8%* of the data within the error bands with a MAE of *85.6%*. The proprieties difference between the fluid used to make the correlation (*FC-84*) and the fluid used in the comparison (*R-134a*) has a strong impact on the prediction accuracy. Figure (72) shows its results.
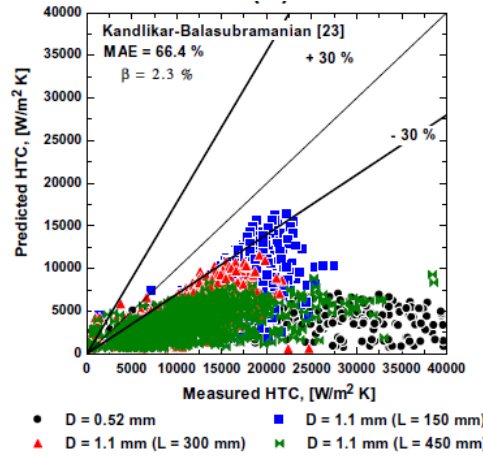
Figure 73: Global comparison of Kandlikar and Balasubramanian correlation

Kandlikar and Balasubramanian correlation predicted *2.3%* of the data within the error band and the MAE of *66.4%* as can be seen in figure (73).
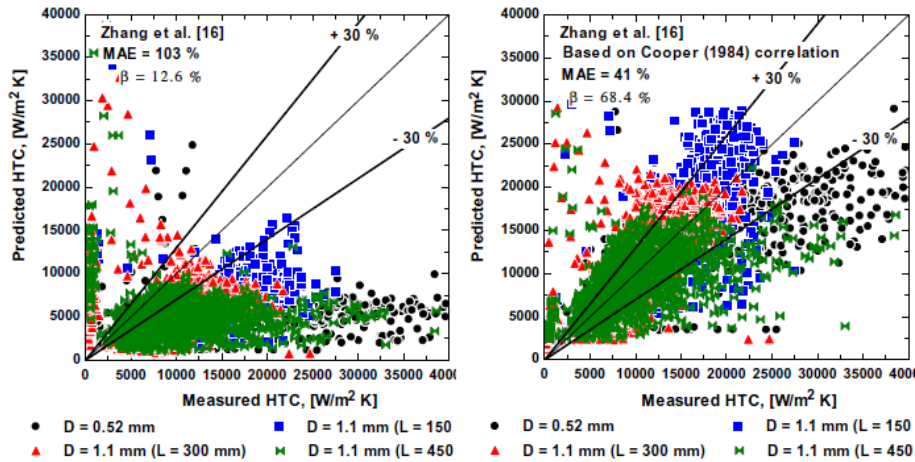
Figure 74, 75: Global comparison of Zhang et al. correlation with Foster-Zuber (first figure) and Cooper (second figure) heat transfer correlation for nucleate boiling.

The best result for Zhang et al. correlation came modifying with the Cooper correlation for the nucleate boiling instead of the Forster-Zuber relation in the original correlation. The figures (74, 75) show the modified correlation. The prediction displacement is *68.4%* within the *±30%* error bands and the MAE is *41%*. The original Zhang et al. correlation predicted only *12.6%* of data within the error bands with a MAE of *103%*. The behavior of the predicted local heat transfer coefficient using Zhang et al. original correlation is like that predicted by Chen correlation. Both correlations predict a heat transfer coefficient with a quick increase related to quality in the very low quality region and a slow increase in the high quality region, which is different from the experimental trend.
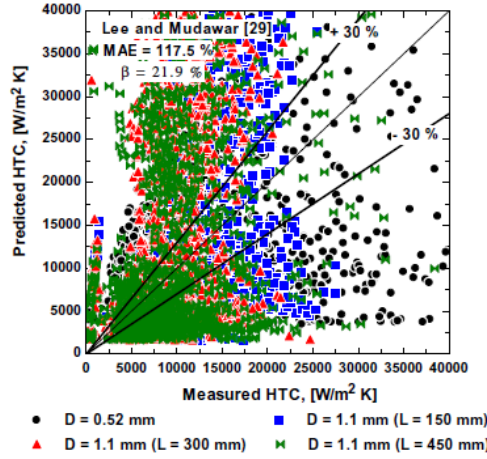
Figure 76: Global comparison of Lee and Mudawar correlation

Lee and Mudawar correlation predicted *21.5%* of the data within the error bands and a MAE of *117.5%*, see figure (76). The correlation predicts poorly the experimental values with a large scatter possibly because it is not capable of predicting the correct experimental trend. The local heat transfer coefficient behaves according to an N-shape trend, which is completely different from the measured experimental trends in all tubes. So, the correlation has captured only a few number of experimental points and either underestimates or overestimates the others. The current experimental data were collected through increasing the heat flux gradually at constant pressure and mass flux.
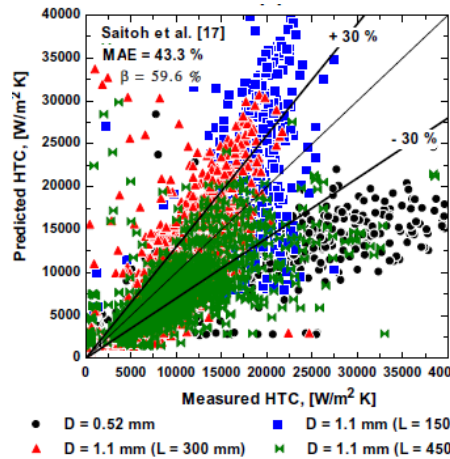
Figure 77: Global comparison of Saithoh et al. correlation

Saitoh et al. correlation predicted only *55.6%* of the data within the error bands with a MAE vale of *43.3%*. According to the figure (77) the correlation predicts the heat transfer coefficient increase with quality in the smallest tube and its slow decrease with vapor quality in the bigger tubes. Moreover, in all tubes the coefficient jumps to a very high value as the quality approaches to unity. Also, by inspecting the performance of the correlation at different operating conditions, it was found that the correlation highly under-predicts the data at low heat flux values. Like the abovementioned correlations, the performance of this correlation gets worse as the heated length increases.
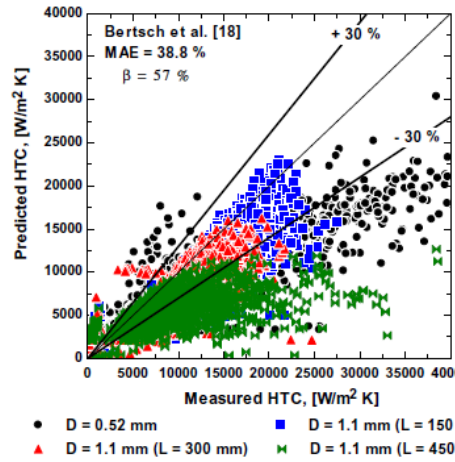
Figure 78: Global comparison of Bertsch et al. correlation

The global comparison of the present data with the correlation of Bertsch et al. is depicted in figure (78). It predicts only *57%* of all data within the error bands with MAE of *38.8%*. For the smallest diameter of tube, the correlation predicted values increase with vapor quality towards the exit. For the bigger tube, the correlation predicted heat transfer coefficient sharply or slightly decrease with vapor quality.
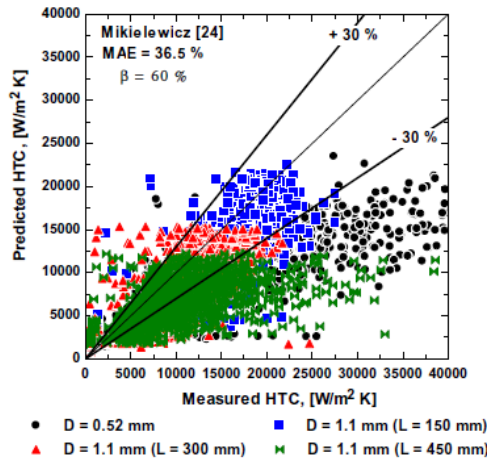
Figure 79: Global comparison of Mikielewicz correlation

Mikielewicz correlation predict up to *60%* of all data within the error bands. Its performance is significantly influenced by the variation of the heated length in the short tubes. The figure (79) shows how the correlation heat transfer coefficient values increase moderately with increasing vapor quality.
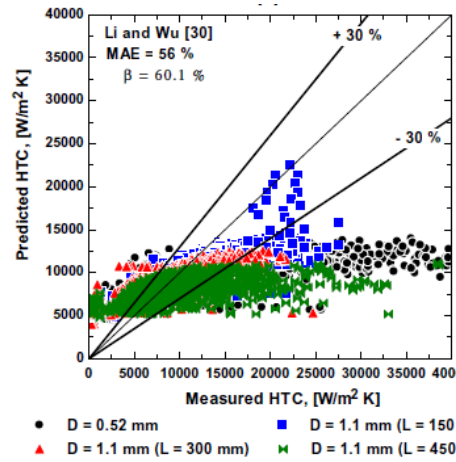
Figure 80: Global comparison of Li and Wu correlation

The correlation predicts *60.1%* of all data within the error bands at a MAE value of *56%* as it showed in figure (80). It highly underestimates the experimental values in the high quality region particularly when the measured heat transfer coefficient increases with vapor quality. Some investigations by other authors reported that the heat transfer coefficients increase with decreasing tube diameter.
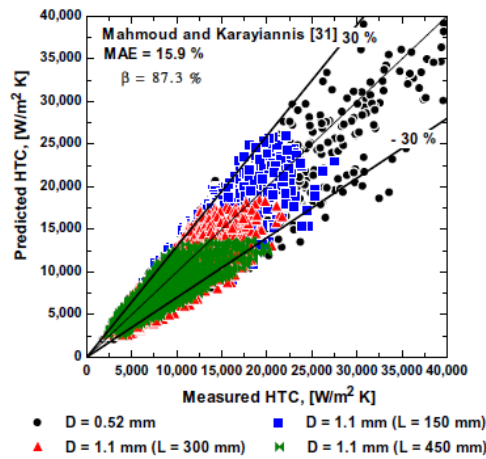
Figure 81: Global comparison of Mahamoud and Karayiannis correlation

This correlation predicted *87.3%* of the data within the *±30%* error bands and a MAE of *15.9%*, as can be seen in figure (81). However, Mahmoud and Karayiannis excluded the data of the two longest *1.1 mm* diameter tubes when developing the correlation.

3.3.5. Heat transfer model summary

In this paragraph all the models and correlations are summarized by category and in their application form.

3.3.5.1. Three-zone model

Table 1: Description of the Thome, Dupont and Jacobi model (2008)

<div align="center">Three-zone model:</div>

Reference heat flux:

$$q_0 = Aq * \left(\frac{P_{sat}}{P_{crit}}\right)^{Nq}$$

Bubble frequency:

$$f_p = \frac{1}{\tau} = \left(\frac{q}{q_0}\right)^{Nf}$$

Initial film thickness:

$$\frac{\delta_0}{d_i} = C_{\delta_0} * \left[3 * \left(\frac{\mu_l}{\rho_l * u_p * d_i}\right)^{\frac{1}{2}}\right]^{0.84} * \left[(0.07 * We_p^{0.41})^{-8} + 0.1^{-8}\right]^{-1/8}$$

Weber bubble-slug:

$$We_p = \frac{\rho_l * u_p^2 * d_i}{\sigma}$$

Film thickness:

$$\delta(z,t) = \delta_0(z) - \frac{q * t}{\rho_l * h_{lg}}$$

Time for dryout:

$$t_{dry,film}(z) = \rho_l * \frac{h_{lg}}{q} * [\delta_0(z) - \delta_{min}]$$

Final film thickness: If $t_{dry,film} => t_G$:

$$\delta_{end}(z) = \delta(z, t_g)$$
$$t_{film} = t_G$$

Else $t_{dry,film} < t_G$:

$$\delta_{end}(z) = \delta_{min}$$
$$t_{film} = t_{dryfilm}$$
$$t_{dry} = t_G - t_{film}$$

Time for next liquid slug:
Film thickness heat transfer coefficient:

$$\alpha_{film}(z) = \frac{k_l}{\delta_0 - \delta_{end} + 10^{-9}} * \ln\left(\frac{\delta_0}{\delta_{end}}\right)$$

Heat transfer coefficient for developed fluxes, Gnielinski:

$$Nu_{\text{lam or turb}}(z) = \frac{h * d_i}{k}$$

Friction coefficient f: If $Re >= 2300$:

$$Nu_{turb} = \frac{Pr * \frac{\xi}{8}(Re - 1000)}{1 + 12.7 * \left(\frac{\xi}{8}\right)^{0.5} * \left(Pr^{\frac{2}{3}} - 1\right)}$$

$$\xi = (1.58 * \ln(Re) - 3.28)^{-2}$$

Else:

$$Nu_{lam} = 4.36$$

Reynolds bubble-slug:

$$Re = \frac{\rho_{l\,or\,v} * u_p * d_i}{\mu_{l\,or\,v}}$$

Medium slugs heat transfer coefficient:

$$\alpha_{slug} = [\alpha_{lam}^4 + \alpha_{turb}^4]^{\frac{1}{4}} = \frac{k_{l\,or\,v}}{d_i} * [Nu_{lam}^4 + Nu_{turb}^4]^{\frac{1}{4}}$$

Heat transfer coefficient:

$$\alpha_{tp} = \frac{t_l}{\tau}\alpha_{slug,l}(z) + \frac{t_{film}}{\tau}\alpha_{film}(z) + \frac{t_{dry}}{\tau}\alpha_{slug,g}(z)$$

3.3.5.2. Bubble Coalescence Model

Table 2: Description of the Bubble Coalescence model (2004)

Slug-coalescence mode:l

Maximum bubble frequency:
$$f_{max} = 0.004 \left(\frac{q}{\sigma}\right)\left(\frac{\sigma^3}{q^2 D^3 \rho_v^2}\right)$$

Transition quality from bubble to coalescence:
$$x_c = 0.763 \left(\frac{q\rho_g \sigma}{\mu_l h_{lv} G^2}\right)^{0.39}$$

Transition quality from coalescence to annular:
$$x_a = 1.4 * 10^{-4}\left(\frac{GD}{\mu_l}\right)^{1.47}\left(\frac{G^2 D}{\rho_l \sigma}\right)^{-1.23}$$

Blasius friction factor:
$$fr_{v,Blasius} = 0.079\, Re^{0.25}$$

Calculated friction factor:
$$fr_q = 304 \left(\frac{GD}{\mu_l}\right)^{-1.16} * \left(\frac{\rho_l}{\rho_v}\right)^{-1.74} * \left(\frac{\mu_l}{\mu_v}\right)^{1.43} x_c^{-2}[1 - e^{-\frac{qD}{h-h_{vl}*\mu_l}}]$$

Shear stress:
$$\tau_i = \left(fr_q - fr_{v,Blasius}\right)G^2 x_c^2 / 2\rho_v$$

Boiling number:
$$Bo = \frac{q}{\rho_g * h_{lv} * D * f_{max}}$$

Coefficients:
$$\gamma = \left(\frac{x_a - x}{x_a - x_c}\right)^{\chi}$$
$$\psi_c = \xi\beta\left(\frac{1 - x_c}{x_a - x_c}\right)$$

Decline in bubble frequency at the transition to annular flow:
$$\beta = 1$$

Empirical parameter:
$$\chi = 3$$

Liquid fraction to film:
$$\xi = 0.002$$

Heat transfer function for $x = x_c$:
$$\Theta_{1c} = \frac{(1 - \psi_c) * \ln^2(1 + \frac{\rho_l}{\rho_v}x_c)}{\Theta_{3c}}$$

$$\Theta_{2c} = \frac{(1 - \psi_c) * \left[\ln(1 + \frac{\rho_l}{\rho_v}x_c) + 4Bo\right]^2}{\Theta_3}$$

$$\Theta_{3c} = 8 * \frac{\mu_l}{\tau_i} * \frac{G}{\rho_v D} * \frac{\rho_l}{\rho_v}x_c - \psi_c \ln^2(1 + \frac{\rho_l}{\rho_v}x_c)$$

Global heat transfer:
$$\alpha(x) = \frac{k_l}{D} * \frac{\left(\frac{\rho_l}{\rho_v}\right) * \left[\left(\frac{x_a - x}{x_a - x_c}\right)^{\beta}\right]^{\gamma} * \ln\left(\frac{1 - \Theta_{1c}}{1 - \Theta_{2c}}\right)}{Bo * (1 - \psi_c)}$$

3.3.5.3. Macroscale Correlations

Table 3: Macroscale Correlations

MACROSCALE

Chen

Martinelli parameter:
$$X_{tt} = \left(\frac{1 - x}{x}\right)^{0.9}\left(\frac{\rho_l}{\rho_v}\right)^{-0.51}\left(\frac{\mu_l}{\mu_v}\right)^{0.1}$$

Convective boiling enhancement factor:
$$F = \begin{cases} 1 & for\ \frac{1}{X_{tt}} \le 0.1 \\ 2.35\left(0.213 + \frac{1}{X_{tt}}\right)^{0.736} & for\ \frac{1}{X_{tt}} \le 0.1 \end{cases}$$

Reynolds Two-Phase:
$$Re_{tp} = Re_L F^{1.25}$$

Liquid fraction Reynolds number:
$$Re_l = \frac{(1 - x)GD}{\mu_l}$$

Bubble growth suppression factor:
$$S = \frac{1}{1 + 2.35 * 10^{-6} Re_{tp}^{1.17}}$$

Forced convection heat transfer coefficient (Dittus-Boelter [39]):	$h_l = 0.023 \dfrac{K_l}{D} Re_l^{0.8} Pr_l^{0.4}$
Nucleate boiling heat transfer coefficient:	$h_f = 0.00122 \dfrac{K_l^{0.79} C_{pl}^{0.45} \rho_l^{0.49}}{\sigma^{0.5} \mu_l^{0.29} h_{lv}^{0.24} \rho_v^{0.24}} (\Delta T_{sat})^{0.24} (\Delta P_{sat})^{0.75}$
Mean heat transfer coefficient:	$h_{tp} = S h_f + F h_l$

Shah

Boiling number:	$Bo = \dfrac{q}{G \Delta H_{lv}}$
Liquid fraction Reynolds number:	$Re_l = \dfrac{(1-x)GD}{\mu_l}$
Prandtl number:	$Pr_l = \dfrac{\mu_l C_p}{k_l}$
Liquid heat transfer coefficient (Dittus-Boelter [39]):	$h_l = 0.023 \dfrac{k_l}{D} Re_l^{0.8} Pr_l^{0.4}$
Convection number:	$N_{Co} = \left(\dfrac{1-x}{x}\right)^{0.8} \left(\dfrac{\rho_v}{\rho_l}\right)^{0.5}$
Convective boiling enhancement factor:	$F = \begin{cases} 14.7 & for\ Bo > 0.0011 \\ 15.43 & for\ Bo < 0.0011 \end{cases}$

Nucleate boiling on liquid heat transfer coefficients:

If $N_{Co} > 1$:

$$\frac{h_{nb}}{h_l} = \begin{cases} 230 Bo^{0.5} & for\ Bo > 0.0003 \\ 1 + 46 Bo^{0.5} & for\ Bo < 0.0003 \end{cases}$$

If $0.1 < N_{Co} < 1$:

$$\frac{h_{nb}}{h_l} = F\ Bo^{0.5} e^{2.74 N_{Co}-0.1}$$

If $0.1 > N_{Co}$:

$$\frac{h_{nb}}{h_l} = F\ Bo^{0.5} e^{2.74 N_{Co}-0.15}$$

Convective boiling on liquid heat transfer coefficients:	$\dfrac{h_{cb}}{h_l} = \dfrac{1.8}{N_{Co}^{0.8}}$
Mean heat transfer coefficient:	$h_{tp} = Max(h_{cb}, h_{nb})$

Gungor and Winterton

Liquid fraction Reynolds number:	$Re_l = \dfrac{(1-x)GD}{\mu_l}$
Prandtl number:	$Pr_l = \dfrac{\mu_l C_p}{k_l}$
Boiling number:	$Bo = \dfrac{q}{G \Delta H_{lv}}$
Reduced pressure:	$P_r = \dfrac{P}{P_{crit}}$
Liquid heat transfer coefficient (Dittus-Boelter [39]):	$h_l = 0.023 \dfrac{k_l}{D} Re_l^{0.8} Pr_l^{0.4}$
Convective boiling enhancement factor:	$E = 1 + 24000 Bo^{1.16} + 1.37(1/X_{tt})^{0.86}$
Bubble growth suppression factor:	$S = \dfrac{1}{1 + 1.15 * 10^{-6} Re_l^{1.17}}$
Nucleate boiling heat transfer coefficients (Cooper [38]):	$h_{nb} = 55 P_r^{0.12} (-log P_r)^{-0.55} M^{-0.5} q^{0.67}$
Mean heat transfer coefficient:	$h_{tp} = S h_f + F h_l$

Kandlikar

All liquid Reynolds number:	$Re_{l0} = \dfrac{GD}{\mu_{Ll}}$
Prandtl number:	$Pr_l = \dfrac{\mu_l C_p}{k_l}$
All liquid heat transfer coefficient (Dittus-Boelter [39]):	$h_{l0} = 0.023 * \dfrac{K_l}{D} Re_{l0}^{0.8} Pr_l^{0.4}$

Convection number:	$N_{Co} = \left(\dfrac{1-x}{x}\right)^{0.8}\left(\dfrac{\rho_v}{\rho_l}\right)^{0.5}$
Froude number:	$Fr^2 = \dfrac{v^2}{gD}$
Orientation flux exponential constant:	$C = 0$ for vertical flux $C = 0.3$ for horizontal flux
Nucleate boiling heat transfer coefficients	$h_{nb} = \left[0.6683 N_{Co}^{-0.2} * (25 Fr_{l0})^c + 1058 Bo^{0.7} F_{fl}\right] h_{l0}$
Convection heat transfer coefficients	$h_{conv} = \left[1.136 N_{Co}^{-0.9} * (25 Fr_{l0})^c + 667.2 Bo^{0.7} F_{fl}\right] h_{l0}$
Mean heat transfer coefficients	$h_{tp} = Max(h_{conv}, h_{nb})$
Liu and Winterton	
All liquid Reynolds number:	$Re_{l0} = \dfrac{GD}{\mu_l}$
Prandtl number:	$Pr_l = \dfrac{\mu_l C_p}{k_l}$
Reduced pressure:	$P_r = \dfrac{P}{P_{crit}}$
Convective boiling enhancement factor:	$F = \left[1 + x\, Pr_l(\dfrac{\rho_l}{\rho_v} - 1)\right]^{0.35}$
Bubble growth suppression factor:	$S = \dfrac{1}{1 + 0.055 F^{0.1} Re_{l0}^{0.16}}$
All liquid heat transfer coefficient (Dittus-Boelter [39]):	$h_{l0} = 0.023 \dfrac{k_l}{D} Re_{l0}^{0.8} Pr_l^{0.4}$
Nucleate boiling heat transfer coefficients (Cooper [38]):	$h_{nb} = 55 P_r^{0.12}(-log P_r)^{-0.55} M^{-0.5} q^{0.67}$
Mean heat transfer coefficients	$h_{tp} = \sqrt[2]{(S h_{nb})^2 + (F h_{l0})^2}$

3.3.5.4. Macroscale Correlations

Table 4: Microscale Correlations

MICROSCALE	
Lazarek and Black	
All liquid Reynolds number:	$Re_{l0} = \dfrac{GD}{\mu_l}$
Boiling number:	$Bo = \dfrac{q}{G \Delta H_{lv}}$
Two-phase heat transfer coefficient:	$h_{tp} = 30 \dfrac{k_l}{D} Re_{l0}^{0.857} Bo^{0.714}$
Tran et al.	
Weber number:	$We_l = \dfrac{G^2 D}{\rho_l \sigma}$
Boiling number:	$Bo = \dfrac{q}{G \Delta H_{lv}}$
Two-phase heat transfer coefficient:	$h_{tp} = 8.4\,10^5 (Bo^2 We_l)^{0.3}\left(\dfrac{\rho_l}{\rho_v}\right)^{-0.4}$
Kew and Cornwell	
All liquid Reynolds number:	$Re_{l0} = \dfrac{GD}{\mu_l}$
Boiling number:	$Bo = \dfrac{q}{G \Delta H_{lv}}$
Two-phase heat transfer coefficient:	$h_{tp} = 30 \dfrac{k_l}{D} Re_{l0}^{0.857} Bo^{0.714}(1-x)^{-0.143}$
Warrier et al.	
Boiling number:	$Bo = \dfrac{q}{G \Delta H_{lv}}$
Two-phase heat transfer coefficient:	$h_{tp} = 4.36 \dfrac{k_l}{D}[1 + 6 Bo^{\frac{1}{16}} - 5.3 x^{0.65}(1 - 855 Bo)]$
Kandlikar and Balasubramanian [33]	

All liquid Reynolds number:	$$\text{Re}_{l0} = \frac{GD}{\mu_{l0}}$$
Boiling number:	$$Bo = \frac{q}{G \Delta H_{lv}}$$
Convection number:	$$N_{Co} = \left(\frac{1-x}{x}\right)^{0.8} * \left(\frac{\rho_v}{\rho_l}\right)^{0.5}$$
Friction factor	$$fr = [1.58 \, ln(\text{Re}_{l0}) - 3.28]^{-2}$$

Liquid laminar heat transfer correlation in function of Reynolds:

$Re_{l0} < 100$ (directly two phase coefficient)

$$h_{tp} = h_{NBD}(1-x)^{0.8}h_{l0}$$

$100 < Re_{l0} < 1600$:

$$h_{l0} = 0.023 \frac{k_l}{D} Re_{l0}^{0.8} \text{Pr}_l^{0.4}$$

$1600 < Re_{l0} < 3 \ 10^3$:

Linear interpolation between upper and lower coefficient

$3*10^3 < Re_{l0} < 10^4$:

$$h_{l0} = \frac{(Re_{l0} - 1000)\text{Pr}_l \left(\frac{fr}{2}\right)\left(\frac{k_l}{D}\right)}{1 + 12.7 \left(\text{Pr}_l^{\frac{2}{3}} - 1\right)\left(\frac{fr}{2}\right)^{0.5}}$$

$10^4 < Re_{l0} < 5 \ 10^6$:

$$h_{l0} = \frac{Re_{l0}\text{Pr}_l \left(\frac{fr}{2}\right)\left(\frac{k_l}{D}\right)}{1 + 12.7 \left(\text{Pr}_l^{\frac{2}{3}} - 1\right)\left(\frac{fr}{2}\right)^{0.5}}$$

Convective boiling heat transfer coefficient:	$h_{CBD} = 1.136 N_{Co}^{-0.9} + 667.2 Bo^{0.7} F_{Fl}$
Nucleate boiling heat transfer coefficient:	$h_{NBD} = 0.6683 N_{Co}^{-0.9} + 1058 Bo^{0.7} F_{Fl}$
Two-phase heat transfer coefficient:	$h_{tp} = \max(h_{CBD}, h_{NBD})(1-x)^{0.8}h_{l0}$

Zhang et al.

Liquid fraction Reynolds number:	$$Re_l = \frac{(1-x)GD}{\mu_l}$$
Vapor fraction Reynolds number:	$$\text{Re}_v = \frac{xGD}{\mu_v}$$
Prandtl liquid number:	$$\text{Pr}_l = \frac{\mu_l C_{pl}}{k_l}$$
Prandtl vapor number:	$$\text{Pr}_v = \frac{\mu_v C_{pv}}{k_v}$$
Martinelli parameter:	$$X_{tt} = \left(\frac{1-x}{x}\right)\left(\frac{f_l}{f_v}\right)^{0.5}\left(\frac{\mu_l}{\mu_v}\right)^{0.5}$$
Expansion coefficient of liquid phase:	$$\beta = \frac{\rho_{bulk} - \rho_{film}}{[\rho_{film}(T_{film} - Tbulk)]}$$

Nusselt relation for or Re_L:

If $Re_L < 2000$ (laminar flow):

$$\max(4.36, Nu_{Collier})$$

$$Nu_{Collier} = 0.17 Re_l^{0.33} Pr_l^{0.43}\left(\frac{\text{Pr}_l}{\text{Pr}_v}\right)^{0.25}\left[\frac{g\beta\rho_l^2 D_h^3 (T_w - T_b)}{\mu_l^2}\right]^{0.1}$$

If $Re_L > 2300$ (Dittus-Boelter):

$$Nu = 0.023 Re_{l0}^{0.8} \text{Pr}_l^{0.4}$$

If $2000 < Re_L < 2300$:

Linear interpolation between upper and lower coefficient

Liquid heat transfer coefficient:

$$h_l = \frac{k_l}{D} Nu$$

Friction factor in function of $Re_{g \, or \, L}$:

If $Re_{g \, or \, L} < 1000$:

$$fr_{l \, or \, v} = \frac{16}{Re_{l \, or \, v}}$$

If $Re_{g \, or \, L} > 2000$:

$$fr_{l \, or \, v} = 0.046 Re_{l \, or \, v}^{-0.2}$$

If $2000 < Re_{L \, or \, g} < 2300$:

Linear interpolation between upper and lower coefficient

Chilsom constant:

For $Re_L < 1000$ and $Re_g < 1000$
$$X = X_{vv} \text{ and } C = 5$$

For $Re_L > 2000$ and $Re_g < 1000$
$$X = X_{tv} \text{ and } C = 10$$

For $Re_L < 1000$ and $Re_g > 2000$
$$X = X_{vt} \text{ and } C = 12$$

For $Re_L > 2000$ and $Re_g > 2000$
$$X = X_{tt} \text{ and } C = 20$$

Else:
Linear interpolation between upper and lower coefficient

Two-phase frictional multiplier:
$$\Phi_l^2 = 1 + \frac{C}{X} + \frac{1}{X^2}$$

Convective boiling enhancement factor:
$$F' = 0.64\Phi_l$$

$$F = Max(F', 1)$$

Nucleate boiling suppression factor:
$$S = (1 + 2.53 \cdot 10^{-6} Re_l^{1.17})^{-1}$$

Nucleate boiling heat transfer coefficient (Foster-Zuber):
$$h_{nb} = 0.00122 * \frac{k_l^{0.79} C_{pl}^{0.45} \rho_l^{0.49}}{\sigma^{0.5} \mu_l^{0.29} h_{lv}^{0.24} \rho_v^{0.24}} (\Delta T_{sat})^{0.24} (\Delta P_{sat})^{0.75}$$

Two-phase heat transfer coefficient:
$$h_{tp} = S h_{nb} + F h_l$$

Lee and Mudawar

Martinelli parameter:
$$X_{vt} = \left(\frac{1-x}{x}\right)^{0.5} \left(\frac{\mu_l}{\mu_v}\right)^{0.5} \left(\frac{\rho_v}{\rho_l}\right)^{0.5}$$

$$X_{vv} = \left(\frac{1-x}{x}\right) \left(\frac{f_l Re_g^{0.25}}{0.079}\right)^{0.5} \left(\frac{\rho_v}{\rho_l}\right)^{0.5}$$

Friction factor in function of $Re_{g \text{ or } L}$:

If $Re_{g \text{ or } L} < 1000$:
$$fr_{l \text{ or } v} = \frac{16}{Re_{l \text{ or } v}}$$

If $Re_{g \text{ or } L} > 2000$:
$$fr_{l \text{ or } v} = 0.046 Re_{l \text{ or } v}^{-0.2}$$

If $2000 < Re_{L \text{ or } g} < 2300$:
Linear interpolation between upper and lower coefficient

Weber number:
$$We_l = \frac{G^2 D}{\rho_l \sigma}$$

Reynolds numbers:
$$Re_v = \frac{xGD}{\mu_v}$$

$$Re_l = \frac{(1-x)GD}{\mu_l}$$

Prandtl numbers:
$$Pr_{l \text{ or } v} = \frac{\mu_{l \text{ or } v} C_{pl \text{ or } v}}{k_{l \text{ or } v}}$$

Liquid or Vapor heat transfer coefficient (Dittus-Boelter):
$$h_{l \text{ or } v} = 0.023 Re_{l \text{ or } v}^{0.8} Pr_{l \text{ or } v}^{0.4} \frac{k_{l \text{ or } v}}{D}$$

Two-phase heat transfer coefficient:

for $x < 0.05$:
$$h_{tp} = 3.856 X_{tt}^{0.267} h_l$$

for $0.05 < x < 0.55$:
$$h_{tp} = 436.48 Bo^{0.522} We_l^{0.351} X_{tt}^{0.665} h_l$$

for $x > 0.55$:
$$h_{tp} = Max(108.6 X_{tt}^{1.665} h_g, h_g)$$

Saitoh et al.

Reynolds numbers:
$$Re_v = \frac{xGD}{\mu_v}$$

$$Re_l = \frac{(1-x)GD}{\mu_l}$$

Weber number:
$$We_l = \frac{G^2 D}{\rho_l \sigma}$$

Martinelli parameter:

for $Re_L > 1000$ and $Re_g > 1000$
$$X_{tt} = \left(\frac{1-x}{x}\right)^{0.9} \left(\frac{\rho_v}{\rho_l}\right)^{0.5} \left(\frac{\mu_l}{\mu_v}\right)^{0.1}$$

for $Re_L < 1000$ and $Re_g > 1000$

$$X_{tt} = (Re_v^{-0.4}) \left(\frac{G_l}{G_v}\right)^{0.5} \left(\frac{f_l}{f_v}\right)^{0.5} \left(\frac{\rho_v}{\rho_l}\right)^{0.5} \left(\frac{\mu_l}{\mu_v}\right)^{0.5}$$

Friction factor in function of $Re_{g\,or\,L}$: If $Re_{g\,or\,L} < 1000$:

$$fr_{l\,or\,v} = \frac{16}{Re_{l\,or\,v}}$$

If $Re_{g\,or\,L} > 2000$:

$$fr_{l\,or\,v} = 0.046 Re_{l\,or\,v}^{-0.2}$$

If $2000 < Re_{L\,or\,g} < 2300$:
Linear interpolation between upper and lower coefficient

Liquid heat transfer coefficient h_L: For $Re_L < 1000$ (Dittus-Boelter):

$$h_l = 0.023 Re_l^{0.8} Pr_l^{0.4} \frac{k_l}{D}$$

For $Re_L > 1000$ (Developed flow):

$$h_l = 4.36 \frac{k_l}{D}$$

Convective boiling enhancement factor:

$$F = 1 + \frac{\left(\frac{1}{X_{tt}}\right)^{1.05}}{1 + We_v^{-0.4}}$$

Bubble growth suppression factor:

$$S = \frac{1}{1 + 0.4(10^{-4} F^{1.25} Re_l)^{1.4}}$$

Bubble diameter:

$$D_b = 0.512 \left[\frac{\sigma}{g}(\rho_l - \rho_v)\right]^{0.5}$$

Nucleate boiling heat transfer coefficient:

$$h_{nb} = 207 \frac{k_l}{D_b} \left(\frac{qD}{k_l T_l}\right)^{0.745} \left(\frac{\rho_v}{\rho_l}\right)^{0.581} Pr_l^{0.533}$$

Two-phase heat transfer coefficient:
$$h_{tp} = S h_{nb} + F h_l$$

Bertsch et al.

Reynolds numbers:

$$Re_{v0} = \frac{GD}{\mu_v}$$
$$Re_{l0} = \frac{GD}{\mu_l}$$

Prandtl numbers:

$$Pr_{l\,or\,v} = \frac{\mu_{l\,or\,v} C_{pl\,or\,v}}{k_{l\,or\,v}}$$

Reduced pressure:

$$P_r = \frac{P}{P_{crit}}$$

Confinement number:

$$Co = \frac{\sqrt{\sigma/g\Delta\rho}}{D}$$

Liquid or Vapor turbulent heat transfer coefficient (Dittus-Boelter):

$$h_{l0\,or\,v0} = 0.023 Re_{l0\,or\,v0}^{0.8} Pr_{l0\,or\,v0}^{0.4} \frac{k_{l0\,or\,v0}}{D}$$

Vapor and liquid laminar heat transfer coefficient:

$$h_{l0\,or\,v0} = \frac{k_{l0\,or\,v0}}{D} \left[3.66 + \frac{0.0668 * \frac{D}{L} Re_{l0\,or\,v0} Pr_{l0\,or\,v0}}{1 + 0.04 * \left(\frac{D}{L} Re_{l0\,or\,v0} Pr_{l0\,or\,v0}\right)^{\frac{2}{3}}}\right]$$

Convective boiling enhancement heat transfer coefficient:
$$h_{conv} = (1-x)h_{l0} + x h_{vo}$$

Convective boiling enhancement factor:
$$F = 1 + 80 * (x^2 - x^6) e^{-0.6*Co}$$

Nucleate boiling heat transfer coefficient (Cooper):
$$h_{nb} = 55 P_r^{0.12 - 0.434 log R_p} (-log P_r)^{-0.55} M^{-0.5} q^{0.67}$$

Bubble growth suppression factor:
$$S = (1-x)$$

Mean heat transfer coefficient:
$$h_{tp} = S h_{nb} + F h_l$$

Mikielewicz

Reynolds number:

$$Re_{l0} = \frac{GD}{\mu_l}$$

Prandtl numbers:

$$Pr_l = \frac{\mu_l C_{pl}}{k_l}$$

Reduced pressure:
$$P_r = \frac{P}{P_{crit}}$$

Nucleate boiling enhancement heat transfer coefficient (Cooper):
$$h_{nb} = 55 P_r^{0.12-0.434 log R_p}(-log P_r)^{-0.55} M^{-0.5} q^{0.67}$$

Friction factor: $Re_{l0} < 4000$:
$$f_1 = \frac{\rho_l}{\rho_v}\left(\frac{\mu_l}{\mu_v}\right)^{0.25}$$
$$f_2 = \frac{k_v}{k_l}$$

Else:
$$f_1 = \frac{\rho_l}{\rho_v}\frac{\mu_l}{\mu_v}$$
$$f_2 = \frac{\mu_v}{\mu_l}\frac{C_{pl}}{C_{pv}}\left(\frac{k_l}{k_g}\right)^{1.5}$$

Convective number of Muller-Steinhagen:
$$\Phi_{MS} = \left[1 + 2\left(\frac{1}{f_1}-1\right)Co^{-1}x\right](1-x)^{\frac{1}{3}} + \frac{x^3}{f_2}$$

Convective additive factor:
$$P = 0.00253 Re_{l0}^{1.17} Bo^{0.6}(\Phi_{MS}-1)^{-0.65}$$

All liquid heat transfer coefficient: If $Re_{l0} < 4000$: $n = 0.9$
$$h_{l0} = \frac{k_l}{D}\left[3.66 + \frac{0.0668\left(\frac{D}{L}\right)Re_{l0}Pr_{l0}}{1 + 0.04\left(\frac{D}{L}\right)Re_{l0}Pr_{l0}}\right]$$

Else: $n = 2$
$$h_{l0} = 0.023 * Re_{l0}^{0.8} Pr_{l0}^{0.4}\frac{k_{l0}}{D}$$

Two-phase on liquid only heat transfer coefficients:
$$\frac{h_{tp}}{h_{l0}} = \sqrt{\Phi_{MS}^n + \frac{1}{1+P}\left(\frac{h_{nb}}{h_{l0}}\right)^2}$$

Li and Wu

Reynolds number:
$$Re_l = (1-x)\frac{GD}{\mu_l}$$

Boiling number:
$$Bo = \frac{q}{G\Delta H_{lv}}$$

Bond number:
$$Bn = \frac{\rho_l g D^2}{\sigma_l}$$

Two-phase heat transfer coefficients:
$$h_{tp} = 334\frac{k_l}{D}Bo^{0.3}(Re_l^{0.36}Bd)^{0.4}$$

Mohamed and Karayiannis

Reynolds numbers:
$$Re_l = \frac{(1-x)GD}{\mu_l}$$

Martinelli parameter:
$$X_{tt} = \left(\frac{1-x}{x}\right)^{0.9}\left(\frac{\rho_v}{\rho_l}\right)^{0.5}\left(\frac{\mu_l}{\mu_v}\right)^{0.1}$$

Nucleate boiling enhancement heat transfer coefficient (Cooper):
$$h_{nb} = 55 P_r^{0.12-0.434 log R_p}(-log P_r)^{-0.55} M^{-0.5} q^{0.67}$$

Confinement number:
$$Co = \frac{\sqrt{\sigma/g\Delta\rho}}{D}$$

Enhancement Factor.
$$F = \left(1 + \frac{2.812 Co^{-0.408}}{X_{tt}}\right)^{0.64}$$

Suppression Factor
$$S = \frac{1}{1 + 2.56 * 10^{-6}(Re_l * F_{new}^{1.25})^{1.17}}$$

Two-phase liquid heat transfer coefficients for turbulent flow:
$$h_l = 0.023 Re_{l0}^{0.8} Pr_{lo}^{0.4}\frac{k_{l0}}{D}$$

Two-phase heat transfer coefficient:
$$h_{tp} = S h_{nb} + F h_l$$

3.1. Applicability ranges

The range of applicability of all the analyzed correlations and models is shown in Tab. 5.

Table 5: Correlation and models applicability ranges

Correlation or Model	Fluid	Pressure kPa	Diameter mm	Mass Flux Kg/m²s	Heat Flux kW/m²
Macro-Scale correlations					
Chen [1]	6 fluids	55-3792			6.2-2400
Shah [28]	R12	40-3308	5-15	70-11071	0.1-1215
Gungor and Winterton [3]	7 fluids	8-20260	5-32	60-8179	2-4579
Kandlikar [2]	10 fluids	100-6400	5-32	67-8179	4.7-2280
Liu and Winterton [29]	water	507-19743	2.95-32	12.4-8189	0.35-262
Micro-Scale correlations					
Lazarek & Black [4]	R113	130-410	3.1	125-751	14-380
Tran et al. [30]	R12	496-827	2.4-2.92	44-832	0.75-12.9
Kew and Cornwell [7]	R141b		1.39-3.69	188-1480	
Warrier et al. [31]	FC84		0.75		
Kandlikar & Balasubramanian [32]	Water, refrigerants	40-6400	0.19-3.2	13-8179	0.3-2280
Zhang et al. [6]	Water, refrigerants	101-866	0.78-6	23.4-2939	2.95-2511
Lee & Mudawar [33]	Water, R134a	144-660	0.35	127-654	159-938
Saitoh et al. [34]	R134a	350-500	0.5-1.1	150-450	0.5-39
Bertsch et al. [5]	12 fluids	100-517	0.16-2.92	20-3000	4-1150
Mikielewicz [8]	Water, refrigerants	767-1155	2-4.26	100-500	11-100
Li and Wu [35]	12 fluids	3471-6412	0.19-2.01	190-570	5-20
Mahmoud and Karayiannis [16]	R134a	600-1400	0.52-4.26	100-500	0.17-158
Mechanicistic models					
Thome [10, 11]	7 fluids	350-793	0.77-3.1	50-347	2-2634
Consolini & Thome [12, 13]	4 fluids	766-811	0.51-0.79	300-200	1-200

3.2. Similarity criteria

A critical issue in utilizing the available correlations and models is their applicability when different fluids are used. To overcome these difficulty, Delhaye et al. (2004) developed criteria based on the Kay and Nedderman (1974) assumptions on enthalpy. These criteria may be applied both to models and correlations and they are useful to understand if the specific correlation is applicable regardless the fluid and the proprieties adopted. The similarity criteria can be summarized in the following requirements:

- Same channel shape: different shapes influence the boundary layers and the heat flux distribution along the channel.
- Same vapor to liquid density ratio at the respective pressures:

$$\left(\frac{\rho_v}{\rho_l}\right)_{p(fluid\ (a))} = \left(\frac{\rho_v}{\rho_l}\right)_{p(fluid\ (b))}$$

To avoid any difference in the volume occupied by every phase the ration between the specific volume of the two phases should be the same at the saturation pressure.

- Same Weber number, to derive the equivalent mass flux G:

$$We \cong \frac{G^2 D}{\sigma \rho_{l,sat}} => G_{fluid(b)} = \sqrt{\frac{We_{fluid(a)} \sigma \rho_{l,sat}}{D}}$$

The inertia/surface tension ratio should be the same to grant the same film, droplet or bubbles dimension.

- Same Boiling Number, to calculate the equivalent heat flux Q:

$$Bo \cong \frac{Q}{GH_{lv}} => Q_{fluid(b)} = \frac{H_{lv,fluid(b)} \cdot Q_{fluid(a)} \cdot G_{fluid(b)}}{H_{lv,fluid(a)} \cdot G_{fluid(a)}}$$

The Boiling number can be thought of as a ratio mass flow rates per unit area. A different mass of vapor generated can change the vapor distribution in the cannel up to the thermal crisis.

- Same equilibrium quality, to calculate the equivalent inlet temperature:

$$x_{eq,in} \cong \frac{H_{l,in} - H_{l,sat}}{H_{lv}} =>$$

$$H(T)_{l,in\ fluid(b)} = H_{l,sat\ fluid(b)} + \frac{H_{lv,fluid(b)}}{H_{lv,fluid(a)}}\left(H_{l,in} - H_{l,sat}\right)_{fluid(a)}$$

The use of the same equilibrium quality to calculate an equivalent inlet temperature is useful to grant the same energetic inlet condition for the fluid.

Due the limited literature concerning the use of FC-72, the similarity criteria have been adopted in this thesis only for pressure drop calculation and for subcooled boiling vapor and void fraction calculation. The use of the criteria for heat transfer models will be done in a further work

3.3. Subcooled model

This section is intended to analyze the subcooled boiling phenomenon with a new model. Subcooled boiling can be the predominant boiling phenomenon at low reduced pressures due to the fluid vaporization inertia. Wetting fluids, as FC-42, shows a high thermal hysteresis in high subcooled condition at the inlet, as reported in the work of Celata et al. (1992). In the paragraph a new model, based on the work of Delhaye et al. (2004), to calculate vapor quality and void fraction is proposed. Figure 82 shows different boiling phases along an experimental section.
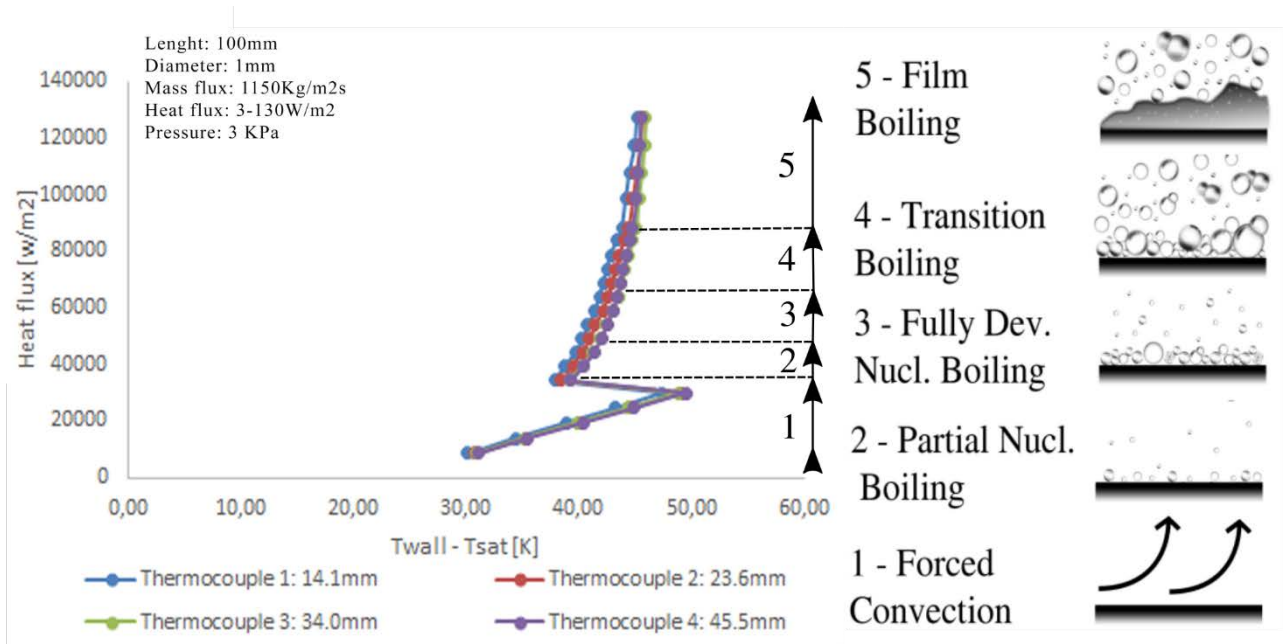
Figure 82: Heat flux vs wall superheating at 1150 Kg/m^{2}s on 100 mm tube, boiling phases.

3.3.1. Subcooled boundaries calculation

Single phase forced convection ends when the first vapor bubbles appear at the first nucleation site at the ONB (Figure 83). When a significant increase in the void fraction occurs, the fluid reaches the "onset of significant void" (OSV). Finally, saturated boiling starts when the whole mixture is in saturated conditions. Once defined ONB and OSV is possible to distinguish two regions in the subcooled zone: the partially developed boiling (PDB) region, delimited by the ONB and the OSV, and the fully developed boiling (FDB) region which is delimited by the OSV and the saturation point.
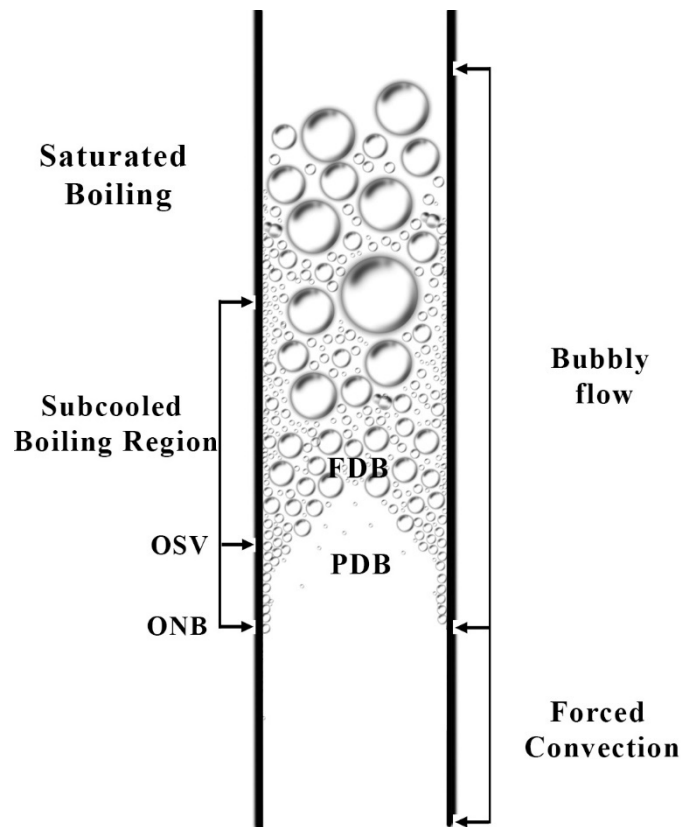
Figure 83: Subcooled flow boiling representation in a vertical channel

The void fraction increases slightly from the ONB to the OSV and it increases much faster in the FDB region. The wall temperature increases linearly in single phase flow and remains almost constant in the boiling region, as shown in Figure 84.
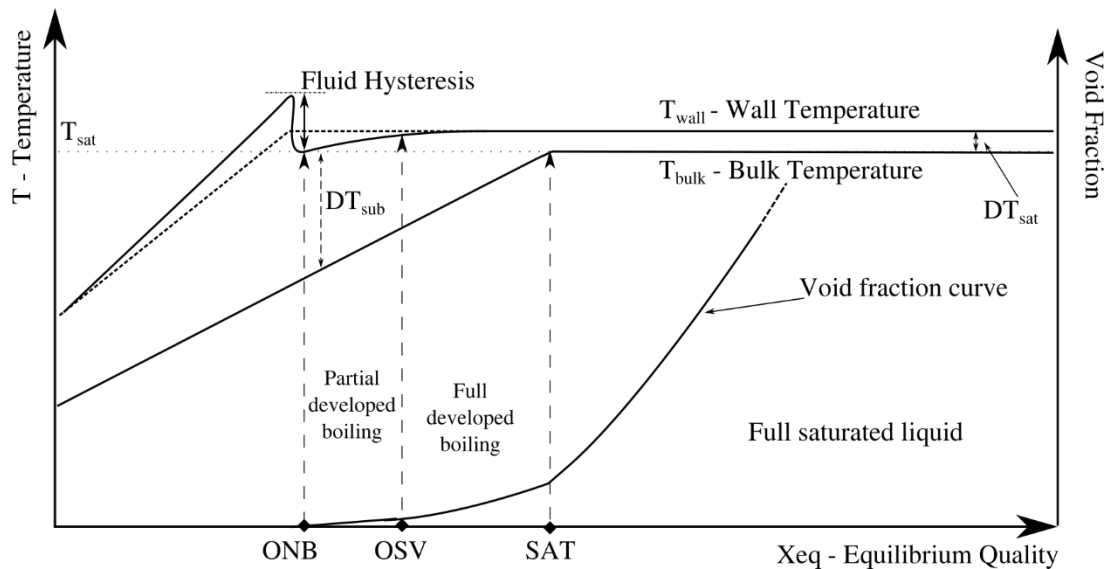
Figure 84: Wall temperature, bulk temperature and void fraction trends at the increasing of equilibrium quality

The Onset Nucleate Boiling (ONB) can be identified by an energy balance, as stated in Delhaye et al. (2004):

$$Z_{ONB} = \frac{Gc_{pl}D}{4} \cdot \left[\frac{\left((T_{sat} - T_{l,in}) + (\Delta T_{sat})_{ONB} \right)}{Q} - \frac{1}{h_{l,conv}} \right]$$

The convective heat transfer coefficient $h_{l,conv}$ can be calculated by the well-known Petukhov-Gnielinskii correlation. The ONB interests only the liquid film around the tube, therefore the fluid properties are evaluated at the film temperature:

$$\frac{\left(T_l(z_{ONB}) + T_{wall}(z_{ONB}) \right)}{2}$$

The only exception is the liquid heat capacity, that is calculated at the average temperature between the inlet and the ONB:

$$\frac{\left(T_l(z_{ONB}) + T_{l,in} \right)}{2}$$

The wall superheating ($\Delta T_{sat} = T_w - T_{sat}$) at the ONB point can be calculated by a modified Frost and Dzakowic (1967) correlation for water:

$$(\Delta T_{sat})_{ONB} = \left(\frac{8\sigma Q T_{sat}}{k_{l,sat}H_{lv,sat}\rho_g} \right)^{0.5} Pr_l^{0.95}$$

The *Pr* number exponent has been changed in this work to 0.95, to better agree with the available experimental results. All the proprieties in last equation are calculated at the saturation temperature T_{sat}. Tab. 5 shows the equivalent applicability range for FC-72 using similarity criterion, as described in previous paragraph:

Table 6: Frost and Dzakowic correlation (1967): applicability range for FC-72

Parameters	Water	FC-72
Pressures	0.1-20 MPa	0.0075-1.57 MPa
Mass velocity	No restriction	No restriction
Heat flux	150 kW/m^2	6.5 kW/m^2

The liquid temperature at the ONB point, to be used in the fluid proprieties calculation, is calculated iteratively from the energy balance:

$$T(x) = T_{in} + 4 \frac{Q \cdot Z_{ONB}}{G \cdot c_{pl} \cdot D}$$

The heat capacity c_{pl} is calculated at the average temperature between T_{in} and $T(x)$ where x is Z_{ONB}.

The Onset of Significant Void point is identified through the Saha and Zuber correlation (1974), as suggested in the Delhaye et al. model (2004). It is calculated starting from the ONB point. The liquid bulk temperature at the OSV is:

$$T_{l,OSV} = \Delta T_{OSV} - T_{sat}$$

Where ΔT_{OSV} is the subcooling degree and it is calculated according to two possible ranges of the Peclet number:

- $Pe < 700000; \quad \Delta T_{OSV} = 0.0022 \cdot \frac{QD}{k_l}$

- $Pe > 700000; \quad \Delta T_{OSV} = 153.8 \cdot \frac{Q}{G \cdot c_{p,l}}$

Where:

$$Pe = \frac{G c_{p,l} \cdot D}{k_l}$$

The fluid properties are calculated at the OSV temperature. From the thermal balance at the OSV point, it is possible to identify the axial position (Z_{osv}) where OSV starts:

$$Z_{OSV} = Z_{ONB} + \left[H_l(T_{l,OSV}) - H_l(T_{l,ONB}) \right] \cdot \frac{GD}{4Q}$$

ONB and OSV points will be used as boundaries in the void fraction calculations for the partial and fully developed boiling regions.

3.3.2. Void fraction calculation

Two-phase pressure drop calculation needs the evaluation of the void fraction. The Zuber and Findlay drift flux model (1965) is widely used in the literature to evaluate the void fraction α.

$$\alpha = \frac{\Gamma_v}{C_0 \Gamma + V_g}$$

Where C_0 is the distribution parameter, that is a function of the local vapor void fraction and the local mixture velocity; V_g is the weighted drift velocity, that physically depends on the radial profile of the void fraction and can be calculated as a function of local the vapor void fraction and the local vapor velocity; Γ is the volumetric flow rate. These parameters, in the original work, are semi-empirical and based on a fluid database. Lahey and Moody (1977) proposed different methods to calculate the void fraction in subcooled boiling, based on the Zuber and Findlay (1965) model, that was developed to estimate the void fraction in the fully developed boiling region.

$$\alpha = \frac{x_v \cdot \rho_l \cdot G}{C_0(x_v \cdot \rho_l + (1 - x_v) \cdot \rho_v)G + V_g \cdot \rho_l \cdot \rho_v}$$

The differences of the Lahey and Moody (1977) model from the original one are: (a) the relation between actual vapor quality and equilibrium quality, (b) the distribution parameter C_0 calculation and (c) the weighted drift velocity V_g calculation. Most of the available models calculate the void fraction in fully developed boiling region assume a zero quality in the partially developed boiling region. However, Levy (1967) and Griffith et al. (1958) proposed correlations for the void fraction at the OSV. Delhaye et al. (2004) improved the Lahey and Moody (1977) extending the range up to the end of subcooled region, concatenating different approaches to different regions of subcooled boiling.

(a) Relation between non-equilibrium and equilibrium vapor quality in the subcooled region

The vapor quality x_v is the vapor mass fraction in a mixture. It is different but related with the equilibrium quality x_{eq}:

$$x_{eq}(z) = \frac{H(Z) - H_{l,sat}}{H_{lv}}$$

The original model from Lahey and Moody (1977) assumes the quality between ONB and OSV (PDB region) equal to zero. However, this approach would lead to an overestimation of the void fraction between the OSV and the saturation point (FDB zone). Therefore, a modified non-equilibrium quality model which adopts an approximation of the subcooled void in PDB and FD regions should be used. Delhaye et al. (2004) proposed a hyperbolic tangent to approximate the transition.

$$x_v(Z) = 0.01\xi \left\{ x_{eq}(Z) - x_{eq}(Z_{ONB}) \left[\tanh\left(\left(\frac{x_{eq(Z)}}{x_{eq}(Z_{ONB})} \right) - 1 \right) + 1 \right] \right\}$$

$$x_v(Z) = x_{eq}(Z) \; if \; x_{eq}(Z) \geq x_v(Z)$$

ξ is a custom constant that must be identified to allow the first order continuity of the quality function between the PDB and FDB regions at the OSV point, where the vapor quality at OSV is expressed by the formula:

$$x_{v,OSV} = \frac{1}{\left(\left(\frac{\rho_l}{\rho_v} \right) \cdot \left(\frac{1 - \alpha_{osv}}{\alpha_{osv}} \right) + 1 \right) \alpha_{OSV}}$$

being α_{OSV} the void fraction at OSV originally calculated by Griffith et al. (1958) for water. Table 6 summarizes the applicability range for the original Griffith et al. (1958) model.

Table 7: Griffith (1958) OSV model applicability range

Parameter	Water	FC-72
Pressure	3.4 – 6.9 – 10.3 MPa	0.25 – 0.57 – 0.8 MPa
Mass velocity	80 – 400 kg/m^{2}s	155 –1500 kg/m^{2}s
Heat flux	1600 – 8500 kW/m^2	80 – 365 kW/m^2

To extend the applicability to other fluids Delhaye et al. (2004) changed that model, introducing the capillarity length:

$$\alpha_{OSV} = \frac{4a}{D}$$

where:

$$a = 7.5 \frac{Q k_l Pr_l}{h_l^2 [T_{sat} - T_l(z_{OSV})]} \frac{L_{cap}}{D}$$

The capillary length L_{cap} is defined as:

$$L_{cap} = \sqrt{\frac{\sigma}{g(\rho_l - \rho_v)}}$$

The single-phase heat transfer coefficient, h_l is evaluated by the Dittus-Boelter correlation and all the fluid properties are calculated at the OSV temperature.

(b) Distribution parameter

The distribution parameter C_0 used is calculated by the equation from Nabizadeh et al. (1980):

$$C_0 = \left(1 + \frac{1 - x_v}{x_v} \cdot \frac{\rho_v}{\rho_l}\right)^{-1} \cdot \left(1 + \frac{1}{n} \cdot Fr^{-0.1} \cdot \left(\frac{\rho_v}{\rho_l}\right)^n \cdot \left(\frac{1 - x_v}{x_v}\right)^{\frac{11*n}{9}}\right)$$

where:

$$n = \sqrt{0.6 \frac{\rho_l - \rho_v}{\rho_l}}$$

Fr is the Froude number defined as:

$$Fr = \frac{G^2}{g \cdot D \cdot \rho_l^2}$$

The void fraction α is largely influenced by the distribution parameter, Delhaye et al. (2004) defines the equation as the most promising in the literature, because it involves pressure, mass flux and quality. Other equations, as from Saha and Zuber (1974), use a constant value and Dix (1971) uses a function of quality. Also in Delayie at al. (2004) a new correlation was proposed, but it is specific for their facility and not suitable. for FC-72.

(c) Weighted drift velocity

Void fraction equation is weakly influenced by the weighted drift velocity and the original formula proposed by Zuber and Findlay (1965) is accurate enough for the calculation, as stated in Delayie at al. (2004).

$$V_g = 1.41 \left(\frac{\sigma \cdot g(\rho_l - \rho_v)}{\rho_l^2}\right)^{0.25}$$

4. Pressure drop methodology

This paragraph analyzes different pressure drop mechanisms considered during pressure drop calculations. Pressure drops in subcooled boiling are different from developed boiling due to a "recovery" effect due to bubble implosion. The paragraph ends with a summary of the most famous literature correlations for subcooled boiling, developed boiling and micro-channels pressure drops. All the correlations are used to calculate pressure drops coefficients

4.1. Pressure drops in flow boiling

Some examples of pressure drop trends at different heat fluxes, from the BOEMIA experiments, are shown in Fig. 85. The same trends were also observed from other authors, as in Kim and Mudawar (2012).

The pressure drop increment is not constant and four different zones can be identified.
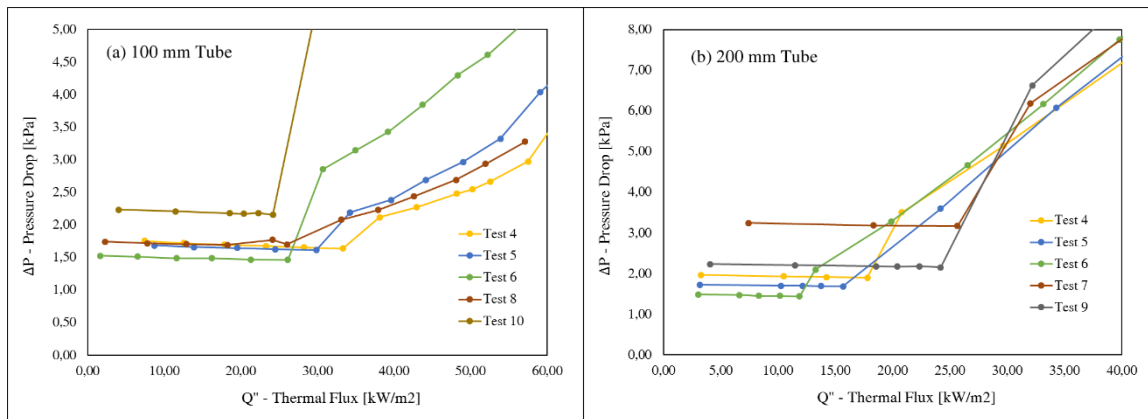
Figure 85: Total pressure drops at different heat fluxes, for 100mm (a) and 200 mm (b) tubes.

The subcooled fluid enters the channel (1) and the pressure drops are related only to the liquid frictional losses *(dp/dz)$_f$*. When the fluid reaches the subcooled boiling point at ONB the bubbles that are formed on the tube reduces the available spaces in the channel accelerating the fluid and consequently the pressure drop increases (2). However, the embryo bubbles at ONB are formed in cavities and when they emerge encounter a large temperature gradient causing bubble reduction or implosion, with the resulting instabilities. The instabilities related to the wall superheating hysteresis are particularly marked for wetting fluids as fluorocarbons (You and Simon (1990)). In the full developed boiling region (3), before the saturation point, the acceleration pressure drop *(dp/dz)$_{acc}$* quickly increases with the void fraction. The frictional losses are higher due to the presence of two phases flowing through the tube. In region (2) and (3), the single-phase model fails to predict pressure drops and it is necessary to adopt a new model. The void fraction, thanks to its relation to the acceleration and frictional pressure drops, can be used as the main parameter to adapt usual two-phase models, such as Lockhart-Martinelli (1979), Friedel (1979), and others. The choice of using two-phase models instead of developing specific correlations is the wide validity range of the model and the possibility of use only one model for all the boiling zones. Margulis and Shwageraus (2014) followed the same approach in their

work, using the Osmachkin and Borisov (1960) correlation. After the saturated point, the pressure drops are well known (4) and the traditional two-phases models can be used.

The total pressure drop is expressed as:

$$-\left(\frac{dp}{dz}\right)_t = -\left(\frac{dp}{dz}\right)_f \pm \left(\frac{dp}{dz}\right)_{acc} \pm \left(\frac{dp}{dz}\right)_g$$

In the single-phase zone, only the friction contribution is considered.

The acceleration contribution, also considered in the subcooled region, is here expressed in terms of the vapor quality x_v instead of the equilibrium quality x_{eq}:

$$-\left(\frac{dp}{dz}\right)_{acc} = \frac{G^2}{\rho_l}\left(\frac{\rho_l}{\rho_v}\frac{x_v^2}{\alpha} + \left(\frac{(1-x_v)^2}{(1-\alpha)} - 1\right)\right)$$

Figure 86 shows the emphasized theoretical trends; the gravitational pressure drop *(dp/dz)$_g$* is null because the channel is horizontal.
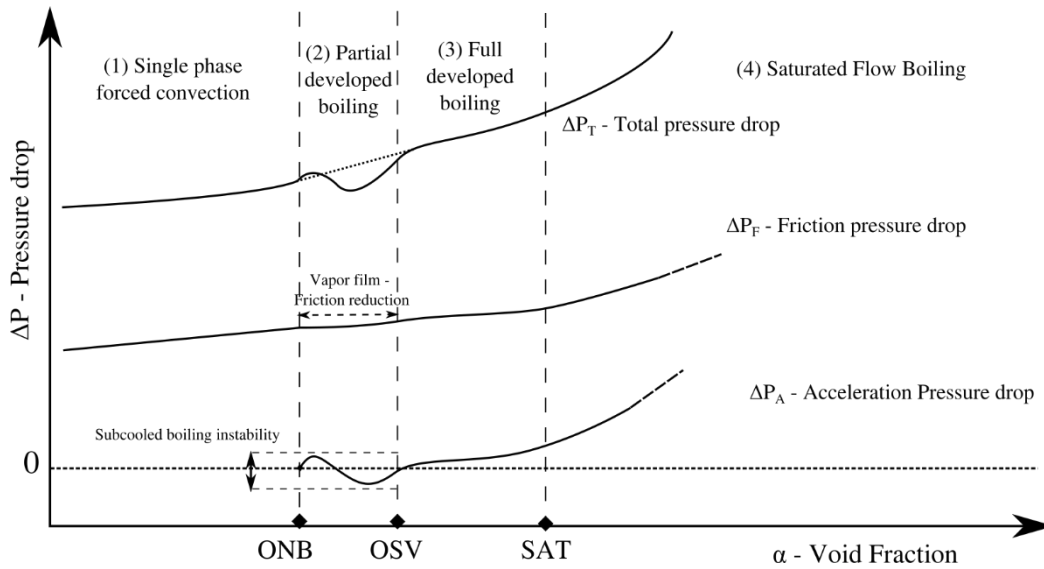
Figure 86: Pressure drop contributions at different void fractions

4.2. Pressure drops in single phase transition flow

In the analyzed tests, the fluid is subcooled at the inlet and a zone of the tube is in single-phase forced convection until the onset of nucleate boiling occurs. As described, the Reynolds' number in the ENEA experiments varied from 2750 to 4500. Being these values between the conservative range $2000 < \mathrm{Re} < 4000$, the flow is mainly in transition between the laminar and turbulent flow. In this region, there are no reliable models able to describe the phenomenon. Several empirical equations have been proposed for computing the transitional pressure drop: Brownlie (1981); Cheng and Chiew (1998); Ligrani and Moffat (1986); Yalin and Da Silva (2001). However, a simple interpolation method may work better in calculating pressure drop in the transition range.

In a first approximation, the pressure drop must vary between the boundaries of laminar and turbulent flow. Thus, if the channel is long enough, it is possible to consider the average pressure drop in a section of the channel, neglecting the physical oscillation between laminar and turbulent flows. In fact, in the same section and over a brief time interval, the fluid statistically changes its behavior cyclically. Then, the friction factor variations can be related to the Reynolds number by a polynomial interpolation between the laminar and turbulent friction factor. To avoid any discontinuity in the functions at the boundaries, a third order polynomial has been adopted. This polynomial function can be expressed as:

$$f_{tran} = \alpha \cdot Re^3 + \beta \cdot Re^2 + \gamma \cdot Re + \delta$$

The 4 constants $\alpha, \beta, \gamma, \delta$ can be obtained by a 4-equations system, where the following boundary conditions are imposed:

$$\begin{cases} A: f_{lam} = f_{tran} & For\ Re = 1100 \\ B: f_{r,trans} = f_{turb} & For\ Re = 8000 \\ C: f_{lam}' = f_{tran}' & For\ Re = 2000 \\ D: f_{tran}' = f_{turb}' & For\ Re = 4000 \end{cases}$$

The first two conditions are taken far from the boundaries, when the fluid is certainly laminar or turbulent; the second two conditions are needed to assure the function continuities at the boundaries. The two well know equations used for laminar and turbulent pressure drops in single phase are:

$$Darcy\ friction\ factor \qquad f_{lam} = \frac{64}{Re}$$

$$Colebrook\ friction\ factor \qquad 1/\sqrt{f_{turb}} = -2\log\left(\frac{\varepsilon}{3.7D} + \frac{2.51}{Re\sqrt{f_{turb}}}\right)$$

The Colebrook equation (1939) is solved recursively. ε is absolute rugosity of the wall, D is the channel diameter, and Re is the Reynold's number. Figure 87 represents schematically the friction factor trend.
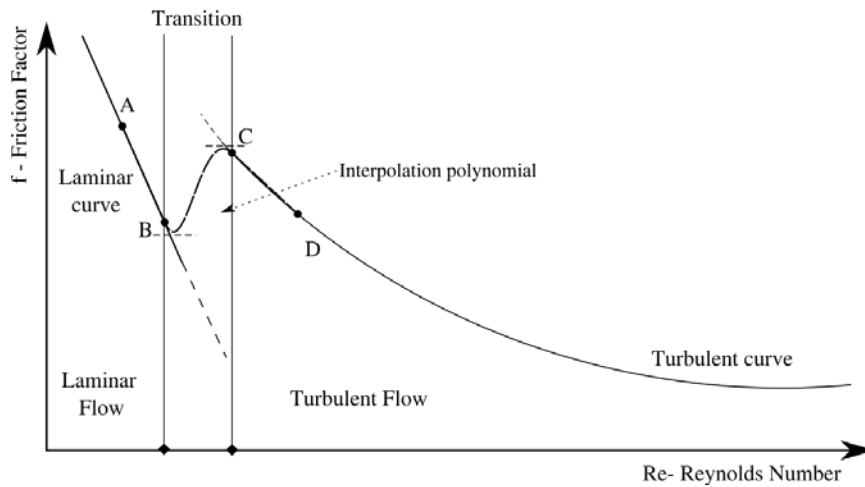
Figure 87: Interpolation curve for the transition friction factor; A, B, C, D are the 4 boundary condition points.

Then, the frictional pressure drop in the subcooled liquid from inlet up to the ONB can be calculated by the equation:

$$\Delta P_f = f \frac{z_{ONB}}{D} \frac{G^2}{2\rho_l}$$

4.3. Pressure drops in subcooled and saturated boiling

In literature, there are few predictive tools specific for subcooled flow boiling, and they are recommended mostly for water in circular tubes. The two-phases models selected to validate the present methodology for the subcooled and saturated boiling zones are: Friedel (1979), Chisholm (1967), Lockhart-Martinelli (1949), Chawla (1967) and, Müller-Steinhagen and Heck (1986), summarized in Table 7.

To compare the methodology with some specific subcooled correlations, those by Owens-Schrock (1960), Kim-Mudawar (2012) and Tong (1997) have been also selected. These correlations have been used to calculate the pressure drop in the subcooled flow boiling region, between ONB and the saturation curve. The ONB and OSV points are calculated by the proposed methodology and used to calculate Z_{sub} and Z_{sat} used in the literature correlations. Owens and Schrock's correlation (1960) was developed for water flow in 3 and 4.6 mm tubes. The correlations of Tong et al. (1997), was developed for water flow in 1.05–2.44 mm tubes and with two different length-to-diameter ratios. Kim and Mudawar`s (2012) correlation was developed for HFE 7100 (and extended for water and R134a) and for 175-415 μm tubes.

The experimental data are related to the total pressure drops from the inlet to the outlet, the fluid enters in the tube in liquid single phase with a high degree of subcooling. Thus, for the calculations, the data has been analyzed calculating the pressure drops from the inlet up to the ONB point (Eq. 5) as in single phase, with the transient single-phase Eq. (32). Furthermore, the points where the fluid being saturated (54 points) are not considered in the assessment of subcooled boiling method but only assessing the whole methodology. The experimental setup is provided with the pressure transducer at inlet and outlet, thus only the total pressure drop, from inlet to outlet, were available for the assessment.

The proposed methodology uses a different correlation to calculate pressure drops for every region; In single phase the standard pressure drop equation from Colebrook (1939) were used, instead, for subcooled and saturated flow boiling the correlations in Tab. 8 were used with the void fraction and quality. However, it should be noted that, theoretically, the subcooled and saturated boiling correlation cannot be the same in the two zones. In fact, the best agreement was obtained using different correlations to best fit the data. For comparisons some literature subcooled boiling correlation are summarized in Table 9.

Table 8: Two-phases pressure drop models

Name	Equations
Lockhart-Martinelli (1949)	$$\left(\frac{dp}{dz}\right)_f = \Phi_l^2 \left(\frac{dp}{dz}\right)_l$$ $$\left(\frac{dp}{dz}\right)_l = 4f_l \frac{1}{D_h} G^2 (1-x_v)^2 \left(\frac{1}{2\rho_l}\right)$$ $$\Phi_l^2 = 1 + \frac{C}{\sqrt{X_{tt}}} + \frac{1}{X_{tt}^2}$$ $$X_{tt} = \left(\frac{\mu_l}{\mu_v}\right)^{0.1} \left(\frac{\rho_v}{\rho_l}\right)^{0.5} \left(\frac{1-x_v}{x_v}\right)^{0.9}$$ $$C = \begin{cases} 20 & Re_l \geq 4000;\ Re_v \geq 4000 \\ 10 & Re_l \geq 4000;\ Re_v \leq 2000 \\ 12 & Re_l \leq 2000;\ Re_v \geq 4000 \\ 5 & Re_l \leq 2000;\ Re_v \leq 2000 \\ interpolated & other\ ranges \end{cases}$$ $$f_l = \frac{0.079}{Re_l^{0.25}}$$ $$Re_{lo} = \frac{GD}{\mu_l}\ ; Re_{vo} = \frac{GD}{\mu_v}$$
Friedel (1979)	$$\left(\frac{dp}{dz}\right)_f = \Phi_l^2 \left(\frac{dp}{dz}\right)_l$$ $$\left(\frac{dp}{dz}\right)_l = 4f_l \frac{1}{D} G^2 (1-x_v)^2 \left(\frac{1}{2\rho_l}\right)$$ $$\Phi_l^2 = E + \frac{3.24 F \cdot M}{Fr_h^{0.045}} We^{0.035}$$ $$f_l = \frac{0.079}{\sqrt[4]{Re_l}}; \quad f_v = \frac{0.079}{\sqrt[4]{Re_v}}$$ $$Fr = \frac{G^2}{\rho_l^2 \cdot g \cdot D}$$ $$We_{lo} = \frac{G^2 D}{\rho_l \sigma}$$ $$E = (1-x_v)^2 + x_v^2 \frac{\rho_l}{\rho_v} \frac{f_v}{f_l}$$ $$F = x_v^{0.78} (1-x_v)^{0.224}$$ $$M = \left(\frac{\rho_l}{\rho_v}\right)^{0.91} * \left(\frac{\mu_v}{\mu_l}\right)^{0.19} \left(1 - \frac{\mu_v}{\mu_l}\right)^{0.7}$$
Chawla (1968)	$$\left(\frac{dp}{dz}\right)_f = \Phi_l^2 \left(\frac{dp}{dz}\right)_l$$ $$\left(\frac{dp}{dz}\right)_l = 4f_l \frac{1}{D} G^2 (1-x_v)^2 \left(\frac{1}{2\rho_l}\right)$$

$$\Phi_l^2 = x^{1.75} \left(1 + S \frac{(1 - x_v)}{x_v} \frac{\rho_v}{\rho_l} \right)^{2.375}$$

$$\frac{1}{S} = 9.1 \frac{1 - x_v}{x_v} (Re_v Fr)^{-0.167} \left(\frac{\rho_l}{\rho_v} \right)^{-0.9} \left(\frac{\mu_l}{\mu_v} \right)^{0.5}$$

$$Fr = \frac{G^2}{\rho_l^2 \cdot g \cdot D}$$

Chisholm (1967)

$$\left(\frac{dp}{dz} \right)_f = \Phi_l^2 \left(\frac{dp}{dz} \right)_l$$

$$\left(\frac{dp}{dz} \right)_l = 4 f_l \frac{1}{D} G^2 \left(\frac{1}{2\rho_l} \right)$$

$$f_{l,v} = \begin{cases} \dfrac{0.079}{\sqrt[4]{Re_{l,v}}} & Re_{l,v} \geq 2000 \\[2mm] \dfrac{16}{Re_{l,v}} & Re_{l,v} < 2000 \end{cases}$$

$$\Phi_l^2 = 1 + (Y^2 - 1) B x_v^{\frac{2-n}{2}} (1 - x_v)^{\frac{2-n}{2}} + x_v^{2-n} \quad \text{where } n = 0.25 \; (Blasius)$$

$$Y = \left(\frac{Y_b}{Y_a} \right)^{1/2}$$

$$Y_a = f_l \frac{2 G^2}{D \rho_l}; \; Y_b = f_v \frac{2 G^2}{D \rho_v}$$

$$B = \begin{cases} \dfrac{55}{G^2} & 0 \leq Y < 9.5; G \geq 1900 \\[2mm] \dfrac{2400}{G} & 0 \leq Y < 9.5; 500 \leq G < 1900 \\[2mm] \dfrac{520}{Y \sqrt{G}} & 0 \leq Y < 9.5; G < 600 \\[2mm] \dfrac{21}{Y} & 9.5 \leq Y < 28; G \geq 600 \\[2mm] \dfrac{15000}{Y^2 \sqrt{G}} & Y \geq 28; G < 1900 \end{cases}$$

Müller-Steinhagen and Heck (1986)

$$\left(\frac{dp}{dz} \right)_f = G(1 - x_v)^{\frac{1}{3}} + B x_v^3$$

$$G = A + 2(B - A) X_v$$

$$A = \left(\frac{dp}{dz} \right)_l = 4 f_l \frac{1}{D} G^2 \left(\frac{1}{2\rho_l} \right)$$

$$B = \left(\frac{dp}{dz} \right)_l = 4 f_v \frac{1}{D} G^2 \left(\frac{1}{2\rho_v} \right)$$

$$f_{l,v} = \begin{cases} \dfrac{0.079}{\sqrt[4]{Re_{l,v}}} & Re_{l,v} \geq 2000 \\[3mm] \dfrac{16}{Re_{l,v}} & Re_{l,v} < 2000 \end{cases}$$

Table 9: Two-phases subcooled and saturated boiling pressure drop models

Name	Equations
Owens-Schrock (1960)	$\dfrac{\left(\dfrac{dp}{dz}\right)_{sub}}{\left(\dfrac{dp}{dz}\right)_{ad}} = \left(0.97 + 0.028 e^{6.13\frac{Z_{sub}}{L_{sat}}}\right)$
Tong (1997)	$\dfrac{\left(\dfrac{dp}{dz}\right)_{sub}}{\left(\dfrac{dp}{dz}\right)_{ad}} = \begin{cases} \left(\dfrac{Z_{sub}}{L_{sat}}\right)^{1.3} e^{\frac{Z_{sub}}{L_{sat}}+0.4} & \dfrac{L}{D} = 50 \\[4mm] \left(\dfrac{Z_{sub}}{L_{sat}}\right)^{1.3} e^{\frac{Z_{sub}}{L_{sat}}+1.35} & \dfrac{L}{D} = 25 \end{cases}$
Kim-Mudawar (2012)	$-\left(\dfrac{dp}{dz}\right)_F = -\left(\dfrac{dp}{dz}\right)_{sub} - \left(\dfrac{dp}{dz}\right)_{TP}$ $\dfrac{\left(\dfrac{dp}{dz}\right)_{sub}}{\left(\dfrac{dp}{dz}\right)_{ad}} = 20.73 \cdot Ja^{-0.98} \left(\dfrac{L}{D}\right)^{-0.54} \dfrac{Z_{sub}}{L_{sat}}$ $Ja = \dfrac{C_{p,l} \cdot \Delta T_{sub,in}}{H_{lv}}$ $L_{sat} = \dfrac{GD}{4Q} C_{p,l}(T_{sat} - T_l)_{inlet}$ $Z_{sub} = \min(L, L_{sat}) - Z_{ONB}$ $\left(\dfrac{dp}{dz}\right)_{ad} = f_l * \left(\dfrac{Z_{ONB}}{D}\right)\left(\dfrac{2G^2}{\rho_l}\right)$ $\left(\dfrac{dp}{dz}\right)_{TP} = \Phi_l^2 \left(\dfrac{dp}{dz}\right)_l$ $\Phi_l^2 = 1 + \dfrac{C}{X} + \dfrac{1}{X^2}$ $X = \sqrt{\dfrac{\left(\dfrac{dp}{dz}\right)_l}{\left(\dfrac{dp}{dz}\right)_v}}$ $\left(\dfrac{dp}{dz}\right)_l = 4f_l \dfrac{1}{D} G^2 (1 - x_{eq})^2 \left(\dfrac{1}{2\rho_l}\right)$ $\left(\dfrac{dp}{dz}\right)_v = 4f_v \dfrac{1}{D} G^2 (x_{eq})^2 \left(\dfrac{1}{2\rho_v}\right)$

$$f_{l,v} = \begin{cases} 0.046 \, Re_{l,v}^{-0.2} & Re_{l,v} \geq 20000 \\ 0.079 \, Re_{l,v}^{-0.25} & 2000 \leq Re_{l,v} < 20000 \\ \dfrac{16}{Re_{l,v}} & Re_{l,v} < 2000 \end{cases}$$

$$C = \begin{cases} 0.048 \, Re_{lo}^{0.451} & Re_l > 2000; Re_v > 2000 \\ 1.45 \, Re_{lo}^{0.25} \, We_{lo}^{0.23} & Re_l \leq 2000; Re_v > 2000 \\ 2.16 \, Re_{lo}^{0.047} \, We_{lo}^{0.6} & Re_l \leq 2000; Re_v \leq 2000 \end{cases}$$

$$We_{lo} = \frac{G^2 D}{\rho_l \sigma}; \quad Re_l = \frac{G(1 - x_{eq})D}{\mu_l}; \quad Re_v = \frac{G x_{eq} D}{\mu_v};$$

$$Re_{lo} = \frac{GD}{\mu_l} \; ; Re_{vo} = \frac{GD}{\mu_v}$$

The proposed methodology provides encouraging results by using Friedel (1979) and Chisholm (1967) correlations in the subcooled boiling zones. A lower agreement has been obtained with the Chawla (1968), Lockhart-Martinelli (1949) and, Müller-Steinhagen and Heck (1986) correlations. The other subcooled boiling correlations have been also considered to compare the results from the present methodology with authoritative and recognized correlations.

4.4. Methodology summary

The total pressure drop in the tube can be calculated as:

$$\int_0^{Z_t} \left(\frac{dp}{dz}\right)_T = \int_0^{Z_{ONB}} \left(\frac{dp}{dz}\right)_{f,SP} + \int_{Z_{ONB}}^{Z_t} \left(\frac{dp}{dz}\right)_{f,TP} + \int_{Z_{ONB}}^{Z_t} \left(\frac{dp}{dz}\right)_{acc} + \int_0^{Z_t} \left(\frac{dp}{dz}\right)_g$$

The gravitational contribution is neglected if the tube is horizontal ($\gamma = 0$):

$$\int_0^{Z_t} \left(\frac{dp}{dz}\right)_g = \int_0^{Z_t} \rho(Z)g \cdot dZ \sin\gamma$$

The acceleration contribution is calculated in two-phase only, neglecting the density variation in the single-phase zone:

$$\int_{Z_{ONB}}^{Z_t} \left(\frac{dp}{dz}\right)_{acc} = \int_{Z_{ONB}}^{Z_t} \frac{G^2}{\rho_l} \left(\frac{\rho_l}{\rho_v} \frac{x_v^2}{\alpha} + \left(\frac{(1 - x_v)^2}{(1 - \alpha)} - 1\right)\right) \cdot dZ$$

A: Regions boundaries (ONB and Saturation points)

The single-phase region ends at the onset of nucleation boiling point, which can be identified as:

$$Z_{ONB} = \frac{G c_{pl} D}{4} \cdot \left[\frac{\left((T_{sat} - T_{l,in}) + (\Delta T_{sat})_{ONB} \right)}{Q} - \frac{1}{h_{l,conv}} \right]$$

where the wall superheating at ONB is obtained from the modified Frost and Dzakowic correlation:

$$(\Delta T_{sat})_{ONB} = \left(\frac{8\sigma Q T_{sat}}{k_{l,sat} H_{lv,sat} \rho_g} \right)^{0.5} Pr_l^{0.95}$$

The saturation length is obtained by a simple energy balance:

$$L_{sat} = \frac{G \cdot D}{4 \cdot Q} \int_{T_{in}}^{T_{sat}} c_{pl} \cdot dT$$

from which the saturation point is identified as $Z_{sat} = L_{sat}$, if L_{sat} is less or equal than the tube length.

B: Single-phase pressure drops

The pressure drops in single phase are evaluated with:

$$\int_0^{Z_{ONB}} \left(\frac{dp}{dz} \right)_{f,SP} = \int_0^{Z_{ONB}} f \cdot \frac{G^2}{2D\rho_l} \cdot dZ$$

where the friction factor *f* is calculated to consider the transition flow regime.

C: Void fraction and actual vapour quality

To calculate the acceleration and the two-phase frictional contributions, the evaluation of the void fraction is needed. It is calculated by the Lahey and Moody model:

$$\alpha = \frac{x_v \cdot \rho_l \cdot G}{C_0(x_v \cdot \rho_l + (1 - x_v) \cdot \rho_v)G + V_g \cdot \rho_l \cdot \rho_v}$$

The distribution parameter C_0 is evaluated and the weighted drift velocity.

In the partial developed (between the ONB and the OSV points) and in the fully developed (from OSV to saturation) boiling regions, the non-equilibrium vapor quality is assumed, following Delaye et al.:

$$x_v(Z) = 0.01\xi \left\{ x_{eq}(Z) - x_{eq}(Z_{ONB}) \left[\tanh \left(\left(\frac{x_{eq(Z)}}{x_{eq}(Z_{ONB})} \right) - 1 \right) + 1 \right] \right\}$$

where the equilibrium quality (negative in this zones) is evaluated. The parameter ξ is evaluated imposing the continuity at Z_{osv} with the quality calculated.

D: Two-phase pressure drops

The Chisolm's model provided the best agreement with ENEA data:

$$\int_{Z_{ONB}}^{Z_t} \left(\frac{dp}{dz}\right)_{f,TP} = \int_{Z_{ONB}}^{Z_t} \Phi_l^2 \left(\frac{dp}{dz}\right)_l$$

$$\left(\frac{dp}{dz}\right)_l = 4f_l \frac{z}{D} G^2 (1 - x_v)^2 \left(\frac{1}{2\rho_l}\right)$$

$$f_{l,v} = \begin{cases} \dfrac{0.079}{\sqrt[4]{Re_{l,v}}} & Re_{l,v} \geq 2000 \\[3mm] \dfrac{16}{Re_{l,v}} & Re_{l,v} < 2000 \end{cases}$$

$$\Phi_l^2 = 1 + (Y^2 - 1)B x_v^{\frac{1.75}{2}} (1 - x_v)^{\frac{1.75}{2}} + x_v^{1.75}$$

$$Y = \left(\frac{Y_b}{Y_a}\right)^{1/2}; \quad Y_a = f_l \frac{2G^2}{D\rho_l}; \quad Y_b = f_v \frac{2G^2}{D\rho_v}$$

$$B = \begin{cases} \dfrac{55}{G^2} & 0 \leq Y < 9.5; G \geq 1900 \\[3mm] \dfrac{2400}{G} & 0 \leq Y < 9.5; 500 \leq G < 1900 \\[3mm] \dfrac{520}{Y\sqrt{G}} & 0 \leq Y < 9.5; G < 600 \\[3mm] \dfrac{21}{Y} & 9.5 \leq Y < 28; G \geq 600 \\[3mm] \dfrac{15000}{Y^2\sqrt{G}} & Y \geq 28; G < 1900 \end{cases}$$

5. Experiment Description

Two different experimental setups were used with a different layout and experimental section. The tubes diameter tested vary from 1mm up to 4mm. The first experimental section was called BO.E.MI.A. (Boiling Experiments in MIcrochannel Apparatus) and developed as micro-boiling ground system. It developed to work with small tubes (0.25-2 mm) and equipped with 0.75 and 1 mm tube with two different tube lengths. In this section, due to the long tube length and smaller diameter, was tested the pressure drop model. The second section is called MicroBo (Microgravity Boiling) and was developed to be used in parabolic flight at near 0 g acceleration. The section can use tube from 1 mm up to 8mm and was equipped with tubes of 2 and 4 mm. Both sections use FC72 as refrigerant and for both were calculated the heat transfer coefficients. The paragraph presents the sections details.

5.1. Uncertainness

Following equations were used to calculate uncertainness and experimental error for the two experimental systems.

C coefficient for thermal heat flux (known value):

$$C = \frac{\Gamma * C_p * \Delta T_{in,out}}{Power}$$

Related error (considering C_p as exact):

$$Er(C) = \sqrt{\left(\frac{C}{\Delta T_{in,out}} * 2Er(T)\right)^2 + \left(\frac{C}{\Gamma} * Er(\Gamma)\right)^2 + \left(-\frac{C}{W^2} * Er(W)\right)^2}$$

T_{bulk} to calculate heat transfer coefficient:

$$T_{bulk} = T_{in} + 4 * \frac{Q * Z}{G * C_p * D} = T_{in} + \frac{\pi * \Gamma * Z * D}{G * C_p}$$

Error on thermal flux Q:

$$Q = \frac{W * C}{\frac{\pi D^2}{4}}$$

$$Er(Q) = \sqrt{\left(Er(W) * \frac{4 * C}{\pi D^2}\right)^2 + \left(Er(D) * \frac{-8 * C * W}{\pi D^3}\right)^2 + \left(Er(C) * \frac{4 * W}{\pi D^2}\right)^2}$$

Error on mass flow rate G:

$$G = \frac{\Gamma}{\frac{\pi D^2}{4}}$$

$$Er(G) = \sqrt{\left(Er(\Gamma) * \frac{4}{\pi D^2}\right)^2 + \left(Er(D) * \frac{-8 * \Gamma}{\pi D^3}\right)^2}$$

Error on T_{bulk} (considering C_p as an exact value):

$$Er(T_{bulk}) = \sqrt{\begin{array}{c}(Er(T))^2 + \left(\frac{T_{bulk} - T_{in}}{Q} * Er(Q)\right)^2 + \left(\frac{T_{bulk} - T_{in}}{Z} * Er(Z)\right)^2 + \\ \left(\frac{T_{bulk} - T_{in}}{G} * Er(G)\right)^2 + \left(\frac{T_{bulk} - T_{in}}{D} * Er(D)\right)^2\end{array}}$$

Heat transfer coefficient H:

$$H = \frac{Q}{T_{sat} - T_{bulk}}$$

Error on heat transfer (considering C_p as an exact value):

$$Er(H) = \sqrt{\left(Er(Q) * \frac{1}{T_{sat} - T_{bulk}}\right)^2 + \left(Er(T_{bulk}) * \frac{Q}{(T_{sat} - T_{bulk})^2}\right)^2}$$

Approximation to avoid T_{sat} calculation:

$$Er(H) = \sqrt{\left(Er(Q) * \frac{H}{Q}\right)^2 + \left(Er(T_{bulk}) * \frac{H^2}{Q}\right)^2}$$

5.1. BO.E.MI.A

The data base used to calculate pressure drops have been obtained in the experimental facility BO.E.MI.A. (Boiling Experiments in MIcrochannel Apparatus), built and operated in the ENEA Laboratory of Thermo-Fluid Dynamics. The facility aim is to perform, at different regimes, heat transfer tests on mini and micro channels, with inner diameter in the range from 0.25 up to 2 mm. A simplified layout of the experimental loop is shown in figure 88. FC-72 (perfluorohexane C6F14), a fluorine liquid manufactured by 3M, was used as working fluid; it is thermally and chemically stable, compatible with sensitive materials, nonflammable, leaves essentially no residue upon evaporation and has no ozone depletion potential, properties that make it ideal for electronics.
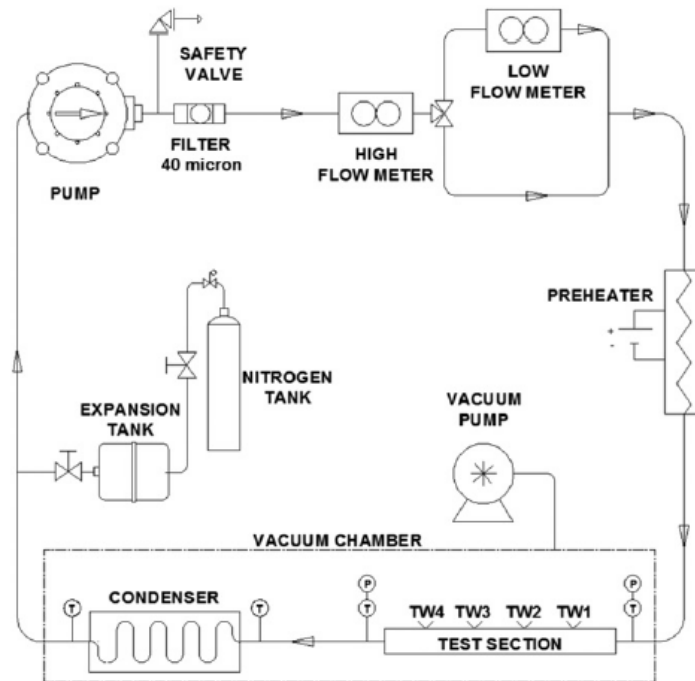
Figure 88: BOEMIA facility simplified layout

The fluid is clean and degassed before entry to the flow loop to remove any non-condensable or impurity. A gear pump can pull the liquid up to 20 bar with a volumetric flow rate in the range 6-552 ml/min. A membrane expansion tank pressurized with nitrogen regulates the operative pressure. Maximum working pressure for the facility is 9 bar. The fluid is filtered after the pump by a 40 μm filter. Two mass flowmeters measure the mass flowrate in two different flow regimes: from 2 up to 500 g/h (low mass flow regime) and from 500 up to 10000 g/h (high mass flow regime). The first range is covered by a digital mass flowmeter based on a thermal

measuring principle (Constant Temperature Anemometry), the second one by a small Coriolis-type flowmeter. A three-way valve operates the two mass flowmeters.

The fluid is electrically preheated upstream the test section inlet up to saturation condition or to a fixed subcooling degree. A counter-current tube in tube condenser cool the fluid with demineralized water at the exit of the experimental section. The thermal balance of the water gives the total heat delivered to the fluid in the microchannel test section.

5.1.1. Test section

The test section consists of a horizontal 1.016 mm (0.04") inner diameter stainless steel tube that have an outer diameter of about 1.6 mm. Two configurations, 100 and 200 mm long, have been tested. Figure 2 shows the instrumentation scheme to measure the heat transfer along the axial coordinate. The test rig includes: pressure taps at the inlet and outlet of the section, inlet and outlet thermocouples for bulk fluid temperature measurement, power supply and four wall thermocouples to localize the local heat transfer coefficient. L_{th} is the heated length, equal to 84 mm and 60 mm in the 200 mm and 100 mm tube, respectively.
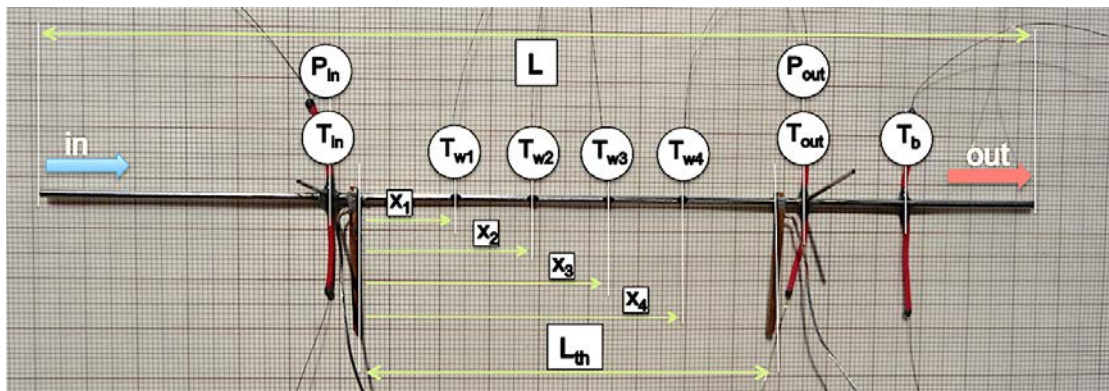
Figure 89 - Test section instrumentation

A constant power DC supply is used to heat the test section by Joule effect; this ensures a uniform heat flux at the wall in the case of uniform wall properties. The electrical power supply is calculated through voltage and current measurements from a 30 A and 60 mV shunt resistor. The pressure drop is investigated by two pressure transducers (0-25 bar) located on either side of the microtube a differential manometer (0-6.895 bar) parallel to the transducers, to take an extra differential pressure measurement, is present. In the 200 mm test tube, a micro-spring is inserted after the outlet pressure tap in order to mix the fluid flow: a more reliable refrigerant bulk temperature, T_b, is then measured by an additional fine-wire thermocouple (50 mm, Type K) directly inserted into the tube, leading to a proper assessment of enthalpy balance both in single-phase and two-phase conditions, above all in laminar flow regime (Fig 2).

5.1.2. Uncertainties

The input uncertainties and the most significant calculated uncertainties are presented in Table 10. The average uncertainty on the experimental heat transfer coefficient has been evaluated between 14% and 17.8% for the 100 mm and 200 mm tube, respectively. The uncertainty on the inner diameter is the major parameter affecting errors. More specific details can be found in the previous work by Saraceno (2012).

Table 10: Measurement uncertainties

Mass flow rate (hi)	0.15	% of Readings
Mass flow rate (low)	1	% on F.S.
Diameter	25	μm
Temperature	0.40	°C
Pressure	0.08	% on F.S.
Differential pressure drop	0.075	% of Calibrated Span
Electrical Power	0.48-1.42	% of Readings

5.2. Experimental data base

The test matrix shown in table 11-12 was used for the experiments: globally, the ranges are: pressure 3-5 bar, mass flux 824-1439 Kg/m²s and heat flux 1.6-181 kW/m². A total of 1244 data points was collected. Not all the points were useful to determinate heat transfer coefficient in saturated boiling. Therefore, only 82 points have been selected in the present study. The aim of a next study will be to investigate the subcooled boiling, thus selecting a larger number of experimental points.

Table 11: Data base for the 200 mm channel

N°	T_{in}	P	Mass flux	q" min	q" max	Data points	Saturated points
-	$C^\bullet$	*MPa*	Kg/m^2s	W/m^2	W/m^2	$n^\bullet$	$n^\bullet$
1	84	0.308	1126	4357	98414	124	**10**
2	88	0.502	1234	4227	181562	128	0
3	87	0.408	1234	4297	170409	72	**3**
4	97	0.404	1030	3297	97900	52	**12**
5	97	0.405	925	3188	99653	60	**19**
6	98	0.404	824	3056	86153	68	**16**
7	84	0.305	1235	4143	71069	60	0

8	97	0.405	1439	7406	87896	32	**3**
9	87	0.304	1132	4070	70838	44	**5**
10	83	0.305	1020	4148	25347	36	0
					Total	**680**	**68**

Table 12: Data base for the 100 mm channel

N°	T_{in}	P	Mass flux	q" min	q" max	Data points	Saturated points
-	$C^{\bullet}$	*MPa*	$Kg/m^2 s$	W/m^2	W/m^2	$n^{\bullet}$	$n^{\bullet}$
1	65	0.304	1149	7685	76510	64	0
2	78	0.302	1131	7687	76510	64	0
3	85	0.,07	1148	2501	47315	40	0
4	86	0.308	1139	7422	80253	68	0
5	86	0.309	1126	8718	127005	84	**7**
6	85	0.304	1032	1612	113401	100	**7**
7	91	0.403	1223	2923	116891	96	0
8	93	0.401	1138	2286	57113	48	0
					Total	**564**	**14**

5.3. MicroBO

The second experimental facility was called *MICROBO*: *MICRO*gravity *BO*iling. The facility was designed at the ENEA laboratories to perform flow-boiling experiments at microgravity and normal gravity conditions to obtain heat transfer coefficients. Figure (90) is a schematic of the loop, that consists of a gear pump (with a maximum flow rate of *500 ml/min)*, a filter, a flow-meter, an electric pre-heater, the flow boiling test section, a condenser, a bellows, and a tank to store the process fluid (*FC-72*).
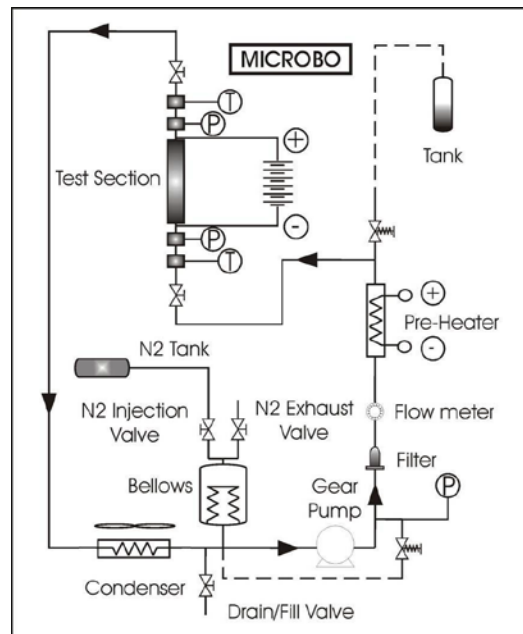
Figure 90: Schematic of the experimental loop (*Air* replaced *N2*)

The experiments that were made are:

   I.   flow boiling in *2.0 mm* tube
  II.   flow boiling in *4.0 mm* tube

The working fluid is *FC-72*, *perfluorohexane, C6F14*, a liquid manufactured by *3M*. It was projected to be employed in electronic cooling and to be used for boiling experiments. Picture in Figure (91) shows the experimental facility mounted in the cabin of an *A300 Zero-G*. A special box of ERTACEL® confine and protect the test section from any leakage, for the same reason all the piping of the facility is contained in a double confinement.
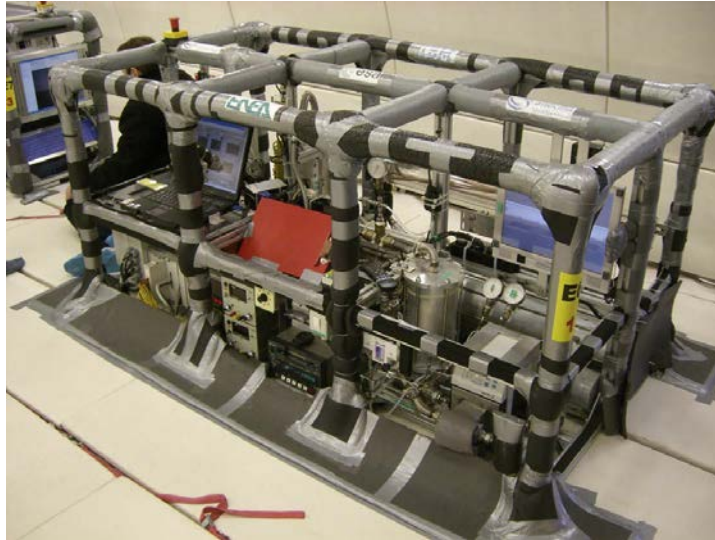
Figure 91: *MICROBO* experimental rack mounted in the cabin of an *A300 Zero-G*

5.3.1. System Description

This section presents each system of the experiment. Each system description should include a written description of how the system function. The experimental loop consists in three main systems:

- main fluid loop,
- second confinement,
- air loop

5.3.1.1. Main Fluid Loop

The main fluid loop consists of components described in the present section. The working fluid was described in the experiment description paragraph. The fluid is contained in the main circuit. A gear pump is used to pump the fluid in the loop. The main provided pressure of the pump is max *5.2 Bar*. The max differential pressure by the pump is *7 Bar*. After the pump, the liquid pass through an impurity filter. FC-72 could reach the maximum temperature of *90°C* due to the saturation pressure.

5.3.1.1.1. 2.0 mm and 4.0 mm Standard Test Sections.

The first test section is made of a Pyrex tube with a transparent metal layer deposited on the outer surface equipped with the electric field. The next figure (86) shows the section.
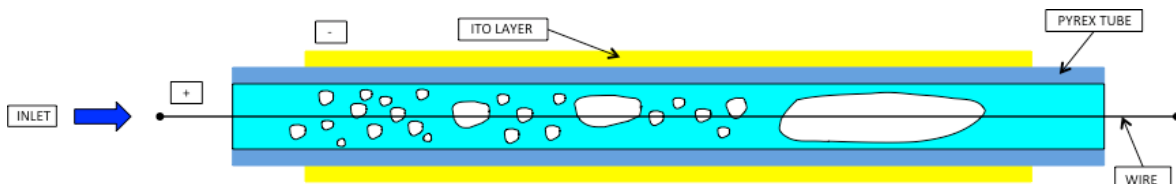
Figure 92: Schematic of the test section for the flow boiling

The deposed metal layer is transparent to allow the flow boiling visualization that is performed by a high-speed digital camera. A set of thermocouples attached to the outer tube wall measures wall temperatures. The configuration is showed in next Figure (87).
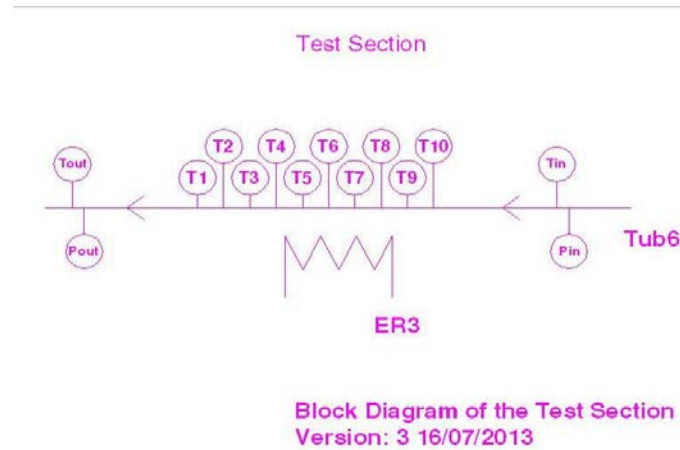
Figure 93: Schematic of the test section

A high-speed digital video camera perform the flow pattern visualisation. Ten thermocouples measure the tube outer wall temperature in different locations. An adhesive tape of *Kapton* attach the thermocouple on the tube and makes a perfect electrical insulation, on the outer surface of the tube.

The *Pyrex* tube is confined in a special box made of Sustarin *C* and closed between two transparent windows of *Lexan* to grant the visualization. The internal maximum temperature expected is in in the range between *45.0 °C* and *55.0 °C*. Figure (94) shows the section and following Figure (89) shows the box.

The standard vertical tube test section is made of *Pyrex* and is equipped with a transparent metal layer deposited on the outer surface. Inner tube diameter is or *4.0 mm* or *2.0mm*. The metal layer is made of *Indium Tin Oxide* and its thickness is of the order of *100-150 nm*. The heated length is *155 mm* and is heated by Joule effect. This configuration allows obtaining constant heat flux at the inner surface of the test section. The metal layer is transparent to allow tube heating as well as boiling phenomena visualization. Figure (94-95) show the test section.
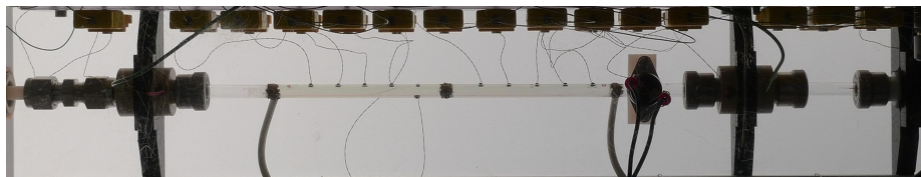
Figure 94: Test section
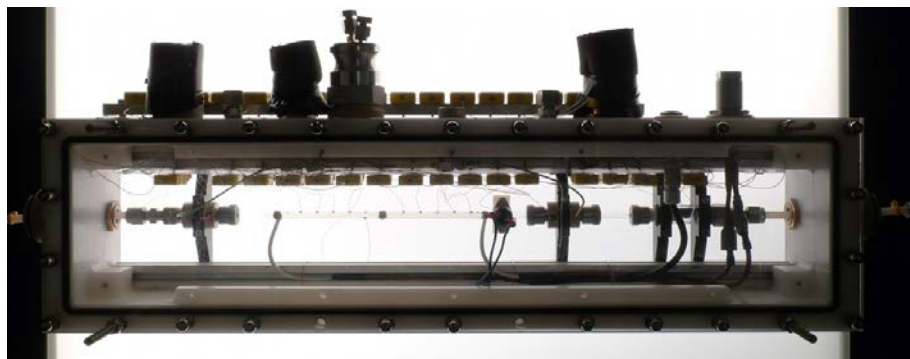
Figure 95: Test Section in the confinement box

5.3.1.1.2. Condenser

The condenser consists of two coaxial tubes. Figure (96) shows the condenser.
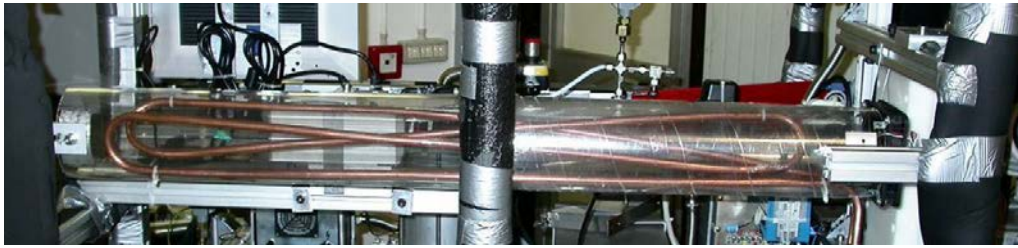
Figure 96: Condenser

The two tubes were made of *copper*; the outer one is a second confinement barrier, while the fluid flows in the inner tube. The condenser is cooled by *a fan* in a forced flow. To avoid any accidental contacts with hot surfaces the bended tubes were placed into a *polycarbonate* cylinder. The expected temperature of the fluid at the entrance is *90°C* and the outer temperature expected is *35°C*. The maximum outer possible temperature is *50°C*. All the second confinement between the test section exit and the condenser inlet is protected with a thermal insulation tube.

5.3.1.1.3. Pre-Heaters

The system is equipped with two pre-heaters.The first pre-heater was realized with a stainless steel tube of *2 m*. The heater elements are inside a tube; the second confinement of the pre-heater is realized with an *Anticorodal* tube of *80 mm* in diameter and *1.2 m* in length. An electric resistance in a metallic tube provides the heat. It is electrically insulated and immersed in *FC72*.

The second pre-heater has the aim to increase the inlet temperature of the fluid. The materials are Sustarin C and POM-C, which support a maximum temperature of *125°C*. A flat electric resistance covered with silicone rubber and attached on the outer surface of the heat exchanger provided the heat. Wall temperature and the exit fluid temperature, which was saturation temperature of *FC-72* at *2.5 Bar* (*86 °C*), were the maximum temperature of the preheaters. There was an insulating foam between the preheater and the outer containment.

5.3.1.1.4. Pressurizer-Tank

The tank containing *FC-72* controls the pressure of the system during the experiments. It consists of a metal body, an external shell, and of an elastic membrane containing the fluid. The membrane separates the air volume of the shell from the fluid. The presence of the air in the shell and the deformation of the membrane absorbs the variation of volume of the main circuit caused by the thermal expansion of the liquid and of the vapour formed in the test section. Moreover, acting on the air pressure inside the shell it is possible to control the system pressure. The air pressure control is sent to the vent line. When the system pressure has to be increase during the experiment, air is injected in the control volume of the tank.

5.3.1.2. Second Confinement

The second confinement of main circuit loop is realized to create a container for any accidental fluid leakage from the mail loop. The volume of the second confinement is three times larger

than the total volume of the main loop which is around to *2.0 l.* The maximum design pressure was *2.5 Bar*, enough to contain all the fluid volume and to resist to the aircraft depressurization. The components of the second confinement system are:

- corrugated tubes,
- cylindrical tanks,
- rectangular tanks.

All the main loop pipes are contained in the corrugated tubes, while the cylindrical tanks contained valves, sensors, and filter. For safety, the second containment has a pressure switch that could shut down the electrical system if the pressure in the containment goes over *2.0 Bar.*

5.3.1.2.1. Tubes

The second confinement of main circuit pipe is realized with an external corrugated tube. The material is stainless steel *AISI 304*. Figure (97) shows the confinement.
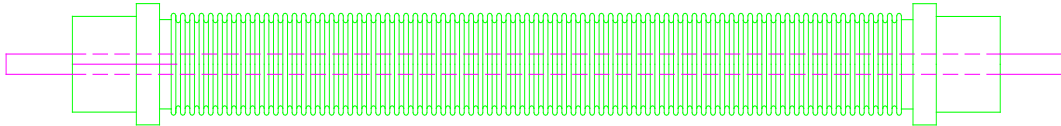
Figure 97: Second confinement of a pipe

5.3.1.2.2. Tanks

The system has two different tanks. One circular to store liquid leakages and one rectangular to store components. The components of the main circuit could not be inserted inside the corrugated tube. For this reason, they will be sited in some special tanks built. Stainless belts and metal brackets guaranteed the holding of the tanks on the rack.

5.3.1.3.   Air Loop

Air loop is used to maintain the pressure of the pressurizer. The air must be pumped by a hand pump in the circuit. A pressurized tank and two different lines are present.

5.3.1.4.   Rack schematic

The components are inserted inside the rack with the disposition showed in the Figure (98)
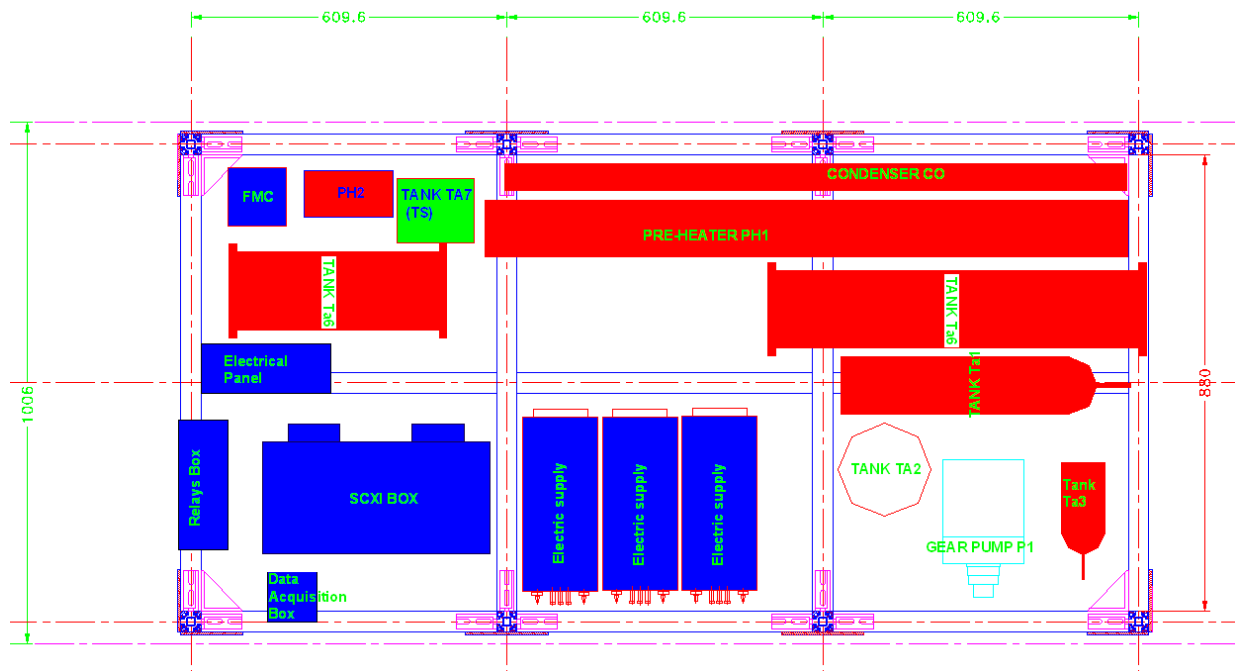
Figure 98*:* Schematization of the position of experimental components in the rack.

5.3.2. Test Route

This section describes the typical test route to flow boiling test. It is divided in two phases:

1. Regulation phase
2. Low gravity experiment

5.3.2.1.   Regulation phase

The experimental loop is regulated to reach the steady condition 10 seconds before the pull up, this regulation is obtained by a specific mass flow rate and heat flux. Steady condition means that all the parameters of the process (fluid temperature, system pressure, mass flow rate, wall temperatures) are stable and do not change with time. In these conditions, flow boiling occurs in the test section. Figure (101) shows the schematization of the loop during the flow boiling with the indication of the fluid phases inside the loop.
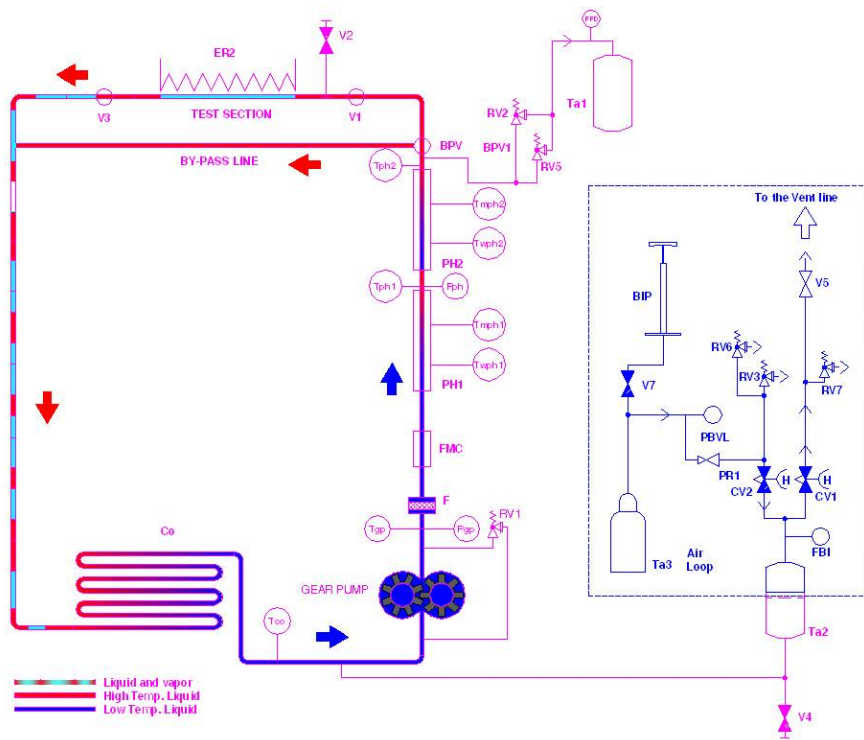
Figure 99: Schematization of the test loop and the two-phase flow during a flow-boiling test

Boiling occurred in the test section and after the test section. The condenser condenses the two-phase fluid. The pre-heater heated the fluid up to a temperature just below the saturation. Hence, the fluid flows from the pre-heater up to the test section as liquid phase. In the by-pass line, during flow boiling, the liquid is stagnant. The fluid temperature, at the exit of the pre-heaters, is measured by thermocouples and is regulated at the desired value automatically by a computer. The pressure transducer, located at the inlet of test section measured the system pressure. The operator, through the valves in the air loop, regulates the pressure. The flow meter measures the mass flow rate, which is regulated by the gear pump controlled by the operator. Ten thermocouples measured the wall temperatures measures the outer wall of the test section. The computer controls fluid temperature at the condenser through the fans, which create a forced airflow on

the serpentine of the condenser. When the regulation phase is concluded, the loop reaches its steady state in less than one minute.

5.3.3. Low gravity experiment

Once the steady condition is reached during the regulation phase, the test loop maintains the steady conditions for long time without any control of the operators. Hence, the loop remains in steady conditions at the pull up announcement for all the duration of the flight parabola. The data and images are recorded during this time to allow the study of gravity on flow boiling and bubble behaviour.

5.3.3.1.1. Pre-heating mode

The objective of the pre-heating phase was to increase the temperature of the loop components from the room values to the equilibrium values before the tests. Once values are reached, by each component, after a period of *15 minutes*, the experiment can start.

5.3.3.1.2. Experimental protocol

This section describes the operations made during parabolas for flow boiling experiments. The minimum time interval between two flight parabolas is *1 minute*. Figure (100) shows the operative sequence.

- *60 s* before the pull up: Regulation.
- *50 s* before the pull up: Start of data acquisition.
- *45 s* before the pull up: Checklist to verify the parameters of the test and the parameters of the experimental loop
- After the end of the parabola. Stop of data acquisition
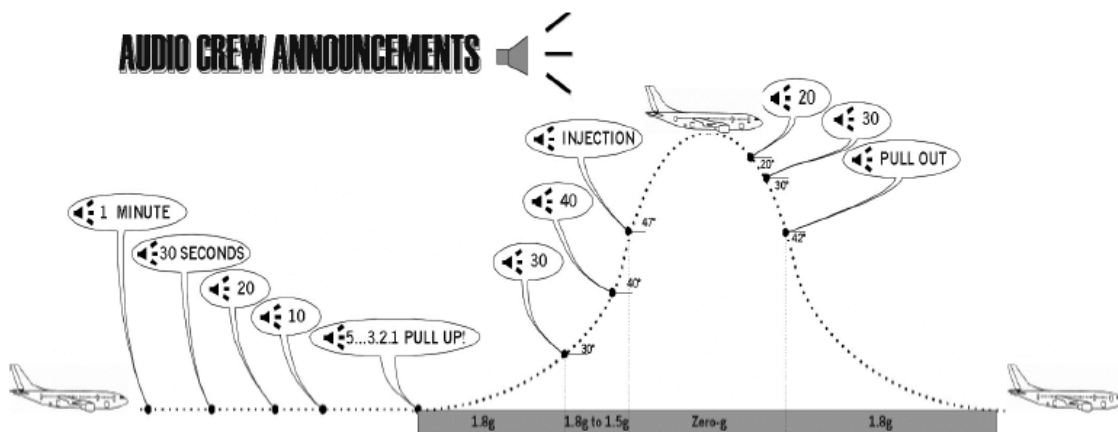
Figure 100: Schematization operations carried out during a typical parabola for a flow-boiling test

The air tank is refilled during the flight every 2 or 3 parabolas by an operator using the hand pump. At the end of parabolic flight pressure in the tank is emptied and bringed to ambient pressure.

5.3.4. Uncertainties

Following the uncertainties of MicroBo are reported in Table 13. The calculations of heat transfer coefficients are refined with the temperature gradient in the thickness of the pyrex tube. Heat transfer coefficients of low gravity tests are compared with those obtained at the same flow conditions (inlet temperature, mass flow rate, pressure, heat flux) at normal gravity with the test section vertically oriented and fluid flowing upwardly. The results of heat transfer coefficients are discussed in the following section and are reported as the ratio between low gravity and normal gravity heat transfer. More details can be found in the work of C.Baltis et al. (2012).

Table 13: Analysis of experimental uncertainty

Electrical tension	0.1	V
Current	0.01	A
Length	$5*10^{-5}$	m
Temperature	0.3	°C
Conductivity	$94014.48*10^{-6}$	W/m^{2}K
Pressure in	$6*10^{-2}$	Bar
Pressure drop	$105*10^{-4}$	Bar
Mass Flux	$163.66*10^{-8}$	Kg/s

6. Assessment

The paragraph is divided into three sections, one for heat transfer correlations and models in both experimental sections (BO.E.MI.A and MicroBo), and one for pressure drop model in BO.E.MI.A. The study of pressure drop has been done only in BO.E.MI.A due to the sufficient length and pressure drop in the channel. In fact, MicroBo, due to the big channel diameter and short channel length compared to sensor's full-scale, MicroBo is inappropriate to measure pressure drops inside the channel.

6.1. Methodology

The proposed method has been applied to the ENEA database from the BOEMIA and MICROBO test sections. The Mean Percentage Error (MPE), the Mean Absolute Percentage Error (MAPE), and the percentage of data within the ±30% error band (±30%) have been used to assess the methodology. The mean percentage error (MPE) is the computed average of percentage errors by which forecasts of a model differ from actual values of the quantity being forecast.

$$MPE = \frac{100\%}{N} \sum_{i=1}^{n} \frac{A - C}{A}$$

A is the actual measured value of the quantity being predicted, *C* is the calculated value and *N* is the number of measured values. The formula is useful to understand how far the mean prediction is from the data and it has the advantage of neglecting any white noise due to the instrumentation.

The Mean Absolute Percentage Error is:

$$MAPE = \frac{100\%}{N} \sum_{i=1}^{n} \frac{\|A - C\|}{A}$$

MAPE is a quantity used to measure how close predictions are to the eventual outcomes and represents the mean error committed for a single forecast.

6.2. BO.E.MI.A heat transfer coefficients

The test matrix shown in table 14 was used for the experiments: globally, the ranges are: pressure 3-5 bar, mass flux 925-1439 Kg/m^{2}s and heat flux 3-181 kW/m^2. A total of 676 data points were collected.

Table 14: Test matrix

N$^\bullet$	T	P	Mass flux	q'' fix min	q'' fix max	Data points
-	C°	MPa	Kg/m^{2}s	W/m^2	W/m^2	n°
1	84	0.308	1126	4357	98414	124
2	88	0.502	1234	4227	181562	128
3	87	0.408	1234	4297	170409	72
4	97	0.404	1030	3297	97900	52
5	97	0.405	925	3188	99653	60
6	98	0.404	824	3056	86153	68
7	84	0.305	1235	4143	71069	60
8	97	0.405	1439	7406	87896	32
9	87	0.304	1132	4070	70838	44
10	83	0.305	1020	4148	25347	36
					Total	676

Not all of the points are in saturated boiling are useful to determinate heat transfer coefficient in those conditions. Therefore, only 68 points have been selected. The channel thickness in the BOEMIA facility is low enough to consider negligible axial conduction and thermal inertia, as shown in Saraceno (2012). Two typical boiling curves inside the channel for different heat fluxes are shown in Figure 101 and Figure 102. At the inlet the fluid is subcooled and it can be assumed to be in forced convection regime. Due to the high thermal flux, boiling starts in the partial nucleate boiling zone and then in the fully developed boiling. The observed occurrence of higher wall superheat degrees at the beginning of the boiling process is known as hysteresis effect and is marked for highly wetting liquids such as refrigerants: the sudden decrease of wall temperatures suggests the onset of nucleate boiling (ONB) in the subcooled flow boiling regime. In the presence of high thermal fluxes then the fluid reaches the film boiling zone. At higher pressures the increase of the saturation temperature determines an increment of the heat flux needed to reach the transition boiling regime. Moreover, the increment of the mass flux reduces the temperature difference between the fluid and the channel wall, due to the increase the heat transfer coefficient in turbulent conditions.
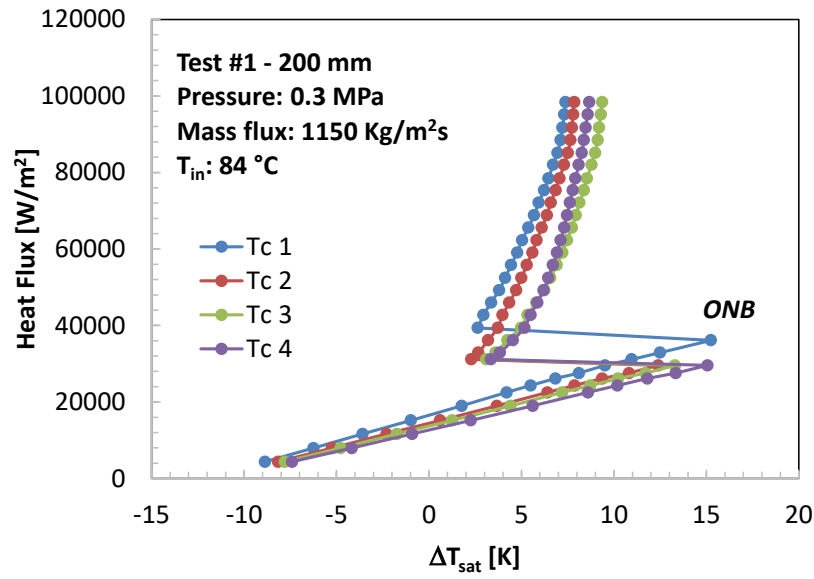
Figure 101: Boiling curve for test #6 – 100 mm
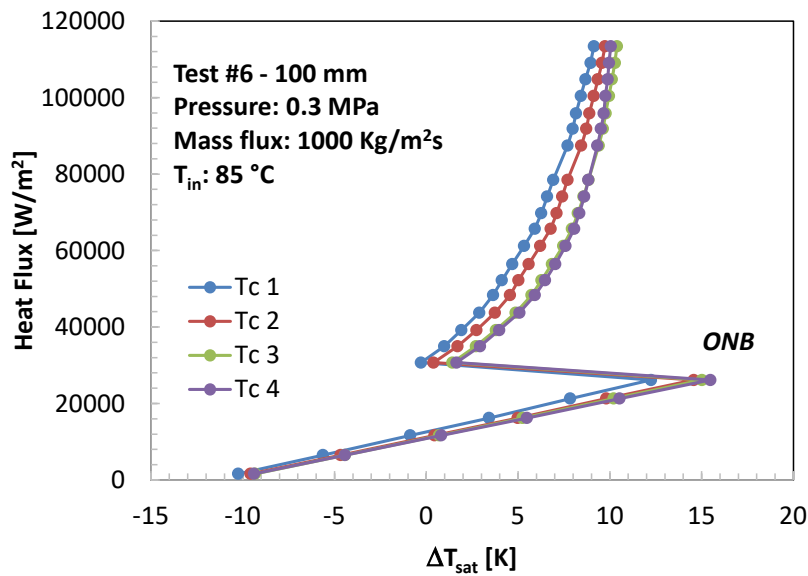
Figure 102: Boiling curve for test #1 – 200 mm

The fluid bulk temperature has been evaluated by a thermal balance, considering the heat losses preliminarily evaluated with the facility empty and in vacuum conditions, as discussed in Saraceno et al. (2012). Thermodynamic properties of FC-72 have been calculated by the REFPROP v. 9.1 program.

During the analysis, the Cooper correlation (1984) for pool boiling was also tested to check if any point, at low mass fluxes, may be referred to that regime. However, the correlation does not provide good results, confirming that the analyzed data are far from pool boiling conditions.

Table 15: Models and correlations assessment

Correlation or Model	MAPE %			% of Points within ±30%		
	100 mm (14 pts.)	200 mm (68 pts.)	both (82 pts.)	100 mm (14 pts.)	200 mm (68 pts.)	both (82 pts.)
Macro-Scale correlations						
Chen [1]	9.52	25.91	23.11	100.0	61.8	68.3
Shah [28]	45.47	35.09	36.86	7.14	33.8	29.3
Gungor and Winterton [3]	121.83	79.65	86.85	0.0	0.0	0.0
Kandlikar [2]	88.35	61.18	65.82	0.0	0.0	0.0
Liu and Winterton [29]	52.05	57.92	56.92	0.0	0.0	0.0
Micro-Scale correlations						
Lazarek & Black [4]	87.90	66.04	69.77	0.0	0.0	0.0
Tran et al. [30]	59.17	55.74	56.33	0.0	0.0	0.0
Kew and Cornwell [7]	62.66	44.07	47.24	0.0	1.47	1.2
Warrier et al. [31]	89.46	89.92	89.84	0.0	0.0	0.0
Kandlikar & Balasubra-manian [32]	60.13	39.83	43.30	0.0	33.8	28.0
Zhang et al. [6]	26.99	18.64	20.07	85.7	82.3	82.9
Lee & Mudawar [33]	325.55	438.37	419.10	28.6	26.5	26.8
Saitoh et al. [34]	41.23	24.69	27.51	7.1	69.12	58.5
Bertsch et al. [5]	66.95	61.85	62.72	0.0	5.9	4.88
Mikielewicz [8]	80.39	82.02	81.74	0.0	0.0	0.0
Li and Wu [35]	12.96	13.51	13.42	100.0	89.7	91.5
Mahmoud and Karayiannis [16]	61.34	67.43	66.39	0.0	0.0	0.0
Mechanicistic models						
Thome [10, 11]	28.21	30.37	30.0	50.00	64.7	62.2
Consolini & Thome [12, 13]	42.05	32.91	34.47	25.00	47.4	43.6

Tab. 15 summarizes the models and correlations assessment based on the average (global) heat transfer coefficients in the test tube. Only the saturated points (10% of the available 680 data points for the 200 mm tube and only 14 points for the 100 mm tube) were elaborated.

6.2.1. Discussion on Models

The Three-Zone model provides the best results for the #4 and #9 tests summarized in table 14 (200 mm). Globally the MAPE is 30.0% and 62.2% of data are predicted within the 30% error range. The model returns the best approximations for low flow rates and heat fluxes. However, the model needs to be adapted to the FC-72 refrigerant in combination with a steel tube, by tuning the empirical parameters. The results of the comparison with the experimental data is shown in Figures 103-104.

The Slug-Coalescence model provides lower errors, but only for few data points. The best predictions occur in the same conditions as in the previous model, suggesting the common nature of the two models. As for the Three-Zone model, however, standard parameters are not suitable for every fluid and conditions and must be found for the employed experimental section and its operating fluid. Considering both tube lengths, the MAPE is around 34.5% and 43.6% of data can be predicted within the 30% error range, as shown in Figure 103. The model has been developed to be applied in the transition between the slug and bubble coalescence regime, which usually appear at positive qualities, this is the reason for the low number of predicable data. However, as reported by Mahmoud and Karayiannis (2014) in their review, the model provides good results in micro-channels where the superficial shear stress are predominant. This situation is more evident at high mass fluxes and reducing the channel size.
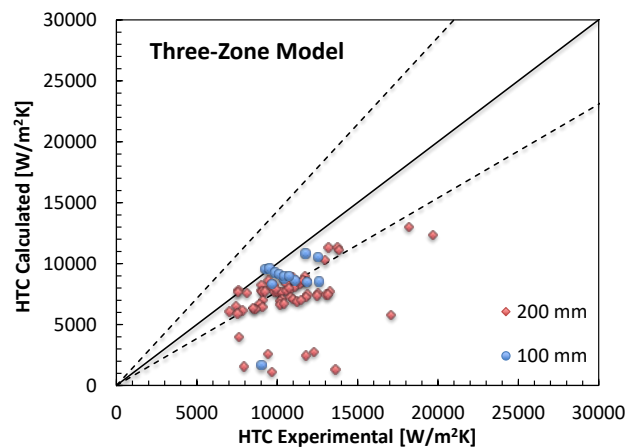
Figure 103: Thome et al. model
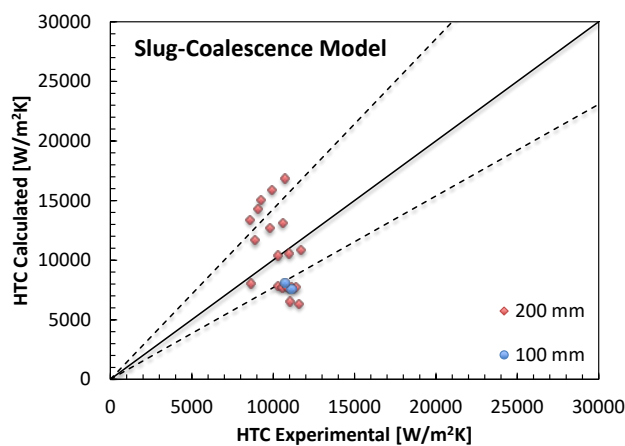
Figure 104: Consolini et al. model

6.2.2. Discussion on Macro-Scale correlations

Macro scale correlations are more suitable for higher channel diameter where the inertia forces dominate the capillarity ones.

The Chen's correlation provides the best results in the macro-scale set of correlations, besides of its simplicity. Globally the MAPE is around 23.11% and 68.3% of data is predicted inside the ±30% error. The model approximate data better in the 1st test matrix of the 200 mm tube. The results worsen with the pressure increment, reaching the lower agreement for the test #6 for the same tube. Figure 101 shows the global comparison.

The Shah's correlation works quite well with the ENEA database: the global MAPE is around 36.9% and 29.3% of data are in the 30% error band, Figure 102 shows the comparison. With reference to the 200 mm tube, the best prediction is obtained in the test #3. This shows how the prediction capability improves with the increment of the heat flux. However, the agreement decreases reducing the mass flux, reaching the lower agreement for the test #6.
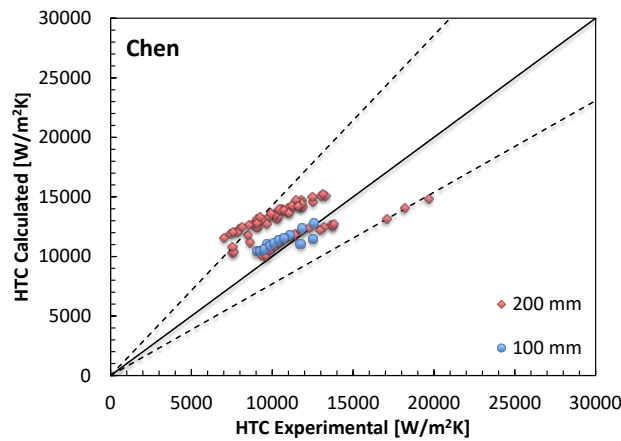
Figure 105: Chen correlation
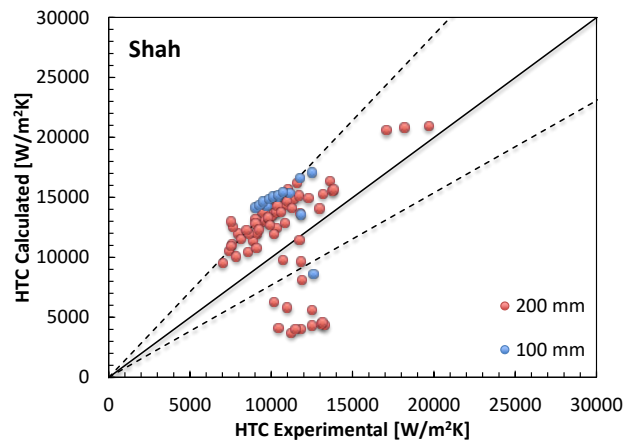
Figure 106: Shah correlation

The correlation from Gungor and Winterton does not provide good predictions. The global MAPE is 86.85% but any point is predicted within the 30% error. The correlation overestimates the heat transfer coefficient for a quite constant value. However, it performs better at high mass

and thermal fluxes. The prediction error is too high to obtain good information from this correlation.

Apparently, Kandlikar's correlation returns results like the Shah correlation; however, all the calculated values are overestimated. The global MAPE is around 65.82% but no data are within the ±30% error range. The best results are obtained with the test #3 with the 200 mm tube for high mass and thermal fluxes. The worst results are for the test #5 (100mm tube) with low mass and thermal flux. This correlation uses a fluid specific factor, assumed to be 1, following the author suggestion. Further studies to obtain this fluid factor are needed to use this correlation.

The Liu and Winterton correlation provides the worst results in this macro-scale category with a MAPE of almost 56.92% and 0% of data within the ±30%. The best results are obtained in the 200 mm tube for the test #9 and the worst for the test #3. However, the difference in the prediction is not so important compared with the magnitude of the error that makes this correlation unsuitable for the present experimental data base. The reason is probably the use of the all-liquid Reynolds number rather than the two-phase one. In fact, this not consider the high percentage of vapor bubbles present in the channel at high thermal fluxes.

6.2.3. Discussion on Micro-Scale correlations

Micro scale correlations are expected to be more suitable for the analyzed channel. However, the behaviors of the correlations are different and not all the correlations produce good results.

The correlation from Lazarek and Black returns a MAPE of 69.8% but with 0% of data within the error range of 30%. Differently from Gungor and Winterton his correlation underestimates by a constant value the heat transfer coefficients. However, it works better at high heat and mass fluxes and the best results have been obtained on the test #6 in the 200 mm tube. Probably changing the non-dimensional constants inside the correlation could lead to better results.

Tran et al. correlation predicts quite well the data: globally the MAPE is about 56.33% and 0% of data is in the ±30% error band. The correlation is quality independent, it does not depend on the assumption made for the test section heat losses. The best results have been obtained for the test #1, and the worst are for the #6, for the longer tube. The correlation is sensible to the mass flux, reducing their accuracy as it decreases.

The correlation from Kew and Cornwell provides globally 1.22% of data predicted into the ±30% error band and the average MAPE is about 47.24%. The correlation performs better at low fluid velocity where 6.25% of data are predicted within ±30% error with an MAPE of 40.1% for the #6 test in the 200 mm tube. The correlation was developed for R141b.

The correlation of Warrier et al. does not provide good results, with a global MAPE of 89.9%. This behavior is due to the presence in the correlation of the Boiling number only. The results obtained are strongly underestimated.

Kandlikar and Balasubramian correlation gives good predictions: the global MAPE is 43.3% and 28% of data are in the 30% error bands, all for the 200 mm tube. The predictions are more accurate for the test #6, where the mass flux is the lower and the worst results are for the test #8 where the mass fluxes are high. However, the relation underestimates the heat transfer coefficients. Figure 107 shows the comparison with the present data.

The correlation of Zhang et al. shows 82.9% of data inside the 30% error bands and a MAPE of 20.1%. The best results are for intermediate heat fluxes and high mass flux in the 6th and 9th tests of the 200 mm tube. The agreement decreases strongly with the increment of pressure reaching a MAPE of 49.1% for the test #3. This is due to the presence of the reduced pressure in the Cooper pool boiling correlation and the subcooled in the Foster and Zuber correlation, by which the liquid heat transfer coefficient is calculated. Globally the correlation underestimates the heat transfer coefficient as shown in Figure 108.
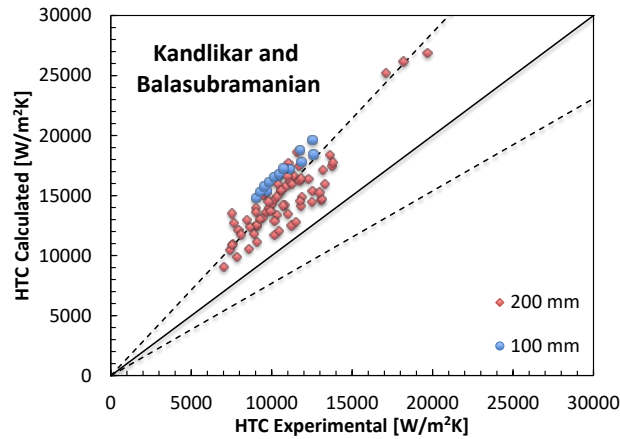
Figure 107: Kandlikar and Balasubramian correlation
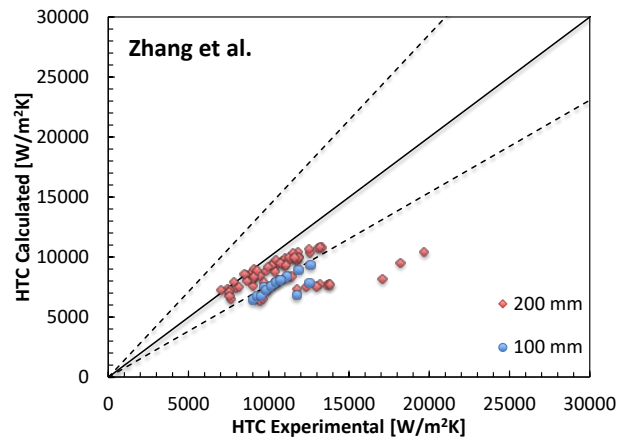
Figure 108: Zhang et al. correlation

Lee and Mudawar correlation overestimates the heat transfer coefficient and returns a global MAPE of more than 419% with 26.8% of data within the error bands. The correlation performs worse at low heat fluxes and high qualities. This depends on the three different relations used to calculate the heat fluxes as functions of quality. Probably changing the equation could improve the prediction capability. However, the best results have been calculated for the dataset #8 in the 200 mm tube, where the model returns a MAPE of about 316% but with more than 66.7% of data inside the 30% error range.

The correlation of Saitoh et al. predicts well the analyzed data. In fact, it returns a total MAPE of 27.5% and 58.5% of data inside the 30% error bands. Limiting to the 200 mm tube tests, those value are 24.7% and 69.1% respectively. The performance can be observed in Figure 109. The model considers the developed and undeveloped turbulent fluxes for liquid and vapor phase

during the evaluation of the friction factor, the Martinelli parameter and the liquid heat transfer. The nucleate boiling is in function of the Prandtl number. The good results are probably due to the layout of the Saitoh's experiment that is like the current test section. The best results are for high mass fluxes and high pressure for the #3 dataset of the 200 mm tube, where all data is within the ±30% error and the correlation presents a MAPE of 13.4%.

Bertsh correlation does not predict well the heat transfer coefficient data, showing a global MAPE of 62.7% and 4.88% data points within the 30% error. The behavior of this correlation is like the macro scale correlation of Liu and Winterton. The correlation performs better at high mass flux.

Mikielewicz correlation does not provide good results (MAPE higher than 81.7% and no data points in the 30% error band). However, like the correlation of Bertsch et al., it works better for high mass fluxes and low heat fluxes. The application range of this correlation is both for micro and macro scale.

The correlation of Li and Wu performs well, as it can be seen in Figure 110; the global MAPE is about 13.4% and 91.5% of data is predicted inside the 30% error. The correlation structure is very simple, it includes only the Boiling number, the Bond number and the Reynolds liquid number. The good agreement with experimental results is probably due to the low-quality values in the data. The prediction capability improves as heat and mass fluxes increase. The best prediction has been obtained for the few data of the 100 mm tube (MAPE between 6% and 17%, 100% data in the 30% error) and in the test #1 of the 200 mm experiments: in this case it returned a MAPE of 4.7% and the 100% of data are predicted within the 30% error.

Mahmoud and Karayiannis correlation is based on suppression and enhancement factors. For the present test section, the correlation does not provide good results. The global average MAPE is about 66.39% and no data points are within the 30% error range. The best prediction has been obtained at high thermal fluxes.
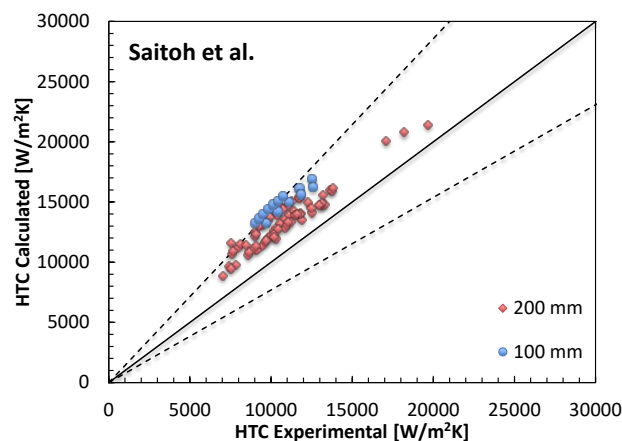
Figure 109: Saitoh et al. correlation
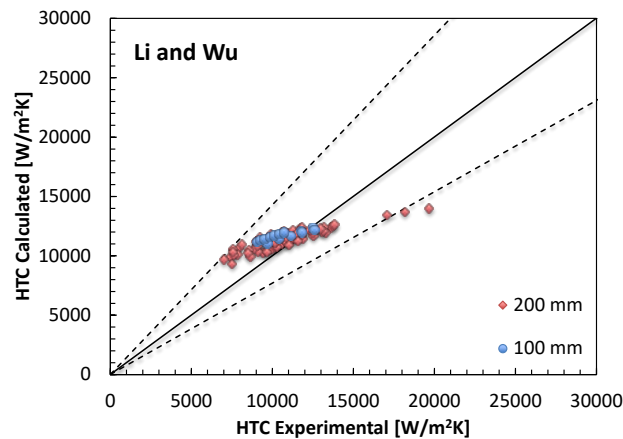
Figure 110: Li and Wu correlation

6.3. MicroBo heat transfer coefficients

For every model were taken the standard recommended data from RERPROP database for all fluids. *FC-72* is not a common fluid and often is difficult to find specific parameters fitted for it, also *Plexiglas* tube does not have a known roughness. Moreover, some models are semi-empirical (as the Three Zone and Slug-Coalescence models) and they need a specific data fitting. Thus, for the present analysis the global parameters are always used and for a more specific analysis further research is suggested.

6.3.1. 2 mm Test Section

The *2 mm* test section has ten different thermocouples at positions indicates in the table 16:

Table 16: *2 mm* test section thermocouples positions

Axial positions									
%									
10	19	28	37	46	63	70	77	84	92
cm									
0,015	0,029	0,043	0,057	0,071	0,0998	0,110	0,1217	0,1330	0,1442

The section was subjected to *four* different sets of tests varying the thermal flux and at operative pressure and bulk flux constants:

I.   The first test set was performed in micro-gravity conditions, during the parabolic flight, with the quantity shows in Table 17:

Table 17: First test quantity on *2 mm* test section

Internal diameter	0.002	m
Channel lenght	0,15754	m
Subcooling	35,400	K
Operative pressure	1,870	bar
Bulk flux	280,000	kg/m^{2}s
Gravity	0	m/s^2
Heat flux	7.3-18.1	kw/m^2

The set consist in *14* different tests with different heat fluxes showed in table 18:

Table 18: First test heat fluxes on *2 mm* test section

Heat flux kw/m^2													
7.2	8.5	9.6	10.8	11.8	12.6	12.7	14.0	14.7	14.7	16.1	16.7	17.3	18.1

Totally there were taken *130* data points from this set.

II. A second set of tests was performed in normal gravity conditions, on earth, with the quantity shows in table 19:

Table 19: Second test on *2 mm* test section

Internal diameter	0.002	m
Channel lenght	0.15754	m
Subcooling	35.00	K
Operative pressure	1.850	bar
Bulk flux	277.00	kg/m^{2}s
Gravity	9.81	m/s^2
Heat flux	7.2-18.22	kw/m^2

The set consist in *14* different tests with different heat fluxes showed in table 20:

Table 20: Second test heat fluxes on *2 mm* test section

Heat flux kw/m^2													
7.1	8.3	9.5	10.6	11.6	12.4	12.6	13.9	14.2	14.8	15.9	16.5	17.1	18.2

Totally there were taken *140* data points from this set.

III. The third set of tests was performed in micro-gravity conditions, during the parabolic flight, with the quantity shows in table 21:

Table 21: Third test on *2 mm* test section

Internal diameter	0.002	m
Channel lenght	0.15754	m
Subcooling	29.40	K
Operative pressure	1.90	bar
Bulk flux	467.00	kg/m^{2}s
Gravity	0	m/s^2
Heat flux	9.6-44.4	kw/m^2

The set consist in *13* different tests with different heat fluxes showed in table 22:

Table 22: Third test heat fluxes on *2 mm* test section micro-gravity

Heat flux kw/m^2												
9.5	12.9	16.7	20.2	23.7	27.5	30.9	34.1	34.7	36.9	38.0	41.3	44.4

Totally there were taken *130* data points from this set.

IV.   The fourth set of tests was performed in normal gravity conditions, on earth, with the quantity shows in table 23:

Table 23: Fourth test on *2 mm* test section

Internal diameter	0.002	m
Channel lenght	0.15754	m
Subcooling	29.4	K
Operative pressure	1.9	bar
Bulk flux	449.00	kg/m^{2}s
Gravity	9.81	m/s^2
Heat flux	9.6-44.4	kw/m^2

The set consist in *13* different tests with different heat fluxes showed in table 24:

Table 24: Fourth test heat fluxes on *2 mm* test section

Heat flux kw/m^2												
9.5	13.0	16.6	20.2	23.7	27.4	31.0	34.1	34.7	36.9	37.9	41.3	44.3

Totally there were taken *130* data points from this set.

6.3.1.1.   Discussion on models

The analysis with the Three-Zone model returned *540* calculated heat transfer coefficients that compared with the expected ones returns a total *RMS* of *217* and *0.16%* of data within the error band of *30%*. Figures 111-112 shows heat transfer coefficient versus quality and experimental heat transfer coefficient versus expected.

Figure 111: Three-Zone 2 mm heat transfer coefficient versus quality

Figure 112: Three-Zone 2 mm experimental heat transfer coefficient versus calculated

Following the results for every test set, that were described in the last paragraph:

- First data set returns *0%* data inside the *30%* error range and an average *RMS* of *322* with the minimum *RMS* of *177* at intermediate heat fluxes of *14.77 kW/m²*.
- Second data set returns *0%* data inside the *30%* error range and an average *RMS* of *407* with the minimum *RMS* of *173* at intermediate heat fluxes of *18.22 kW/m²*.
- Third data set returns *33%* data inside the *30%* error range and an average *RMS* of *130* with the minimum *RMS* of *95* at intermediate heat fluxes of *44.76 kW/m²*.
- Fourth data set returns *32%* data inside the *30%* error range and an average *RMS* of *94* with the minimum *RMS* of *95* at intermediate heat fluxes of *34.76 kW/m²*.

Using the thermodynamic qualities for the fourth set of data gives an *RMS* of *91* and 11.53% of data inside the *30%* error band.

The analysis with Slug-Coalescence model returned *153* calculated heat transfer coefficients that compared with the expected ones returns a total *RMS* of *735* and *0%* of data within the error band of *30%*. Figures 113-114 shows heat transfer coefficient versus quality and experimental heat transfer coefficient versus expected.

Figure 113: Slug-Coalescence 2 mm heat transfer coefficient versus quality

Figure 114: Slug-Coalescence model *2mm* experimental heat transfer coefficient versus calculated

Following the results for every test set, that were described in the last paragraph:

- First data set returns *0%* data inside the *30%* error range and an average *RMS* of *640* with the minimum *RMS* of *499* at intermediate heat fluxes of *14.48 kW/m²*.
- Second data set returns *0%* data inside the *30%* error range and an average *RMS* of *743* with the minimum *RMS* of *519* at intermediate heat fluxes of *18.22 kW/m²*.
- Third data set returns *33%* data inside the *30%* error range and an average *RMS* of *870* with the minimum *RMS* of *415* at intermediate heat fluxes of *16.70 kW/m²*.
- Fourth data set returns *32%* data inside the *30%* error range and an average *RMS* of *671* with the minimum *RMS* of *437* at intermediate heat fluxes of *16.63 kW/m²*.

For this model is impossible to use the thermodynamic qualities because it did not work with negative values for quality.

6.3.1.2. Discussion on macro-Scale correlations

Following correlations are studied by authors for macro-scale tubes. The definition of macro-channel is in the first chapter.

The analysis with the Chen's correlation returned *540* calculated heat transfer coefficients that compared with the expected ones returns a total *RMS* of *103* and *34.03%* of data within the error band of *30%*. Figures 115-116 shows heat transfer coefficient versus quality and experimental heat transfer coefficient versus expected.

Figure 115: Chen 2 mm heat transfer coefficient versus quality

Figure 116: Chen 2 mm experimental heat transfer coefficient versus calculated

Following the results for every test set, that were described in the last paragraph:

- First data set returns *48.6%* data inside the *30%* error range and an average *RMS* of *133* with the minimum *RMS* of *94* at intermediate heat fluxes of *20.6 kW/m²*.
- Second data set returns *31.4%* data inside the *30%* error range and an average *RMS* of *163* with the minimum *RMS* of *255* at intermediate heat fluxes of *9.6 kW/m²*.
- Third data set returns *33%* data inside the *30%* error range and an average *RMS* of *248* with the minimum *RMS* of *90* at intermediate heat fluxes of *25.4 kW/m²*.
- Fourth data set returns *26.1%* data inside the *30%* error range and an average *RMS* of *73* with the minimum *RMS* of *86* at intermediate heat fluxes of *15.1 kW/m²*.

The analysis with the Shah's correlation returned *461* calculated heat transfer coefficient that compared with the expected ones returns a total *RMS* of *192* and *23.6%* of data within the error band of *30%*. Figures 117-118 shows heat transfer coefficient versus quality and experimental heat transfer coefficient versus expected.
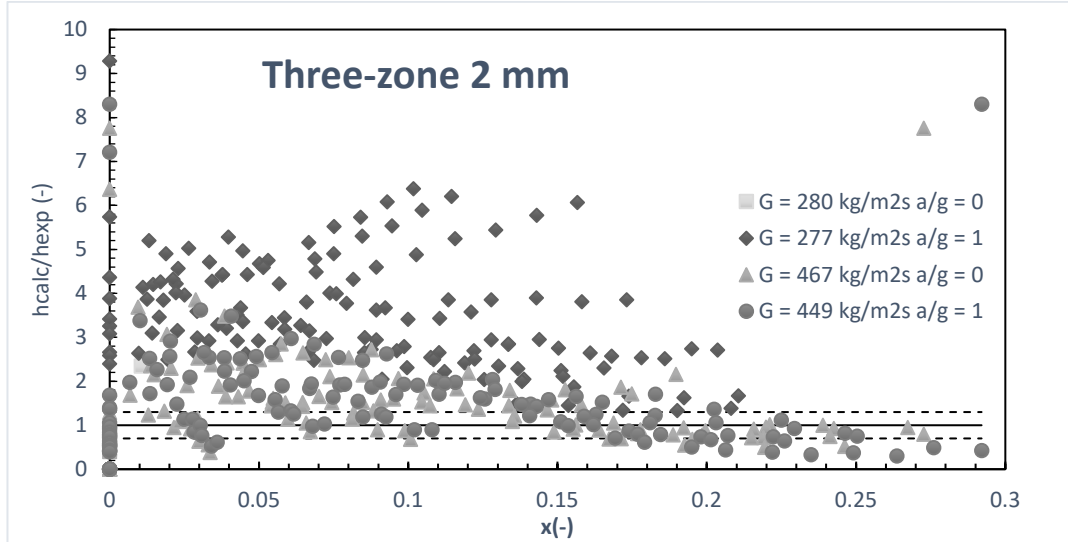
Figure 117: Shah 2 mm heat transfer coefficient versus quality

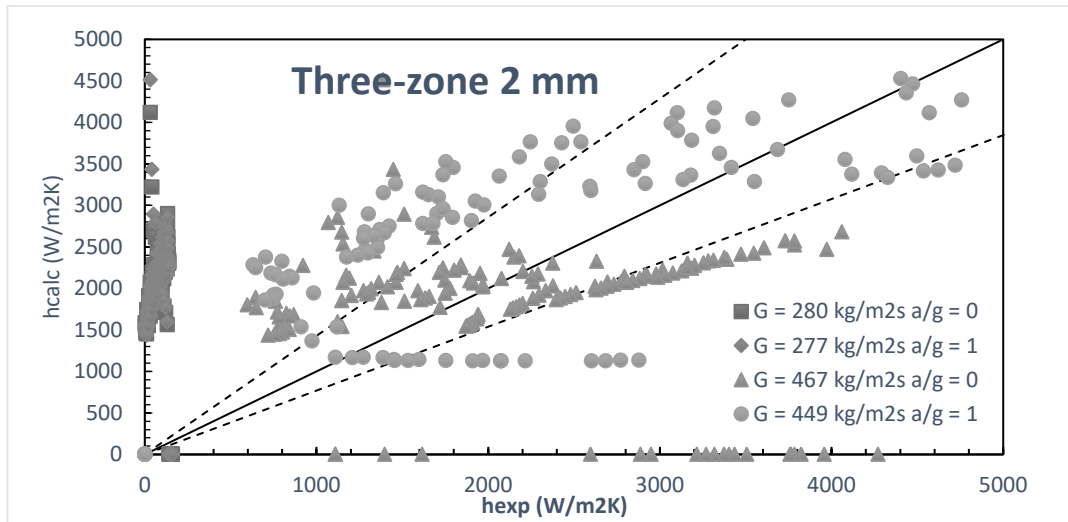Figure 118: Shah 2 mm experimental heat transfer coefficient versus calculated

Following the results for every test set, that were described in the last paragraph:

- First data set returns *19.84%* data inside the *30%* error range and an average *RMS* of *258* with the minimum *RMS* of *171* at intermediate heat fluxes of *14.78 kW/m²*.
- Second data set returns *8.73%* data inside the *30%* error range and an average *RMS* of *319* with the minimum *RMS* of *165* at intermediate heat fluxes of *18.22 kW/m²*.
- Third data set returns *31.73%* data inside the *30%* error range and an average *RMS* of *130* with the minimum *RMS* of *99* at intermediate heat fluxes of *34.76 kW/m²*.
- Fourth data set returns *34.28%* data inside the *30%* error range and an average *RMS* of *127* with the minimum *RMS* of *98* at intermediate heat fluxes of *34.75 kW/m²*.

The analysis with the Gungor and Winterton correlation returned *504* calculated heat transfer coefficient that compared with the expected ones returns a total *RMS* of *282* and *3.97%* of data within the error band of *30%*. Figures 119-120 shows heat transfer coefficient versus quality and experimental heat transfer coefficient versus expected.
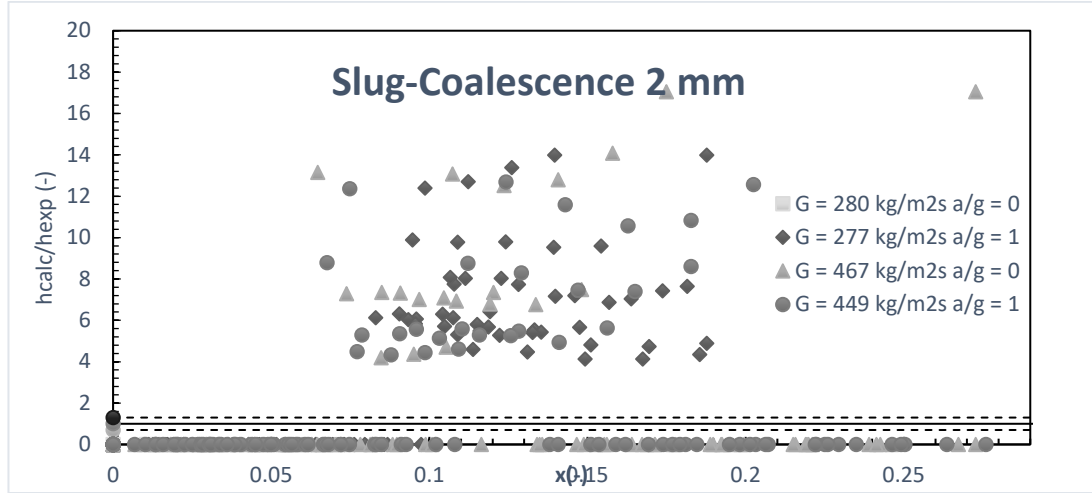
Figure 119: Gungor and Winterton 2 mm heat transfer coefficient versus quality
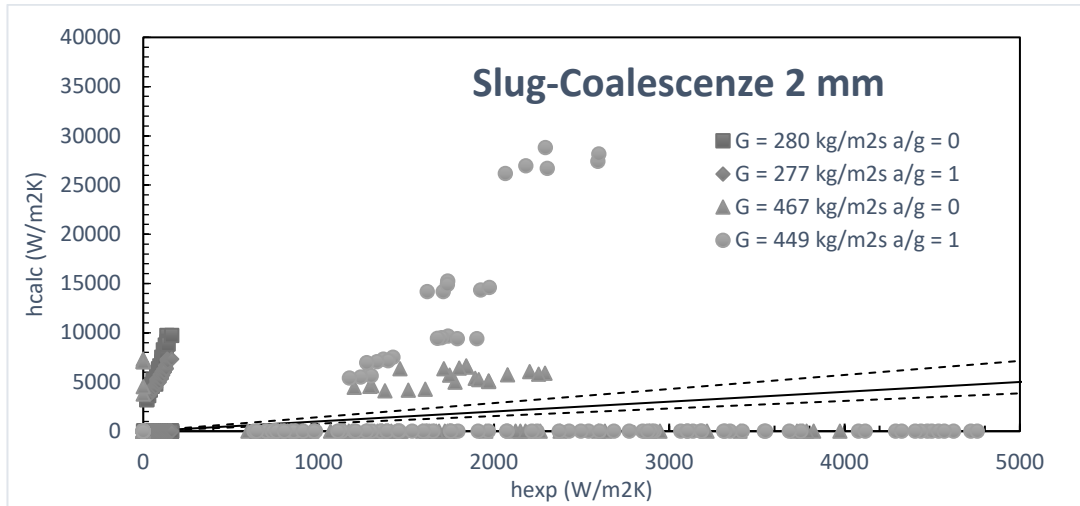

Figure 120: Gungor and Winterton 2 mm experimental heat transfer coefficient versus calculated

Following the results for every test set, that were described in the last paragraph:

- First data set returns *0%* data inside the *30%* error range and an average *RMS* of *339* with the minimum *RMS* of *246* at intermediate heat fluxes of *14.78 kW/m²*.
- Second data set returns *0%* data inside the *30%* error range and an average *RMS* of *416* with the minimum *RMS* of *226* at intermediate heat fluxes of *18.22 kW/m²*.
- Third data set returns *6.35%* data inside the *30%* error range and an average *RMS* of *211* with the minimum *RMS* of *114* at intermediate heat fluxes of *44.42 kW/m²*.
- Fourth data set returns *9.52%* data inside the *30%* error range and an average *RMS* of 213 with the minimum *RMS* of *101* at intermediate heat fluxes of 44.39 *kW/m²*.

The analysis with the Kandlikar's correlation returned *504* calculated heat transfer coefficient that compared with the expected ones returns a total *RMS* of *309* and *5.36%* of data within the error band of *30%*. Figures 121-122 shows heat transfer coefficient versus quality and experimental heat transfer coefficient versus expected.
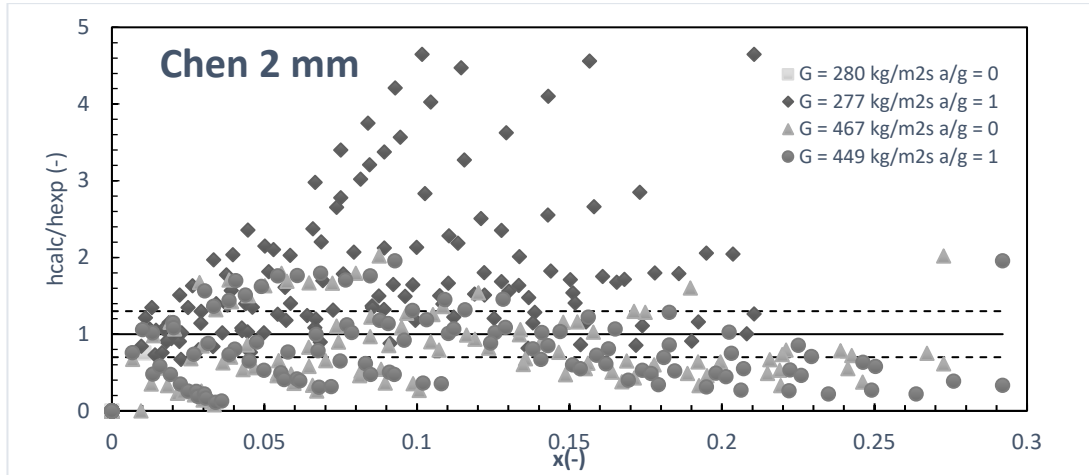
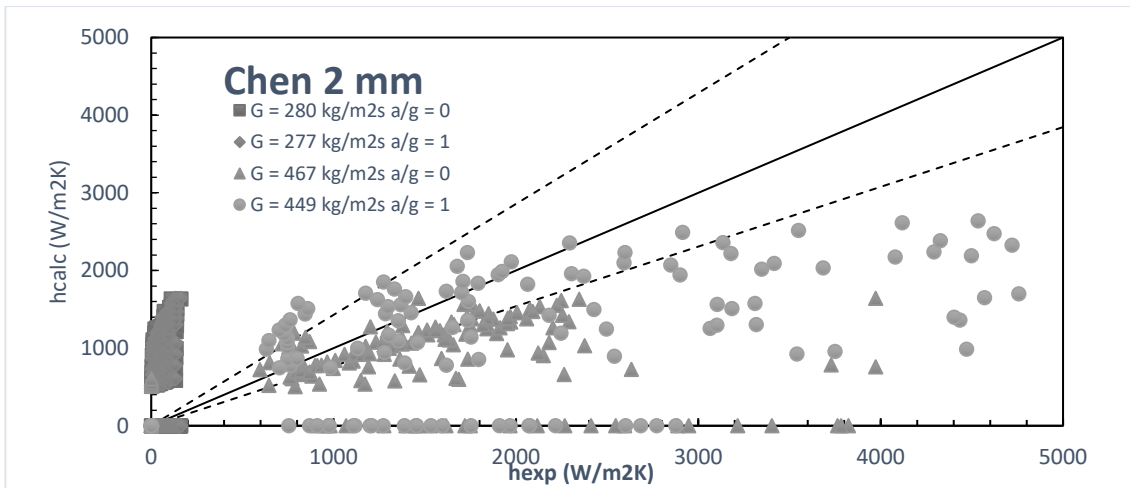Figure 121: Kandlikar 2 mm heat transfer coefficient versus quality

Figure 122: Kandlikar 2 mm experimental heat transfer coefficient versus calculated

Following the results for every test set, that were described in the last paragraph:

- First data set returns *0%* data inside the *30%* error range and an average *RMS* of *386* with the minimum *RMS* of *269* at intermediate heat fluxes of *14.78 kW/m²*.
- Second data set returns *0%* data inside the *30%* error range and an average *RMS* of *473* with the minimum *RMS* of *273* at intermediate heat fluxes of *18.22 kW/m²*.
- Third data set returns *9.52%* data inside the *30%* error range and an average *RMS* of *224* with the minimum *RMS* of *102* at intermediate heat fluxes of *44.42 kW/m²*.
- Fourth data set returns *11.90%* data inside the *30%* error range and an average *RMS* of *224* with the minimum *RMS* of *98* at intermediate heat fluxes of *41.33 kW/m²*.

The analysis with the Liu and Winterton correlation returned *560* calculated heat transfer coefficient that compared with the expected ones returns a total *RMS* of *164* and *17.67%* of data within the error band of *30%*. Figures 123-124 shows heat transfer coefficient versus quality and experimental heat transfer coefficient versus expected.
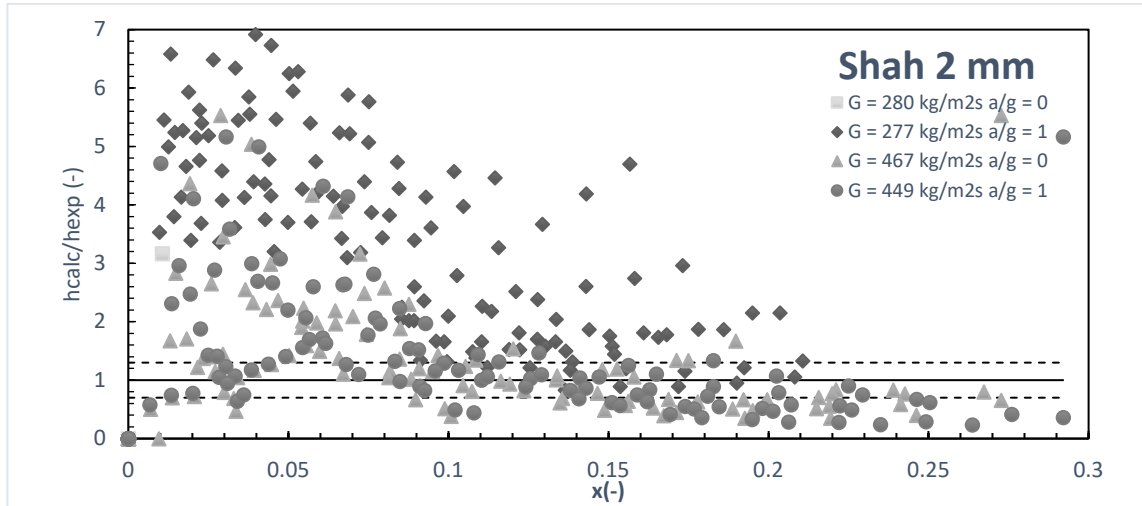
Figure 123: Liu and Winterton 2 mm heat transfer coefficient versus quality
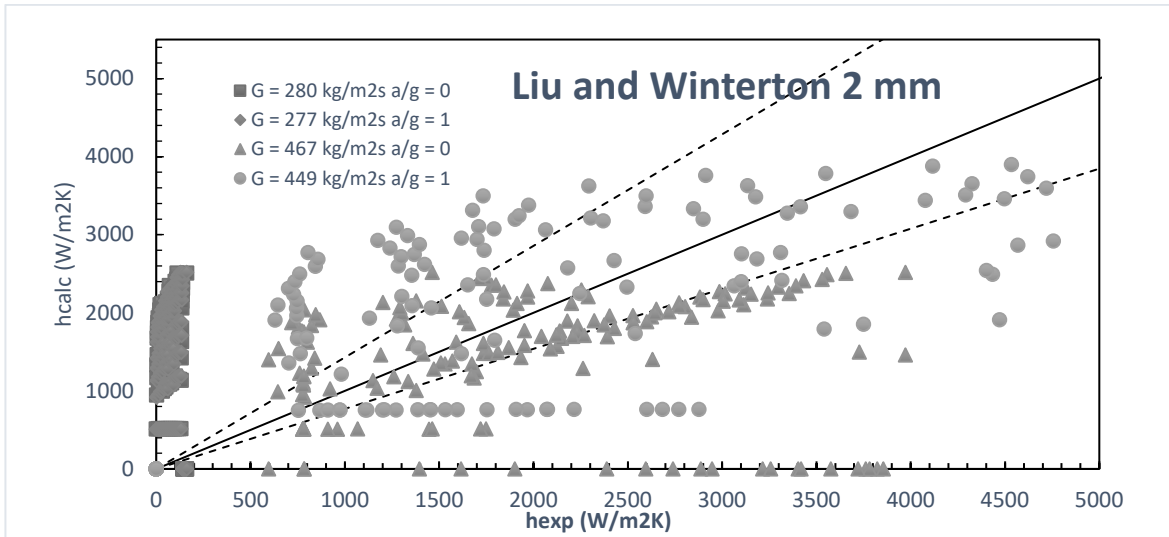
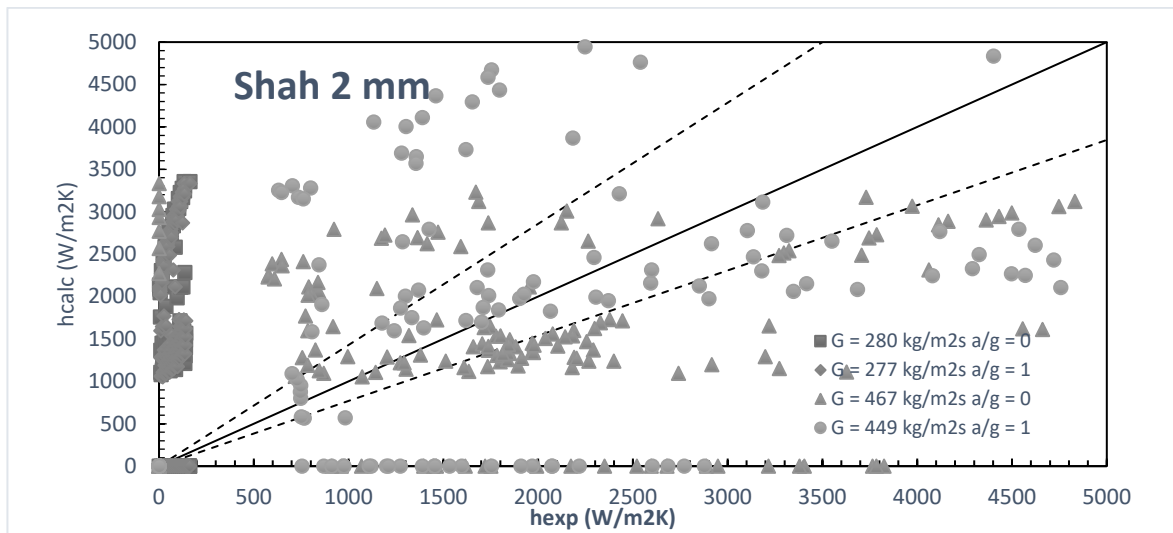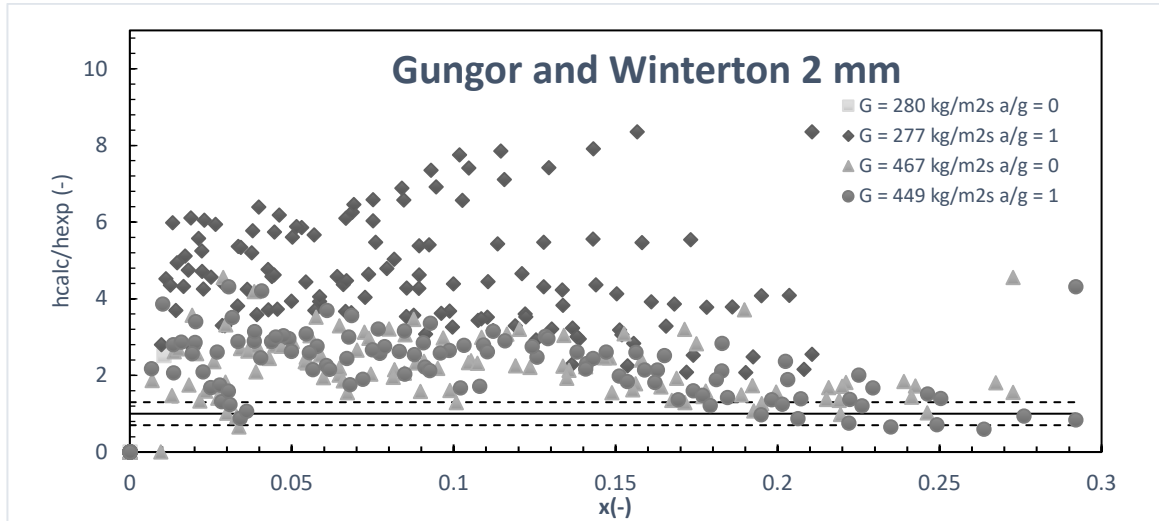Figure 124: Liu and Winterton 2 mm experimental heat transfer coefficient versus calculated
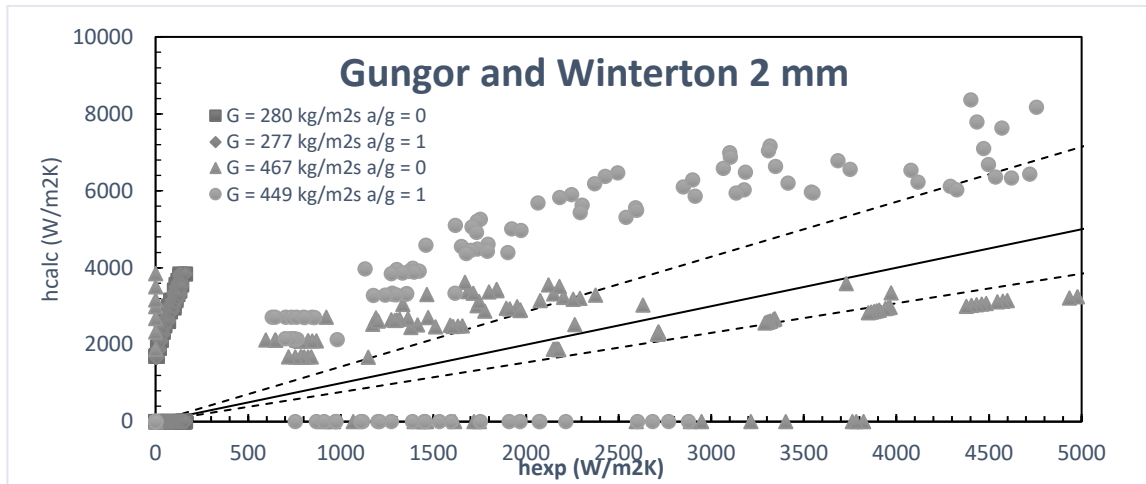
Following the results for every test set, that were described in the last paragraph:

- First data set returns *3.57%* data inside the *30%* error range and an average *RMS* of *218* with the minimum *RMS* of *145* at intermediate heat fluxes of *17.3 kW/m²*.
- Second data set returns *7.86%* data inside the *30%* error range and an average *RMS* of *269* with the minimum *RMS* of *141* at intermediate heat fluxes of *18.22 kW/m²*.
- Third data set returns *31.42%* data inside the *30%* error range and an average *RMS* of *112* with the minimum *RMS* of *95* at intermediate heat fluxes of *36.99 kW/m²*.
- Fourth data set returns *27.85%* data inside the *30%* error range and an average *RMS* of *110* with the minimum *RMS* of *102* at intermediate heat fluxes of *34.12 kW/m²*.

6.3.1.3.   Discussion on micro-Scale correlations

Following correlations are studied by authors for micro-scale tubes. The definition of micro-channel is in the first chapter.

The analysis with the Lazarek and Black correlation returned *540* calculated heat transfer coefficient that compared with the expected ones returns a total *RMS* of *275* and *5%* of data within the error band of *30%*. Figures 125-126 shows normalized heat transfer coefficient versus quality and expected heat transfer coefficient versus quality and experimental heat transfer coefficient versus expected.
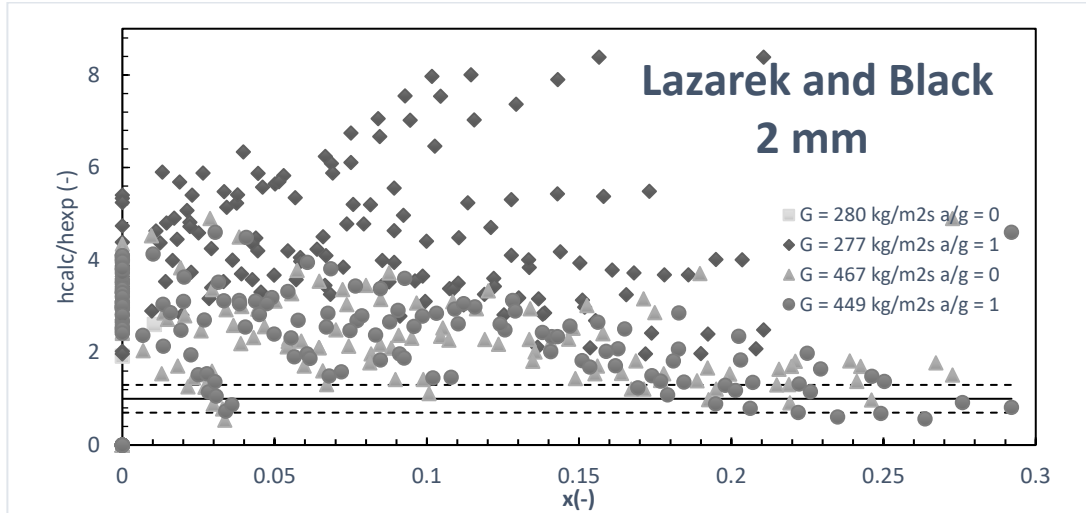
Figure 125: Lazarek and Black 2 mm heat transfer coefficient versus quality

Figure 126: Lazarek and Black 2 mm experimental heat transfer coefficient versus calculated

Following the results for every test set, that were described in the last paragraph:

- First data set returns *0%* data inside the *30%* error range and an average *RMS* of *331* with the minimum *RMS* of *237* at intermediate heat fluxes of *14.78 kW/m²*.
- Second data set returns *0%* data inside the *30%* error range and an average *RMS* of *405* with the minimum *RMS* of *245* at intermediate heat fluxes of *18.22 kW/m²*.
- Third data set returns *9.23%* data inside the *30%* error range and an average *RMS* of *206* with the minimum *RMS* of *103* at intermediate heat fluxes of *41.32 kW/m²*.
- Fourth data set returns *10.76%* data inside the *30%* error range and an average *RMS* of *207* with the minimum *RMS* of *98.52* at intermediate heat fluxes of *37.91 kW/m²*.

The analysis with the Tran et al. correlation returned *540* calculated heat transfer coefficient that compared with the expected ones returns a total *RMS* of *395* and *2.88%* of data within the error band of *30%*. Figures *127-128* shows normalized heat transfer coefficient versus quality and experimental heat transfer coefficient versus expected.

Figure 127: Tran et al. 2 mm heat transfer coefficient versus quality

Figure 128: Tran et al. 2 mm experimental heat transfer coefficient versus calculated

Following the results for every test set, that were described in the last paragraph:

- First data set returns *0%* data inside the *30%* error range and an average *RMS* of *514* with the minimum *RMS* of *361* at intermediate heat fluxes of *14.78 kW/m²*.
- Second data set returns *0%* data inside the *30%* error range and an average *RMS* of *629* with the minimum *RMS* of *366* at intermediate heat fluxes of *18.22 kW/m²*.
- Third data set returns *3.84%* data inside the *30%* error range and an average *RMS* of *273* with the minimum *RMS* of *128* at intermediate heat fluxes of *41.33 kW/m²*.
- Fourth data set returns *7.69%* data inside the *30%* error range and an average *RMS* of *275* with the minimum *RMS* of *113* at intermediate heat fluxes of *41.33 kW/m²*.

The analysis with the Kew and Cornwell correlation returned *540* calculated heat transfer coefficient that compared with the expected ones returns a total *RMS* of *242* and *7.84%* of data within the error band of *30%*. Figures *129-130* shows heat transfer coefficient versus quality and experimental heat transfer coefficient versus expected.
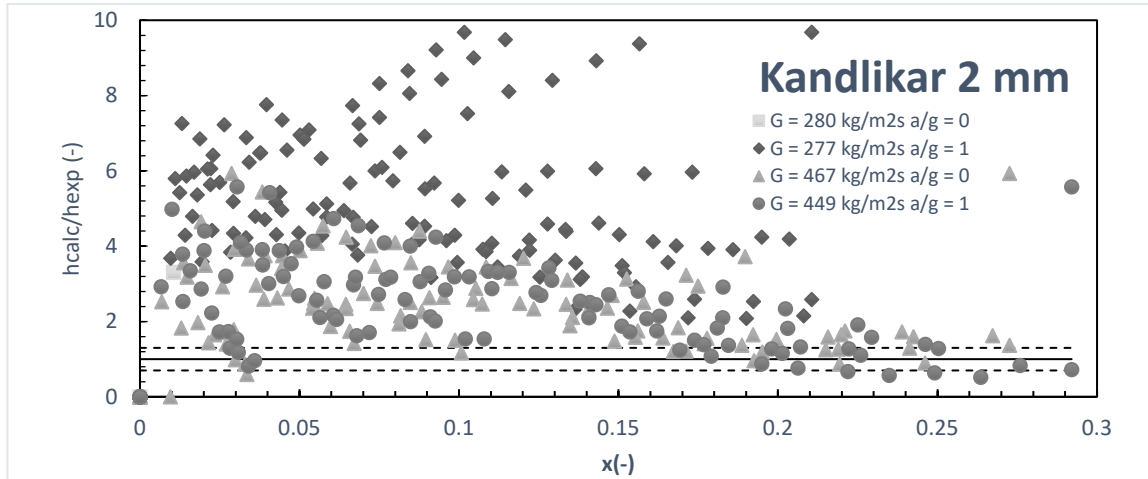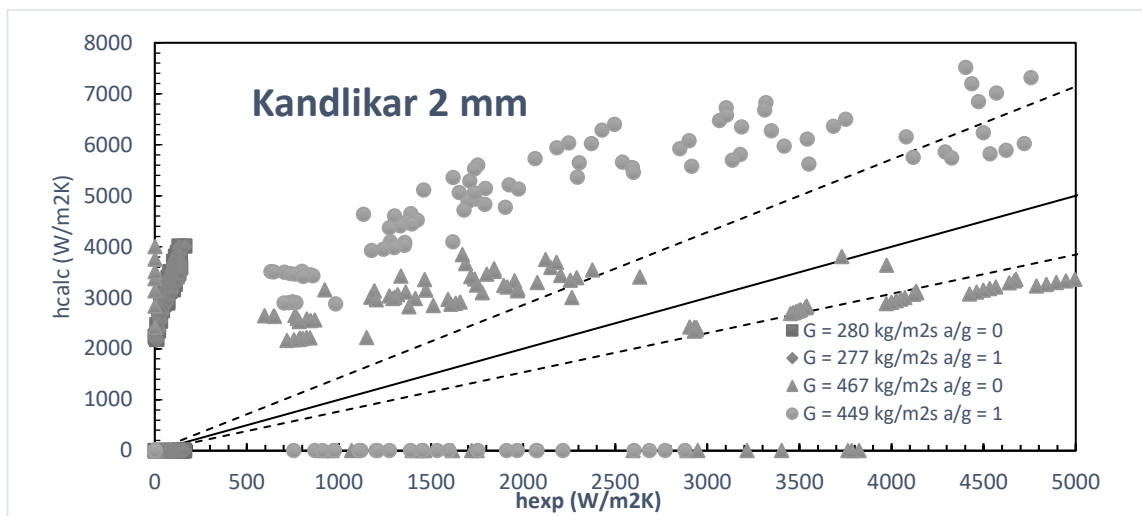
Figure 129: Kew and Cornwell 2 mm heat transfer coefficient versus quality

Figure 130: Kew and Cornwell 2 mm experimental heat transfer coefficient versus calculated

Following the results for every test set, that were described in the last paragraph:

- First data set returns *0%* data inside the *30%* error range and an average *RMS* of *292* with the minimum *RMS* of *210* at intermediate heat fluxes of 14.78 kW/m^2.
- Second data set returns *0%* data inside the *30%* error range and an average *RMS* of *358* with the minimum *RMS* of *218* at intermediate heat fluxes of *18.22 kW/m²*.
- Third data set returns *16.15%* data inside the *30%* error range and an average *RMS* of *181* with the minimum *RMS* of *90.52* at intermediate heat fluxes of *41.32 kW/m²*.
- Fourth data set returns *15.38%* data inside the *30%* error range and an average *RMS* of *182* with the minimum *RMS* of *87.23* at intermediate heat fluxes of *37.91 kW/m²*.

The analysis with the Kandlikar and Balasubramanian correlation returned *540* calculated heat transfer coefficient that compared with the expected ones returns a total *RMS* of *39* and *22.22%* of data within the error band of *30%*. Figures 131-132 shows heat transfer coefficient versus quality and experimental heat transfer coefficient versus expected.
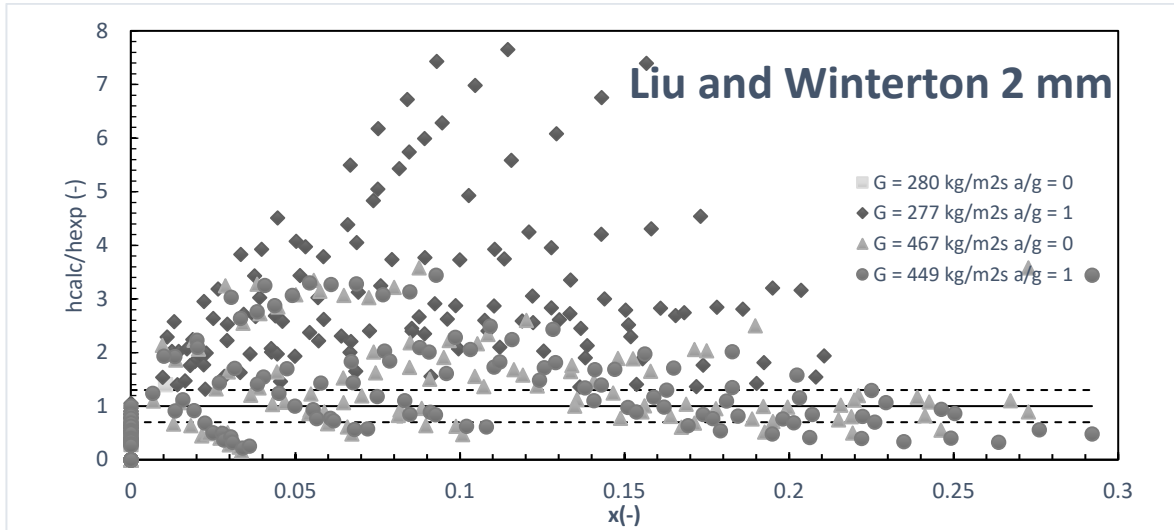
Figure 131: Kandlikar and Balasubramanian 2 mm heat transfer coefficient versus quality

Figure 132: Kandlikar and Balasubramanian 2 mm experimental heat transfer coefficient versus calculated

Following the results for every test set, that were described in the last paragraph:

- First data set returns *39.28%* data inside the *30%* error range and an average *RMS* of *61* with the minimum *RMS* of *95* at intermediate heat fluxes of *8.50 kW/m²*.
- Second data set returns *45%* data inside the *30%* error range and an average *RMS* of *76* with the minimum *RMS* of *105* at intermediate heat fluxes of *10.64 kW/m²*.
- Third data set returns *2.30%* data inside the *30%* error range and an average *RMS* of *23* with the minimum *RMS* of *62* at intermediate heat fluxes of *12.99 kW/m²*.
- Fourth data set returns *2.31%* data inside the *30%* error range and an average *RMS* of *23* with the minimum *RMS* of *62* at intermediate heat fluxes of *9.54 kW/m²*.

The analysis with the Warrier et al. correlation returned *462* calculated heat transfer coefficient that compared with the expected ones returns a total *RMS* of *126* and *43.05%* of data within the error band of *30%*. Figures 133-134 shows heat transfer coefficient versus quality and experimental heat transfer coefficient versus expected.

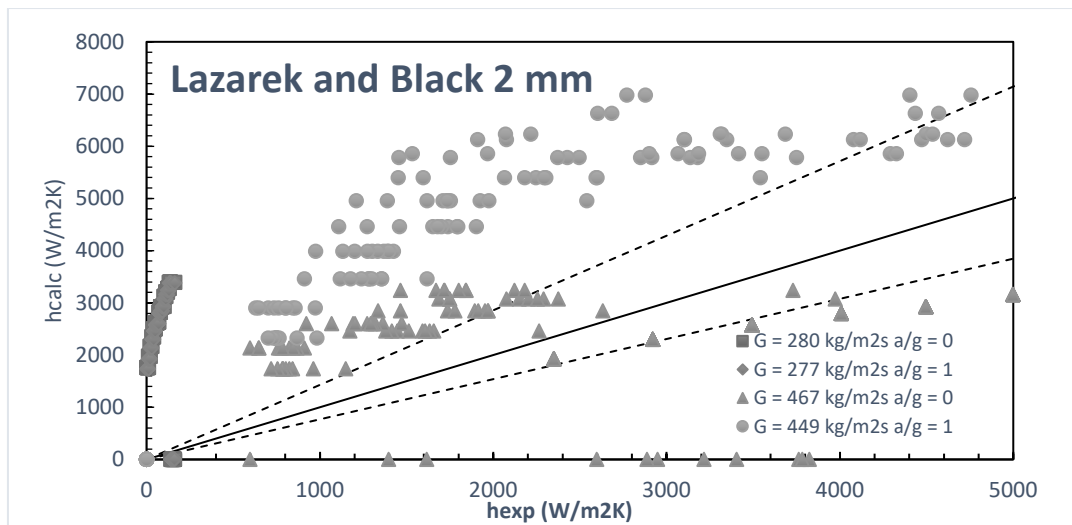Figure 133: Warrier et al. 2 mm heat transfer coefficient versus quality

Figure 134: Warrier et al. 2 mm experimental heat transfer coefficient versus calculated

Following the results for every test set, that were described in the last paragraph:

- First data set returns *61.11%* data inside the *30%* error range and an average *RMS* of *97* with the minimum *RMS* of 103 at intermediate heat fluxes of *9.68 kW/m²*.
- Second data set returns *48.41%* data inside the *30%* error range and an average *RMS* of *117* with the minimum *RMS* of *102* at intermediate heat fluxes of *14.04 kW/m²*.
- Third data set returns *39.04%* data inside the *30%* error range and an average *RMS* of *160* with the minimum *RMS* of *100* at intermediate heat fluxes of *44.42 kW/m²*.
- Fourth data set returns *27.61%* data inside the *30%* error range and an average *RMS* of *145* with the minimum *RMS* of *98* at intermediate heat fluxes of *41.33 kW/m²*.

The analysis with the Zhang et al. correlation returned *462* calculated heat transfer coefficient that compared with the expected ones returns a total *RMS* of 58.56 and *23.79%* of data within the error band of *30%.* Figures 135-136 shows heat transfer coefficient versus quality and experimental heat transfer coefficient versus expected.
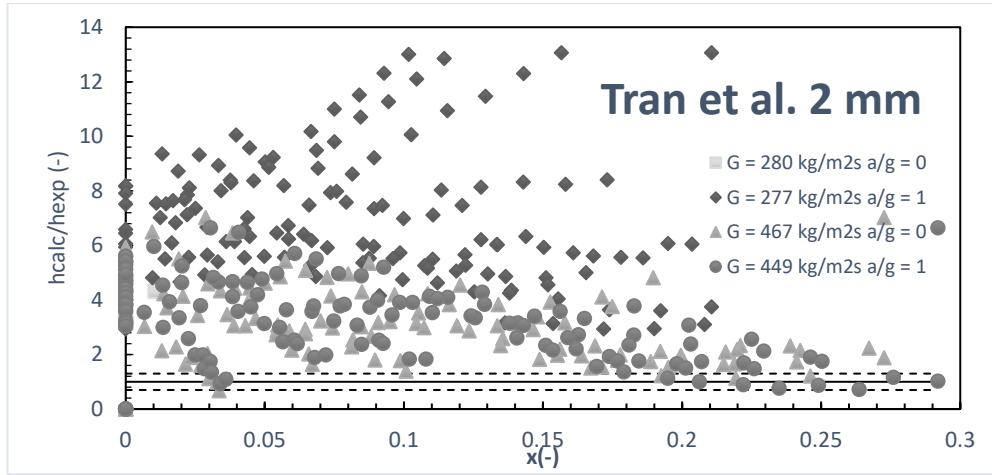
Figure 135: Zhang et al. 2 mm heat transfer coefficient versus quality
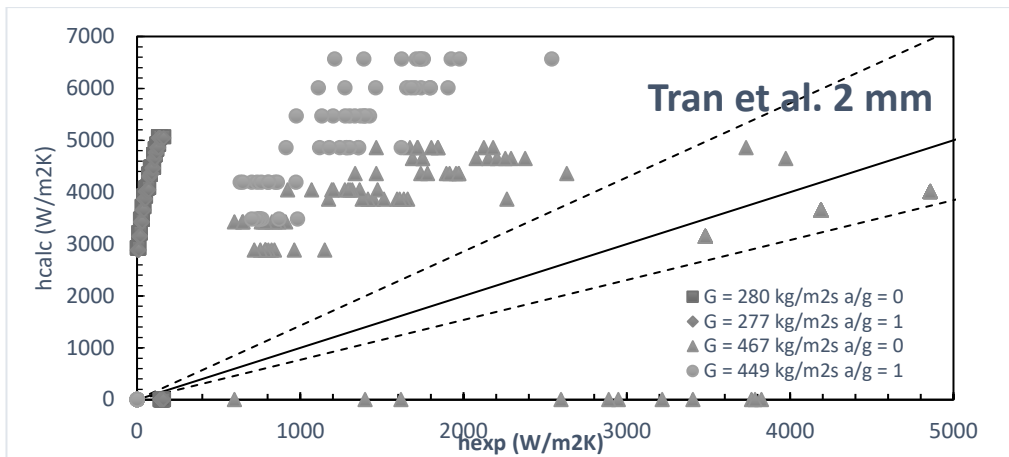

Figure 136: Zhang et al. 2 mm experimental heat transfer coefficient versus calculated

Following the results for every test set, that were described in the last paragraph:

- First data set returns *11.90%* data inside the *30%* error range and an average *RMS* of *40* with the minimum *RMS* of *60* at intermediate heat fluxes of *9.68 kW/m²*.
- Second data set returns *17.46%* data inside the *30%* error range and an average *RMS* of *49* with the minimum *RMS* of *73* at intermediate heat fluxes of *12.45 kW/m²*.
- Third data set returns *33.33%* data inside the *30%* error range and an average *RMS* of *79* with the minimum *RMS* of *100* at intermediate heat fluxes of *23.78 kW/m²*.
- Fourth data set returns *32.38%* data inside the *30%* error range and an average *RMS* of *76* with the minimum *RMS* of *111* at intermediate heat fluxes of *27.48 kW/m²*.

The analysis with the Lee and Mudawar correlation returned *462* calculated heat transfer coefficient that compared with the expected ones returns a total *RMS* of *1375* and *2.62%* of data within the error band of *30%*. Figures 137-138 shows heat transfer coefficient versus quality and experimental heat transfer coefficient versus expected.
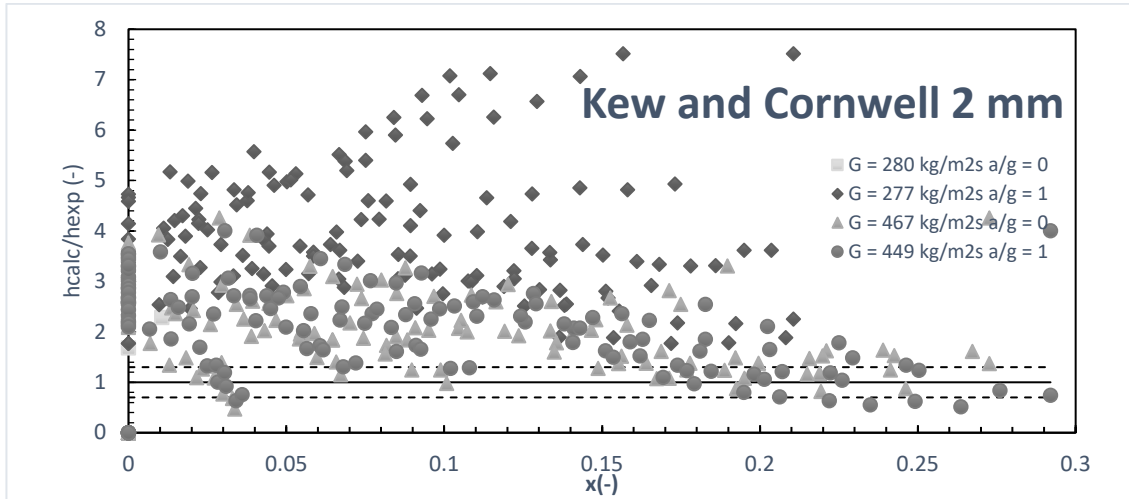
Figure 137: Lee and Mudawar 2 mm heat transfer coefficient versus quality

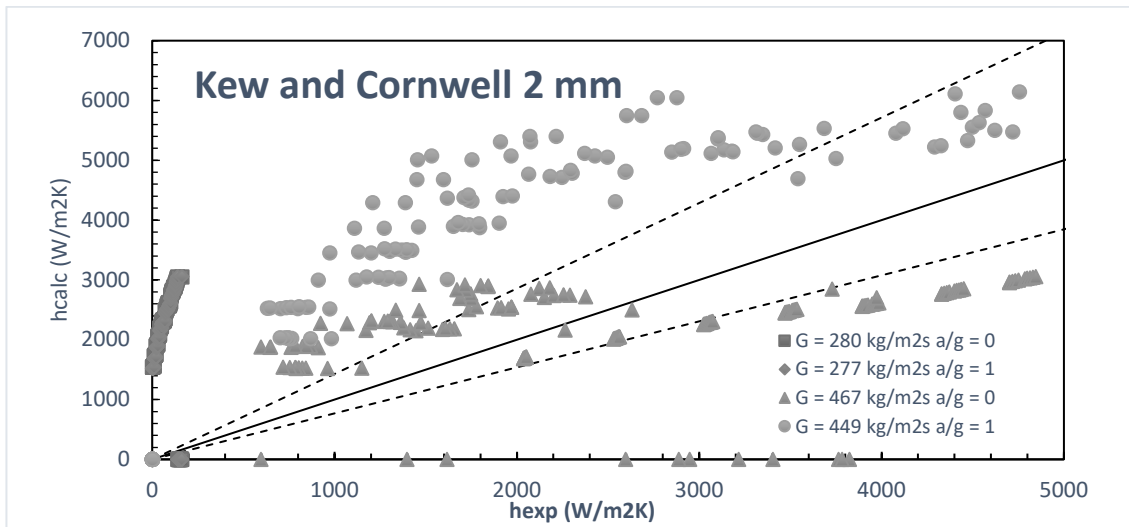
Figure 138: Lee and Mudawar 2 mm experimental heat transfer coefficient versus calculated

Following the results for every test set, that were described in the last paragraph:

- First data set returns *0%* data inside the *30%* error range and an average *RMS* of *2969* with the minimum *RMS* of *2340* at intermediate heat fluxes of *14.78 kW/m²*.
- Second data set returns *0%* data inside the *30%* error range and an average *RMS* of *3549* with the minimum *RMS* of *1877* at intermediate heat fluxes of *18.22 kW/m²*.
- Third data set returns 5.71% data inside the *30%* error range and an average *RMS* of *601* with the minimum *RMS* of *267* at intermediate heat fluxes of *44.42 kW/m²*.
- Fourth data set returns *4.77%* data inside the *30%* error range and an average *RMS* of *565* with the minimum *RMS* of *234* at intermediate heat fluxes of 44.39 *kW/m²*.

The analysis with the Saitoh et al. correlation returned *501* calculated heat transfer coefficient that compared with the expected ones returns a total *RMS* of *241* and *11.44%* of data within the error band of *30%*. Figure 139-140 shows heat transfer coefficient versus quality and experimental heat transfer coefficient versus expected.
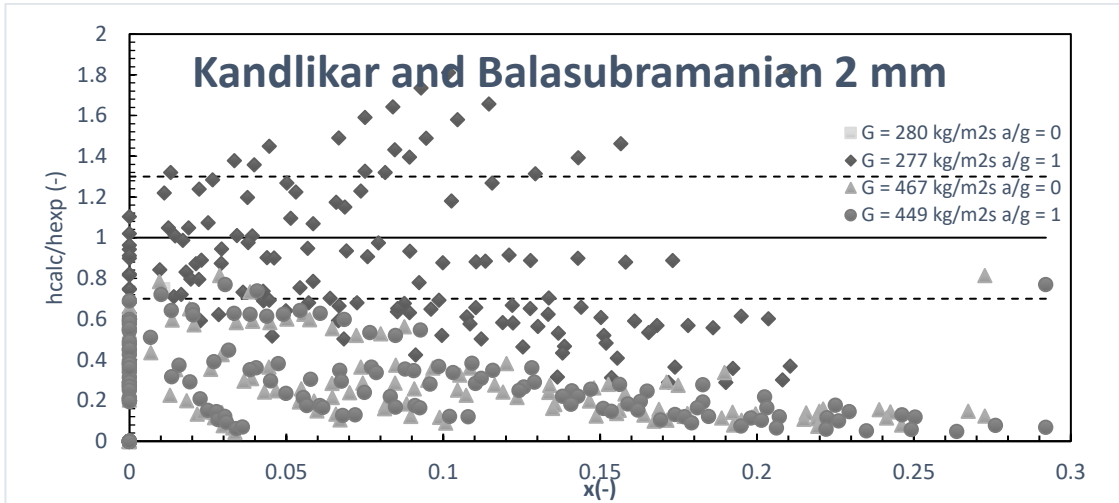
Figure 139: Saitoh et al. 2 mm normalized heat transfer coefficient versus quality
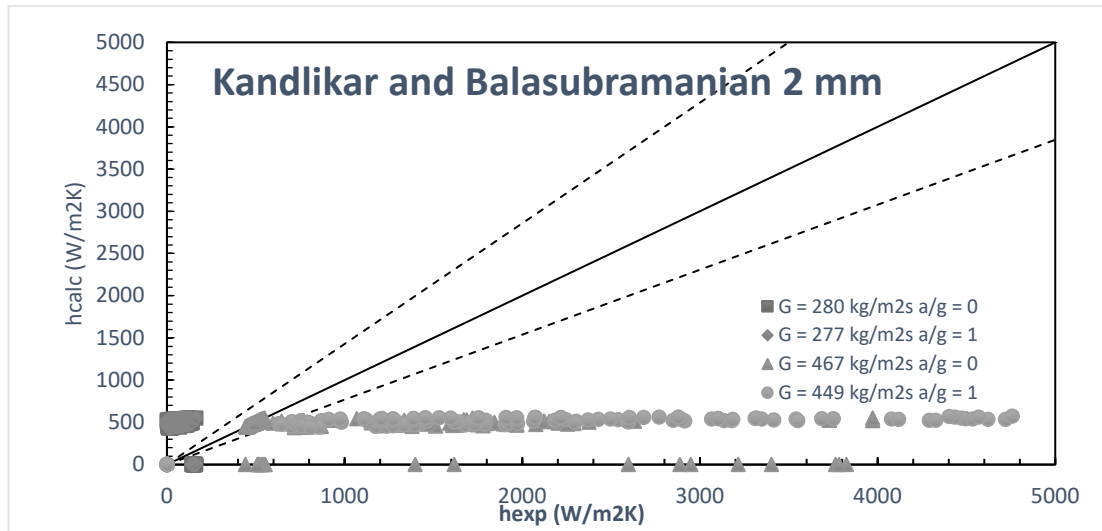

Figure 140: Saitoh et al. 2 mm experimental heat transfer coefficient versus calculated

Following the results for every test set, that were described in the last paragraph:

- First data set returns *1.6%* data inside the *30%* error range and an average *RMS* of *177* with the minimum *RMS* of *155* at intermediate heat fluxes of *14.78 kW/m²*.
- Second data set returns *0%* data inside the *30%* error range and an average *RMS* of *470* with the minimum *RMS* of *274* at intermediate heat fluxes of *18.22 kW/m²*.
- Third data set returns *32.28%* data inside the *30%* error range and an average *RMS* of *137* with the minimum *RMS* of *104* at intermediate heat fluxes of *34.76 kW/m²*.
- Fourth data set returns *11.9%* data inside the *30%* error range and an average *RMS* of *208* with the minimum *RMS* of *93* at intermediate heat fluxes of *41.33 kW/m²*.

The analysis with the Bertsch et al. correlation returned *540* calculated heat transfer coefficient that compared with the expected ones returns a total *RMS* of 56 and *26.33%* of data within the error band of *30%*. Figures 141-142 shows heat transfer coefficient versus quality and experimental heat transfer coefficient versus expected.
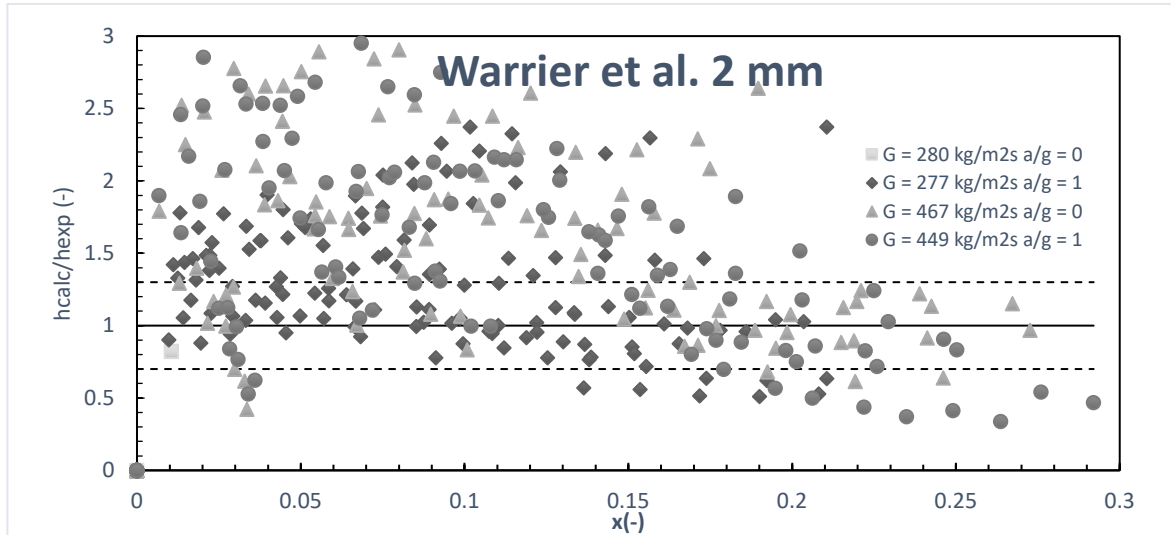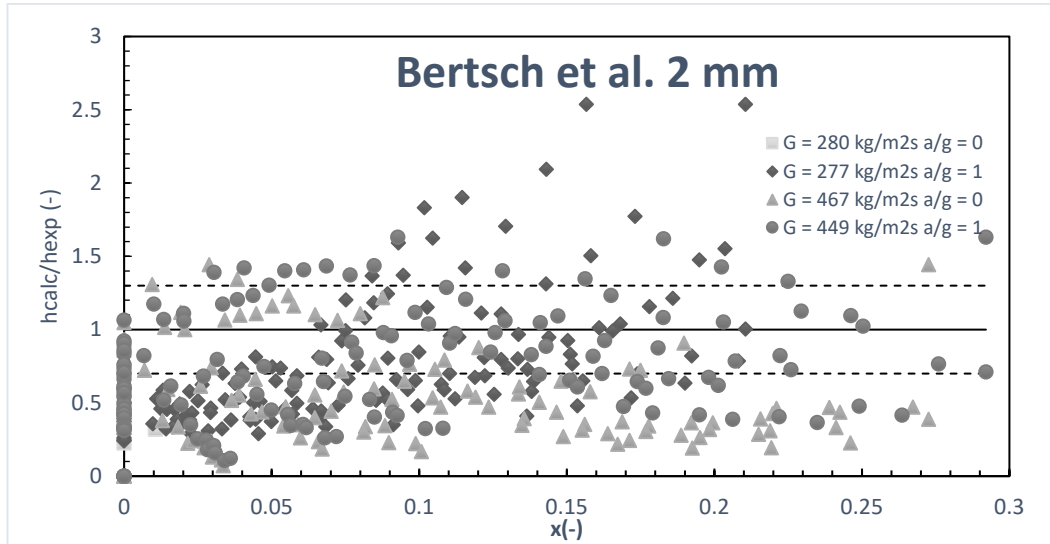
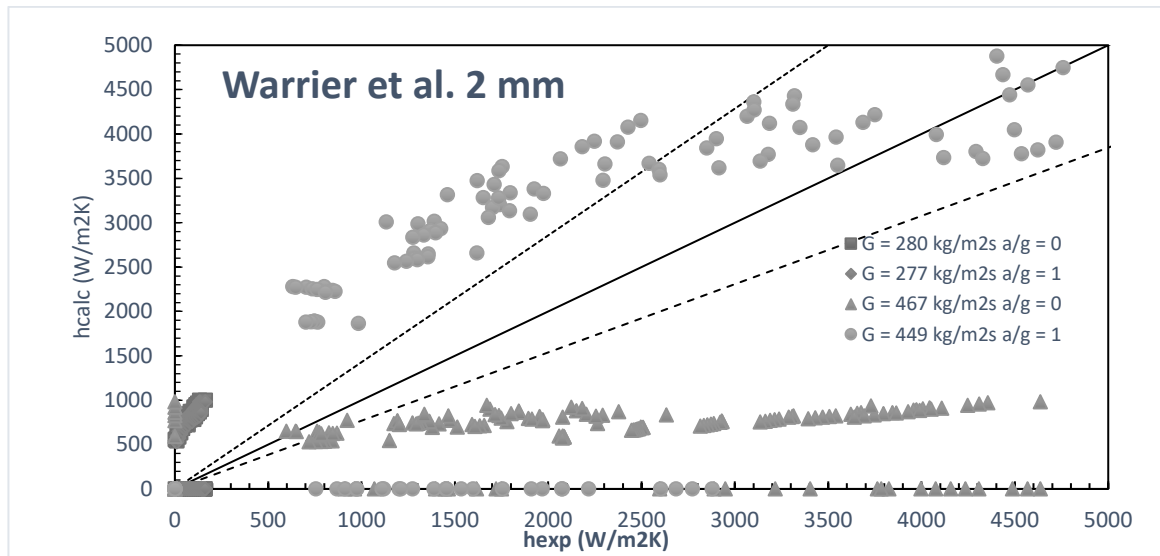Figure 141: Bertsch et al. 2 mm heat transfer coefficient versus quality
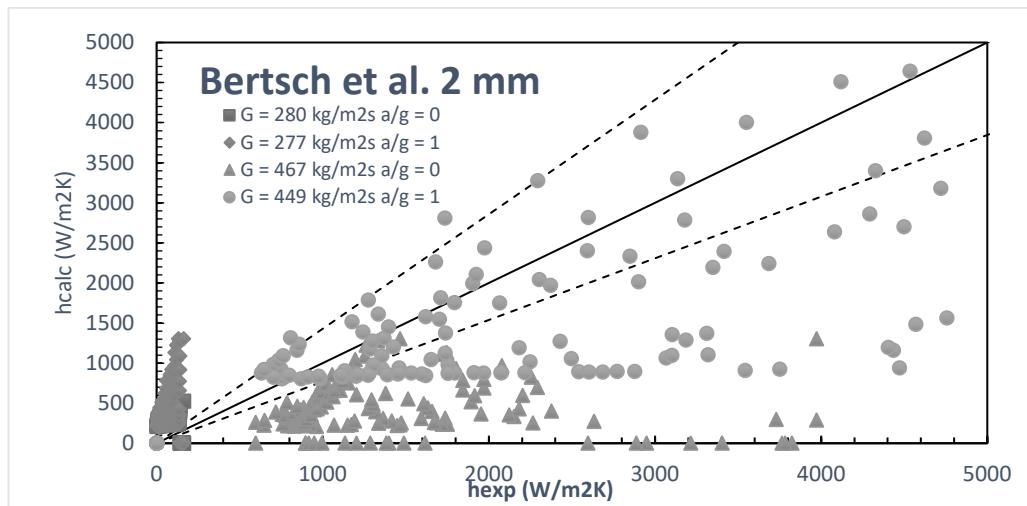
Figure 142: Bertsch et al. 2 mm experimental heat transfer coefficient versus calculated

Following the results for every test set, that were described in the last paragraph:

- First data set returns *10%* data inside the *30%* error range and an average *RMS* of *39* with the minimum *RMS* of *58* at intermediate heat fluxes of *9.68 kW/m²*.
- Second data set returns *31%* data inside the *30%* error range and an average *RMS* of 73 with the minimum *RMS* of *103* at intermediate heat fluxes of *14.29 kW/m²*.
- Third data set returns *23%* data inside the *30%* error range and an average *RMS* of *45* with the minimum *RMS* of *100* at intermediate heat fluxes of *9.59 kW/m²*.
- Fourth data set returns *42%* data inside the *30%* error range and an average *RMS* of 76 with the minimum *RMS* of *95* at intermediate heat fluxes of *20.26 kW/m²*.

The analysis with the Mikielewicz's correlation returned *540* calculated heat transfer coefficient that compared with the expected ones returns a total *RMS* of *64* and *27%* of data within the error band of *30%*. Figures 143-144 shows heat transfer coefficient versus quality and experimental heat transfer coefficient versus expected.
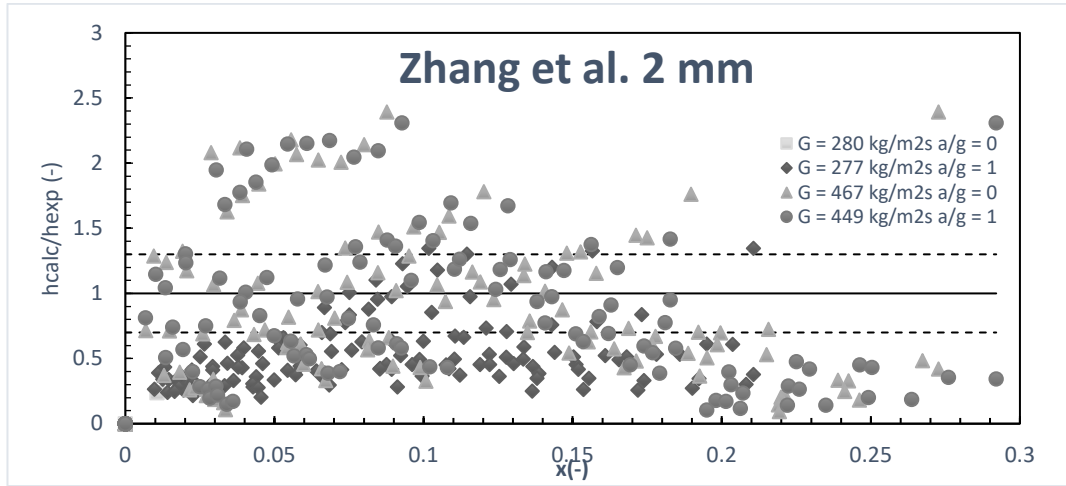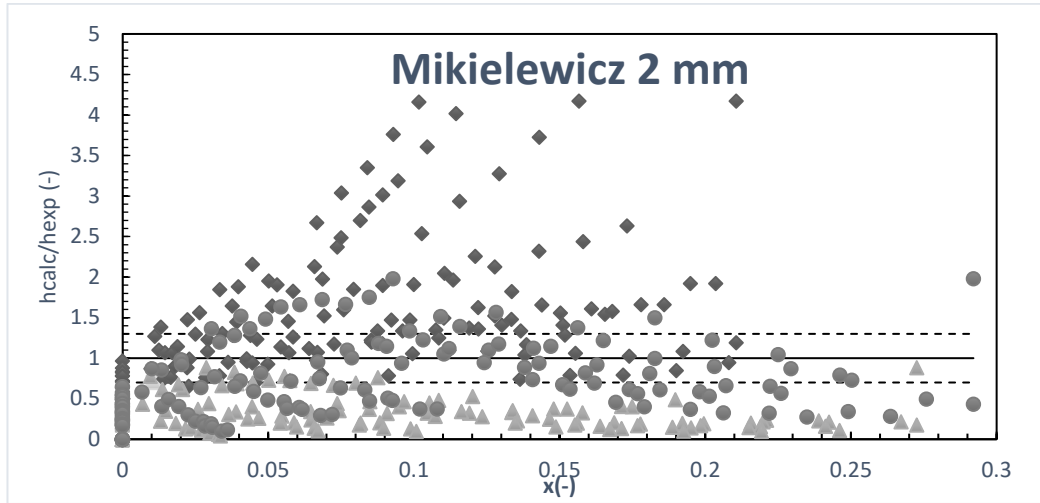
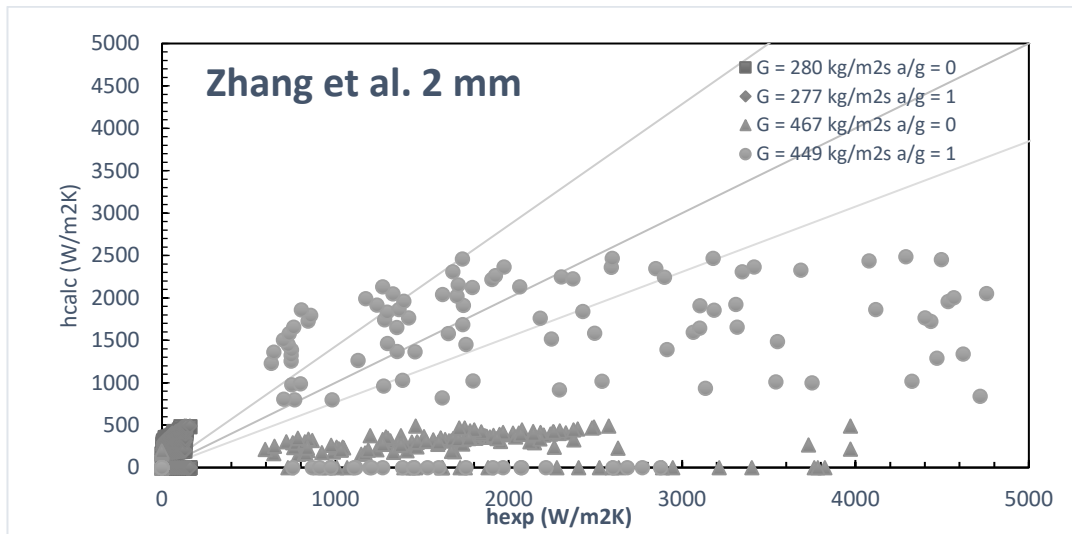Figure 143: Mikielewicz 2 mm heat transfer coefficient versus quality
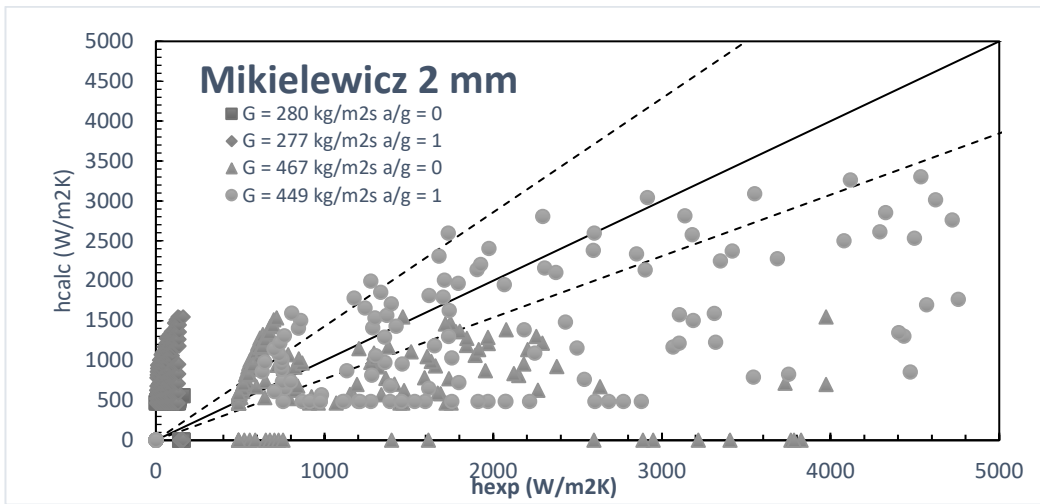
Figure 144: Mikielewicz 2 mm experimental heat transfer coefficient versus calculated

Following the results for every test set, that were described in the last paragraph:

- First data set returns *28.57%* data inside the *30%* error range and an average *RMS* of *63* with the minimum *RMS* of *101* at intermediate heat fluxes of 9.68 *kW/m²*.
- Second data set returns *45%* data inside the *30%* error range and an average *RMS* of *143* with the minimum *RMS* of *103* at intermediate heat fluxes of 14.86 *kW/m²*.
- Third data set returns *6.15%* data inside the *30%* error range and an average *RMS* of *26* with the minimum *RMS* of *71* at intermediate heat fluxes of *12.99 kW/m²*.
- Fourth data set returns *30%* data inside the *30%* error range and an average *RMS* of *71* with the minimum *RMS* of *103* at intermediate heat fluxes of *20.26 kW/m²*.

The analysis with the Li and Wu correlation returned *540* calculated heat transfer coefficient that compared with the expected ones returns a total *RMS* of *221* and *21.68%* of data within the error band of *30%*. Figures 145-146 shows heat transfer coefficient versus quality and experimental heat transfer coefficient versus expected.
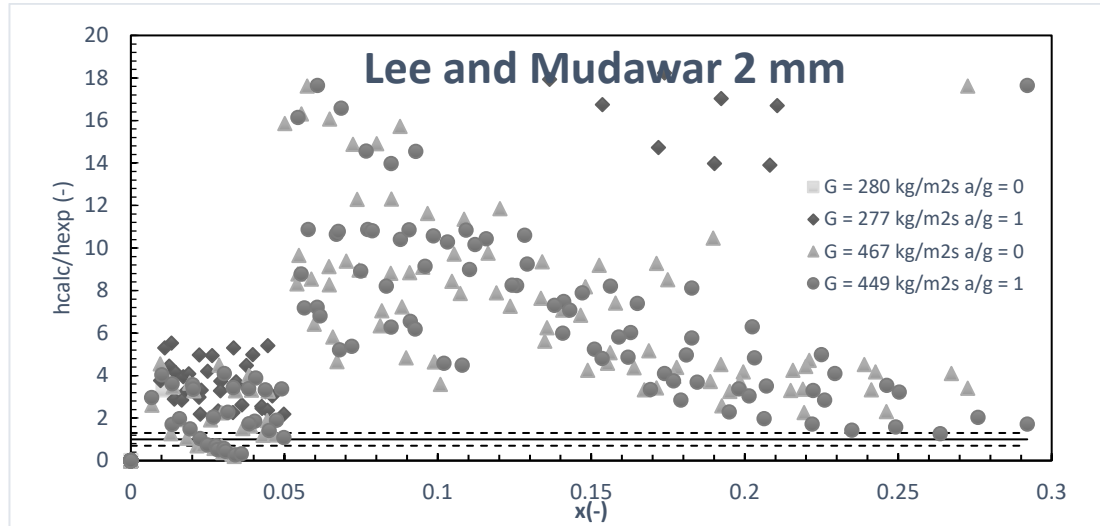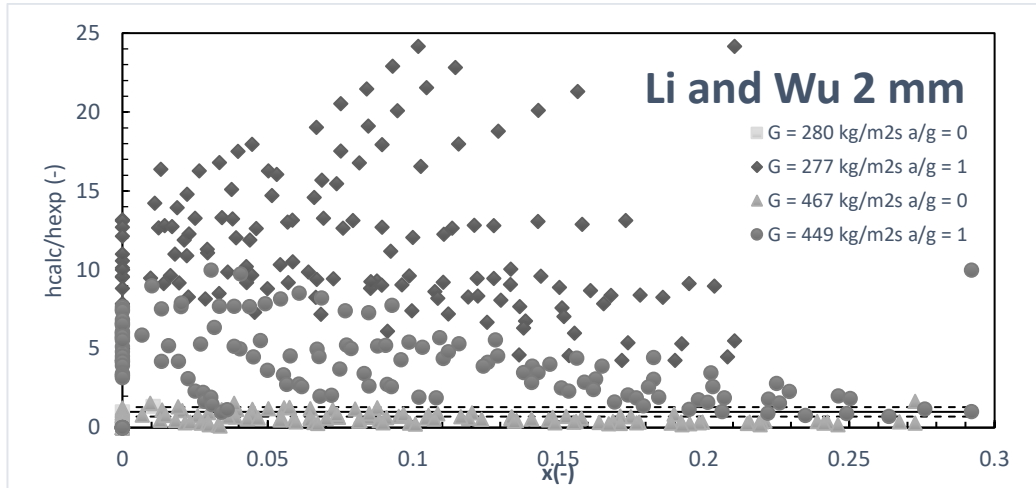
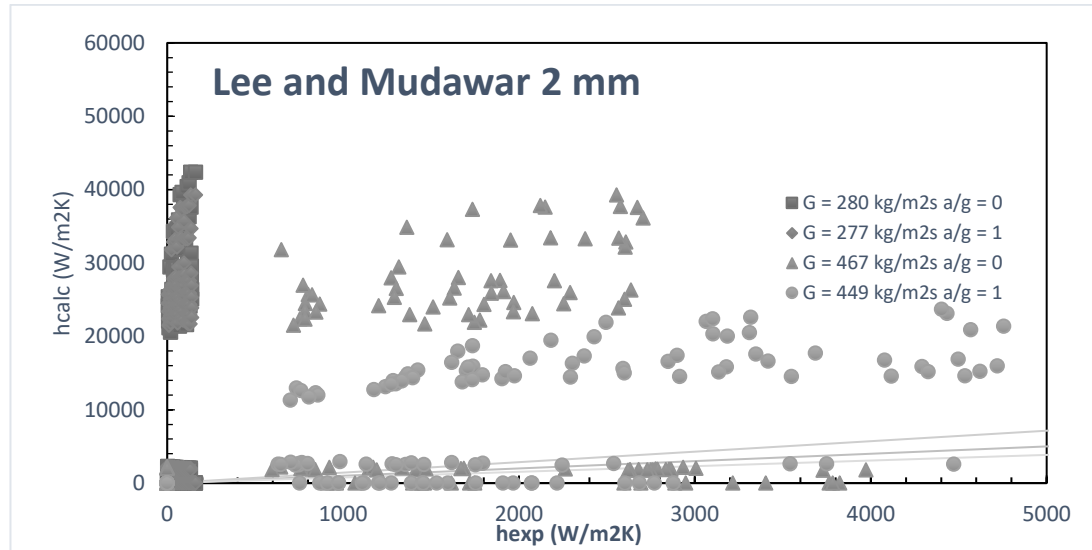Figure 145: Li and Wu model *2mm* heat transfer coefficient versus quality

Figure 146: Li and Wu model *2mm* experimental heat transfer coefficient versus calculated

Following the results for every test set, that were described in the last paragraph:

- First data set returns *42.14%* data inside the *30%* error range and an average *RMS* of *133* with the minimum *RMS* of *101* at intermediate heat fluxes of *16.14 kW/m²*.
- Second data set returns *0.71%* data inside the *30%* error range and an average *RMS* of *1034* with the minimum *RMS* of *536* at intermediate heat fluxes of *18.22 kW/m²*.
- Third data set returns *36.16%* data inside the *30%* error range and an average *RMS* of *52* with the minimum *RMS* of *107* at intermediate heat fluxes of *9.59 kW/m²*.
- Fourth data set returns *7.69%* data inside the *30%* error range and an average *RMS* of *333* with the minimum *RMS* of *116* at intermediate heat fluxes of *44.39 kW/m²*.

The analysis with the Mohamed and Karayiannis correlation returned 462 calculated heat transfer coefficient that compared with the expected ones returns a total *RMS* of *280* and *15.35%* of data within the error band of *30%*. Figure 147-148 shows heat transfer coefficient versus quality and experimental heat transfer coefficient versus expected.
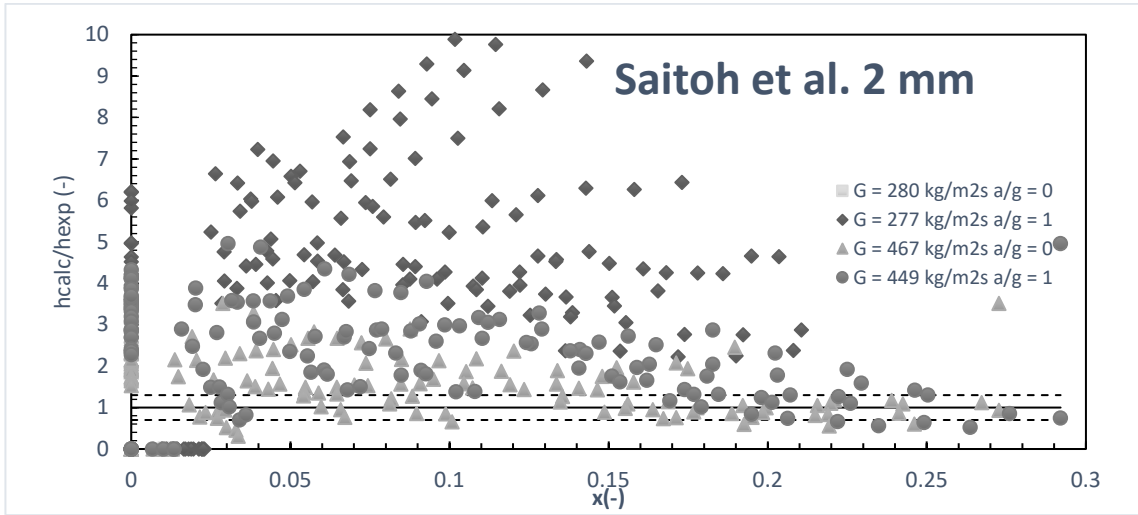
Figure 147: Mohamed and Karayiannis 2 mm heat transfer coefficient versus quality

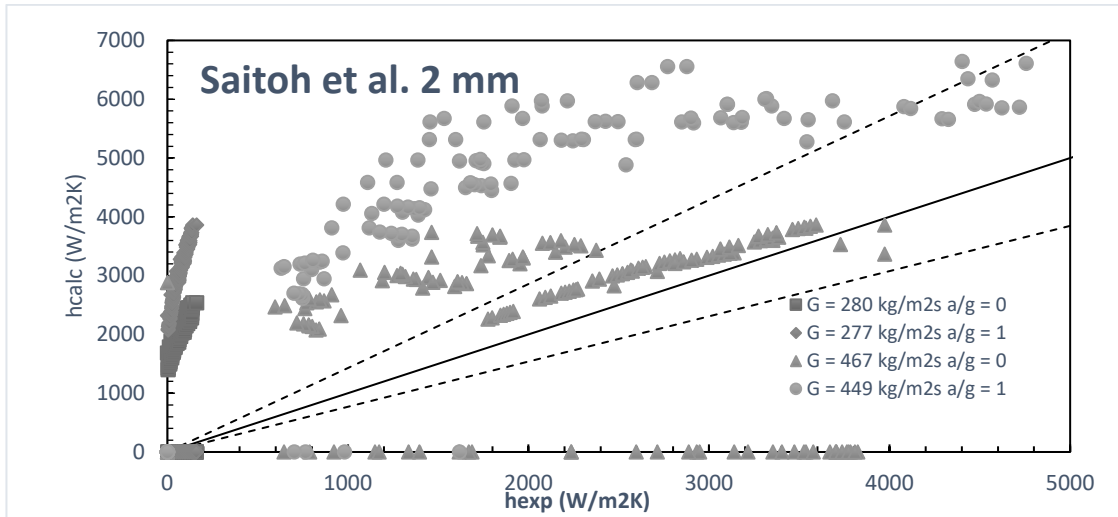Figure 148: Mohamed and Karayiannis 2 mm experimental heat transfer coefficient versus calculated

Following the results for every test set, that were described in the last paragraph:

- First data set returns *11.9%* data inside the *30%* error range and an average *RMS* of *187* with the minimum *RMS* of *132* at intermediate heat fluxes of *14.78 kW/m²*.
- Second data set returns *0%* data inside the *30%* error range and an average *RMS* of *911* with the minimum *RMS* of *534* at intermediate heat fluxes of *18.22 kW/m²*.
- Third data set returns *45.71%* data inside the *30%* error range and an average *RMS* of *95* with the minimum *RMS* of *98* at intermediate heat fluxes of *27.59 kW/m²*.
- Fourth data set returns *3.8%* data inside the *30%* error range and an average *RMS* of *380* with the minimum *RMS* of *158* at intermediate heat fluxes of *44.39 kW/m²*.

6.3.2. 4 mm Test Section

The *4 mm* test section has ten different thermocouples at positions indicates in the table 25:

Table 25: *4 mm* test section thermocouples positions

Axial positions									
%									
11	19	27	35	42	60	68	77	85	93
cm									
0.017	0.030	0.042	0.054	0.065	0.094	0.106	0.119	0.132	0.144

However, the thermocouple number *6th* broke during one of the experiments. Thus, test number *5th* has less data points. The section was subjected to *5th* different sets of tests where the thermal flux change and the operative pressure and bulk flux remain constants:

I.   First test set was performed in normal gravity conditions, on earth, with the quantity shows in table 26:

Table 26: First test quantity on *4 mm* test section

Internal diameter	4E-03	m
Channel lenght	0.15	m
Subcooling	29.64	K
Operative pressure	1.86	bar
Bulk flux	177.06	kg/m^{2}s
Gravity	9.81	m/s^2
Heat flux	5.1-28.8	kw/m^2

The set consist in *16th* different tests with different heat fluxes showed in table 27:

Table 27: First test heat fluxes on *4mm* test section

Heat flux kw/m^2															
5.1	6.6	8.2	9.6	11.1	12.7	15.1	17.3	19.3	20.6	22.2	23.7	24.9	25.4	27.0	28.8

Totally there were taken *160* data points from this set.

II.   Second test was performed in miro-gravity conditions, during the parabolic flight, with the quantity shows in table 28:

Table 28: Second test on *4 mm* test section

Internal diameter	4E-03	m
Channel lenght	0.15	m
Subcooling	27.43	K
Operative pressure	1.80	bar
Bulk flux	179.67	kg/m^{2}s
Gravity	0	m/s^2
Heat flux	5.1-28.8	kw/m^2

The set consist in *16th* different tests with different heat fluxes showed in table 29:

Table 29: Second test heat fluxes on *4 mm* test section

Heat flux kw/m^2															
5.1	6.6	8.1	9.6	11.1	12.7	15.1	17.3	19.3	20.6	22.2	23.7	24.8	25.4	26.9	28.8

Totally there were taken *160* data points from this set.

III.   Third test was performed in normal gravity conditions, on earth, with the quantity shows in table 30:

Tabella 30: Third test on *4 mm* test section

Internal diameter	4E-03	m
Channel lenght	0.15	m
Subcooling	27.43	K
Operative pressure	1.86	bar
Bulk flux	244.23	kg/m^{2}s
Gravity	9.81	m/s^2
Heat flux	6.7-42.1	kw/m^2

The set consist in *15th* different tests with different heat fluxes showed in table 31:

Table 31: Third test heat fluxes on *4 mm* test section

Heat flux kw/m^2														
6.7	11.3	15.8	20.1	24.9	29.3	30.5	32.0	34.0	35.6	36.3	37.0	38.6	40.3	42.1

Totally there were taken *150* data points from this set.

IV.   Fourth test was performed in miro-gravity conditions, during the parabolic flight, with the quantity shows in table 32:

Table 32: Fourth test on *4 mm* test section

Internal diameter	0.004	m
Channel lenght	0.15	m
Subcooling	25.36	K
Operative pressure	1.74	bar
Bulk flux	250.20	kg/m^{2}s
Gravity	0	m/s^2
Heat flux	6.7-42	kw/m^2

The set consist in *16th* different tests with different heat fluxes showed in table 33:

Table 33: Fourth test heat fluxes on *4 mm* test section

Heat flux KW/M²														
6.7	11.3	15.8	20.1	24.9	29.3	30.5	32.0	34.0	35.6	36.3	36.9	38.6	40.3	42.0

Totally there were taken *160* data points from this set.

V. Fifth test was performed in normal gravity conditions, on earth, with the quantity shows in table 34:

Table 34: Fifth test on *4 mm* test section

Internal Diameter	0.004	m
Channel lenght	0.15	m
Subcooling	29.64	K
Operative Pressure	1.86	bar
Bulk flux	177.06	kg/m²s
Gravity	9.81	-
Heat flux	33.3-65.9	kW/m²

The set consist in *14th* different tests with different heat fluxes showed in table 35:

Table 35: Fifth test heat fluxes on *4 mm* test section

Heat flux kw/m²													
33.3	35.5	38	39.8	42.4	44.9	47.2	50.2	52.6	55	57.5	60.4	63.2	65.9

Totally there were taken *126* data points from this set. The *6th* thermocouple broke during experiments.

6.3.2.1. Discussion on models

The analysis with the model returned *756* calculated heat transfer coefficient that compared with the expected ones returns a total *RMS* of *348* and *21.34%* of data within the error band of *30%*. Figures 149-150 shows heat transfer coefficient versus quality and experimental heat transfer coefficient versus expected.

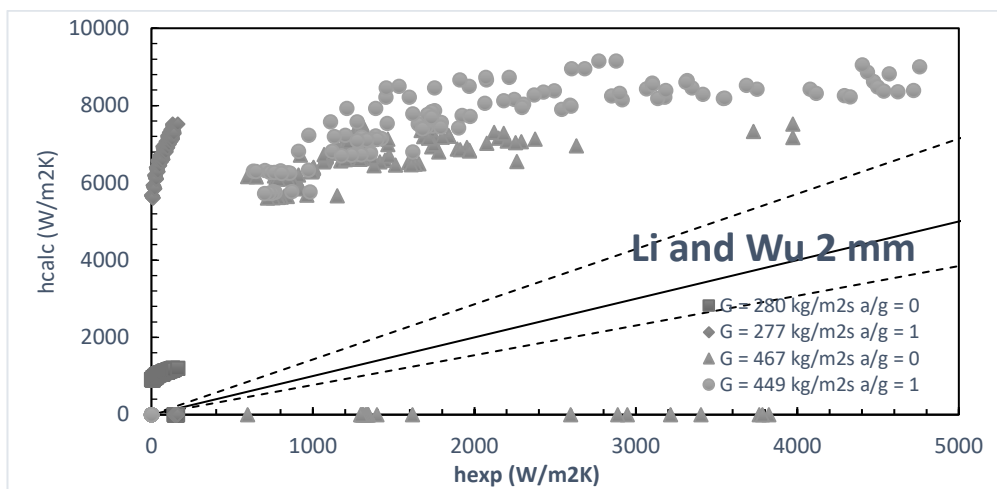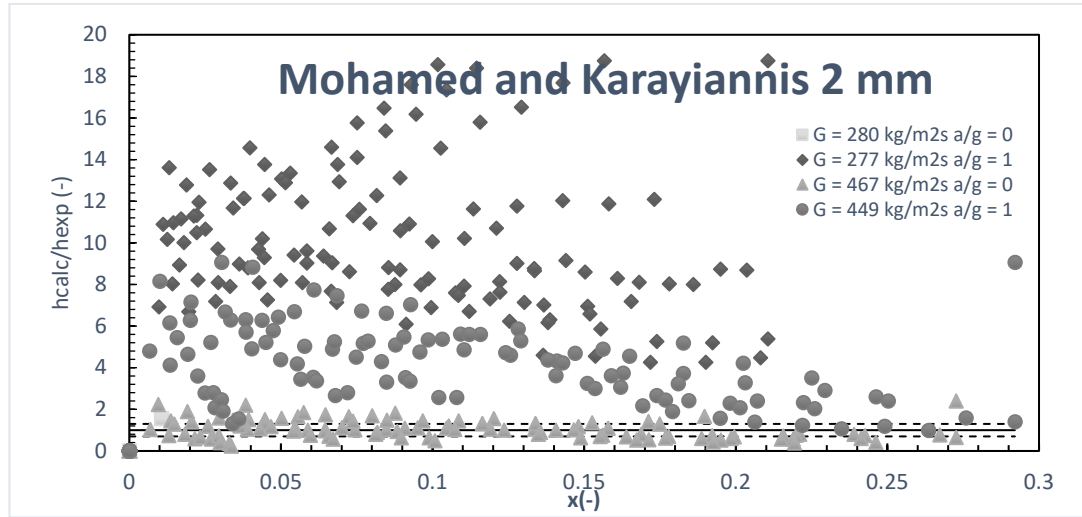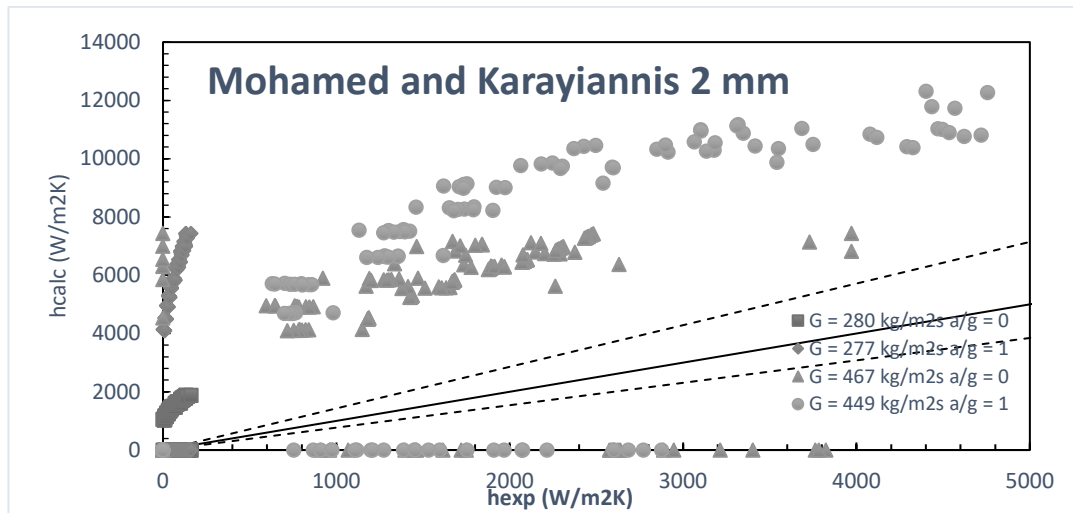Figure 149: Three-Zone 4 mm heat transfer coefficient versus quality

Figure 150: Three-Zone 4 mm experimental heat transfer coefficient versus calculated

Following the results for every test set, that were described in the last paragraph:

- First data set returns *9.38%* data inside the *30%* error range and an average *RMS* of *400* with the minimum *RMS* of *352* at intermediate heat fluxes of *28.8 kW/m²*.
- Second data set returns *8.75%* data inside the *30%* error range and an average *RMS* of *424* with the minimum *RMS* of *360* at intermediate heat fluxes of *28.8 kW/m²*.
- Third data set returns *17.33%* data inside the *30%* error range and an average *RMS* of *356* with the minimum *RMS* of *311* at intermediate heat fluxes of *12.7 kW/m²*.
- Fourth data set returns *17.33%* data inside the *30%* error range and an average *RMS* of *361* with the minimum *RMS* of *310* at intermediate heat fluxes of *42 kW/m²*.
- Fifth data set returns *53.17%* data inside the *30%* error range and an average *RMS* of *233* with the minimum *RMS* of *226* at intermediate heat fluxes of *63.2 kW/m²*.

Using the thermodynamic qualities for the fifth set of data gives an *RMS* of *176* and *54.76%* of data inside the *30%* error band.

The analysis with the Slug-Coalescence model returned *229* calculated heat transfer coefficient that compared with the expected ones returns a total *RMS* of *1006* and *3.43%* of data within the error band of *30%*. Figures 151-152 shows heat transfer coefficient versus quality and expected heat transfer coefficient versus calculated graphics for every set with corrected vapor quality.

Figure 151: Slug-Coalescence 4 mm heat transfer coefficient versus quality

Figure 152: Slug-Coalescence 4 mm experimental heat transfer coefficient versus calculated

Following the results for every test set, that were described in the last paragraph:

- First data set returns *0%* data inside the *30%* error range and an average *RMS* of *1625* with the minimum *RMS* of *875* at intermediate heat fluxes of *11.1 kW/m²*.
- Second data set returns *0%* data inside the *30%* error range and an average *RMS* of *1739* with the minimum *RMS* of *978* at intermediate heat fluxes of *11.1 kW/m²*.
- Third data set returns *0%* data inside the *30%* error range and an average *RMS* of *941* with the minimum *RMS* of *485* at intermediate heat fluxes of *11.1 kW/m²*.
- Fourth data set returns *32%* data inside the *30%* error range and an average *RMS* of *477* with the minimum *RMS* of *177* at intermediate heat fluxes of *8.2 kW/m²*.

For this model is impossible to use the thermodynamic qualities because it did not work with negative qualities. Using the thermodynamic qualities for the fifth set of data gives an *RMS* of *582* and 0% of data inside the 30% error band.

6.3.2.1.   Discussion on macro-Scale correlations

Following correlations are studied by authors for macro-scale tubes. The definition of macro-channel is in the first chapter.

The analysis with the Chen's correlation returned *580* calculated heat transfer coefficient that compared with the expected ones returns a total *RMS* of *86.41* and *62.71%* of data within the error band of *30%*. Figueres 153-154 shows heat transfer coefficient versus quality and expected heat transfer coefficient versus calculated graphics for every set with corrected vapor quality.

Figure 153: Chen 4 mm heat transfer coefficient versus quality

Figure 154: Chen 4 mm experimental heat transfer coefficient versus calculated

Following the results for every test set, that were described in the last paragraph:

- First data set returns *67.18%* data inside the *30%* error range and an average *RMS* of *96* with the minimum *RMS* of *99* at intermediate heat fluxes of *11.1 kW/m²*.
- Second data set returns *57.81%* data inside the *30%* error range and an average *RMS* of *104* with the minimum *RMS* of *99* at intermediate heat fluxes of *15.1 kW/m²*.
- Third data set returns *65.83%* data inside the *30%* error range and an average *RMS* of *90* with the minimum *RMS* of *93* at intermediate heat fluxes of *25.9 kW/m²*.
- Fourth data set returns *60%* data inside the *30%* error range and an average *RMS* of *96* with the minimum *RMS* of *97* at intermediate heat fluxes of *15.1 kW/m²*.

- Fifth data set returns *0%* data inside the *30%* error range and an average *RMS* of *55* with the minimum *RMS* of *56* at intermediate heat fluxes of *42.4 kW/m²*.

Using the thermodynamic qualities for the fifth set of data gives an *RMS* of *35* and *0%* of data inside the *30%* error band.

The analysis with the Shas's correlation returned *580* calculated heat transfer coefficient that compared with the expected ones returns a total *RMS* of *235* and *32.1%* of data within the error band of *30%*. Figures 155-156 shows heat transfer coefficient ve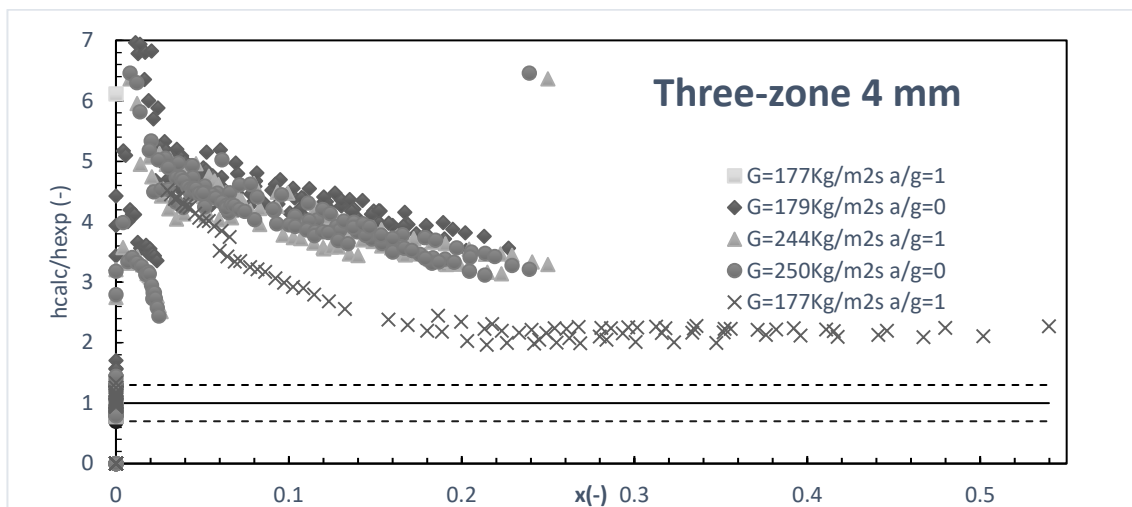rsus quality and expected heat transfer coefficient versus calculated graphics for every set with corrected vapor quality.

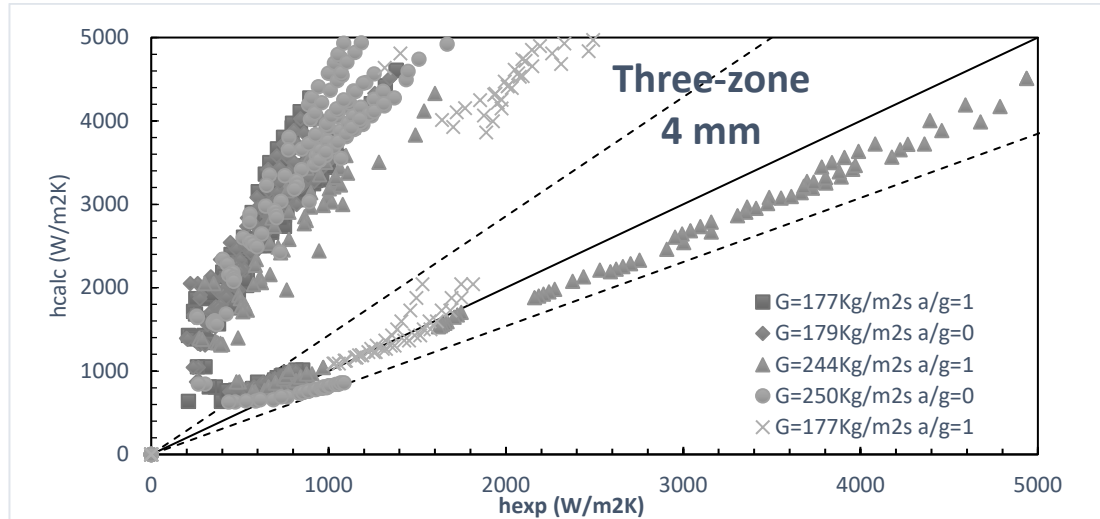Figure 155: Shah 4 mm heat transfer coefficient versus quality

Figure 156: Shah 4 mm experimental heat transfer coefficient versus calculated

Following the results for every test set, that were described in the last paragraph:

- First data set returns *32.03%* data inside the *30%* error range and an average *RMS* of *293* with the minimum *RMS* of *214* at intermediate heat fluxes of *24.9 kW/m²*.
- Second data set returns *27.34%* data inside the *30%* error range and an average *RMS* of *315* with the minimum *RMS* of *228* at intermediate heat fluxes of *24.8 kW/m²*.
- Third data set returns *43.33%* data inside the *30%* error range and an average *RMS* of *252* with the minimum *RMS* of *196* at intermediate heat fluxes of *38.6 kW/m²*.

- Fourth data set returns *39.16%* data inside the *30%* error range and an average *RMS* of *264* with the minimum *RMS* of *205* at intermediate heat fluxes of *38.6 kW/m²*.
- Fifth data set returns *7.14%* data inside the *30%* error range and an average *RMS* of *117* with the minimum *RMS* of *102* at intermediate heat fluxes of *63.2 kW/m²*.

Using the thermodynamic qualities for the fifth set of data gives an *RMS* of *120* and *8.89%* of data inside the *30%* error band.

The analysis with the Gungor and Winterton correlation returned *580* calculated heat transfer coefficient that compared with the expected ones returns a total *RMS* of *499* and *0%* of data within the error band of *30%*. Figures 157-158 shows heat transfer coefficient versus quality and expected heat transfer coefficient versus calculated graphics for every set with corrected vapor quality.
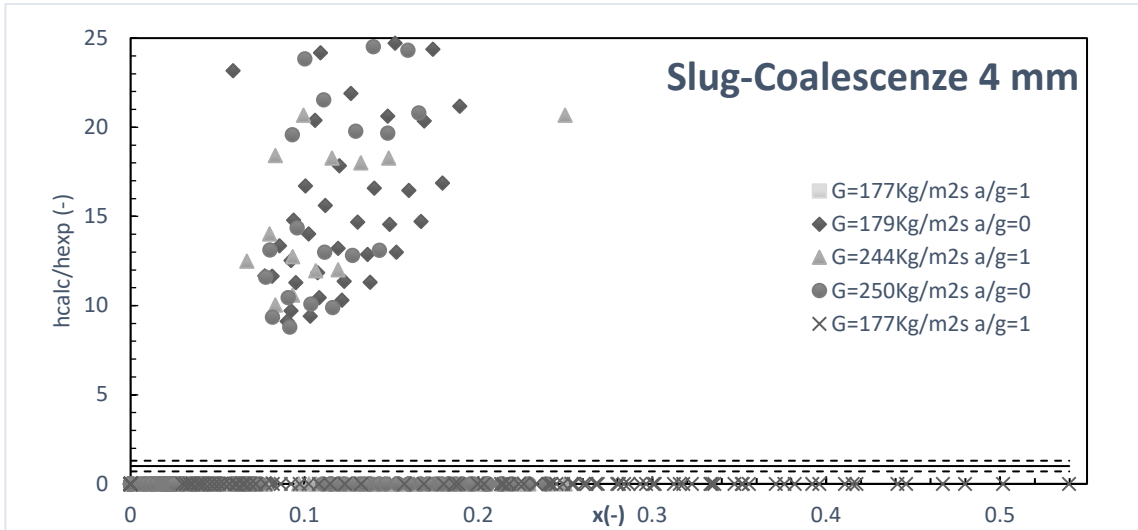

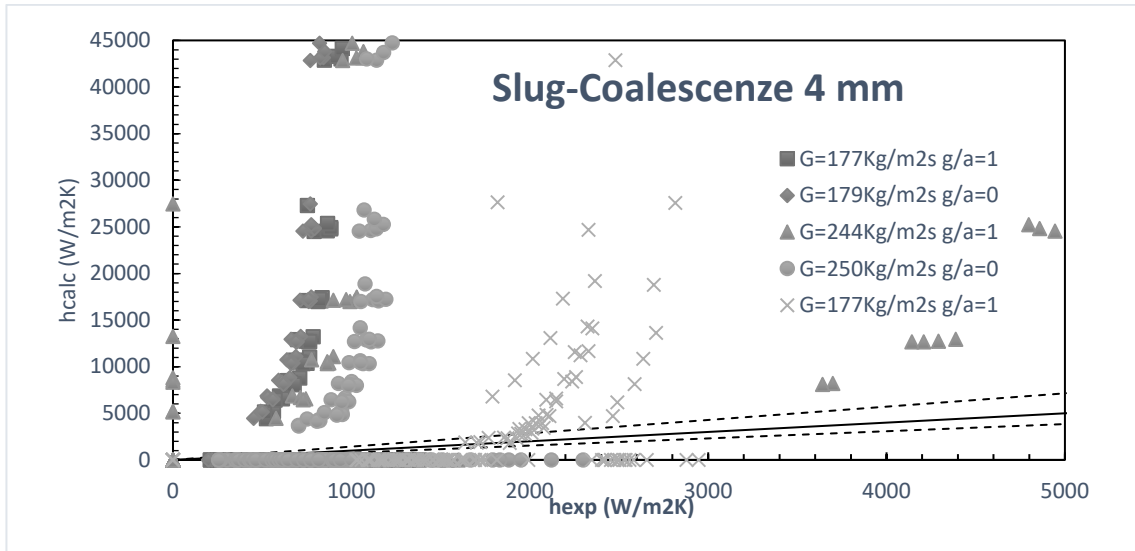Figure 157: Gungor and Winterton 4 mm heat transfer coefficient versus quality

Figure 158: Gungor and Winterton 4 mm experimental heat transfer coefficient versus calculated

Following the results for every test set, that were described in the last paragraph:

- First data set returns *0%* data inside the *30%* error range and an average *RMS* of *479* with the minimum *RMS* of *440* at intermediate heat fluxes of *11.1 kW/m²*.
- Second data set returns *0%* data inside the *30%* error range and an average *RMS* of *509* with the minimum *RMS* of *483* at intermediate heat fluxes of *11.1 kW/m²*.
- Third data set returns *0%* data inside the *30%* error range and an average *RMS* of *505* with the minimum *RMS* of *521* at intermediate heat fluxes of *24.9 kW/m²*.
- Fourth data set returns *0%* data inside the *30%* error range and an average *RMS* of *520* with the minimum *RMS* of *527* at intermediate heat fluxes of *24.9 kW/m²*.
- Fifth data set returns *0%* data inside the *30%* error range and an average *RMS* of *482* with the minimum *RMS* of *468* at intermediate heat fluxes of *42.4 kW/m²*.

Using the thermodynamic qualities for the fifth set of data gives an *RMS* of *526* and *0%* of data inside the *30%* error band.

The analysis with the Kandlikar's correlation returned *580* calculated heat transfer coefficient that compared with the expected ones returns a total *RMS* of *416* and *0%* of data within the error band of *30%*. Figures 159-160 shows heat transfer coefficient versus quality and expected heat transfer coefficient versus calculated graphics for every set with corrected vapor quality.
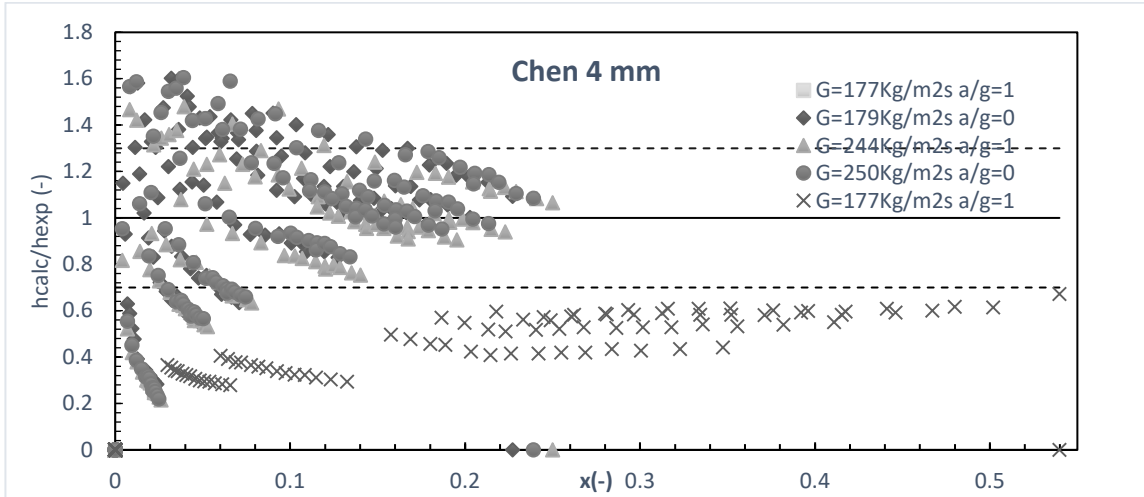

Figure 159: Kandlikar 4 mm heat transfer coefficient versus quality

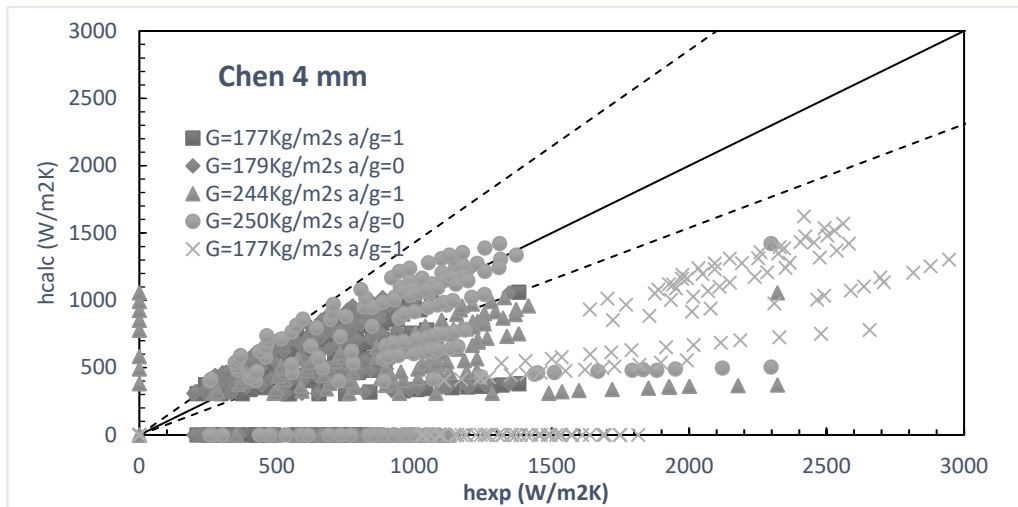Figure 160: Kandlikar 4 mm experimental heat transfer coefficient versus calculated

Following the results for every test set, that were described in the last paragraph:

- First data set returns *0%* data inside the *30%* error range and an average *RMS* of *453* with the minimum *RMS* of *418* at intermediate heat fluxes of *24.9 kW/m²*.
- Second data set returns *0%* data inside the *30%* error range and an average *RMS* of *486* with the minimum *RMS* of *443* at intermediate heat fluxes of *24.8 kW/m²*.
- Third data set returns *0%* data inside the *30%* error range and an average *RMS* of *437* with the minimum *RMS* of *407* at intermediate heat fluxes of *36.3 kW/m²*.
- Fourth data set returns *0%* data inside the *30%* error range and an average *RMS* of *456* with the minimum *RMS* of *419* at intermediate heat fluxes of *36.3 kW/m²*.
- Fifth data set returns *0%* data inside the *30%* error range and an average *RMS* of *283* with the minimum *RMS* of *262* at intermediate heat fluxes of *63.2 kW/m²*.

Using the thermodynamic qualities for the fifth set of data gives an *RMS* of *310* and *0%* of data inside the *30%* error band.

The analysis with the Liu and Winterton correlation returned *746* calculated heat transfer coefficient that compared with the expected ones returns a total *RMS* of *130* and *27.24%* of data within the error band of *30%*. Figures 161-162 shows heat transfer coefficient versus quality and expected heat transfer coefficient versus calculated graphics for every set with corrected vapor quality.
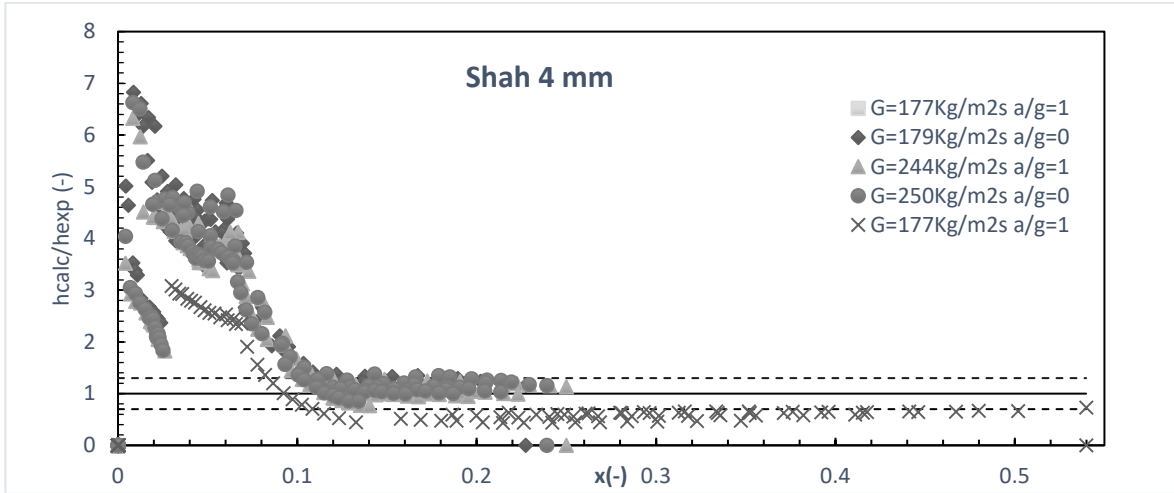
Figure 161: Liu and Winterton 4 mm heat transfer coefficient versus quality

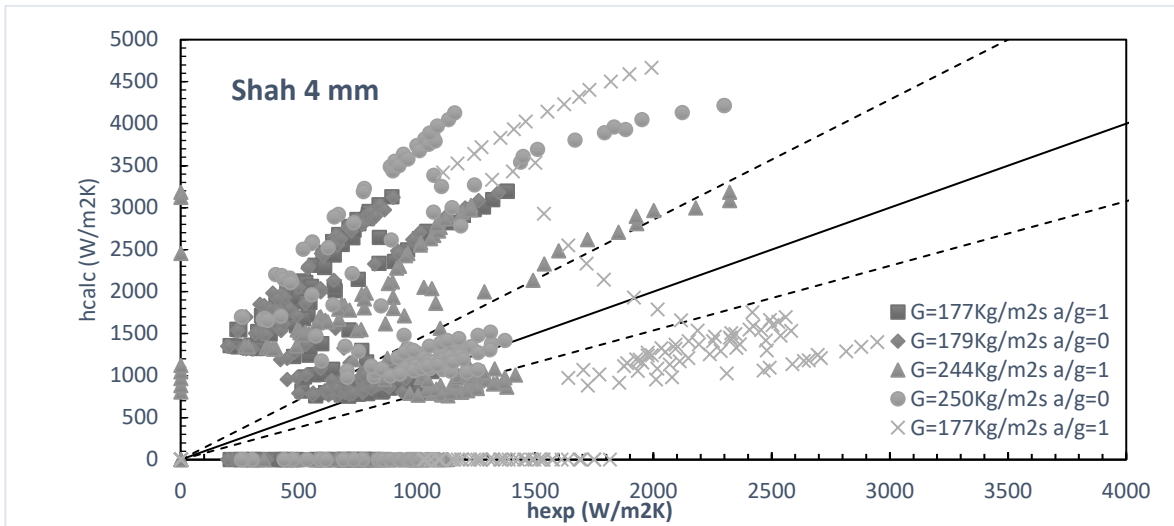Figure 162: Liu and Winterton 4 mm experimental heat transfer coefficient versus calculated

Following the results for every test set, that were described in the last paragraph:

- First data set returns *18.75%* data inside the *30%* error range and an average *RMS* of *154* with the minimum *RMS* of *122* at intermediate heat fluxes of *24.9 kW/m²*.
- Second data set returns *15.63%* data inside the *30%* error range and an average *RMS* of *169* with the minimum *RMS* of *131* at intermediate heat fluxes of *23.7 kW/m²*.
- Third data set returns *31.42%* data inside the *30%* error range and an average *RMS* of *112* with the minimum *RMS* of *95* at intermediate heat fluxes of *37 kW/m²*.
- Fourth data set returns *18.67%* data inside the *30%* error range and an average *RMS* of *136* with the minimum *RMS* of *116* at intermediate heat fluxes of *36.9 kW/m²*.
- Fifth data set returns *14.67%* data inside the *30%* error range and an average *RMS* of *150* with the minimum *RMS* of *124* at intermediate heat fluxes of *42.4 kW/m²*.

Using the thermodynamic qualities for the fifth set of data gives an *RMS* of *58* and *6.67%* of data inside the *30%* error band.

Following correlations are studied by authors for micro-scale tubes. The definition of micro-channel is in the first chapter.

6.3.2.1. Discussion on micro-Scale correlations

The analysis with the Lazarek and Black correlation returned *746* calculated heat transfer coefficient that compared with the expected ones returns a total *RMS* of *369* and *0%* of data within the error band of *30%*. Figures 163-164 shows heat transfer coefficient versus quality and expected heat transfer coefficient versus calculated graphics for every set with corrected vapor quality.
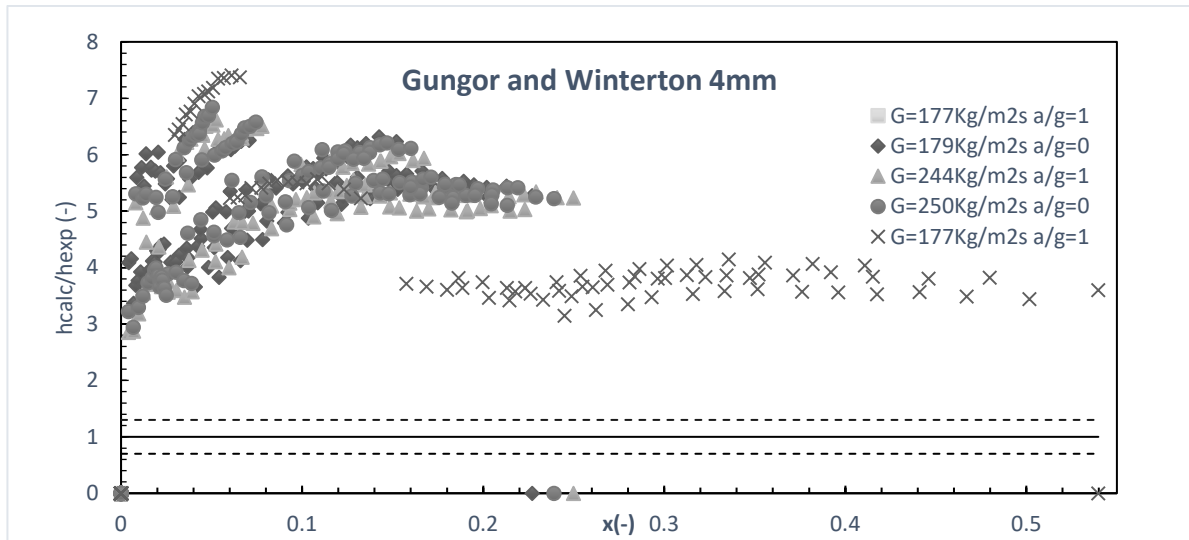

Figure 163: Lazarek and Black 4 mm heat transfer coefficient versus quality
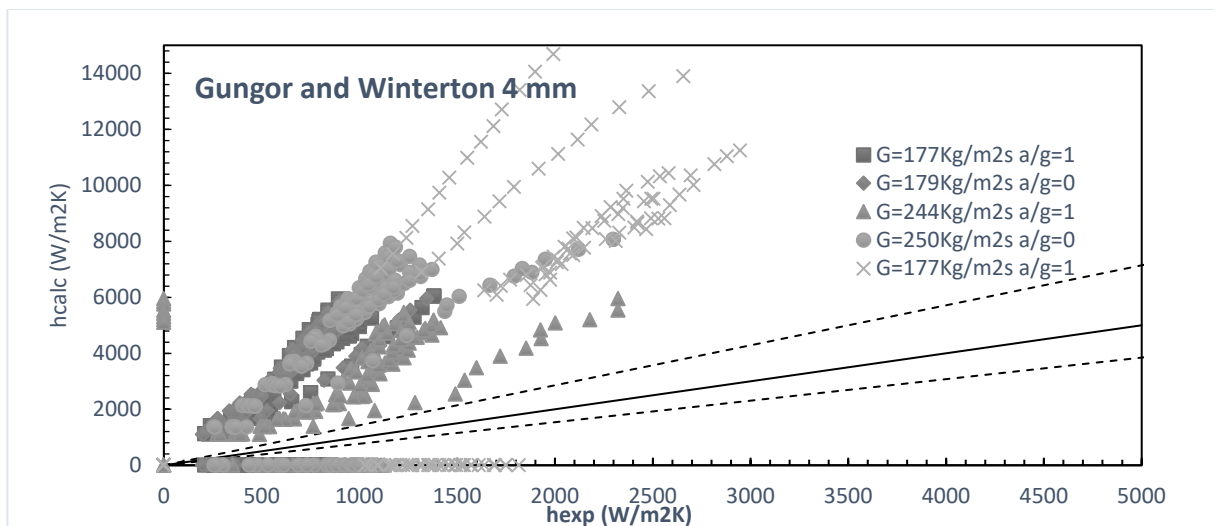

Figure 164: Lazarek and Black 4 mm experimental heat transfer coefficient versus calculated

Following the results for every test set, that were described in the last paragraph:

- First data set returns *0%* data inside the *30%* error range and an average *RMS* of *408* with the minimum *RMS* of *401* at intermediate heat fluxes of *11.1 kW/m²*.
- Second data set returns *0%* data inside the *30%* error range and an average *RMS* of *434* with the minimum *RMS* of *421* at intermediate heat fluxes of *24.8 kW/m²*.
- Third data set returns *0%* data inside the *30%* error range and an average *RMS* of *415* with the minimum *RMS* of *403* at intermediate heat fluxes of *36.3 kW/m²*.
- Fourth data set returns *0%* data inside the *30%* error range and an average *RMS* of 427

with the minimum *RMS* of *409* at intermediate heat fluxes of *36.6 kW/m²*.
- Fifth data set returns *0%* data inside the *30%* error range and an average *RMS* of *310* with the minimum *RMS* of *306* at intermediate heat fluxes of *42.4 kW/m²*.

Using the thermodynamic qualities for the fifth set of data gives an *RMS* of *310* and *0%* of data inside the *30%* error band.

The analysis with the Trasn et al. correlation returned *746* calculated heat transfer coefficient that compared with the expected ones returns a total *RMS* of *811* and *0%* of data within the error band of *30%*. Figures 165-166 shows heat transfer coefficient versus quality and expected heat transfer coefficient versus calculated graphics for every set with corrected vapor quality.
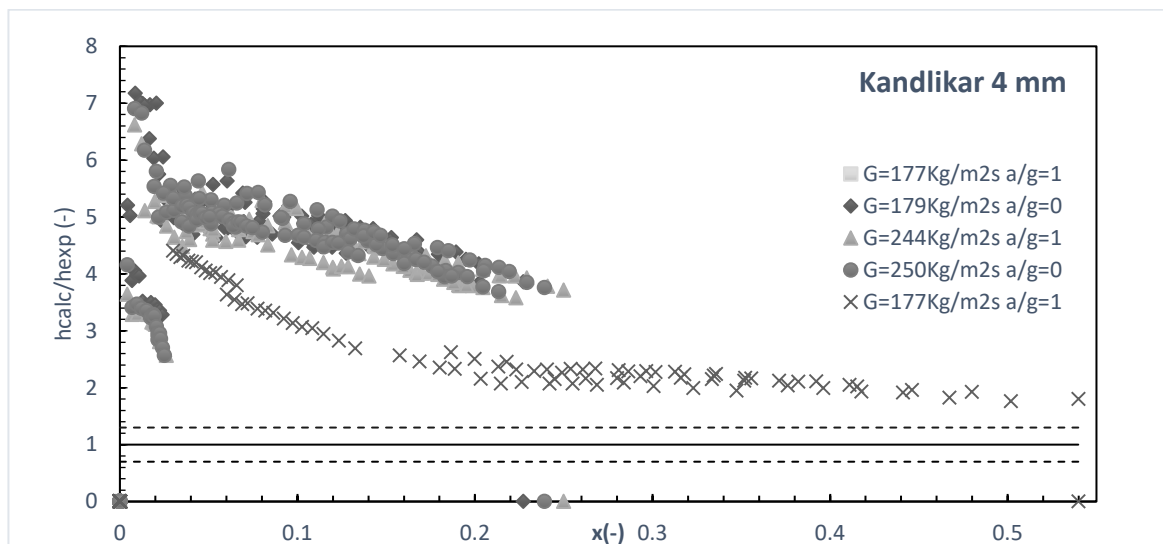

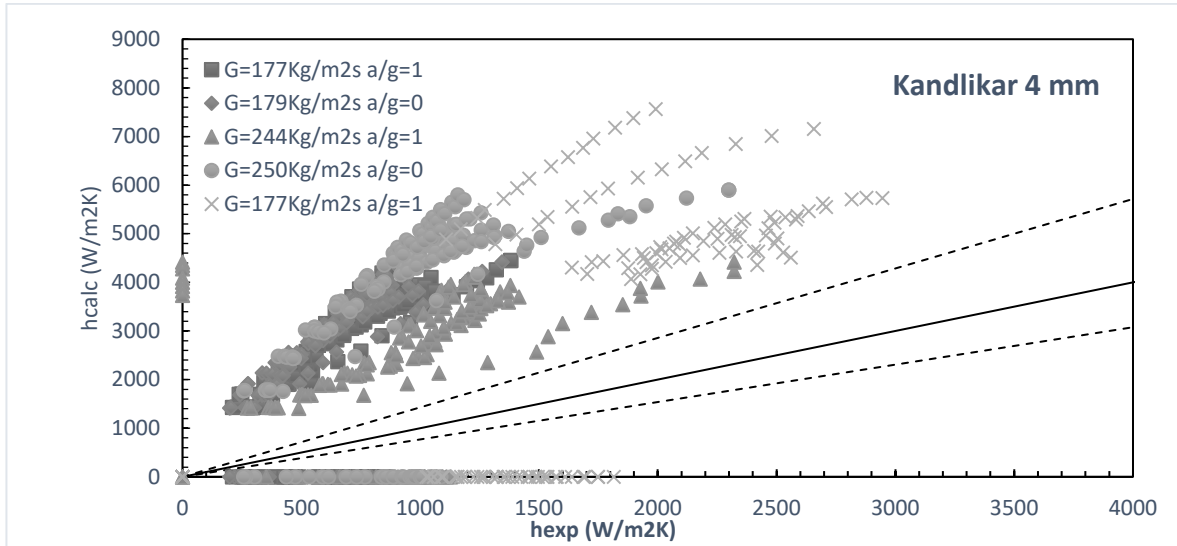Figure 165: Tran et al. 4 mm heat transfer coefficient versus quality

Figure 166: Tran et al. 4 mm experimental heat transfer coefficient versus calculated

Following the results for every test set, that were described in the last paragraph:

- First data set returns *0%* data inside the *30%* error range and an average *RMS* of *906* with the minimum *RMS* of *835* at intermediate heat fluxes of *24.9 kW/m²*.
- Second data set returns *0%* data inside the *30%* error range and an average *RMS* of *954* with the minimum *RMS* of *868* at intermediate heat fluxes of *24.8 kW/m²*.
- Third data set returns *0%* data inside the *30%* error range and an average *RMS* of *818*

with the minimum *RMS* of *762* at intermediate heat fluxes of *36.3 kW/m²*.

- Fourth data set returns *0%* data inside the *30%* error range and an average *RMS* of *827* with the minimum *RMS* of *759* at intermediate heat fluxes of *36.3 kW/m²*.
- Fifth data set returns *0%* data inside the *30%* error range and an average *RMS* of *599* with the minimum *RMS* of *586* at intermediate heat fluxes of *57.5 kW/m²*.

Using the thermodynamic qualities for the fifth set of data gives an *RMS* of *599* and *0%* of data inside the *30%* error band.

The analysis with the Kew and Conrwell correlation returned *746* calculated heat transfer coefficient that compared with the expected ones returns a total *RMS* of *348* and *0%* of data within the error band of *30%*. Figures 167-168 shows heat transfer coefficient versus quality and expected heat transfer coefficient versus calculated graphics for every set with corrected vapor quality.
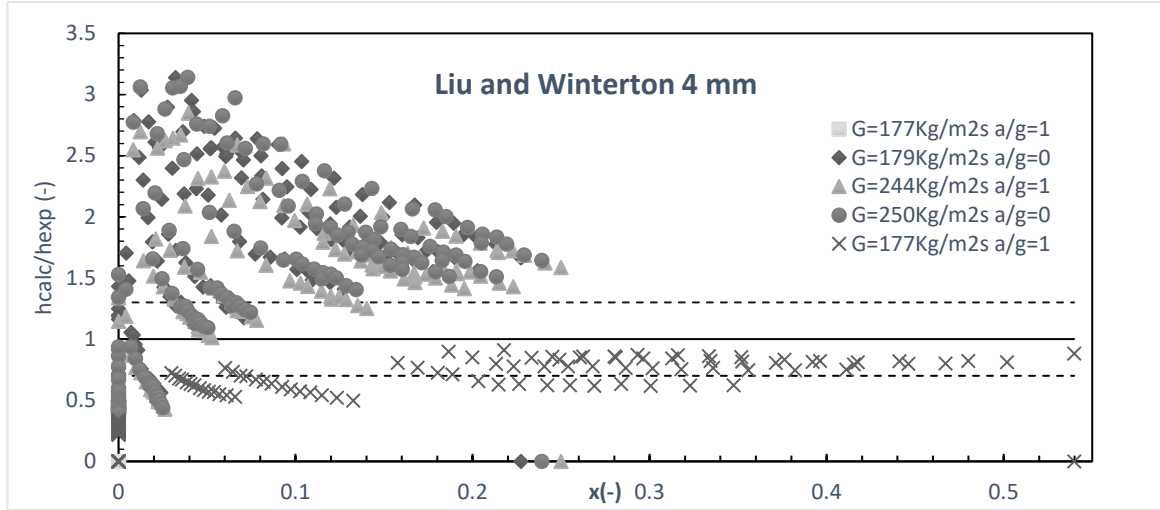

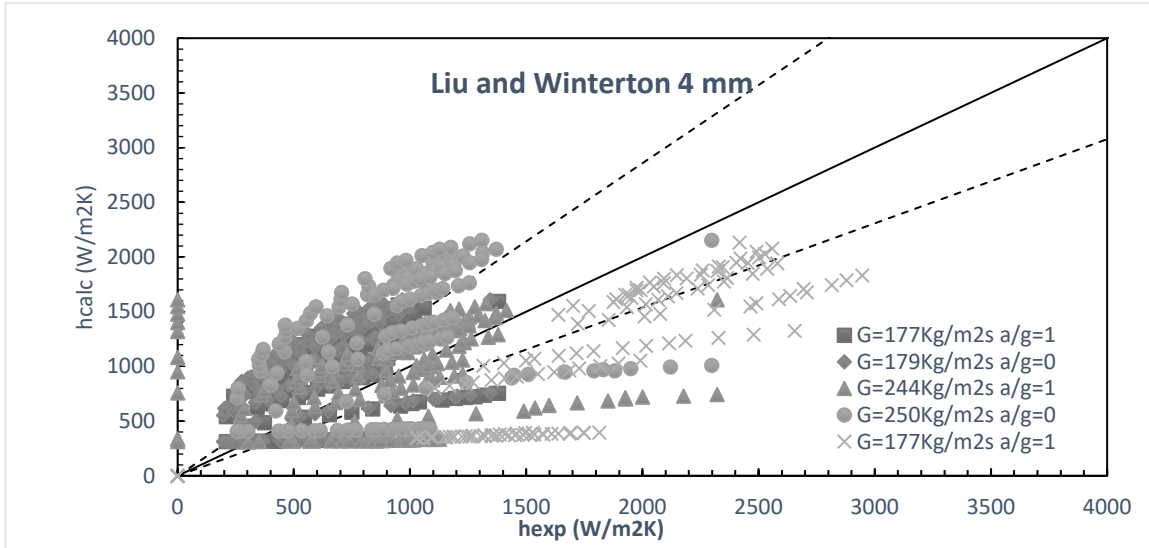Figure 167: Kew and Cornwell 4 mm heat transfer coefficient versus quality

Figure 168: Kew and Cornwell 4 mm experimental heat transfer coefficient versus calculated

Following the results for every test set, that were described in the last paragraph:

- First data set returns *0%* data inside the *30%* error range and an average *RMS* of *358* with the minimum *RMS* of *351* at intermediate heat fluxes of *11.1 kW/m²*.
- Second data set returns *0%* data inside the *30%* error range and an average *RMS* of *381* with the minimum *RMS* of *371* at intermediate heat fluxes of *17.3 kW/m²*.
- Third data set returns *0%* data inside the *30%* error range and an average *RMS* of *363* with the minimum *RMS* of *354* at intermediate heat fluxes of *36.3 kW/m²*.
- Fourth data set returns *0%* data inside the *30%* error range and an average *RMS* of *374* with the minimum *RMS* of *359* at intermediate heat fluxes of *36.3 kW/m²*.
- Fifth data set returns *0%* data inside the *30%* error range and an average *RMS* of *277* with the minimum *RMS* of *272* at intermediate heat fluxes of *42.4 kW/m²*.

Using the thermodynamic qualities for the fifth set of data gives an *RMS* of *268* and *0%* of data inside the *30%* error band.

The analysis with the Warrier et al. correlation returned *580* calculated heat transfer coefficient that compared with the expected ones returns a total *RMS* of *204* and *23.45%* of data within the error band of *30%*. Figures 169-170 shows heat transfer coefficient versus quality and expected heat transfer coefficient versus calculated graphics for every set with corrected vapor quality.
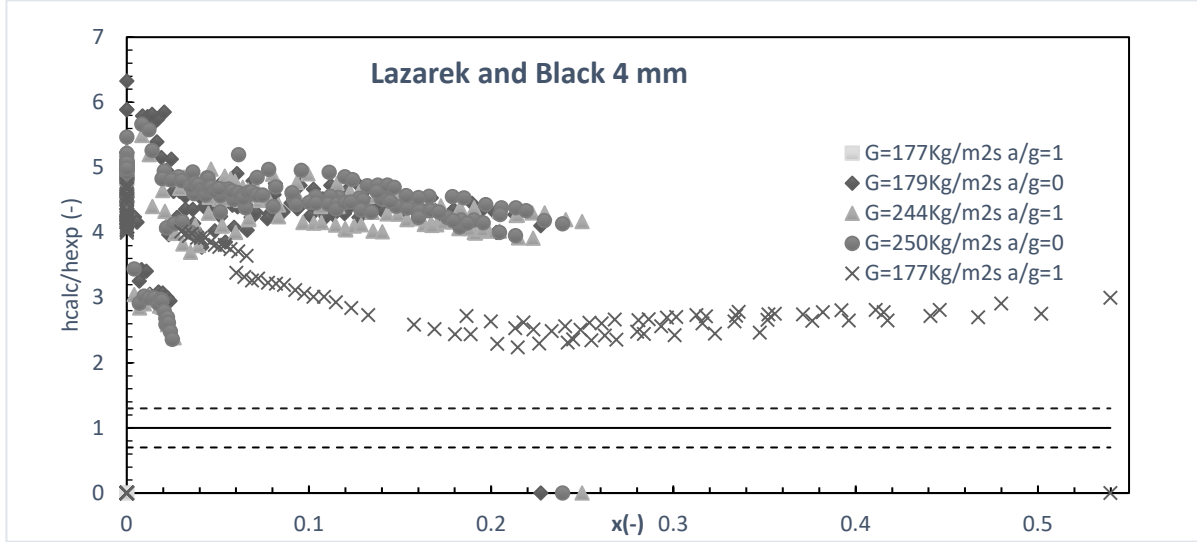

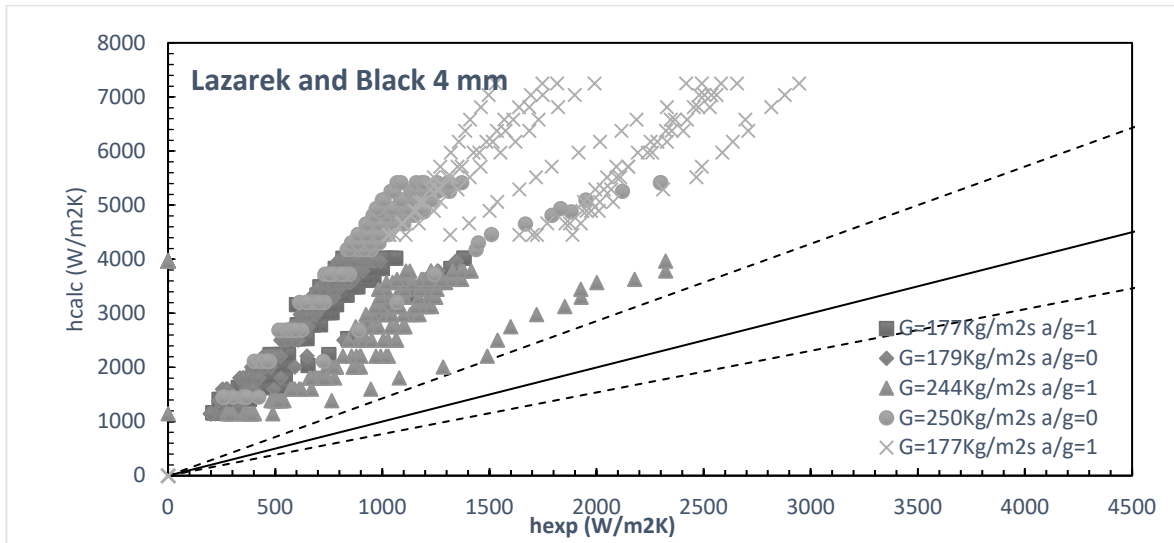Figure 169: Warrier et al. 4 mm heat transfer coefficient versus quality

Figure 170: Warrier et al. 4 mm experimental heat transfer coefficient versus calculated

Following the results for every test set, that were described in the last paragraph:

- First data set returns *8.59%* data inside the *30%* error range and an average *RMS* of *168* with the minimum *RMS* of *155* at intermediate heat fluxes of *24.9 kW/m²*.
- Second data set returns *7.81%* data inside the *30%* error range and an average *RMS* of *180* with the minimum *RMS* of *164* at intermediate heat fluxes of *24.9 kW/m²*.
- Third data set returns *0%* data inside the *30%* error range and an average *RMS* of *326* with the minimum *RMS* of *304* at intermediate heat fluxes of *36.3 kW/m²*.
- Fourth data set returns *0%* data inside the *30%* error range and an average *RMS* of *339* with the minimum *RMS* of *312* at intermediate heat fluxes of *36.3 kW/m²*.
- Fifth data set returns *77.38%* data inside the *30%* error range and an average *RMS* of *105* with the minimum *RMS* of *100* at intermediate heat fluxes of *60.4 kW/m²*.

Using the thermodynamic qualities for the fifth set of data gives an *RMS* of *58* and *0%* of data inside the *30%* error band.

The analysis with the Kandlikar and Balasubramanian correlation returned *746* calculated heat transfer coefficient that compared with the expected ones returns a total *RMS* of *37* and *8.99%* of data within the error band of *30%*. Figures 171-172 shows heat transfer coefficient versus quality and expected heat transfer coefficient versus calculated graphics for every set with corrected vapor quality.
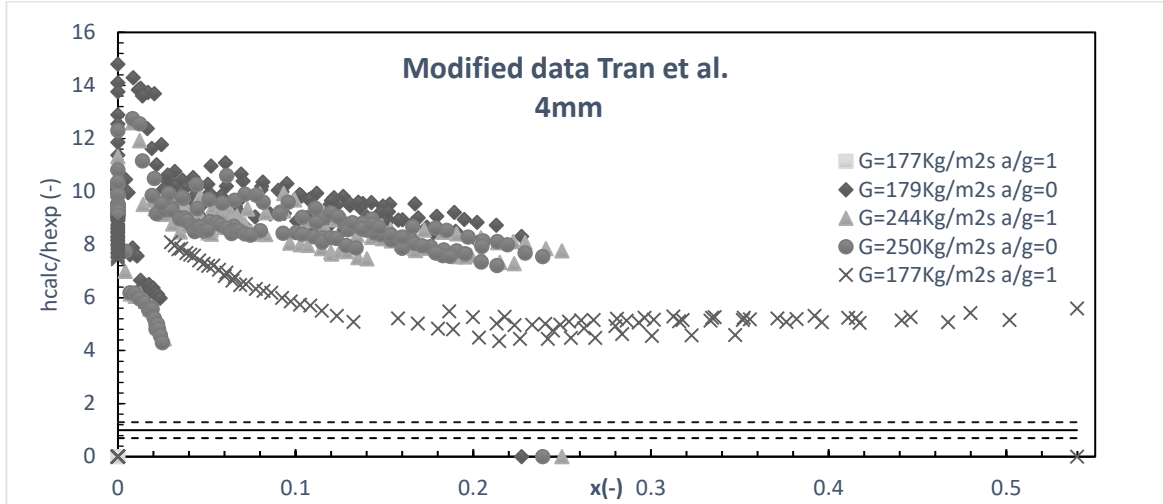
Figure 171: Kandlikar and Balasubramanian 4 mm heat transfer coefficient versus quality

Figure 172: Kandlikar and Balasubramanian 4 mm experimental heat transfer coefficient versus calculated

Following the results for every test set, that were described in the last paragraph:

- First data set returns *13.75%* data inside the *30%* error range and an average *RMS* of *47* with the minimum *RMS* of *52* at intermediate heat fluxes of *11.1 kW/m²*.
- Second data set returns *16.86%* data inside the *30%* error range and an average *RMS* of *52* with the minimum *RMS* of *58* at intermediate heat fluxes of *11.1 kW/m²*.
- Third data set returns *2.66%* data inside the *30%* error range and an average *RMS* of *32* with the minimum *RMS* of *33* at intermediate heat fluxes of *24.9 kW/m²*.
- Fourth data set returns *2.67%* data inside the *30%* error range and an average *RMS* of *34* with the minimum *RMS* of *34* at intermediate heat fluxes of *24.9 kW/m²*.
- Fifth data set returns *0%* data inside the *30%* error range and an average *RMS* of *25* with the minimum *RMS* of *27* at intermediate heat fluxes of *60.4 kW/m²*.

Using the thermodynamic qualities for the fifth set of data gives an *RMS* of *14* and *0%* of data inside the *30%* error band.

The analysis with the Zhang et al. correlation returned *580* calculated heat transfer coefficient that compared with the expected ones returns a total *RMS* of *72* and *44.8%* of data within the error band of *30%.* Figures 173-174 shows heat transfer coefficient versus quality and expected heat transfer coefficient versus calculated graphics for every set with corrected vapor quality.

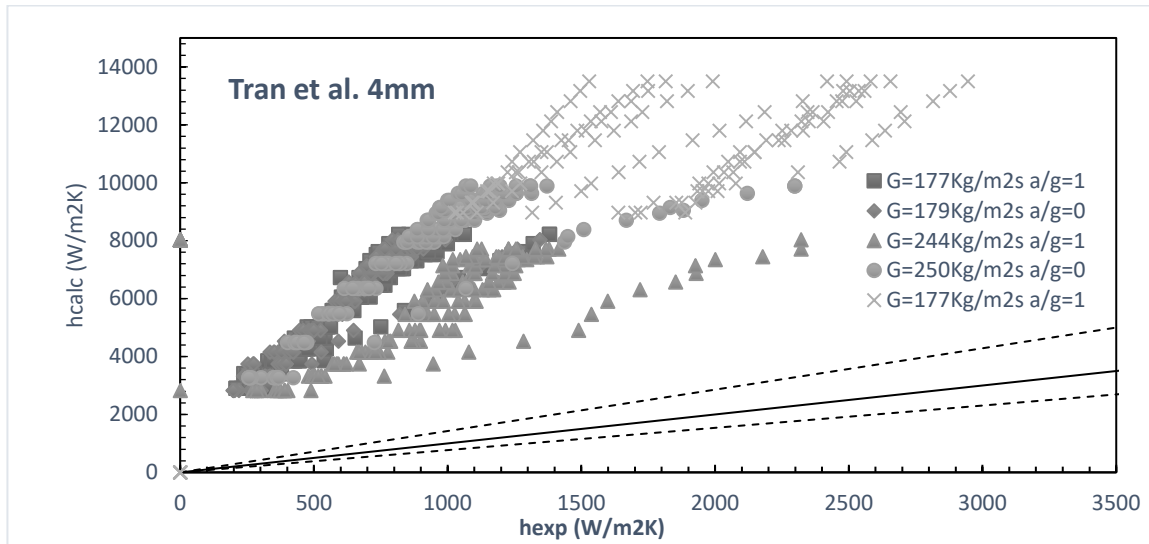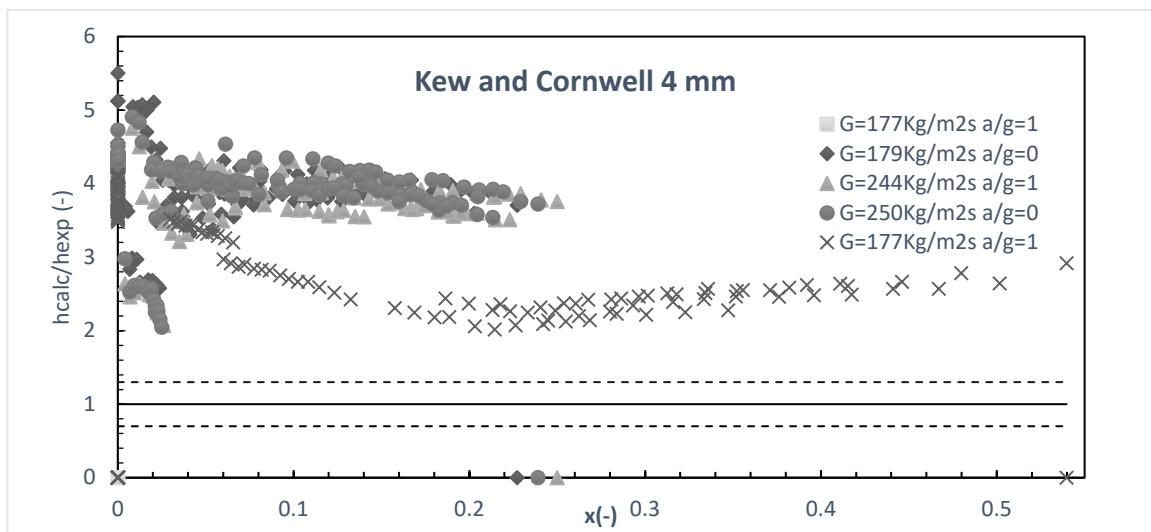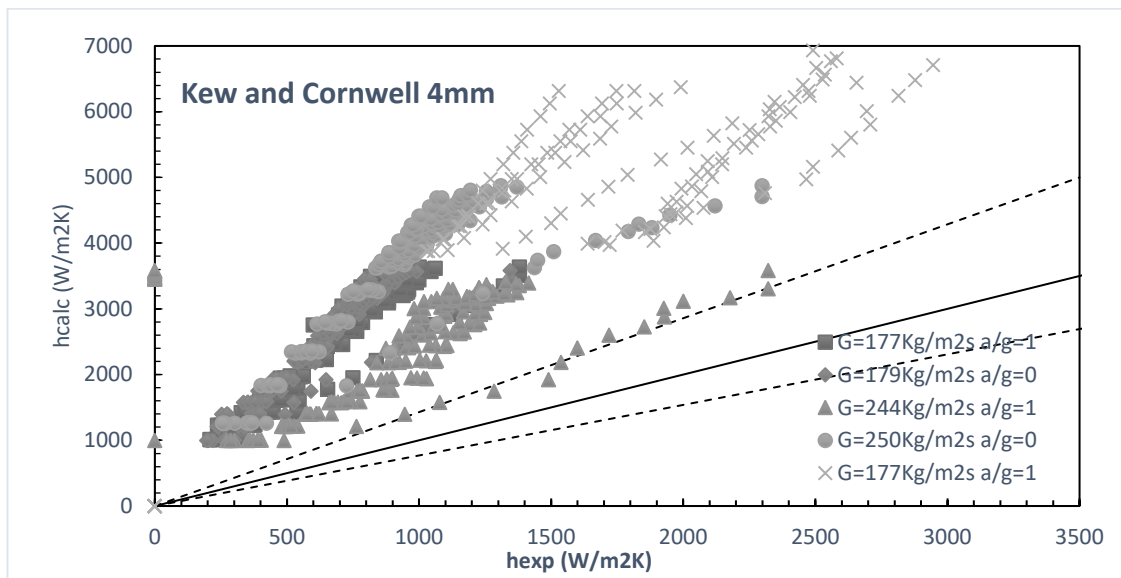Figure 173: Zhang et al. 4 mm heat transfer coefficient versus quality

Figure 174: Zhang et al. 4 mm experimental heat transfer coefficient versus calculated

Following the results for every test set, that were described in the last paragraph:

- First data set returns *34.36%* data inside the *30%* error range and an average *RMS* of *75* with the minimum *RMS* of *96* at intermediate heat fluxes of *12.7 kW/m²*.
- Second data set returns *27.34%* data inside the *30%* error range and an average *RMS* of *77* with the minimum *RMS* of *104* at intermediate heat fluxes of *12.7 kW/m²*.
- Third data set returns *63.33%* data inside the *30%* error range and an average *RMS* of *112* with the minimum *RMS* of *100* at intermediate heat fluxes of *35.6 kW/m²*.
- Fourth data set returns *54.16%* data inside the *30%* error range and an average *RMS* of *117* with the minimum *RMS* of *100* at intermediate heat fluxes of *36.9 kW/m²*.
- Fifth data set returns *0%* data inside the *30%* error range and an average *RMS* of *27* with the minimum *RMS* of *30* at intermediate heat fluxes of *50.2 kW/m²*.

Using the thermodynamic qualities for the fifth set of data gives an *RMS* of *26* and *0%* of data Lee and Mudawar

The analysis with the Lee and Mudawar correlation returned *580* calculated heat transfer coefficient that compared with the expected ones returns a total *RMS* of *1058* and *12.59%* of data within the error band of *30%*. Figures 175-176 shows normalized heat transfer coefficient versus quality and expected heat transfer coefficient versus calculated graphics for every set with corrected vapor quality.
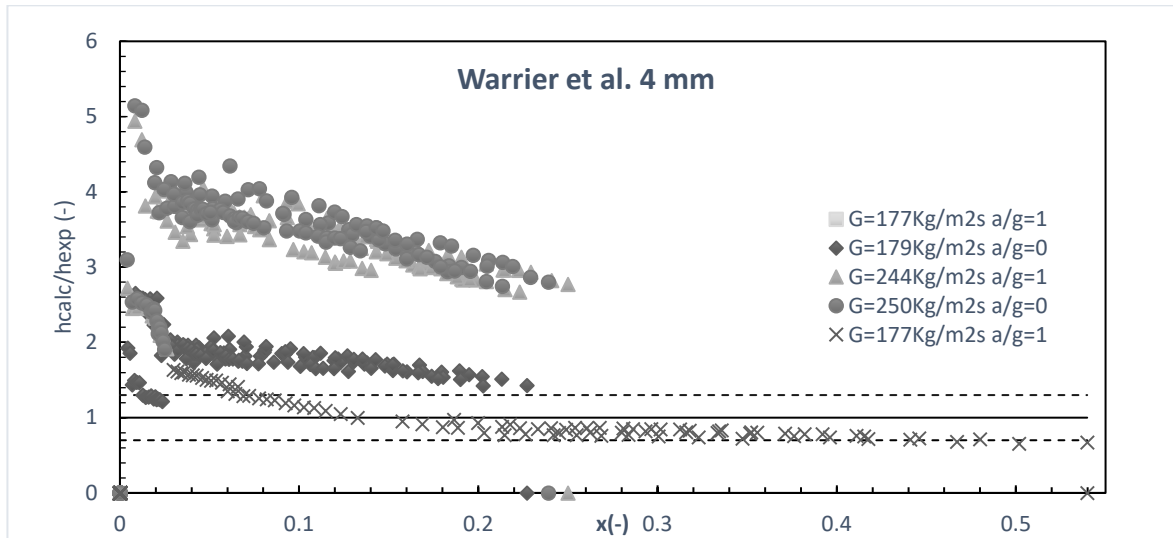

Figure 175: Lee and Mudawar 4 mm heat transfer coefficient versus quality

Figure 176: Lee and Mudawar 4 mm experimental heat transfer coefficient versus calculated

Following the results for every test set, that were described in the last paragraph:

- First data set returns *10.15%* data inside the *30%* error range and an average *RMS* of *1321* with the minimum *RMS* of *821* at intermediate heat fluxes of *11.1 kW/m²*.
- Second data set returns *9.36%* data inside the *30%* error range and an average *RMS* of *1415* with the minimum *RMS* of *909* at intermediate heat fluxes of *11.1 kW/m²*.
- Third data set returns *10.83%* data inside the *30%* error range and an average *RMS* of

786 with the minimum *RMS* of *736* at intermediate heat fluxes of *37 kW/m²*.

- Fourth data set returns *11.67%* data inside the *30%* error range and an average *RMS* of *816* with the minimum *RMS* of *766* at intermediate heat fluxes of *36.9 kW/m²*.
- Fifth data set returns *8.33%* data inside the *30%* error range and an average *RMS* of *1105* with the minimum *RMS* of *918* at intermediate heat fluxes of *50.2 kW/m²*.

Using the thermodynamic qualities for the fifth set of data gives an *RMS* of *663* and *2.22%* of data inside the *30%* error band.

The analysis with the Saitoh et al. correlation returned *702* calculated heat transfer coefficient that compared with the expected ones returns a total *RMS* of *370* and *0%* of data within the error band of *30%*. Figures 177-178 shows heat transfer coefficient versus quality and expected heat transfer coefficient versus calculated graphics for every set with corrected vapor quality.

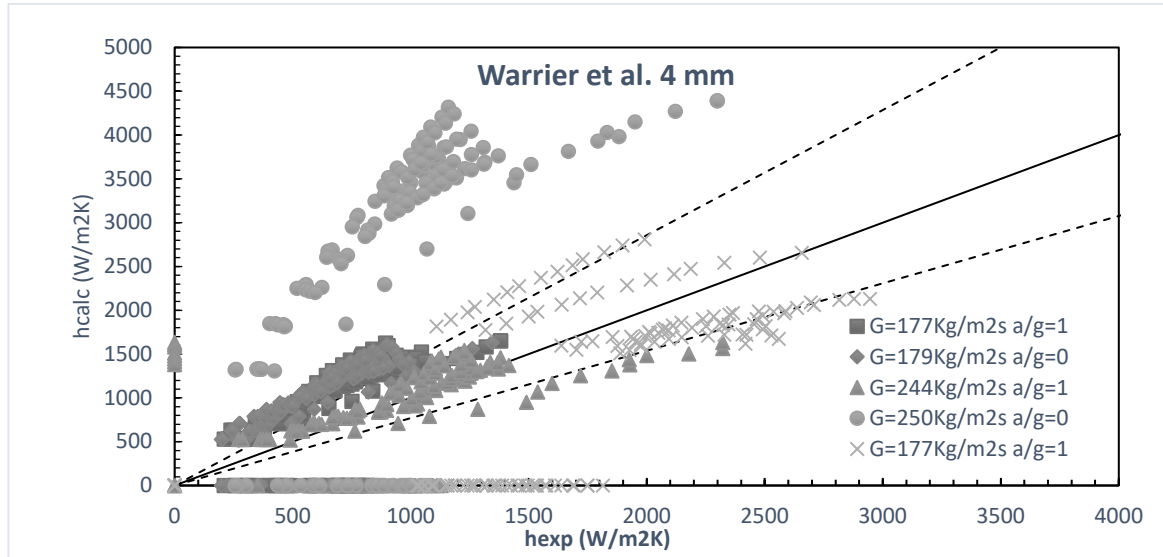Figure 177: Saitoh et al. 4 mm heat transfer coefficient versus quality

Figure 178: Saitoh et al. 4 mm experimental heat transfer coefficient versus calculated

Following the results for every test set, that were described in the last paragraph:

- First data set returns *0%* data inside the *30%* error range and an average *RMS* of *488* with the minimum *RMS* of *460* at intermediate heat fluxes of *24.9 kW/m²*.
- Second data set returns *0%* data inside the *30%* error range and an average *RMS* of *325* with the minimum *RMS* of *293* at intermediate heat fluxes of *24.8 kW/m²*.
- Third data set returns *0%* data inside the *30%* error range and an average *RMS* of *446* with the minimum *RMS* of *419* at intermediate heat fluxes of *36.3 kW/m²*.
- Fourth data set returns *0%* data inside the *30%* error range and an average *RMS* of *286* with the minimum *RMS* of *259* at intermediate heat fluxes of *36.3 kW/m²*.
- Fifth data set returns *0%* data inside the *30%* error range and an average *RMS* of 336 with the minimum *RMS* of *329* at intermediate heat fluxes of *63.2 kW/m²*.

Using the thermodynamic qualities for the fifth set of data gives an *RMS* of *344* and 0% of data inside the *30%* error band.

The analysis with the Bertsch et al. correlation returned *746* calculated heat transfer coefficient that compared with the expected ones returns a total *RMS* of *66* and *32%* of data within the error band of *30%*. Figures 179-180 shows heat transfer coefficient versus quality and expected heat transfer coefficient versus calculated graphics for every set with corrected vapor quality.
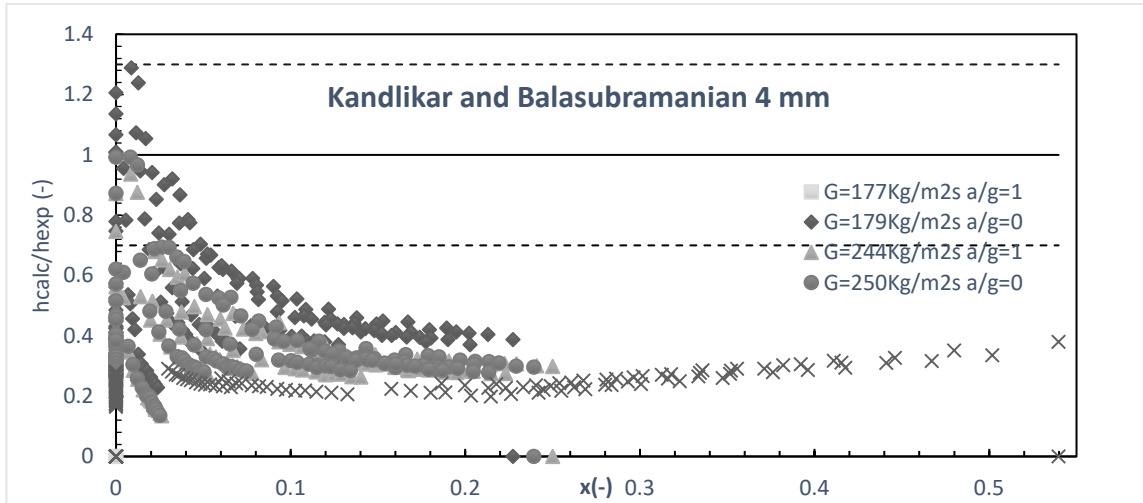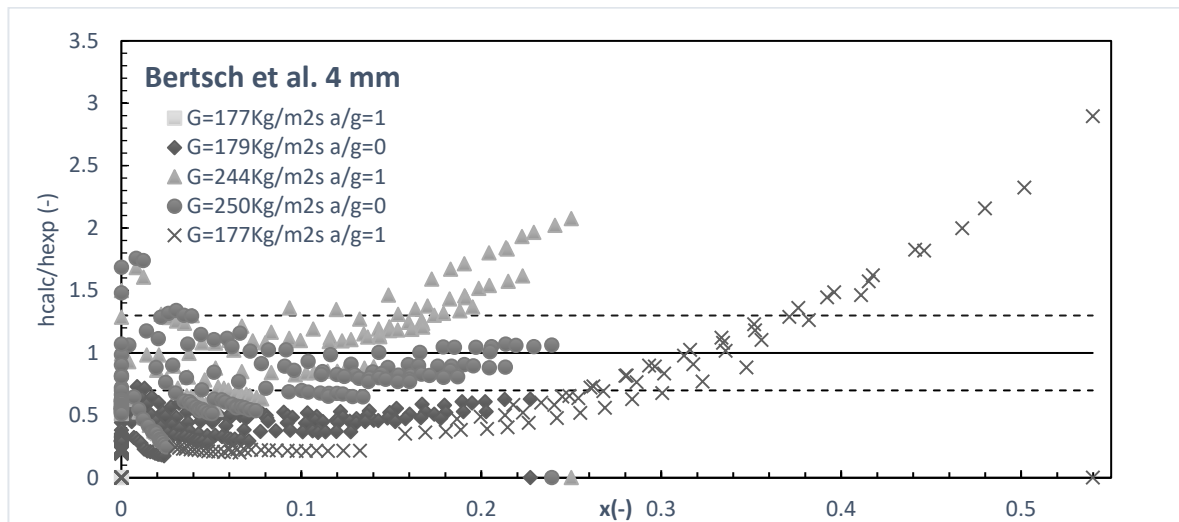

Figure 179: Bertsch et al. 4 mm heat transfer coefficient versus quality
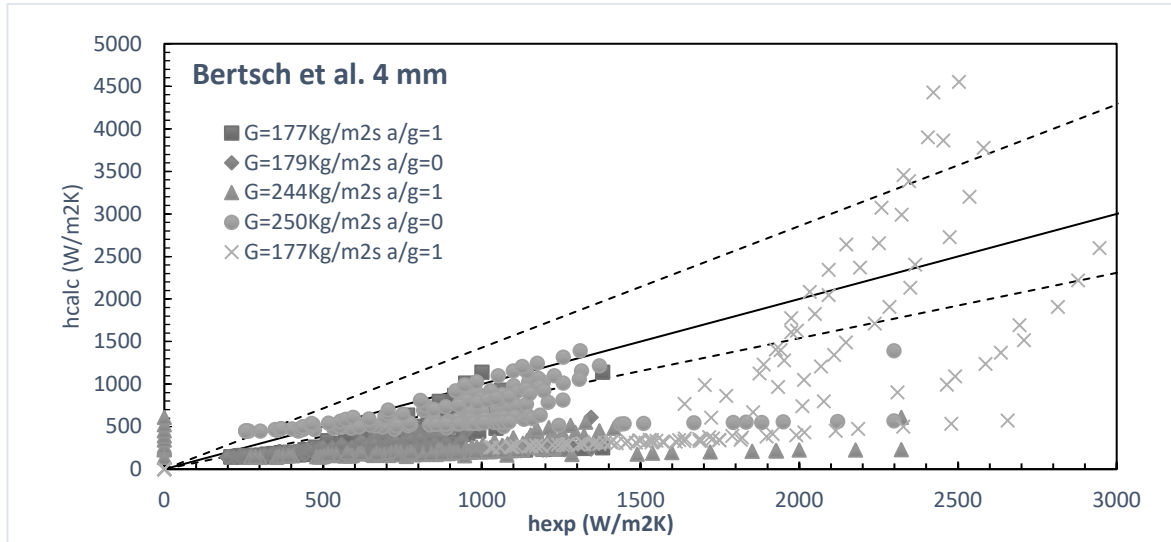
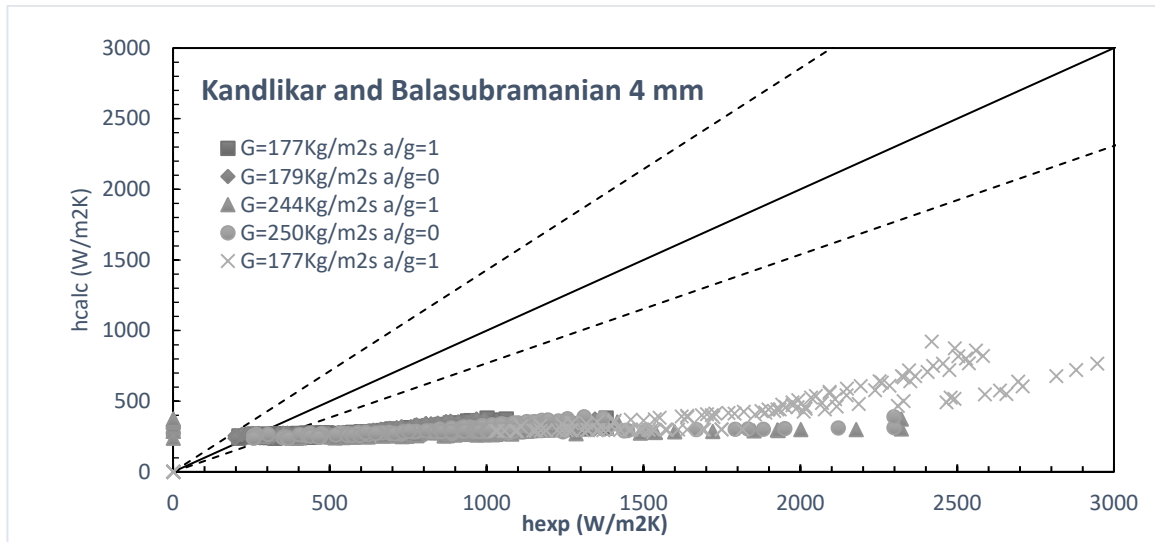Figure 180: Bertsch et al. 4 mm experimental heat transfer coefficient versus calculated

Following the results for every test set, that were described in the last paragraph:

- First data set returns *12.5%* data inside the *30%* error range and an average *RMS* of *49* with the minimum *RMS* of *54* at intermediate heat fluxes of *24.9 kW/m²*.
- Second data set returns *1.25%* data inside the *30%* error range and an average *RMS* of *43* with the minimum *RMS* of *42* at intermediate heat fluxes of *11.1 kW/m²*.
- Third data set returns *45.33%* data inside the *30%* error range and an average *RMS* of *78* with the minimum *RMS* of *100* at intermediate heat fluxes of *35.6 kW/m²*.
- Fourth data set returns *52.67%* data inside the *30%* error range and an average *RMS* of *136* with the minimum *RMS* of *101* at intermediate heat fluxes of *24.9 kW/m²*.
- Fifth data set returns *16.67%* data inside the *30%* error range and an average *RMS* of *76* with the minimum *RMS* of *102* at intermediate heat fluxes of *57.5 kW/m²*.

Using the thermodynamic qualities for the fifth set of data gives an *RMS* of *17* and *2.38%* of data inside the *30%* error band.

The analysis with the Mikielewicz correlation returned *746* calculated heat transfer coefficient that compared with the expected ones returns a total *RMS* of *85* and *30.83%* of data within the error band of *30%*. Figures 181-182 shows heat transfer coefficient versus quality and expected heat transfer coefficient versus calculated graphics for every set with corrected vapor quality.
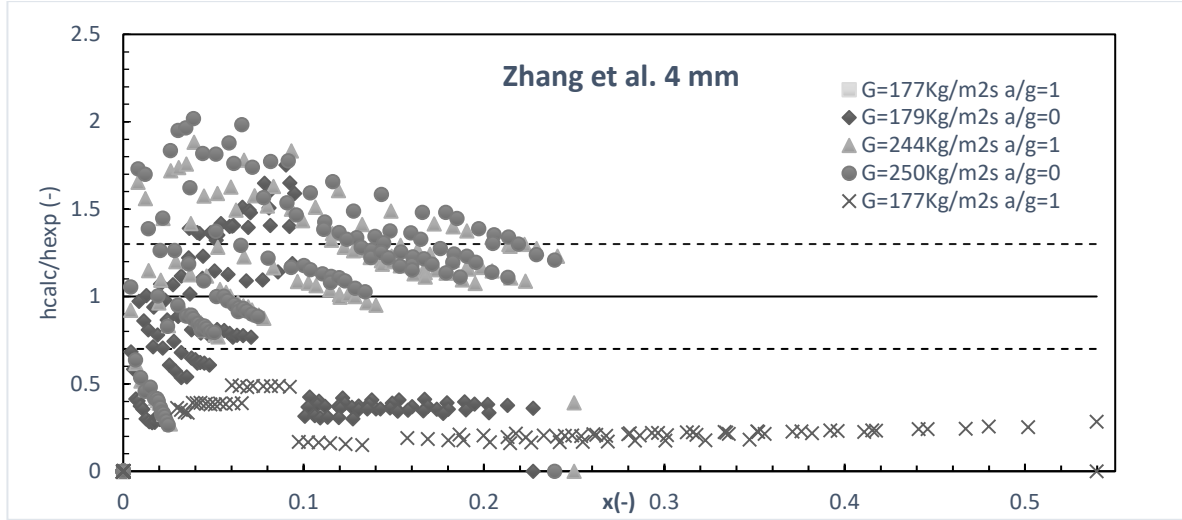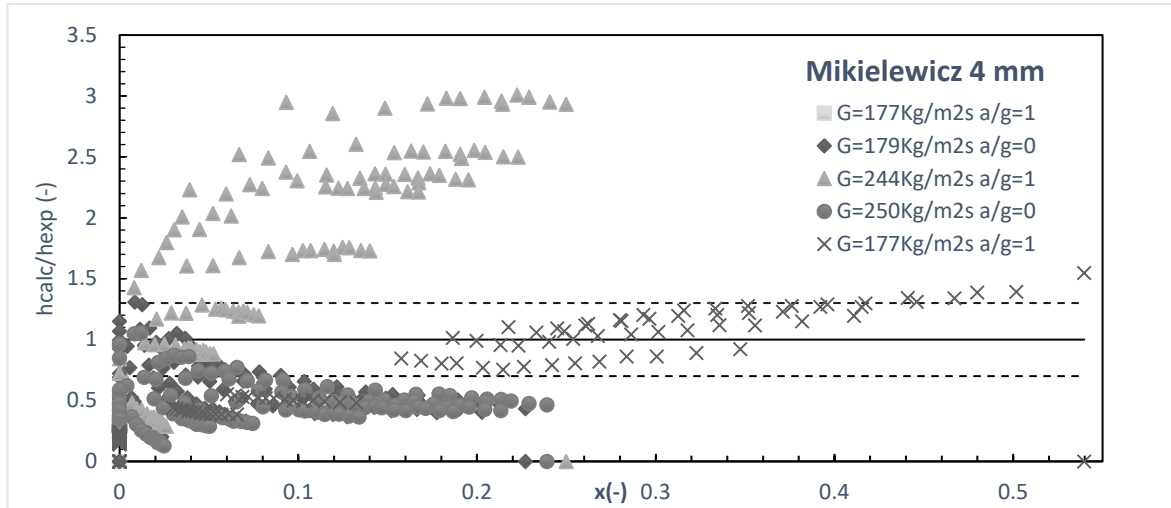
Figure 181: Mikielewicz 4 mm heat transfer coefficient versus quality
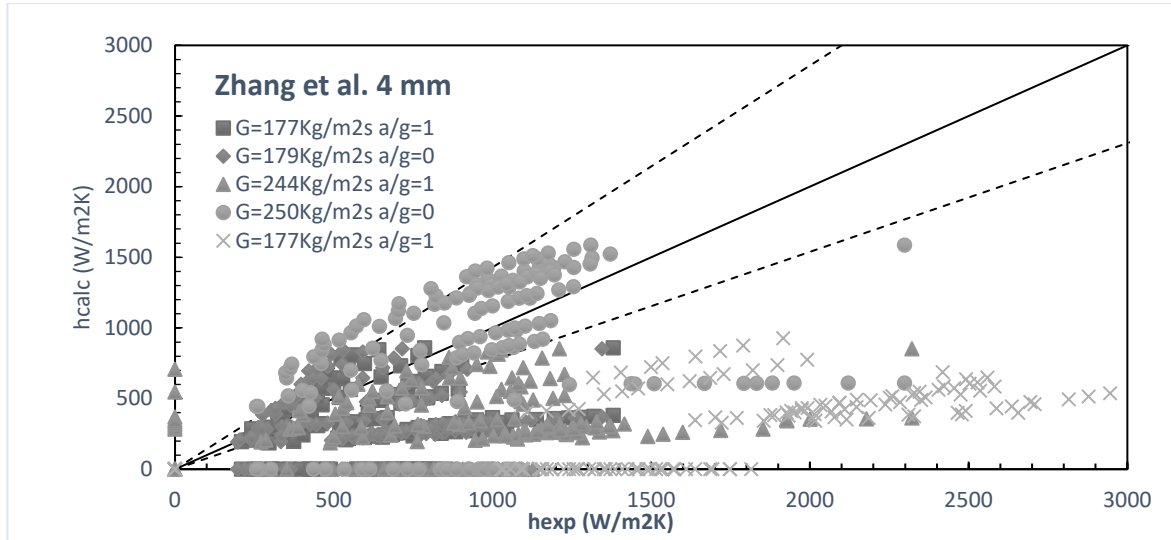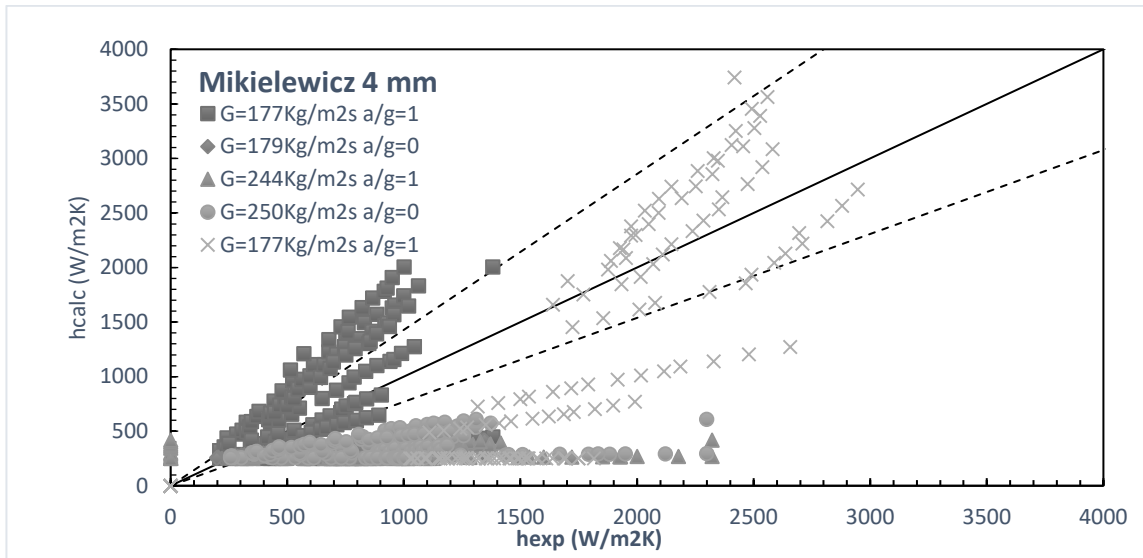

Figure 182: Mikielewicz 4 mm experimental heat transfer coefficient versus calculated

Following the results for every test set, that were described in the last paragraph:

- First data set returns *31.25%* data inside the *30%* error range and an average *RMS* of *127* with the minimum *RMS* of *122* at intermediate heat fluxes of *17.3 kW/m²*.
- Second data set returns *23.75%* data inside the *30%* error range and an average *RMS* of *54* with the minimum *RMS* of *62* at intermediate heat fluxes of *11.1 kW/m²*.
- Third data set returns *31.42%* data inside the *30%* error range and an average *RMS* of *42* with the minimum *RMS* of *43* at intermediate heat fluxes of *36.3 kW/m²*.
- Fourth data set returns *8.67%* data inside the *30%* error range and an average *RMS* of *136* with the minimum *RMS* of *116* at intermediate heat fluxes of *24.9 kW/m²*.
- Fifth data set returns *39.68%* data inside the *30%* error range and an average *RMS* of *89* with the minimum *RMS* of *95* at intermediate heat fluxes of *63.2 kW/m²*.

Using the thermodynamic qualities for the fifth set of data gives an *RMS* of *80* and *28.57%* of data inside the *30%* error band.

The analysis with the Li and Wu correlation returned *746* calculated heat transfer coefficient that compared with the expected ones returns a total *RMS* of *442* and *8.75%* of data within the

error band of *30%.* Figures 183-184 shows heat transfer coefficient versus quality and expected heat transfer coefficient versus calculated graphics for every set with corrected vapor quality.
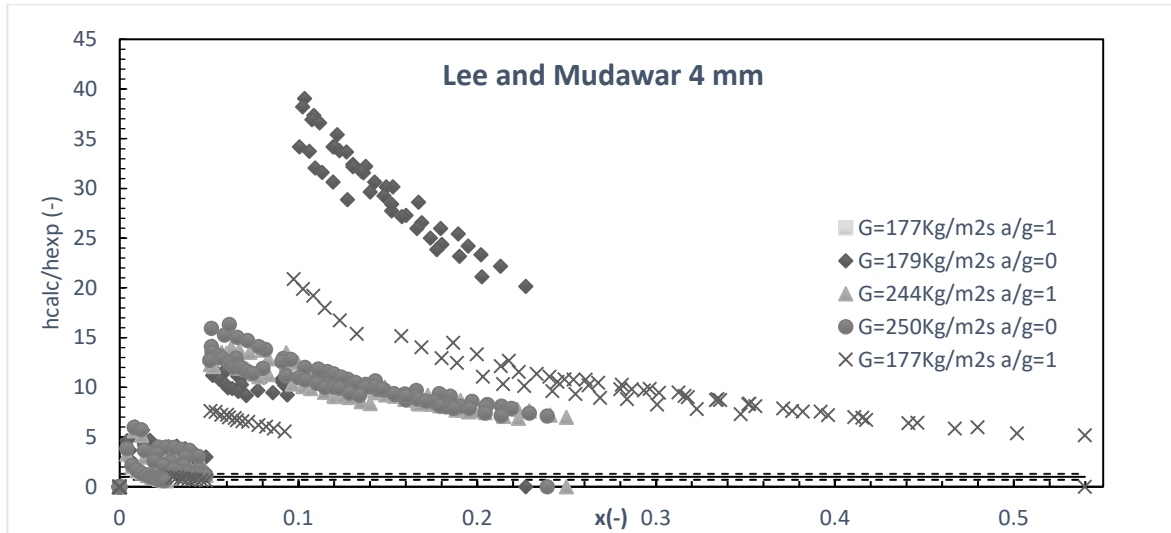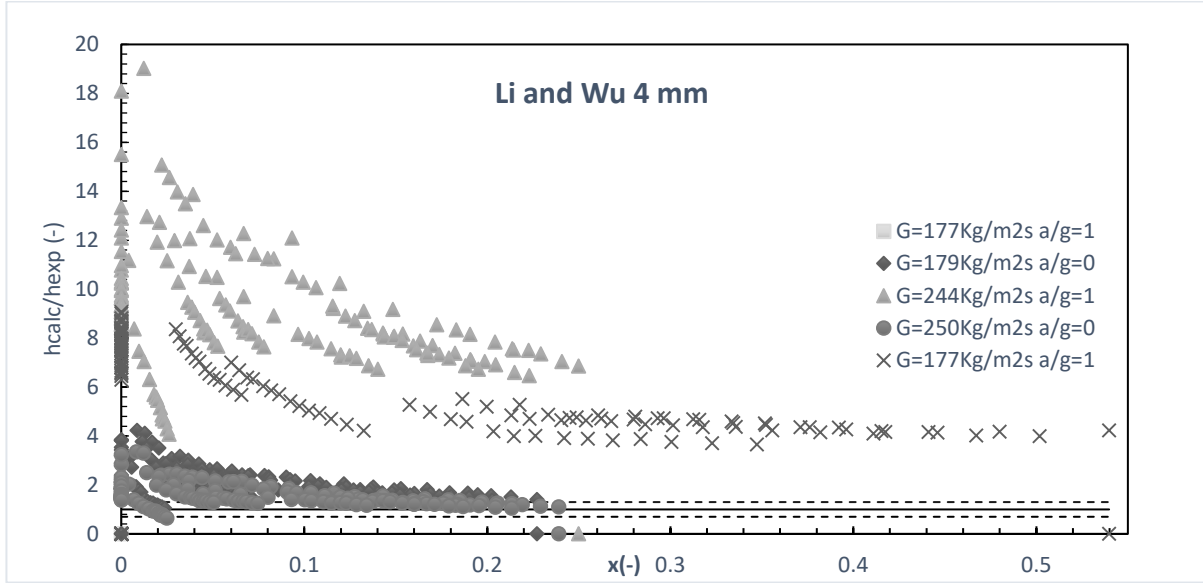

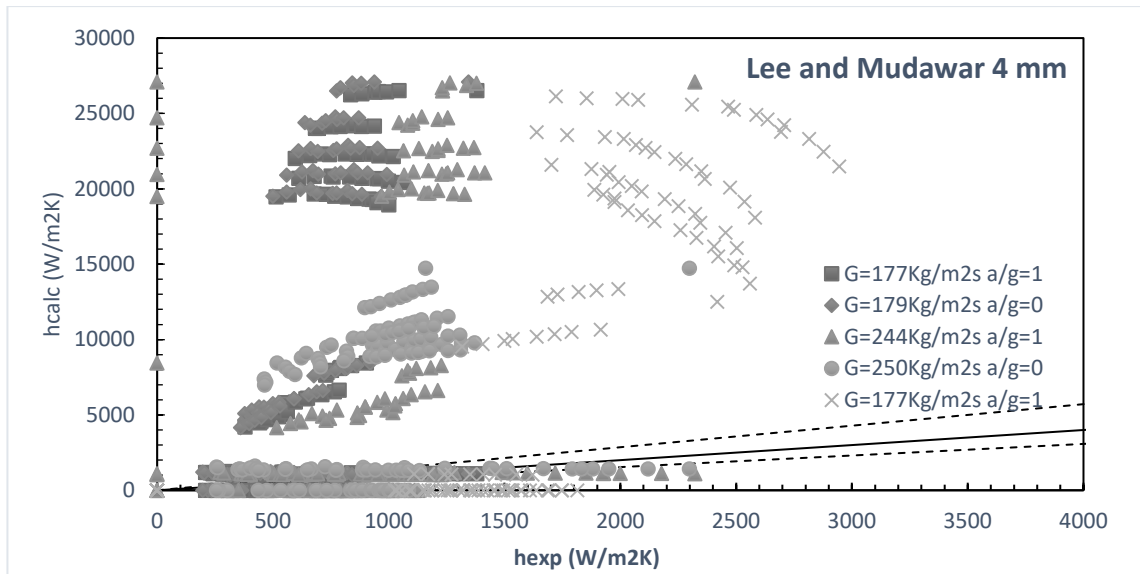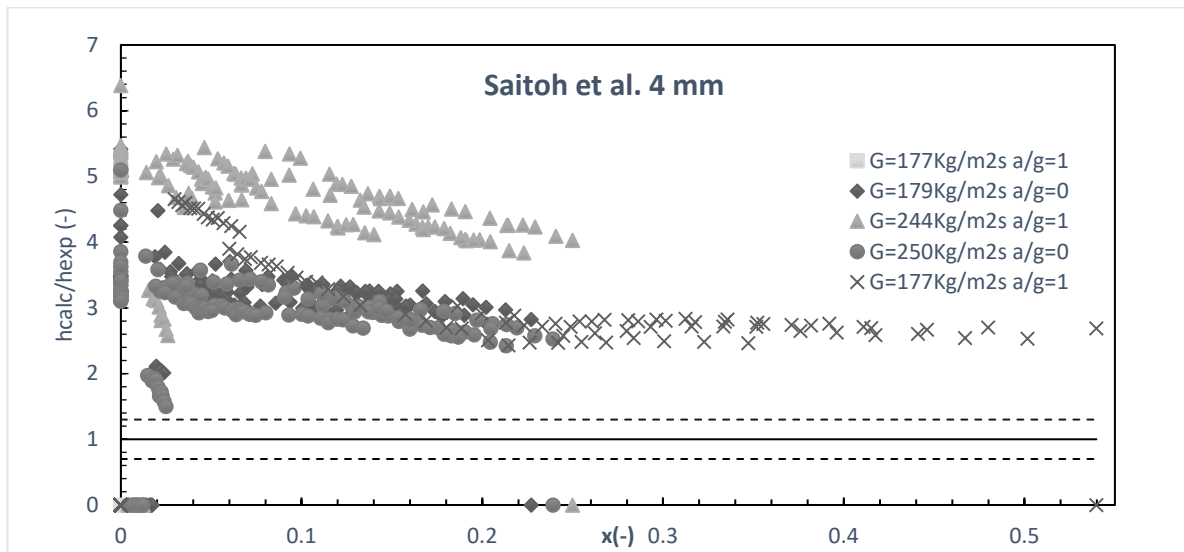Figure 183: Li and Wu 4 mm heat transfer coefficient versus quality
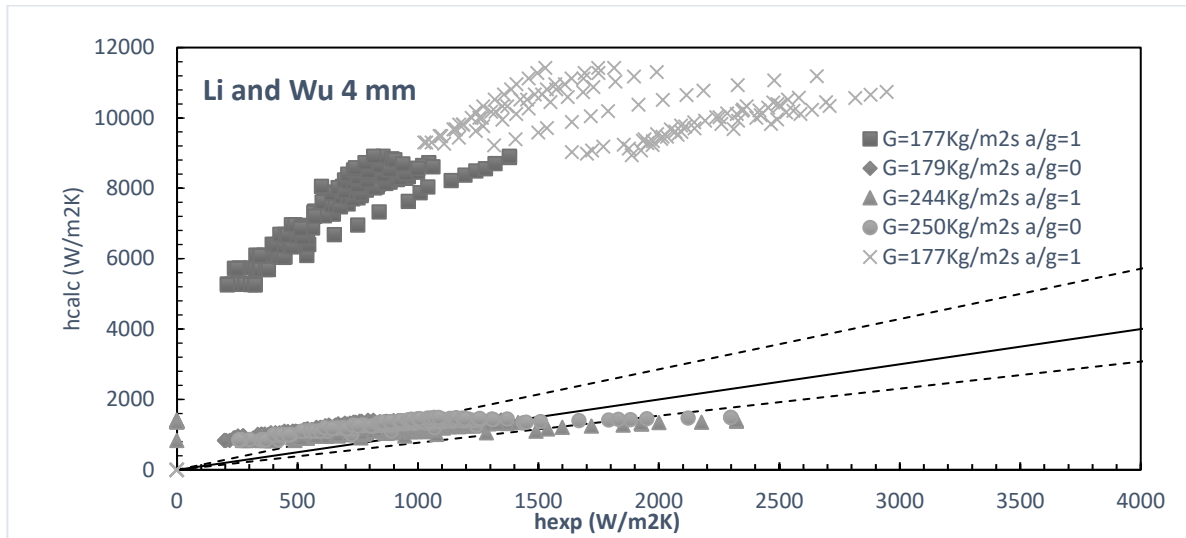
Figure 184: Li and Wu 4 mm experimental heat transfer coefficient versus calculated

Following the results for every test set, that were described in the last paragraph:

- First data set returns *0%* data inside the *30%* error range and an average *RMS* of *1204* with the minimum *RMS* of *932* at intermediate heat fluxes of *24.9 kW/m²*.
- Second data set returns *5%* data inside the *30%* error range and an average *RMS* of *205* with the minimum *RMS* of *157* at intermediate heat fluxes of *24.8 kW/m²*.
- Third data set returns *0%* data inside the *30%* error range and an average *RMS* of *868* with the minimum *RMS* of *713* at intermediate heat fluxes of *38.6 kW/m²*.
- Fourth data set returns *30%* data inside the *30%* error range and an average *RMS* of *144* with the minimum *RMS* of *117* at intermediate heat fluxes of *38.6 kW/m²*.
- Fifth data set returns *0%* data inside the *30%* error range and an average *RMS* of *543* with the minimum *RMS* of *483* at intermediate heat fluxes of *63.2 kW/m²*.

Using the thermodynamic qualities for the fifth set of data gives an *RMS* of *561* and *0%* of data inside the *30%* error band.

The analysis with the Mohamed and Karayiannis correlation returned *580* calculated heat transfer coefficient that compared with the expected ones returns a total *RMS* of *547* and *0.2%* of data within the error band of *30%*. Figures 185-186 shows heat transfer coefficient versus quality and expected heat transfer coefficient versus calculated graphics for every set with corrected vapor quality.
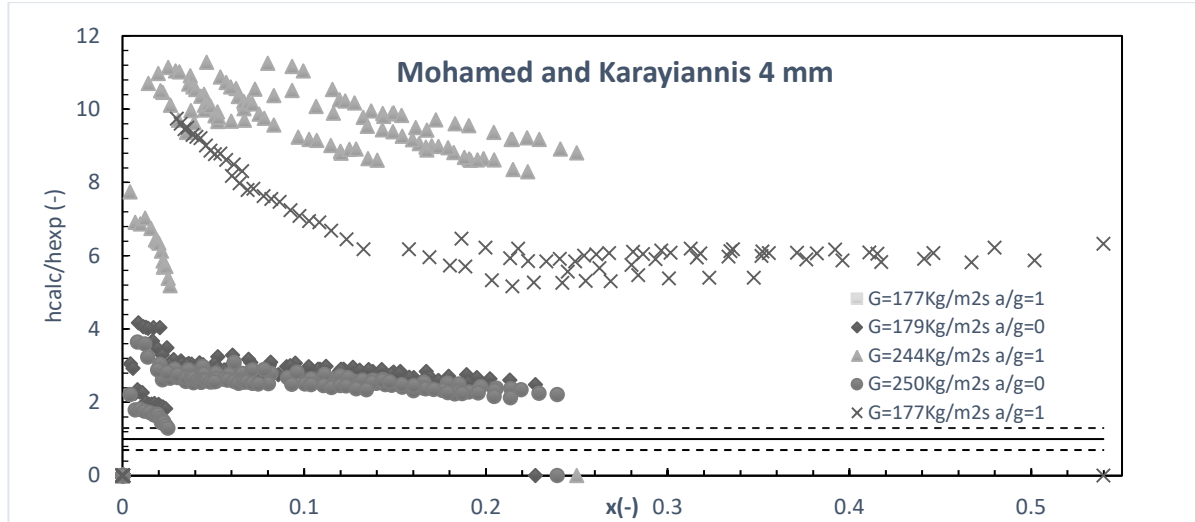
Figure 185: Mohamed and Karayiannis 4 mm heat transfer coefficient versus quality

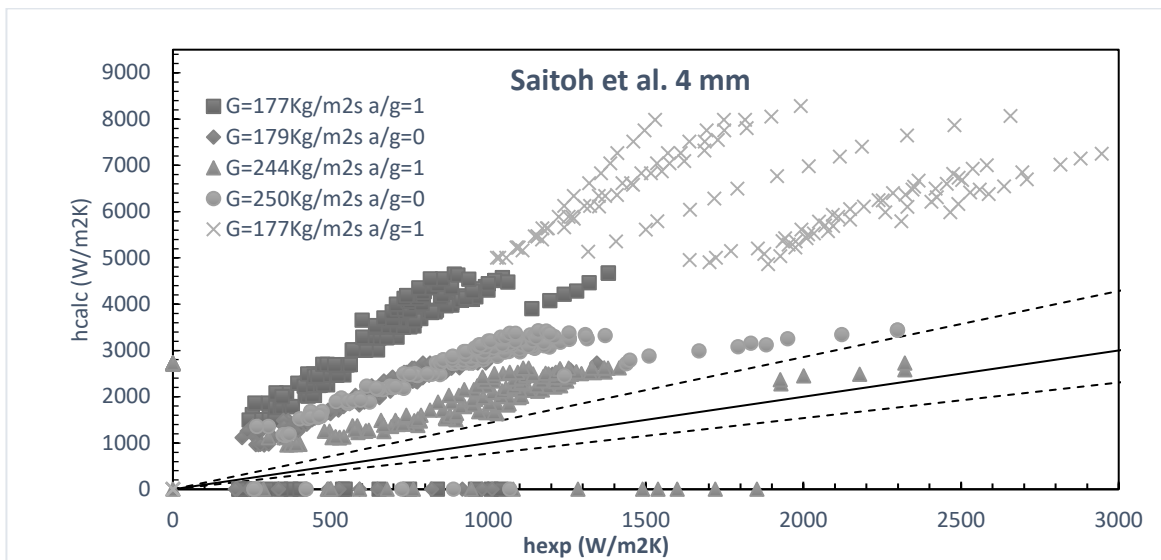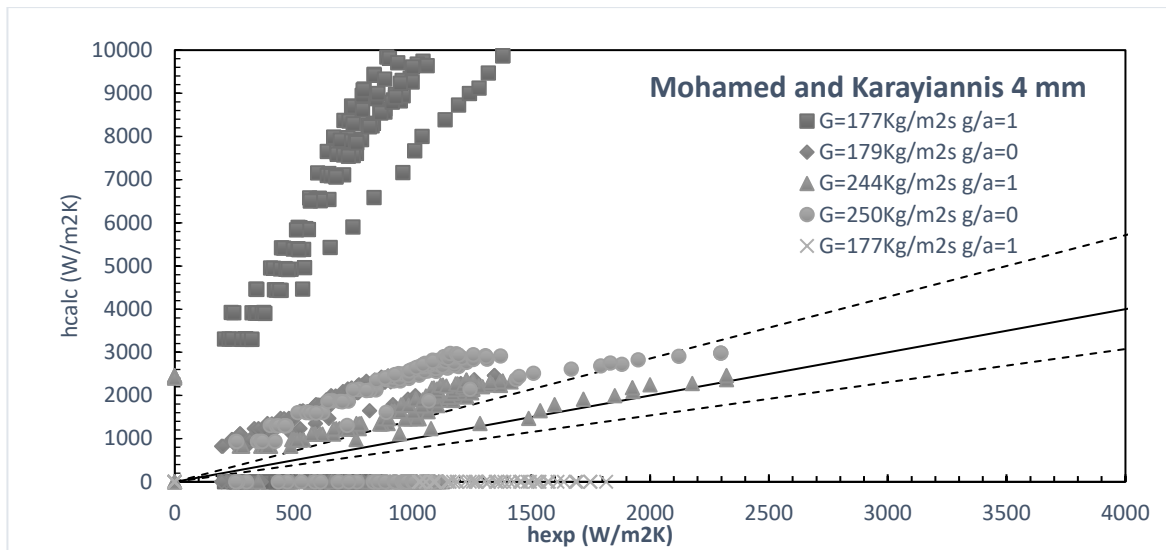Figure 186: Mohamed and Karayiannis 4 mm experimental heat transfer coefficient versus calculated

Following the results for every test set, that were described in the last paragraph:

- First data set returns *0%* data inside the *30%* error range and an average *RMS* of *1058* with the minimum *RMS* of *986* at intermediate heat fluxes of *24.9 kW/m²*.
- Second data set returns *0%* data inside the *30%* error range and an average *RMS* of *285* with the minimum *RMS* of *262* at intermediate heat fluxes of *24.8 kW/m²*.
- Third data set returns *0%* data inside the *30%* error range and an average *RMS* of *934*

with the minimum *RMS* of *877* at intermediate heat fluxes of *38.6 kW/m²*.

- Fourth data set returns *0.83%* data inside the *30%* error range and an average *RMS* of *244* with the minimum *RMS* of *225* at intermediate heat fluxes of *38.6 kW/m²*.
- Fifth data set returns *0%* data inside the *30%* error range and an average *RMS* of *710* with the minimum *RMS* of *692* at intermediate heat fluxes of *63.2 kW/m²*.

Using the thermodynamic qualities for the fifth set of data gives an *RMS* of *58* and *6.67%* of data inside the *30%* error band.

6.4. BO.E.MI.A pressure drops

6.4.1. Single-phase transient flow

Assessing the equation for single phase transient pressure drop a good agreement were obtained: 100% of the predicted data (79 points) have an error <30%, the MAPE is 4.71% and the MPE 0.79%. However, the pressure drop values are quite close to the differential pressure instrument error, ±510 Pa, both in 100 and 200 mm channels, thus the measurements may be affected by an experimental error that can strongly affect the model uncertainty. A graphical representation of the results is shown in Figure 189:
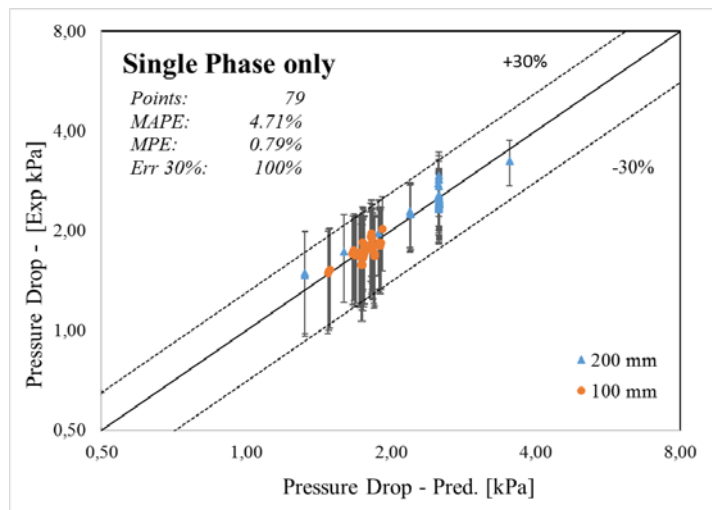
Figure 187: Pressure drop, experimental vs predicted in 100 mm (orange) and 200 mm (blue) tubes.

During the experiment, the average measured single-phase pressure drops were about 2.3 kPa for the 200 mm tube and 1.7 kPa for the 100 mm. The maximum and minimum values were respectively 3.95 kPa and 1.49 kPa for the 200 mm tube and 1.76 kPa and 1.44 kPa for the 100 mm tube. Comparing the results with the laminar and turbulent equations, the experimental data are respectively ÷1/3 of the laminar results and ÷15 times compared to the turbulent. Thanks to its good agreement, before the ONB point, once the void fraction is calculated, it can be used in any of the available pressure drop models. However, must be noted that the single-phase pressure drops are quite low (few kPa), thus the instrumentation error is high if compared with the pressure drops. If all the 139 subcooled points (subcooled boiling only) are considered in single phase, the pressure drop is lower than the expected, as shown in Figure 188. Despite the average enthalpy is lower than the saturation value and the equilibrium quality x_{eq} is negative, the single-phase model is not able to predict the pressure drops in the subcooled flow.
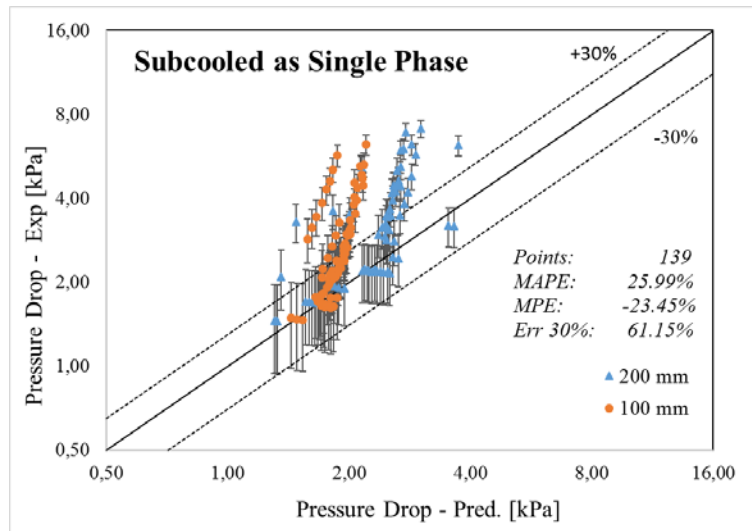
Figure 188: Single-Phase pressure drops

6.4.2. Subcooled flow boiling

The assessments for the subcooled flow boiling equations of Table 8 are reported in Table 36, where all the points are assessed considering the saturated correlations of Müller-Steinhagen and Heck, Friede, Lockhart-Martinelli, Chisholm and Chawla calculated with the vapour quality and void fraction from, and the literature correlations of Kim-Mudawar, Owens-Schrock and Tong, specifically developed for subcooled flow boiling. The partial results for the total pressure drops in the 100 mm and the 200 mm tubes are shown in in Tables 37 and 38, respectively.

Table 36: Global results for subcooled flow foiling points with new-model and literature subcooled correlation

Global (139 points)								
	Present methodology					Subcooled boiling correlations		
Sub-cooled boiling model	Chisholm	Friedel	Müller-Steinhagen and Heck	Lockhart-Martinelli	Chawla	Owens-Schrock	Tong	Kim-Mudawar
MPE	-2,83%	13,48%	22,41%	-32,25%	51,30%	-13,78%	26,09%	-118,77%
MAPE	21,57%	19,02%	24,12%	40,35%	51,32%	32,78%	29,05%	128,40%
±30%	79,86%	76,26%	67,63%	61,87%	15,11%	65,47%	52,52%	20,86%

Table 37: 100mm results for subcooled flow foiling points with new-model and literature subcooled correlation

100 mm (76 points)								
	Present methodology					Subcooled boiling correlations		
Subcooled boiling model	Chisholm	Friedel	Müller-Steinhagen and Heck	Lockhart-Martinelli	Chawla	Owens-Schrock	Tong	Kim-Mudawar
MPE	-2,44%	14,87%	24,44%	-33,75%	51,38%	-10,46%	29,89%	-107,18%
MAPE	20,82%	17,45%	24,44%	40,42%	51,38%	28,64%	29,89%	111,78%
±30%	78,95%	78,95%	68,42%	60,53%	15,79%	73,68%	52,63%	19,74%

Table 38: 200mm results for subcooled flow foiling points with new-model and literature sub-cooled correlation

200 mm (63 points)								
	Present methodology					Subcooled boiling correlations		
Subcooled boiling model	Chisholm	Friedel	Müller-Steinhagen and Heck	Lockhart-Martinelli	Chawla	Owens-Schrock	Tong	Kim-Mudawar
MPE	-3,29%	11,81%	19,95%	-30,44%	51,20%	-17,79%	21,50%	-132,76%
MAPE	22,47%	20,90%	23,72%	40,27%	51,25%	37,78%	28,03%	148,45%
±30%	80,95%	73,02%	66,67%	63,49%	14,29%	55,56%	52,38%	22,22%

The subcooled boiling pressure drops trends by using the Kim and Mudawar and Owens and Schrock and Tong correlations, are shown in Figure 189; The same trends for the proposed methodology, adopting different models, are shown in Figure 190.
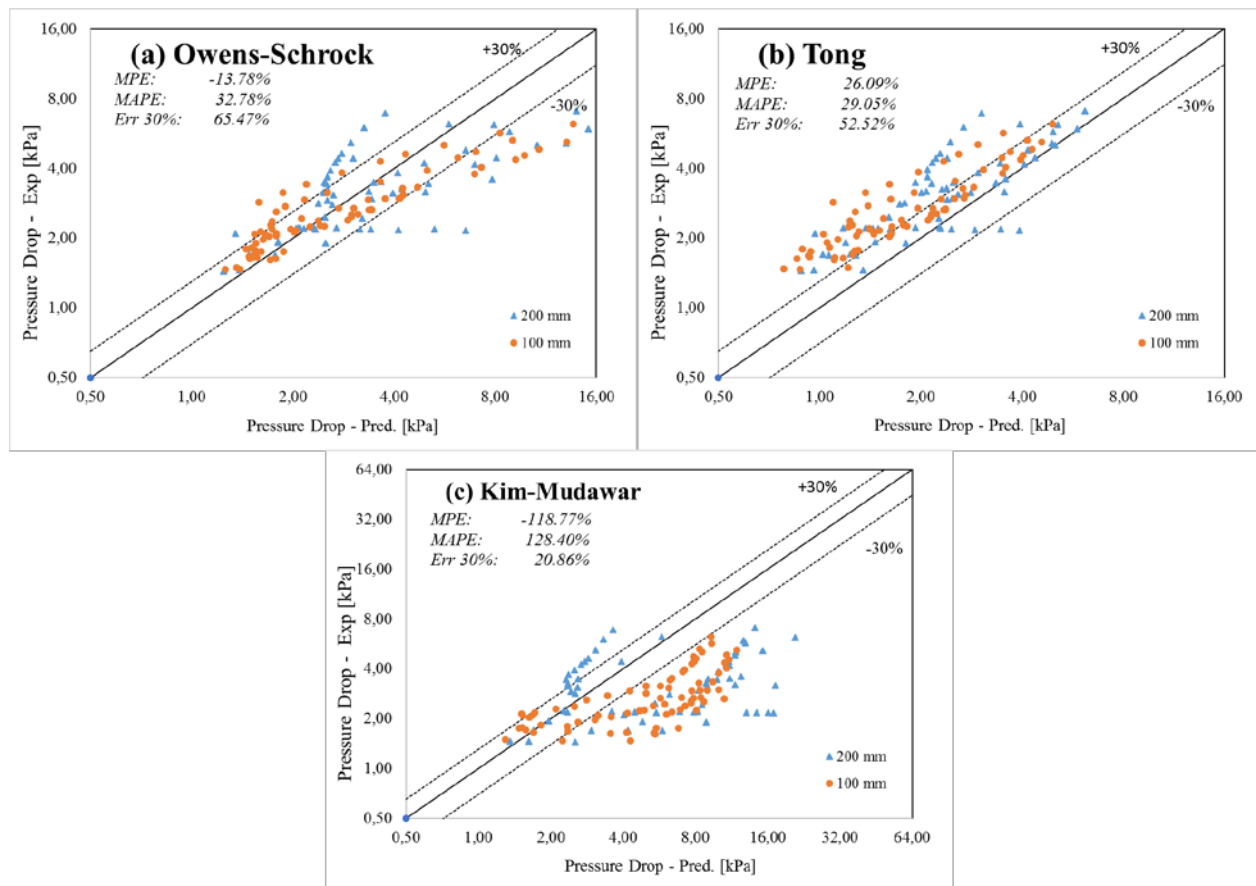
Figure 189: Pressure drop prediction for specific subcooled boiling correlations: (a) Owens-Schrock, (b) Tong and (c) Kim-Mudawar.
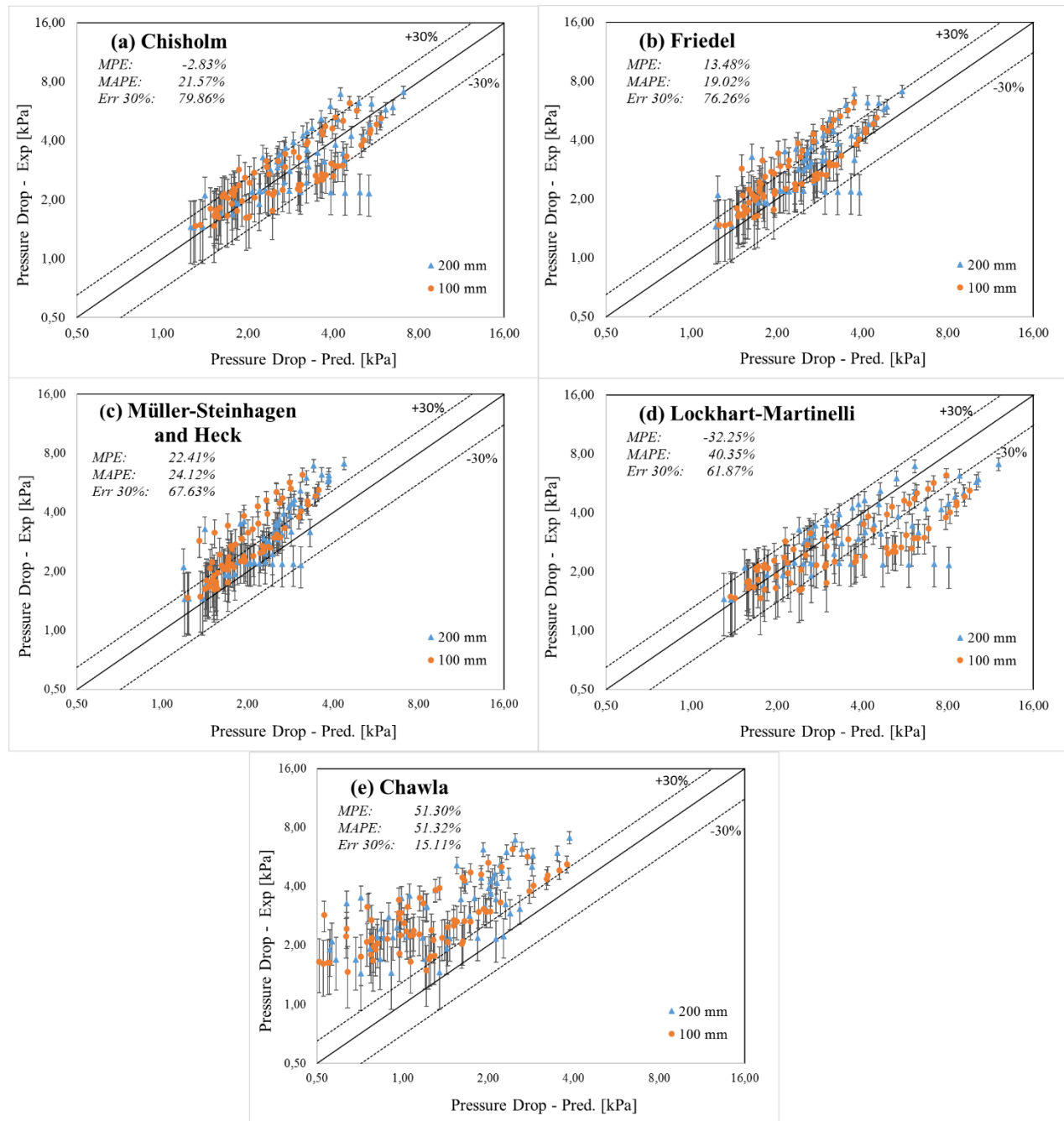
Figure 190: Pressure drop predictions with the applied methodology: (a) Chisholm, (b) Friedel, (c) Müller-Steinhagen and Heck , (d) Lockhart-Martinelli , and (e) Chawla.

The average experimental error is ±9.5%, ranging between a minimum of ±3% for high pressure drop values and ±35.4% for the lower ones.

From Figures 189, 190 and the results in Tab. 36, it appears how the analysed experimental data are well predicted when the Chisholm correlation is used. It presents a MAPE of 21.57% and a MPE of -2.83%, and it is capable of predict up to 79.86% of the points with an error lower than ±30%. The best results are for the 100 mm tube, where the Chisholm correlation obtain a

MAPE of 20.82% and a MPE of -2.44% with the 78.95% of data below the 30% error. How showed by Figures 189-190 and Tab. 36-37-38 the MAPE alone is not always the best instrument to evaluate the prediction accuracy for a correlation, alone cannot fully describes the quality of a prediction. In fact, any deviation from the mean values is not evident by this statistical instrument, neither the error sign. The lower MAPE is for Friedel correlation, but the trends, the MPE and the ±30% error bands are better for Chisholm correlation how showed in Figure 190. The best results obtained from the literature specific subcooled correlations comes from the Owens-Schrock correlation where the MPE is -13.78%, MAPE 32.78 and 65.47% of the data has an error lower then ±30%. The correlations have a wider error then the ones proposed within the methodology and show a wider dispersion, particularly marked for the 200mm data. The present conclusion agrees with Friedel and Tribbe and Müller-Steinhagen, where the Chisholm correlation was identified as the most suitable one, performing very well in calculating pressure drops for $\mu_l/\mu_g > 1000$ and with mass velocities greater than 100 kg/m^{2}s, as in the BOEMIA set-up.

6.4.3. Saturated flow boiling

At saturation is possible to use another correlation to best fit the experimental data. The chosen correlations are the same for subcooled flow boiling: Müller-Steinhagen and Heck, Friedel, Lockhart-Martinelli, Chisholm and Chawla. For the assessment, the vapor qualities and the real void fraction are used following the proposed methodology. If the equilibrium quality is higher than the vapor quality, the equilibrium quality is used in the correlations, instead the void fraction is always calculated regardless the kind of quality used. Table 39 reports global results for the total pressure drops (only for the point when the saturation in reached) and Tables 40-41 respectively shows the results for the 100 mm and 200 mm tubes.

Table 39: Global results for saturated flow foiling points

Global (84 points)					
	Present methodology				
Subcooled boiling model	Lockhart-Martinelli	Chisholm	Chawla	Friedel	Müller-Steinhagen and Heck
MPE	-15,71%	29,55%	44,09%	45,43%	56,77%
MAPE	26,54%	30,25%	44,09%	45,43%	56,77%
±30%	70,24%	44,05%	15,48%	14,29%	0,00%

Table 40: 100mm results for saturated flow foiling points

100 mm (24 points)				
	Present methodology			
Subcooled boiling model	Lockhart-Martinelli	Chisholm	Chawla	Friedel	Müller-Steinhagen and Heck
MPE	-20,35%	24,26%	39,05%	41,28%	53,23%
MAPE	24,67%	25,73%	39,05%	41,28%	53,23%
±30%	75,00%	54,17%	41,67%	20,83%	0,00%

Table 41: 200mm results for saturated flow foiling points

200 mm (60 points)				
	Present methodology			
Subcooled boiling model	Lockhart-Martinelli	Chisholm	Chawla	Friedel	Müller-Steinhagen and Heck
MPE	-13,86%	31,67%	46,11%	47,09%	58,19%
MAPE	27,29%	32,06%	46,11%	47,09%	58,19%
±30%	68,33%	40,00%	5,00%	11,67%	0,00%

The saturated flow boiling pressure drops trends by using the proposed methodology, adopting different models, are shown in Figure 191.
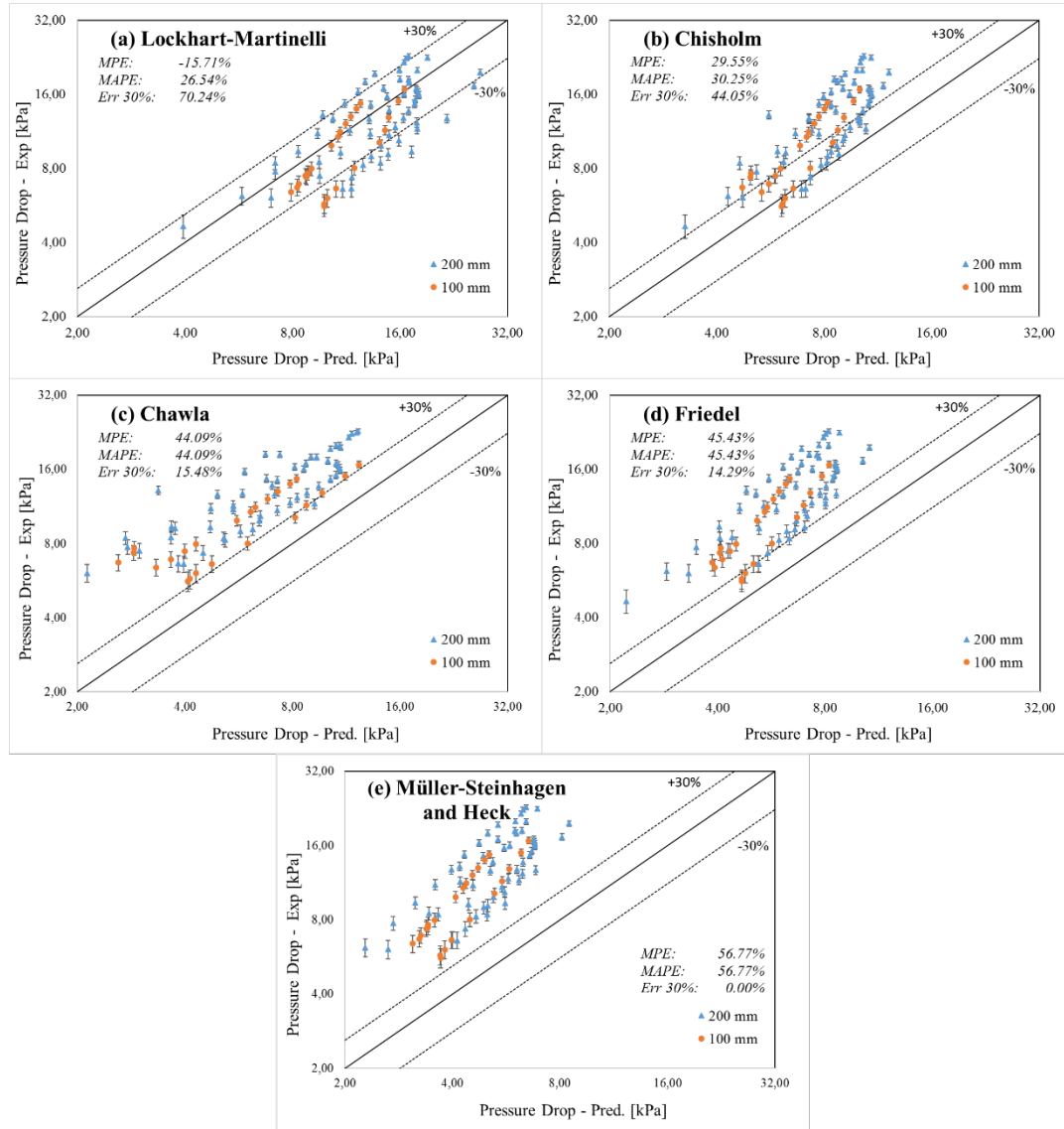
Figure 191: Saturated pressure drop predictions predicted: (a) Lockhart-Martinelli, (b) Chisholm, (c) Chawla, (d) Friedel and (e) Müller-Steinhagen and Heck.

Figure 191 and the results in Table 39 show how the predictions underestimate the experimental data in most of the correlations, suggesting using a higher void fraction in the channel. However, the Lockhart-Martinelli correlation, that overestimated the data in subcooled flow boiling region, had a low error at saturated conditions; its MPE is -15,71%, the MAPE 26,54% and 70,24% of the data have an error lower than ±30%. The second-best correlation is the Chisholm one, with and MPE of 29,55% a MAPE of 30,25% and 44,05% of the data with an error lower than ±30%. It suggests using the Lockhart-Martinelli correlation to obtain a good prediction and Chisholm correlation in first approximation. A further study should be a better calculation of the void fraction to use always the same correlation for all the subcooled and saturated length.

6.4.4. Full methodology

Merging the best results obtained from the single phase transient pressure drop obtained, the best results from subcooled flow boiling model of Chisholm and the best saturated flow boiling results obtained from Lockhart-Martinelli (both calculated with the void fraction and vapor quality), the data in Tab. 42 is obtained. The 100 mm tube get the best results with an MPE of -5.25% a MAPE of 16.60% and 84.40% of the data with an error lower than ±30%. The global results, for both 100 mm and 200 mm channels, are quite good and near to the 100 mm tube results; the MPE is -5.88%, MAPE is 18.54% and 82.45% of the data has an error lower than ±30%.

Table 42: Global results for the methodology

Methodology global results			
	100 mm	200 mm	Global
Points	141,00	161	302
MPE	-5,25%	-6,43%	-5,88%
MAPE	16,60%	20,24%	18,54%
±30%	84,40%	80,75%	82,45%

The total pressure drops trends obtained by using the proposed methodology, and adopting the transient model for single-phase, Chisholm for subcooled boiling and Lockhart-Martinelli for saturated boiling, as described above, are shown in Figure 192. It is possibile to use also Friedel in the methodology, The choice of using Chisholm is due to the lower MPE joined to the biggest number of data predicted with an error lower of 30%.
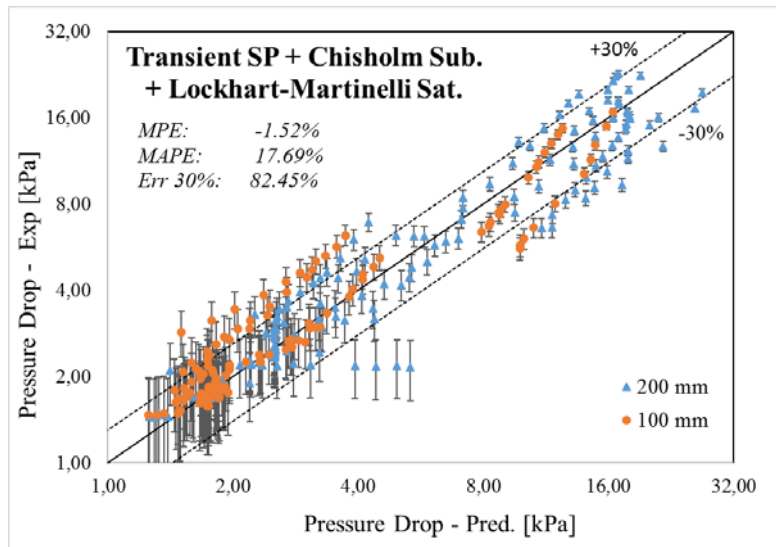
Figure 192: Global methodology drop predictions; Transient pressure drop for Single Phase, Chisholm for subcooled flow boiling and Lockhart-Martinelli for saturated flow boiling.

The average pressure drops (experimental) was 3.69 kPa in the 100 mm channel, the minimum value was 1.47 kPa and the maximum 16.74 kPa; for the 200 mm channel, the three values were: 6.87 kPa, 1.44 kPa and 22.87 kPa, respectively.

7. Conclusions

This thesis presented an assessment for seventeen correlations as well as two mechanistic models and their application on microgravity and normal gravity on two different experimental facilities. The assessment has been conducted using local heat transfer coefficients calculated along the experimental section on the thermocouples position and with the pressure drops between the entrance and the end of experimental sections.

7.1. Heat transfer

The comparison demonstrated that all examined correlations are not general enough and/or could not predict the current experimental data with a reasonable accuracy. A depth remark for MICROBO is necessary, due to microgravity applicaiton, for every correlation to understand the possible causes of a bad prediction or the insufficient accuracy of the model/correlation. However, no one of the correlation is expected to work with *FC-72* as refrigerant fluid. To examine the difference in data between the micro and standard gravity, a brief description of the results for every model and with every section is proposed.

7.1.1. BO.E.MI.A

A comparison of several models and correlations available in the literature, for flow boiling heat transfer in micro and macro tubes, has been performed using experimental data obtained by ENEA through the facility BOEMIA on 1 mm tubes, 100 mm and 200 mm long. In this preliminary phase of the study, only saturated boiling points have been considered. Macro scale correlations provide quite better results than expected, especially the Chen correlation that is the oldest one. However, the micro scale correlations provide a better agreement than the macro scale ones. The correlations of Zhang et al. and Li and Wu give more than 83% of data within ±30% error band, with a MAPE lower than 27%. This behavior is due to the dimension of the 1 mm channel that is close to the micro scale. The mechanistic "Three-zone model" provides a better agreement than the "Slug-Coalescence model" with more experimental points. More experiments are needed with different fluids to increase the database range.

7.1.2. MicroBo

Also, the mechanistic models failed to predict the experimental data of all tubes, especially the Slug-Coalescence model, which may be attributed to the fact that these models are not totally based on theory but depend on empirical parameters. They are semi-mechanistic models and needs to be fitted on the experimental section.

The Three-Zone model returns the best results for the *4 mm* test section in terrestrial gravity conditions when the vapor and thermodynamic quality are positive. Begin the model theoretically independent from gravity, the *2 mm* test section the model returns almost the same approximation micro and normal gravity with *+1%* error in the zero gravity case. Instead for *4 mm* the prediction is worse. Globally the model needs to be adapted with *FC-72* refrigerant e with *Pyrex*

tube, by tuning the empirical parameters. up to *50%* of data is well predicted (when the model is used inside their normal hypothesis). Globally the *RMS* is around *200* and *10%* of data con be predicted within the *30%* error range.

The Slug-Coalescence model returns bad results. Standard parameters are not suitable with the analyzed experimental section and its operating fluid. The model is developed for the transition between the slug and bubble coalescence regime that usually appear at positive qualities far from the experiment's range. In addition, the model works only in micro-channels where the superficial shear stress is predominant. This situation rises with high mass flux and reducing the channel size. The error magnitude makes the analysis of the gravity related phenomena totally impossible. Globally the RMS is around 800 and 1.5% of data can be predicted within the 30% error range.

Macro scale correlations are more suitable in the *4 mm* channel where the transition between micro and macro scale is not clearly defined. Most of the correlation does not take in account the gravity term. Chen correlation returns the better results, followed by Shas and Liu and Winterton correlation.

The Chen correlation returns the better results for both *2 mm* and *4 mm* channel in all the analyzed cases. The model approximate data better in the terrestrial gravity experiments. The better results were obtained with *4 mm* tube excluding with the higher heat fluxes. Moreover, the difference between micro and standard gravity data reduces with the decrement of channel diameter. Gravity term does not appear in the correlation expression. Globally the *RMS* is around *95* and *45%* of data is predicted well. The model approximate data better in the terrestrial gravity experiments with an average increment of *+5\10%* in the error range e *-10\100* in the global *RMS*. The better results were obtained with *4 mm* tube excluding for the last data set, with the higher heat fluxes, that returns *0%* of data within the *30%* error range.

The Shas correlation works well with the database, the better prediction is obtained with *4 mm* tubes. The predictions are better in the terrestrial gravity experiments. Gravity term does not appear in the correlation expression. The global *RMS* is around *215* and *27%* of data are in the *30%* error band.

Gungor and Winterton correlation does not returns a good prediction on the database. The prediction boundary of the correlation is out of the experimental range and *FC-72* was not included in its originally experimental data. The prediction error is too high to obtain some information between gravity and zero gravity conditions from the model. The difference between micro and standard gravity data reduces with the decrement of channel diameter. Gravity term does not appear in the correlation expression. The global *RMS* is *370* and *2%* of data are predicted within the *30%* error band.

Kandlikar's correlation returns similar results to the Gungor and Winterton correlation. The better results are with the *2 mm* channel for the higher mass and thermal fluxes. The gravity presence improves the results. The correlation use a fluid specific factor that was impose arbitrary to *1* and takes into account the gravity force. The global *RMS* is around *350* and 2.5% of data are within the *30%* error range. The gravity presence improves the results of about *+2%* on the data between the *30%* error ranges.

The Liu and Winterton correlation works quite well with the database. The best results are obtained with *4 mm* channel and in standard gravity conditions. The model does not take into account the gravity term. Moreover, the difference between micro and standard gravity data reduces with the decrement of channel diameter. The correlation works quite well with the database and returns almost *32%* of data within the *30%* error bands with a global *RMS* of *145*. The difference in the prediction between the *2 mm* and *4 mm* channels is about *-30* on *RMS* and *-10%* of data between the error bands. Moreover, the difference from standard and micro gravity conditions *+3\5%* in prediction capacity (data between error bands of *30%*) and *2\50* for accuracy (*RMS*).

Micro scale correlations are theoretically more suitable in the *2 mm* channel where the transition between micro and macro scale is more accentuated to micro scale. Also in this case most of the correlation does not take in account the gravity therm. Zhang, Kandlikar, Bertsch and Mikielewicz correlation returns the better results. The two best correlations for general purpose are from Bertsch and Mikielewicz. The difference in the results is important to define the transition between micro and macro scales.

Lazarek and Black correlation works better with the *2 mm* channel, how expected, and with higher heat and mass fluxes. Moreover, the difference between micro and standard gravity data reduces with the decrement of channel diameter. This difference is important because denotes how the reduction in channel size is correlated with the increment of superficial forces despite the buoyancy. The correlation is simple (it remembers the Gnieliwski correlation of Nusselt number) and does not consider the gravity therm. Globally the correlation returns an *RMS* of *300* and *2.5%* of data within the error range *of 30%*. The difference in *RMS* between the *2 mm* and *4 mm* channels is about *+110* and the data between *30%* error bands increment is about *5%*. The difference between zero gravity and terrestrial gravity in the predicted data is about *1-50* on *RMS* and *1-2%* of data within the *30%* error bands.

Tran's correlation not predict well the data with the 4mm channel. The correlation is quality independent, results does not change using or not the modified quality. Globally the *RMS* is about *550* and *1.5%* of data is between the *30%* error bands. However if considered only the *2 mm* channel the *RMS* increase up to *273* and *8%* of data predicted within the *30%* error bands with higher mass and heat fluxes.

Kew and Cornwell correlation not predict very well the heat transfer coefficients. The correlation is projected to work in the micro scale and in fact it predicts better the results with the *2 mm* channel, especially at high mass and bulk flux. Moreover, the difference between standard and micro gravity is not evident. The correlation does not consider the gravity force and is designed to work with *R141b*. The correlation not predict very well the heat transfer coefficients, globally only *4%* of data are predicted into the *30%* error bands and the average *RMS* is about *300*.

Warrier et al. better prediction relates to the reduction on the scale. The better prediction is for higher heat fluxes for 4mm channel. This correlation does not consider the gravity term. The correlation returns a global *RMS* of about *150* and *30%* of data within the *30%* error bands. The results improve in the *2 mm* channel where the medium *RMS* is *128* and *43%* of data is predicted within the *30%* error bands. Moreover the difference between predictions in standard gravity

and in micro gravity is about *+20%* of data within the *30%* error bands ad *-15-20* on *RMS* for standard gravity cases.

Kandlikar and Balasubramanian correlation strongly underestimate the heat transfer coefficients. The predictions are more accurate in the *2 mm* channel where the micro scale behavior is more marked. The correlation underestimating the heat transfer coefficients and works better with low heat and mass fluxes. The correlation is based on the Kandlikar correlation for macro scale, it uses a fluid specific factor that was impose arbitrary to *1* and but not takes into account the gravity force. The global *RMS* is *40* and *15%* of data are in the *30%* error bands. In the *2 mm* channel up to *45%* of data is predicted in the *30%* error bands with an average *RMS* of *76*. Moreover, the correlation works better on normal gravity conditions with an increment of *15%* of data within the error bands of *30%* and a difference between the microgravity of *15* points on *RMS*.

Zhang et al. correlation results with the 4 mm channel are better than the *2 mm*. The best predictions are for intermediate heat fluxes and high mass flux. The model accuracy falls quickly with the increment of heat fluxes. The difference between corrected and not corrected quality is negligible. The model does not consider the gravity force. The correlation shows *33%* of data inside the *30%* error bands and an average *RMS* of *75* underestimating the heat fluxes. The results with the 4 mm channel are better than the *2 mm*, another *20%* of data is within the *30%* error bands and *RMS* is improve of *30*. The difference between the normal and micro gravity case is low; *5\10%* of data in the *30%* error range and *1\5* points of *RMS* (in favor of normal gravity).

Lee and Mudawar correlation high overestimate the heat transfer coefficient. The data is in the correct range only for low qualities. This depends on the different structure of the relations with the increment of quality. Probably changing the equation could improve the prediction capacity. However, the best results are for *4 mm* tube with the increment of mass and heat fluxes. The correlation does not consider the gravity force. The correlation high overestimate the heat transfer coefficient and returns a global *RMS* of about *1150* with *7.5%* of data within the error bands of *30%*. The increment of prediction in standard gravity case is about of *1%* of data in the *30%* error range and *40* points on *RMS*.

Saitoh et al. correlation is used outside their projected diameter range and heat fluxes range, in fact the globally results are bad. The *4 mm* results are the worst. However, is interesting to observe that the model take into account the gravity force and works better in the microgravity cases. Only *6%* of data is in the *30%* error bands and the global *RMS* is about *300*.

The Bertsh's correlation predict quite well heat transfer coefficient data. The behavior of this correlation is like Saitoh correlation. The best predicted data are for *4 mm* channel in micro gravity (outside from the declared application range). Instead, for the *2 mm* channel general trend is inverted and the best prediction is with standard gravity data. The correlation works better at high mass flux and heat fluxes. Moreover, the correlation takes into account the gravity force. The Bertsh's correlation predict data with a global *RMS* of *75* and *17%* of data points within the *30%* error bands. The difference between micro e standard gravity in this second case is around *10%* of data inside the 30% error bands and *30* on *RMS*.

Mikielewicz correlation correlation generally works better with *4 mm* tube but the best prediction is with *2 mm*. The application range of this correlation is for both micro and macro scale.

The correlation works better in standard gravity. This correlation considers the gravity force. The correlation predicts quite well the data with *30%* of data within the *30%* error band and an average global value of *75* on *RMS*. The best prediction is with *45%* of data within the *30%* error bands and an average *RMS* of *145*. The correlation works better in standard gravity with a difference up to *+20%* of data inside the *30%* error bands and *60* points on *RMS* value.

Li and Wu correlation has a strange behavior, for the *4 mm* tube the correlation predicts only the data in micro gravity and the best prediction are with the *2 mm* tube is in standard gravity. The correlation is applied inside their application range but with a fluid that was not take in consideration by the author. The prediction capacity improves with heat and mass flux. And the difference with and without gravity is not clear. The model considers the gravity force. The global *RMS* is about *450* and *15%* of data is predicted inside the *30%* error bands. The best prediction with the *2 mm* tube has *36%* of data inside the *30%* error bands and *RMS* of about *52*.

The Mohamed and Karayiannis correlation change with the hydraulic diameter. Both *2 mm* and *4 mm* channel use the same correlation. The *4 mm* channel returns the worst results. Moreover, the correlation considers the gravity effect. The global average *RMS* is about *400* and *8%* of data points are within the *30%* error range. However, the 2 channel returns an *RMS* of about *280* and *15%* of points predicted within the error band of *30%*. The micro gravity predictions return up to *45%* of data within the *30%* error bands and an average *RMS* of *95*.

Most of the correlation returns the expected behavior. Macro correlations works better with the *4 mm* tube and micro scale correlation with *2 mm*. However, there are some exceptions like Mikielewicz, Chen and Liu and Winterton correlation that works always well. This behavior is due to the dimension of the *2mm* channel that is close yet to the macro scale. The prediction power of the correlations is better in standard gravity with some exceptions by Saitoh, Bertsch and Mohamed and Karayiannis. The mechanistic Three-zone model works better in standard gravity. The Slug-Coalescence model does not return satisfying results. The best results are from macro-scale correlations.

7.2. Pressure drops

A flow boiling pressure drop calculation methodology, is described; its main features are the capability to be used also in transition flow and in the use of the non-equilibrium vapor quality instead of the equilibrium thermodynamic quality. The model includes single phase, subcooled and saturated boiling conditions, identifying their boundaries. Employing a third order interpolation curve, the pressure drop for subcooled liquid in transition flow can be calculated. The methodology is based on the work of Delhaye et al.. The model considers the fluid proprieties, the energy, mass and momentum conservation to predict the ONB, OSV points and a hyperbolic function is adopted to calculate the non-equilibrium vapor quality in the subcooled boiling region.

The vapor quality and void fraction are used in the well-known pressure drop models, such as: Friedel, Chisholm, Chawla, Lockhart-Martinelli and Müller-Steinhagen and Heck. The results have been also compared with the correlations from Owens-Schrock, Tong, and Kim-Mudawar , specific for subcooled flow boiling. The best agreement with the ENEA experimental data has

been obtained using a transient model for the Single-Phase flow region, the Chisholm model for the subcooled flow boiling region followed by Lockhart-Martinelli for the saturated flow boiling region. The resulting MAPE is of 18,54%, a MPE of -5,88% and 82,45% of the predicted points with an error lower than 30%. The results are very encouraging because none of the employed correlation was developed specifically for the ENEA database or adapted on it, with the only exception of a small reduction of the Pr number exponent (0.95 instead of 1) in the Frost and Dzakowic correlation for ONB prediction. Further pressure drop correlations that can be used with the proposed methodology are available in the literature. Moreover, all the methodology steps have been checked with an "applicability model", proposed by Delhaye et al. , to assure the compatibility with the fluid and ranges used in the experimental facility.

8. Annex A: Programs Validation

A programs validation is necessary to assure the quality of the obtained results. The validation is made confronting the literature data by Mohamed and Karayiannis (2012), for the Multiple Correlation Model, Thome et al. (2004), for the Three-Zone Model, and Consoloni et al. (2010), for the Bubble Coalescence Model, with the program ones.

The fluid proprieties database used for every model is *RefProp v.9.1*.

8.1. Three-Zone model

The overlook starts with the Three-Zone Model and the results obtained by Thome et al. (2004) confronting heat transfer data with a big database from different studies:

- Lazarek and Black (1982)
- Wambsganss et al. (1993)
- Tran et al. (1996)
- Yan and Lin (1998)
- Bao et al. (2000)
- Baird et al. (2000)
- Lin et al. (2001)
- Agostini (2002)

The validation analysis is made on the data that were obtained from digitalizing published graphs. These results are for a single flow channel except for that of Yan and Lin (1998) and Agostini (2002). As most of the results are for low to intermediate vapor qualities, it will be assumed here that all these data fall in the elongated bubble regime where the Consolini and Thome (2010) model works.

The global parameters for the correlations are showed in the following Tab. (43):

Table 43: Global parameters for Three-Zone model.

Minimum film thickness:	0.3	[μm]
Correcting factor for initial film thickness:	0.29	[-]
Frequency bubble exponential factor:	1.74	[-]
Reference heat exponential factor:	-0.5	[-]
Reference heat multiplication factor:	3328.00	[-]

8.2. Lazarek and Black

The first such study was of Lazarek and Black (1982), who investigated evaporation of *R-113* in a *3.1 mm* stainless tube. They performed experiments starting from subcooled inlet conditions with a two-part vertical test section heated by direct current. The confrontation on the data shows a strong difference on the value of the heat transfer coefficient. The trend is the same, but the value seems to be translated with a proportional factor on the vertical axis. Probably the difference is due to the fluid database used. The following two Figures 193-194 are the original and obtained trends. Dotted lines are for optimized parameters.
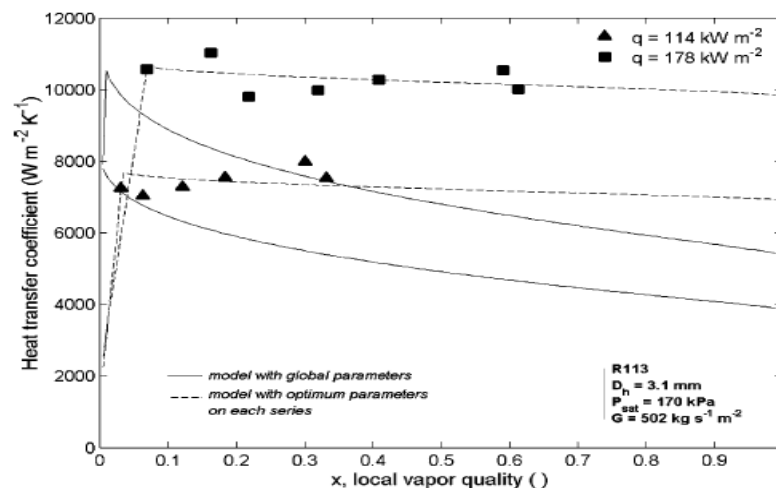
Figure 193: Lazarek and Black (1982) data on Thome et al. (2004) study for *R113*.
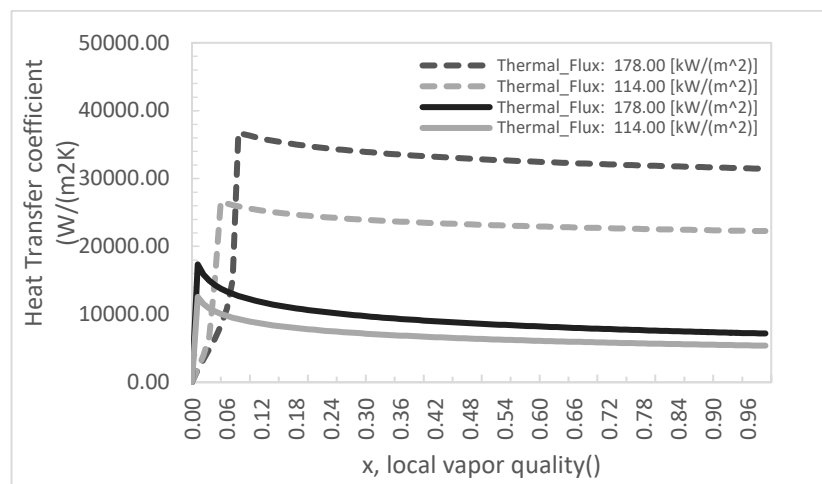
Figure 194: Lazarek and Black (1982) data obtained with *Refprop 9.1* for *R113*.

The specific parameters for the correlations are showed in the following Tab (44):

Table 44: Lazarek and Black (1982) parameters for Three-Zone model.

Minimum film thickness:	1.00E-02	[µm]
Correcting factor for initial film thickness:	1.18	[-]
Frequency bubble exponential factor:	1.80	[-]
Reference heat exponential factor:	-0.54	[-]
Reference heat multiplication factor:	3319.00	[-]

8.3. Wambsganss et al.

Next, is analyzed the study, at Argonne Laboratory, of Wambsganss et al. (1993). They worked on *R-113* evaporating in a circular channel of *2.92 mm*. They used a test section heated by direct current and the liquid enters sub-cooled. They gave a complete description of the test set-up and the diameter of the tube is near the maximum value of the database at the limit of the meso-tube classification. Like the previous analysis the confrontation on the data shows a strong difference on the value of the heat transfer coefficient, the trend is the same, but the mean value seems to be translated with a proportional factor on the vertical axis. Figure 195 show the original trend and Figure 196 the obtained trends. Dotted lines are for optimized parameters.

Figure 195: Wambsganss et al. (1993) data on Thome et al. (2004) study for *R113*.
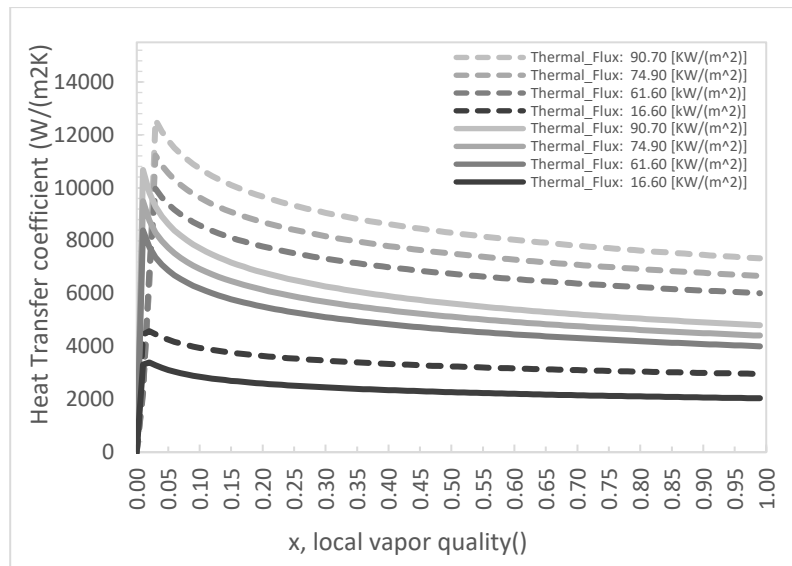
Figure 196: Wambsganss et al. (1993) data obtained with *Refprop 9.1* for *R113*.

The specific parameters for the correlations are showed in the following Table 45:

Table 45: Wambsganss et al. (1993) parameters for Three-Zone model.

Minimum film thickness:	4.70E-01	[μm]
Correcting factor for initial film thickness:	0.77	[-]
Frequency bubble exponential factor:	1.72	[-]
Reference heat exponential factor:	-0.47	[-]
Reference heat multiplication factor:	3298.00	[-]

8.4. Tran et al.

Tran et al. (1996) reported results for *R-12* evaporating in a *2.46 mm* circular channel. The experimental test section was electrically heated with four clamps to change the heated length. After each clamp a thermocouple measured the bulk temperature of the fluid. The trend is the same, but are translated up on the vertical axis. Figures 197-198 show the original trend and the obtained trends. Dotted lines are for optimized parameters.

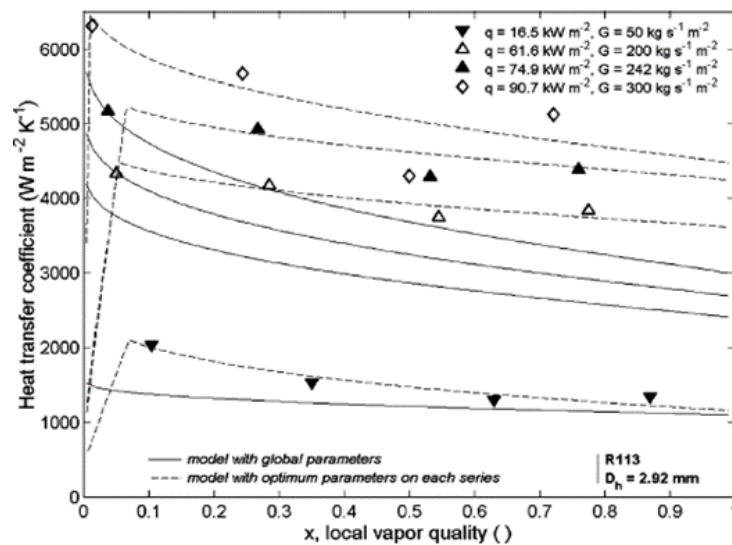Figure 197: Tran et al. (1996) data on Thome et al. (2004) study for *R12*.

Figure 198: Tran et al. (1996) data obtained with *Refprop 9.1* for *R12*.

The specific parameters for the correlations are showed in the following Table 46:

Table 46: Tran et al. (1996) parameters for Three-Zone model.

Minimum film thickness:	3.60E-01	[µm]
Correcting factor for initial film thickness:	0.87	[-]
Frequency bubble exponential factor:	1.71	[-]
Reference heat exponential factor:	-0.57	[-]
Reference heat multiplication factor:	3321.00	[-]

8.5. Yan and Lin

Yan and Lin (1998) investigated flow boiling of *R-134a* inside a bundle of *28* pipes with an internal diameter of *2 mm*. This set of tests is the only one in the database where a preheater has been used to control the vapor quality at the inlet of the test section. The diameter of the tube of the preheater and the heat flux associated are unknown at the location where the bubbles were created. In this study, the mass flux was varied from *50* to *200 kg/m²s*, heat flux from *5* to *20 kW* and saturation temperature from *5* to *31 °C*. For the fourth time the trend is the same but are translated up on the vertical axis. Figures 199-200 show the original trend and the obtained trends. Dotted lines are for optimized parameters.
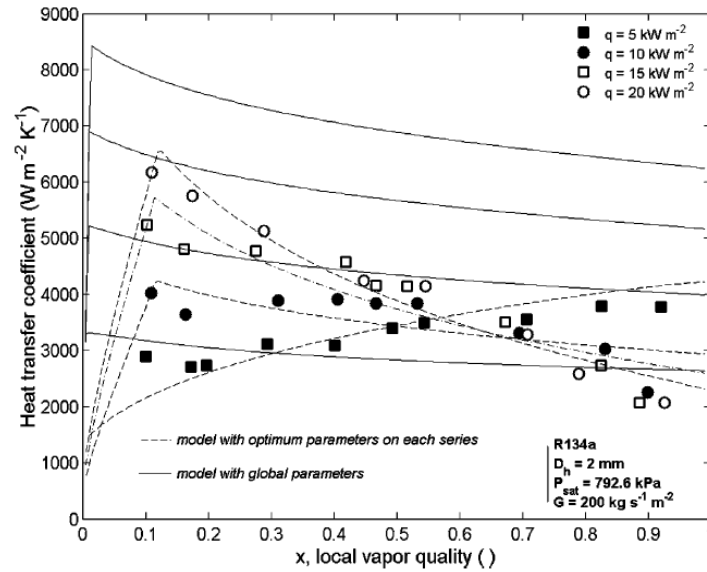
Figure 199: Yan and Lin (1998) data on Thome et al. (2004) study for *R134a*.
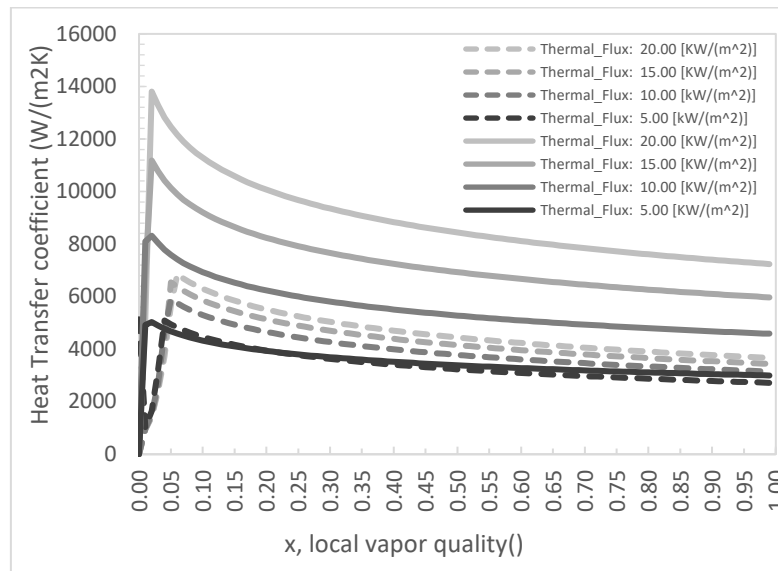
Figure 200: Yan and Lin (1998) data obtained with *Refprop 9.1* for *R134a*.

The specific parameters for the correlations are showed in the following Table 46:

Table 47: Yan and Lin (1998) parameters for Three-Zone model.

Minimum film thickness:	1.92E+00	[µm]
Correcting factor for initial film thickness:	1.20	[-]
Frequency bubble exponential factor:	1.27	[-]
Reference heat exponential factor:	-0.44	[-]
Reference heat multiplication factor:	3551.00	[-]

8.6. Bao et al.

Bao et al. (2000) reported local flow boiling coefficients for *R-11* and *R-123* inside a copper tube with a diameter of 1.95 mm. They used a single piece of tubing, *870 mm* long. The first

400 mm of the tube was unheated, providing an entrance region; that section was followed by a *270 mm* long test zone and then by a *200 mm* unheated exit zone. Tests were made over a wide range of conditions: mass velocities from *50* to *1800 kg/m²s*, vapor qualities from *0%* to *90%*, heat fluxes from *5* to *200 kW/m²* and a range of saturation pressures. For every study the trend is the same but translated up on the vertical axis, the parameters correction does not affect how expected the data. Figures 201-202 show the original trend and Figures 203-204 the obtained trends. Dotted lines are for optimized parameters.
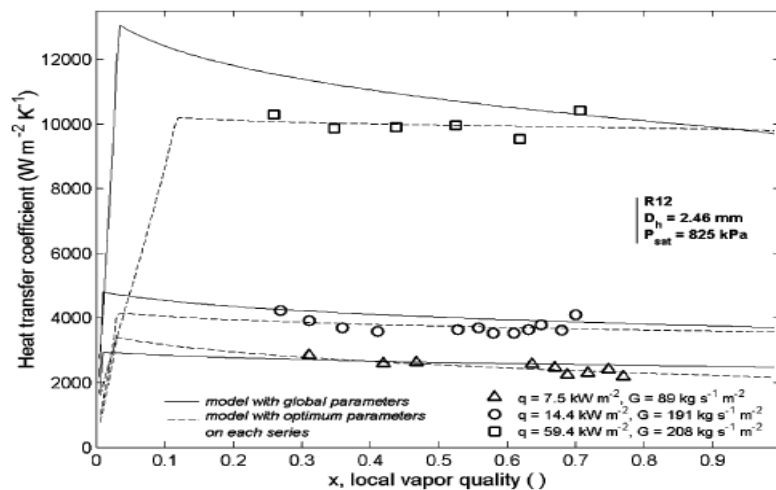

Figure 201: Bao et al. (2000) data on Thome et al. (2004) study for *R11*.

Figure 202: Bao et al. (2000) data obtained with *Refprop 9.1* for *R11*.

Figure 203: Bao et al. (2000) data on Thome et al. (2004) study for *R123*.
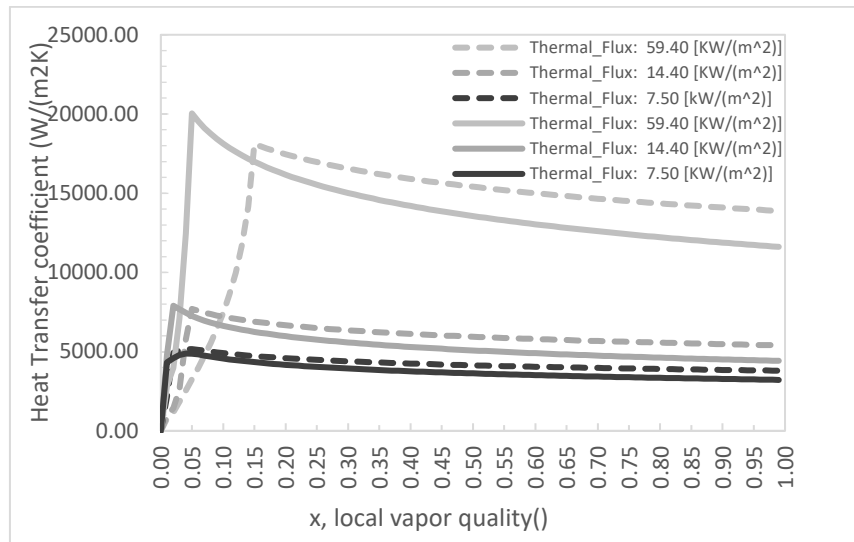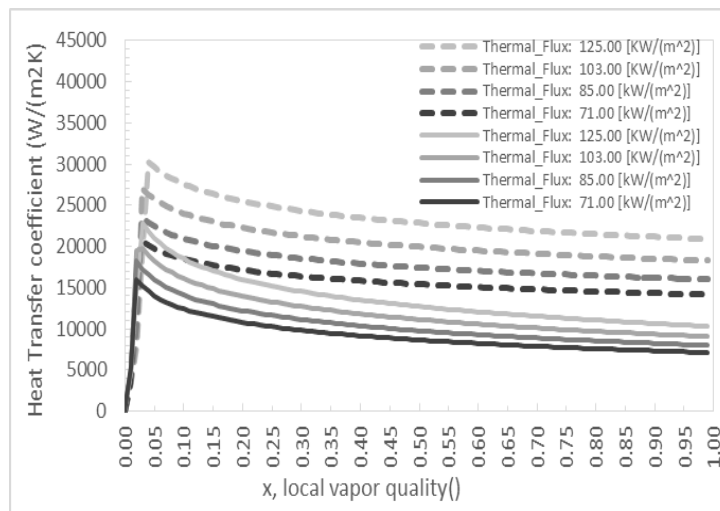

Figure 204: Bao et al. (2000) data obtained with *Refprop* 9.1 for *R123*.

The specific parameters for the correlations are showed in the following tables Tables 48-49.

Table 48: Bao et al. (2000) parameters for Three-Zone model for *R11*.

Minimum film thickness:	2.00E-02	[μm]
Correcting factor for initial film thickness:	0.59	[-]
Frequency bubble exponential factor:	1.72	[-]
Reference heat exponential factor:	-0.59	[-]
Reference heat multiplication factor:	3334.00	[-]

Table 49: Bao et al. (2000) parameters for Three-Zone model for *R123*.

Minimum film thickness:	8.00E-02	[µm]
Correcting factor for initial film thickness:	0.44	[-]
Frequency bubble exponential factor:	1.73	[-]
Reference heat exponential factor:	-0.55	[-]
Reference heat multiplication factor:	3324.00	[-]

8.7. Baird et al.

Baird et al. (2000) studied *R-123* in a *0.92 mm* diameter tube and *CO2* in *1.95 mm* tube. In this work was analyzed the local heat transfer coefficients of *CO2*. In the heating system used the thermal inertial of the tube wall is large. Differently, this time the trend is the same but are translated not only to the vertical axis but also on the horizontal. This phenomenon is due to the starting quality of the model. Figures 205-206 show the original trend and the obtained trends. Dotted lines are for optimized parameters.

Figure 205: Baird et al. (2000) data on Thome et al. (2004) study for *CO2*.
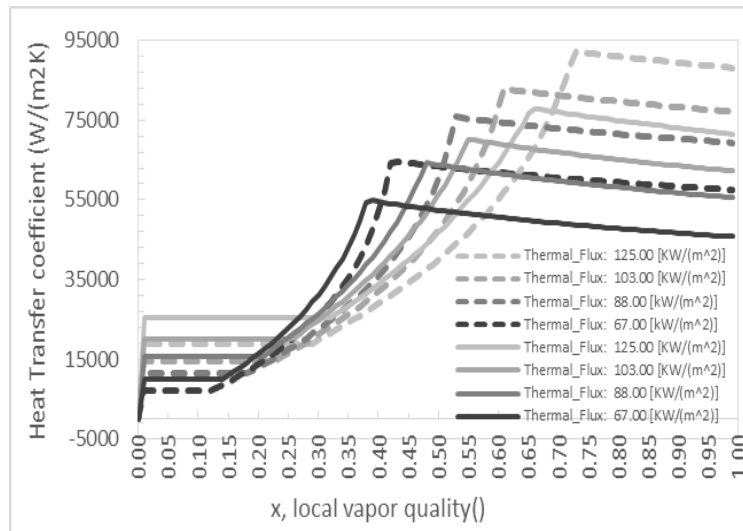
Figure 206: Baird et al. (2000) data obtained with *Refprop 9.1* for *CO2*.

The specific parameters for the correlations are showed in the following Table 50:

Table 50: Baird et al. (2000) parameters for Three-Zone model.

Minimum film thickness:	1.50E-01	[μm]
Correcting factor for initial film thickness:	0.34	[-]
Frequency bubble exponential factor:	1.70	[-]
Reference heat exponential factor:	-0.55	[-]
Reference heat multiplication factor:	3323.00	[-]

8.8. Lin et al.

Lin et al. (2001) database were made on *R-141b* in a vertical *1.1 mm* tube test section. The mass velocity range was from *300* to *2000 kg/m²s* and heat flux range was of *18-72 kW/m2*, however the only presented data was at the mass velocity of *510 kg/m²s*. The outlet pressure of the test section was atmospheric while the inlet pressure varied from *1.34* to *2.19 bar* depending the flow conditions. The trend is the same, but the value seems to be translated with a proportional factor on the vertical axis. The following Figures 207-208 are the original and obtained trends. Dotted lines are for optimized parameters.
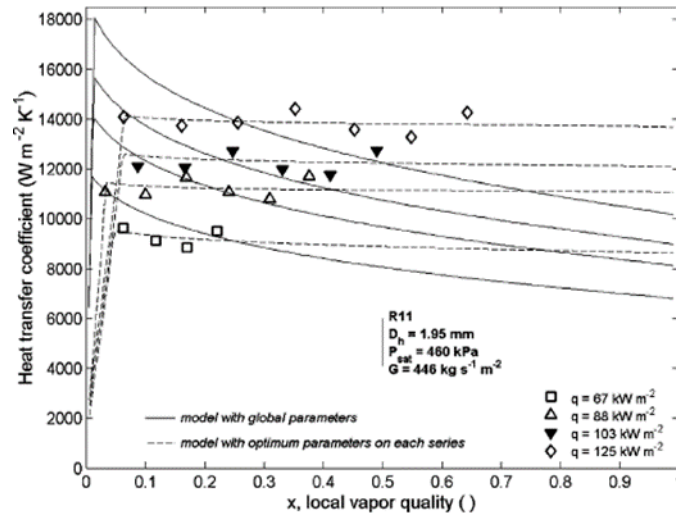
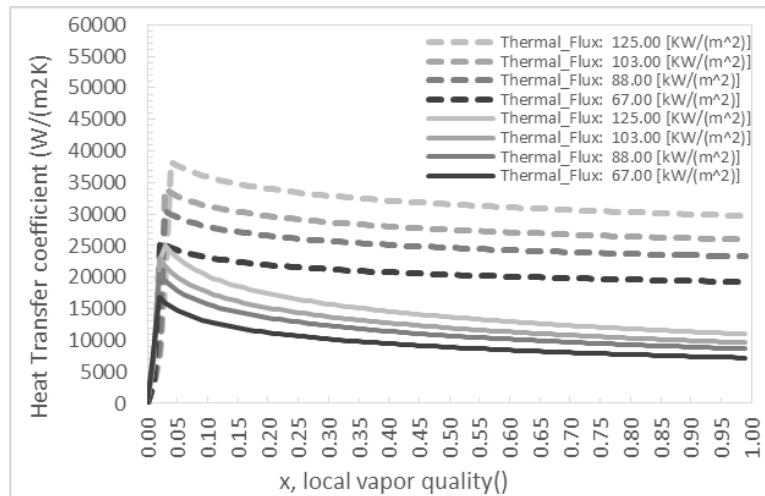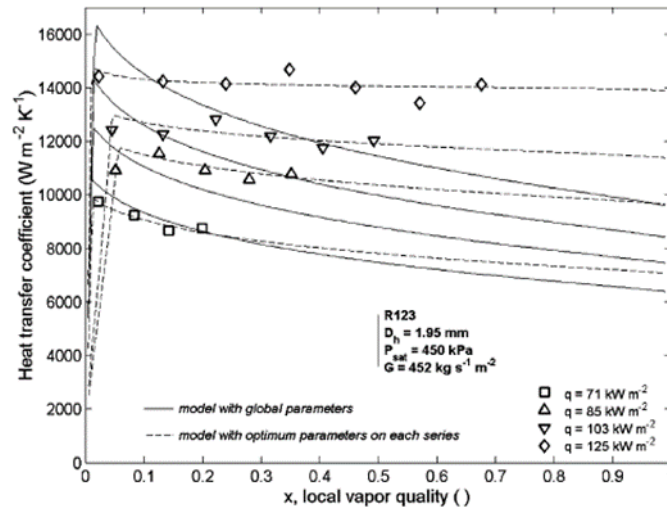Figure 207: Lin et al. (2001) data on Thome et al. (2004) study for *R141b*
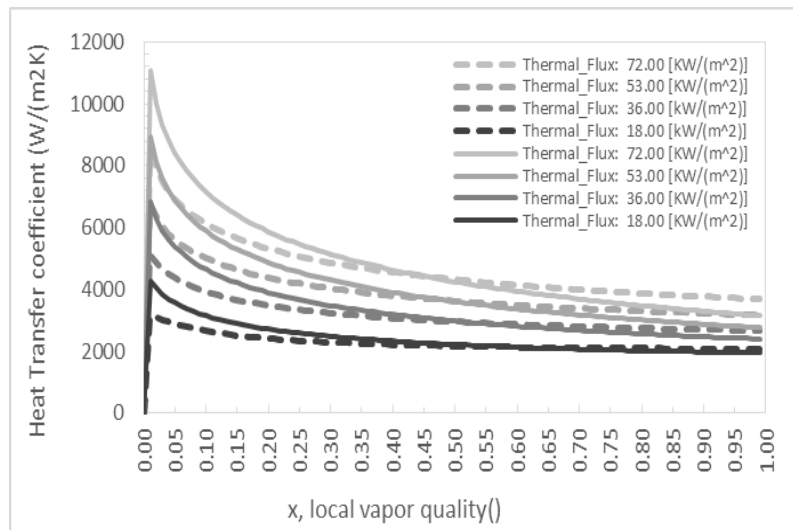
Figure 208: Lin et al. (2001) data obtained with *Refprop 9.1* for *R141b*.

The specific parameters for the correlations are showed in the following Table 51:

Table 51: Lin et al. (2001) parameters for Three-Zone model.

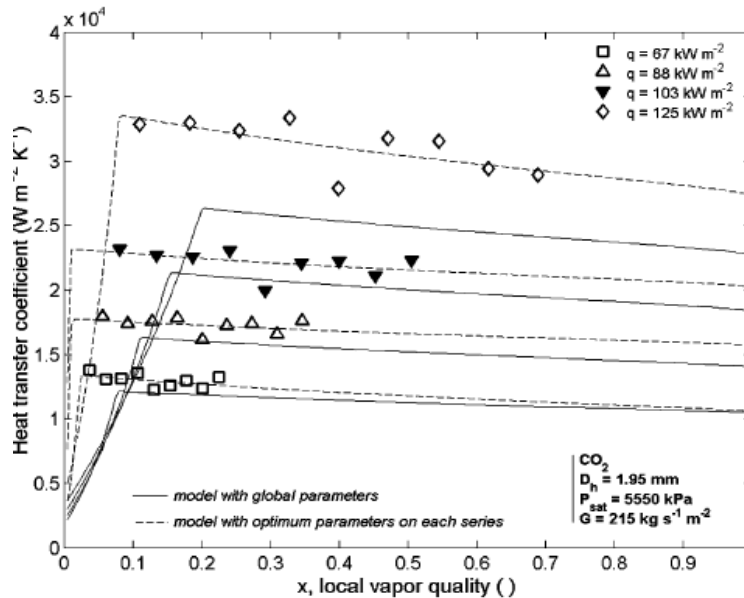|		
Minimum film thickness:	5.80E-01	[μm]
Correcting factor for initial film thickness:	0.86	[-]
Frequency bubble exponential factor:	1.79	[-]
Reference heat exponential factor:	-0.60	[-]
Reference heat multiplication factor:	3324.00	[-]

8.9. Agostini

Agostini (2002) studied *R134a* in a multichannel experiment section two different values of hydraulic diameter, $d_h = 0.77\ mm$ (*18* channels) and *2.01 mm* (*11* channels) and with rectangular

shape of the channel. For every study the trend is the same and match the original data. Figures 209-210 show the original trend within the different channel diameter and Figures 211-211 the obtained trends. Dotted lines are for optimized parameters.
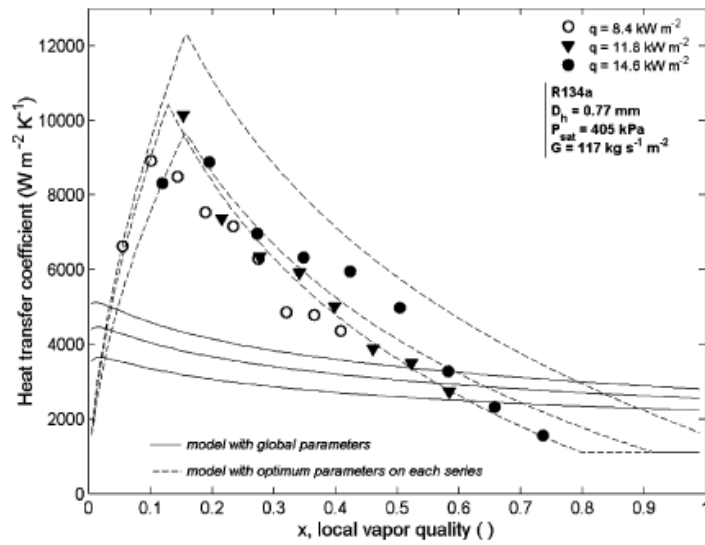
Figure 209: Agostini (2002) data on Thome et al. (2004) study for *R134a* in a *0.77 mm* channel.
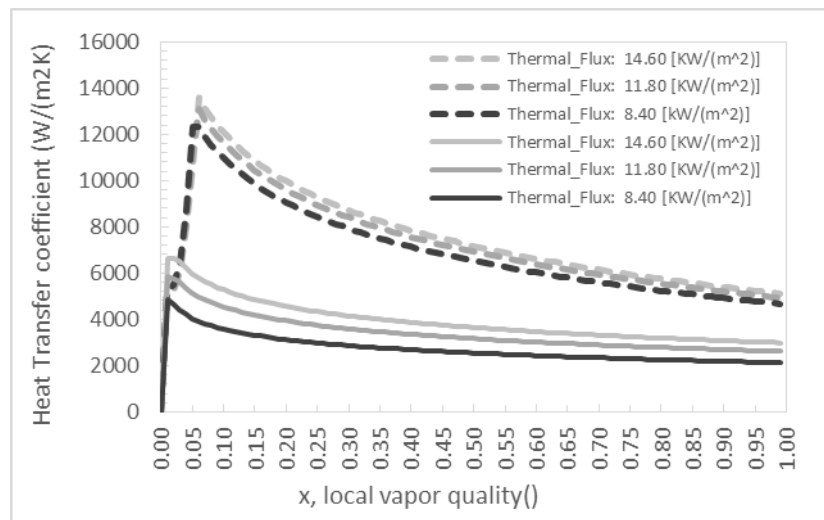
Figure 210: Agostini (2002) data obtained with *Refprop 9.1* for *R134a* in a *0.77 mm* channel.
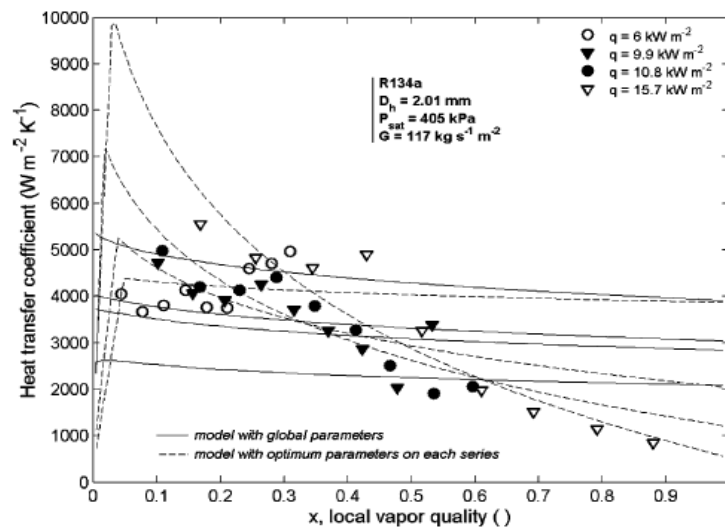
Figure 211: Agostini (2002) data on Thome et al. (2004) study for *R134a* in a *2.01 mm* channel.
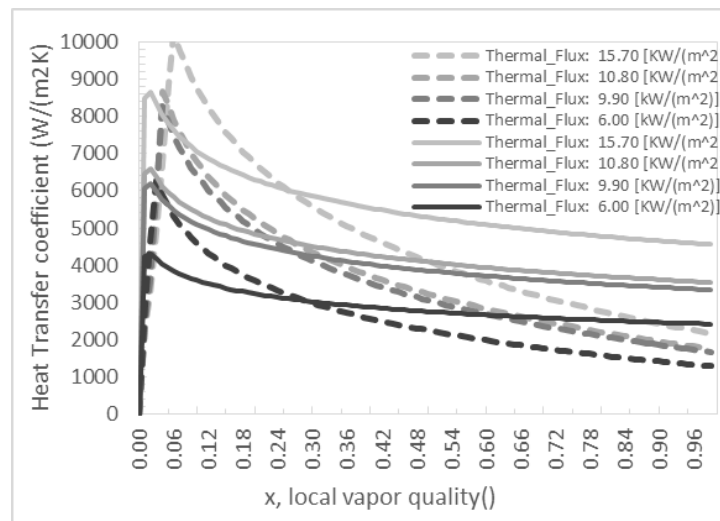
Figure 212: Agostini (2002) data obtained with *Refprop 9.1* for *R134a* in a *2.01 mm* channel.
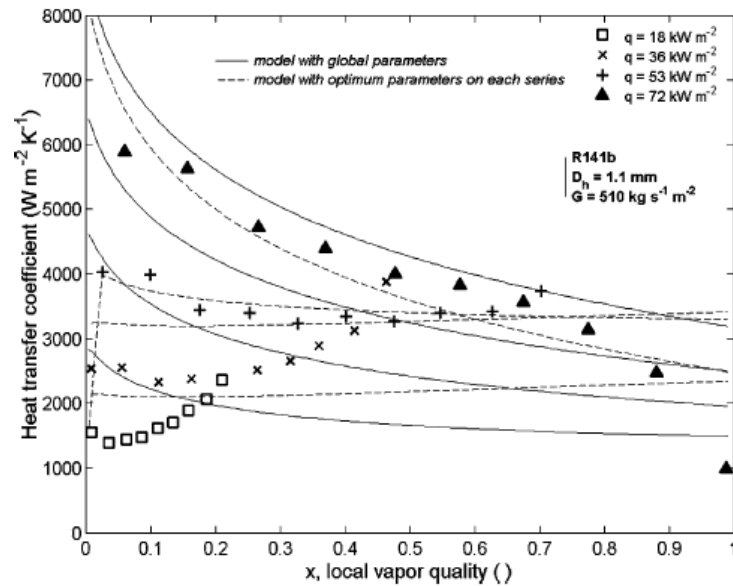
The specific parameters for the correlations are showed in the following Tables 52-53:

Table 52: Agostini (2002) parameters for Three-Zone model for *0.77 mm* channel.

Minimum film thickness:	1.82	[μm]
Correcting factor for initial film thickness:	1.23	[-]
Frequency bubble exponential factor:	1.18	[-]
Reference heat exponential factor:	-0.05	[-]
Reference heat multiplication factor:	3272.00	[-]

Table 53: Agostini (2002) parameters for Three-Zone model for *2.01 mm* channel.

Minimum film thickness:	3.00E+00	[μm]
Correcting factor for initial film thickness:	0.80	[-]
Frequency bubble exponential factor:	1.70	[-]
Reference heat exponential factor:	-0.24	[-]
Reference heat multiplication factor:	3452.00	[-]

8.10. Bubble Coalescence model

Following is reported the validation procedure for the Bubble Coalescence model of Consolini e Thome (2010). The overlook starts with results obtained during the model validation confronting heat transfer data with their database for fluids:

- R-134a
- CO2
- R141-b
- R-236fa

The validation analysis is made on the data that were obtained from digitalizing published graphs. These results are for a single flow channel.

The global parameters for the correlations are showed in the following Table 54:

Table 54: Global parameters for Bubble-Coalescence model.

beta:	1	[-]
chi:	3	[-]
eta:	0.02	[-]

8.10.1.   Validation R-134a

The trend is the same, but the value seems to be translated with a proportional factor on the vertical axis. Probably the difference is due to the fluid database used. The following two Figures 213-214 are the original and obtained trends.
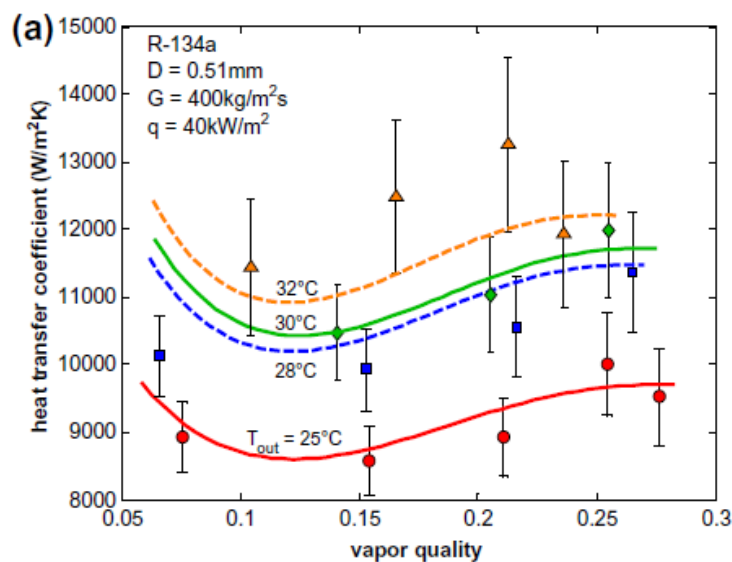
Figure 213: Validation R-134a data on Consolini et al. (2010) study.
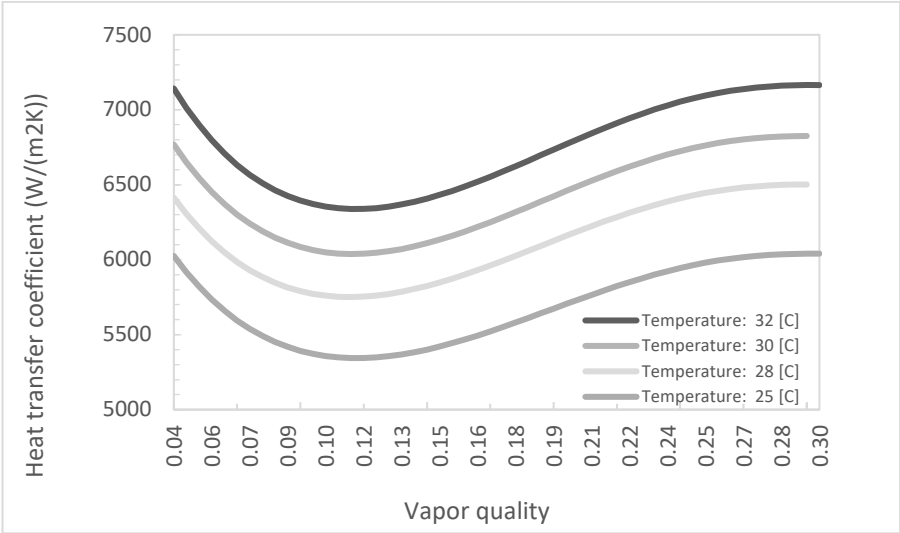
Figure 214: R-134a data obtained with *Refprop 9.1.*

8.10.1.   Validation thermal flux

The trend is the same but the value seems to be translated with a proportional factor on the vertical axis. Probably the difference is due to the fluid database used. The following two Figures 214-215 are the original and obtained trends.
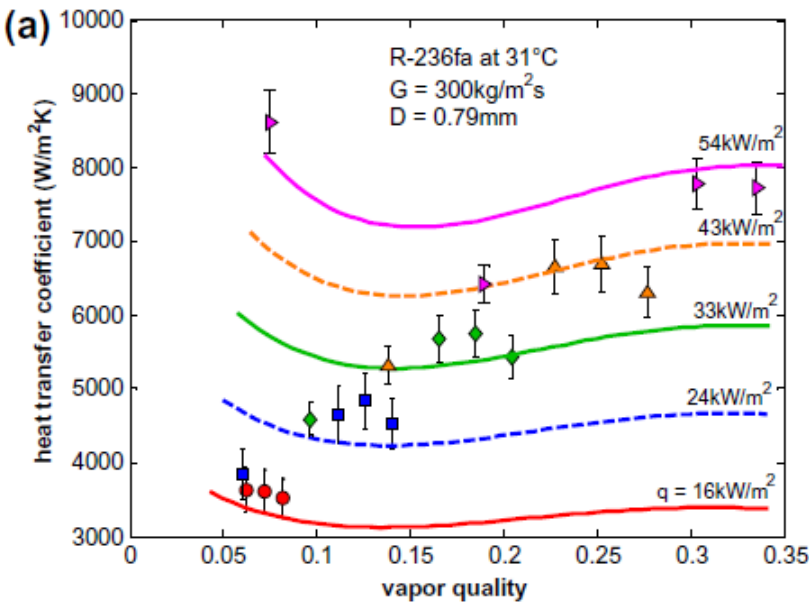
Figure 215: Validation thermal flux data on Consolini et al. (2010) study for *R236fa.*
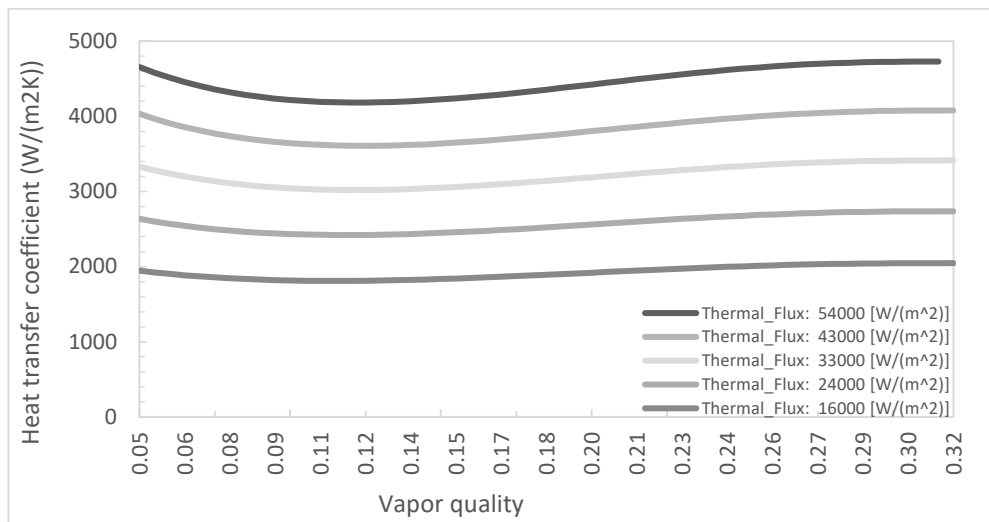
Figure 216: Validation thermal flux data obtained with *Refprop 9.1* for *R236fa*.

8.10.1.   Validation mass flux

The trend is the same, but the value seems to be translated with a proportional factor on the vertical axis. Probably the difference is due to the fluid database used. The following two Figures 217-218 are the original and obtained trends.
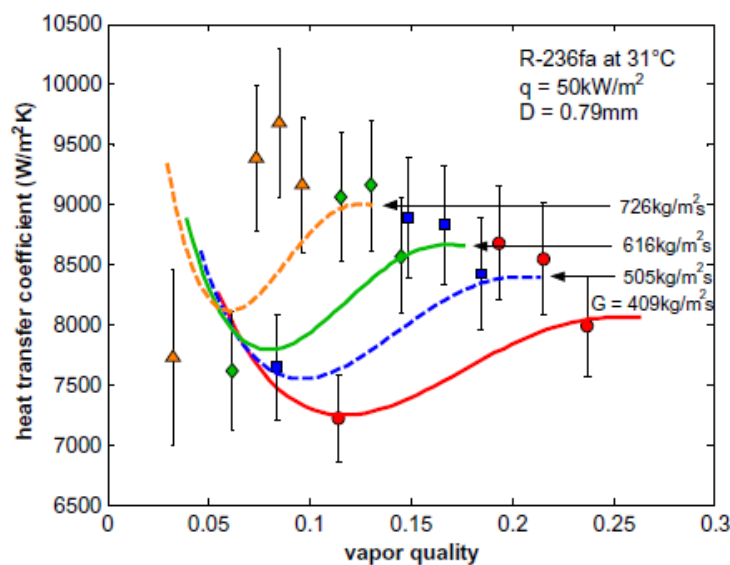
Figure 217: Validation mass flux data on Consolini et al. (2010) study for *R236fa*.
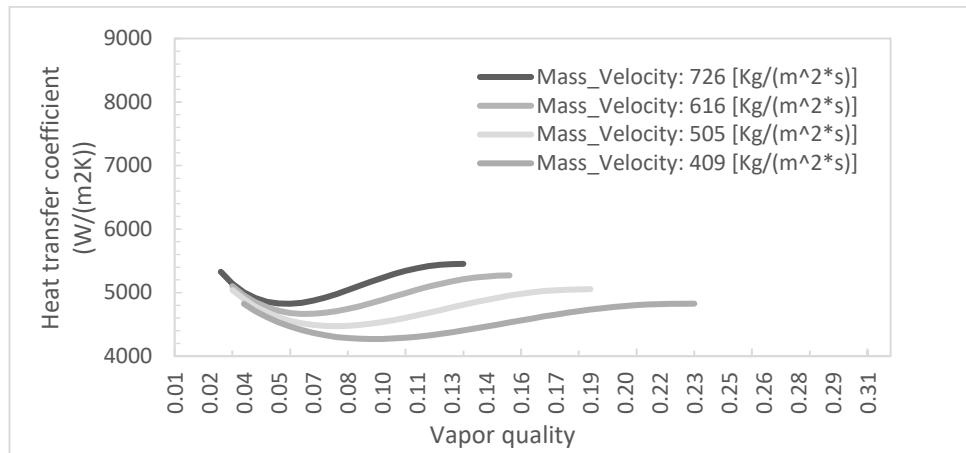
Figure 218: Validation mass flux data obtained with *Refprop 9.1* for *R236fa.*

8.10.1.   Validation CO2

The trend is the same, but the value seems to be translated with a proportional factor on the vertical axis. Probably the difference is due to the fluid database used. The following two Figures 219-220 are the original and obtained trends.
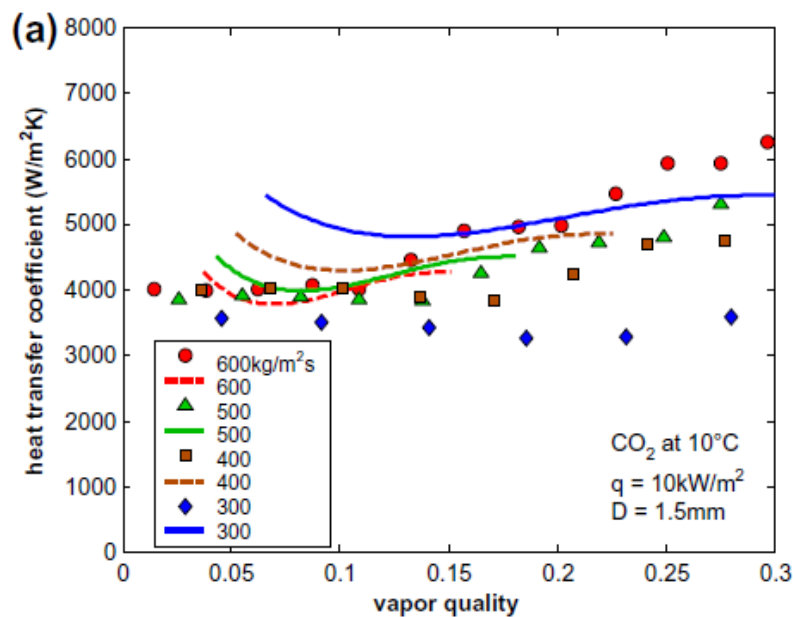
Figure 219: Validation CO2 data on on Consolini et al. (2010) study.
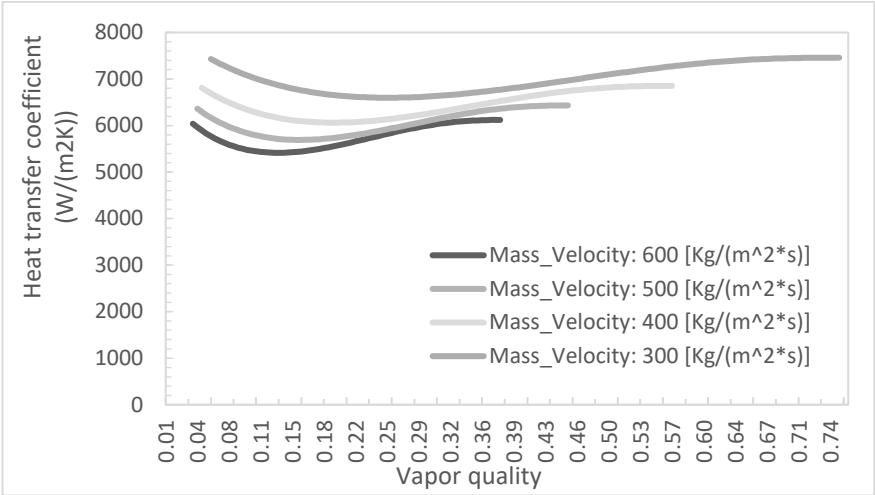
Figure 220: Validation CO2 data obtained with *Refprop 9.1*.

8.10.1.   Validation R-141b

The trend is the same, but the value seems to be translated with a proportional factor on the vertical axis. Probably the difference is due to the fluid database used. The following two Figures 221-222 are the original and obtained trends.
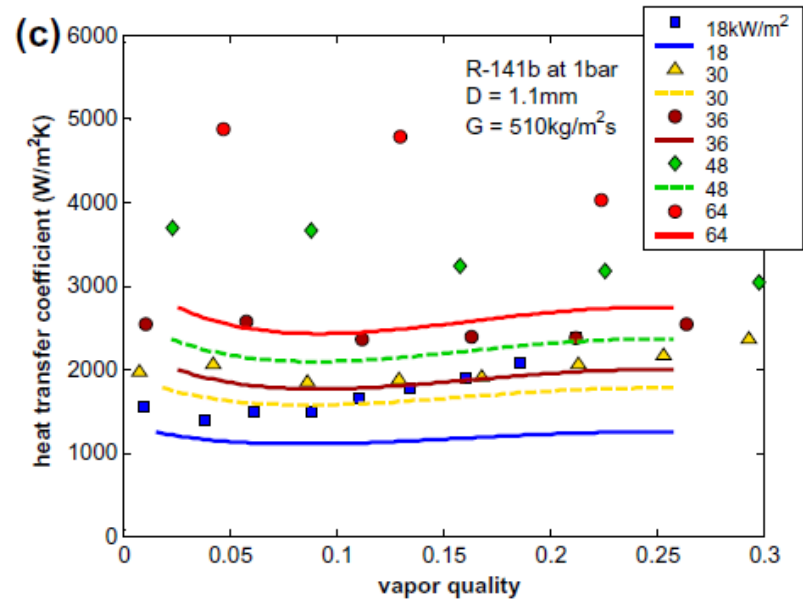
Figure 221: Validation R-141bdata on Consolini et al. (2010) study.
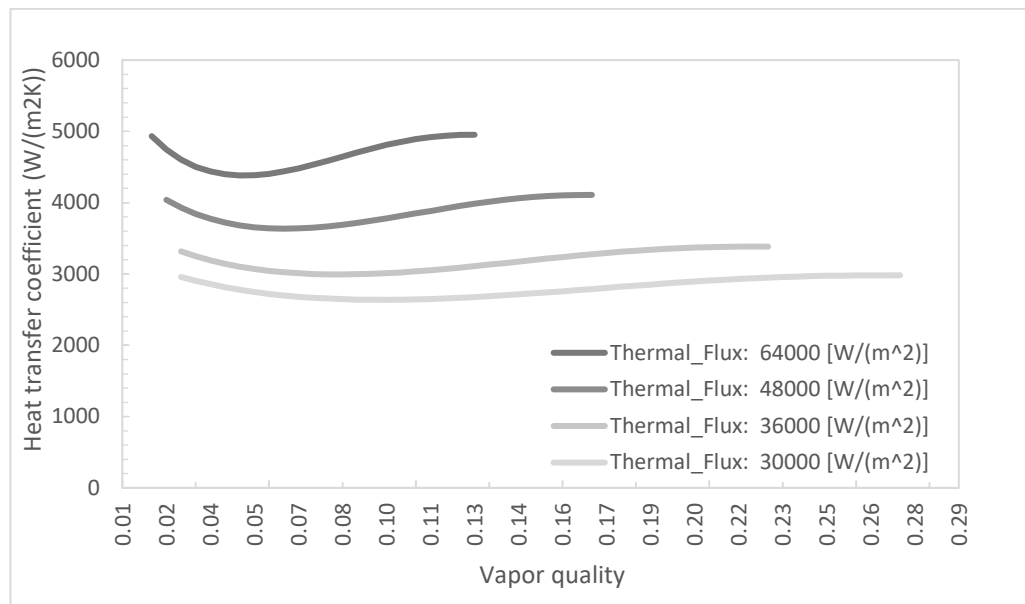
Figure 222: Validation R-141b data obtained with *Refprop 9.1.*

8.11. Correlations

Following is reported the validation procedure for the Correlations. The overlook starts with re-sults obtained during the model validation confronting heat transfer data with the database of Mohammed and Krayannis during the experiment reported in the Table 55:

Table 55: Correlation validation experiment proprieties

Mass Velocity:	300	[Kg/(m²s)]
Thermal Flux:	56000	[W/(m²)]
Internal Channel Diameter:	0.52	[mm]
Channel Length:	-	[m]
Pressure:	600	[KPa]
Temperature:	-	[C]

The validation analysis is made on the data that were obtained from digitalizing published graphs. These results are for a single flow channel.

The global parameters for the correlations are showed in the following Table 56:

Table 56: Global parameters for Bubble-Coalescence model.

Fluid:	R134a	[file-name]
Gravity:	9.81	[m/s²]
Roughness:	0.001	[mm]

The trend is the same, but the value seems to be translated with a proportional factor on the ver-tical axis. Probably the difference is due to the fluid database used. The following two Figures 223-224 are the original trends. Figures 225-226 shows obtained trends.
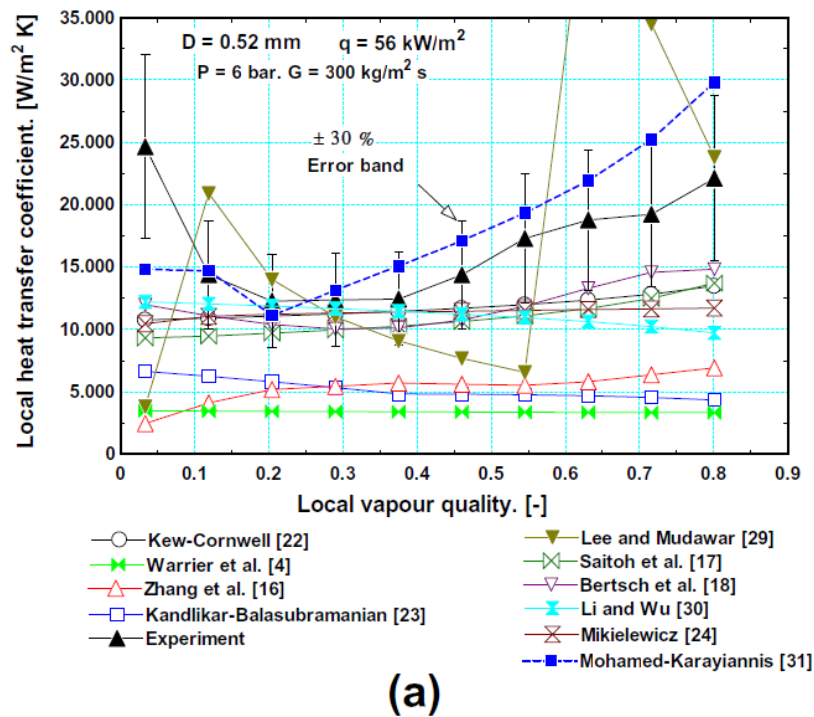
(a)

Figure 223: Correlation data from Mohammed and Krayiannis studies (2012) for microchannels.
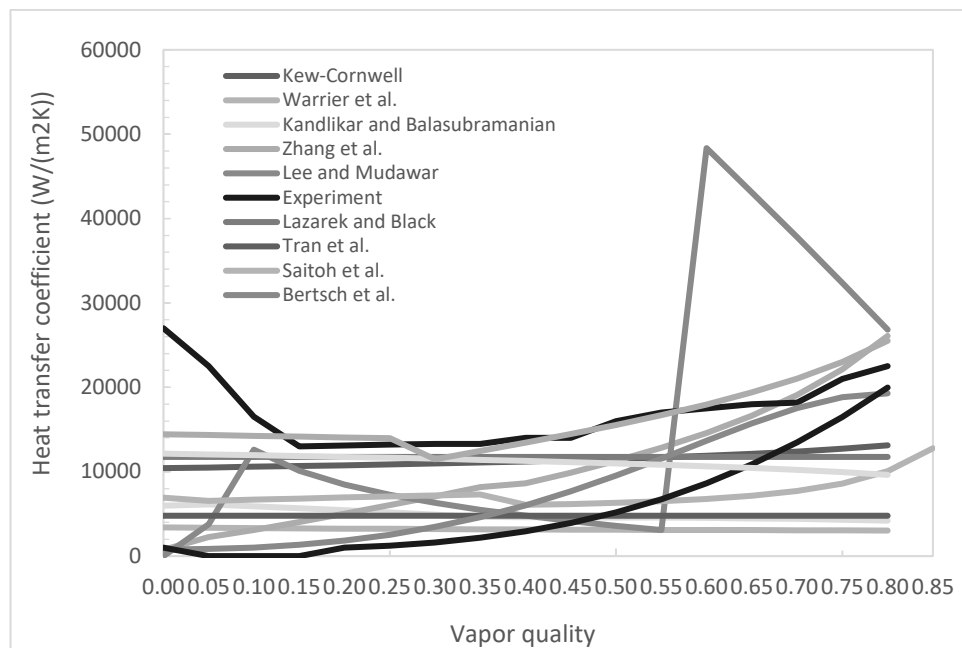
Figure 224: Correlation data obtained with *Refprop 9.1* for microchannels.
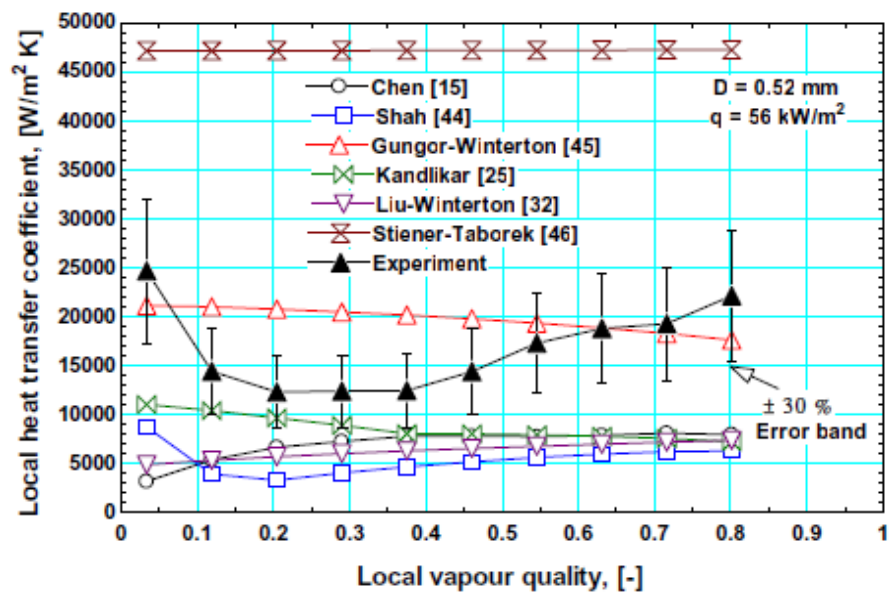
Figure 225: Correlation data from Mohammed and Krayiannis studies (2012) for macrochannels.
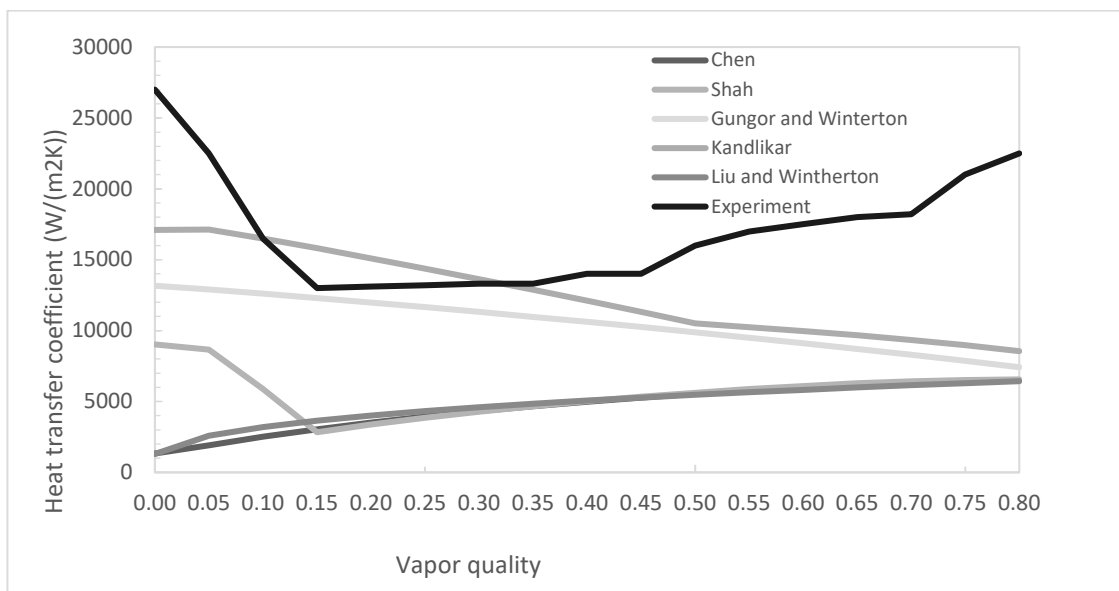
Figure 226: Correlation data obtained with *Refprop 9.1* for macrochannels.

9. Annex B: Programs Schematics

Following are reported the operative diagram flux for every program used. Schematics will not have any description because they are proposed only for a description purpose.

- **Three-Zone program:**
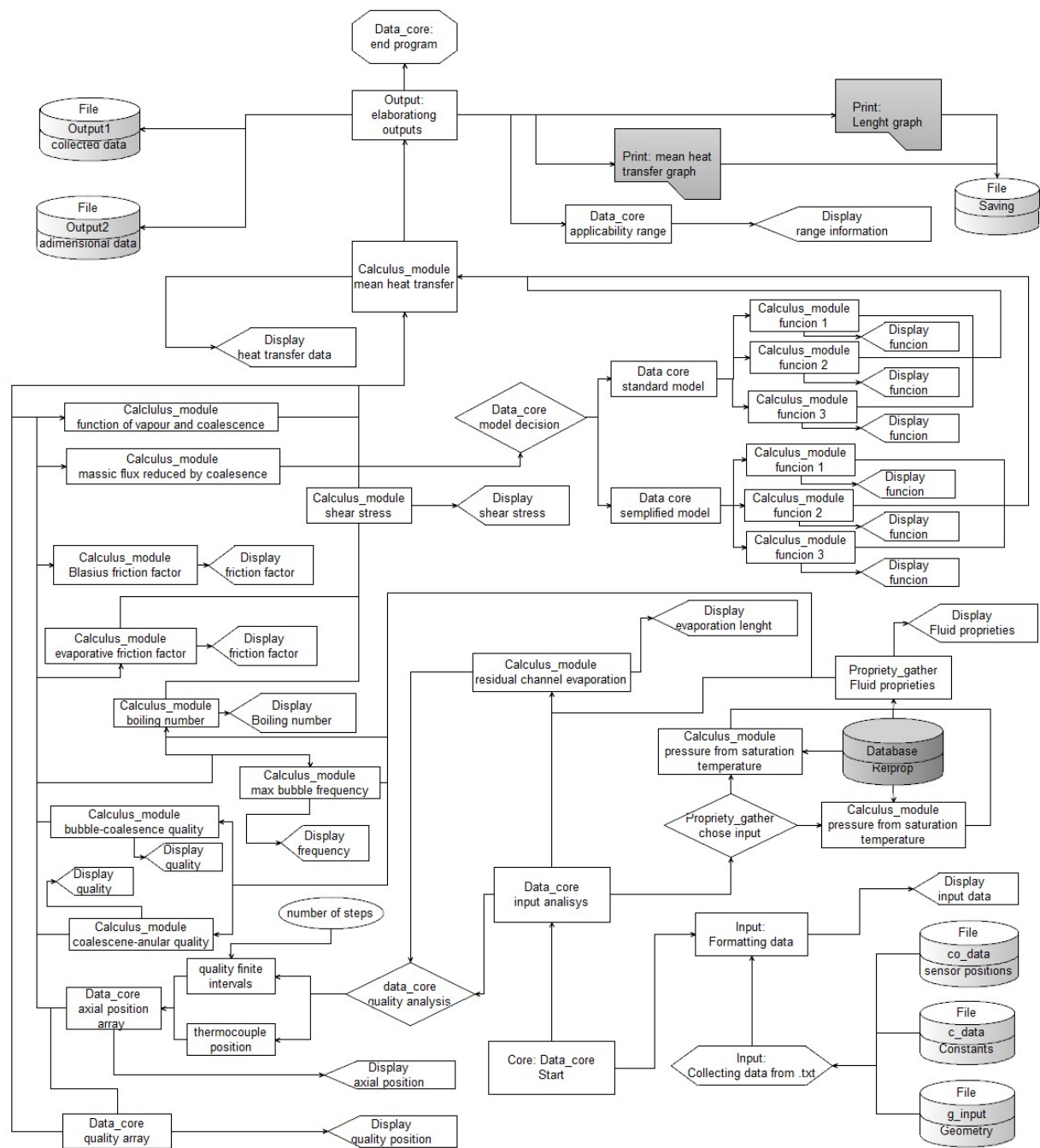
Figure 227: Three-zone program flux diagram

- ## **Slug-Coalescence program:**
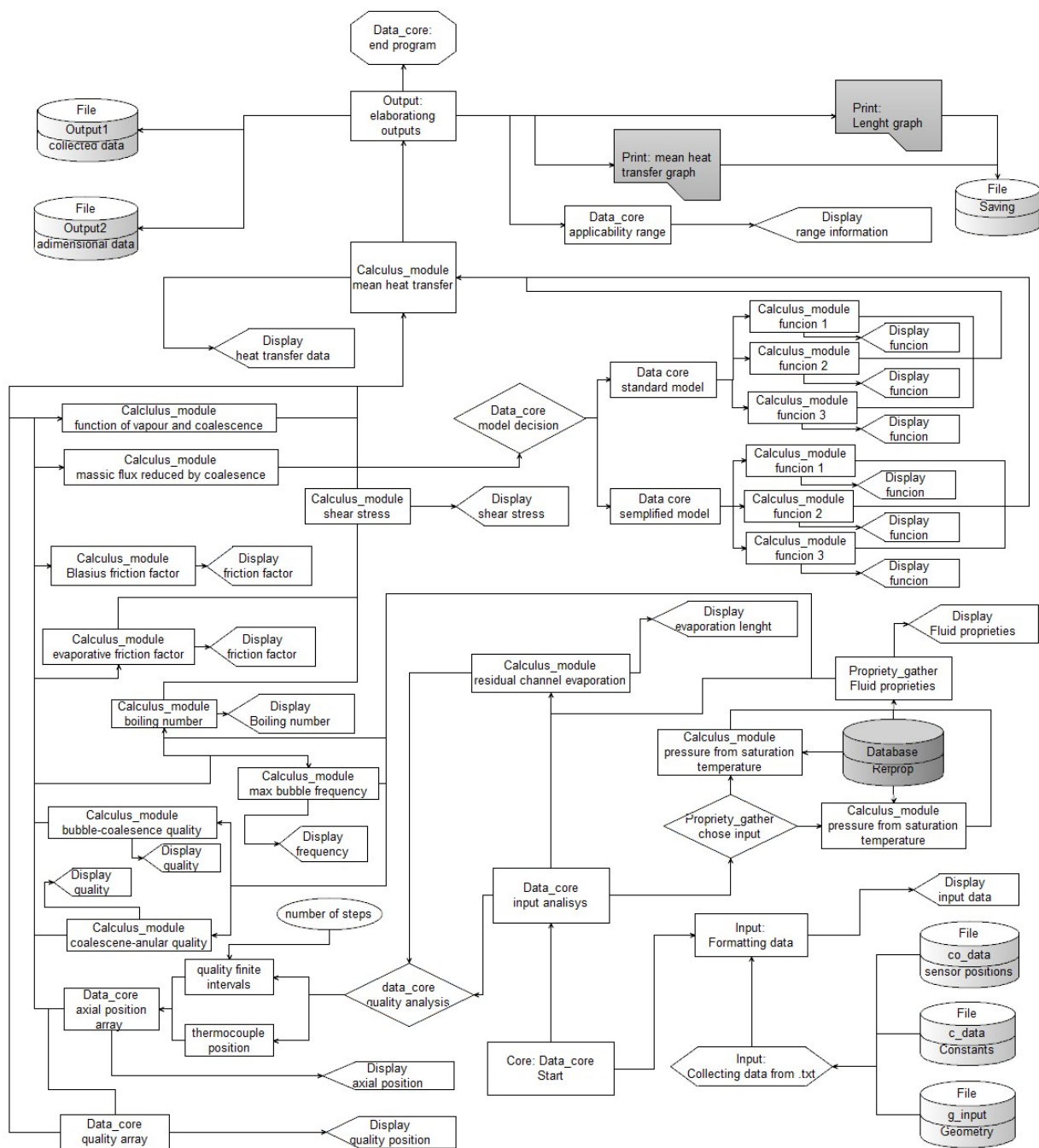
Figure 228: Slug-Coalescence flux diagram

- ## **Correlations main program:**

The program is divided in the main program and correlations subroutines.
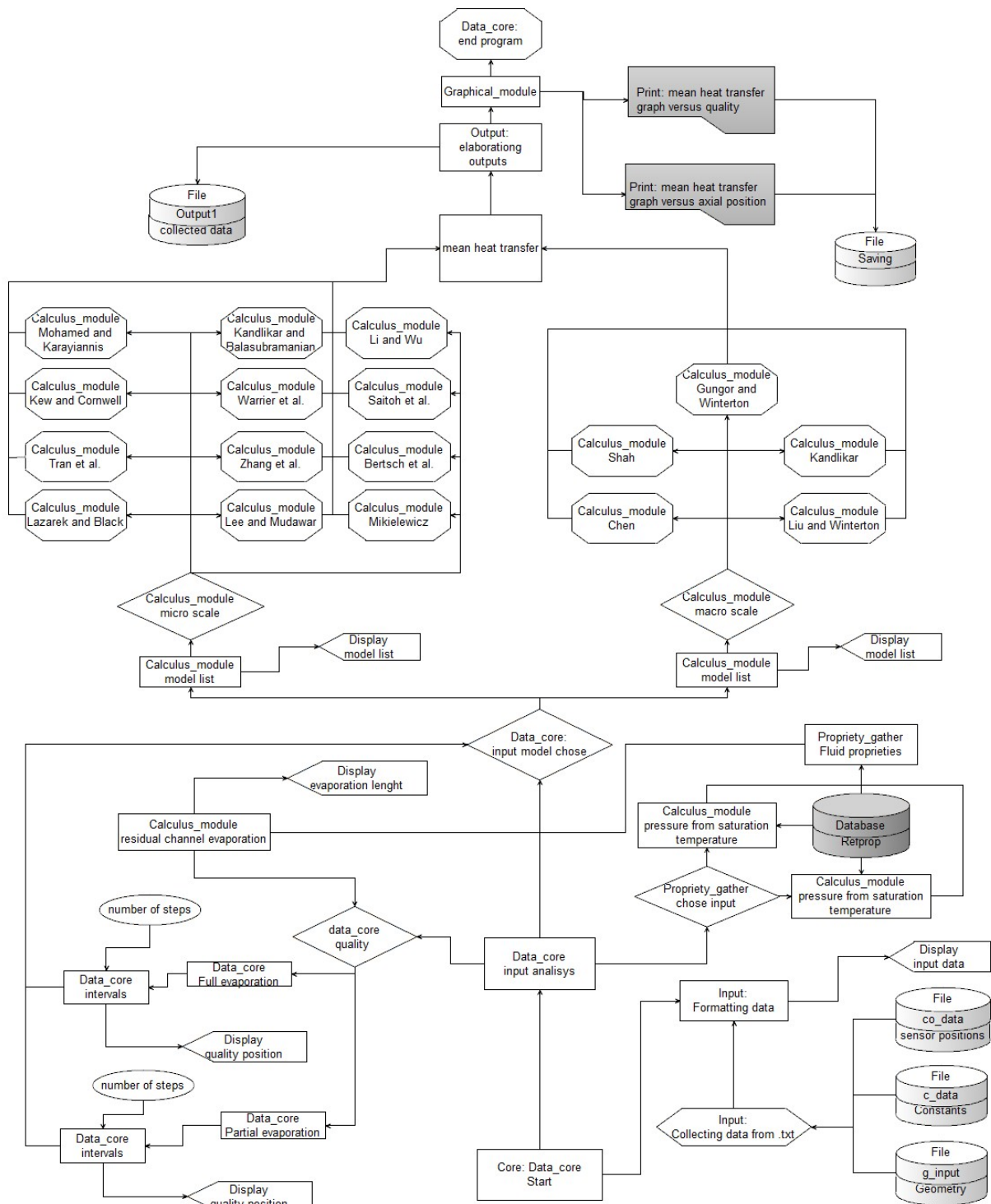
Figure 229: Correlation main program flux diagram
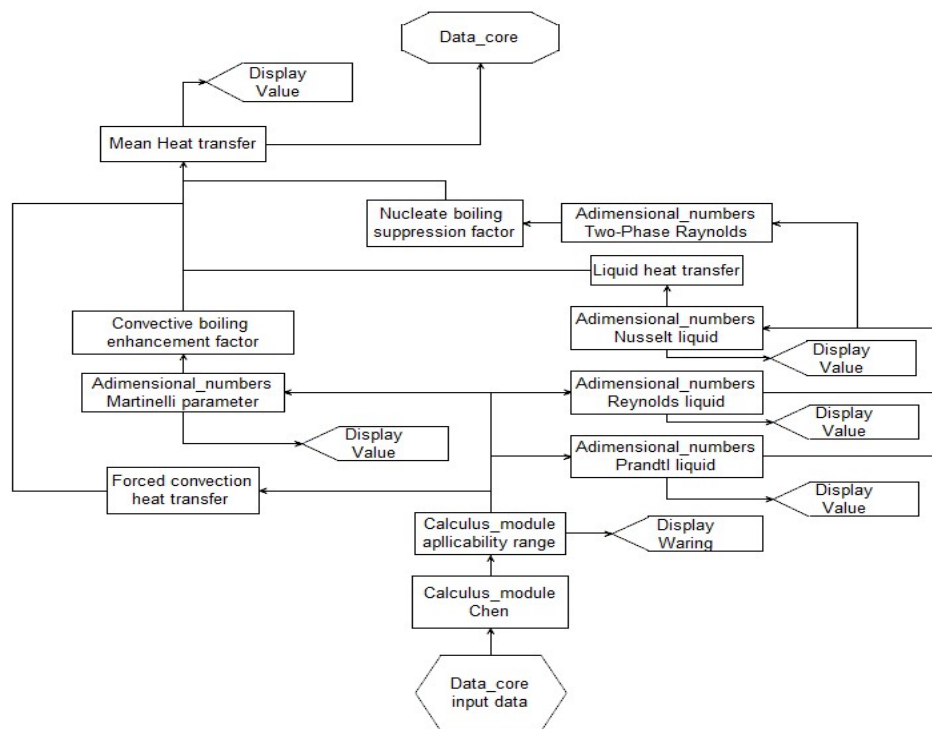
o **Chen subroutine:**

Figure 230: Chen subroutine flux diagram
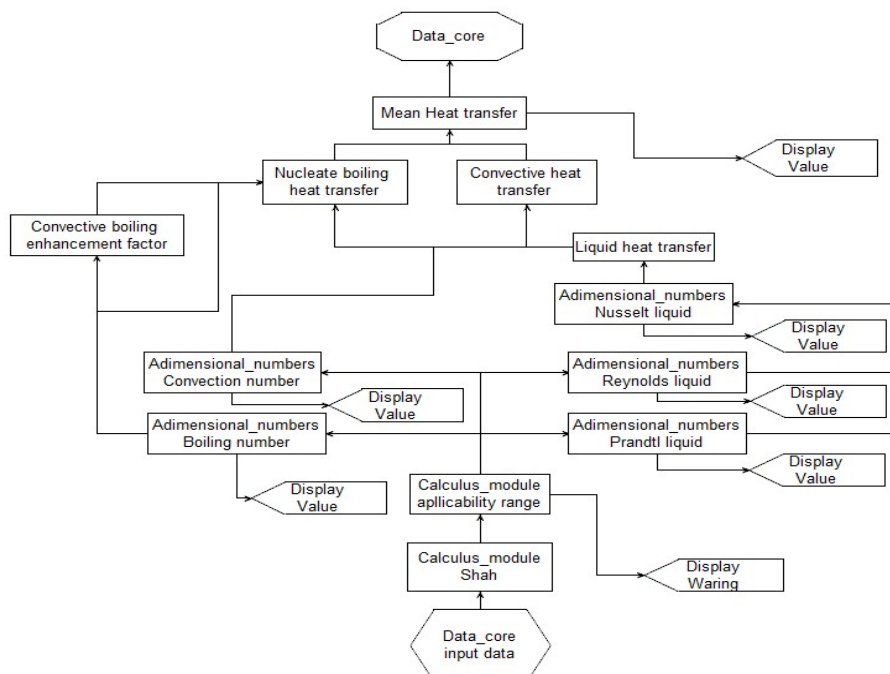
o **Shah subroutine:**

Figure 231: Shah subroutine flux diagram

o **Gungor and Winterton subroutine:**
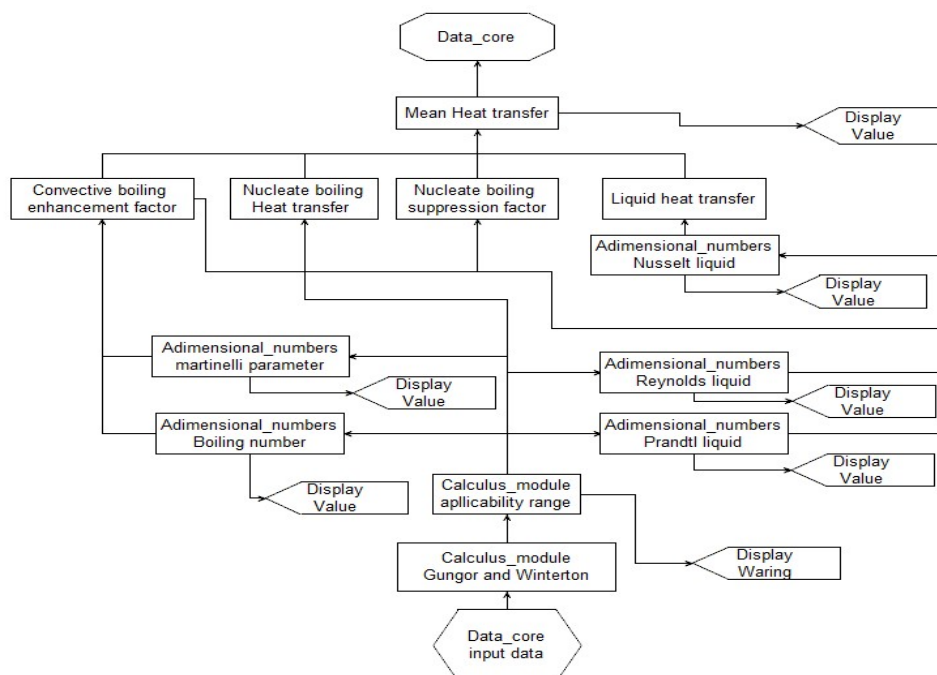
Figure 232: Gungor and Winterton subroutine flux diagram

o **Kandlikar subroutine:**
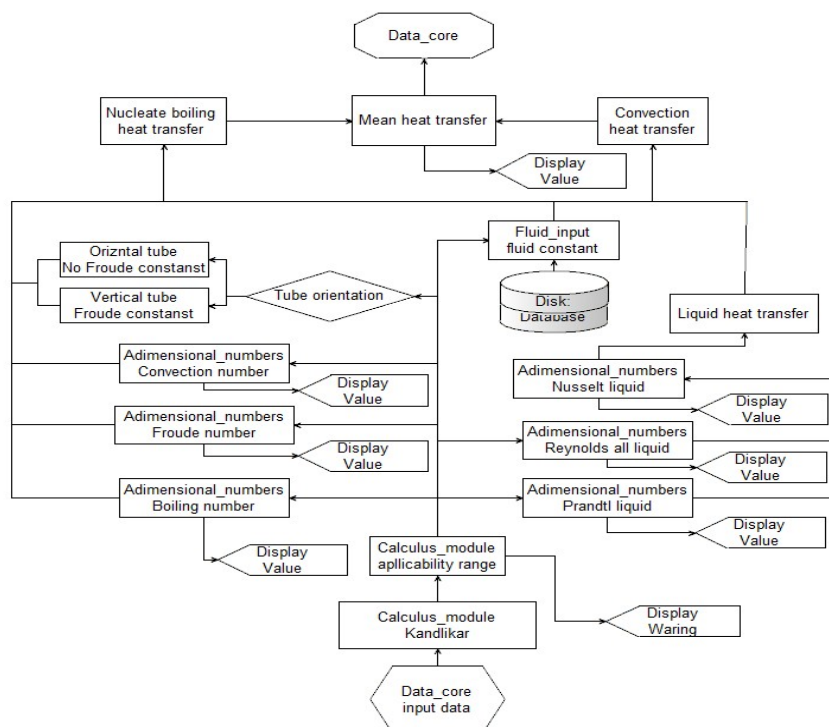
Figure 233: Kandlikar subroutine flux diagram

o **Liu and Winterton subroutine:**
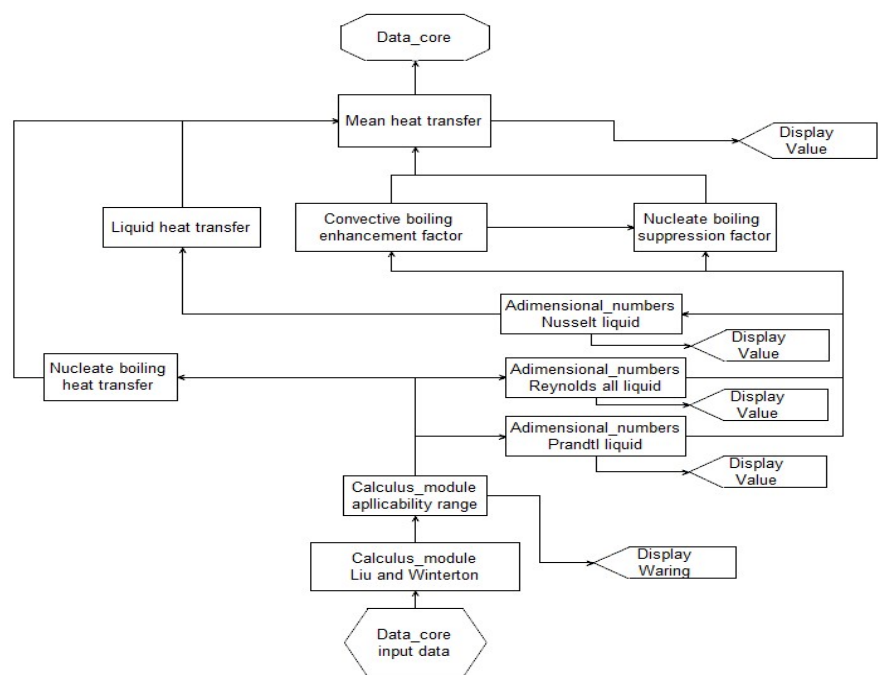
Figure 234: Liu and Winterton subroutine flux diagram

o **Lazarek and Black subroutine:**
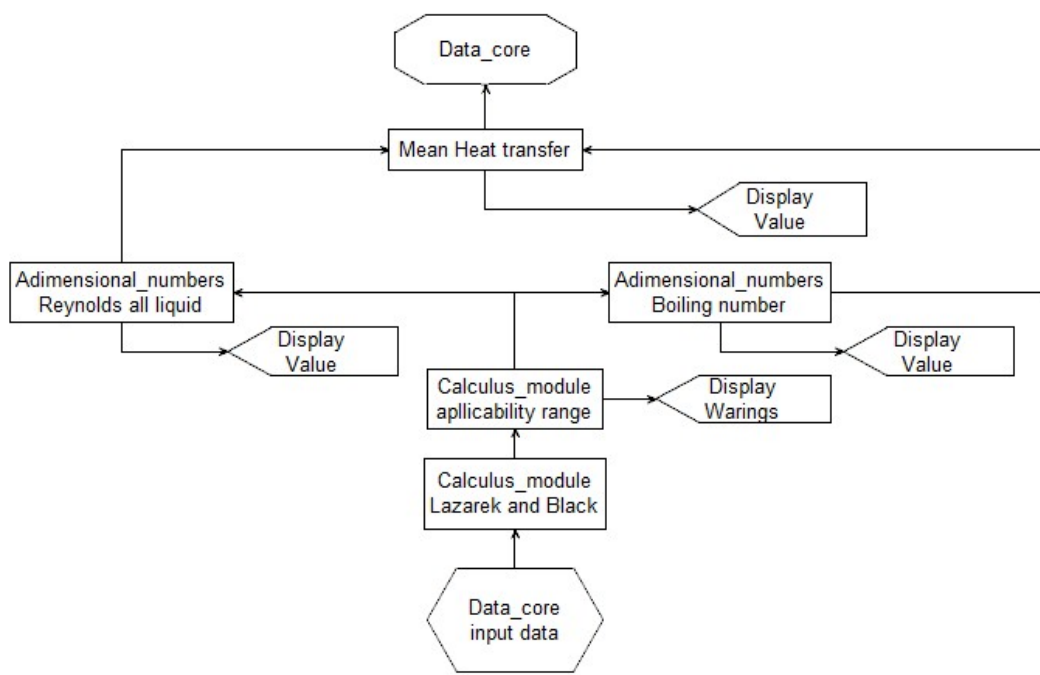
Figure 235: Lazarek and Black subroutine flux diagram

o **Tran et al. subroutine:**
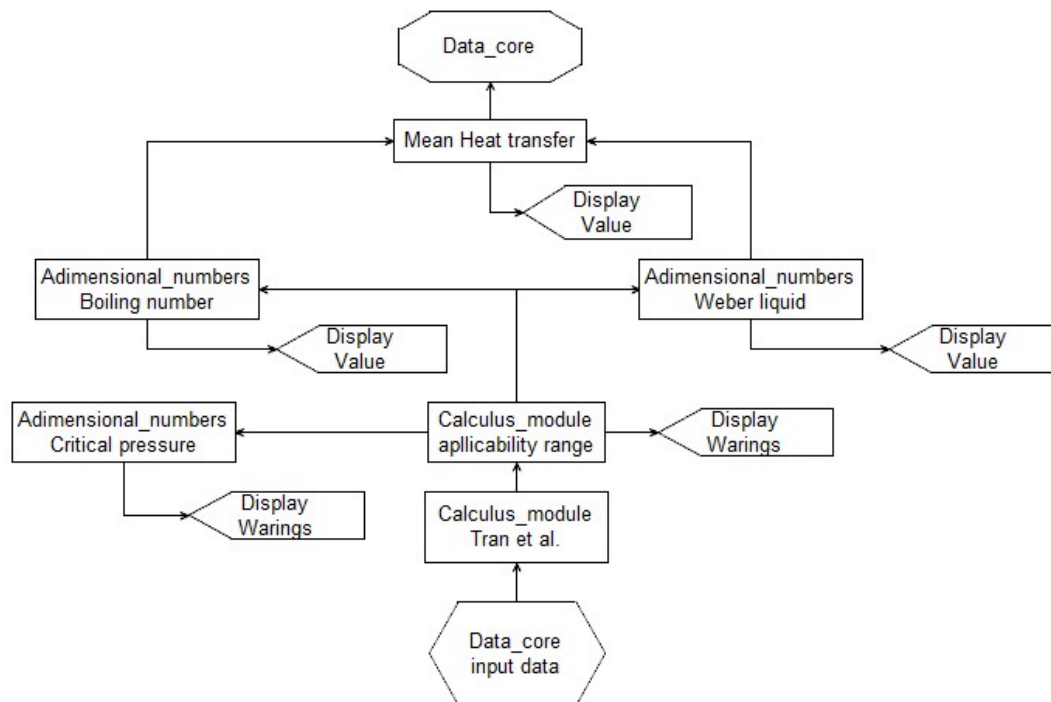
Figure 236: Tran et al. subroutine flux diagram

o **Kew and Cornwell subroutine:**
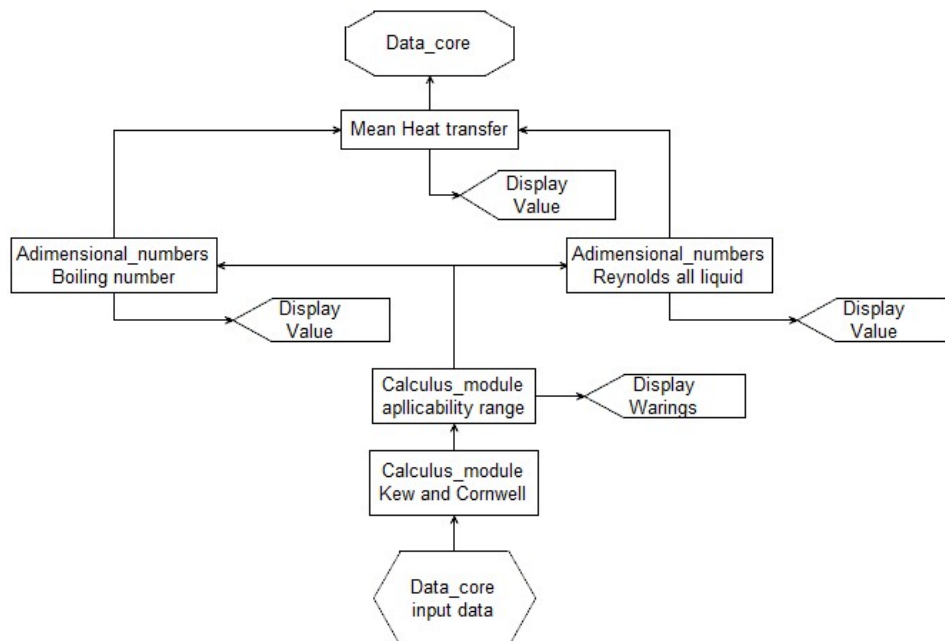
Figure 237**:** Kew and Cornwell subroutine flux diagram

o **Warrier et al. subroutine:**
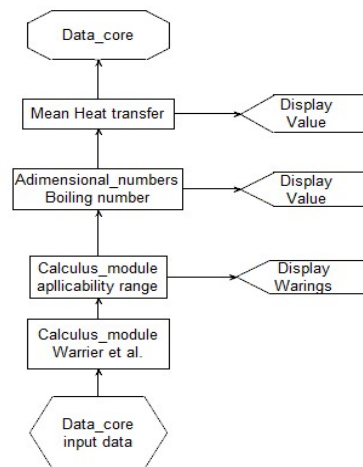
Figure 238: Warrier et al. subroutine flux diagram

o **Kandlikar and Balasubramanian subroutine:**
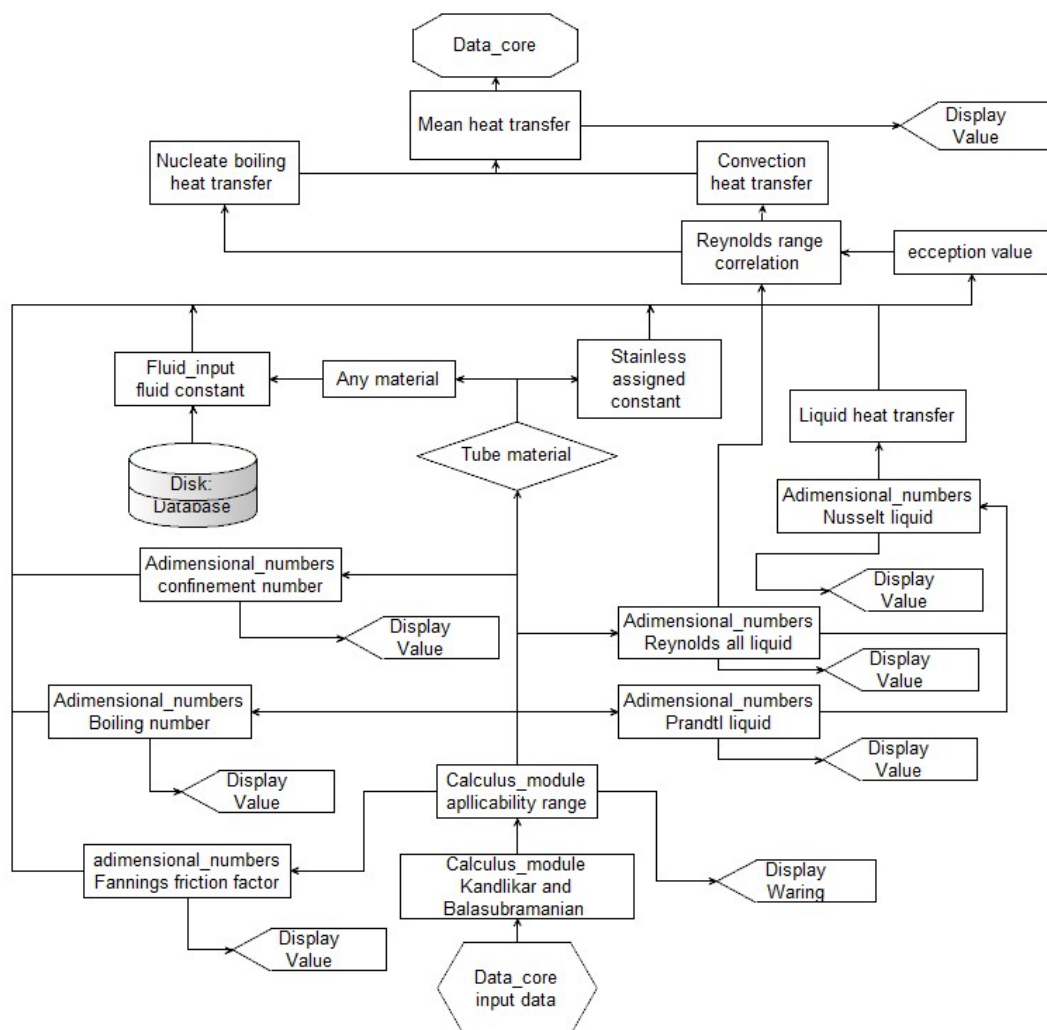
Figure 239: Kandlikar and Balasubramanian subroutine flux diagram

o **Zhang et al. subroutine:**
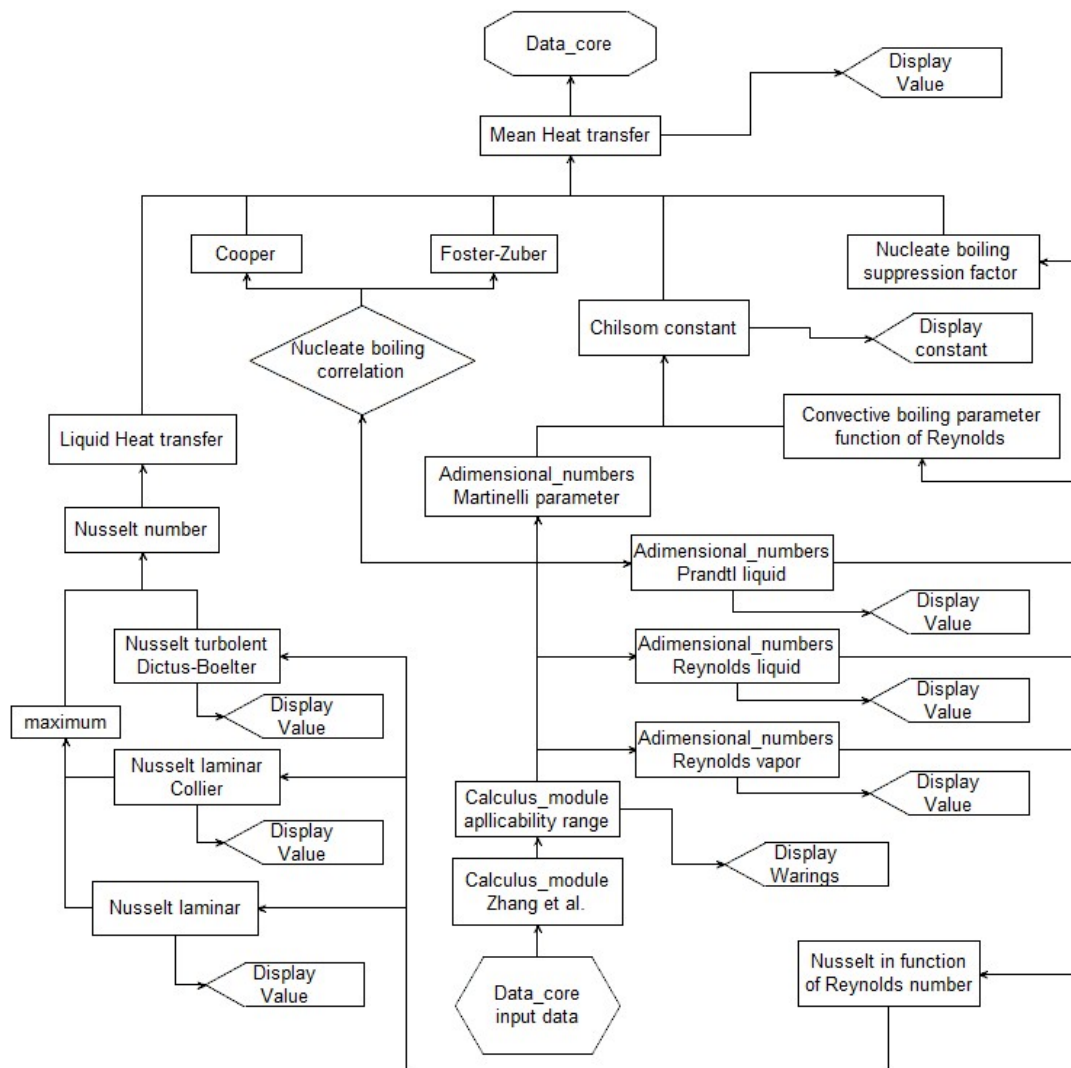
Figure 240: Zhang et al. subroutine flux diagram

o **Lee and Mudawar subroutine:**
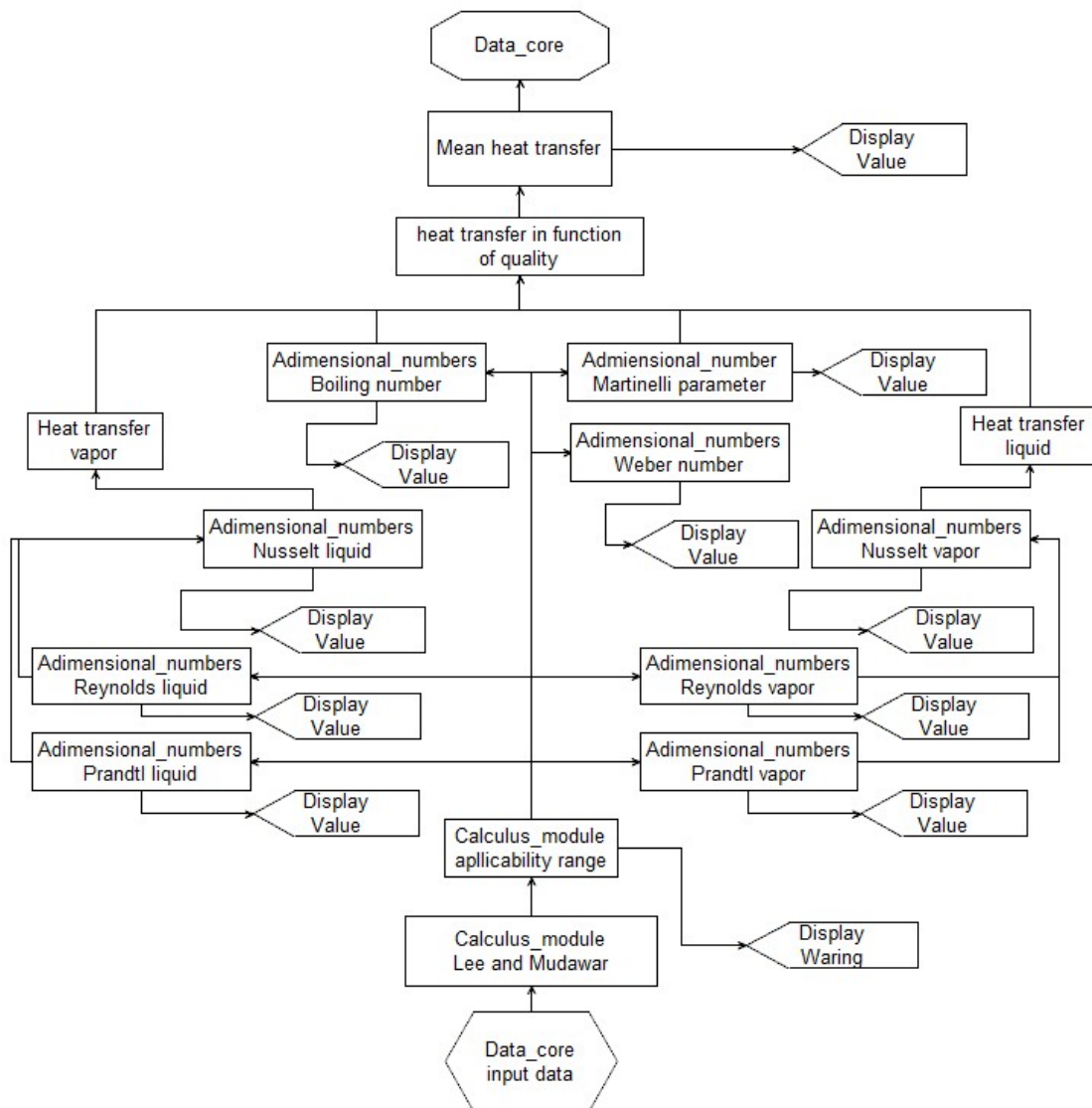
Figure 241: Lee and Mudawar subroutine flux diagram

o **Saitoh et al. subroutine:**
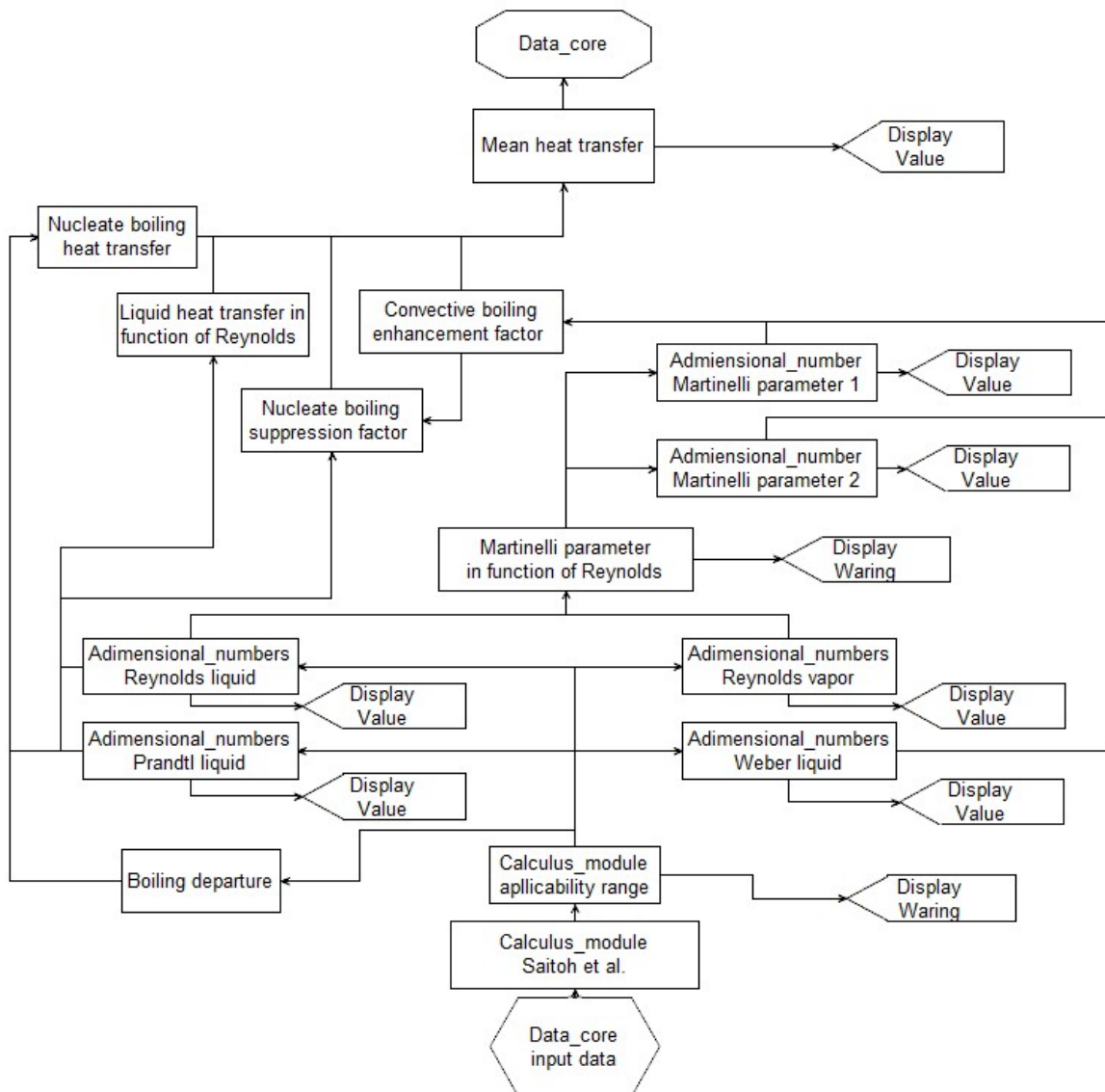
Figure 242: Saitoh et al. subroutine flux diagram

o **Bertsch et al. subroutine:**
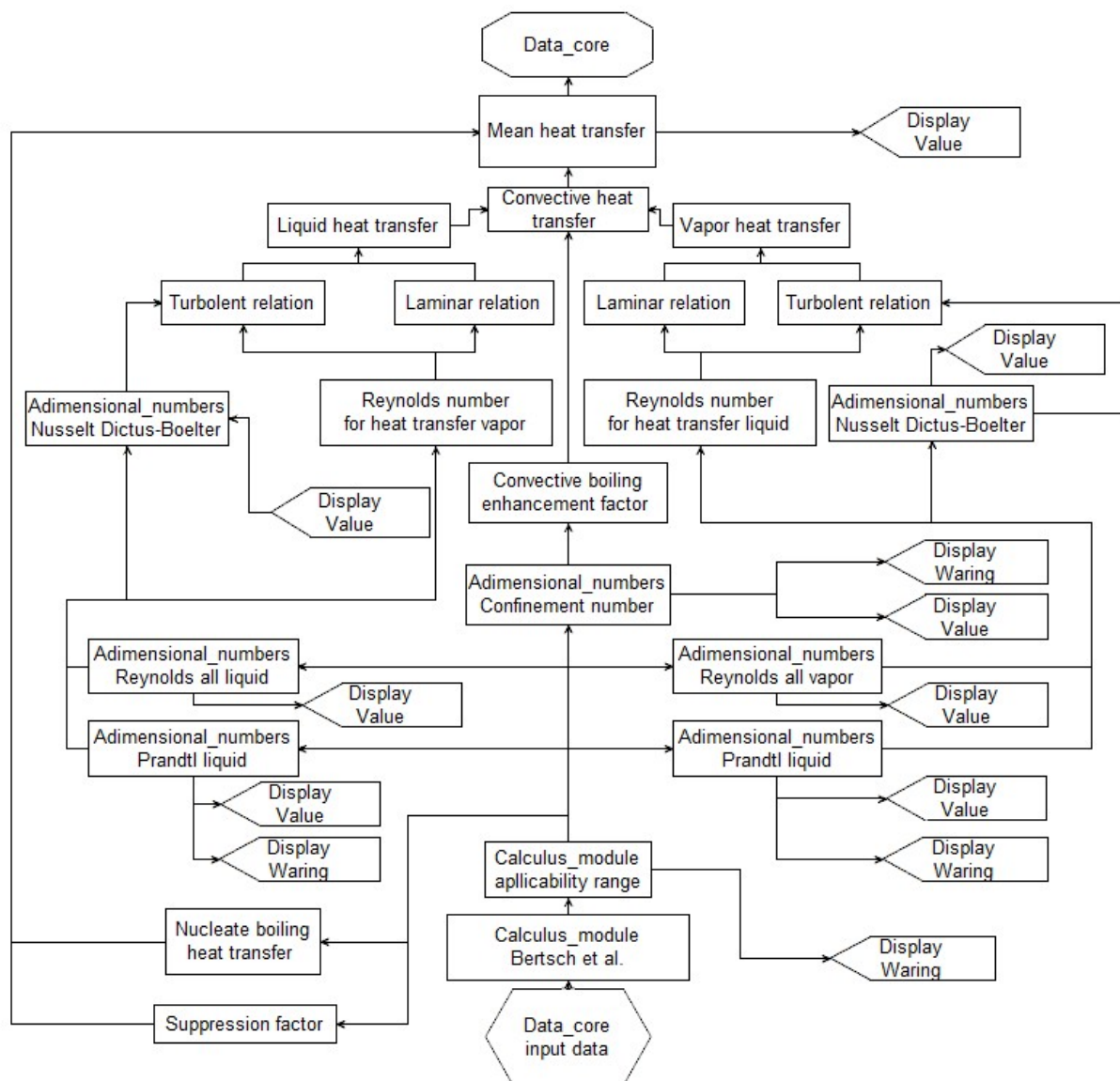
Figure 243: Bertsch et al. subroutine flux diagram

o **Mikielewicz subroutine:**
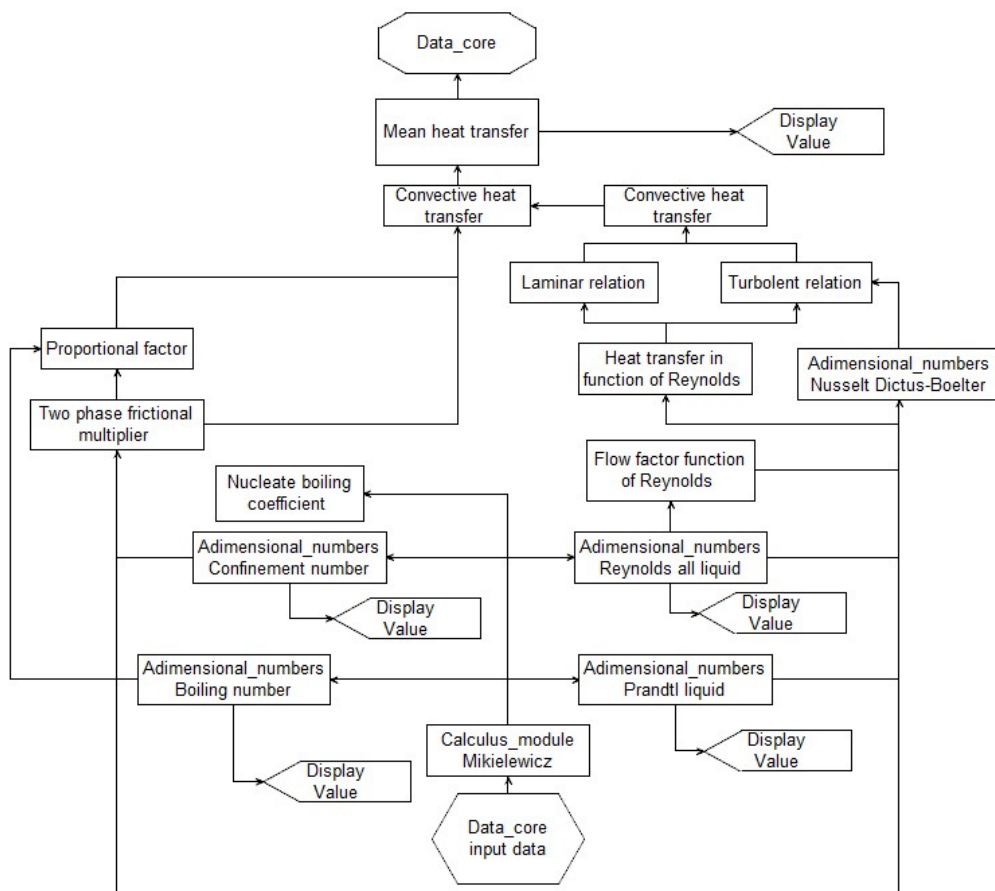
Figure 244: Mikielewicz subroutine flux diagram

o **Li and Wu subroutine:**
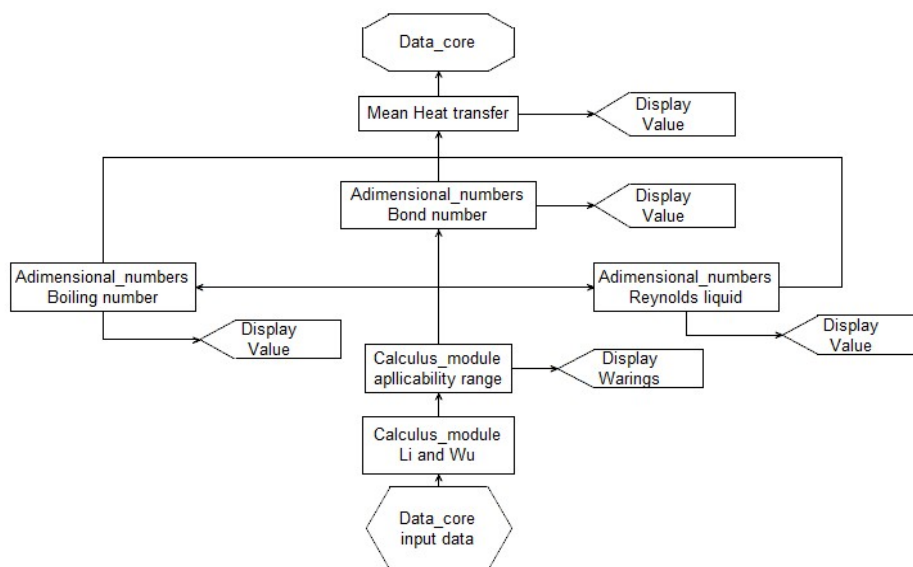
Figure 245: Li and Wu subroutine flux diagram

o **Mohamed and Karayiannis subroutine:**
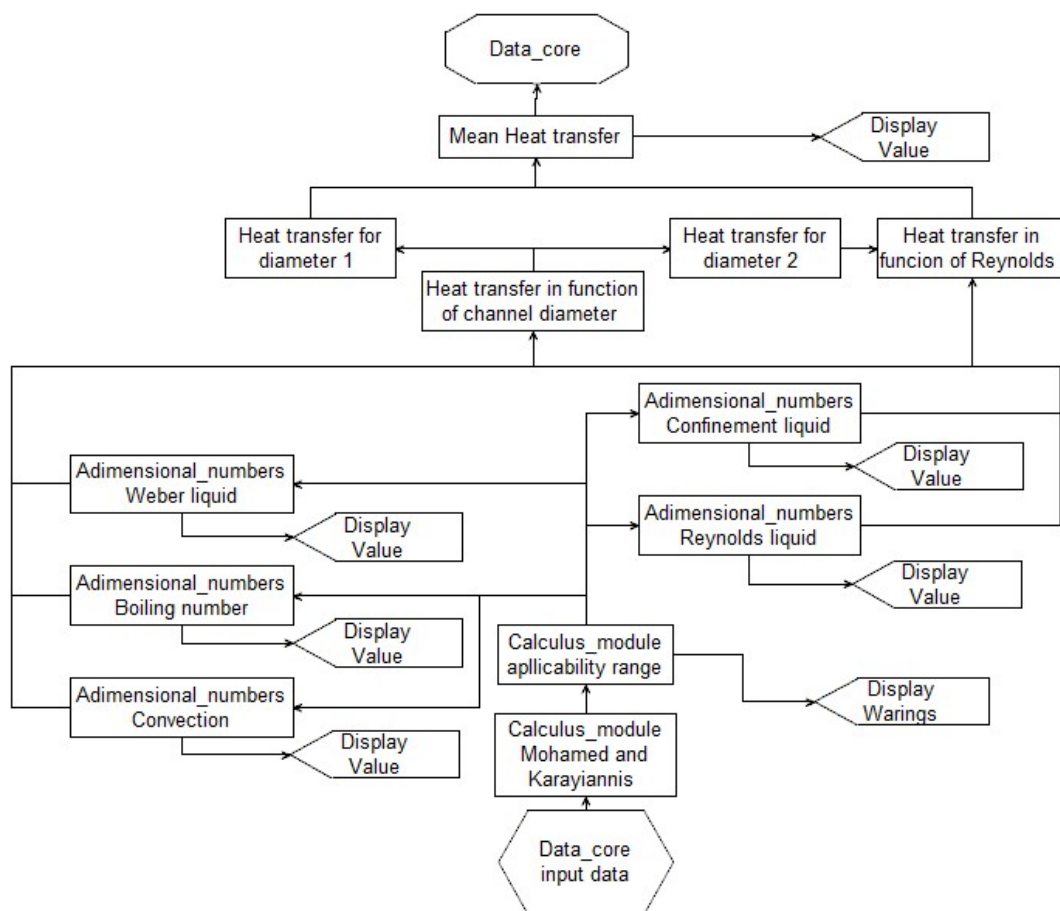
Figure 246: Mohamed and Karayiannis subroutine flux diagram

Bibliography

[1]   A.M. Jacobi, S.S. Mehendale, R.K. Shah, Fluid flow and heat transfer at micro- and meso-scales with application to heat exchanger design, Applied mechanics review, 53 (2000), 175–193.

[2]   Addlesee J. and Kew P. A. (2002). Development of the liquid film thickness above a sliding bubble. Transactions of Institute of Chemical Engineering, 80:272–277.

[3]   Agostini B. and Bontemps A. (2005). Vertical flow boiling of refrigerant R134a in small channels. Inter- national Journal of Heat and Fluid Flow, 26:296–306, 2005.

[4]   Agostini B., and Thome J. R. (1012). Experimental study on flow boiling heat trnasfer of multiport tubes with R245fa and R1234ze(E). In ECI 8th International Conference on Boiling and Condensation Heat Transfer.

[5]   Agostini B., Bontemps A., and Thonon B. (2006). Effects of geometrical and thermophysical parameters on heat transfer measurements in small-diameter channels. Heat Transfer Engineering, 27(1):14–24.

[6]   Agostini B., Fabbri M., Park J. E., Wojtan L., Thome J. R., and Michel B. (2007). State of the art of high heat flux cooling technogies. Heat Transfer Engineering, 28(4):258–281.

[7]   Agostini B., Revellin R., Thome J. R., Fabbri M., Michel B., Calmi D., and Kloter. U. (2008) High heat flux flow boiling in silicon multi-microchannels – Part III: Saturated critical heat flux of R236fa and two-phase pressure drops. International Journal of Heat and Mass Transfer, 51:5426–5442.

[8]   Agostini B., Thome J. R., Fabbri M., and Michel B. (2008). High heat flux two-phase cooling in silicon multimicrochannels. IEEE Transactions on Components and Packaging Technologies, 31:691– 701.

[9]   Agostini B., Thome J. R., Fabbri M., Michel B., Calmi D., and Kloter U. (2008). High heat flux flow boiling in silicon multi-microchannels – Part I: Heat transfer characteristics of refrigerant R236fa. International Journal of Heat and Mass Transfer, 51:5400–5414.

[10] Agostini, B., and Thome, J. R. (2005), Comparison of an Extended Database for Flo Boiling Heat Transfer Coeficients in Multi-Micro-channel Elements With the Three-Zone Model, ECI Heat Transfer and Fluid Flow in Micro-scale, Castelvecchio Pascoli, Italy, September 25–30.

[11] Agostini, B., Thome, J. R., Fabbri, M., Calmi, D., Kloter, U., and Michel, B., High (2008) Heat Flux Flow Boiling in Silicon Multi-Micro channels: Part II—Heat Transfer Characteristics of R-245fa, International Journal of Heat Mass Transfer, doi:10.1016/j.ijheatmasstransfer.2008.03.007.

[12] Arcanjo A., Tibirica C. B., and Ribatski G. (2010). Evaluation of flow patterns and elongate bubble characteristics during the flow boiling of halocarbon refrigerants in a microscale channel. Experimental Thermal and Fluid Science, 34:766–775.

[13] Baker O. (1954). Simultaneous flow of oil and gas. Oil and Gas Journal, 53:185–190.

[14] Bao, Z. Y., Fletcher, D. F., and Haynes, B. S. (2000), Flow Boiling Heat Transfer of Freon R11 and HCFC123 in Narrow Passages, International Journal of Heat and Mass Transfer, vol. 43, pp. 3347– 3358.

[15] Baranek, P., Marsden, K.C., and Best, F.R., (1994), "Zero-G Annular Flow and 1-G Stratified Flow Single Component Two-Phase Condensation Modeling," Proceedings of the ASME 1994 WAM, pp. 1137-1142.

[16] Barber J., Brutin D., Sefiane K., Gardarein J. L., and Tadrist L. (2011). Unsteady-state fluctuation analysis during bubble growth in a rectangular microchannel. International Journal of Heat and Mass Transfer, 54:4784–4795.

[17] Barber J., Sefiane K., Brutin D., and Tadrist L. (2009). Hydrodynamics and heat transfer during flow boiling instabilities in a single microchannel. Applied Thermal Engineeging, 29:1299–1308.

[18] Bergles, A. E., and Kandlikar, S. G. (2005), On the Nature of Critical Heat Flux in Micro channels, Journal of Heat Transfer, vol. 127, pp. 101–107.

[19]   Bertsch S. S., Groll E. A., and Garimella S. V. (2008), "Review and Comparative Analysis of Studies on Saturated Flow Boiling in Small Channels," Nanoscale and Microscale Thermophysical Engineering.

[20]   Bertsch S. S., Groll E. A., and Garimella S. V. (2009). A composite heat transfer correlation for saturated flow boiling in small channels. International Journal of Heat and Mass Transfer, 52:2110– 2118.

[21]   Bhide R., Singh S. G., Sridharan A., Duttagupta S. P., and Agrawal A. (2009). Pressure drop and heat transfer characteristics of boiling water in sub-hundred micron channel. Experimental Thermal and Fluid Science, 33:963–975.

[22]   Bilir S. (1995). Laminar flow heat transfer in pipes including two-dimensional wall and fluid axial conduction. International Journal of Heat and Mass Transfer, 38(9):1619–1625, 1995.

[23]   Bogojevic D., Sefiane K., Walton A. J., Lin H., Cummins G., Kenning D. B. R., and Karayiannis T. G. (2011), Experimental investigation of non-uniform heating effect on flow boiling instabilities in a microchannel-based heat sink. International Journal of Thermal Sciences, 50:309–324.

[24]   Borhani N., Agostini B., and Thome J. R. (2010). A novel time strip flow visualisation technique for investigation of intermittent dewetting and dryout in eleongated bubble flow in a microchannel evaporator. International Journal of Heat and Mass Transfer, 53:4809–4818.

[25]   Bower, J.S., Klausner, J.F., Sathyanarayan, S., (2002), "High Heat Flux, Gravity Independent, Two-Phase Heat Exchangers for Spacecraft Thermal Management," SAE Journal of Aerospace, Paper 2002-01-3196, pp. 747-755

[26]   Boye H., Staate Y., and Schmidt J. (2007). Experimental investigation and modelling of heat transfer during convective boiling in a minichannel. International Journal of Heat and Mass Transfer, 50(1-2): 208–215.

[27]   Brauner N. and Ullmann A. (2006). The prediction of flow boiling maps in minichannels. In 4th Japanese-European Two-Phase Flow Set Meeting, Kyoto, 24-28 September.

[28]   Brusstar, M.J., Merte, H., (1997), "Effects of Heater Surface Orientation"

[29]   C. Tribbe, H. Müller-Steinhagen. An Evaluation of the Performance of Phenomenological models for Predicting Pressure Gradient during Gas-Liquid Flow in Horizontal Pipelines, Int. J. Multiphase Flow 26 (2000), 1019-1036.

[30]   C.F. Colebrook, Turbulent flow in pipes with particular reference to the transition region between the smooth and rough pipe laws, Proceedings of the Institution of Civil Engineers, 12 (1939), 393-422.

[31]   Carey, V., (1992), Liquid-Vapor Phase-Change Phenomena, Hemishpere Publishing, New York.

[32]   Celata G. P., Cumo M., Marconi V., McPhail S. J., and Zummo G. (2006). Microtube liquid single- phase heat transfer in laminar flow. International Journal of Heat and Mass Transfer, 49:3538–3546.

[33]   Celata G. P., Saha S. K., Zummo G., and Dossevi D. (2010). Heat transfer characteristics of flow boiling in a single horizontal microchannel. International Journal of Thermal Sciences, 49:1086–1094.

[34]   CELATA G.P.; CUMO M.; D' ANNIBALE F.; F. GUGLIERMETTI; INGUÌ G. (1995). "A theoretical model for evaluation of direct boiling of R114 jets in water" REVUE GENERALE DE THERMIQUE (ISSN:0035-3159), 417- 425, 34;

[35]   Chen T. and Garimella S. V. (2006). Measurement and high-speed visualization of flow boiling of a dielectric fluid in a silicon microchannel heat sink. International Journal of Heat and Mass Transfer, 32:957–971.

[36]   Chen, J.C., (1966), "Correlation for Boiling Heat Transfer to Saturated Fluids in Convective Flow," I & EC Process Design and Development, Vol. 5. No. 3, pp. 322-329

[37]   Cheng L., Ribatski G., and Thome J. R. (2008). Two-phase flow patterns and flow-pattern maps: Fundamentals and applications. Applied Mechanics Reviews, 61:1–28.

[38]   Cheng P. and Wu H.Y. (2006). Mesoscale and microscale phase-change heat transfer. Advances in Heat Transfer, 39:469–573.

[39] Chisholm C. and Laird A. D. K. (1958). Two-phase flow in rough tubes. Journal of Heat Transfer (Transactions of the ASME), 80:276–286.

[40] Chisholm. D. (1967), A theoretical basis for the Lockhart-Martinelli correlation for two-phase flow. International Journal of Heat and Mass Transfer, 10:1767–1778.

[41] Chung P.M.Y. and Kawaji M. (2004). The effect of channel dialeter on adiabatic two-phase flow characteristics in microchannels. International Journal of Multiphase Flows, 30:735–761.

[42] Churchill S. W. and Usagi R. (1972). A general expression for the correlation of rates of transfer and the other phenomena. American Institute of Engineering of Chemical Engineering Journal, 18:1121–1128.

[43] Cicchitti, C. Lombardi, M. Silvestri, G. Soldaini, and R. Zavattarelli (1960). Two-phase cooling experiments – pressure drop, heat transfer and burnout measurements. Energia Nucleare, 7: 407–425.

[44] Cioncolini and J. R. Thome (2011). Algebraic turbulence modeling in adiabatic and evaporating annular two-phase fow. International Journal of Heat and Fluid Flow, 32:805–817.

[45] Cioncolini and John Richard Thome (2012). Entrained liquid fraction prediction in adiabatic and evaporating annular two-phase flow. Nuclear Engineering and Design, 243:200–213.

[46] Cioncolini, J. R. Thome, and C. Lombardi. (2009), Unified macro-to-microscale method to predict two-phase frictional pressure drops of annular flows. International Journal of Multiphase Flow, 35: 1138–1148.

[47] Coleman J.W. and Garimella S. (2003). Two-phase flow regimes in round, square and rectangular tubes during condensation of refrigerant r134a. International Journal of Refrigeration, 26:117–128.

[48] Collier J.G. and Thome J.R. (1994). Convective boiling and condensation. Oxford Univesity Press.

[49] Consolini L. and Thome J. R. (2010). A heat transfer model for evaporation of coalescing bubbles in micro-channel flow. International Journal of Heat and Fluid Flow, 31:115–125.

[50] Consolini, L. (2008), Convective Boiling Heat Transfer in a Single Micro-Channel, Ph.D. Dissertation, Ecole Polytechique F´ed´erale de Lausanne, Switzerland, http://library.epfl.ch/theses/?nr=4024.

[51] Consolini, L., and Thome J. R. (2008),Micro-Channel Flow Boiling Heat Transfer of R-134a, R-236fa, and R-245fa, J. Microfluidics and Nanofluidics: 10.1007/s10404-008-0348-7.

[52] Cooper G. (1984). Heat flow rates in saturated nucleate pool boiling - a wide-ranging experimentation using reduced properties. Advances in Heat Transfer, 16:157–239..

[53] Cooper, M.G., (1989), "Flow Boiling – the 'Apparently Nucleate' Regime" International Journal of Heat and Mass Transfer, Vol. 32, No.3, pp. 459-464.

[54] Cooper, M.G., Mori, K., and Stone, C.R., (1983), "Behavior of Vapour Bubbles"

[55] Cornwell, K., and Kew, P. A.(1993), Boiling in Small Parallel Channels, in Energy Efficiency in Process Technology, Elsevier Applied Science, London, pp. 624–638.

[56] Cortina Diaz M. and Schmidt J. (2007). Flow boiling of n-hexane in small channels heat transfer measurements and flow pattern observations. Chemical Engineering Technology, 3:389–394.

[57] Cortina Diaz M. and Schmidt J. (2007). Experimental investigation of transient boiling heat transfer in microchannels. International Journal of Heat and Fluid Flow, 28(1):95–102.

[58] Cortina Diaz M., Boye H., Hapke I., Schmidt J., Staate Y., and Zhekov Z. (2006). Investigation of flow boiling in narrow channels by thermographic measurements of local wall temperatures. Microfluidics and Nanofluidics, 2(1):1–11.

[59] Coskun A.K., Rosing T., Whisnant K., and Gross. K. (2008) Static and dynamic temperature- aware scheduling for multiprocessor SoCs. IEEE Transactions on Very Large Scale Integration (VLSI) Systems, 16(9):1127–1140..

[60] Costa-Patry E. and Thome J. R. (2012). Flow pattern based flow boiling heat transfer model for mi- crochannels. In ECI 8th International Conference on Boiling and Condensa-

tion Heat Transfer.

[61] Costa-Patry E. (2011). Cooling high heat flux micro-electronic systems using refrigerants in high aspect ratio multi-microchannel evaporators. PhD thesis, Ecole Polytechnique Federale de Lausanne.

[62] Costa-Patry E. and Thome J. R. (2011). Two-phase flow boiling in microchannels for cooling of micro- electronics. In 8th International Conference on Heat Transfer, Fluid Mechanics and Thermodynamics.

[63] Costa-Patry E., Nebuloni S., Olivier J., and Thome J. R. (2012). On-chip two-phase cooling with refrigerant 85 μm-wide multi-microchannel evaporator under hot-spot conditions. IEEE Transactions on Components, Packaging and Manufacturing Technology, 2(2):311–320.

[64] Costa-Patry E., Olivier J., Michel B., and Thome J. R. (2011). Two-phase flow of refrigerant in 85 μm-wide multi-microchannels: Part II – Heat transfer with 35 local heaters. International Journal of Heat and Fluid Flow, 32:464–476.

[65] Costa-Patry E., Olivier J., Nichita B. A., Michel B., and Thome J. R. (2011). Two-phase flow of refrigerant in 85 μm-wide multi-microchannels: Part I – Pressure drop. International Journal of Heat and Fluid Flow, 32:451–463.

[66] Costa-Patry E., Olivier J., Paredes S., and Thome J. R. (2010). Hot-spot self-cooling effects on two- phase flow of R245fa in 85 μm-wide multi-microchannels. In 16th International Workshop on Thermal Investigation of ICs and Systems (THERMINIC).

[67] Critical Heat Flux – II," International Journal of Heat and Mass Transfer, Vol. 40, No. 17, pp. 4021-4030.

[68] Crowley, C. J. and Sam. R. G. (1991) 'Microgravity Experiments with a Simple Two-Phase Thermal System', 8th Symposium on Space Nuclear Power Systems.

[69] Crowley, C.J., and Sam, R.G., (1991), "Microgravity Experiments with a Simple Two-Phase Thermal System," Proceedings of the Eighth Symposium on Space Nuclear Power Systems, pp. 1207-1213.

[70] Cubaud T., and Ho, C.-M. (2004), Transport of Bubbles in Square Micro- Channels, Physics of Fluids, vol. 16, no. 12, pp. 4575–4585.

[71] D. Chisholm, A theoretical basis for the Lockhart-Martinelli correlation for two-phase flow, Int. J. Heat Mass Transf. 10-18 (1967), 1767–1778.

[72] D.A. Mikielewicz, A new method for determination of flow boiling heat transfer coefficient in conventional-diameter channels and minichannels, Heat Transfer Eng. 31 (4) (2010) 276–287.

[73] Damianides C.A. and Westwater J.W. (1988). Two-phase flow patterns in a compact heat exchanger and in small tubes. 2nd Proceedings of the UK National Conference on Heat Transfer, Glasglow, Mechanical Engineering Publications, pages 1257–1268, Sept.

[74] Davis E. J. and Cooper T. J. (1969). Thermal entrance effects in stratified gas-liquid flow: experimental investigation. Chemical Engineering Science, 24:509–520.

[75] Departure in Forced Convection Boiling," International Journal of Heat and Mass Transfer, Vol. 36, No. 3, pp 651-662.

[76] Dhir, V.K., (1990), "Nucleate and transition boiling heat transfer under pool and external flow conditions," Proceedings of the 9th International Heat Transfer Conference, Jerusalem, Vol. 1, pp. 129-156.135

[77] Dupont and Thome J. R. (2005). Evaporation in microchannels: influence of the channel diameter on heat transfer. Microfluidics and Nanofluidics, 1:119–127.

[78] Dupont, Thome J. R., and Jacobi A. M. (2004). Heat transfer model for evaporation in microchannels. Part II: comparison with the database. International Journal of Heat and Mass Transfer, 47:3387–3401.

[79] Flow Boiling at Various Orientations," Transactions of the ASME, Vol.117, pp. 380-386.

[80] Forster, H. K., and Zuber, N. (1955), Dynamics of Vapor Bubbles and Boiling Heat Transfer, AIChe Journal, vol. 1, p. 531.

[81] Fu X., Qi S. L., Zhang P., and Wang R. Z. (2008). Visualization of flow boiling of liquid nitrogen in a vertical mini-tube. International Journal of Multiphase Flow, 34:333–351, 2008.

[82]   G. Hetsroni, A. Mosyak, Z. Segal, G. Ziskind, A uniform temperature heat sink for cooling of electronic devices, Int. J. Heat Mass Transfer 45 (2002), 3275– 3286.

[83]   G. Hetsroni, A. Mosyak, Z. Segal, G. Ziskind, A uniform temperature heat sink for cooling of electronic devices, Int. J. Heat Mass Transfer 45 (2002), 3275– 3286.

[84]   G. Kandlikar, Scale effect on flow boiling heat transfer in microchannels: a fundamental perspective. International journal of thermal sciences, 49 (2010), 1073–1085.

[85]   G. R Celata, M. Cumo, and T. Setaro Hysteresis phenomena in subcooled flow boiling of well-wetting fluids, Experimental Heat Transfer 5-4 (1992), 54-75.

[86]   G. Ribatski, L. Wojtan, J.R. Thome, An analysis of experimental data and prediction methods for two-phase frictional pressure drop and flow boiling heat transfer in micro-scale channels. Experimental thermal and fluid science 31-1 (2006), 1–19.

[87]   G. Ribatski, L. Wojtan, J.R. Thome, An analysis of experimental data and prediction methods for two-phase frictional pressure drop and flow boiling heat transfer in micro-scale channels. Experimental thermal and fluid science 31-1 (2006), 1–19.

[88]   G.E. Dix G.E., Vapor Void Fractions for Forced Convection with Subcooled Boiling at Low Flow Rate, Ph.D. Thesis, University of California (1971).

[89]   G.M. Lazarek, S.H. Black, Evaporative heat transfer, pressure drop and critical heat flux in a small vertical tube with R-113, Int. J. Heat Mass Transfer 25 (1982) 945–960.

[90]   G.M. Lazarek, S.H. Black, Evaporative heat transfer, pressure drop and critical heat flux in a small vertical tube with R-113, Int. J. Heat Mass Transfer 25 (1982) 945–960.

[91]   G.R. Warrier, V.K. Dhir, L.A. Momoda, Heat transfer and pressure drop in narrow rectangular channels, Exp. Therm. Fluid Sci. 26 (2002) 53–64.

[92]   Galvis E. and Culham R. (2012). Measurements and flow pattern visualizations of two-phase flow boiling in single channel evaporators. International Journal of Multiphase Flow, 42:52–61.

[93]   Gersey, C.O., and Mudawar, I., (1995), International Journal of Heat and Mass Transfer, Vol. 38, No. 4, pp. 629-641, "Effects of Heater Length and Orient tion on the Trigger Mechanism for Near-Saturated Flow Boiling Critical Heat Flux – II,"

[94]   Gersey, C.O., and Mudawar, I., (1995), Photomicrography and High-Speed Video Imaging," International Journal of Heat and Mass Transfer, Vol. 36, pp. 2511-2526. "Effects of Heater Length and Orientation on the Trigger Mechanism for Near-Saturated Flow Boiling Critical Heat Flux – I,"

[95]   Gnielinski V. (1976). New equations for heat and mass transfer in turbulent pipe and channel flow. Int. Chem. Eng 16(2):359—368.

[96]   Gungor, K.E., and Winterton, R.H.S., (1986), International Journal of Heat and Mass Transfer, Vol. 38, No. 4, pp. 643-654. "A General Correlation for Flow Boiling in Tubes and Annuli," International Journal of Heat and Mass Transfer, Vol. 29, pp. 351-358.

[97]   H. Müller-Steinhagen, K. Heck, A simple friction pressure drop correlation for two-phase flow in pipes, Chem. Process Engineering, Vol. 20 (1986), pp. 297-308.

[98]   H. Muller-Steinhagen, K. Heck. A simple friction pressure drop correlation for two-phase flow in pipes. Chem. Eng. Processing 20 (1986), 297–308.

[99]   H. Nabizadeh, Ubertragungsgesetze fur den Dampfvolum-enanteil zwischen Freon und Wasser, Kolloquium uber Aehnlichkeitsgesetze in Zweiphasenstromungen, Institut fur Verfahrenstechnik der T.U. Hannover (1980).

[100]   H.Y Wu, P. Cheng, An experimental study of convective heat transfer in silicon micro-channels with different surface conditions, Int. J. Heat and Mass Transfer, 46 (14) (2003) 2547–2556

[101]   Hapke, H. Boye, and J. Schmidt (2002). Flow boiling of water and n-heptane in micro channels. Microscale Thermophysical Engineering, 6(2):99–115.

[102]   Haramura, Y., and Katto, Y., (1982), "A New Hydrodynamic Model of Critical Heat Flux, Applicable Widely to Both Pool and Forced Boiling on Submerged Bodies in Saturated Liquids", International Journal of Heat and Mass Transfer. 26, No. 3, pp. 389- 399.

[103]   Hardt S., Schilder B., Tiemann D., Kolb G., Hessel V., and Stephan P. (2007). Analysis of flow patterns emerging during evaporation in parallel microchannels. International Journal of Heat and Mass Transfer, 50(1-2):226–239.

[104]   Harirchian T. and Garimella S. V. (2008). Microchannel size effects on local flow boiling heat transfer to a dielectric fluid. International Journal of Heat and Mass Transfer, 51:3724–3735.

[105]   Harirchian T. and Garimella S. V. (2009). Effects of channel dimension, heat flux, and mass flux on flow boiling regimes in microchannels. International Journal of Multiphase Flow, 35:349–362.

[106]   Harirchian T. and Garimella S. V. (2009). The critical role of channel cross-sectional area in microchan- nel. International Journal of Multiphase Flow, 35:904–913.

[107]   Harirchian T. and Garimella S. V. (2010). A comprehensive flow regime map for micro-channel flow boiling with quantitative transition criteria. International Journal of Heat and Mass Transfer, 53: 2694–2702.

[108]   Harirchian T. and Garimella S. V. (2012). Flow regime-based modeling of heat transfer and pressure drop in microchannel flow boiling. International Journal of Heat and Mass Transfer, 55:1246–1260.

[109]   Hetsroni G., Mosyak A., and Segal Z. (2001). Nonuniform temperature distribution in electronic devices cooled by flow in parallel microchannels. IEEE Transactions on Components and Packaging Technolo- gies, 24:16–23.

[110]   Hetsroni G., Mosyak A., Pogrebnyak , and Rozenblit R. (2011). Infrared temperature measurements in micro-channels and micro-fluid systems. International Journal of Thermal Sciences, 50:853– 868.

[111]   Hetsroni G., Mosyak A., Pogrebnyak E., and Segal Z. (2005). Explosive boiling of water in parallel micro-channels. International Journal of Multiphase Flow, 31(4):371–392.

[112]   Hetsroni G., Mosyak A., Pogrebnyak E., and Segal Z. (2009). Heat transfer of gas-liquid mixture in micro-channel heat sink. International Journal of Heat and Mass Transfer, 52:3963–3971.

[113]   Hetsroni G., Mosyak v, Pogrebnyak E., and Segal Z. (2006). Periodic boiling in parallel micro- channels at low vapor quality. International Journal of Multiphase Flow, 32:1141– 1159.

[114]   Hetsroni G., Mosyak, A. Segal Z., and Pogrebnyak E. (2003). Two-phase flow patterns in parallel micro-channels. International Journal of Multiphase Flow, 29(3):341–360, 2003.

[115]   Hewitt G.F. and Roberts D.N. (1969). Studies of two-phase flow patterns by simultaneous x-ray and flash photography. Technical report, Atomic Energy Research Establishment, Harwell, Report No. AERE-M 2159.

[116]   Hill W.S., and Best F.R., (1991), "Microgravity Two-Phase Flow Experiment and Test Results," 21st Conference on Environmental Systems, SAE Technical Paper Series 911556.

[117]   Hinze J.O., (1975), Turbulence, 2nd Edition, McGraw-Hill, New York. Ivey, H.J., and Morris, D.J., 1962, "On the Relevance of the Vapor-Liquid Exchange Mechanism for Sub-cooled Boiling Heat Transfer at High Pressure, UKAEA, AEEW-R 137.

[118]   Huo X., Chen L., Tian Y. S., and Karayiannis T. G. (2004). Flow boiling and flow regimes in small diameter tubes. Applied Thermal Engineering, 24:1225–1239.

[119]   J. Lee, I Mudawar, Fluid flow and heat transfer characteristics of low temperature two-hase micro-channel heat sinks – part 2. Subcooled boiling pressure drop and heat transfer, Int. J. Heat Mass Transfer 51 (2008) 4327– 4341.

[120]   J. Lee, I. Mudawar, Fluid flow and heat transfer characteristics of low temperature two-phase micro-channel heat sinks – part 1 experimental methods and flow visualization re-sults, Int. J. Heat Mass Transfer 51 (2008), 4315–4326.

[121]   J. Lee, I. Mudawar, Two-phase flow in high heat flux microchannel heat sink for refrigera-tion cooling applications. Part II: Heat transfer characteristics, Int. J. Heat Mass Transfer 48 (2005) 941–955.

[122]   J. Lee, I. Mudawar, Two-phase flow in high-heat-flux micro-channel heat sink for refrig-eration cooling applications: part I – pressure drop characteristics, Int. J. Heat mass transf. 48 (2005), 928–940.

[123]   J. M. Delhaye, F. Maugin, J.M. Ochterbeck, Void fraction predictions in forced convective subcooled boiling of water between 10 and 18 MPa, International Journal of Heat and

Mass Transfer 47 19-20 (2004), 4415-4425.

[124]   J. W. Coleman, S. Garimella, Characterization of two-phase flow patterns in small diameter round and rectangular tubes, Int. J. Heat and Mass Transfer, 42 (15) (1999) 2869–2881

[125]   J.C. Chen, A correlation for boiling heat transfer to saturated fluids in convective flow, Ind. Eng. Chem. 5 (1966) 322–329

[126]   J.M. Chawla, Wärmeübergang und Druckabfall in Waagerechten Rohren bei der strömung von Verdampfenden Kältemitteln, VDI-Verlag (1967).

[127]   J.M. Kay, R.M. Nedderman, An Introduction to Fluid Mechanics and Heat Transfer, third ed., Cambridge University Press, Cambridge (1974), 134-144.

[128]   J.R. Thome, V. Dupont, A.M. Jacobi, Heat transfer model for evaporation in microchannels. Part I: Presentation of the model, Int. J. Heat Mass Transfer 47 (2004) 3375–3385.

[129]   Jabardo J.M.S. and Filho E.P.B. (2000). Convective boiling of halocarbon refrigerants floying in a horizontal copper tube - an experimental study. Experimental Thermal Fluid Science, 23:93–104.

[130]   Jacobi A.M., Mehendale S.S. and Shah R.K. (2000). Fluid flow and heat transfer at micro- and meso-scales with applicaition to heat exchanger design. Applied Mechanics Review, 53:175–193, 2000.

[131]   Jacobi M. and Thome J. R. (2002). Heat transfer model for evaporation of eleongated bubble flows in microchannels. Journal of Heat Transfer, 124:1131–1136.

[132]   Jacobi, A. M., and Thome, J. R. (2002), Heat Transfer Model for Evaporation of Elongated Bubble Flows in Micro-channels, Journal of Heat Transfer, vol. 124, pp. 1131–1136.

[133]   Jiang L., Koo J. M., Zhang L., Wang E., Im S., Yao S., Zeng S., Bari A., Santiago J. G., Kenny T. W., and Goodson K. E. (2002). Progress on two-phase convection in microchannel heat sinks. In Proceedings of 4th Pacific Rim Thermal Science and Energy Engineering Workshop (PaRTSEE-4).

[134]   Jung, D.S., Venart, J.S., and Sousa, A.M., (1987), "Effects of Enhanced Surfaces and Surface Orientation on Nucleate and Film Boiling Heat Transfer in R111," International Journal of Heat and Mass Transfer, Vol. 30, No. 12, pp. 2627-2639.

[135]   K. Kuwahara, S. Koyama, K. Kazari, Experimental study of flow boiling of HFC134a in a multi-port extruded tube, ICMM2004, Rochester, New York, USA (2004).

[136]   K. Mishima, T. Hibiki, Some characteristics of air–water two-phase flow in small diameter vertical tubes, Int. J. Multiphase Flow 22 (1996) 703–712

[137]   K.A. Triplett, S.M. Ghiaasiaan, , S.I. Abdel-Khalik, D.L. Sadowski, Gas–liquid two-phase flow in microchannels Part I: two-phase flow patterns, Int. J. of Multiphase Flow, 25 (3) (1999) 377–394.

[138]   K.A. Triplett, S.M. Ghiaasiaan,, S.I. Abdel-Khalik, D.L. Sadowski, Gas–liquid two-phase flow in microchannels Part II: void fraction and pressure drop, Int. J. of Multiphase Flow, 25 (3) (1999) 395–410

[139]   K.E. Gungor, R.H.S. Winterton, A general correlation for flow boiling in tubes and annuli, Int. J. Heat Mass Transfer 29 (1986) 351–358.

[140]   Kandlikar G. (2010). Scale effectd on flow boiling heat transfer in microchannels: A fundamental perspective. International Journal of Thermal Sciences, 49:1073–1085.

[141]   Kandlikar S.G. (2001). Critical heat flux in sub-cooled flow boiling: An assesment of current understanding and future directions for research. Multiphase Science and Technology, 13, No. 3:207–232.

[142]   Kandlikar S.G. (2002). Two-phase flow patterns, pressure drop and heat transfer during boiling in minichannel flow passages of compact evaporators. Heat Transfer Engineering, 23:5–23.

[143]   Kandlikar, S. G. (2004), Heat Transfer Mechanisms During Flow Boiling in Micro channels, Journal of Heat Transfer, vol. 126, pp. 8–16.

[144]   Kandlikar, S. G., and Balasubramanian, P. (2004), An Extension of the Flow Boiling Correlation to Transition, Laminar, and Deep Laminar Flows in Mini-Channels and Micro-Channels, Heat Zhang, W., Hibiki, T., and Mishima, K., Correlation for Flow Boiling Heat Transfer in Mini-Channels, International Journal of Heat and Mass Transfer, vol. 47, pp.

5749–5763.

[145] Karayiannis G., Shiferaw D., Kenning D. B. R., and Wadekar V. V. (2010). Flow patterns and heat transfer for flow boiling in small to micro diameter tubes. Heat Transfer Engineering, 31(4): 257–275.

[146] Karayiannis T.G., Mahmoud M.M., Kenning D.B.R. (2012), A study of discrepancies in flow boiling results in small to micro diameter metallic tubes, Exp. Therm. Fluid Sci. 36 126–142.

[147] Kattan N., Thome J.R., and Favrat D. (1998). Flow boiling in horizontal tubes: Part 3 - Development of a new heat transfer model based on flow pattern. Journal of HeatTransfer - Trans of the ASME, 120:156–165.

[148] Katto Y. and Ohno H. (1984). An improved version of generalized correlation of critical heat flux for the forced convective boiling in uniformly heated vertical tubes. International Journal of Heat and Mass Transfer, 27(9):1641–1648.

[149] Kawahara, Sadatomi, Okayama, Kawaji, and Chung (2005). Effects of channel diameter and liquid properties on void fraction in adiabatic two-phase flow through microchannels. Heat Transfer Engineering, 26(3):13–19.

[150] Kenning, D.B.R., (1991), "Wall Temperature Patterns in Nucleate Boiling," International Journal of Heat and Mass Transfer, Vol. 35, No. 1, pp. 73-86.

[151] Kenning, D.B.R., and Cooper, M.G., (1989), "Saturated Flow Boiling of Water in Vertical Tubes," International Journal of Heat and Mass Transfer, Vol. 32, No. 3, pp. 445-458.136

[152] Kew, P. A., and Cornwell, K. (1997), Correlations for the Prediction of Boiling Heat Transfer in Small-Diameter Channels, Applied Thermal Engineering, vol. 17, pp. 705–715

[153] Kim T. H., Kommer E., Dessiatoun S. (2012), and J. Kim. Measurement of two-phase flow and heat transfer parameters using infrared thermography. International Journal of Multiphase Flow, 40:56–67.

[154] Kirby, D.B., and Westwater, J.W., (1965), "Bubble and Vapor Behavior on a Heated Horizontal Plate During Pool Boiling Near Burnout," Chemical Engineering Progress Symposium Series, Vol. 61, No. 57, pp. 238-247.

[155] Kirk, K.M., Merte, H., and Keller, R., (1995), "Low-Velocity Sub-cooled Nucleate boling"

[156] Klausner, J. F., Mei, R., Bernhard, D.M., and Zeng, L.Z., (1993), "Vapor Bubble Departure in Forced Convection Boiling," International Journal of Heat and Mass Transfer, Vol. 36, No. 3, pp 651-662.

[157] Klausner, J.F., and Mei, R., (1993), "A Unified Model for the Prediction of Bubble Detachment Diameters in Boiling Systems – I. Pool Boiling," International Journal of Heat and Mass Transfer, Vol. 36, No. 9, pp. 2261-2270.

[158] Klausner, J.F., Mei, R., and Zeng, L.Z., (1997), "Predicting Stochastic Features of Vapor Bubble Detachment in Flow Boiling," International Journal of Heat and Mass Transfer, Vol. 40, No. 15, pp3547-3552.

[159] Kohl M. J., Abdel-Khalik S. I., Jeter S. M., and Sadowski D. L. (2005). An experimental investigation of microchannel flow with internal pressure measurements. International Journal of Heat and Mass Transfer, 48:1518–1533.

[160] Kommer E., Scammell A., Solotych V., Dessiatoun S., and Kim. J. (2012), Multiphase convective heat transfer in microgravity via infrared thermography. In ECI 8th International Conference on Boiling and Condensation Heat Transfer.

[161] Krebs D., Narayanan V., Liburdy J., and Pence D. (2010), Spatially resolved wall temperature mesure- ments during flow boiling in microchannels. Experimental Thermal and Fluid Science, 34:434–445.

[162] L. Consolini, J.R. Thome, A heat transfer model for evaporation of coalescing bubbles in micro-channel flow, Int. J. Heat Fluid Flow 31 (1) (2010) 115–125.

[163] L. Consolini, J.R. Thome, Micro-channel flow boiling heat transfer of R-134a, R- 236fa, and R-245fa, Microfluid. Nanofluid. 6 (6) (2009) 731–746.

[164] L. Friedel, Improved friction pressure drop correlations for horizontal and vertical two-phase pipe flow, European Two-Phase Flow Group Meeting, Ispra, Italy, Paper E2 (1979).

[165] L. Friedel, Momentum exchange and pressure drop in two-phase, NATO Advanced Study

Institute, Istanbul, Turkey (1975) (Also Appendix B, P. Whalley "Boiling Condensation and Gas-Liquid Flow", Oxford, 1987).

[166] L. Friedel, Momentum exchange and pressure drop in two-phase, NATO Advanced Study Institute, Istanbul, Turkey (1975) (Also Appendix B, P. Whalley "Boiling Condensation and Gas-Liquid Flow", Oxford, 1987).

[167] L. Gugliermetti, G. Caruso, L. Saraceno, G. Zummo, G.P. Celata, Saturated flow boiling of FC-72 in 1 mm diameter tube, International Communications in Heat and Mass Transfer 75 (2016), 115-123.

[168] L. Saraceno, G.P. Celata, M. Furrer, A. Mariani, G. Zummo, Flow boiling heat transfer of refrigerant FC-72 in microchannels, Int. J. of Thermal Sciences, 53 (2012) 35-41

[169] L. Wojtan, R. Revellin, J. R. Thome, Investigation of saturated critical heat flux in a single, uniformly heated microchannel, Exp. Therm. Fluid Sci., 30 (8) (2006) 765–774

[170] Lallemand M., Branescu C., and Haberschill P. (2001). Local heat transfer coefficients during boiling of R22 and R407c in horizontal and smooth microfin tubes. International Journal of Refrigeration, 24:57–72.

[171] LATINI G.; PASSERINI G.; POLONARA F.; F. GUGLIERMETTI (1998) " Applicability of theoretical models to evaluation of thermal conductivity in microgravity". Proceeding of Congress STAIF, Albuquerque, 25-20 Jan., 20-25 Jan. Albuquerque,

[172] Lazarek, G. M., and Black, S. H. (1982), Evaporative Heat Transfer, Pressure Drop and Critical Heat Flux in a Small Vertical Tube with R-113, International Journal of Heat and Mass Transfer, vol. 25, no. 7, pp. 945–960.

[173] Lee J., Mudawar I. (2005), Two-phase flow in high heat flux microchannel heat sink for refrigeration cooling applications. Part II: Heat transfer characteristics, Int. J. Heat Mass Transfer 48 941–955.

[174] Lee P. S. and Garimella S. V. (2008). Saturated flow boiling heat transfer and pressure drop in silicon microchannel array. International Journal of Heat and Mass Transfer, 51:789–806.

[175] Lee, R.C., and Nydahl, J.E. (1989), "Numerical Calculation of Bubble Growth in Nucleate Boiling from Inception through Departure," Transactions of the ASME, Vol. 111, pp. 474-478.

[176] Lelea C. (2007). The conjugate heat transfer of the partially heated microchannels. Heat and Mass Transfer, 44:33–41.

[177] Li J.M. and Wang B.K. (2003). Size effect on two-phase flow regime for condensarion in micro/mini tubes. Heat Transfer-Asian Research, 32:65–71.

[178] Li W., Wu Z. (2010), A general correlation for evaporative heat transfer in micro/minichannels, Int. J. Heat Mass Transfer 53, 1778–1787.

[179] Lienhard, J.H., and Dhir, V.K., (1973), "Hydrodynamic Prediction of Peak Pool-boiling Heat Fluxes from Finite Bodies," Transactions of the ASME, Series C, Journal of Heat Transfer, Vol. 95, pp. 152-158.

[180] Lihong, W., Min, C., and Groll, M. (2005), Experimental Study of Flow Boiling Heat Transfer in Mini-Tube, ICMM2005.

[181] Lin S., Kew P. A., and Cornwell K. (2001). Flow boiling of refrigerant R141b in small tubes. Trans IChemE, 79, Part A:417–424.

[182] Lin T.-Y. and Kandlikar S. G. (2012). A theoretical model for axial heat conduction effects during single- phase flow in microchannels. Journal of Heat Transfer, 134:1–6.

[183] Lin, S., Kew, P. A., and Cornwell, K. (2001), Two-Phase Heat Transfer to a Refrigerant in a 1mm Diameter Tube, International Journal of Refrigeration, vol. 24, pp. 51–56.

[184] Liu Z., Winterton R.H.S. (1991), A general correlation for saturated and subcooled flow boiling in tubes and annuli, based on a nucleate pool boiling equation, Int. J. Heat Mass Transfer 34 (II), 2759–2766.

[185] Liu Z., Zhao Y., and Takei M. (2997). Experimental study on axial wall heat conduction for convective heat transfer in stainless steel tube. Heat and Mass Transfer, 43:587–594.

[186] Lockhart R. W. and Martinelli R. C. (1949). Proposed correlation of data for isothermal two-phase, two-component flow in pipes. Chemical Engineering Progress, 45:39–48.

[187] Lowe D.C. and Rezkallah K.S. (1999). Flow regime identification in microgravity two-

phase flow using void fraction signals. International Journal of Multipjhase Flow, 25:433–457.

[188] M. Caira, G. Caruso, A. Naviglio, A correlation to predict CHF in subcooled flow boiling, Int Comm. in Heat and Mass Transfer, Vol. 22 (1995), 35-45.

[189] M. K. Akbar, S. M. Ghiaasiaan Simulation of Taylor Flow in Capillaries Based on the Volume-of-Fluid Technique, Ind. Eng. Chem. Res., 45 (15) (2006) 5396–5403

[190] M. M. Mahmoud, T. G. Karayiannis, Heat transfer correlation for flow boiling in small to micro tubes, Int. J. Heat and Mass Transfer, 66 (2013) 553–574

[191] M. Margulis, E. Shwageraus, Extending Two-Phase Capabilities of Thermal-Hydraulic Module in BGCore, Reactor Physics and Technology II (In memory of Dr. Uri Mintzer) (2014).

[192] M. S. Yalin, A.M.A.F. Da Silva, Fluvial processes, IAHR, Delft, Netherlands (2001).

[193] M. Zhang, R.L. Webb, Correlation of two-phase friction for refrigerants in small-diameter tubes, Exp. Thermal Fluid Sci. 25 (2001) 131–139.

[194] M.B. Bowers, I. Mudawar, Two-phase electronic cooling using mini-channel and micro-channel heat sinks: part 1 – Design Criteria and Heat Diffusion Constraints, J. Electron. Packag. 116 (1994), 290–297.

[195] M.B. Bowers, I. Mudawar, Two-phase electronic cooling using mini-channel and micro-channel heat sinks: Part 2— flow rate and pressure drop constraints, J. Electron. Packaging 116 (1994) 298–305.

[196] M.B. Ould Didi, N. Kattan, J.R. Thome, Prediction of Two-Phase Pressure Gradients of Refrigerants in Horizontal Tubes, International Journal of Refrigeration 25 (2002), 935-947.

[197] M.G. Cooper, Saturated nucleate pool boiling – a simple correlation, in: First UK National Heat Transfer Conference, IChemE Symposium, Series 86, vol. 2, 1984, pp. 785–793.

[198] M.M. Shah, Chart correlation for saturated boiling heat transfer: equations and further study, ASHRAE Trans. 88 (pt 1) (1982) 185–196.

[199] Ma Y. and Chung J. N. (2001), "A study of bubble dynamics in reduced gravity forced-convection boiling," Int. J. Heat Mass Transfer, vol. 44, pp. 399–415.

[200] Martin-Callizo C., Palm B., Owhaib W., and Ali R. (2010). Flow boiling visualization of R-134a in a vertical channel of small diameter. Journal of Heat Transfer, 132(3):1–8.

[201] Martin-Callizo, C., Ali, R. and Palm, B. (2007), New Experimental Results on Flow Boiling of R-134a in a Vertical Micro channel, UK Heat Transfer 2007 Proceedings, Edinburgh.

[202] Mauro W., Thome J. R., Toto D., and Vanoli G. P. (2010). Saturated critical heat flux in a multi- microchannel heat sink fed by a split flow system. Experimental Thermal and Fluid Science, 34:81–92.

[203] Mei, R., Chen W., and Klausner J.F., (1995), "Vapor Bubble Growth in Heter geneous Boiling – I. Formulation," International Journal of Heat and Mass Transfer, Vol. 38, No. 15, pp. 909-919.

[204] Mei, R., Chen W., and Klausner J.F., (1995), "Vapor Bubble Growth in Heterogeneous Boiling – II. Growth Rate and Thermal Fields," International Journal of Heat and Mass Transfer, Vol. 38, No. 15, pp. 921-934.

[205] Mikic, B.B., Rohsenow, W.M., and Griffith, P., (1970), "On Bubble Growth Rates," International Journal of Heat and Mass Transfer, Vol. 13, pp. 657-666.

[206] Mikielewicz D.A (2010)., A new method for determination of flow boiling heat transfer coefficient in conventional-diameter channels and minichannels, Heat Transfer Eng. 31 (4) 276–287.

[207] Miller, K.M., Ungar, E.K., Dzenitis, J.M., and Wheeler, M., (1993), "Microgravity Two-Phase Pressure Drop Data in Smooth Tubing," Fluid Mechanics Phenomena in Microgravity, ASME FED-Vol.175, 00. 37-50.

[208] Mishima K. and Hibiki T. (1996). Some characteristics of air-water two-phase flow in small diameter vertical tubes. International Journal of Multiphase Flow, 22(4):703–712.

[209] Mohamed M. Mahmouda, Tassos G. Karayiannis (2012), Heat transfer correlation for flow boiling in small to micro tubes.

[210]   Moharana M. K., Singh P. K., and Khandekar S. (2011). Axial heat conduction in the context of developing flows in microchannels. In 9th International Conference on Nanochannels, Microchannels, and Minichannels.

[211]   Moharana M. K., Singh P. K., and Khandekar S. (2012). Optimum Nusselt number for simulataneously developing internal flow under conjugate conditions in a square microchannel. Journal of Heat Transfer, 134:1–10.

[212]   Morini G. L. (2006). Scaling effects for liquid flows in microchannels. Heat Transfer Engineering, 27(4): 64–73.

[213]   Moriyama K. and Inoue A. (1996). Thickness of the liquid film formed by a growing bubble in a narrow gap between two horizontal plates. Journal of Heat Transfer, 118:132–139.

[214]   Muzychka Y. S. and Yovanovich M. M. (2004). Laminar forced convection heat transfer in the combined entry region of non-cicular ducts. Transactions of the ASME, 54126:54–61.

[215]   N. Ullmann and N. Brauner, The Prediction of Flow Pattern Maps In Mini Channels, Multiphase Science and Technology, 19 (2007) 49-73.

[216]   N. Zuber, J.A. Findlay, Average volumetric concentration in two phase flow systems, J. Heat Transfer 87 (1965), 453–467.

[217]   N.S. Cheng, Formulas for friction factor in transitional regions, Journal of Hydraulic Engineering, ASCE 134-9 (2008)., 1357-1362.

[218]   N.S. Cheng, Formulas for friction factor in transitional regions, Journal of Hydraulic Engineering, ASCE 134-9 (2008)., 1357-1362.

[219]   N.S. Cheng, Y.M. Chiew, Modified logarithmic law for velocity distribution subjected to upward seepage, Journal of Hydraulic Engineering, ASCE 124-12 (1998), 1235-1241.

[220]   Nishikawa, K., Fujita, Y., Ohta, H., and Hidaka, S. (1982). "Effect of the Surface Roughness on the Nucleate Boiling Heat Transfer over the Wide Range of Pressure". Heat Transfer 1982, Proc. 7th Int. Heat Transfer Conf., Vol. 4, pp. 61–66. 30.

[221]   Ong L. and Thome J. R. (2009). Flow boiling heat trasnfer of R134a, R236fa and R245fa in a horizontal 1.030 mm circular channel. Experimental Thermal and Fluid Science, 33:651–663.

[222]   Ong. L. (2010) Macro-to-microchannel transition in two-phase flow and evaporation. PhD thesis, Ecole Polytechnique Federale de Lausanne.

[223]   P. Griffith, J.A. Clark, W.M. Roshenow, Void volumes in subcooled boiling systems, ASME Paper 58-T-19, New York (1958).

[224]   P. Saha, N. Zuber, Point of net vapor generation and vapor void fraction in subcooled boiling, Fifth Int. Heat Transfer Conf., Tokyo, Paper B4.7 (1974).

[225]   P.A. Kew, K. Cornwell, Correlations for the prediction of boiling heat transfer in small diameter channels, Appl. Therm. Eng. 17 (8-10) (1997) 705–715

[226]   P.M. Ligrani, R.J. Moffat, Structure of Transitionally Rough and Fully Rough Turbulent Boundary-Layers, Journal of Fluid Mechanics 162 (1986), 69-98.

[227]   P.S. Lee, S.V. Garimella, Saturated flow boiling heat transfer and pressure drop in silicon microchannel arrays, Int. J. Heat mass transf. 51 (2008), 789–806.

[228]   Park J. E. and Thome J. R. (2010). Critical heat flux in multi-microchannel copper elements with low pressure refrigerants. International Journal of Heat and Mass Transfer, 53:110–122.

[229]   Park J. E. (2008). Critical heat flux in multi-microchannel copper elements with low pressure refrigerants. PhD thesis, Ecole Polytechnique Federale de Lausanne.

[230]   Park J. E., Thome J. R., and Michel B. (2009). Effect of inlet orifices on saturated CHF and flow visualisation in multi-microchannel heat sinks. In 25th IEEE Semiconductor Thermal Measurement and Management (SEMI-THERM) Symposium.

[231]   Patil V. A. and Narayanan V. (2005). Measurement of near wall liquid temperatures in single-phase flow through silicon microchannels. In Proceedings of the 3rd International Conference on Microchannels ans Minichannels.

[232]   Patil V. A. and Narayanan V. (2006). Spatially resolved temperature measurement in micro channels. Microfluidics and Nanofluidics, 2:291–300.

[233] Peterson R.B. (1999). Numerical modeling of conduction effects in microscale counter flow heat exchangers. Microscale Thermophysical Engineering, 3(1):17–30.

[234] Piasecka M., Hozejowska S., Poniewski M.E. (2004), Experimental evaluation of flow boiling incipience of subcooled flow in a narrow channel, Int. J. Heat Fluid Flow 25 159–172

[235] Pierre-Gilles; Brochard-Wyart, Françoise; Quéré, David (2004). Capillarity and Wetting Phenomena: Drops, Bubbles, Pearls, Waves. New York: Springer. p. 119. ISBN 978-0-387-00592-8.

[236] R. Gronnerud, Investigation of liquid hold up, flow resistance and heat transfer in circulation type evaporators, Part IV: two phase flow resistance in boiling refrigerants, Annex 1972-1, Bull Del'Inst. Du Froid (1972).

[237] R. Revellin, V. Dupont, T. Ursenbacher, J. R. Thome, I. Zunc, Characterization of diabatic two-phase flows in microchannels: Flow parameter results for R-134a in a 0.5 mm channel, Int. J. of Multiphase Flow, 32 (7) (2006) 755–774

[238] R.K. Shah, Classification of heat exchangers. In heat exchangers: thermal hydraulic fundamentals and design (S. Kakac, A.E. Bergles, F. Mayinger, eds.), Hemisphere, Washington D. C. (1991), 9-14.

[239] R.T.Jr. Lahey, F.T. Moody F.J., The Thermal Hydraulics of a Boiling Water Nuclear Reactor, American Nuclear Society, LaGrange Park (1977).

[240] R.W. Lockhart, R.C. Martinelli, Proposed correlation of data for isothermal two-phase two-component flow in pipes, Chem. Eng. Progr. 45-1 (1949), 39–48.

[241] Revellin R. (2005). Experimental two-phase fluid flow in microchannels. PhD thesis, Ecole Polytechnique Federale de Lausanne.

[242] Revellin R. and Thome J. R. (2008). A theoretical model for the prediction of the critical heat flux in heated microchannels. International Journal of Heat and Mass Transfer, 51:1216–1225.

[243] Revellin R., Dupont V., Ursenbacher T., Thome J. R., and Zun I. (2006). Characterization of two- phase flows in microchannels: Optical measurement technique and flow parameter results for R-134a in a 0.5 mm channel. International Journal of Multiphase Flow, 32(7):755–774.

[244] Revellin, R., Agostini, B., and Thome, J. R. (2008), Elongated Bubbles in Micro channels Part II: Experimental Study and modeling of Bubble Collisions, International Journal of Multiphase Flow, doi:10.1016/j.ijmultiphaseflow.2007.07.006.

[245] Revellin, R., and Thome, J. R. (2006), A New Type of Diabatic Flow Pattern Map for Boiling Heat Transfer in Micro channels, Journal of Micromechanics and Micro engineering, vol. 17, pp. 788–796.

[246] Revellin, R., Dupont, V., Thome, J. R., and Zun, I (2006)., Characterization of Diabatic Two-Phase Flows in Micro-Channels: Flow Parameter Results for R-134a in a 0.5 mm Channel, International Journal of Multiphase Flow, vol. 32, pp. 755–774.

[247] Ribatski G., Wojtan L., and Thome J. R. (2006). An analysis of experimental data and prediction methods for two-phase frictional pressure drop and flow boiling heat transfer in micro-scale channels. Experimental Thermal and Fluid Science, 31:1–19.

[248] Rite, R.W., and Rezkallah, K.S., (1993), "An Investigation of Transient Effects on Heat Transfer Measurements in Two-Phase, Gas-Liquid Flows Under Microgravity Conditions," Heat Transfer in Microgravity Systems, ASME HTD-Vol. 235, pp. 49-57.

[249] Rite, R.W., and Rezkallah, K.S., (1997), "Local and Mean Heat Transfer Coefficients in Bubbly and Slug Flows Under Microgravity Conditions," International Journal of Multiphase Flow, Vol. 23, No. 1, pp. 37-54.137

[250] Roshenow, W.M., (1952), "Heat Transfer, A Symposium," Engineering Research Institute, University of Michigan, Ann Arbor, Michigan

[251] S. Levy, Forced convection subcooled boiling-prediction of vapor volumetric fraction, Int. J. Heat Mass Transfer 19 (1967), 99–113.

[252] S. Levy, Forced convection subcooled boiling-prediction of vapor volumetric fraction, Int. J. Heat Mass Transfer 19 (1967), 99–113.

[253] S. Saitoh, H. Daiguji, E. Hihara, Correlation for boiling heat transfer of R134a in horizon-

tal tubes including effect of tube diameter, Int. J. Heat Mass Transfer 50 (2007) 5215–5225.

[254]   S.G. Kandlikar, A general correlation for saturated two-phase flow boiling heat transfer inside horizontal and vertical tubes, J. Heat Transfer Trans. ASME 112 (1990) 219–228.

[255]   S.G. Kandlikar, M.E. Steinke, S. Tian, L.A. Campbell, High-speed photographic observation of flow boiling of water in parallel mini-channels, Proceedings of 35th National Heat Transfer Conference, ASME, Anaheim, CA (2001), 675–684.

[256]   S.G. Kandlikar, P. Balasubramanian, An extension of the flow boiling correlation to transition, laminar, and deep laminar flows in minichannels and microchannels, Heat Transfer Eng. 25 (3) (2004) 86–93.

[257]   S.M. Kim, I. Mudawar, Consolidated method to predicting pressure drop and heat transfer coefficient for both subcooled and saturated flow boiling in micro-channel heat sinks, International Journal of Heat and Mass Transfer, Volume 55 13–14 (2012), 3720-3731.

[258]   S.M. Kim, I. Mudawar, Theoretical model for local heat transfer coefficient for annular flow boiling in circular mini/micro-channels, Int. J. Heat and Mass Transfer, 73 (2014) 731–742.

[259]   S.M. Kim, I. Mudawar, Universal approach to predicting two-phase frictional pressure drop for mini/micro-channel saturated flow boiling, Int. J. Heat Mass Transf. 58 (1–2) (2013), 718–734.

[260]   S.M. You, T.M. Simon, A. Bar-Cohen, Experiments on Nucleate Boiling Heat Transfer with a Highly-Wetting Dielectric Fluid: Effects of Pressure, Subcooling and Dissolved Gas Content, Cryogenic and Immersion Cooling of Optics and Electronic Equipment, HTD-Vol. 131 (1990), 45–52.

[261]   S.M. You, T.M. Simon, A. Bar-Cohen, Experiments on Nucleate Boiling Heat Transfer with a Highly-Wetting Dielectric Fluid: Effects of Pressure, Subcooling and Dissolved Gas Content, Cryogenic and Immersion Cooling of Optics and Electronic Equipment, HTD-Vol. 131 (1990), 45–52.

[262]   S.S. Bertsch, E.A. Groll, S.V. Garimella, A composite heat transfer correlation for saturated flow boiling in small channels, Int. J. Heat Mass Transfer 52 (7–8) (2009) 2110–2118.

[263]   S.S. Bertsch, E.G. Groll, S.V. Garimella, Review and comparative analysis of studies on saturated flow boiling in small channels, Nanoscale Microscale Thermophys. Eng. 12 (3) (2008) 187–227.

[264]   Sabry M., Sridhar A., Atienza D., Temiz Y., Leblebici Y., Szczukiewicz S., Borhani N., White M. (1999). Fluid mechanics. McGraw-Hill, 4th edition.

[265]   Saisorn S., Kaew-On J., and Wongwises S. (2010). Flow pattern and heat transfer characteristics of R-134a refrigerant during flow boiling in a horizontal circular mini-channel. International Journal of Heat and Mass Transfer, 53:4023–4038.

[266]   Saitoh S., Daiguji H., and Hihara E. (2005). Effect of tube diameter on boiling heat transfer of R-134a in horizontal small-diameter tubes. International Journal of Heat and Mass Transfer, 48:4973–4984.

[267]   Saitoh S., Daiguji H., and Hihara E. (2007). Correlation for boiling heat trnasfer of R-134a in horizontal tubes including effect of tube diameter. International Journal of Heat and Mass Transfer, 50:5215–5225.

[268]   Sathyanarayan, S., (2003), "Gravity Dependent/Independent Regime Maps for Subcooled Flow Boiling", Masters Thesis, Department of Mechanical and Aerospace Engineering, University of Florida.

[269]   Sato T., Minamiyama T., Yanai M., Tokura T., and Ito Y. (1971). Study of heat transfer in boiling two-phase channel flow-part 2: Heat transfer in the nucleate boiling region. Heat Transfer Japanese Research, 1(1):15–30.

[270]   Schneider B., Kosar A., and Peles Y. (2007). Hydrodynamic cavitation and boiling in refrigerant (R-123) flow inside microchannels. International Journal of Heat and Mass Transfer, 50:2838–2854.

[271]   Serizawa A., Fukano T., Bataille J. (1995), Multiphase Flow.

[272]   Serizawa, A., Feng, Z., and Kawara, Z. (2002), Two-Phase Flow in Micro-channels, Experimental Thermal and Fluid Science, vol. 26, pp. 703–714.

[273] Shah R. K. and London A. L. (1978). Laminar flow forced convection in ducts. Academic Press.

[274] Shah R.K. (1986). Classification of heat exchangers. In Heat Exchangers: Thermal Hydraulic Fundamentals and Design, S. Kakac, A.E. Bergles, F. Mayinger, eds., Hemisphere, Washington D.C.

[275] Shah, M.M., (1982), "Chart Correlation for Saturated Boiling Heat Transfer: Equations and Further Study," ASHRAE Trans., Vol. 88, pp. 185-196.

[276] Shiferaw D., Karayiannis T. G., and Kenning D. B. R. (2009). Flow boiling in a 1.1 mm tube with R134a: Experimental results and comparison with model. International Journal of Thermal Sciences, 48(2):331–341.

[277] Shiferaw, D., Huo, X., Karayiannis, T. G., and Kenning, D. B. R. (2007), Examination of Heat Transfer Correlations and a Model for Flow Boiling of R-134a in Small Diameter Tubes, International Journal of Heat and Mass Transfer, vol. 50, pp. 5177–5193.

[278] Standley, V.H., and Fairchild, J.F., (1991), "Boiling and Condensing Pumped Loop Micro-gravity Experiment," Proceedings of the Eighth Symposium on Space Nuclear Power Systems, pp. 1224-1229.

[279] Steiner (1993). VDI-Warmeatlas (VDI Heat Atlas). Verein Deutscher Ingenieure, Dusseldorf, Chapter Hbb.

[280] Steiner D. and Taborek J. (1992). Flow boiling heat transfer in vertical tubes correlated by an asymptotic model. Heat Transfer Engineering, 13(2):43–69.

[281] Su S., Huang S., and Wang X. (2005). Study of boiling ncipience and heat transfer enhancement in forced flow through narrow channels. International Journal of Multiphase Flow, 31:253–260.

[282] Sumith, B., Kaminaga, F., and Matsumura, K (2003)., Saturated Flow Boiling of Water in a Vertical Small Diameter Tube, Experimental Thermal and Fluid Science, vol. 27, pp. 789–801.

[283] Suo M. (1963). Two-phase flow in capillary tubes. PhD thesis, Massachusetts Institute of Technology.

[284] T. Harirchian, S. V. Garimella, Boiling Heat Transfer and Flow Regimes in Microchannels—A Comprehensive Understanding, Journal of Electronic Packaging, MARCH 2011, Vol. 133 / 011001-1

[285] T.N Tran, M.-C Chyu, M.W Wambsganss, D.M France, Two-phase pressure drop of refrigerants during flow boiling in small channels: an experimental investigation and correlation development, International Journal of Multiphase Flow 26-11 (2000), Pages 1739-1754.

[286] T.N. Tran, M.W. Wambsganss, M.-C. Chyu, D.M. France, A correlation for nucleate flow boiling in small channels, in: Compact Heat Exchangers for the Process Industries Conference, Snowbird, Utah, June 22 – 27, 1997.

[287] Taitel Y. and Dukler A.E. (1976). A model for predicting flow regime transitions in horizontal and near horizontal gas-liquid flow. AIChE Journal, 22:47–55.

[288] the Effects of Body Force, Surface Tension Force, and Inertia on Flow Boiling CHF," International Journal of Heat and Mass Transfer, Vol. 45, pp. 4079-4095.

[289] Thome (2006). State-of-the-art overview of boiling and two-phase flows in microchannels. Heat Transfer Engineering, 27(9):4–19.

[290] Thome J. R. and Consolini L. (2010). Mechanisms of boiling in micro-channels: Critical assessment. Heat Transfer Engineering, 31(4):288–297.

[291] Thome J. R. (2004). Boiling in microchannels: a review of experiment and theory. International Journal of Heat and Fluid Flow, 25:128–139.

[292] Thome J. R. (2010). Wolverine Engineering Data Book III. http://www.wlv.com.

[293] Thome J. R., Brunschwiler T., and Michel B. (2011). Towards thermally-aware design of 3D MPSoCs with inter-tier cooling. In Design, Automation and Test in Europe.

[294] Thome, J. R., Dupont, V., and Jacobi, A.M. (2004), Heat Transfer Model for Evaporation in Micro-channels. Part I: Presentation of the Model, International Journal of Heat and Mass Transfer, vol. 47, pp. 3375–3385.

[295] Thorncroft, G.E, and Klausner, J.F., (1997), "Visual Observations of Vapor Bubble Dy-

namics in Vertical Flow Boiling," Proceedings of the Engineering Foundation International Conference, on Convective Flow and Pool Boiling II, Irsee, Germany, May 18-23, paper VIII-1.

[296]   Thorncroft, G.E., and Klausner, J.F., (1999), "The Influence of Vapor Bubble Sliding on Forced Convection Boiling Heat Transfer," Journal of Heat Transfer, Vol. 121, pp. 73-79.

[297]   Thorncroft, G.E., Klausner, J.F., and Mei, R., (2001), "Bubble Forces and Detachment Models,"Multiphase Science and Technology, Vol. 13, Nos. 3 & 4, pp. 1- 42.

[298]   Thorncroft, G.E., Klausner, J.F., and Mei, R., (2001), "Bubble Forces and Detachment Models," Multiphase Science and Technology, Vol. 13, Nos. 3 & 4, pp. 1- 42.

[299]   Tibirica B., Ribatski G., and Thome J. R. (2012). Flow boiling characteristics for R1234ze(E) in 1.0 and 2.2 mm circular channels. Journal of Heat Transfer, 134:1–8.

[300]   Tran T.N, Chyub M.-C, Wambsganssa M.W, Francec D.M (2000),Two-phase pressure drop of refrigerants during flow boiling in small channels: an experimental investigation and correlation development International Journal of Multiphase Flow, Volume 26, Issue 11, 1 November 2000, Pages 1739–1754

[301]   Tran, T. N., Wambsganss, M. W., and France, D. M. (1996), Small Circular- and Rectangular-Channel Boiling with Two Refrigerants, International Journal of Multiphase Flow, vol. 22, no. 3, pp. 485–498.

[302]   Triplett K.A., Ghiaasiaan S.M., Abdel-Khalik S.I. and Sadowski D.L. (1999). Gas liquidtwo-phase flow in microchannels. part 1 - Two-phase flow patterns. International Journal of Multiphase Flow, 25:377–394.

[303]   Triplett K.A., Ghiaasiaan S.M., Abdel-Khalik S.I., LeMouel A., and. McCord B.N (1999). Gas liquid two-phase flow in microchannels. part 2- Void fraction and pressure drop. International Journal of Multiphase Flow, 25:395–410.

[304]   Tripplett, K. A., Ghiaasiaan, S. M., Abdel-Khalik, S. I., and Sadowski, D. L. (1999), Gas–Liquid Two-Phase Flow in Micro-Channels Part I: Two-Phase Flow Patterns, International Journal of Multiphase Flow, vol. 25, pp. 377–394.

[305]   UNFCCC. Kyoto Protocol to the United Nations Framework Convention on Climate Change (1997). http://unfccc.int/kyoto_protocol/items/2830.php/.

[306]   V. Dupont, J.R. Thome, A.M. Jacobi, Heat transfer model for evaporation in microchannels. Part II: Comparison with the database, Int. J. Heat Mass Transfer 47 (2004) 3387–3401.

[307]   V.S. Osmachkin, V. Borisov, Pressure drop and heat transfer for flow boiling water in vertical rod bundles, Paper B4.9, IVth International Heat Transfer Conference Paris-Versailles (1970).

[308]   V.S. Osmachkin, V. Borisov, Pressure drop and heat transfer for flow boiling water in vertical rod bundles, Paper B4.9, IVth International Heat Transfer Conference Paris-Versailles (1970).

[309]   Van Helden, W.G.J., Van der Geld, C.W.M., and Boot, P.G.M., (1995), "Forces on Bubbles Growing and Detaching in Flow Along a Vertical Wall," International Journal of Heat and Mass Transfer, Vol. 38, No. 11, pp. 2075-2088.

[310]   Van Stralen, S.J.D., Cole, R., Sluyter, W.M., and Sohal, M.S., (1975), "Bubble Growth Rates in Nucleate Boiling of Water at Subatmospheric Pressures", International Journal of Heat and Mass Transfer, Vol. 18, pp. 655-669.

[311]   Vick C. and Ozisik M. N. (1981). An exact analysis of low Peclet number heat transfer in laminar flow with axial conduction. Letter in Heat and Mass Transfer, 8:1–10.

[312]   W. Frost, G.S. Dzakowic, An extension of the method of predictive incipient boiling on commercially finished surfaces, ASME-AIChE Heat Transfer Conference, Seattle (1967).

[313]   W. Li, Z. Wu, A general correlation for evaporative heat transfer in micro/minichannels, Int. J. Heat Mass Transfer 53 (2010) 1778–1787.

[314]   W. Qu, I. Mudawar, Measurement and prediction of pressure drop in two-phase microchannel heat sinks, int. J. Heat mass transf. 46 (2003), 2737–2753.

[315]   W. Tong, A.E. Bergles, M.K. Jensen, Pressure drop with highly subcooled flow boiling in small-diameter tubes, Exp. Therm. Fluid Sci. 15 (1997), 202–212.

[316]   W. Zhang, T. Hibiki, K. Mishima, Correlation for flow boiling heat transfer in mini-

channels, Int. J. Heat Mass Transfer 47 (2004) 5749–5763.

[317] W.L. Owens, V.E. Schrock, Local pressure gradients for subcooled boiling of water in vertical tubes, ASME Paper No. 60-WA-249 (1960).

[318] W.R. Brownlie, Reexamination of Nikuradse roughness data, Journal of the Hydraulics Division-ASCE, 107-1 (1981), 115-119.

[319] Wang R. Z., Cheng P., and Bergles A. E. (2008). Effects of inlet and outlet configurations on flow boiling instabilities in parallel microchannels. International Journal of Heat and Mass Transfer, 51:2261–2281, 2008.

[320] Wang R. Z., Cheng P., and Wu H. (2007). Unstable and stable flow boiling in parallel microchannels and in a single microchannel. International Journal of Heat and Mass Transfer, 50:4297–4310, 2007.

[321] Warrier G.R., Dhir V.K., Momoda L.A. (2002), Heat transfer and pressure drop in narrow rectangular channels, Exp. Therm. Fluid Sci. 26 53–64.

[322] Westheimer, D. and Peterson, G. P. (2001), Visualization of Flow Boiling in an Annular Heat Exchanger under Micro Gravity Conditions, AIAA J. Thermophysics and Heat Transfer, Vol. 15, no. 3, pp. 333-340.

[323] Wojtan L., Revellin R., and Thome (2006). Investigation of saturated critical heat flux in a single uniformly heated microchannel. Experimental Thermal and Fluid Science, 30:765–774.

[324] Wojtan L., Ursenbacher T., and Thome J. R. (2005). Investigation of flow boiling in horizontal tubes: Part i - a new diabatic two-phase flow pattern map. International Journal of Heat and Mass Transfer, 48:2955–2969.

[325] Woldesemayat M.A. and Ghajar A. J. (2007). Comparison of void fraction correlations for different flow patterns in horizontal and upward inclined pipes. International Journal of Multiphase Flow, 33: 347–370.

[326] Wu H. Y. and Cheng P. (2004). Boiling instability in parallel silicon microchannels at different heat flux. International Journal of Heat and Mass Transfer, 47:3631–3641.

[327] Wu H. Y., Cheng P., and Wang H. (2006). Pressure drop and flow boiling instabilities in silicon microchannel heat sinks. Journal of Micromechanics and Microengineering, 16:2138–2146.

[328] Wu Y. and Cheng P. (2004). Visualization and measurement of periodic boiling in silicon microchannels.

[329] Wu Y. and Cheng P. (2003). An experimental study of convective heat transfer in silicon microchannels with different surface conditions. International Journal of Heat and Mass Transfer, 46:2547–2556.

[330] X. Xu and V. P. Carey. "Film evaporation from a micro-grooved surface - An approximate heat transfer model and its comparison with experimental data", J. of Thermophysics and Heat Transfer, 4 (4) (1990), 512-520.

[331] Xu L., Zhang W., Wang Q. W., and Su Q.C. (2006). Flow instability and transient flow patterns inside intercrossed silicon microchannel array in a micro-timescale. International Journal of Multiphase Flow, 32(5):568–592.

[332] Xu, Shen S., Gan Y., Li Y., Zhang W., and Su Q. (2005). Transient flow pattern based microscale boiling heat transfer mechanisms. Journal of Micromechanics and Microengineering, 15(6):1344–1361.

[333] Yang C.-Y. and Shieh C.-C. (2001). Flow pattern of air-water and two-phase R-134a in small circular tubes. International Journal of Multiphase Flow, 27:1163–1177.

[334] Z. Liu, R.H.S. Winterton, A general correlation for saturated and subcooled flow boiling in tubes and annuli, based on a nucleate pool boiling equation, Int. J. Heat Mass Transfer 34 (11) (1991) 2759–2766.

[335] Zeng, L.Z., (1999), "Growth Rates in Nucleate Boiling of Water at Subatmospheric Pressures", International Journal of Heat and Mass Transfer, Vol. 18, pp. 655-669

[336] Zeng, L.Z., Klausner, J.F., Bernhard, D. M., and Mei R., (1993), "A Unified Model for the Prediction of Bubble Detachment Diameters in Boiling Systems– II. Flow Boiling," International Journal of Heat and Mass Transfer, Vol. 36, No. 9, pp. 2271-2279.138

[337] Zhang P. and Fu X. (2009). Two-phase flow characteristics of liquid nitrogen in vertically

upward 0.5 and 1.0 mm micro-tubes: Visualization studies. Cryogenics, 49:565–575.

[338]   Zhang T., Peles Y., Wen J. T., and Jensen M. K. (2010). Two-phase flow instability analysis for transient electronics cooling. In 12th IEEE Intersociety Conference on Thermal and Thermomechanical Phenomena in Electronic Systems.

[339]   Zhang T., Wen J. T., Peles Y., Catano J., Zhou R., and Jensen M. K. (2011). Two-phase refrigerant flow instability analysis and active control in transient electronics cooling systems. International Journal of Multiphase Flow, 37:84–97.

[340]   Zhang w., Koo J.-M., Jiang L., Asheghi M., Goodson K. E., Santiago J. G., Kenny W. (2002). Measurements and modeling of two-phase flow in microchannels with nearly constant heat flux boundary conditions. Journal of Microelectromechanical Systems, 11(1):12–19.

[341]   Zuber, N., (1958), "On the Stability of Boiling Heat Transfer," Series C, Journal of Heat Transfer, Vol. 80, No. 4, pp. 711-720.

[342]   Zuber, N., (1961), "The Dynamics of Vapor Bubbles in Non Uniform Temperature Fields," International Journal of Heat and Mass Transfer, Vol. 2, pp. 83-98.